## *Pharmaceutical Co-crystals; Screening Optimisation, Utility and Performance*

CORNER, PHILIP,ANTHONY

# Pharmaceutical Co-crystals; Screening Optimisation, Utility and Performance

Exploring the application and performance of binary systems in pharmaceutical development.

Philip A. Corner MPharm

Submitted for the degree of
Doctor of Philosophy

Division of Pharmacy
School of Medicine, Pharmacy and Health


**2017**

# Abstract

Pharmaceutical Co-crystals; Utility, Formulation and Performance

Philip A. Corner MPharm

**Key words:** Pharmaceutical, co-crystal, screening, optimisation, co-amorphous, ROY, ornidazole, zafirlukast.

Co-crystallisation is currently a 'hot topic' in pharmaceutical development among other fields. Modification of the physicochemical properties of the parent material by inclusion of a second component within the crystal structure, with the potential to lead to large improvements in useful attributes, being the key reason for the interest in co-crystals. Being able to efficiently utilise co-crystallisation to ameliorate problem properties of drugs or other compounds would be a boon to many industries, the pharmaceutical being an ideal example. Limitations in current ability to predict co-crystal formation and potential property modification presents a great opportunity for development in this research area.

The work presented in this thesis encompasses the optimisation of a high-throughput ultrasonication based physical co-crystal screen paired with a computational pre-screen, the application of this optimised screen and the analysis of both co-crystalline and co-amorphous materials resulting from the screening. An initial optimisation of a manual physical co-crystal screen was later transferred to an automated screen implemented on a robotics platform. The implementation of the screen and subsequent analysis of products led to the discovery of the stabilisation of an amorphous form of highly polymorphic compound, ROY, through a predicted co-former interaction. The interactions responsible for the stabilisation were further investigated in the ROY:pyrogallol co-amorphous material and it was found that certain analogues of pyrogallol exhibit the same behaviour with ROY depending on the presence and position of specific functionality.

Implementation of the optimised co-crystal screen to the antiprotozoal drug ornidazole led to the detection of 23 hits and the crystal structure of the 1:1 co-crystal of ornidazole and 5-nitroisophthalic acid being determined by single crystal X-ray diffraction. Characterisation of this co-crystal found that it crystallised much more readily than pure ornidazole, potentially improving its processing characteristics, but that unexpectedly had a lower intrinsic dissolution rate than either of the parent components. In comparison, formulation and characterisation of the already known zafirlukast:piperazine co-crystals showed that large improvements in dissolution rates and oral bioavailability in relation to the parent drug are possible. Specifically, the 1:1 zafirlukast:piperazine co-crystal showed a large increase in dissolution rate *in vitro* and an accompanying six-fold increase in *in vivo* oral bioavailability.

# Acknowledgements

Firstly, I'd like to thank my primary supervisor Dave for all of his help and guidance throughout my PhD and for making time for me whenever needed. More importantly, for making sure at least a significant portion of that time was dedicated to the exchange of hilarious anecdotes of some form or other.

My gratitude is also extended to my other supervisors Jon and Jon for their assistance, specifically; Jon for expert guidance, especially in the synthetic lab, and Jon for project ideas and providing such thorough feedback on all of my work.

For making the task of working in a lab which started almost empty a lot easier than it may otherwise have been, I am grateful to the technical staff – you shall be remembered as the 'heroines of Holliday'! Other members of staff from the now defunct Division of Pharmacy at Durham, especially the Pharmaceutics team, for technical assistance. I should also like to thank Durham University itself and AstraZeneca for funding of the project.

I'd also like to acknowledge the help received from the industrial team at AZ – Jim, Zoe, Tudor and Martin for their provision of a welcoming and friendly environment, extensive knowledge and entertaining discussions. Time spent at AZ has always been enjoyable and fondly anticipated.

Thanks also to The Pharmbabes of G115 and associated satellite offices for friendly discussion, camaraderie and the sustenance of morale, it would have been rather dull without you. Most importantly, Kim, for being a beacon of hope, joy and hilarity, thus making the undertaking of this arduous academic endeavour all the more enjoyable, worthwhile…and abundant in catisfaction.

My other thanks are handed out to friends – near and far – and family for continued encouragement throughout my studies (and pretending to remember what a co-crystal is when taking to me about my work), especially Susan and Lucy for helping to lead me into the field of pharmacy to begin with. Finally, my parents for all of their support during my current work and everything heretofore, except when they weren't in Alaska, Jamaica?...cheese on toast.

# Table of contents

# List of publications

**Research papers**

The work presented in Chapter 4 of this thesis has also been published in the following research paper:

P. A. Corner, J. J. Harburn, J. W. Steed, J. F. McCabe and D. Berry, *Stabilisation of an amorphous form of ROY through a predicted co-former interaction.* Chem. Commun., 2016, 52, 6537.

The work presented in Chapter 7 of this thesis has been written into a research paper and submitted to Chemical Communications (RSC) for consideration for publication, the title is as follows:

Philip Corner, David Berry, James McCabe, Rafael Barbas, Rafel Prohens, Hongwen Du, Hongyu Zhou and Antonio Llinas, *Property Prediction and Pharmacokinetic Evaluation of Mixed Stoichiometry Cocrystals of Zafirlukast, a Drug Delivery Case Study.*

Contributions in the form of experimental and analytical assistance using dynamic vapour sorption techniques were made to a project resulting in the following research paper:

Andrea Perrin, Melissa J. Goodwin, Osama M. Musa, David J. Berry, Philip Corner, Katharina Edkins, Dmitry S. Yufit, and Jonathan W. Steed, *Hydration Behavior of Polylactam Clathrate Hydrate Inhibitors and Their Small-Molecule Model Compounds.* Cryst. Growth Des., 2017.

These can be found in Appendix 1.

**Oral presentations**

An Optimised Co-crystal Screen, presented at the Academy of Pharmaceutical Sciences (APS) PharmSci 2014, University of Hertfordshire, Hatfield, UK.

Applying an Optimised Co-crystal Screen Utilising Ultrasonication to Active Pharmaceutical Ingredients, presented at the British Crystallographic Association (BCA) Spring Meeting 2016, University of Nottingham, Nottingham, UK.

**Poster presentations**

Using the Design of Experiments Approach to Optimise Co-crystal Screening, presented at International School of Crystallisation (ISC) Granada 2014, San Anton Hotel, Granada, Spain.

Using the Design of Experiments Approach to Optimise Co-crystal Screening, presented at the Academy of Pharmaceutical Sciences (APS) PharmSci 2014, University of Hertfordshire, Hatfield, UK.

Applying an Optimised Co-crystal Screen Utilising Ultrasonication to Active Pharmaceutical Ingredients, presented at the British Crystallographic Association (BCA) Spring Meeting 2015, University of York, York, UK.

# List of symbols and abbreviations

Symbols

| | |
|---|---|
| $\Delta H$ | Enthalpy change |
| λ | Wavelength |
| $F$ | Bioavailability (%) |
| $H$ | Enthalpy |
| $H_{ex}$ | Excess enthalpy |
| $M^+$ | Molecular ion |
| $M_r$ | Relative molecular mass |
| $Q^2$ | Goodness of predication |
| $R^2$ | Coefficient of determination (goodness of fit) |
| T | Temperature |
| $T_g$ | Glass transition |

Abbreviations

| | |
|---|---|
| API | Active pharmaceutical ingredient |
| ATR | Attenuated total reflectance |
| AUC | Area under the curve |
| AZ | AstraZeneca |
| CCDC | Cambridge Crystallographic Data Centre |
| CIF | Crystallographic information file |
| CIRCE | Centre for Intelligent Research in Crystal Engineering |
| COSMO | Conductor-like screening model |
| CSD | Cambridge Structural Database |
| DCM | Dichloromethane |
| DFT | Density functional theory |
| DMF | Dimethylformamide |
| DOE | Design of experiments |
| DSC | Differential scanning calorimetry |
| DVS | Dynamic vapour sorption |
| EAFUS | Everything added to food in the United States |

| | |
|---|---|
| ESI | Electrospray ionisation |
| FaSSIF | Fasted state simulated intestinal fluid |
| FDA | Food and Drug Administration |
| FTIR | Fourier transform infrared (spectroscopy) |
| FWHM | Full width at half maximum |
| GC | Glass-crystal |
| GRAS | Generally recognized as safe |
| HME | Hot-melt extrusion |
| HPLC | High performance liquid chromatography |
| HPMC | Hydroxypropyl methylcellulose |
| IDR | Intrinsic dissolution rate |
| IR | Infrared |
| IV | Intravenous |
| LAG | Liquid-assisted grinding |
| MLR | Multiple linear regression |
| NMR | Nuclear magnetic resonance |
| PABA | *p*-Aminobenzoic acid |
| PAT | Process analytical technology |
| PTFE | Polytetrafluoroethylene |
| PVP | Polyvinylpyrrolidone |
| PVPVA | Polyvinylpyrrolidone vinyl acetate |
| PXRD | Powder X-ray diffraction |
| RH | Relative humidity |
| ROC | Receiver operating characteristic (curve) |
| ROY | 5-Methyl-2-[(2-nitrophenyl)amino]-3-thiophenecarbonitrile |
| SDI | Surface dissolution imager |
| SGF | Simulated gastric fluid |
| TGA | Thermogravimetric analysis |
| THF | Tetrahydrofuran |
| TLC | Thin layer chromatography |
| UV | Ultraviolet |

# List of figures

# List of tables

# Chapter 1 – Introduction

## 1.1 General introduction to pharmaceutical co-crystals

Crystalline material can be defined as '*a regular arrangement of the constituent molecules, atoms or ions into some fixed and rigid pattern known as a lattice*'.[1] A co-crystal can very simply be described as a crystalline solid containing two or more different substances, however this is an oversimplified description. A multicomponent crystal is an umbrella term which can be used to describe many types of compounds including: salts, hydrates and solvates, and inclusion compounds such as clathrates. A universally accepted definition of a co-crystal has yet to be recognized and as such, debate continues within the community as to what should and should not be given this label. A recently proposed definition, '*cocrystals are solids that are crystalline single phase materials composed of two or more different molecular and/or ionic compounds generally in a stoichiometric ratio which are neither solvates nor simple salts.',* attempts to be broad whilst still maintaining consistency with the scientific literature.[2] This proposed definition is, on the whole, successful at differentiating co-crystals from other multicomponent complexes, however a prior debate regarding the state of matter of the constituents is left unclarified.

Previously it had been suggested that only multicomponent crystals formed from reactants that were in the solid state under ambient conditions should be classed as co-crystals,[3,4] and arguments made against this definition resulted.[5] The importance of this is that if co-crystals could be formed from reactants in the liquid state, this would encompass solvates. Although relatively recent FDA guidance on pharmaceutical co-crystals states that co-crystals should be treated as drug product intermediates rather than a new drug entity,[6] solvates and co-crystal are still different from a patentability perspective. This is because for a material to be patentable it must be novel, useful and non-obvious. Solvates, it could be argued, are obvious to someone skilled in the art, due to the quantity of prior art in existence. The desire for the definition of pharmaceutical co-crystals to be specific around this point is that they would therefore be more readily patentable as a novel phase.

As well as in the pharmaceutical field, co-crystals have garnered interest in other communities such as those investigating porous solids for gas storage and separation applications, and those involved in ferroelectrics research.[7] Broader areas in which co-crystals have potential application are agrochemicals,[7] photographic film formulation,[4] solid-state organic synthesis,[8] and semiconductor,[9] optical[10] and explosive materials.[11,12,13] Thus pharmaceutical co-crystals are a subset of a larger group and are distinguished by containing an active pharmaceutical ingredient

(API) as at least one of the constituent components. To be termed a pharmaceutical co-crystal the other non-API component(s) of the co-crystal should be safe for use in humans with no toxic or serious adverse effects. Although theoretically any co-former could be used, human safety testing would be required to be performed if not previously completed for any particular substance, adding significant cost to the development process. Therefore co-formers for pharmaceutical co-crystals are generally limited to substances found in the FDA's Generally Recognized as Safe (GRAS) or Everything Added to Food in the United States (EAFUS) lists.[7]

## 1.2 Crystallisation

### 1.2.1 Crystal growth from solution

The formation of a crystal is a two-step process of nucleation followed by crystal growth. These processes will only occur when there is supersaturation of the solute, that is, when the concentration of material in question is higher than its thermodynamic solubility, as this is the driving force for crystallisation. There are three categories of nucleation: homogeneous primary nucleation, heterogeneous primary nucleation and secondary nucleation. The first of these describes nucleation which occurs spontaneously in a supersaturated solution without the presence of any other matter. The second is when nucleation is induced by foreign particles which act as a template for growth. Finally, secondary nucleation is that which is induced by 'seeding' with the desired crystallite.

In terms of homogeneous primary nucleation, classical nucleation theory suggests that the formation of a nucleus occurs through a sequence of bimolecular additions, where collisions between molecules form a cluster which grows in size with the further addition of molecules. As a cluster grows, its free energy increases until it reaches a threshold size known as a critical nucleus, at which point it becomes stable and as size increases further, free energy decreases, leading to further growth. Before reaching this critical point, the cluster is likely to dissolve due to its unfavorable energetic situation. With an increase in supersaturation, the free energy barrier and the size of the critical nuclei decrease to the point where it becomes possible for nucleation to occur spontaneously.[1]

Once a critical nucleus has formed, the crystal growth process will occur. There are a number of theories for crystal growth and the model that is followed is influenced by the surface roughness of the growing crystal, a property which is commonly characterised by the α-factor. Low values indicate a rough crystal surface with a low energy barrier for continued growth and high values

a smooth surface with a greater energy barrier. Rough crystal surfaces, with an α-value of less than two, will allow continuous growth to proceed which will be diffusion controlled. This is where molecular diffusion to the crystal surface occurs, followed by a first order 'reaction' of the solute molecules arranging in the lattice. The growth rate in this case would be linear with respect to supersaturation. Smooth surfaces, with an α-value of greater than five, lead to growth proceeding via the screw dislocation mechanism. This is where a dislocation occurs on the surface of the crystal and thus prevents the need for surface nucleation to occur. Instead growth can occur perpetually in a spiral manner. In surface roughness between α-values of two and five, the birth and spread mechanism of growth is most probable. In this mechanism, surface nucleation occurs followed by a monolayer spreading outwards from the initial nucleation at the centre. Further surface nuclei can develop on these 'islands'.[1] These growth mechanisms are described in Figure 1.1.

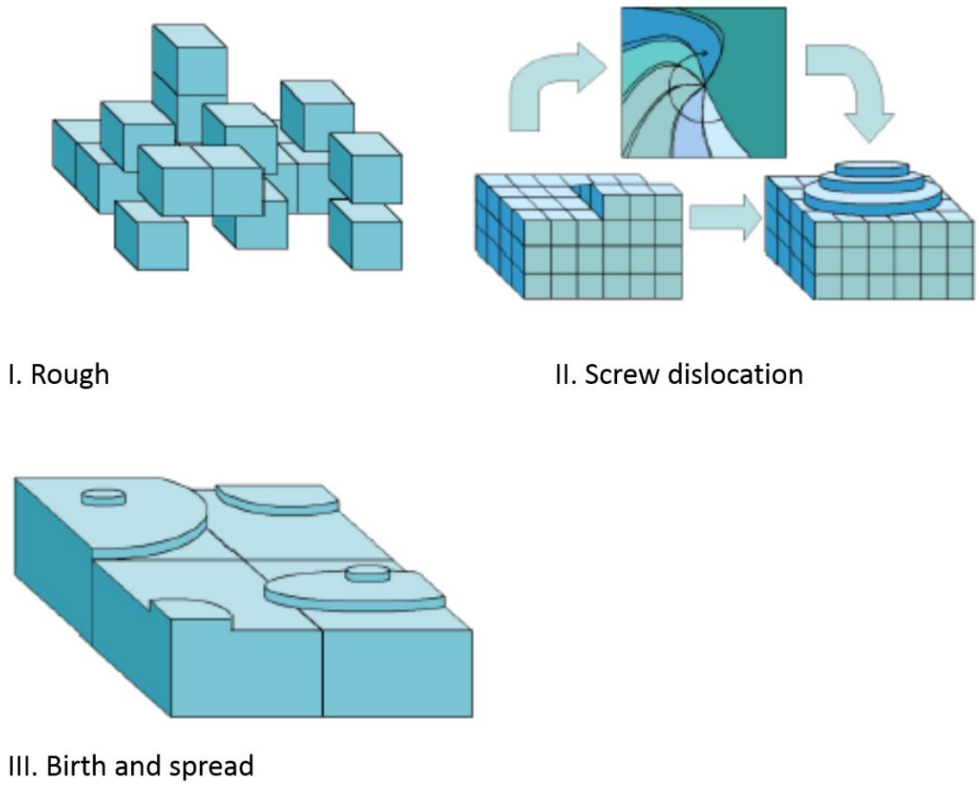


***Figure 1.1*** Mechanisms of crystal growth. I. Rough, II. Screw dislocation, III. Birth and spread. Adapted from reference.[14]

### 1.2.2 Glass-to-crystal growth

Certain materials which form glasses display a fast mode of crystal growth known as the glass-crystal (GC) mode which occurs near the glass transition temperature. This phenomenon was first observed in a study of *o*-terphenyl by Greet and Turnbull,[15] and has since been observed in many other small molecule organic compounds including: phenyl salicylate,[16] indomethacin[17] and ROY.[18,19] The GC mode of crystal growth is not limited by molecular diffusion in the bulk liquid, leading some to term it 'diffusionless',[20] and crystal growth in this mode has been shown to occur orders of magnitude faster than those predicted by standard models.[17]

## 1.3 Phase diagrams

Binary (two component) and ternary (three component) phase diagrams can be produced for multicomponent systems to show the environment in which each phase will be present. These are of use as the phase relationships between the two constituent components of a co-crystal can be quantitatively described by the construction of a phase diagram.

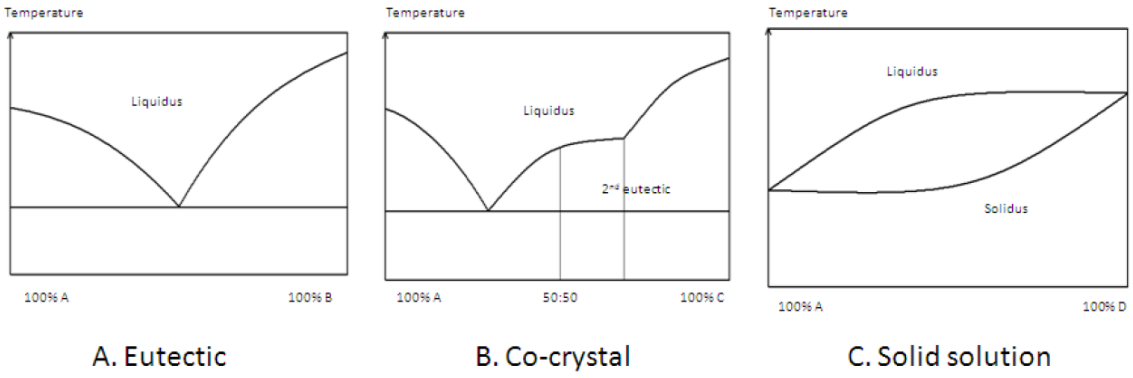


***Figure 1.2*** *The three fundamental types of binary phase diagram. Reproduced, with permission, from reference.[14]*

The three fundamental types of binary phase diagram are: eutectic, co-crystal and solid solution, as seen in Figure 1.2. In the eutectic binary phase diagram, there are two immiscible (in the solid state) components with a submerged eutectic, the lower melting point caused by the presence of the second component. The co-crystal diagram shows a solid co-crystal phase between the first and second eutectics, and the solid solution diagram shows two components which are miscible in the solid state.[14]

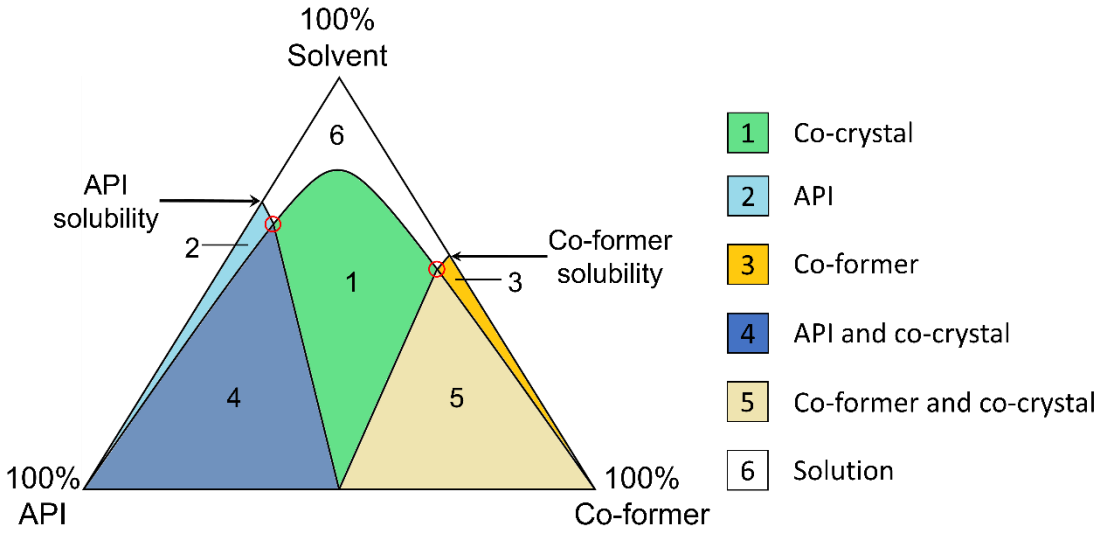


***Figure 1.3*** *Example of ternary phase diagram for a 1:1 stoichiometric ratio co-crystal in which the API and co-former have different solubilities in the solvent. Adapted from reference.*[21]

Ternary phase diagrams introduce solvent to the represented substances. These diagrams are often displayed as a triangle and show the compositions at a specific temperature. They can show that, for example, evaporation of solvent would lead to the movement from one region to another (away from the solvent apex) and potentially into the co-crystal phase.[22] This would be seen as moving from the white solution phase into the green co-crystal phase in the example ternary phase diagram in Figure 1.3.

## 1.4 Crystal engineering

Crystal engineering is a term used to describe the utilisation of the knowledge of intermolecular interactions in crystal structures in designing new crystalline materials with desired properties.[23] Much research into the rational design of co-crystals has been based on the crystal engineering approach of identification and utilisation of supramolecular synthons.[24] Synthons are non-covalent bonds which reliably and reproducibly form the same kind of supramolecular interaction when forming between molecules with particular kinds of functional groups, known as tectons.[25] The most significant interactions in synthon based design are conventional hydrogen bonds (OH···O and NH···O), however weaker bonds (e.g. CH···O, CH···N, O···I) are also used. Due to the directional nature of these interactions, the orientation of the molecules within the crystal structure can be

predicted reasonably accurately. This allows the necessary functional groups to be placed in the correct area of the molecule to produce the desired synthon and hence, in theory, the crystal structure designed.[26]

For the successful design of co-crystals, this means that the co-former selected should possess complimentary functional groups to those of the API, thereby being able to form the intermolecular interactions constituting the supramolecular synthon selected. Examples of synthons commonly used in the design of co-crystals include the amide-amide synthon, the acid-amide heterosynthon and the acid-pyridine heterosynthon.[27]

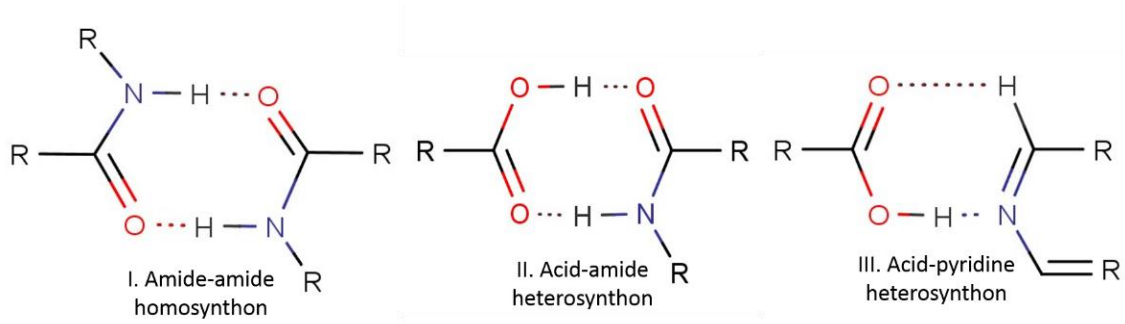


***Figure 1.4*** *Examples of synthons. I. Amide-amide homosynthon, II. Acid-amide heterosynthon, III. Acid-pyridine heterosynthon.*

This approach however doesn't take into consideration all of the weaker interactions that may be present between the two components of a co-crystal and thus a co-crystal designed in this way may not always be able to be produced experimentally.

The Cambridge Structural Database (CSD) is a repository for small-molecule organic and metal-organic crystal structures, currently containing over 875,000 structures. Statistical analysis of the large amount of data in the CSD can be carried out and analysis of data relating to co-crystal specific subset of the CSD has been reported.[28] The aim was to identify factors beyond synthon matching that would be indicative of the ability to form a co-crystal. The strongest correlations found related to the polarity and the shape of the co-crystal components, whereas number of hydrogen bond donors and acceptors showed no obvious statistical relationship.[28] This kind of statistical analysis can be used as a predictor for components likely to form co-crystals and could be used as an initial step in reducing the number of co-formers for physical screening.

## 1.5 Production of co-crystals

In terms of high-throughput screening both reaction crystallisation and sonic methods have been employed.[29,30] Many other methods of co-crystal production are possible, not all amenable to high-throughput work, the sections 1.51-1.5.5 below describe many of which that have been reported in the literature.

### 1.5.1 Evaporative and reaction crystallisation

Solution crystallisation methods can be used to produce co-crystals by, for example, evaporation of an undersaturated solution to form a supersaturated solution and induce crystallisation of the co-crystal. Ternary phase diagrams can be made use of in this method, for example to determine the region in the phase diagram in which the co-crystal is most likely to be stable in the solid phase and perform the necessary actions to reach this environment, as alluded to above.[22] Reaction crystallisation involves the intentional addition of an excess of either of the co-crystal components to a solution which is undersaturated with respect to the co-crystal. This addition of excess component reduces the solubility of, and causes supersaturation with respect to, the co-crystal, leading to nucleation and co-crystallisation. [31,32,33]

### 1.5.2 Sonication

The use of sonochemical techniques to produce co-crystals was introduced with the SonicSlurry method in which an ultrasonic probe is used to subject a slurry of the reactants and solvent to pulses of ultrasound.[34] An alternative method for the successful production of co-crystals using sonication employed an ultrasonicator water bath rather than probe and was implemented as a high-throughput screening technique using the 96-well plate format.[30]

### 1.5.3 Grinding and liquid-assisted grinding

Another method of screening for co-crystals is by grinding. This can be solid-state ('dry' or 'neat') grinding, devoid of solvent use, or can use a small amount of solvent, a technique which is known as solvent-drop grinding or liquid-assisted grinding (LAG). Grinding can be carried out by hand, using a pestle and mortar, or mechanically, employing a ball or vibratory mill.[35] This process can be time consuming and hence limits the speed at which screening can occur, however the use of this mechanochemical process has led to the obtaining of certain structures or stoichiometries of co-crystals which are unobtainable by other routes.[36] The addition of a small amount of solvent in LAG, typically only a few microlitres, can provide further benefits, such as improved yield and a larger scope of reactants and products, compared to neat grinding.[35] It can also act in a catalytic role, reducing the time taken for co-crystals to form versus solid-state grinding and in addition may

enable selective polymorphic and stoichiometric co-crystal synthesis.[37] Although the mechanism is not fully understood, it has been suggested that the addition of the solvent improves effiency either by facilitating molecular diffusion or effecting the course of mechanochemical co-crystallisation.[35] The fact that solid-state grinding is a solvent-free process and only a very limited amount of solvent is used in LAG, means both of these processes are favourable from an environmental perspective due to the reduction or eradication of solvent waste. An additional benefit to the solvent-free nature of dry grinding is that the solubility of starting materials is no longer an issue and the problem of unexpected solvate formation is removed.[36] It is also possible to use co-crystals obtained from these methods as seeds to induce crystallisation from solution.[27]

### 1.5.4 Crystallisation from the melt

Thermal methods such as hot-stage microscopy employing the Kofler technique have been used to determine the binary phase behaviour of co-crystal systems. This involves one component being melted, then re-crystallised, before the molten second component is brought into contact with the first. This causes solubilisation of a portion of the first component and a zone of mixing is created which is comparable to the composition of the binary phase diagram; one side representing 100% of one component and the other side representing 100% of the other component, with a concentration gradient across the zone. Once it has been determined from the melt that a co-crystal exists, production can be eased by seeding from melt material.[38]

### 1.5.5 Others

Freeze-drying has been demonstrated as an alternative technique for co-crystallisation and it has been suggested that it may be more suitable for large scale manufacture of co-crystals than other methods as the process is already used on an industrial scale.[39] Formation of co-crystals by spray drying, a process which is in use in the pharmaceutical industry to produce amorphous material, has been reported.[40] The large scale production of co-crystals by this method could be particularly useful due to its speed and the fact that it is a continuous, one-step process. Supercritical fluid technology, which again already has industrial use, has been shown to have feasible application to co-crystal screening methods and potential particle engeneering.[41] Another method of co-crystal production which has been proposed as suitable for large scale manufacture is an extrusion based co-crystallisation process which is both solvent free and continuous. These attributes, along with process analytical technology (PAT), which has been demonstrated can be applied to this process, make it particularly relevant to industrial manufacture.[42] Microwave synthesis has been attempted, both solvent-free without success, and with the addition of small amounts of solvent leading to the successful production of a number of co-crystals.[43] In the attempted solvent-free

synthesis the molecular mobility of the reactants, compared to that in the presence of solvent, is likely to have been restricted to the extent that co-crystallisation could not occur. The addition of solvent therefore facilitating the interaction of the reacting components.

## 1.6 Property modification by co-crystallisation

Crystal structure can have a great influence on the physical properties of a material. This is seen in polymorphism, which is where molecules of a particular compound, that are identical in the liquid and vapour states, can form solid crystalline phases in at least two different arrangements. Polymorphs contain exactly the same molecules with the only difference between two polymorphic forms being the crystal structure, yet significant differences in physical properties can be displayed.[44] Ibuprofen is an example of a compound which can exist in more than one crystal structure with molecules in the same conformation, this is known as packing polymorphism and is shown in Figure 1.5 below.

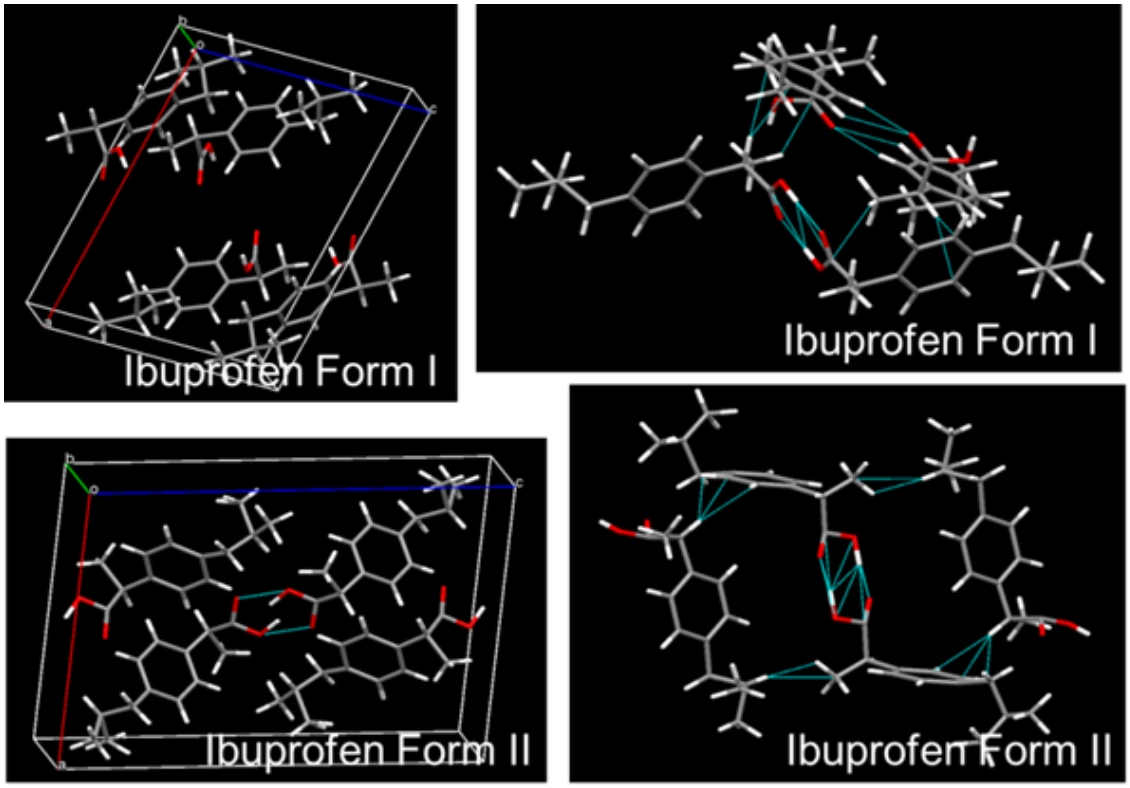


***Figure 1.5*** *Polymorphic form I and II of ibuprofen.*

Figure 1.6, below, shows the categories by which materials in the solid form can be defined. It is worth noting that multicomponent crystals including co-crystals can also be polymorphic in nature, and as such the categories listed in Figure 1.6 are not necessarily exclusive. Examples of polymorphism in co-crystals include the phenazine:mesaconic acid system in which three polymorphic forms have been discovered,[45] and the 3-hydroxybenzoic acid:acridine system which was found to be dimorphic. The second of these examples was found in a study looking at polymorphism in co-crystals formed from polymorphic co-formers, and in the limited number of systems under investigation it was found that the co-crystals produced were not inherently less prone to polymorphism than the individual components.[46]

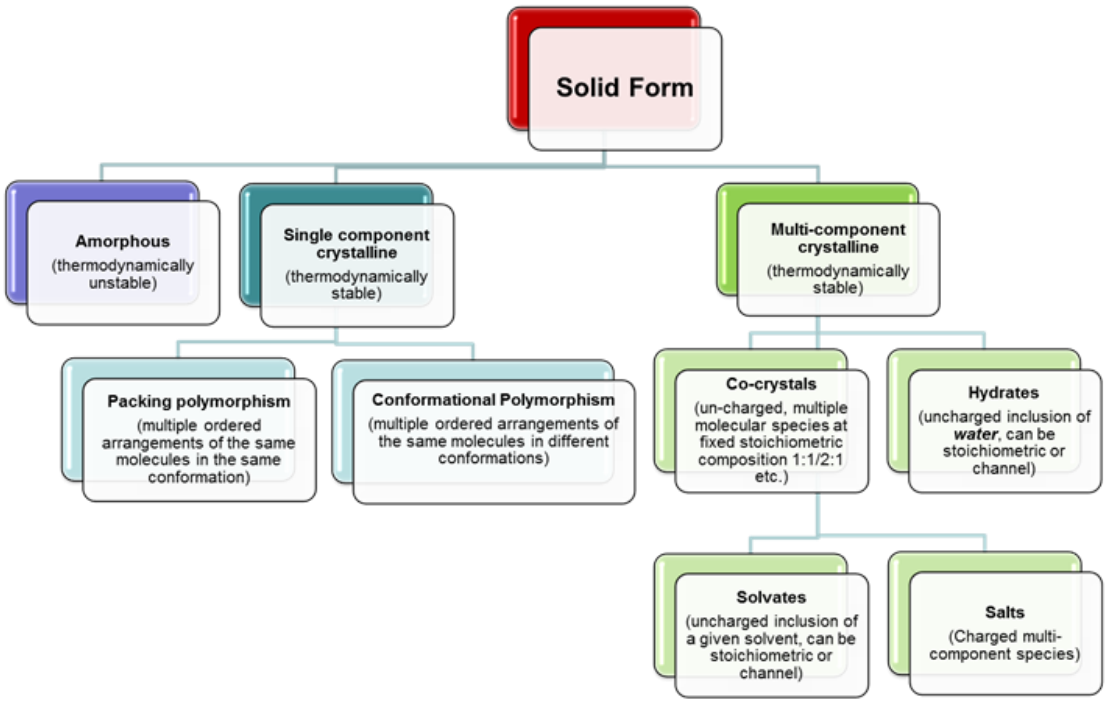


***Figure 1.6*** *A chart showing the categories of forms in which materials can exist in the solid form. Adapted from reference.*[7]

Figure 1.7 below gives a structural representation of some of the solid forms described in Figure 1.6 and introduces ionic co-crystals and solid solutions as potential forms in which materials may exist in the solid form. Hydrogen bond donor and acceptor regions are indicated by the blue and red colouration. It is worth noting that although the inclusion compound shown (Figure 1.7, H) is stoichiometric, there is the potential for non-stoichiometric inclusion compounds to form, for example a channel hydrate; and that more complex multicomponent crystalline forms are possible such as ionic co-crystal hydrates or solvates, and polymorphs thereof.[21,47]

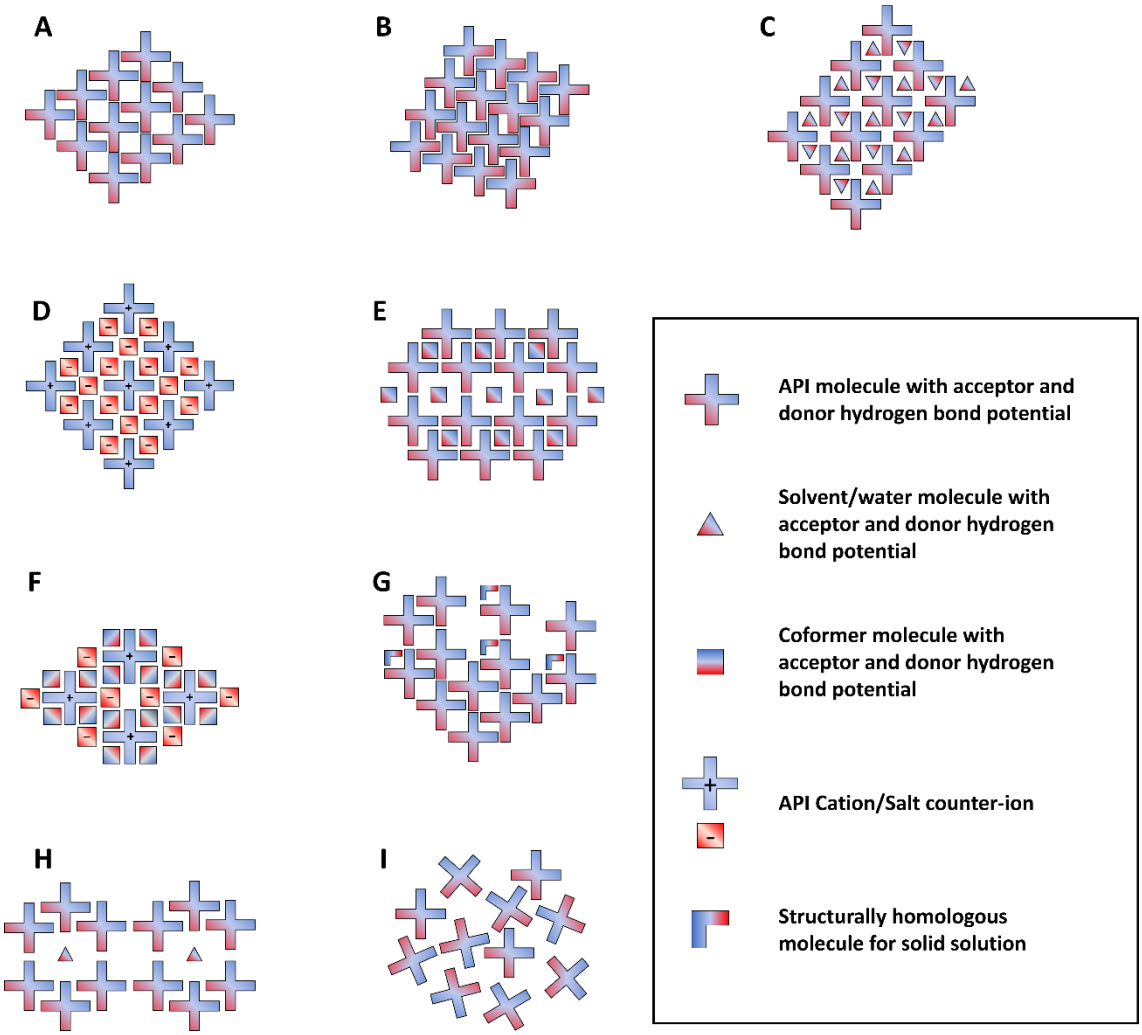


***Figure 1.7*** *Structural representation of forms in which materials can exist in the solid form: A. polymorph A of API, B. polymorph B of API, C. stoichiometric solvate or hydrate, D. salt, E. molecular co-crystal, F. ionic co-crystal, G. solid solution, H. inclusion compound (stoichiometric), I. amorphous API. Adapted from reference.*[21]

Co-crystals, by virtue of modifying the crystal structure, are also able to improve the properties of an API without altering its molecular structure, or necessarily reducing its physical or chemical stability. A large proportion of research into the improvements in properties that co-crystals can attain has been focused on solubility and dissolution rate, leading to many examples of co-crystals achieving improvements in these areas.[27,48] It has been noted however that improvements in measured solubility in co-crystals should be treated with caution as they can transform via recrystallisation to the most stable form when brought into contact with a solvent.[7,49] In terms of administering a pharmaceutical product, this could include the dissolution of the drug in the stomach and if the stable form of the drug was to be formed the improvement

in solubility the co-crystal achieved would be affected. The advantage in solubility offered by the co-crystal may not be entirely lost in this case though, as the route to the stable form of the drug may extend over a period of time of increased apparent solubility, sufficient for the required absorption for therapeutic effect. This has been explained by Babu and Nangia by the adaptation of the 'spring and parachute' concept for amorphous drug dissolution and its application to co-crystals.[48] Indeed accounts of co-crystals improving the bioavailability of the drug by as much as three fold have been published.[50] The modification of solubility by a co-crystal does not necessarily have to be an increase in order for it to be of benefit from a formulation perspective. Reducing the solubility could prove useful in the formulation of a slow release dosage form and a lower solubility could be of benefit when needing to mask the taste of a drug product, as long as the necessary balance between this and bioavailability is achieved.

In addition to improving solubility and dissolution rate, there are several other benefits that can be realised by utilising co-crystallisation, such as improved hygroscopicity, and physicochemical and photo-stability compared to the parent API.[51,52] Hygroscopicity can be of particular importance in substances liable to hydrate at certain levels of humidity due to its implications for formulation, processing and storage.[53] It is easy to overlook the fact that if the new 'wonder-drug', that has been formulated to improve its solubility to allow for a satisfactory bioavailability via the oral route, has a hygroscopicity which would prevent effective processing to the extent that tablet production was unfeasible, then the drug might never reach the market, The reason being that it may not be economically viable to formulate the drug in any other manner for oral delivery and reduction in patient acceptance could negate the production of any other dosage form. The capacity for co-crystallisation to reduce hygroscopicity and thus improve stability to humidity has been demonstrated with co-crystals of caffeine and a number of co-formers.[51] Enhancement of stability in terms of photodegradation has also been displayed in co-crystal of nitrofurantoin and 4-hydroxybenzoic acid compared to the drug alone, this in addition to its increased stability to varying humidity and temperatures.[52]

## 1.7 Amorphous solids

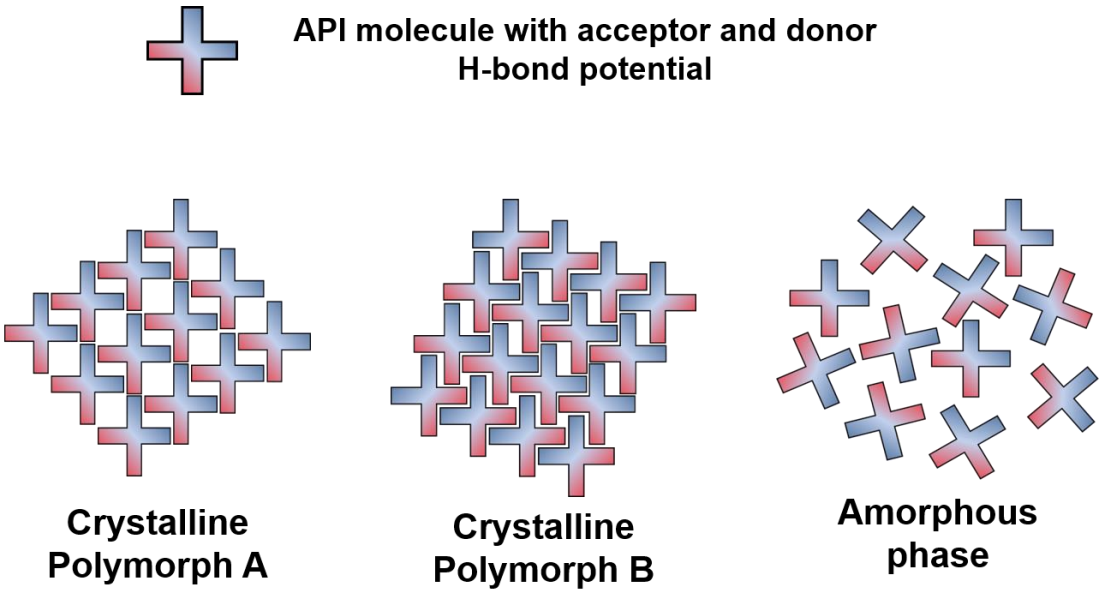


***Figure 1.8*** *Diagrammatic representation of crystalline polymorphs and the amorphous phase of the same API.*

Solubility advantage can be conferred by the amorphous form of a given compound. Given the possibility for improvement in apparent solubility, the amorphous form is considered of great interest in the pharmaceutical industry when developing formulations of poorly soluble drugs.[54,55,56] These phases however also have the potential to convert to a thermodynamically more stable crystalline form; the timescale of this conversion dictates the degree of opportunity or risk associated with the phase.[57] Stabilisation techniques such as formulating the product with the addition of a polymer have been widely studied[58,59,60] and can yield suitable stability at a cost – financial in terms of greater development needed for the formulation, additional regulatory requirements and issues surrounding drug loading. This refers to the quantity of API that is contained within a formulation.[61]

### 1.7.1 Amorphous solid dispersions

Current marketed products which contain the API in the amorphous form include: Sporanox®, Isoptin® SR-E and Gris-PEG®, these all employ polymeric compounds as stabilising agents in the formulation.[54] Many of the polymers used in stabilising drugs in this way (such as PVP, PVPVA and HPMC)[54] are hygroscopic[62] and can lead to faster re-crystallisation of the drug through modification of the glass transition ($T_g$), removing the solubility benefit. There are also issues associated with HPMC which can cause a laxative effect.[63]

Polymer stabilised amorphous formulations may only be able to support a limited quantity of API while maintaining stability as increasing the API loading could lead to crystallisation of the drug. If the maximum drug loading afforded is poor then larger or multiple tablets/doses will be required; drug loading in amorphous-solid-dispersion formulations means that for one part of API there needs to be generally somewhere between 2.5 to 9 parts polymer. With drugs where a single dose is only a few milligrams or less this is not a problem but if a 100mg dose is needed with a 10% drug loading limit then each tablet would need to be a gram in weight and at that size the acceptability to the patient may come into question. If the formulation no longer meets patient acceptability, the drug product will not be used, no matter how innovative a formulation or extensively developed the API.

## 1.7.2 Co-amorphous materials

The deficiencies in polymer stabilised amorphous formulations discussed above have led to an expansion in research in co-amorphous materials.[64,65] Co-amorphous phases have been the subject of significant study since 2009 as they have the potential to solve the problems of drug loading and toxicity. The co-amorphous approach has been defined as 'the combination of two or more low molecular weight components that form a homogeneous amorphous single-phase system'.[66] The stabilising interactions have been seen to occur via a number of mechanisms including hydrogen bonding, π- π stacking and salt formation. There are currently no purported means of predicting which small molecules will create such interactions and stabilise APIs in the desired fashion. This means many thousands of potential molecules could be used as the second entity, therefore some mechanism for practical selection would be beneficial.

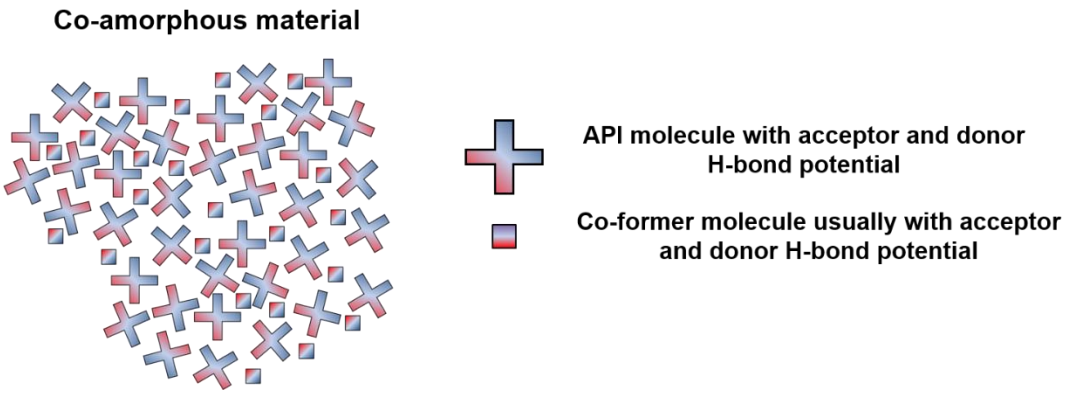


***Figure 1.9*** *Diagrammatic representation of a co-amorphous material consisting of an API and co-former.*

## 1.8 Summary

Research into the ability to predict suitable co-formers and the prediction of property modification is taking place in the academic community. Aakeröy *et al*. have investigated the ability to predict the changes in certain properties including the melting point, which would occur in the production of co-crystals using a particular set of co-formers. Their predictions of co-crystal properties were based on an observed trend in a small number of co-formers, they then produced the co-crystals and measured the actual properties compared to those predicted.[67] This, although a process involving prediction and physical characterisation, did not employ computational prediction and was limited to a small population of co-formers and not a large scale screen for an API of interest.

Research into computational prediction specifically of co-crystals has shown that methods used to calculate whether a potential co-crystal is thermodynamically more stable than the crystals of its components, can reliably predict whether the co-crystal can form.[68,69] These studies were focused on the computational methods and did not feature physical co-crystal production or apply the process to a larger screen for a particular API.

Luu *et al*. reported a high-throughput co-crystal screen using solvent mediated sonic blending. The process involved physical screening followed by analysis of the properties to identify improvements in solubility and physical stability. This investigation however did not employ any initial co-former prediction prior to the physical screening, instead selecting many of the potential co-formers from those previously shown to form co-crystals.[30] A situation which is not always achievable and may not lead to the determination of the most appropriate co-former.

A staged approach to screening has been suggested as the most sensible and efficient method for discovery of novel co-crystals. An initial stage to select the most promising co-formers for a given API would be carried out, either by computational prediction or by utilising informatics tools such as the CSD. This would allow for a reduction in the overall cost associated with screening, as the physical, resource intensive, screening can be reduced to only those potential co-formers which display a high likelihood of successful co-crystal formation, without wasting resources on the many materials that are unlikely to do so.[37,70]

In this project, a two-step process for co-crystal screening was employed. Computational prediction was carried out to determine the most likely co-formers to form co-crystals with a number of chosen APIs and a physical screen of this shortlist of co-formers followed, with the resultant co-crystals analysed. The project not only aims to develop an optimised, efficient high-

throughput screening methodology which can be applied to a range of APIs, but also to determine structure property relationships between the co-formers and the modified properties of the co-crystals compared to the API, by analysis of the co-crystals obtained from applying the screen.

## 1.9 Aims and objectives

The overall aim of the project is to allow prediction of the most suitable co-former selection for a given API, to produce a co-crystal with desired alterations in properties compared to the API alone. To achieve this, a robust, reliable screening method must be determined and utilised to ensure all reasonably accessible potential co-crystals are found for a given system, to allow a robust dataset to be built for subsequent property prediction. Determination of the property modification that will occur based upon the structure of the co-former used must then be developed. Further aims of the project include the determination of robust formulation approaches for co-crystal materials to facilitate their wider use and to predict and control *in-vivo* behaviour of co-crystals.

### 1.9.1 Aims

1. Produce co-crystals of model APIs with a range of chemistries representative of compounds relevant to the pharmaceutical industry.
2. Characterise the produced co-crystals, the APIs and the co-formers.
3. Measure the performance and properties of the co-former and parent compounds.
4. Determine the predictability of property modifications based on API and co-former properties.

### 1.9.2 Objectives

1. In order to efficiently produce co-crystals, necessary for use throughout the project, the following set of objectives were devised.
    a. Optimise a co-crystal screen for the efficient production of co-crystals. To do this a number of sub-objectives must be carried out:
        i. Produce a manual co-crystal screening procedure to best mimic the high-throughput robotic co-crystal screening process currently being implemented in industry.
        ii. Utilise a suitably efficient yet thorough method for optimisation of the chosen screening method.

iii. Undertake validation testing of the newly optimised screening procedure to ensure it achieves the required performance.
iv. Depending upon adequate access to the robotics platform, transfer the optimised parameters from the manual co-crystal screen to the automated process and carry out a further optimisation.

b. Implement the optimised and validated co-crystal screening process to multiple APIs which represent a range of chemistries. More thoroughly this will require:
i. Choosing and sourcing relevant model APIs for co-crystal screening based on their structure and properties.
ii. Performing a computational pre-screen to determine a shortlist of potential co-formers, calculated to be most likely to co-crystallise with the API, for physical co-crystal screening.
iii. Performing the physical co-crystal screen for each API against the shortlisted co-formers, using the optimised parameters.

c. Perform efficient analysis of the co-crystal screens in order to detect 'hits' (any product of the screen which could potentially be a co-crystal). Steps necessary to accomplish this are:
i. Utilise an available analytical technique which allows relatively rapid analysis of material produced from the physical co-crystal screen and that is capable of detecting solid state form change between samples.
ii. If necessary, perform further analysis of the material to confirm its status as a 'hit', to prevent inefficiencies in the screening process developing by unnecessary characterisation of material.

2. Characterisation of the parent components (API and co-former) and co-crystal is necessary to understand the nature of the binary system. For the purposes of identifying the make-up of said system the following objectives are set.
a. Measure characteristic properties e.g. melting point and thermal behaviour of the materials.
b. Determine from these results and any necessary characterisation, for example single crystal X-ray diffraction, the form of the material, i.e. co-crystal or otherwise.

3. Measuring the properties of both the co-crystal and the parent materials is useful for determining the improvements or modifications available by co-crystallisation compared to those inherent to the pure API. Specifically looking at those relevant to

pharmaceuticals affords the following objectives:

a. Investigate properties such as solubility and dissolution to determine the potential improvements relating to bioavailability of the co-crystal compared to the API.
b. Investigate properties related to processing of material to determine the potential improvements of the co-crystal in this regard. For example, measuring:
    i. Moisture sorption to aid in informing of potential improvements in powder handling, stability and tableting.
    ii. Physical stability to investigate potential enhancement of shelf life and/or storage requirements.
    iii. Outcomes of alternative methods of manufacture to guide potential scale-up of co-crystal production.

4. Using the results from the measurements of co-crystal and parent material properties, correlations between the properties and/or structure of the APIs and co-formers and the effect of these on the properties and performance of the co-crystals, should be sought. This could lead to the resolution of the final objectives:
    a. Determine structure-property relationships between the APIs, co-formers and co-crystal to allow prediction of property modification between the API and co-crystal based on the structure or properties of the chosen co-former.
    b. Relate these such findings to those already present in the literature.

# Chapter 2 – Materials and methods

## 2.1 Materials

### 2.1.1 Solids

Most of the materials used as part of the work presented in this thesis were the co-formers for the co-crystal screens. Two full co-crystal screens are documented, each of which required 48 co-formers that were selected from a computational pre-screen as detailed both later in this chapter and in Chapter 4. Many of the co-formers featured in both co-crystal screens however there were over 60 unique compounds used as co-formers for the two co-crystal screens (see Table 2.1 (list) and Figure 2.1 (structures)). Sourcing eight of these compounds in their pure form, either at all, or in sufficient time, proved unfeasible and they were substituted with alternative stock. The eight compounds where this was necessary are highlighted in Table 2.1 along with the substituents which were either a salt or hydrate form or not enantiomerically pure forms of the original chemicals. The structures of the seven compounds used in the place of those unavailable are shown in Figure 2.2. Note that DL-isocitric acid trisodium salt hydrate was used in place of both isocitric acid and allocitric acid.

It was chosen to substitute the compounds which were unavailable with similar material containing the same chemical either with the addition of a second substance (in the case of salts and hydrates) or a stereoisomeric variation, rather than excluding the compounds. The rationale for this decision was that individual molecules of the material must become available for the formation of a co-crystal, whether by solvation, melting, sublimation or other means, and given the inclusion of solvent in the physical screening method employed, molecules of the predicted co-formers would be present for co-crystallisation to occur. In the case of stereoisomeric variation, the different enantiomers often show very little difference, if any, in calculated excess enthalpy and as such a substitution would allow for much less variation from predicted co-former excess enthalpy than excluding the compound and including the compound with the incrementally next most calculated excess enthalpy.

Table 2.2 and Figure 2.4 show the list and structures, respectively, of compounds used in the validation testing of the optimised co-crystal screen in Chapter 3 (where not already listed). The model APIs used are listed in Table 2.3 and their structures displayed in Figure 2.5.

***Table 2.1*** *List of compounds used. (*substituted compounds and their replacements (#65-71))*

| # | Compound | Alternative name |
|---|---|---|
| 1 | Acesulfame* | - |
| 2 | Aconitic acid | 1-Propene-1,2,3-tricarboxylic acid |
| 3 | Allocitric acid* | *erythro*-Isocitric acid |
| 4 | 4,4-Bipyridine | 4,4'-Bipyridyl |
| 5 | Carnitine* | - |
| 6 | Catechol | 1,2-Dihydroxybenzene |
| 7 | 5-Chlorosalicylic acid | 5-Chloro-2-hydroxybenzoic acid |
| 8 | Citric acid | - |
| 9 | 2,4-Dihydroxybenzoic acid | - |
| 10 | 2,5-Dihydroxybenzoic acid | Gentisic acid |
| 11 | 3,4-Dihydroxybenzoic acid | Protocatechuic acid |
| 12 | 3,5-Dihydroxybenzoic acid | 3,5-Dihydroxybenzoic acid |
| 13 | 2,6-Dimethylpyrazine | - |
| 14 | 3,5-Dinitrobenzoic acid | - |
| 15 | DL-Valine* | - |
| 16 | Ethanesulfonic acid | - |
| 17 | Etidronic acid* | - |
| 18 | Fumaric acid | 2-Butenedioic acid |
| 19 | Gallic acid | 3,4,5-Trihydroxybenzoic acid |
| 20 | 4-Hexylresorcinol | 4-Hexylbenzene-1,3-diol |
| 21 | Hydroquinone | 1,4-Dihydroxybenzene |
| 22 | 1-Hydroxy-2-naphthoic acid | - |
| 23 | 3-Hydroxy-2-naphthoic acid | - |
| 24 | 6-Hydroxy-2-naphthoic acid | - |
| 25 | 3-Hydroxybenzoic acid | - |
| 26 | 4-Hydroxybenzoic acid | *p*-carboxyphenol |
| 27 | Indole | 2,3-Benzopyrrole |
| 28 | Isocitric acid* | - |
| 29 | Ketoglutaric acid | 2-Oxoglutaric acid |
| 30 | L-Lysine | - |
| 31 | Maleic acid | 2-Butenedioic acid |
| 32 | Malonic acid | 1,3-Propanedioic acid |
| 33 | Methanesulfonic acid | - |
| 34 | Methyl gallate | Methyl 3,4,5-trihydroxybenzoate |
| 35 | 3-Methyl-2-oxobutanoic acid* | α-Ketoisovaleric acid |
| 36 | *m*-Nitrobenzoic acid | 3-Nitrobenzoic acid |
| 37 | 5-Nitroisophthalic acid | - |
| 38 | *o*-Cresol | 2-Methylphenol |
| 39 | Octadecylamine | Stearylamine |
| 40 | *o*-Phenylphenol | 2-Phenylphenol |
| 41 | Orcinol | 3,5-Dihydroxytoluene |
| 42 | Oxalic acid | - |

***Table 2.1*** *(Continued)*

| # | Compound | Alternative name |
|---|---|---|
| 43 | 2-Oxo-3-phenylpropionic acid | Phenylpyruvic acid |
| 44 | *p*-*tert*-butylphenol | 4-*tert*-Butylphenol |
| 45 | *p*-Cresol | 4-Methylphenol |
| 46 | Pentafluorophenol | 2,3,4,5,6-Pentafluorophenol |
| 47 | *p*-Ethylphenol | 4-Ethylphenol |
| 48 | Phenol | Hydroxybenzene |
| 49 | Piperazine | 1,4-Diazacyclohexane |
| 50 | Quercetin | 3,3’,4’,5,7-Pentahydroxyflavone |
| 51 | Resorcinol | 1,3-Benzenediol |
| 52 | Salicylic acid | 2-Hydroxybenzoic acid |
| 53 | Skatole | 3-Methylindole |
| 54 | Succinic acid | 1,4-Butanedioic acid |
| 55 | Sulfamic acid | Amidosulfonic acid |
| 56 | Tartaric acid* | 2,3-Dihydroxysuccinic acid |
| 57 | *tert*-Butylhydroquinone | TBHQ |
| 58 | Thymol | 2-Isopropyl-5-methylphenol |
| 59 | 1,2,3-Trihydroxybenzene | Pyrogallol |
| 60 | Trimesic acid | 1,3,5-Benzenetricarboxylic acid |
| 61 | 2,5-Xylenol | 2,5-Dimethylphenol |
| 62 | 2,6-Xylenol | 2,6-Dimethylphenol |
| 63 | 3,4-Xylenol | 3,4-Dimethylphenol |
| 64 | 4-Aminobenzoic acid | PABA |
| 65 | Acesulfame K* | Acesulfame potassium |
| 66 | (±)-Carnitine hydrochloride* | - |
| 67 | DL-Isocitric acid trisodium salt hydrate* | - |
| 68 | Etidronic acid monohydrate* | - |
| 69 | L-(+)-Tartaric acid* | - |
| 70 | L-Valine* | - |
| 71 | 3-Methyl-2-oxobutanoic acid sodium salt* | - |

***Table 2.2*** *List of compounds used for validating co-crystal screen optimisation (excluding those present in Table 2.1).*

| # | Compound | Alternative name |
|---|---|---|
| 72 | Aspirin | Acetylsalicylic acid |
| 73 | Benzoic acid | - |
| 74 | Caffeine | - |
| 75 | Carbamazepine | Tegretol |
| 76 | Glutaric acid | 1,5-Pentanedioic acid |
| 77 | Ibuprofen | - |
| 78 | Nicotinamide | Niacinamide |
| 79 | Paracetamol | Acetaminophen |
| 80 | Saccharin | - |
| 81 | Sulfamethazine | Sulfadimidine |
| 82 | Sulfamethoxypyridazine | - |
| 83 | Trimethoprim | - |

***Table 2.3*** *List of model APIs used.*

| # | Compound | Alternative name |
|---|---|---|
| 84 | Ornidazole | Xynor |
| 85 | ROY | 5-Methyl-2-[(2-nitrophenyl)amino]-3-thiophenecarbonitrile |
| 86 | Zafirlukast | Accolate |

All compounds listed in Tables 2.1 to 2.3 were purchased from Sigma-Aldrich and used as received, with the exceptions of ROY which was synthesised in-house (see Chapter 4 for details) and zafirlukast which was supplied by AstraZeneca.

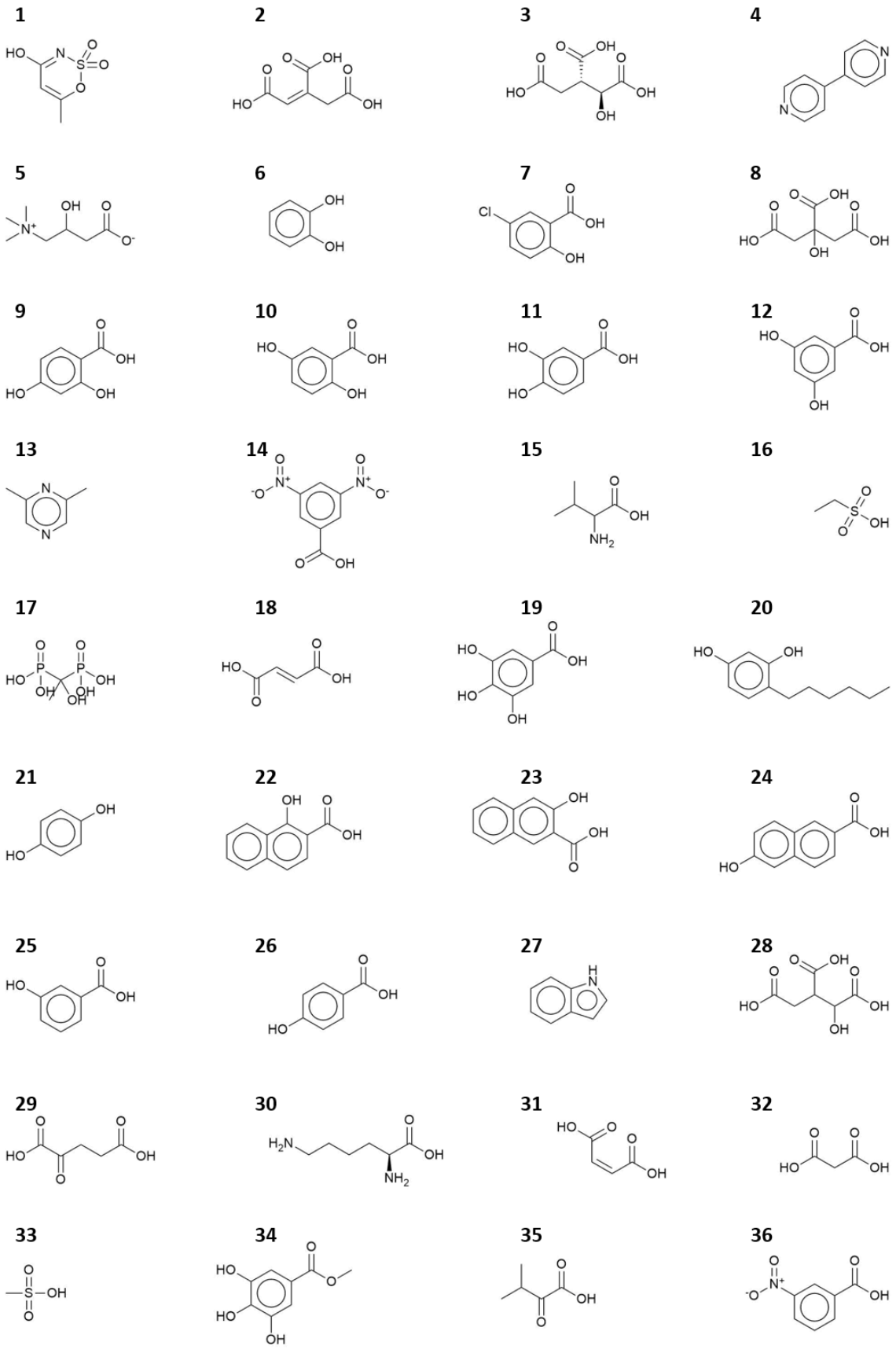


***Figure 2.1*** *Chemical structures of compounds used as co-formers in co-crystal screens.*

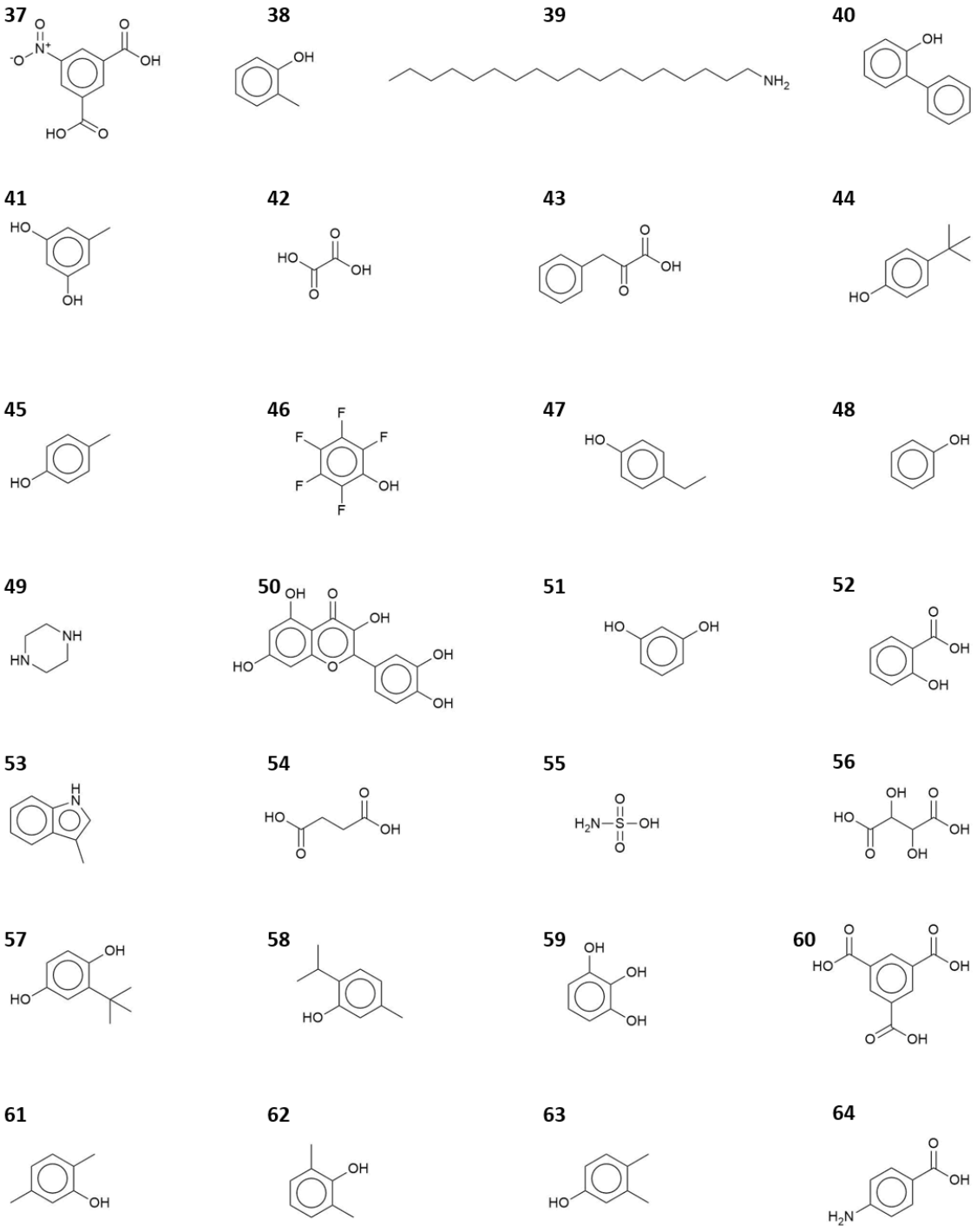


***Figure 2.2*** *Chemical structures of compounds used as co-formers in co-crystal screens. Continued from Figure 2.1.*

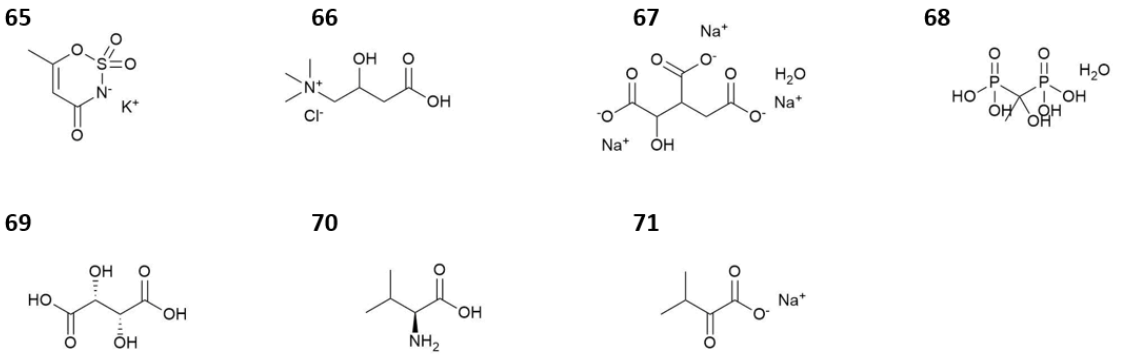


***Figure 2.3*** *Chemical structures of compounds substituted for unavailable compounds, for use as co-formers in co-crystal screens.*

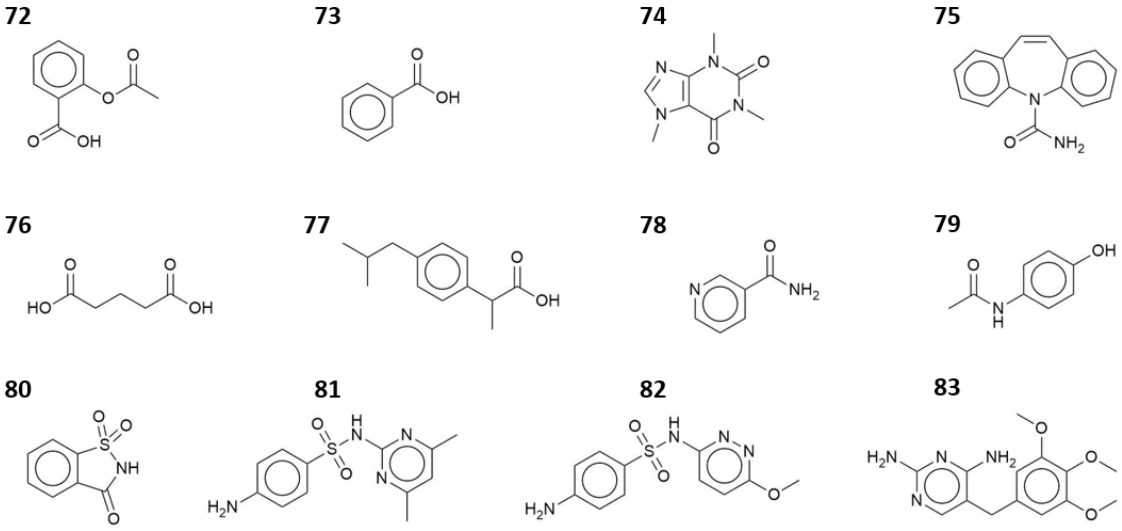


***Figure 2.4*** *Chemical structures of compounds (not previously listed), which were used for validation testing of the optimised co-crystal screening method.*

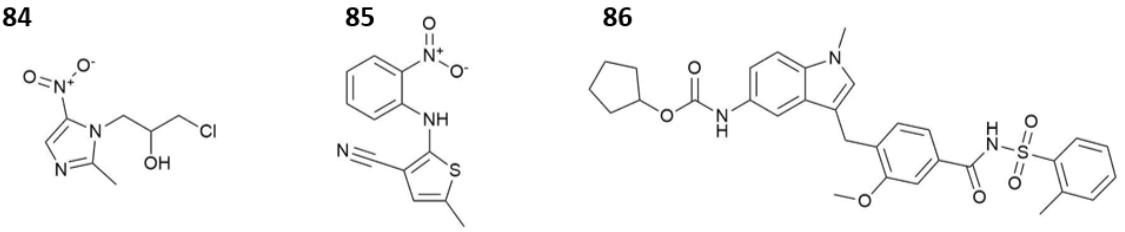


***Figure 2.5*** *Model APIs: Ornidazole (left) and ROY (middle), the two APIs used for co-crystal screening, and zafirlukast (right).*

### 2.1.2 Solvents

Acetone, acetonitrile, dichloromethane (DCM), ethanol and hexane were used in the co-crystal screening procedure. In addition, toluene and tetrahydrofuran (THF) were used in the second optimisation experiments (Chapter 3). These were all of at least reagent grade and purchased from Sigma-Aldrich. Water was obtained from the on-site Purelab Option-Q purification system, and the acetonitrile used for HPLC mobile phase was purchased from Fisher Scientific and was of HPLC grade.

## 2.2 Methods

### 2.2.1 Differential scanning calorimetry

Differential Scanning Calorimetry (DSC) is a technique used to investigate the thermal behaviour of materials. An accurate definition of DSC is given by Höhne *et al*. as '*the measurement of the change of the difference in the heat flow rate to the sample and to a reference sample while they are subjected to a controlled temperature program*'.[71] The DSC technique is able to measure the heat capacity of materials and detect the temperature at which phase transitions occur, as well as being able to, with the appropriate method, quantify such phenomena.[72,73] The equipment used to perform DSC is the differential scanning calorimeter, of which there are two fundamental designs: power compensation and heat flux.

The concept of power compensation DSC is to measure the energy required to keep two sample containers (pans) and their contents at the same temperature as each other, as the immediate environmental temperature is altered. One of these pans contains the sample material and the other, reference pan, is empty. In heat flux DSC, the sample and reference pans are heated in the same furnace and the signal measured is derived from the difference in temperature of the sample and reference pans detected by the temperature sensors under each pan. To achieve this, the calorimeter consists of four main parts: furnace, sample stages, temperature sensors and a controller, a diagrammatic representation of which is shown in Figure 2.6.

The stage assembly consists of a stage each for the sample and reference pans, attached to which are thermocouples to monitor the temperature of each pan. All of this in housed within a sealable furnace which is used to vary the temperature external to the pans. The final fundamental part is the controller which sets the temperatures and measures the energy use of the heating stages and temperatures of the pans.[73] Nitrogen can be flowed through the furnace to keep the samples under an inert atmosphere in many contemporary DSCs, and amenities such as autosamplers are widely available.

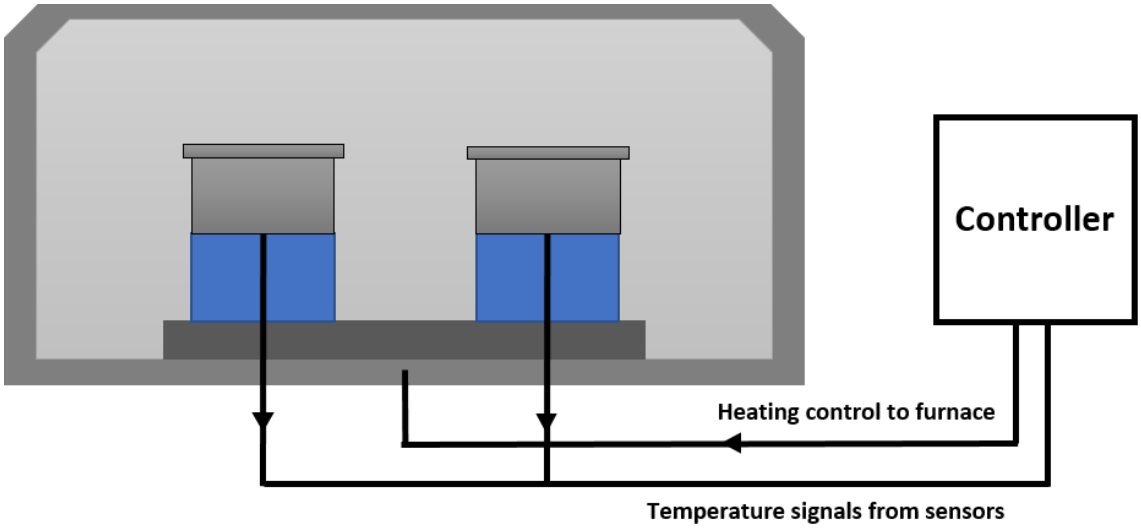


***Figure 2.6*** *Diagrammatic representation of a heat flux differential scanning calorimeter.*

In this thesis, DSC was used for various purposes, the most basic of which was to determine the melting point of certain materials for identification. A significant use was to probe crystallisation behaviour of many materials investigated which required the use of a 'heat-cool-heat' method. DSC was also employed as a useful tool for investigating combinations of compounds where presence of multiple melting endotherms, or lack thereof, is effective information for determination of the binary behaviour of the components.[74]

The following sets of parameters were used as the standard ramp and standard heat-cool-heat methods respectively for collecting DSC thermograms throughout this thesis unless stated otherwise.

Experimental DSC method

DSC thermograms were recorded on a TA Q2000 using standard aluminium pans. Standard mode was used throughout and a heating rate of 10°C/min up to 300°C was used for the standard ramp method. Where heat/cool/heat cycles were used, the initial heating phase was at a rate of 10°C/min to a maximum temperature slightly above the melting point of the material (from literature if experimental data not available and of the component with the higher melting point if a multicomponent system), cooling cycle at 50°C/min to -90°C and the second heating cycle at 10°C/min to the maximum temperature described above.

## 2.2.2 Thermogravimetric analysis

Thermogravimetric analysis (TGA) is another technique used to investigate the thermal behaviour of materials. Specifically with TGA, the mass of sample is measured as temperature is varied; a definition given by the International Confederation for Thermal Analysis and Calorimetry states that TGA '*is a technique in which the mass change of a substance is measured as a function of temperature whilst the substance is subjected to a controlled temperature programme*'.[75] This program is usually in the form of a steadily increasing temperature and a detection of a loss of mass, either at a given temperature where desolvation or dehydration occurs and at a higher temperature where decomposition may occur.[76]

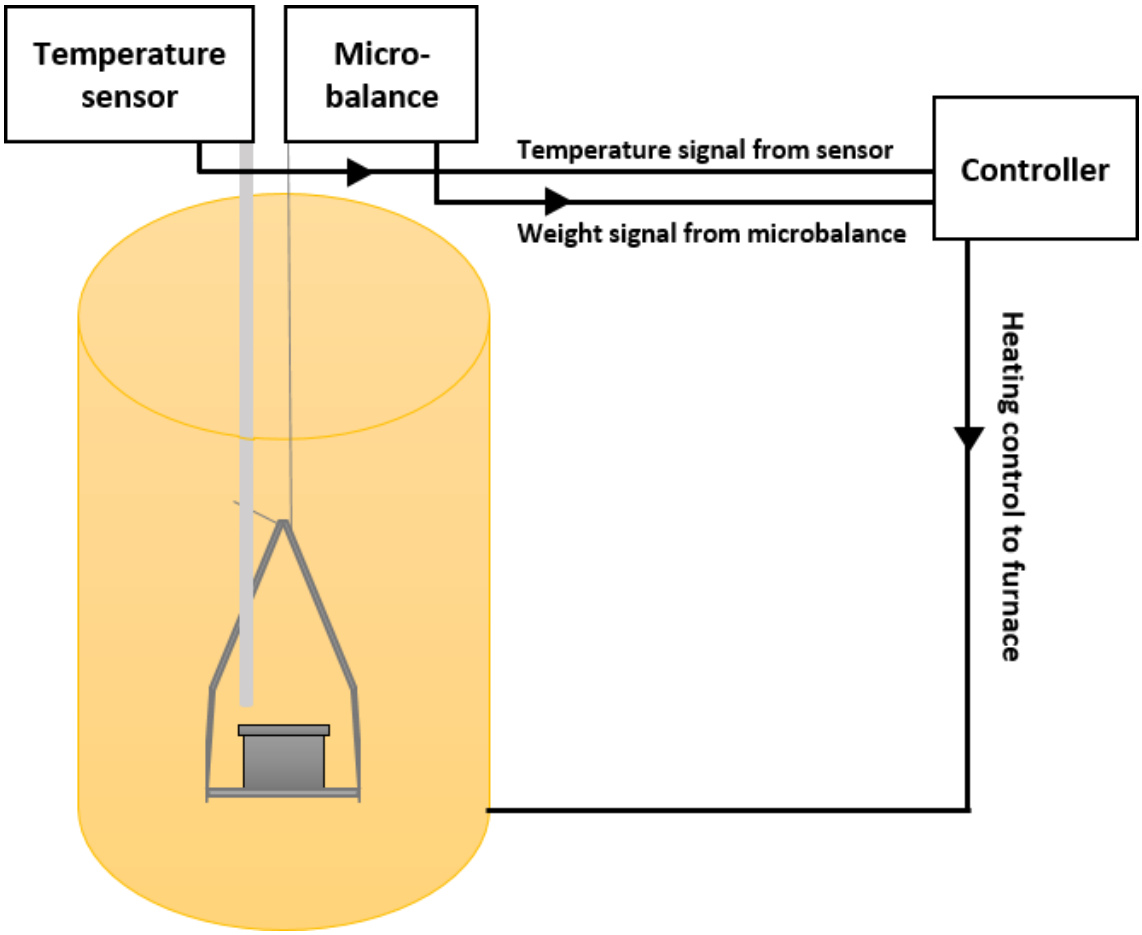


***Figure 2.7*** *Diagrammatic representation of a thermogravimetric analyser.*

The equipment required to perform this technique is called a thermogravimetric analyser, shown in diagrammatic for in Figure 2.7, and consists of a microbalance with two sample holders, one for a reference pan (not shown in Figure 2.7) and the other for the sample pan. The

sample pan is encased in a furnace during the running of an experiment and the temperature varied according to the method parameters set. As temperature increases, any solvent present, either residual or present in the crystal structure of a solvate for example, will be released and a consequent reduction in weight of the sample will be detected. A controller is present to monitor and record the temperature and weight and control the furnace temperature.[76] Nitrogen can be flowed through the furnace to keep the samples under an inert atmosphere and with some TGA equipment secondary apparatus can be connected to an exhaust port to analyse the exhaust gases. As an example, a mass spectrometer could be used to identify the solvent which is released from the material during the experiment.[77]

The following sets of parameters were used as the standard method for collecting TGA profiles throughout this thesis unless stated otherwise.

Experimental TGA method

TGA profiles were recorded on a TA Q500 using standard platinum pans. The method used was a ramp at a rate of 10°C/min to 300°C maximum.

### 2.2.3 Powder X-ray diffractometry

Powder X-ray diffraction (PXRD) is used mainly for the identification of compounds based on their diffraction pattern, which is unique to each crystalline material.[78] Measurements are undertaken using an X-ray diffractometer in which X-rays are generated, a monochromatic beam of which the rotated powdered crystalline sample is exposed to over a range of angles, and the intensity of the resulting diffracted X-rays detected. The X-rays are generated in a vacuum tube in which a large voltage (around 40kV) is applied, resulting in a beam of electrons from the cathode which impinge on an anode, which is in the form of a pure metal plate usually copper or molybdenum.[79] This causes X-rays to be generated in the surface layers of the anode, both by deceleration of the impinging high-energy electrons by the atomic electrons of the target metal ions, resulting in continuous radiation; and by the production of fluorescent X-ray photons by the transfer of electrons from outer orbitals to fill vacancies produced by the ejection of electrons by incident particles with greater energy than that binding the ejected electrons to the nucleus – characteristic radiation.[78,79]

Characteristic radiation, so called as it is of a defined wavelength related to the energy difference between the shells from which an electron falls from and to when filling a vacancy, as described above, is of higher intensity than continuous radiation. For a copper anode, the wavelengths of this characteristic radiation are $K\alpha_1$ 1.5406Å, $K\alpha_2$ 1.5444Å and $K\beta_1$ 1.3922Å.[78]

When X-rays interacts with matter, such as sample material in a diffractometer, photons of the incident beam are either scattered (either coherently where no energy is absorbed (Thomson scattering) or incoherently where some of the energy of the photon is absorbed and the rest reemitted as an X-ray photon of lower energy (Compton scattering)) or absorbed by the atoms of the target, increasing its temperature.[80] Each scattering point can be thought of as a source of reemitted spherical waves, expanding outwards with the consequence of interference between waves. This may be constructive or destructive interference and in crystalline material where scattering atoms are arranged in a periodic manner and given that the wavelength of the X-rays are on the order of the interplanar distance between these, diffraction will occur at specific angles.[78]

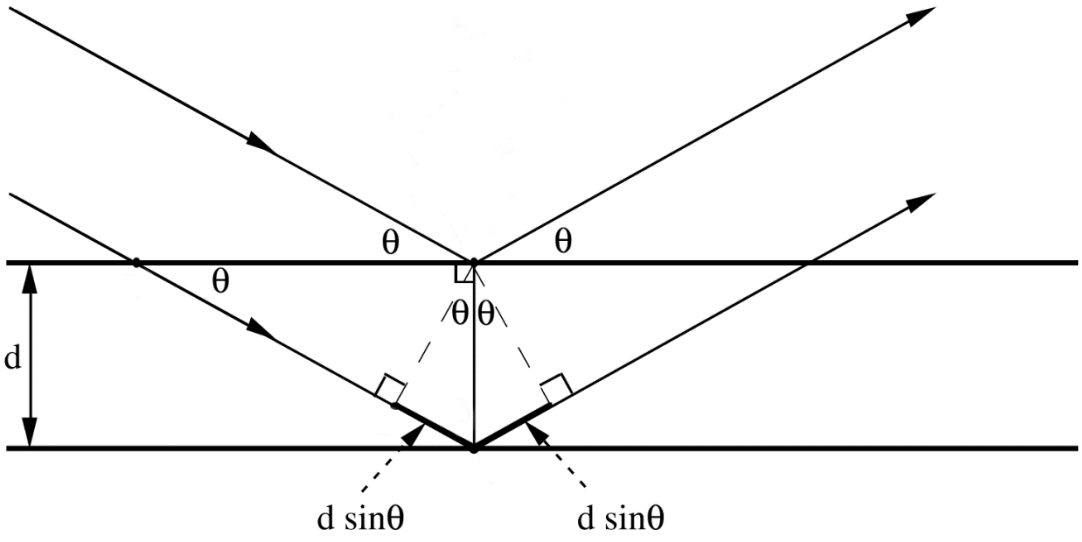


***Figure 2.8*** *An optical analogy to crystallographic planes reflecting X-rays, representing the geometry for interference of a wave scattered from two planes separated by the spacing given by d. Adapted from reference.*[81]

W. L. Bragg reported in 1912 an equation for calculating the angle at which the reflection conditions for diffraction are satisfied;[82] it has come to be known as Bragg's Law and is given below.

$$n\lambda = 2d \sin\theta$$

Where n is an integer representing number of planes, λ is the wavelength of the X-rays, d is the distance between lattice planes and θ the angle of incidence of the X-ray beam, which is equal to the scattering angle. In Figure 2.8 the two horizontal parallel lines represent lattice planes in

a crystal and X-ray beams are shown by the two parallel lines coming from the left and reflecting from each of the two lattice planes. The angle of incidence of the two parallel X-rays is θ and the difference in path length between the top and bottom X-rays is 2d sinθ, shown by the thicker line highlighted in the figure. Due to the additional path length, waves that reflect from lower planes will be phase retarded with respect to the first wave resulting in interference. When the difference in path length between the two X-rays in Figure 2.8 is equal to one wavelength, and multiples of this for further planes, the wave interference is maximally constructive and this is diffraction.[78,80,81] Although the Bragg equation was developed from an analogy, it was later proven correct using the concept of reciprocal space as introduced by P. P. Ewald.[83]

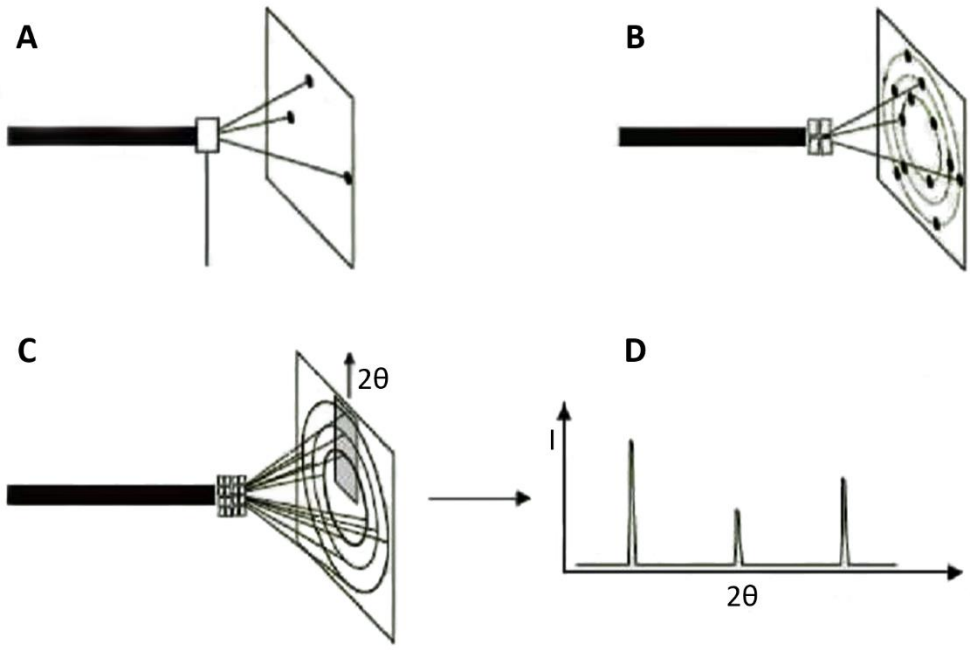


***Figure 2.9*** *Diagram showing diffraction from: a single crystal (A), four single crystals of different orientations (B), a polycrystalline material with multiple orientations (C) and a diffraction pattern (D), produced from the extracted intensities from (C) plotted against the 2*θ *angle. Adapted from reference.*[84,85]

The intensity of the diffraction from a material is determined by a number of factors, and in the case of single crystal X-ray diffraction, when diffracted X-rays are recorded on photographic film (an outdated technique, now replaced by electronic detectors), the result is spots of differing brightness being observed, when the position of the crystal allows for the diffraction conditions of the Bragg equation to be satisfied. As these conditions are limited, a fixed single crystal produces few reflections and must be rotated to generate a complete diffraction pattern.[86] With

PXRD, there are many crystals in different orientations, all exposed to the radiation at the same time, each which diffract, given the correct geometry, and the diffraction patterns are superimposed producing a complete circle (Debye ring) for each reflection.[78,86]

Figure 2.9 shows the relationship between increasing number of crystals or crystallites and the resulting diffraction patterns. The rings are converted into an intensity and plotted against the 2θ angle to produce the unique powder pattern for the material being analysed.

In this work PXRD was used for the analysis of samples from co-crystal screening and its optimisation, in Chapters 6 and 3 respectively; the detection of crystallisation from amorphous material in Chapters 4 and 5 and for material identification throughout, with the following parameters used as the standard method for collecting powder patterns unless stated otherwise.

Experimental PXRD method

Powder diffraction patterns were recorded on a PANalytical Empyrean diffractometer using Cu Kα radiation (λ = 1.54Å), tube voltage of 40kV and 40mA current. Intensities were measured from 2° to 40° 2θ with 0.04 rad. Soller silts and an incident beam divergent slit of 1/8°, anti-scatter slit of 1/4° and diffracted beam anti-scatter slit of 7.5mm (PIXcel).

### 2.2.4 Infrared spectroscopy

The basis of infrared (IR) spectroscopy is the measurement of the absorption of infrared radiation, that which falls within the region of the electromagnetic spectrum having wavelengths of between 0.8 and 1000μm, at specific wavelengths due to vibrational transitions in molecules.[87] The frequency at which absorption occurs is dependent upon vibrational modes present in the molecule and give rise to peaks in the spectrum which are characteristic of many specific functional groups. The environment of the analyte molecule may influence the IR absorption, for example molecular interactions such as hydrogen bonding may cause alterations in vibration and thus the frequency at which absorption occurs.[88] A complex absorption spectrum is produced due to the multiplicity of simultaneously occurring vibrations which is uniquely characteristic of the overall configuration of the molecule.[89] As such the IR spectrum can be thought of as a fingerprint, making it useful for the identification of substances,[90] or changes therein, which is pertinent to its use in this work for the analysis of co-crystal screening.

The following parameters were used as the standard method for collecting spectra throughout this thesis unless stated otherwise.

Experimental FTIR method

FTIR spectra of solid phases were collected on either an Agilent Cary 630 FTIR spectrometer with diamond attenuated total reflectance (ATR) crystal accessory and 128 scans for each sample were collected at a resolution of 2 $cm^{-1}$ over a wavenumber region of 4000-650 $cm^{-1}$; or a PerkinElmer Spectrum Two FTIR spectrometer with diamond universal ATR accessory and 4 scans for each sample were collected at a resolution of 2 $cm^{-1}$ over a wavenumber region of 4000-600 $cm^{-1}$.

## 2.2.5 Dynamic vapour sorption

Dynamic vapour sorption (DVS) is a gravimetric technique which measures moisture sorption behaviour of materials over a range of solvent vapour concentrations. Although the sorption of other solvents may be investigated, water is the most commonly used solvent, applicable especially in the pharmaceutical field as atmospheric water vapour may be influential in the physical and chemical stability of drugs and dosage forms and thus study of material behaviour in relation to relative humidity (RH) is particularly useful.

The apparatus used for DVS is somewhat like that of a thermogravimetric analyser (see Section 2.2.2) but which measures sample mass change over a range of relative humidities at a constant temperature. To achieve this a sample and reference pan, attached to a microbalance, are held in two separate chambers which are kept at the same RH as each other. The RH is changed in a stepwise manner according to the programmed method and held at each RH until the mass of the sample equilibrates to within a defined ranged. The difference in weight between the sample and reference pans can be attributed to the uptake or release of water by the sample. Water uptake can either be by adsorption onto the surface of the material, or by absorption, into the bulk material if amorphous or by hydrate formation if crystalline.[91]

The measurement of moisture sorption and hydration behaviour of materials was the main use of DVS in this work, however it is also a sensitive technique for the detection of small quantities of amorphous content in otherwise crystalline samples,[92] as seen with some samples in Chapter 7. The following parameters were used as the standard method for DVS analysis throughout this thesis unless stated otherwise.

Experimental DVS method

DVS was undertaken using a Surface Measurement Systems (London UK) DVS-1 with a 10% RH step between humidity values with equilibrium achieved at 0.1% weight change before moving to the next step. Methods were started at the humidity of the room at ambient (to the nearest 10% RH, measured by a Rotronic A/H hygrometer) with subsequent increase to 90% RH before cycling to 0% RH, to 90% RH, to 0% RH. Sample weights of between 5-20mg were used for all samples.

## 2.2.6 Chromatography

### 2.2.6.1 General

Chromatography encompasses a number of techniques which separate individual components from a mixture based on the rates in which they move through a medium. Chromatographic techniques can be gas or liquid based and the two types used in this thesis, both forms of liquid chromatography, are thin layer and high-performance liquid chromatography.

### 2.2.6.2 Thin layer chromatography

Thin layer chromatography (TLC) involves using a plate coated with a thin layer of stationary phase; commonly, and used in this work, a sheet of aluminium coated in silica. The procedure to separate components begins by adding an amount of mobile phase to the development tank sufficient to give an approximately 5mm depth of liquid. The range of solvents available to use as the mobile phase for TLC is extensive and combinations of solvents are often used to vary polarity and eluting power.[87] Small amounts of other components can be added to alter the solubility of acidic or basic solutes, for example the mobile phase used in this work was DCM:ethanol:ammonia in the ratio 200:8:1.

After allowing the atmosphere in the tank to become saturated with the solvent vapour, the plate is spotted with the liquid samples to be analysed along with any necessary standards and placed in the tank. As the mobile phase is drawn through the thin layer of stationary phase by capillary action, the sample components are separated by their adsorption affinity to the stationary phase, and are observed as spots at varying distances along the plate. The plate may require viewing under a UV lamp, or the use of a locating agent which reacts chemically with the solute resulting in coloured spots, for visible observation. The distance these spots have migrated in relation to the solvent front can then be measured to characterise the solute.[87] TLC was used to monitor the course of reactions during the synthesis of ROY in Chapter 4.

#### 2.2.6.3 High performance liquid chromatography

High performance liquid chromatography (HPLC) is a more advanced form of chromatography in which a mechanical pump is used to pass mobile phase, at a constant flow rate, through a column which is packed with a microparticulate stationary phase. Similarly, to TLC, a wide range of solvents and mixtures thereof can be used for the mobile phase. The stationary phase used for HPLC and found within the column is predominantly a chemically modified silica, although unmodified silica and polymeric resins or gels can also be used.[87]

To conduct HPLC, a constant pressure flow of mobile phase is achieved before injection of the sample for analysis. The sample is injected, via a valve from the sample loop, into the mobile phase stream resulting in no significant interruption to the flow. The sample, now within the flowing mobile phase, is passed through the column. The differential in affinity of the solute for the mobile and stationary phases determines the retention time in the column for the components of the sample. Each species from the sample will elute from the column and be presented to the detector after differing periods of time since injection. Numerous types of detector can be used with HPLC including: mass spectrometers, fluorometric, electrochemical and UV-vis spectrophotometers, with the latter the most widely used.[87,89] In this work, a UV-vis spectrophotometer was used as a detector, in which, similar to the other detector types, an electrical signal is generated, amplified and processed by a computer to produce a chromatogram of solute concentration over time.

### 2.2.7 Intrinsic dissolution

Intrinsic dissolution rate (IDR) is the rate of mass transfer per area of dissolving surface and is a useful parameter to measure which is independent of many of the factors that affect the standard the dissolution rate. For example, the effect of varying exposed surface area, unavoidable due to disintegration in traditional dosages forms,[93] can be nullified when measuring the IDR. If sink conditions are assumed, the IDR is therefore directly proportional to the solubility of the drug in the dissolution media.[94] IDR is commonly determined using the rotating disk method, whereby the compound to be assessed is compressed into a non-disintegrating disc which is placed into the dissolution medium with only one face exposed. The disc is then rotated at a fixed speed and samples from the dissolution medium are taken at specific time points, filtered and analysed, usually by UV spectrometry, to monitor release of the compound, with IDR being obtained by the amount of substance dissolved per unit surface area and time.[95]

The Sirius surface dissolution imager (SDI) is a piece of apparatus used for IDR determination which differs from the rotating disc method. It is a flow through cell approach that maintains sink conditions and exposed sample surface area using a laminar flow cell, with concentration detected by a UV sensor array. Figure 2.10 shows a false colour image as an example output from an IDR experiment. The red arrow indicates the direction of flow of the dissolution medium and the green arrow the position of the sample in the cell. The UV senor array allows visualisation of the increased downstream concentration of the sample compound, which is interpreted by the software to allow calculation of the IDR.

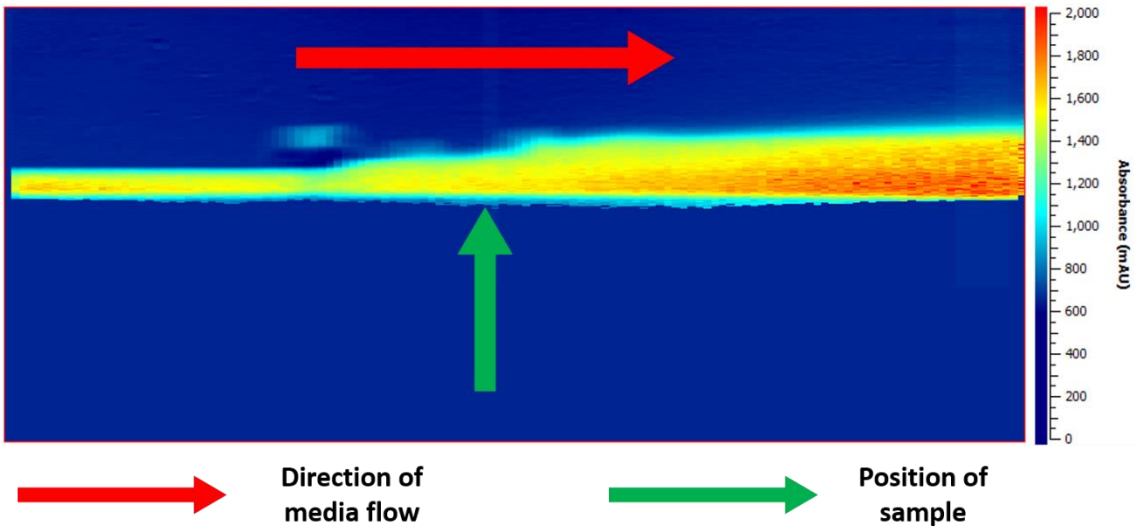


***Figure 2.10*** *False colour image from an IDR experiment, annotated to show media flow and sample position.*

Intrinsic dissolution testing was employed for the determination of IDR of ornidazole, 5-nitroisophthalic acid and the 1:1 co-crystal of these compounds in Chapter 6, and using a modified method to compare the intrinsic dissolution profiles of co-crystals of zafirlukast and the parent API in Chapter 7. Details of the experimental parameters for the intrinsic dissolution testing performed are given in the appropriate sections of the relevant chapters.

## 2.2.8 Computational methods

### 2.2.8.1 COSMOtherm

COSMOtherm is a computer program designed for predictive property calculation of liquids and is based on the COSMO-RS theory of interacting molecular surface charges.[96,97] The Conductor-like Screening Model (COSMO) is the quantum chemical basis of COSMO-RS and is an efficient form of quantum mechanical dielectric continuum solvation methods.[98] In COSMO calculations, a virtual conductor environment is used to calculate solute molecules in which a polarisation charge density (σ) is induced on the molecular surface, where there is an interface with the conductor. The molecule is converged into a state in which it is energetically optimal in terms of electron density within the conductor. From this a σ-profile is produced by converting the polarisation charge density, which is related to molecular surface polarity, into a distribution-function. Hydrogen bonding interactions are identified based on the polarisation charges of the interacting surfaces where hydrogen bond donor and acceptor atoms are located, with less specific van der Waals interactions being accounted for in a more approximate manner. The time-consuming quantum chemical calculations to produce the σ-profile only need to be performed once per molecule as the σ-profiles are stored for future use.[99,100]

Computational co-crystal screening in COSMOtherm is achieved by calculating the excess enthalpy ($H_{ex}$) of an API (A) and co-former (B) pair, which is obtained by mixing the two components from a virtually subcooled liquid to yield the subcooled co-crystal ($A_mB_n$). The mole fractions are accounted for by $x_m=m/(m+n)$ and $x_n=n/(m+n)$ and the $H_{ex}$ calculated by the following equation.

$$H_{ex} = H_{AB} - x_m H_{pure,A} - x_n H_{pure,B}$$

Where $H_{AB}$ and $H_{pure}$ represent the molar enthalpies in the pure reference state and in the m:n molar mixture. The $H_{ex}$ of the API and co-former pairs, relative to the pure components, represents the predicted propensity for co-crystallisation and can then be ranked to find the most highly predicted API-co-former pairs. This method neglects the long-range interactions in the crystals and there are a number of known limitations and approximations inherent to the method,[100] which could lead to artefacts in the calculated API:co-former enthalpies resulting in higher or lower ranking for certain co-formers than may be achieved with more complex methods. However, the approximations and method employed by COSMOtherm has been shown to give accurate and efficient results on a set of potential co-crystal formers.[101]

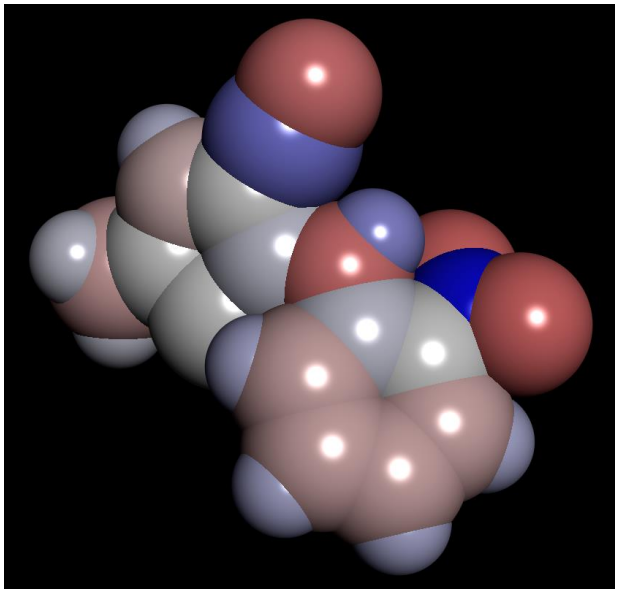

***Figure 2.11*** *Charge surface for a molecule of ROY where blue indicates positive and red negative.*

A similar approach to computational co-crystal screening was reported by Musumeci *et al.*,[102] in which sets of potential hydrogen bond donor and acceptor sites were identified on calculated gas phase molecular electrostatic potential surfaces to estimate interaction site pairing energies in the solid form. An example of a calculated charge surface is shown in Figure 2.11 and the method by which the interaction site pairing energies are calculated depicted in Figure 2.12.

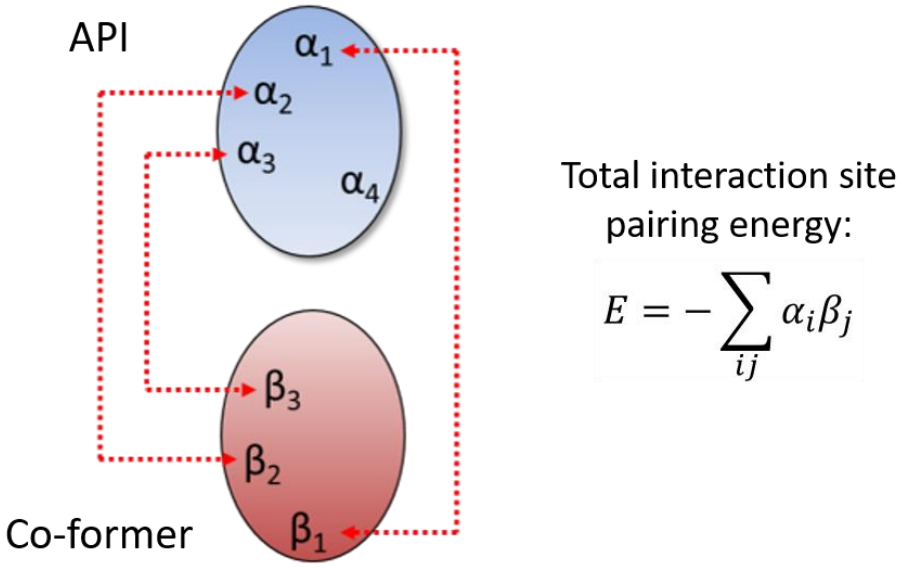


***Figure 2.12*** *Diagram depicting the method by which the interaction site pairing energies are calculated in the computational co-crystal screening method used by Musumeci et al.,*[102] *showing interactions between hydrogen bond donors (α) and acceptors (β) in the API (blue) and co-former (red) molecules.*

The co-crystal prediction method is based on the concept that the best hydrogen bond donor ($\alpha_1$) and best acceptor ($\beta_1$) will form the strongest hydrogen bond, followed by the next best of each donor ($\alpha_2$) and acceptor ($\beta_2$), until all of the interaction sites are satisfied. At this point a set of hydrogen bond interaction sites $\alpha_i$ (hydrogen bond donor parameters) and $\beta_j$ (hydrogen bond acceptor parameters) are defined and the total interaction site pairing energy of the solid is estimated as the sum over all contacts given by the equation in Figure 2.12. The difference in this total interaction site pairing energy between the API and co-former pair and the two pure components, which is based on the formation of the most favourable intermolecular interactions, provides a measure of the probability of co-crystallisation occurring.[102] This method of computational co-crystal screening has also proved largely successful.[103,104]

The computational co-crystal screening undertaken in this work (the computational pre-screen for the co-crystal screening of ROY (Chapter 4) and ornidazole (Chapter 6)), used COSMOtherm software (F. Eckert and A. Klamt, COSMOtherm, Version C3.0, Release 16.01; COSMO logic GmbH & Co. KG, Leverkusen, Germany, 2015) and screen specific details are given in the respective chapters.

#### 2.2.8.2 Design of experiments

Design of experiments (DOE) is a statistical based method for developing a set of experiments to more efficiently perform an investigation as compared to standard experimental undertaking. The concept of DOE was first introduced by Fisher in 1935,[105] and the field has since developed, more recently making use of the advances in computer technology leading to software applications allowing for rapid construction and evaluation of designs and improved features such as complex plots for visualisation of experimental models.[106] DOE is often used for optimisation and improving efficiency of processes and has been demonstrated in many disciplines such as biofuel production,[107] process engineering[108] and pharmaceuticals.[109]

Factorial designs are the basis for all classical designs used in optimisation, screening and robustness testing, and are used in this work. Factorial designs involve the varying of variables (factors) simultaneously between separate experiments which allows for the investigation of interaction effects between factors, which cannot be achieved by a series of 'one-at-a-time' experiments. Each factor, for example temperature or pressure, can be varied between different settings (levels) which must be defined in the experimental design. Factorial designs can either be full factorial, in which observations are made for every level of each setting, or fractional factorial, in which a reduced set of observations is made.[110]

For a process with many factors, each with multiple levels, a full factorial design can require an extremely large number of observations, i.e. experiments repeated with varying levels of the variables. To reduce the resource burden the number of levels for each factor can be reduced to a high and low level, with a centre level or midpoint. This is called a two-level full factorial design and an example of an experimental plan for a process with two factors is shown in Table 2.4. The other option is to use a fractional factorial design in which all possible combinations of levels for factor are not observed but which can still feasibly result in good estimates of main effects and interaction effects between factors.[110]

***Table 2.4*** *Example of a full factorial experimental design for two variables (factors) at high (+), low (-) and midpoint (M) levels.*

| **Experiment number** | **Factor** | |
|---|---|---|
| | **Variable A** | **Variable B** |
| Experiment 1 | + | + |
| Experiment 2 | + | - |
| Experiment 3 | - | + |
| Experiment 4 | - | - |
| Experiment 5 | M | M |
| Experiment 6 | M | M |
| Experiment 7 | M | M |

Factorial designs can be represented geometrically, with an example for the experimental design given in Table 2.4 shown in Figure 2.13, where the points at the edges of the rectangle represent high and low levels of variable A (x-axis) and variable B (y-axis), and the points in the centre relate to the three repeated midpoints. In designs where more factors are involved the number of dimensions of the geometric representation increases, such that a design with three variables would result in a three-dimensional cube and so on.[111]

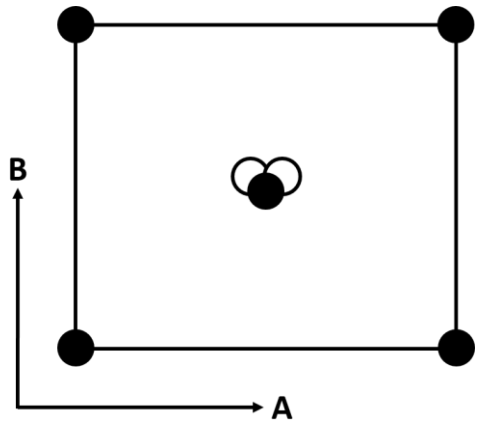


***Figure 2.13*** *Geometric representation of a two-level full factorial design with two variables and a midpoint with two replicates (three total).*

After a design is defined, it is carried out experimentally and the responses, also previously defined, are measured and recorded. Regression analysis, of which numerous variations are available depending upon the design, is undertaken computationally and the data fit to a model. Assuming a good statistical fit of the model, the effect of alterations to variable settings on the measured response(s) can be determined and visualised, for example as response surface or contour plots,[111] an example of which is shown in Figure 2.14.

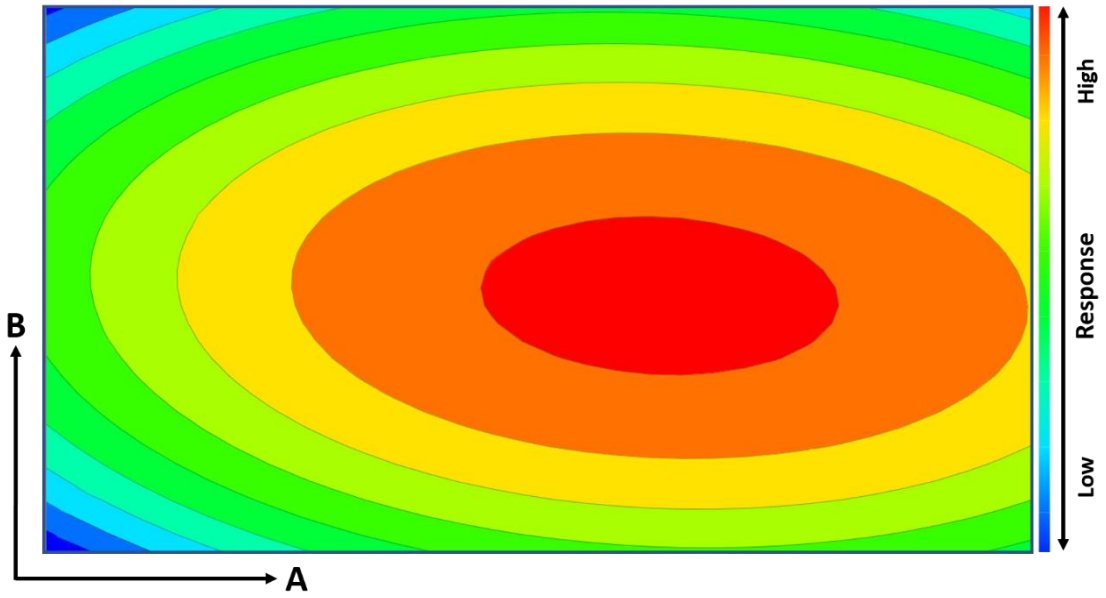


***Figure 2.14*** *Example of a two-dimensional contour plot showing the response (red = high, blue = low) in the plot area with variable A increasing along the x-axis and variable B increasing along the y-axis. The highest response is seen at approximately the midpoint for both variables.*

In this work, DOE was utilised in the optimisation of a physical co-crystal screening method (Chapter 3), employing Umetrics MODDE (version 10) software for both experimental design and analysis. An initial manual screen was first optimised using a fractional factorial design as numerous variables were involved and a smaller set of experiments was required to ensure practicality of the optimisation. A second stage of optimisation was applied to the automated version of the physical screening procedure and a reduced set of variables, which made the use of a full factorial design feasible in this instance.

### 2.2.9 Summary

This section has covered most of the methods used within this body of work, especially those which feature in multiple chapters. Where methods have been used which deviate from those described here, or where they are specific to one particular piece of work and not covered here, they are detailed in the appropriate sections.

# Chapter 3 – Optimisation of physical co-crystal screening

## 3.1 Introduction

### 3.1.1 Screening

There has been much interest in recent times in pharmaceutical co-crystals and their ability to modify the physical and chemical properties of a parent drug. There is little surprise considering the improvements in many pharmaceutically relevant characteristics that have been reported. From orders of magnitude greater solubility and dissolution behaviour,[27] to large reductions in hygroscopicity and photodegradation.[51,52] The ability to obtain these improvements in properties without modifying the molecular makeup of the active pharmaceutical ingredient (API), and before any further formulation, is another advantage of employing co-crystals in development of pharmaceuticals and other solid forms. The downside is that there is no guarantee that the formation of a co-crystal will bring about an improvement in a particular property of interest, or that there will be any improved characteristic at all. There is also no fool-proof method of predicting which compounds will form co-crystals, although advancements in computational prediction are certainly helping in this respect. These *in silico* approaches will be discussed later within this thesis (Chapter 4).

Even with perfect prediction an optimised method of physical screening is required to assess the ease of production of the co-crystal phase, so a robust physical screening retains an inescapable presence within the development process of co-crystals. Therefore, the current best practice for developing pharmaceutically relevant co-crystals must encompass a screening process which includes many potential co-formers to, hopefully, produce a number of co-crystals.[112] Analysis of the co-crystals obtained allows the determination of the improvements, or lack thereof, in relevant properties, and a decision as to which, if any, co-crystals to take into further development.

Methods of co-crystal screening utilising ultrasonication have been reported which demonstrate the feasibility of the technique.[30,34,113,114] Details of optimisation of this type of screening process have not been published and so any method for screening for co-crystals in an efficient manner using ultrasonication requires development. A screening process which is not optimised increases the likelihood of under detection of drug-co-former pairs which can form co-crystals

and as such will lead to a screen which is not effective or fit for purpose. For these reasons, a body of work focused on optimisation for a co-crystal screening method has been undertaken.

### 3.1.2 Computational pre-screen

Prior to physical screening for co-crystals, an optional, but advantageous step, is a computational pre-screen. This involves the use of computational chemistry to predict drug-co-former pairs that are likely to form co-crystals.[112] Different methods are available including comparison of lattice energies calculated using anisotropic intermolecular atom-atom potentials,[69] to full crystal structure prediction[115] and the decision on which is most appropriate will be based on the size of the screen and the resources available. The benefit of employing a computational pre-screen is that a reduction in the scale of physical screening can be justified based on the outcome of the pre-screen. The co-formers predicted most likely to form a co-crystal with the API being investigated can be prioritised for physical screening and any co-formers predicted to be unlikely to form co-crystals can be dropped from the physical screen. Although current computational methods have been shown to be effective,[103,115] the extent to which this influences the inclusion of compounds in the physical screen must be considered as it is likely that some inconsistencies may occur due to methodological artefacts. These are discussed in more depth in Chapter 2.

### 3.1.3 Design of experiments

Throughout this project, the computational pre-screen has been undertake using COSMOtherm, a piece of commercial off-the-shelf software, which by its nature is already optimised by its designers. The aim for this section of work is to optimise the screening process and as the computational pre-screen is 'taken care of', the physical section of the screen is the focus. To perform the optimisation, the design of experiments approach has been identified as a suitable methodology to employ based on its advantages as laid out in Chapter 2.

### 3.1.4 Automation

Automation, for example by the use of robotics, is used extensively in industry to improve the efficiency of many processes of which solid form screening is included. Therefore, automation should be a primary consideration to improve the practical relevance of any high-throughput co-crystal screening optimisation work. The work presented in this chapter is divided into an initial or preliminary screen optimisation in which a manual method which aimed to be a close representation of an automated process was first carried out. The results from this were then used to inform the design of a second optimisation of an actual automated process. Gaining

access to the use of an industrial robotics platform was vital for this work to be carried out. Several limitations in relation to the customisation of the processes, which were required for optimisation testing purposes, presented themselves. However, with state of the art technology which is designed to solely run validated screening processes and is currently implemented in active projects some limitations are inevitable. The issue that arose and the solutions used to overcome them are discussed in a later section of this chapter.

### 3.1.5 Physical screening

Salt and polymorph screening are common practice in the pharmaceutical industry and high-throughput methods of both have been developed to make extensive investigation feasible.[29] Co-crystal screening is much like salt screening, in that the production of new solid forms consisting of an API and second entity is the desired outcome and that similar high-throughput screening methods can be employed. However, due to the significantly greater number of acceptable co-formers compared to counter-ions, the necessity for a high-throughput process is even greater. There are a relatively limited number of well-established pharmaceutically acceptable counter ions; those which are safe for human consumption at the required dosage.[116,117]

As co-crystals rely on weaker intermolecular forces rather than ionic bonding there are more potential second entities which can be combined with the API. The constituent molecules are not required to be ionisable, but those that are, are not necessarily excluded from a co-crystal screen, as such a much wider range of potential co-formers are available than salt counterions. Given that all pairs of compounds will display some intermolecular interaction, no matter how weak, there is potential for almost all compounds to be co-formers if paired with a suitable API to overcome the thermodynamic and kinetic factors prerequisite for a viable crystal structure containing the two compounds to form.

With seemingly endless possible co-formers available, a commonly applied practical solution is to screen against one or more lists which are available containing compounds regarded to be safe to be used in products for humans. These include the ‘generally recognized as safe’ (GRAS) list and the ‘everything added to food in the United States’ (EAFUS) list, both maintained by the FDA.[118,119] This approach improves the feasibility of co-crystal screening however it limits the investigated co-formers to a fraction of the potential candidates as the lists mentioned contain only around 4000 compounds combined. A co-former not present in these lists of compounds may still be pharmaceutically acceptable and if it forms a co-crystal with desired properties it

could prove worthwhile to perform the necessary toxicity studies to gain approval for its use in a product.

Regarding the methodologies for screening for co-crystals, numerous techniques have been assessed. These methods include: dry or solid-state grinding,[35] solvent-drop or liquid assisted grinding (LAG),[35,36] microwave,[43] hot-stage microscopy,[38] hot-melt extrusion (HME)[42] and freeze-drying.[39] These techniques are all relatively time consuming or impractical in terms of high-throughput screening and so for more situations where efficient screening of a large number co-formers is required, other methods have been considered such as reaction crystallisation and sonic methods.[29,30]

It is accepted that the method implemented for producing co-crystals can influence the formation or lack of formation of certain co-crystals. For example, it has been reported that when utilising LAG a particular co-crystal form can be produced, whereas the same reagents when processed using solid-state grinding form a different co-crystal,[120] or no co-crystal at all.[121,122] A co-crystal screen incorporating multiple methods for producing co-crystals may be argued to be the ideal, however practicality in terms of time and resources is likely to render this unfeasible. The use of automation is highly prized in the modern pharmaceutical development process.[29,123] No literature method presented has yet detailed a means by which an optimised screen could be applied to a robotics platform. As such we set out to determine a method by which this could be readily and robustly achieved to deliver an efficient physical screening process to build into a broader screening paradigm. To achieve this an ultrasonication based screening method utilising an ultrasonic probe on a 96-well plate format was chosen due to its ability to be easily implemented on a robotics platform allowing automation of the process. This approach, by replacing mechanical grinding with sonication and including a small amount of solvent during the process, enabled the advantages of solvent drop grinding methods and the robotics practicality that was our ambition. The parameters at which features of the screen will be carried out are the focus of the optimisation.

# 3.2 Initial optimisation

## 3.2.1 Methods

### 3.2.1.1 General

For the initial round of optimisation, the caffeine and malonic acid system was selected. It is known that a co-crystal can form between these two materials and the optimisation approach was based around tuning the parameters of the screening method to lead to the greatest

proportion of conversion of these starting materials to the caffeine:malonic acid co-crystal. The co-crystal is also known to form spontaneously,[33] but it has been shown that the spontaneous formation is humidity dependent and that formation of the co-crystal from contact of the two starting materials at ambient relative humidity (≤40%) over multiple days is negligible, requiring a much higher relative humidity to cause significant conversion.[124] This environment was not present in the laboratory in which the work was undertaken and as such any co-crystal formation seen is due to experimental factors and not spontaneity.

The caffeine:malonic acid co-crystal has also been reported to form by shaking of the two starting components, with the rate that this occurs influenced by particle size.[125] Although shaking was used to produce the physical mixture of the components for comparative analysis, the length of time shaking was used in this work (combined total of 10 minutes at a low shaking rate) was much less than the time required for even the smallest particle size (fastest rate) to form the co-crystal in the referenced article which was on the order of days. This, again, substantiating the lack of influence of spontaneous co-crystal formation on the co-crystalline material produced throughout the experimentation presented in this work. Three solvents were used in the screening process as part of the optimisation; these were: acetone, ethanol and hexane. These solvents were chosen to cover a range of solvent properties and represent the three main categories of solvent: non-polar (hexane), polar protic (ethanol) and polar aprotic (acetone).

#### 3.2.1.2 Design of experiments

The Design of Experiments (DOE) approach was used for the optimisation of the screening parameters. Umetrics MODDE software was used both for experimental planning and analysis of the results. The parameters chosen to investigate were: ultrasonication power, ultrasonication time, temperature, solvent and solvent amount. A larger set of potential parameters were considered for investigation which also included: light exposure, humidity and pressure; most of these proved to be impractical to investigate requiring either the purchase of equipment and/or extensive modification to the experimental setup. The response which was selected to be measured was percentage conversion of starting material to co-crystal. Although other parameters were considered for study such as pressure and light exposure, the feasibility of implementing them in the screening process prevented them from warranting inclusion in the optimisation experiments.

The method used in the DOE software was an optimisation and the experimental plan laid out in Table 3.1 was produced. This was a fractional factorial design which was deemed to be the

most appropriate type given the number of factors being investigated. This approach was suitable as a relatively large number of experiments were carried out, meaning a good model could be achieved without the need for a full factorial design which would have required an unreasonably large amount of time and resources given the number of variables implicated in the optimisation.

***Table 3.1*** *Experimental plan as produced by MODDE DOE software.*

| Experiment number | Ultrasonication power (%) | Ultrasonication time (minutes) | Temperature (°C) | Solvent | Solvent volume (µl) |
|---|---|---|---|---|---|
| 1 | 0 | 0 | 20 | Acetone | 5 |
| 2 | 100 | 20 | 20 | Acetone | 5 |
| 3 | 100 | 0 | 60 | Acetone | 5 |
| 4 | 0 | 20 | 60 | Acetone | 5 |
| 5 | 100 | 0 | 20 | Acetone | 50 |
| 6 | 0 | 20 | 20 | Acetone | 50 |
| 7 | 0 | 0 | 60 | Acetone | 50 |
| 8 | 100 | 20 | 60 | Acetone | 50 |
| 9 | 0 | 10 | 40 | Acetone | 27.5 |
| 10 | 0 | 20 | 20 | Ethanol | 5 |
| 11 | 0 | 0 | 60 | Ethanol | 5 |
| 12 | 100 | 20 | 60 | Ethanol | 5 |
| 13 | 100 | 20 | 20 | Ethanol | 50 |
| 14 | 100 | 0 | 60 | Ethanol | 50 |
| 15 | 0 | 20 | 60 | Ethanol | 50 |
| 16 | 0 | 0 | 20 | Ethanol | 27.5 |
| 17 | 0 | 0 | 40 | Ethanol | 50 |
| 18 | 0 | 10 | 20 | Ethanol | 50 |
| 19 | 100 | 0 | 40 | Ethanol | 5 |
| 20 | 100 | 10 | 20 | Ethanol | 5 |
| 21 | 50 | 0 | 20 | Ethanol | 50 |
| 22 | 50 | 20 | 40 | Ethanol | 27.5 |
| 23 | 50 | 10 | 60 | Ethanol | 27.5 |
| 24 | 100 | 0 | 20 | Hexane | 5 |
| 25 | 0 | 20 | 20 | Hexane | 5 |
| 26 | 0 | 0 | 60 | Hexane | 5 |
| 27 | 100 | 20 | 60 | Hexane | 5 |
| 28 | 0 | 0 | 20 | Hexane | 50 |
| 29 | 100 | 20 | 20 | Hexane | 50 |
| 30 | 100 | 0 | 60 | Hexane | 50 |
| 31 | 0 | 20 | 60 | Hexane | 27.5 |
| 32 | 50 | 20 | 60 | Hexane | 50 |
| 33 | 50 | 10 | 40 | Hexane | 5 |
| 34 | 50 | 10 | 40 | Hexane | 27.5 |
| 35 | 50 | 10 | 40 | Hexane | 27.5 |

### 3.2.1.3 Physical DOE experiments

The experimental setup used during the optimisation experimentation consisted of an ultrasonic probe (Sonics Vibra Cell, 130W, 20kHz) with 8-tip adapter positioned using a retort stand above a 96-well plate (borosilicate glass, Zinsser). The well plate was positioned on a hot plate (IKA C-MAG HP 4). Infrared spectroscopy was carried out using an Agilent Technologies Cary 630 FTIR spectrometer with diamond ATR.

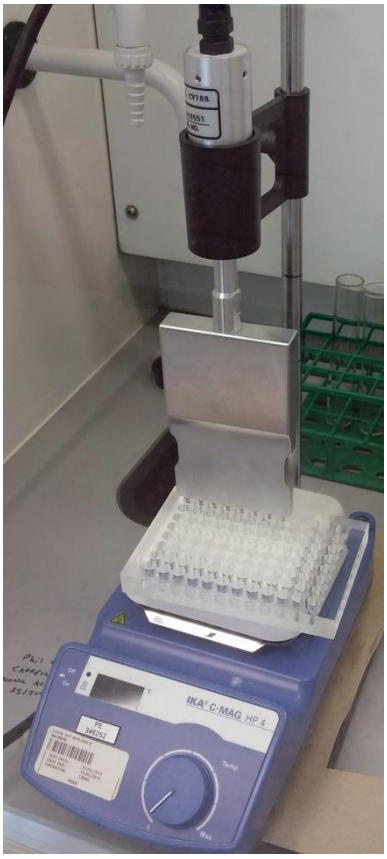


***Figure 3.1*** *Photograph showing experimental setup.*

The experimental plan listed which experiments to carry out with variations in the parameter values between each experiment. The method implemented for the undertaking of these experiments was as follows:

Approximately 50mg of the physical mixture of caffeine and malonic acid in a 2:1 molar ratio was weighed out into each of the required number of wells in the 96-well plate as dictated by the experimental plan. This required the use of multiple plates as experiments were carried out at different temperatures. The powder was gently compacted to the bottom of each well before the plate was placed on the hot plate and allowed to reach the instructed temperature. The plate was then removed and a Gilson pipette was used to quickly add the correct amount of the

appropriate solvent to the wells, again as stated in the experimental plan. Immediately after addition of the solvent, the plate was returned to the hot plate and the 8 tips of the ultrasonic probe placed in the necessary wells. The ultrasonic probe was set at the desired power setting and left for the stipulated time. Upon completion, the resultant material was removed from the wells using a spatula and analysed by infrared spectroscopy. For analysis, infrared spectroscopy was used to measure the response of conversion of starting material to co-crystal. This required a set of reference standards to be produced and analysed so that comparisons of the spectra of experiment samples could be carried out to determine the quantity of co-crystal present in said samples.

#### 3.2.1.4 Preparation of calibration standards for analysis

Using infrared spectroscopy to successfully detect and quantify the presence of particular solid forms within a sample has been reported previously for both polymorphs[126,127] and co-crystals.[128] A method similar to those used in the referenced literature was employed in which calibration standards containing varying ratios of co-crystal to parent components were produced.

An amount each of caffeine and malonic acid were milled separately at 25Hz for 15 minutes in a Retsch Mixer Mill MM 400 ball mill using PTFE coated balls and vessels. The resultant powders were used to produce a 2:1 molar ratio physical mix of the two components. This was achieved by weighing out the appropriate amount of each component, transferring into ball mill vessels and shaking at 10Hz for 5 minutes without the presence of the balls.

The 2:1 caffeine:malonic acid co-crystal was produced, following the method published by Trask *et al.*,[51] by weighing out the appropriate amount of each component, transferring into a ball mill vessel and milling at 25Hz for 30 minutes (with the ball bearing present). Subsequent to this, six 100mg samples were produced by weighing out the necessary quantity of both the 2:1 mixture and co-crystal (as described by Table 3.2 below) into a small sample vial and blending in the ball mill, again at 10Hz for 5 minutes without the presence of the ball bearings, in order to thoroughly mix the materials. The vials were wrapped in paper to prevent breakage during blending.

### 3.2.1.5 Infrared spectroscopy

Each sample was analysed by infrared spectrometry using an Agilent Cary 630 FTIR spectrometer with diamond ATR and a resolution of 2cm$^{-1}$, see Appendix 3.1 for spectra.

***Table 3.2*** *Compositions of the caffeine:malonic acid calibration standards.*

| Sample (co-crystal content) | Percentage of co-crystal by mass (%) | Mass of co-crystal weighed (mg) | Percentage of physical mixture by mass (%) | Mass of physical mixture weighed (mg) |
|---|---|---|---|---|
| 0% | 0 | 0 | 100 | 99.65 |
| 20% | 20 | 20.06 | 80 | 80.76 |
| 40% | 40 | 40.38 | 60 | 59.99 |
| 60% | 60 | 59.74 | 40 | 41.61 |
| 80% | 80 | 79.76 | 20 | 19.91 |
| 100% | 100 | 100.22 | 0 | 0 |

The infrared spectra for the 0% and 100% sample are shown in the plot below (Figure 3.2).

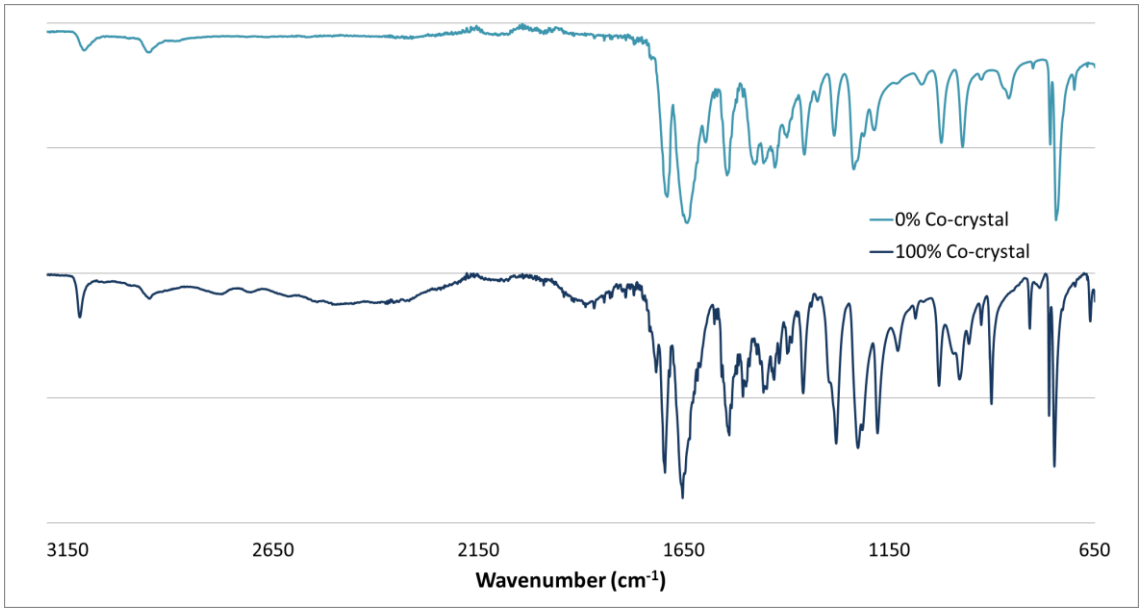


***Figure 3.2*** *Infrared spectra of 0% co-crystal (2:1 molar ratio physical mixture of milled caffeine and milled malonic acid, top) and 100% co-crystal (bottom).*

There are differences in these spectra and the most prominent is the peak at a wavenumber around 3100cm$^{-1}$, an enlargement of which is shown below (Figure 3.3). The wavelength range in which this peak occurs corresponds to the literature values for a C-H stretch.[129] Figure 3.4 shows the hydrogen bonding present in the 2:1 caffeine:malonic acid co-crystal; the image was produced from the entry in the CSD (GANYAW) using Mercury. It is evident that there are two

hydrogen bonds between each molecule of caffeine and malonic acid. One between the carboxylic O-H of malonic acid and one of the nitrogen atoms in the imidazole ring of caffeine, and the second between the C-H of the imidazole ring of caffeine and carbonyl O of malonic acid. This second hydrogen bond, when formed would alter the environment of the C-H bond, causing the difference in the peak observed in the spectra.

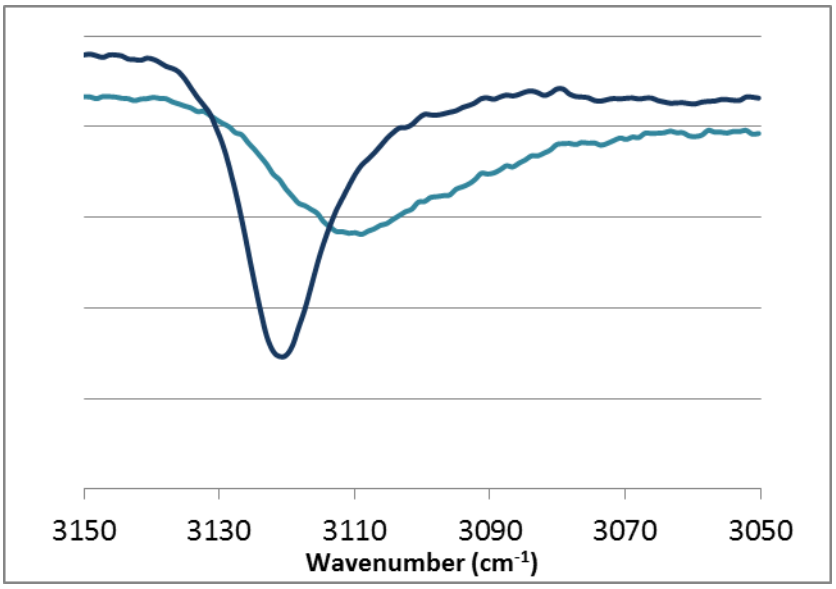


***Figure 3.3*** *Enlargement of peak used for comparison.*

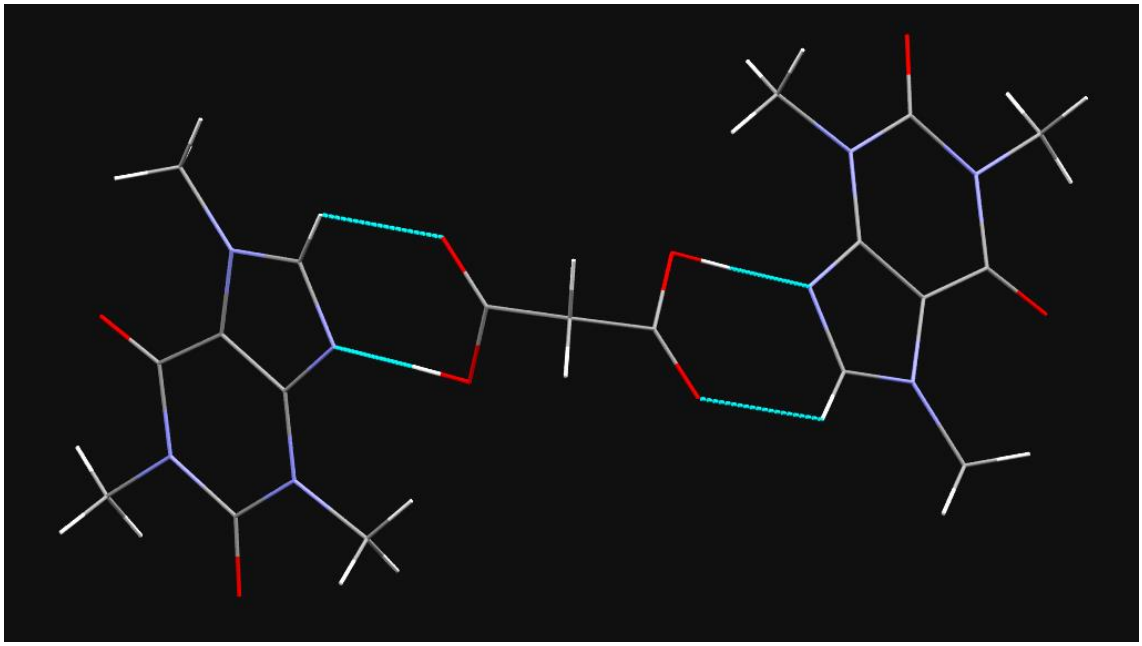

***Figure 3.4*** *Image showing the hydrogen bonding (cyan dotted lines) between molecules of caffeine and malonic acid in the 2:1 caffeine:malonic acid co-crystal.*

A scatter graph was produced using this data and the 40% sample data pointed omitted due to its deviation from the trend. The graph with trend line and equation are shown in Figure 3.5.

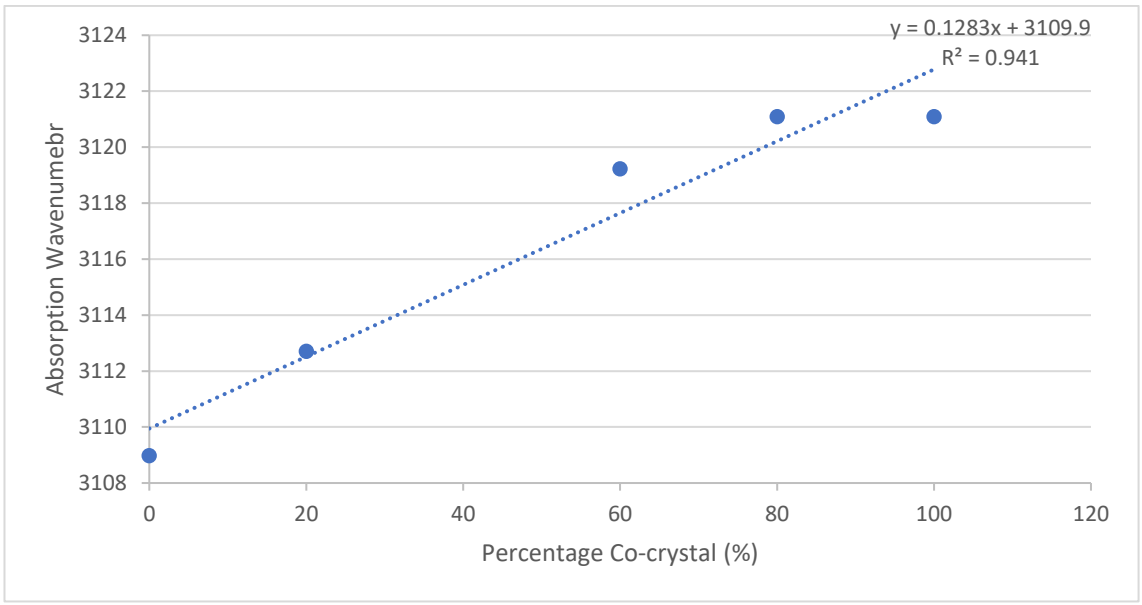


***Figure 3.5*** *Scatter graph showing the wavenumber of absorption for the peak maximum for samples of varying co-crystal composition.*

The $R^2$ value of 0.941 indicates a reasonably good correlation, however determination of percentage co-crystal content calculated using the equation obtained from this data will only be an approximate value due to the less than perfect correlation. The resolution of the spectra achievable from the spectrometer used is great enough that multiple steps based on peak position between the spectra for 0% and 100% co-crystal are detectable. A minimum useful number of steps for the purposes of evaluating the parameters of the screening method would be two, equivalent to co-crystal is produced and co-crystal is not produced. The FTIR analysis used allows greater separation of the outcome of the experiments and in turn an improved DOE analysis. Although multiple steps in terms of co-crystal conversion could be detected, this was over a relatively narrow wavelength range (3109 to 3121) and the resolution of the spectrometer resulted in six detectable measurements, based on increments of $2cm^{-1}$ throughout the range. The results are listed as a calculated conversion to co-crystal (Table 3.3), however it can be seen that only certain values are possible due to the grouping based on the detectable ranges. These values then can be thought of as an indicator of the amount of conversion to co-crystal without being misinterpreted as an exact expected value.

### 3.2.2 Results

The approximate percentage conversion to co-crystal observed in the experimental samples as determined by infrared analysis (spectra presented in Appendix 3.2) is shown in Table 3.3 below. Where there is no value in the result column, that particular experiment was not carried out. This was due to improving efficiency in the practical undertaking of the experiments; in order to minimise the number of consecutive runs required, multiple experiments were carried out on the same plate. By planning to combine certain experiments for example those requiring the same temperature, a resource efficient experimental plan was produced and followed. This however led to the exclusion of five out of the 35 experiments due to the limits of the experimental setup, for example by the layout of the 8-tip ultrasonic probe preventing adjacent wells to be sonicated at different sonication intensities.

***Table 3.3*** *Experimental plan showing approximate percentage conversion to co-crystal as determined by infrared analysis of experimental samples.*

| Exp. number | Sonication power (%) | Sonication time (minutes) | Temp. (°C) | Solvent | Solvent volume (µl) | Conversion to co-crystal (%) |
|---|---|---|---|---|---|---|
| 1 | 0 | 0 | 20 | Acetone | 5 | 80 |
| 2 | 100 | 20 | 20 | Acetone | 5 | 65 |
| 3 | 100 | 0 | 60 | Acetone | 5 | 73 |
| 4 | 0 | 20 | 60 | Acetone | 5 | 73 |
| 5 | 100 | 0 | 20 | Acetone | 50 | 80 |
| 6 | 0 | 20 | 20 | Acetone | 50 | 80 |
| 7 | 0 | 0 | 60 | Acetone | 50 | 73 |
| 8 | 100 | 20 | 60 | Acetone | 50 | 80 |
| 9 | 0 | 10 | 40 | Acetone | 27.5 | 80 |
| 10 | 0 | 20 | 20 | Ethanol | 5 | 73 |
| 11 | 0 | 0 | 60 | Ethanol | 5 | 80 |
| 12 | 100 | 20 | 60 | Ethanol | 5 | 80 |
| 13 | 100 | 20 | 20 | Ethanol | 50 | 80 |
| 14 | 100 | 0 | 60 | Ethanol | 50 | 80 |
| 15 | 0 | 20 | 60 | Ethanol | 50 | 80 |
| 16 | 0 | 0 | 20 | Ethanol | 27.5 | - |
| 17 | 0 | 0 | 40 | Ethanol | 50 | 73 |
| 18 | 0 | 10 | 20 | Ethanol | 50 | 80 |
| 19 | 100 | 0 | 40 | Ethanol | 5 | 80 |
| 20 | 100 | 10 | 20 | Ethanol | 5 | - |
| 21 | 50 | 0 | 20 | Ethanol | 50 | 80 |
| 22 | 50 | 20 | 40 | Ethanol | 27.5 | 80 |
| 23 | 50 | 10 | 60 | Ethanol | 27.5 | - |
| 24 | 100 | 0 | 20 | Hexane | 5 | 22 |
| 25 | 0 | 20 | 20 | Hexane | 5 | 22 |
| 26 | 0 | 0 | 60 | Hexane | 5 | 73 |
| 27 | 100 | 20 | 60 | Hexane | 5 | 73 |
| 28 | 0 | 0 | 20 | Hexane | 50 | 29 |
| 29 | 100 | 20 | 20 | Hexane | 50 | 22 |
| 30 | 100 | 0 | 60 | Hexane | 50 | 80 |
| 31 | 0 | 20 | 60 | Hexane | 27.5 | - |
| 32 | 50 | 20 | 60 | Hexane | 50 | - |
| 33 | 50 | 10 | 40 | Hexane | 5 | 65 |
| 34 | 50 | 10 | 40 | Hexane | 27.5 | 73 |
| 35 | 50 | 10 | 40 | Hexane | 27.5 | 73 |

## 3.2.3 DOE analysis

### 3.2.3.1 Model fitting

Table 3.3 contains the experiments and the resultant conversion to co-crystal calculated. These results were input into the MODDE software and analysis undertaken. The outcome was data fit to a multiple linear regression (MLR) model which overall did not show a good fit. Figure 3.6 shows the summary of fit with good $R^2$ (goodness of fit) and reproducibility but not satisfactory $Q^2$ (goodness of prediction) or model validity. Following further processing of the results which involved excluding two data points which did not fit the trend line (highlighted in Table 3.3), as advised in the software literature,[130] the fit of the data to the model was much improved as is evidenced by the updated summary of fit plot in Figure 3.7.

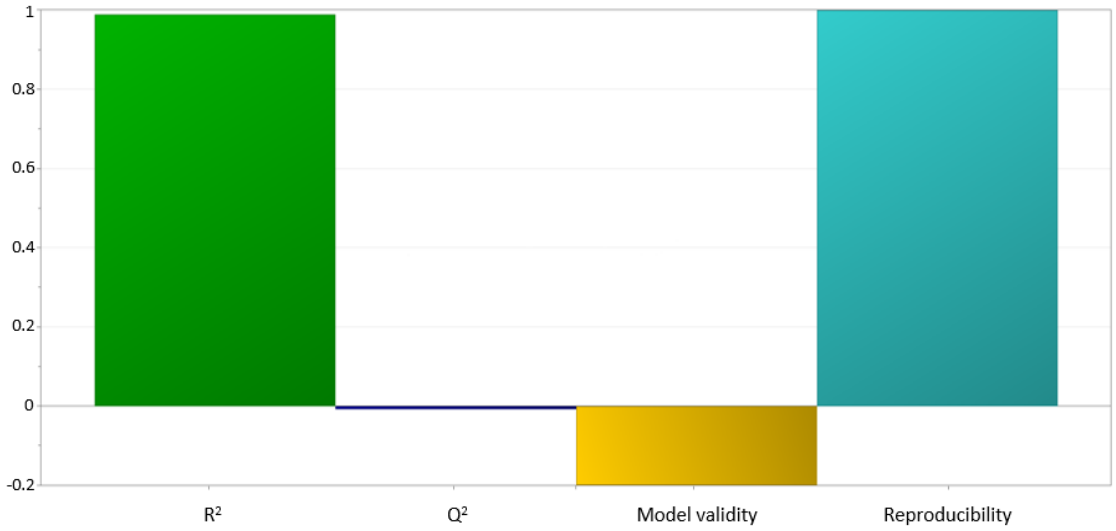


***Figure 3.6*** *Plot showing the summary of fit for the model after initial DOE analysis, with bars representing $R^2$ (green), $Q^2$ (dark blue), model validity (yellow) and reproducibility (light blue).*

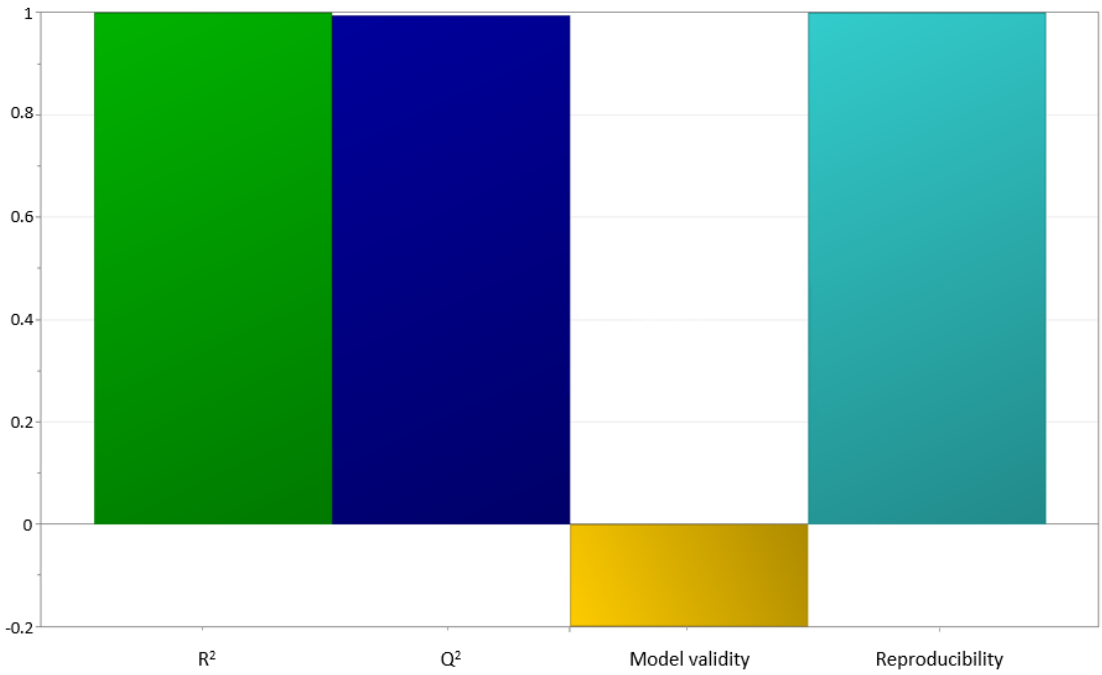


***Figure 3.7*** *Plot showing summary of fit for the model after further processing, with bars representing $R^2$ (green), $Q^2$ (dark blue), model validity (yellow) and reproducibility (light blue).*

The improvement in the fit of the model is demonstrated by the increased $Q^2$ seen in Figure 3.7. The model validity does not see the same improvement, however as the $R^2$ and $Q^2$ are high, the likelihood is that the lack of fit is artificial. This is a known issue with the chosen analysis method whereby an artificial error can lead to a model validity calculated to be low, ostensibly indicating a lack of fit, when all other indicators show excellent calculated values.[130]

### 3.2.3.2 Analysis and plot generation

Using the improved model, the following contour plots resulted from the data analysis.

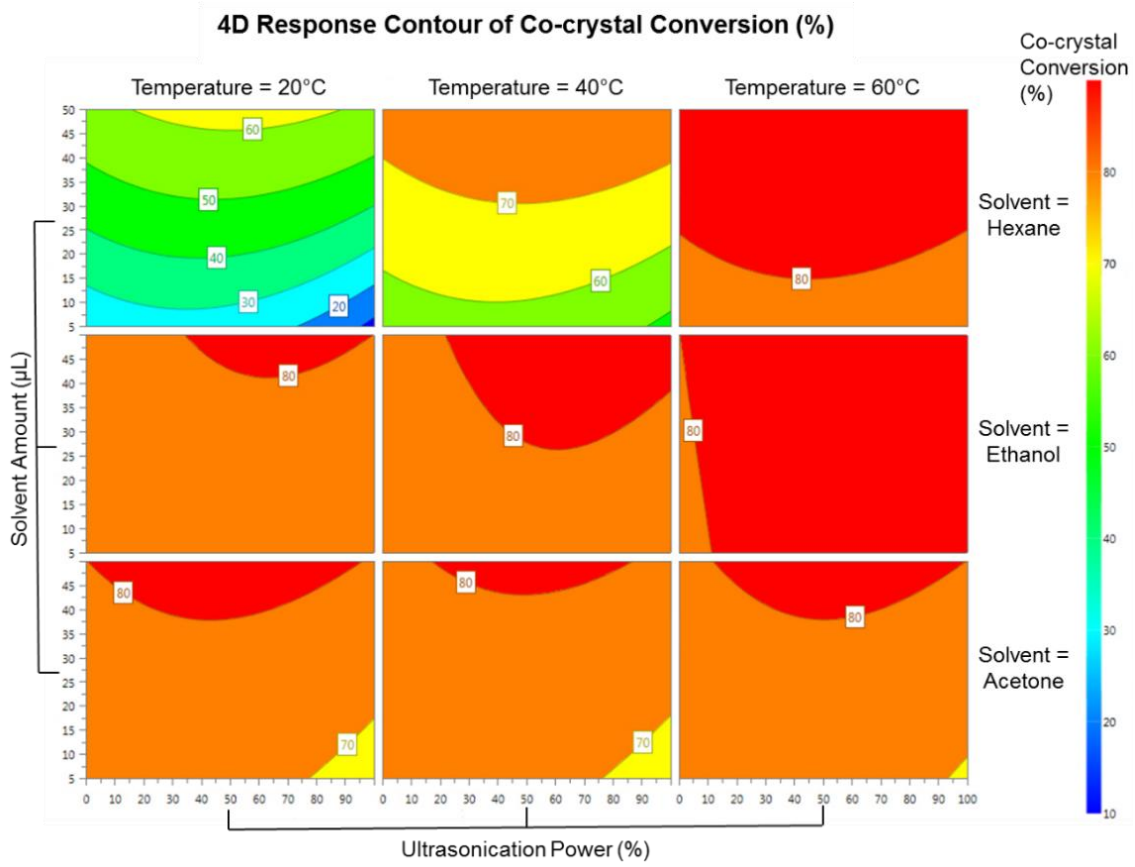


***Figure 3.8*** *A 4D contour plot showing the relationship between ultrasonication power, temperature, solvent and solvent amount on the conversion of starting material to co-crystal, with the ultrasonication time set at 20 minutes.*

The above 4D response contour plot (Figure 3.8) shows the effects of the variables on the conversion of starting materials to co-crystal, with the exception of ultrasonication time which is fixed at 20 minutes, the maximum value. By determining from the 4D contour plots the best settings for each variable the below 2D contour plot was produced (Figure 3.9), with the parameters ultrasonication time, temperature and solvent, set at their 'best' values i.e. those that led to the greatest conversion to the co-crystal from the starting components. This leads to the plot area showing the effect on response of the final two variables, ultrasonication power and solvent amount.

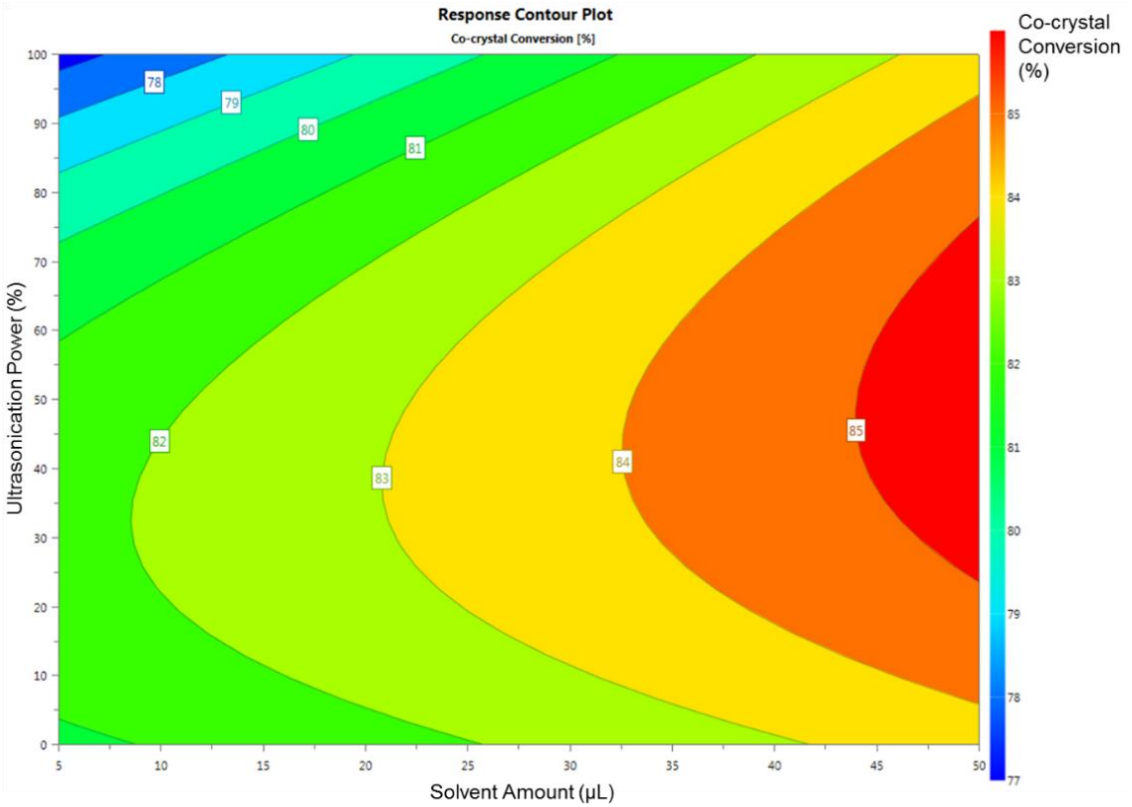


***Figure 3.9*** *A contour plot showing the relationship between ultrasonication power and solvent amount on the conversion of starting material to co-crystal when using acetone as the solvent, with all other parameters fixed at their optimum levels, showing the best possible response in the plot area. Ultrasonication time: 10 minutes, Temperature: 20°C, Solvent: acetone.*

The results as displayed in the 4D contour plot allow the observation that when using acetone or ethanol as the solvent, the settings of the other parameters did not significantly influence the response as a large conversion to co-crystal occurred at all of the values. Similarly, with a temperature of 60°C the same applies. There is however a general trend that increasing ultrasonication power and solvent amount show a higher conversion to co-crystal. When using hexane as the solvent the conversion to co-crystal is much more dependent on temperature and solvent amount. Optimum and 4D contour plots for each of the three solvents which graphically represent these findings are presented in Appendix 3.3.

The 2D contour plot allows 'best' values for the two variables which are not already fixed at their optimum to be determined. Using these values for all of the parameters should allow for the most conversion to co-crystal from starting material possible with the method used for screening.

### 3.2.4 Validation testing

Before applying this optimised screening process to APIs of interest, it was deemed prudent to perform some validation activities to ensure the physical screening methods used would produce the required outcomes i.e. detectable form change from the starting components.

#### 3.2.4.1 Method

A number of co-crystal systems had previously been found, in unpublished work (see Appendix 3.4), to be producible using ultrasonication. These materials were used to test the utility of the ultrasonication based well plate method with optimised parameters with material other than that which it was optimised. To be valid the optimised process should produce co-crystal from the starting materials, as to not achieve this would indicate that although optimised for the caffeine:malonic acid co-crystal the method would not be appropriate for other materials. The method used was to apply the ultrasonication screening process using the optimised parameters to a single sample for each of the systems used and measure the response by comparison of FTIR data. The spectra from the IR analysis are shown in Appendix 3.5. Multiple reference data for each system were not produced for the validation activities as the comparison of the IR data for the product of the method to a single spectrum of the physical mixture was decided to be sufficient to determine whether production of a new form had occurred.

### 3.2.4.2 Results

***Table 3.4*** *List of API and co-former pairs, which have previously been determined to form co-crystals using liquid assisted sonication, the stoichiometric ratio used and whether conversion to a new form was detected based on FTIR analysis. *Uncertain due to very subtle changes in spectra.*

| API | Co-former | Stoichiometric ratio | Detection of conversion based on IR |
|---|---|---|---|
| Caffeine | Oxalic acid | 2:1 | Yes* |
| Caffeine | Maleic acid | 2:1 | Yes* |
| Caffeine | Malonic acid | 2:1 | Yes |
| Caffeine | Oxalic acid | 1:1 | Yes |
| Caffeine | Maleic acid | 1:1 | Yes |
| Caffeine | Malonic acid | 1:1 | Yes |
| Caffeine | Glutaric acid | 1:1 | Yes |
| Sulfamethazine | Aspirin | 1:1 | Yes |
| Sulfamethazine | Benzoic acid | 1:1 | Yes |
| Ibuprofen | 4,4-bipyridine | 2:1 | Yes |
| Ibuprofen | 4,4-bipyridine | 1:1 | Yes |
| Ibuprofen | Nicotinamide | 1:1 | Yes |
| Trimethoprim | Sulfamethoxypyridizine | 1:1 | Yes |
| Carbamazepine | Saccharin | 1:1 | Yes |
| Carbamazepine | Nicotinamide | 1:1 | Yes |
| Paracetamol | 4,4-bipyridine | 1:1 | Yes |
| Aspirin | 4,4-bipyridine | 1:1 | Yes |

Having verified that the optimised settings determined in the initial screening optimisation were applicable to efficient detection, across a broad range of chemistries, of known co-crystals we then employed the screen to find a new co-crystal in order to undertake a second round of optimisation. To achieve this, model APIs: ROY and ornidazole, were chosen to represent a range of drug like chemistry, which was of interest to the project team. A co-crystal screen was then conducted in both systems. The experimental details, analysis and results of these screens are presented in Chapters 4 and 6; in summary, no co-crystals were discovered in the ROY screen however a total of 23 hit were found from the ornidazole screen.

### 3.2.5 Summary of initial optimisation

***Table 3.5*** *Optimised values determined for the investigated variables specific for each solvent.*

| Solvent | Sonication time (minutes) | Sonication power (% of full power) | Solvent volume (µl) | Temperature (°C) |
|---|---|---|---|---|
| Acetone | 10 | 50 | 50 | 20 |
| Ethanol | 10 | 65 | 50 | 20 |
| Hexane | 20 | 55 | 50 | 60 |

The screening method employed combines aspects of other methods to give a procedure that is effective at producing hits and is efficient for high-throughput screening. Considering the plate preparation where the API in solution is added to the co-former, assuming that the co-former has equal to or greater solubility in the solvent as the API then the drying stage is effectively an evaporative crystallisation step. This will not always be the case as it is very unlikely that all co-formers would have greater solubility than the API but even if the solubility was only half that of the API there is still the possibility of a 2:1 co-crystal forming. It is therefore possible that in some cases a co-crystal may form before the addition of the solvent drop and sonication steps. This second part of the method mimics solvent drop grinding (LAG) by simply replacing grinding, either by hand, or using a mill, with sonication using an ultrasonic probe. By adding the small amount of solvent to the 1:1 molar ratio of compounds it is more likely that the system will be in a favourable position of its ternary phase diagram to result in the formation of a co-crystal.[22] By combining these two steps there are effectively two chances for co-crystallisation to occur and this is perhaps a factor in the consistently high conversion to co-crystal seen in the DOE experiments and the successful detection of all hits in the validation testing.

## 3.3 Second optimisation

### 3.3.1 Methods

#### 3.3.1.1 General

The initial optimisation experiment and associated validation proved successful in indicating that the physical screening method employed was adequate to detect conversion of starting components to new, potentially co-crystalline, forms. It was also shown to be robust in terms of reproducibly causing a large percentage conversion to co-crystal over a wide range of settings for the variables investigated. This screening method was the best manual representation achievable to the automated screening process which was the ultimate target for optimisation. The automation involved a robotics platform as depicted in Figures 3.10 and 3.11. The process began by manually filling a vial with stock API solution and a deep-well plate with the required co-former stock solutions. These were placed in the appropriate place in the robot along with a quartz plate into which the materials would be dispensed. A method file with parameters for the experiment was input into the control computer and the program initiated. The robotic arm moved the plates to the required locations within the robot and the volumes of API and co-former solution dictated in the method file were dispensed into the 96-well plate by the dispensing needles. The solvents were evaporated and the solvent drop for 24 of the 96 well added followed by sonication of said wells. This last section was repeated a further three times until all 96 wells had been sonicated. The plate was finally moved to the optical microscopy area for imaging which is the last stage of the automated process.

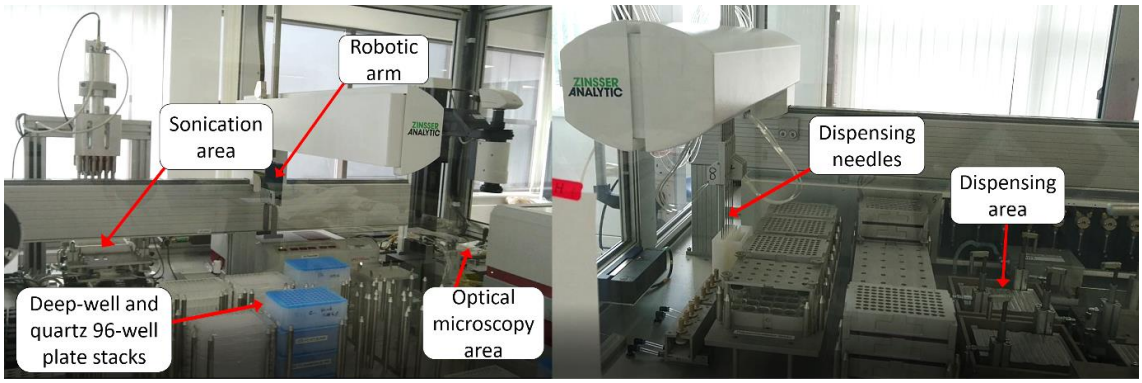


***Figure 3.10*** *Split image of robot with key areas labelled.*

***Figure 3.11*** *Photograph of sonication stage showing the 24-tip adapter in the wells of a quartz 96-well plate mid sonication.*

When access to the robotics platform was gained, a second optimisation was planned using the optimal parameters determined from the initial experiments as a guide from which to set appropriate limits. Four hits from the ornidazole screen (see Chapter 6 for full details of this screen) were used in this second experiment to attempt to broaden the range of representative compounds employed for the optimisation. Only four co-formers were chosen as the number was limited by the layout of the 96-well plates used as a compromise to be able to run the experiments as efficiently as possible by varying multiple factors per plate. The co-formers picked were based on the crystallisation propensity of the materials produced compared to other hits from the screen, with the chosen four taking less time to crystallise than others. Four solvents were used for this second optimisation, these were: acetonitrile, ethanol, tetrahydrofuran (THF) and toluene. These solvents were again chosen to cover a wide range of solvent properties and represent the three main categories of solvent: non-polar (toluene), polar protic (ethanol) and polar aprotic (acetonitrile and THF).

#### 3.3.1.2 DOE plan and plate layout

The plate diagram in Figure 3.12 displays the layout used for the second optimisation experiments. The colours of the well in columns one and two indicate the co-former used: orange for 5-nitroisophthalic acid, purple for oxalic acid, green for 2,4-dihydroxybenzoic acid

and blue for trimesic acid. The letters each well is labelled with identifies the solvent used: A for acetonitrile, E for ethanol, O for oxolane (tetrahydrofuran (THF)) and T for toluene. This layout meant that for each run in which sonication time and solvent volume were being altered, four co-formers and four solvents were also being included to produce a full factorial dataset. Theoretically columns three and four, and five and six could have been used to increase the number of co-formers investigated however given that the PXRD analysis stage of these experiments was still being carried out manually, this was not a feasible option due to the excessive increase in time required per experiment. The design of the robot and the software limitations alluded to in the introduction to this chapter, specifically that the software was written to follow a set method which did not inherently allow for the use of different solvents for the solvent-drop on one plate, meant that the maximum number of solvents able to be tested per plate was limited to four. The platform uses a 24-tip probe for sonication which sonicates one quadrant of the plate immediately after solvent addition. The plate is then returned for the addition of solvent to the next quadrant of wells before the process repeats until all four quadrants have had solvent added and sonication occurred. This gives rise to the layout of the solvent and co-former placements on the plate. The second half of the plate denoted by the yellow wells had the API to co-former ratio at 2:1. This was not a significant part of the experiment and an unfortunate waste of material but again a necessary limitation of using a platform which must adhere to strict validated processes in an industrial setting.

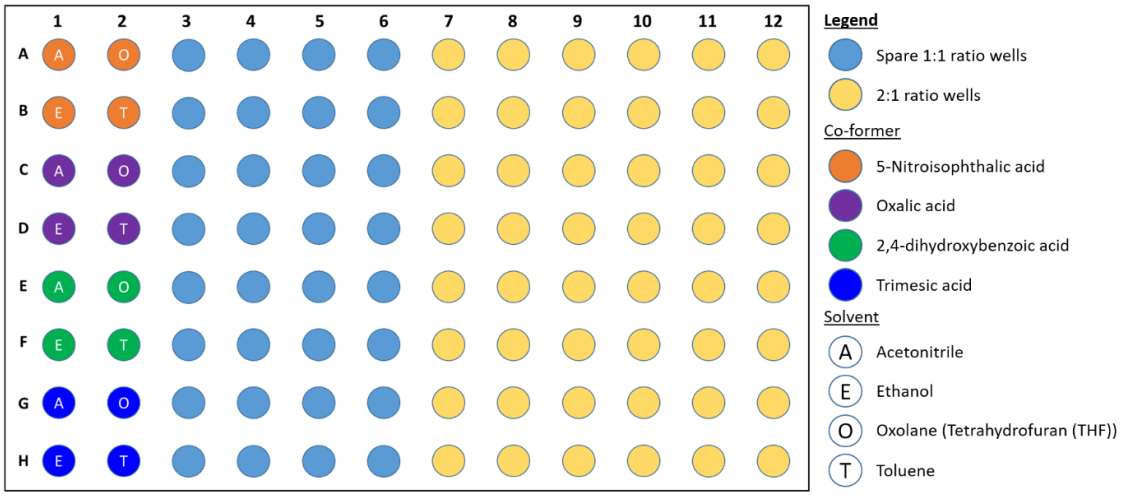


***Figure 3.12*** *Layout of the 96-well plates used for the second optimisation DOE experiments. Wells of interest are those in columns 1 and 2 and are colour coded by co-former and labelled by solvent.*

***Table 3.6*** *Experimental plan for the second optimisation listing the settings used for each of the seven runs.*

| Plate number | Sonication time | | Solvent volume | |
|---|---|---|---|---|
| | Minutes | DOE setting | µL | DOE setting |
| 1 | 6 | High | 10 | Low |
| 2 | 6 | High | 25 | High |
| 3 | 2 | Low | 25 | High |
| 4 | 2 | Low | 10 | Low |
| 5 | 4 | Mid | 17.5 | Mid |
| 6 | 4 | Mid | 17.5 | Mid |
| 7 | 4 | Mid | 17.5 | Mid |

### 3.3.1.3 Physical DOE experiments

Although the co-formers chosen were based on the crystallisation propensity of the product of the co-former:API material ('hit'), the time scale (and/or variation in scaling the method to the robotics platform) at which the second optimisation experiment was run and then analysed, resulted in only two of the four co-formers tested (5-nitroisophthalic acid and trimesic acid) crystallising within a sufficiently short time as to be analysed fully. One of the other co-former:API pairs (2,4-dihydroxybenzoic acid) showed minimal signs of crystallisation in most plates, however mainly sticky, possibly partially amorphous material was present at the at time of analysis and so suitable analysis was not possible. The products of the final co-former:API (oxalic acid) pair had not crystallised at all, or not sufficiently, on any of the plates in the given timescale and were excluded from any PXRD analysis. Figure 3.13 shows an example tiled image of the optical micrographs of each well of a 96-well plate (plate number 7 but representative of all plates) after the sonication stage of the automated process. It can be seen that the wells containing ornidazole and 5-nitroisophthalic acid or trimesic acid (see Figure 3.12 for reference) already show signs of significant crystallisation, whereas those containing ornidazole and 2,4-dihydroxybenzoic acid or oxalic acid do not. These images were taken immediately after the last sonication step and further time for crystallisation to occur was left before analysis, however it is evidence of the disparity in crystallisation propensity between the ornidazole:co-former systems. This highlights a potential flaw in the screening method from a practicality point of view. Unless automated PXRD plate reading is introduced then manual recovery of the sample from the plate is required and can be very difficult depending on the properties/behaviour of the material under investigation.

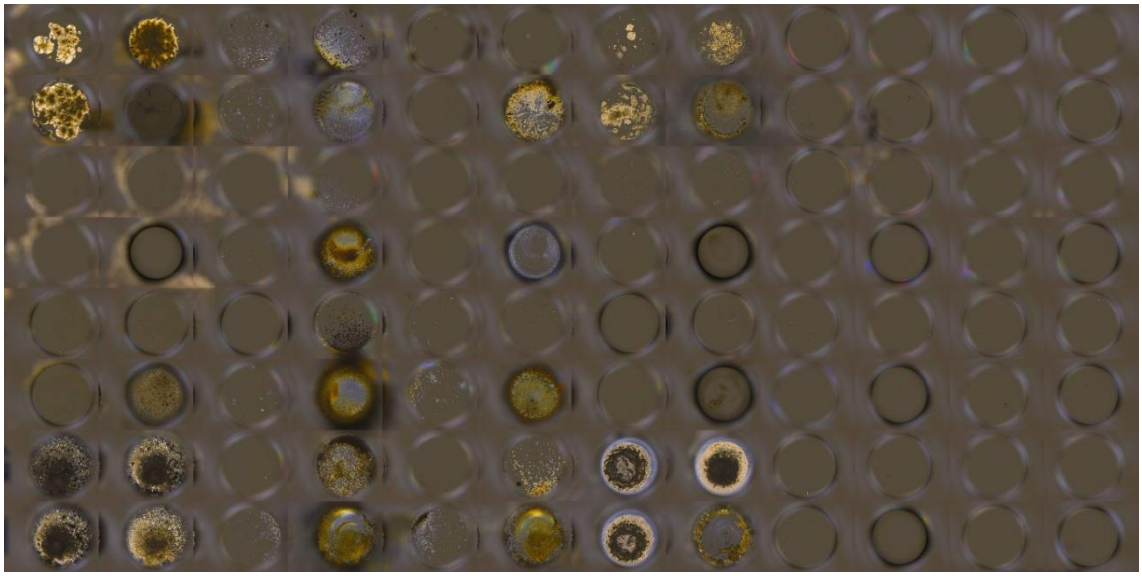

***Figure 3.13*** *Tiled image of the optical micrographs of each well of a 96-well plate (number 7) after the sonication stage of the automated process.*

A potential improvement would be to add a stage in the automated process on the robot, in which induced crystallisation is attempted by either temperature cycling or humidity cycling if sufficient crystallisation has not occurred by the time analysis is performed. This may not be as advantageous as it might seem initially though, as although more hits may be identified, that they were not produced easily and required further processing may be an indication that their manufacture could also require extensive processing in comparison to those more readily accessed co-crystals identified by the standard screening procedure i.e. the accessibility of a co-crystal phase is in and of itself a criterion for its selection for future development where all else is equal. This potential discrimination between relatively easy and difficult to form co-crystal phases could be seen as an advantage to the current screen – effective enough to identify the majority of readily accessed co-crystal systems and acting as an indicator that if a hit isn't detected then it is probably/possibly too hard to produce to be worthy of consideration for a pharmaceutical form for development.

#### 3.3.1.4 PXRD analysis

After running the experiments using the automated robotic process, the material from the wells was to be manually removed and prepared for PXRD analysis (plots of the PXRD patterns can be found in Appendix 3.6). The condition/physical state of the materials meant that all of the samples for two of the co-formers (oxalic acid and 2,4-dihydroxybenzoic acid) were excluded from analysis and all of the samples for the two co-formers in which sufficiently crystalline material was present (5-nitroisophthalic acid and trimesic acid) were analysed. This was carried out at AstraZeneca and so the standard method detailed in Chapter 2 was not followed. Instead

X-ray powder diffraction patterns were recorded on a Bruker D4 Endeavor diffractometer with intensities measured from 2° to 40° 2θ.

Subsequent to the discovery of the 1:1 ornidazole:5-nitroisophthalic acid co-crystal (see Chapter 6 for details), its crystal structure was determined and a powder pattern from this, calculated using Mercury, was used in this analysis to allow a comparison of peak data of experimental samples to take place. The comparison focused on a specific peak unique to the co-crystal and measurements of its intensity and shape were used for the comparative analysis. For the products of the screen containing ornidazole and trimesic acid, an identical approach was not possible as crystal structure data was not available. Therefore, several similar methods were attempted identifying key characteristics of a peak unique to the powder pattern of the 'hit' from the co-crystals screen, and comparing these between the power patterns from the optimisation experiment to allow analysis using MODDE and ultimately optimisation of process parameters.

The methods for the analysis of the ornidazole:trimesic acid samples included comparing net peak height (intensity) and the full width at half maximum (FWHM) between the individual sample patterns. A further comparison involved a combined function of the FWHM and peak height as an indicator of conversion to co-crystal/crystallinity and relative amount of the co-crystal as part of the whole sample. The equation used to calculate this value is shown below, with the 100,000 term simply to produce more convenient numbers.

$$FWHM{:}\,peak\ height\ value = \frac{FWHM \times 100{,}000}{net\ peak\ height}$$

This is of course affected by the quantity of sample recovered which differed between wells, but as this is an optimisation of the method as a whole, and not just a quantification of co-crystal producible, then the optimisation based on this FWHM-peak height derivative number takes into account the practicalities of the method in as much as where less sample is able to be retrieved from the well, the value for the FWHM-peak height will be proportionally lower. i.e.

Low amount of sample + low co-crystal content/crystallinity = higher value = bad
Low amount of sample + high co-crystal content/crystallinity = mid value = reasonable
High amount of sample + low co-crystal content/crystallinity = mid value = reasonable
High amount of sample + high co-crystal content/crystallinity = low value = good

These values depend on the parameters of the PXRD analysis and of the material under investigation but are designed to be compared between samples of the same system and therefore as low a value as possible would be the aim of the optimisation.

### 3.3.2 Results

***Table 3.7*** *Experimental plan showing measured FWHM as determined by PXRD analysis of experimental samples and FWHM as a percentage of that of the calculated powder pattern for ornidazole:5-nitroisophthalic acid samples.*

| Plate/Run | Well | Solvent | Solvent volume (µL) | Sonication time (minutes) | FWHM | FWHM as % of calculated |
|---|---|---|---|---|---|---|
| 4 | A1 | Acetonitrile | 10 | 2 | 0.141 | 136.9% |
| 1 | A1 | Acetonitrile | 10 | 6 | 0.084 | 81.6% |
| 4 | B1 | Ethanol | 10 | 2 | 0.107 | 103.9% |
| 1 | B1 | Ethanol | 10 | 6 | 0.122 | 118.4% |
| 4 | A2 | THF | 10 | 2 | 0.098 | 95.1% |
| 1 | A2 | THF | 10 | 6 | 0.139 | 135.0% |
| 4 | B2 | Toluene | 10 | 2 | 0.098 | 95.1% |
| 1 | B2 | Toluene | 10 | 6 | 0.120 | 116.5% |
| 3 | A1 | Acetonitrile | 25 | 2 | 0.141 | 136.9% |
| 2 | A1 | Acetonitrile | 25 | 6 | 0.120 | 116.5% |
| 3 | B1 | Ethanol | 25 | 2 | 0.134 | 130.1% |
| 2 | B1 | Ethanol | 25 | 6 | 0.104 | 101.0% |
| 3 | A2 | THF | 25 | 2 | 0.104 | 101.0% |
| 2 | A2 | THF | 25 | 6 | 0.118 | 114.6% |
| 3 | B2 | Toluene | 25 | 2 | 0.108 | 104.9% |
| 2 | B2 | Toluene | 25 | 6 | 0.111 | 107.8% |
| 5 | A1 | Acetonitrile | 17.5 | 4 | 0.102 | 99.0% |
| 6 | A1 | Acetonitrile | 17.5 | 4 | 0.116 | 112.6% |
| 7 | A1 | Acetonitrile | 17.5 | 4 | 0.123 | 119.4% |
| 5 | B1 | Ethanol | 17.5 | 4 | 0.125 | 121.4% |
| 6 | B1 | Ethanol | 17.5 | 4 | 0.107 | 103.9% |
| 7 | B1 | Ethanol | 17.5 | 4 | 0.147 | 142.7% |
| 5 | A2 | THF | 17.5 | 4 | 0.138 | 134.0% |
| 6 | A2 | THF | 17.5 | 4 | 0.108 | 104.9% |
| 7 | A2 | THF | 17.5 | 4 | 0.118 | 114.6% |
| 5 | B2 | Toluene | 17.5 | 4 | 0.120 | 116.5% |
| 6 | B2 | Toluene | 17.5 | 4 | 0.107 | 103.9% |
| 7 | B2 | Toluene | 17.5 | 4 | 0.133 | 129.1% |

***Table 3.8*** *Experimental plan showing measured FWHM and net peak height as determined by PXRD analysis of experimental samples and a calculated derivative of FWHM and net peak height for ornidazole:trimesic acid samples.*

| Plate/Run | Well | Solvent | Solvent volume (µL) | Sonication time (minutes) | FWHM | Net peak height | FWHM: peak height value |
|---|---|---|---|---|---|---|---|
| 4 | G1 | Acetonitrile | 10 | 2 | 0.076 | 1757.3 | 4.32 |
| 1 | G1 | Acetonitrile | 10 | 6 | 0.064 | 1021.5 | 6.27 |
| 4 | H1 | Ethanol | 10 | 2 | 0.082 | 380.6 | 21.54 |
| 1 | H1 | Ethanol | 10 | 6 | 0.064 | 782.2 | 8.18 |
| 4 | G2 | THF | 10 | 2 | 0.077 | 282.0 | 27.30 |
| 1 | G2 | THF | 10 | 6 | 0.069 | 411.0 | 16.79 |
| 4 | H2 | Toluene | 10 | 2 | 0.050 | 180.3 | 27.73 |
| 1 | H2 | Toluene | 10 | 6 | 0.073 | 1322.1 | 5.52 |
| 3 | G1 | Acetonitrile | 25 | 2 | 0.072 | 587.7 | 12.25 |
| 2 | G1 | Acetonitrile | 25 | 6 | 0.071 | 575.2 | 12.34 |
| 3 | H1 | Ethanol | 25 | 2 | 0.074 | 251.2 | 29.46 |
| 2 | H1 | Ethanol | 25 | 6 | 0.083 | 3262.9 | 2.54 |
| 3 | G2 | THF | 25 | 2 | 0.076 | 120.6 | 63.02 |
| 2 | G2 | THF | 25 | 6 | 0.071 | 1064.7 | 6.67 |
| 3 | H2 | Toluene | 25 | 2 | 0.124 | 725.6 | 17.09 |
| 2 | H2 | Toluene | 25 | 6 | 0.123 | 1243.7 | 9.89 |
| 5 | G1 | Acetonitrile | 17.5 | 4 | 0.084 | 442.3 | 18.99 |
| 6 | G1 | Acetonitrile | 17.5 | 4 | 0.161 | 496.1 | 32.45 |
| 7 | G1 | Acetonitrile | 17.5 | 4 | 0.138 | 577.2 | 23.91 |
| 5 | H1 | Ethanol | 17.5 | 4 | 0.093 | 314.0 | 29.62 |
| 6 | H1 | Ethanol | 17.5 | 4 | 0.114 | 375.8 | 30.34 |
| 7 | H1 | Ethanol | 17.5 | 4 | 0.110 | 400.3 | 27.48 |
| 5 | G2 | THF | 17.5 | 4 | 0.094 | 272.5 | 34.50 |
| 6 | G2 | THF | 17.5 | 4 | 0.079 | 465.0 | 16.99 |
| 7 | G2 | THF | 17.5 | 4 | 0.085 | 521.9 | 16.29 |
| 5 | H2 | Toluene | 17.5 | 4 | 0.098 | 322.1 | 30.43 |
| 6 | H2 | Toluene | 17.5 | 4 | 0.135 | 593.4 | 22.75 |
| 7 | H2 | Toluene | 17.5 | 4 | 0.112 | 771.8 | 14.51 |

Data viewer software (PANalytical) was used to automatically pick the peaks with manual verification and for samples where this was not possible, manual picking of peaks was undertaken (highlighted in Table 3.8).

### 3.3.3 DOE analysis

For DOE analysis FWHM as a percentage of that of the calculated powder pattern for ornidazole:5-nitroisophthalic acid was used as the outcome measured for ornidazole:5-nitroisophthalic acid samples and FWHM, net peak height and the caluclated FWHM:peak height value were all used in separate analyses for the ornidazole:trimesic acid samples.

### 3.3.3.1 Model fitting

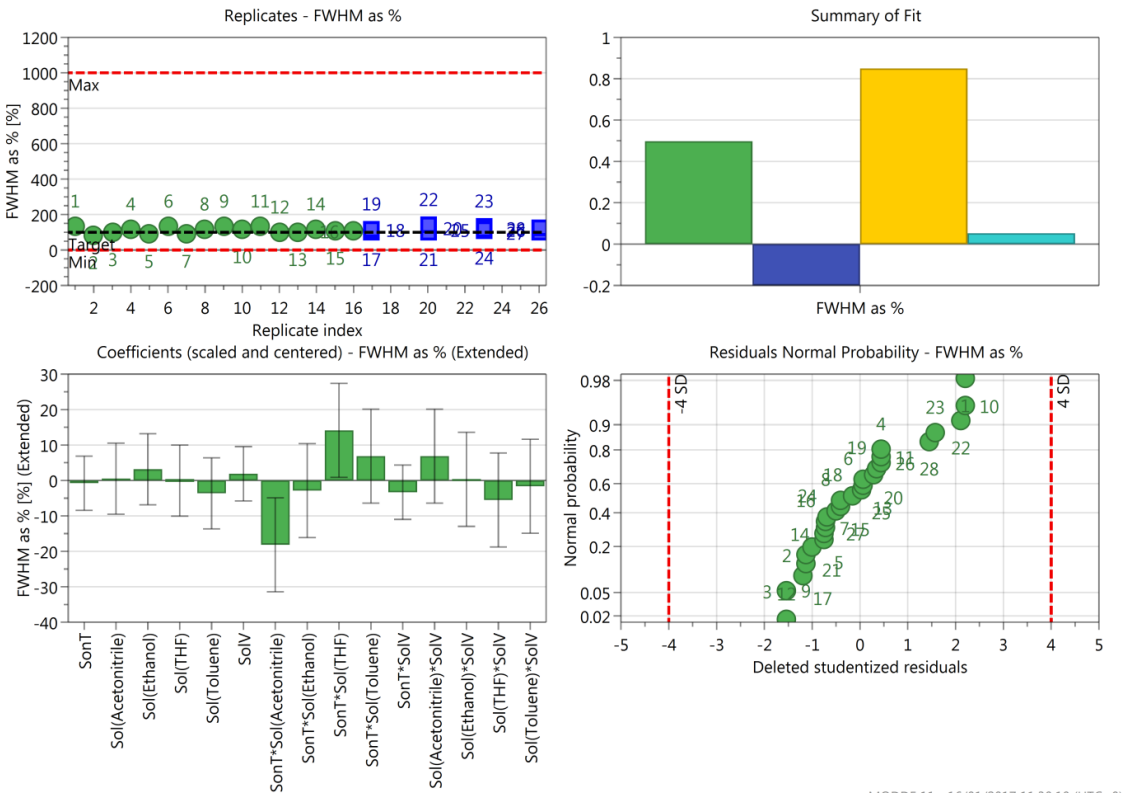


***Figure 3.14*** *Plots detailing model summary for ornidazole:5-nitroisophthalic acid results. Clockwise from top left: Replicates (results of repeated experiments shown by blue squares), summary of fit ($R^2$ (green), $Q^2$ (dark blue), model validity (yellow) and reproducibility (light blue)), residuals and coefficients.*

The results from the experiments show that conversion to co-crystal occurred in all cases for the ornidazole:5-nitroisophthalic acid samples. Figure 3.14 displays the model summary for this data and it is apparent that the variation in measured outcome from the experiments is very small relatively between the entire set of samples. This has led to a model from which gleaning useful parameter optimisation is not possible as any perceived possible improvements are not statistically significant. The same is true for the analysis of the ornidazole:trimesic acid data, in that conversion from starting components was seen in all of the samples to a relatively similar degree and as such the model's ability to produce optimisation of any significance is diminished. Model summary plots from the analysis of the ornidazole:trimesic acid data are presented in Appendix 3.7.

### 3.3.3.2 Analysis and plot generation

Due to none of the DOE analysis for the second optimisation experiments leading to models with statistical significance, any attempt to use the models to influence parameter value optimisation would be unfounded. That all of the samples showed easily detectable conversion from starting materials and within a similar enough range that meaningful models could not be produced from the data suggests that further optimisation may not be necessary and that the current process is at a suitable level of optimisation. This section then is a purely academic tangent into the type of optimisation that was envisioned may have resulted from the second optimisation experiment.

Using the data from the ornidazole:5-nitroisophthalic acid samples, both FWHM and peak height were set as measured outcomes and a model produced which inevitably was not significant. Regardless, a plot was produced to show how using the DOE analysis, it is possible to determine the optimal parameters for certain variables so that two outcomes can be maximised. In this case setting sonication time to 6 minutes and solvent volume to 25µl would give high peak height but low FWHM. It is therefore necessary to compromise the outright maximum of both peak height and FWHM to be able to set the parameters so that reasonable values of each are achieved. The exact point at which parameter must be set to maximise both outcomes, assuming they are of equal importance, is shown in Figure 3.15.

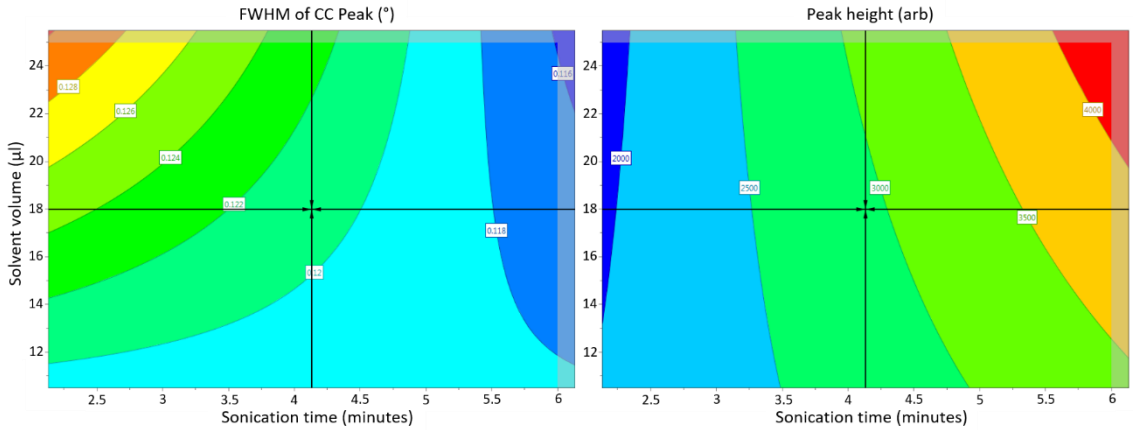


***Figure 3.15*** *Response contour plots for FWHM and peak height from the orindazole:5-nitroisophthalic acid data showing the settings at which both outcomes are maximised. Note: this plot was produced from a statistically insignificant model, is for illustration of the concept only and was not used to inform optimisation.*

### 3.3.4 Summary of second optimisation

Similarly to the initial optimisation, to which this second optimisation shared a very comparable procedure, a combination of aspects from different screening techniques are incorporated. Unlike the initial method where API in solution was added to dry co-former, in the second method implemented on the robot, both the API and co-formers were added to the wells in solution. In the case of the four co-formers used in this work the same solvent, methanol, was used to make the solutions of the API and all co-formers. This may not always be the case though as if the API and any of the co-formers are not sufficiently soluble in the same solvent then different solvents would need to be used. This could lead to a situation where this first, plate preparation step of the procedure, is effectively an antisolvent crystallisation step. Again, this is a well-documented method of co-crystal production[131] and may be a contributing factor to the expected efficacy of the screening method used for the second optimisation.

## 3.4 Conclusions

The first section of this chapter dealt with the initial optimisation of a manual co-crystal screen mimicking an automated procedure. The result of the experiments enabled the determination of a set of optimised values for each of the variables to be used with three different solvents. This outcome was of great importance for much of the work presented in the following chapters as it afforded an efficient and robust process for co-crystal screening employing the available resources. The latter section of the chapter involving the second optimisation experiment of the automated process can be seen as somewhat of a validation of the outcome of the initial optimisation and its scalability to a higher throughput, more efficient process. No further optimisation of the variables was achievable with the parameters used and the analysis method employed. As the detection rate for the co-crystal of the samples analysed was maximal, this serves only to confirm the effectiveness and suitability of the overall method. Using the DOE approach, it may still be possible to improve the efficiency of the process in some ways, such as reducing material use. This may require the investigation of different factors and use of alternative analysis techniques which could detect greater variation in the measured outcomes to allow for more meaningful variable optimisation.

# Chapter 4 – ROY synthesis, co-crystal screen and discovery and analysis of a co-amorphous binary material

## 4.1 Introduction

Having developed and optimised a co-crystal screen in the previous chapter, the next step was to put the optimised method into practice and perform a screen on a novel material, i.e. a compound for which there were no reported co-crystals and which had not previously been screened. This chapter presents this work and includes a co-crystal screen of ROY, findings from the analysis and the investigation into an interaction which stabilised the binary composition as a co-amorphous material.

ROY (5-methyl-2-[(2-nitrophenyl)amino]-3-thiophenecarbonitrile) is a highly polymorphic compound and is a precursor in the synthesis of the antipsychotic drug olanzapine. It is so named due to the red, orange and yellow crystal colours of its polymorphs and has been reported to exist in at least 10 polymorphic forms.[132] With seven of these forms structurally characterised, it was until recently,[133,134] the compound with the most polymorphs recorded in the Cambridge Structural Database(CSD).[135] Due to its drug-like characteristics, being a precursor to and thus sharing some similar structure to a marketed drug, as well as its highly polymorphic nature, ROY was chosen as a model compound upon which to implement the optimised co-crystal screen.

Availability of ROY commercially is limited and small quantities in the range of 10mg can cost hundreds of pounds. In order to carry out a full co-crystal screen we would require a significant amount of API, in the region of 5g, and so purchasing of ROY was not a feasible option. Although within my work this was inconvenient, this problem highlights why the optimisation of screening processes to improve efficiency is relevant. Limited and expensive API is often an issue in the early stages of drug development and any way to reduce the amount required, such as by making screening processes more efficient, is paramount. The development of microfluidics to further reduce the required API amount compared to well plate screening is an example of this trend.[136,137] The acquisition and deployment of a new technology in industry can take many years and although microfluidic co-crystal screening may be implemented in the future, the currently accessible high-throughput co-crystal screening processes use the robotic well plate platform, hence its use in this work.

In order to achieve the required quantity of ROY the decision was taken to synthesise it in house. To achieve this a synthetic route to produce ROY was found in the literature[138] and, as the starting materials were accessible financially and readily available, synthesis of a sufficient quantity of ROY for screening was undertaken.

## 4.2 Synthesis of ROY

### 4.2.1 Method

The synthesis of ROY was conducted with the assistance of Dr Jonathan Harburn (Durham University), and followed a two-step process as detailed in the patent for olanzapine,[138] with further guiding information found in a PhD thesis.[139]

#### 4.2.1.1 Step 1

An amount of 11.68g (0.364mol) sulfur, 25.33g (31.5ml, 0.436mol) propionaldehyde and 75ml DMF were placed in a flange-necked flask fitted with an overhead stirrer, air condenser, thermometer, and dropping funnel. Triethylamine (30.9ml, 0.222mol) was added dropwise over 35 minutes to the cooled stirred reaction mixture whilst maintaining the pot temperature between -5 and 10°C with an ice-bath. After addition, the pot was allowed to warm up to 20°C over 45 minutes, whilst keeping the mixture well stirred. A solution of 24.1g (0.365mol) malononitrile in 50ml dimethylformamide (DMF) was added drop-wise over 60 minutes keeping the pot temperature between 8-20°C throughout the addition. Once complete the mixture was stirred at 15-20°C for a further 45 minutes then sampled for thin layer chromatography (TLC). Having confirmed, from TLC, that a new chemical species was present, the mixture was then poured into a beaker containing approximately 600ml ice/water with stirring to cause the required product to precipitate for around 1 hour. After 10 minutes, the stirrer was switched off and the solid allowed to settle. The aqueous liquor was decanted away and the solid isolated by filtration. The solid was left to dry for approximately 65 hours. The isolated solid was further washed with 215ml deionised water, then subjected to a further drying cycle overnight *in vacuo* at 70-75°C to give 2-amino-5-methylthiophene-3-carbonitrile.

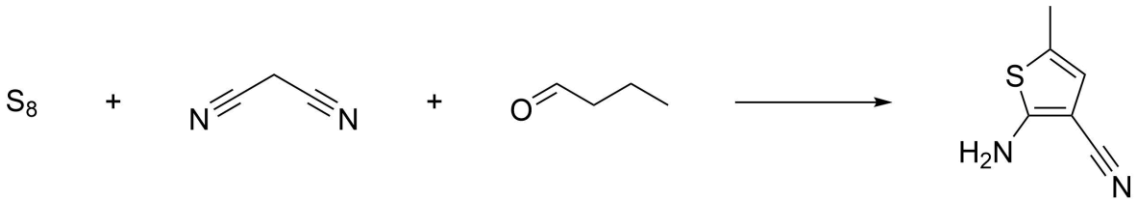


***Figure 4.1*** *A schematic diagram of the first step of ROY synthesis.*

#### 4.2.1.2 Step 2

A solution of 32.05g (0.227mol) 2-fluoronitrobenzene and 31.36g (0.227mol) 2-amino-5-methylthiophene-3-carbonitrile in 285ml dry tetrahydrofuran (THF) was added dropwise to a stirred slurry of 16.36g (0.682mol) sodium hydride in 57ml dry THF under nitrogen. The mixture was stirred at 25°C for 24 hours, poured onto cracked ice and extracted into dichloromethane (DCM) (3 x 570ml). The combined extracts were washed with 2M HCl (2 x 225ml) and water (2 x 225ml), dried over magnesium sulfate and the solvent removed under reduced pressure using a rotary evaporator. The residue was crystallised from ethanol by evaporation to give ROY.

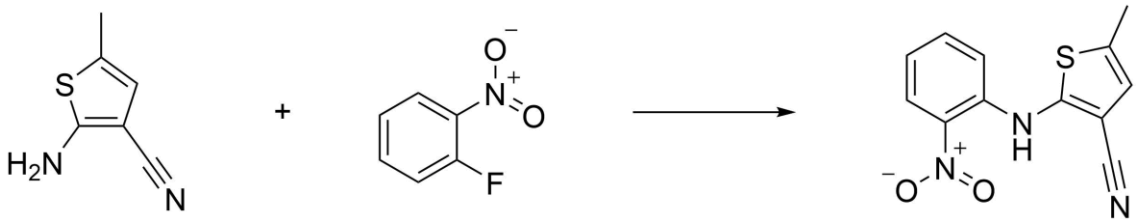


***Figure 4.2*** *A schematic diagram of the second step of ROY synthesis.*

### 4.2.2 Analysis of synthesised ROY

Samples from batch one were analysed by $^{1}$H NMR (Figure 4.3), $^{13}$C NMR (Figure 4.4) and mass spectrometry (Figure 4.5) to confirm the identity of the synthesised material as ROY. The peaks observed in the $^{1}$H NMR spectrum integrate to represent the nine hydrogen atoms, as present in the ROY molecule. There are 12 peaks detected in the $^{13}$C NMR spectrum also representative of the 12 unique carbon atoms of ROY. The peaks observed in both NMR spectra correspond to those in a previously reported synthesis of ROY by Hartwig *et.al*.[140]

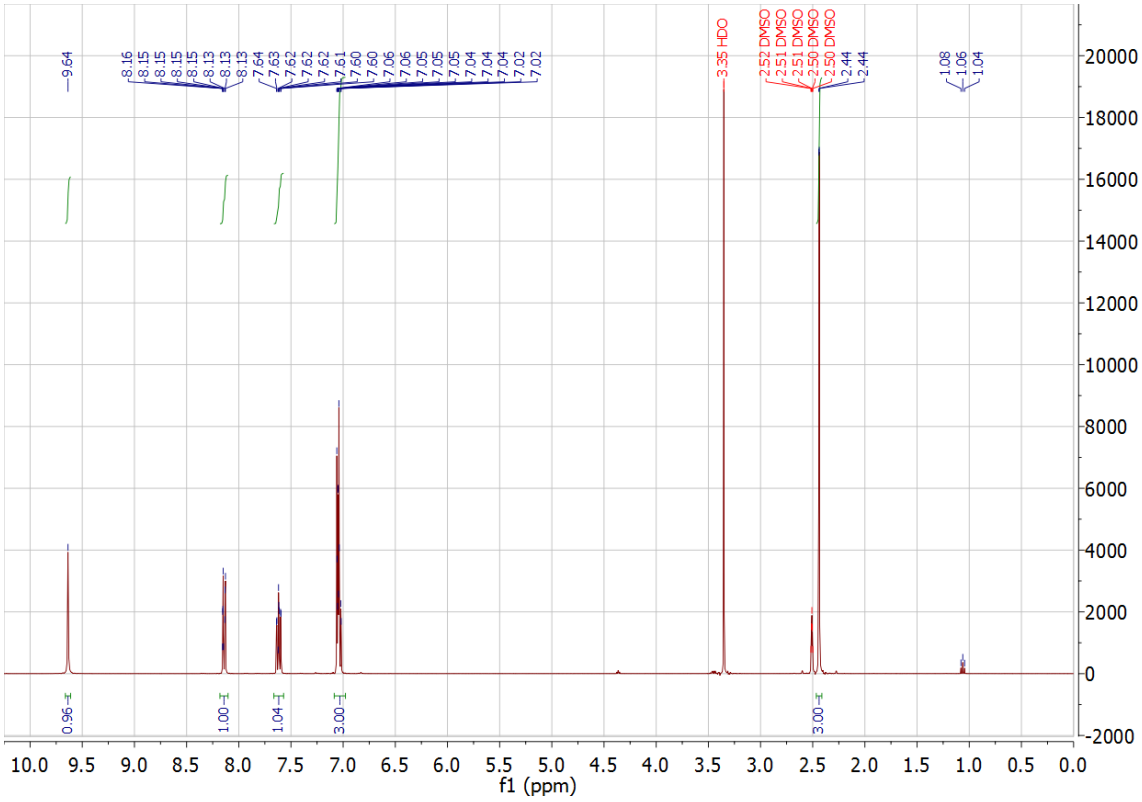


***Figure 4.3*** *$^{1}$H NMR spectrum of synthesised ROY.*

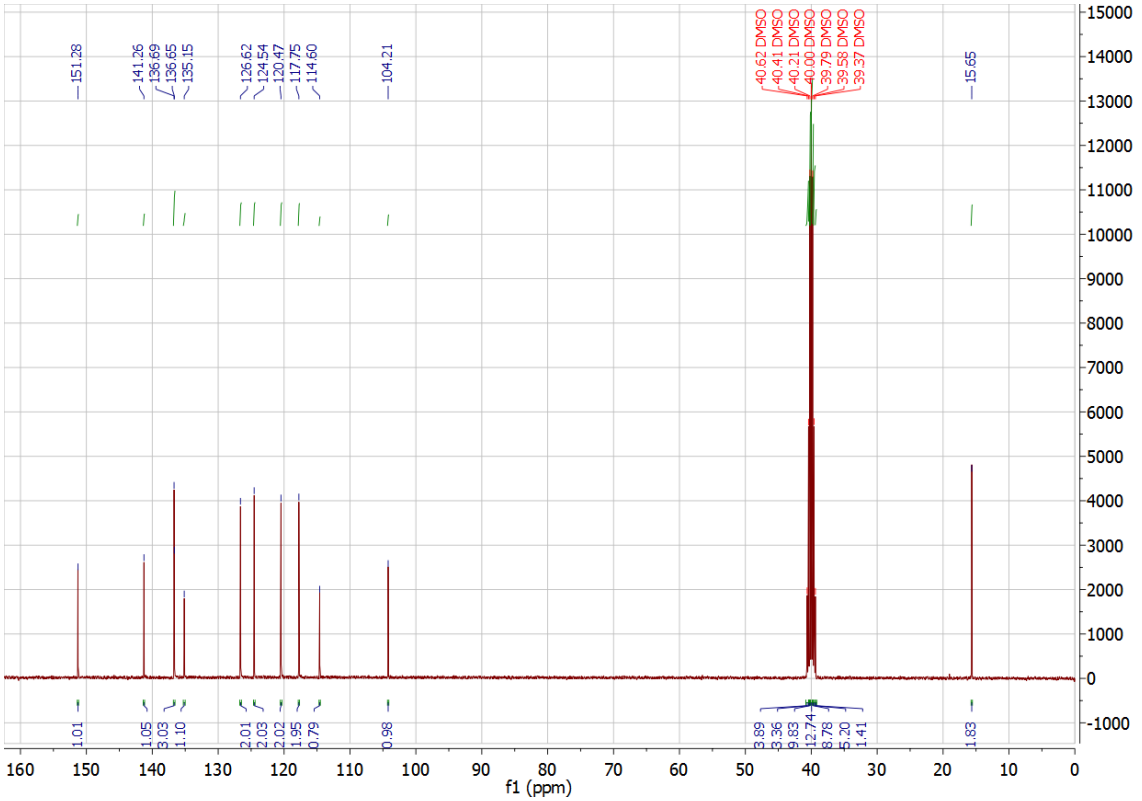


***Figure 4.4*** *$^{13}$C NMR spectrum of synthesised ROY.*

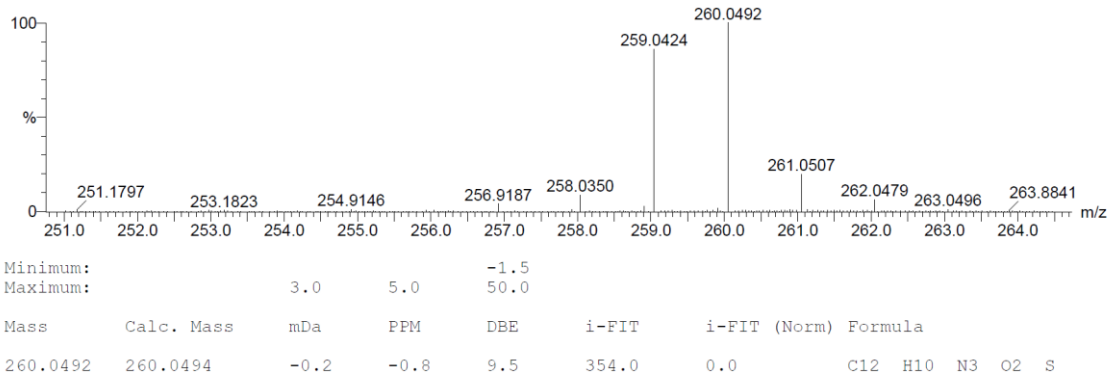


| | | | | | | | |
|---|---|---|---|---|---|---|---|
| Minimum: | | | | -1.5 | | | |
| Maximum: | | 3.0 | 5.0 | 50.0 | | | |
| Mass | Calc. Mass | mDa | PPM | DBE | i-FIT | i-FIT (Norm) | Formula |
| 260.0492 | 260.0494 | -0.2 | -0.8 | 9.5 | 354.0 | 0.0 | C12 H10 N3 O2 S |

***Figure 4.5*** *Mass spectrum of synthesised ROY, focused around the molecular ion peak.*

The calculated exact mass of isotopically pure ROY ($C_{12}H_9N_3O_2S$) is 259.041549. Due to the electrospray ionisation (ESI) method being used in positive mode, the $[M+H]^+$ peak is observed at 260.0492 and $[M]^+$ at 259.0424 m/z. The NMR and mass spectroscopy analysis of batch one of synthesised ROY in combination with the PXRD analysis, detailed below, provide evidence of its identity as ROY.

The ability of ROY to crystallise in multiple polymorphic forms simultaneously, due to the small differences in enthalpy between the forms, was observed in the crystallisation phase of the procedure. A number of polymorphic forms were recovered from consecutive crystallisations and collected into vials, a photograph of these is shown in Figure 4.6.

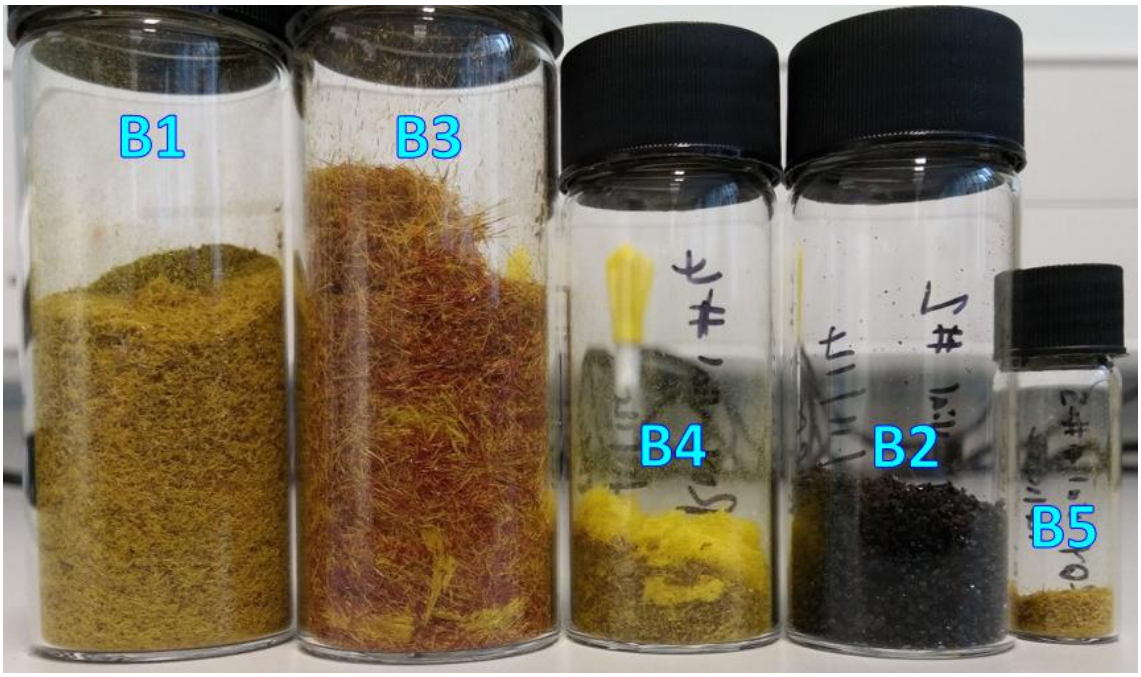


***Figure 4.6*** *Synthesised ROY in vials. Each batch was collected from consecutive crystallisations from the one synthesis. The batches are, from left to right: one, three, four, two and five.*

Only material from batches one and three were used for work presented in this thesis. There are clear visual differences between all batches which can be attributed to the multiple polymorphic forms of ROY present with the exception of batches one and five in which the same polymorph is observed, and batch two. Batch two does not resemble any of the discovered forms of ROY and therefore might be suspected to be either a new polymorph or not in fact ROY at all. However, when crushed, the appearance of batch two is similar to other batches in that yellow crystals are present and the PXRD pattern obtain matches that of the calculated pattern of polymorph Y[141] of ROY (Figure 4.7).

It is therefore likely that the appearance of the batch two material is due to a fine coating of impurity on small 'pellets' of polymorph Y of ROY. The PXRD patterns for batches one and three of the synthesised ROY contain all of the peaks in the calculated pattern of polymorph Y, however the patterns of both batches also contain the peaks present in ROY polymorph R to differing extents. Only a very small peak at approximately 7.5° 2θ identifies batch one as containing a detectable quantity of polymorph R whereas the pattern for batch three contains much more prominent peaks associated with polymorph R indicating that it contains a much more even mixture of both polymorphs Y and R, as apparent by its visual appearance.

The reference patterns for the known polymorphs of ROY were calculated using the CCDC's Mercury software,[142] from the CSD entry codes: QAXMEH (ON), QAXMEH01 (Y), QAXMEH02 (R), QAXMEH03 (OP), QAXMEH04 (YN), QAXMEH05 (ORP) and QAXMEH12 (YT04). PowDLL software[143] was used to convert the data files to match those used for the experimentally obtained samples to facilitate the plotting of diffractograms.

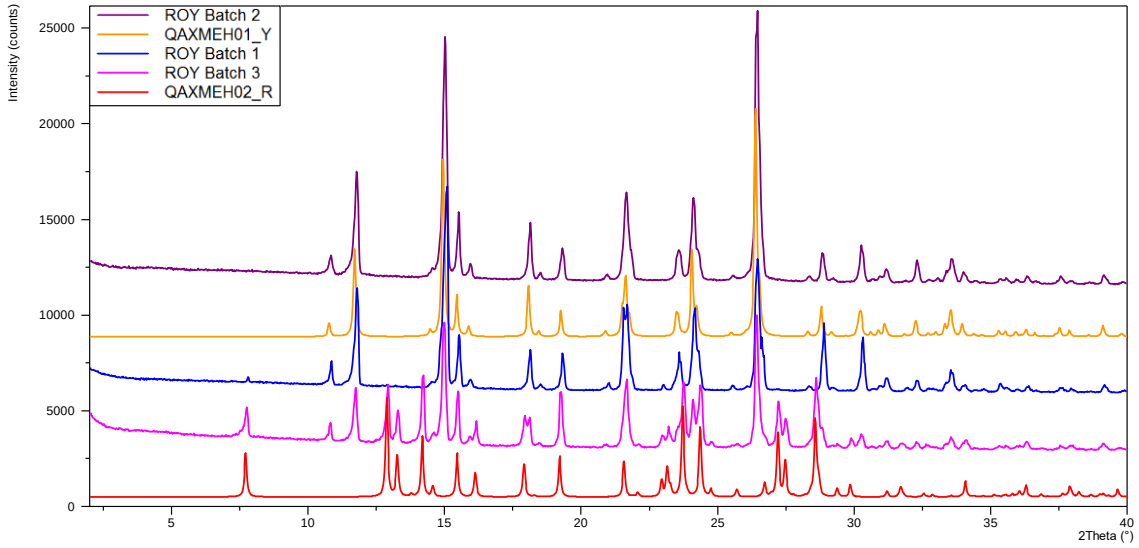


***Figure 4.7*** *Powder patterns of batches one, two and three of synthesised ROY and calculated powder patterns of known ROY polymorphs Y and R for comparison.*

Samples from both batch one and three were analysed by DSC (Figure 4.8) and the melting points measured compared to the literature values for ROY polymorphs (Table 4.1).

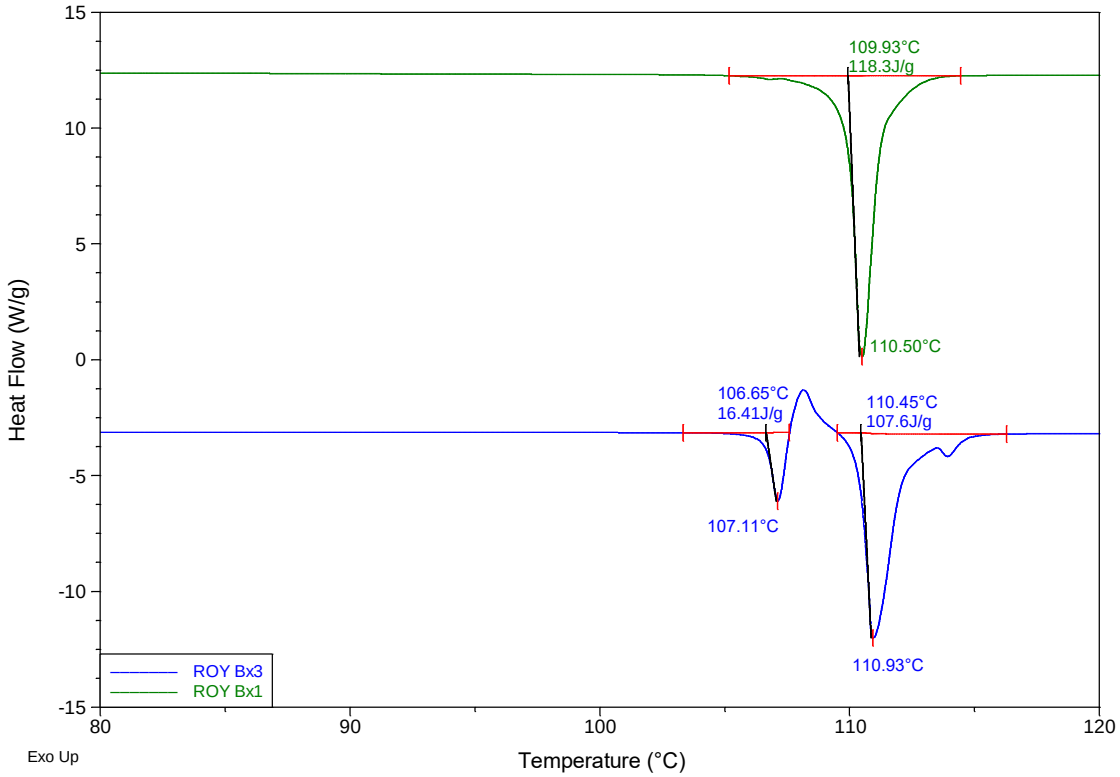


***Figure 4.8*** *DSC traces for batches one (green) and three (blue) of synthesised ROY.*

Figure 4.8 shows the DSC curves produced for samples from two of the batches of synthesised ROY using the standard ramp method detailed in Chapter 2. On heating of the batch one sample, there is a large endothermic peak with an onset temperature of 109.9°C indicating melting of the sample. This melting point value is commensurate with the literature melting point of polymorph Y of ROY, which is the most thermodynamically stable form under ambient conditions.[132] Heating of the batch three sample in the same manner gives rise to a more complex DSC trace. There is an initial small endothermic peak with an onset temperature of 106.7°C, followed by an exothermic peak and a final larger endothermic peak with a 110.5°C onset. The likely explanation for these events is the melting of polymorph R contained within the sample, as identified by PXRD (Figure 4.7) and its melting point fitting that of the endothermic peak (Table 4.1). Following this, a conversion of polymorphic form by crystallisation from the now molten ROY to a second polymorph (Y) which then melted at a higher

temperature. This is not uncommon in polymorphic systems[144] and is known as a melt recrystallisation melt event.

***Table 4.1*** *Selected properties of ROY polymorphs.*[132]

| Form | ORP | YN | R | YT04 | Y | OP | ON |
|---|---|---|---|---|---|---|---|
| **Description** | Orange-red plate | Yellow needle | Red prism | Yellow prism | Yellow prism | Orange plate | Orange needle |
| **Melting point (°C)** | 97 | 99 | 106.2 | 106.9 | 109.8 | 112.7 | 114.8 |

## 4.3 Co-crystal screen

The optimised method from the previous chapter was used for the co-crystal screen of ROY. The initial step was to use COSMOtherm[101] to predict the most likely co-formers to co-crystallise with ROY by performing calculations on a list of potential co-formers. This process is discussed in more detail in the method section below. After obtaining the results from this computational pre-screen, any of the top 48 predicted co-formers (Table 4.2) which were not already in stock, were obtained and the physical screen carried out using the parameters determined by the optimisation experiments. An issue in acquiring all of the required co-formers was caused by a lack of availability of one co-former which was ranked number 17 (*p*-vinylphenol) and was rectified by substituting it with the co-former ranked number 49 (2-oxo-3-phenylpropionic acid) at the appropriate place in the list.

***Table 4.2*** *COSMOtherm rank order of co-formers used for ROY screen (48 selected from the top 49 predicted using COSMOtherm with one excluded due to availability (p-vinylphenol #17)).*

| Rank | Co-former | Rank | Co-former |
|---|---|---|---|
| 1 | Pentafluorophenol | 25 | Indole |
| 2 | Acesulfame | 26 | 3-Hydroxy-2-naphthoic acid |
| 3 | Oxalic acid | 27 | 2,5-Xylenol |
| 4 | Quercetin | 28 | Salicylic acid |
| 5 | Sulfamic acid | 29 | *m*-Nitrobenzoic acid |
| 6 | 3,5-Dinitrobenzoic acid | 30 | Skatole |
| 7 | 1,2,3-Trihydroxybenzene | 31 | Hydroquinone |
| 8 | 2,4-Dihydroxybenzoic acid | 32 | Fumaric acid |
| 9 | 5-Nitroisophthalic acid | 33 | Methyl gallate |
| 10 | Gallic acid | 34 | *p*-Cresol |
| 11 | *tert*-Butylhydroquinone | 35 | Methanesulfonic acid |
| 12 | 1-Hydroxy-2-naphthoic acid | 36 | *p*-Ethylphenol |
| 13 | Catechol | 37 | 3-Hydroxybenzoic acid |
| 14 | 4-Hexylresorcinol | 38 | 6-Hydroxy-2-naphthoic acid |
| 15 | 5-Chlorosalicylic acid | 39 | Ethanesulfonic acid |
| 16 | Resorcinol | 40 | Allocitric acid |
| 17 | 3,5-Dihydroxybenzoic acid | 41 | *p-tert*-butylphenol |
| 18 | Orcinol | 42 | 3,4-Xylenol |
| 19 | 2,5-Dihydroxybenzoic acid | 43 | 2,6-Xylenol |
| 20 | *o*-Cresol | 44 | Citric acid |
| 21 | 3,4-Dihydroxybenzoic acid | 45 | Etidronic acid |
| 22 | Thymol | 46 | 4-Hydroxybenzoic acid |
| 23 | Phenol | 47 | *o*-Phenylphenol |
| 24 | Trimesic acid | 48 | 2-Oxo-3-phenylpropionic acid |

## 4.3.1 Methods

### 4.3.1.1 Computational pre-screen

The method used to produce the list of most favourable potential co-formers was to first gather the required COSMO files containing the optimised sigma surfaces for use with the COSMOtherm software. An AZ in-house list of potential co-formers with files in the correct format was made available for the computational pre-screen. This left calculation of the API of interest's, in this case ROY, sigma surface to be calculated in order for the screen to proceed. Using the COSMOconf software this was a simple yet computationally time-consuming task. The SMILES string for the compound was entered into the software which then performed density functional theory (DFT) calculations to produce the COSMO file of the compound for further use. This is computationally intensive and can take multiple hours or longer per molecule; for the

combination of types of molecules and computer hardware used in this work, a time of 12 to 24 hours would be normal.

Once the COSMO file exists it can be used thereafter, so this time-consuming step need only be performed once per molecule. Having access to the precompiled list of potential co-formers helped greatly in this respect as it is not inconceivable that with its size (342 compounds) and only moderate computational resources available, it could take over a year to recreate it from scratch. COSMOtherm was then employed to systematically work through the list, in each case calculating the enthalpy excess of interaction of co-former to API compared to the sum of interactions of API to API and co-former to co-former. The end result was a list which could be sorted by excess enthalpy allowing the more likely potential co-formers to be identified.

A table containing the full list of co-formers with excess enthalpy calculated for the given stoichiometry with ROY as produced by COSMOtherm can be found in Appendix 4.1.

#### 4.3.1.2 Physical screen

The procedure for the physical screening was based on the optimised parameters previously determined (as outlined in Chapter 3). Three sets of the physical screening process were performed using separate 96-well plates for the screen, one for each solvent tested (acetone, ethanol and hexane). For each set of the screening process, 25mg of ROY dissolved in a DCM solution was added to an equimolar amount of solid, previously weighed, potential co-former in 48 wells of a borosilicate glass 96-well plate. After leaving the initial solvent to evaporate, 50µl of appropriate solvent was added to eight wells and the 8-tips of the ultrasonic probe were placed in these wells and sonicated at the power setting, and for the time, dictated by the results from the optimisation experiment, using a Sonics Vibra Cell 130W 20kHz ultrasonic processor. This process was repeated for the remaining wells and the whole process repeated a further two times replacing the solvent and sonication parameters as required; thereby completing the screening process in three solvents for 48 potential co-formers. The optimal parameters for each solvent varied slightly, for example a higher temperature was used with hexane. See Figure 4.9 for a diagrammatic representation of this process along with example images of the plate after each step.

Once all of the wells on the plate had undergone sonication a spatula was used to remove as much of the contents as possible into small sample vials, these had lids attached and were then shaken by hand to distribute the material before undergoing analysis.

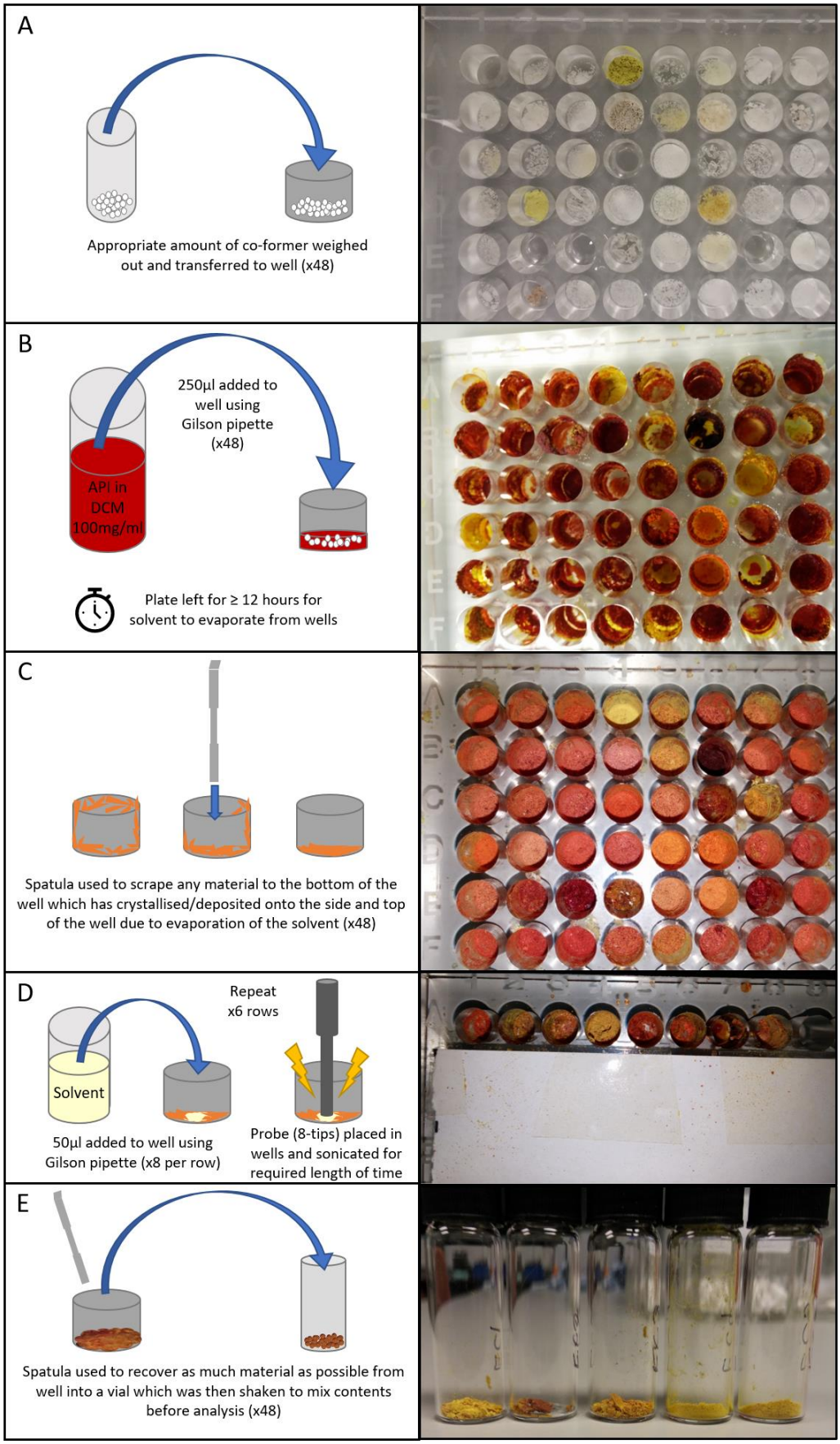


***Figure 4.9*** *Steps involved in the physical co-crystal screening process, represented diagrammatically (A to E) with example images of a plate after each step from the ROY screen.*

### 4.3.2 FTIR analysis

Infrared spectra for all of the samples from the screen as well as those of the individual starting components were obtained using the method detailed in Chapter 2 on approximately 5-10mg of material which had been removed from the well as described above. Analysis was carried out by manually comparing the spectra of the screen product for each ROY:co-former pair to those of the two pure compounds using BioRad Know-it-all spectral viewing software. As infrared spectroscopy is additive in nature, the peaks found in the two pure components should also be found in the spectrum of the product. Intermolecular bond formation between the molecules of the two constituent components, as is the case when a co-crystal forms, would cause slight variation in the intramolecular bond length of the interacting atoms. This change in bond length would lead to variation in the position of the peak detected allowing the identification of a hit in screening terms.

A hit would indicate only that a change in bonding or bond behaviour had occurred and not necessarily that a co-crystal had formed. Follow up investigation would be needed to confirm the nature of the resultant material and this level of identification is adequate for the type of high-throughput screening being employed. The forming of a salt or even degradation of the starting components are examples of other transformations which could lead to changes in IR spectra and possibly misidentification of a hit as a co-crystal. Much less subtle changes in spectra would be expected in these cases though and it is likely that such material could be discounted as a potential co-crystal with minor further analyses. Analysis of samples in which the wavenumbers at which the peaks are positioned are the same as the parent compounds, with no peak shift occurring, would be suggestive of no form change occurring and would be considered not hits.

### 4.3.3 Results

The results of the FTIR analysis of the ROY screen are presented in Table 4.3 in the form of a list of peak maxima relating to two peaks present in all spectra. A full set of spectra are presented in Appendix 4.2. The two peaks at wavenumbers of approximately 3300 and 2220$cm^{-1}$, were identified due frequent variation of these peaks between samples. The variations in peaks positions occur in all samples from the screen and are therefore related to a covalent bond of the ROY molecule rather than the co-formers. These slight variations suggest a solid-state form change but the lack of any peaks not accounted for in the spectra of the parent compounds indicates that covalent bonding within the two molecules has not been altered. The

wavenumbers listed in Table 4.3 are however, all explained by conversion of ROY polymorphs as the peak maxima observed are all commensurate (within the accuracy of the instrument used) with those obtained for one or more polymorphs of ROY (Figure 4.10).

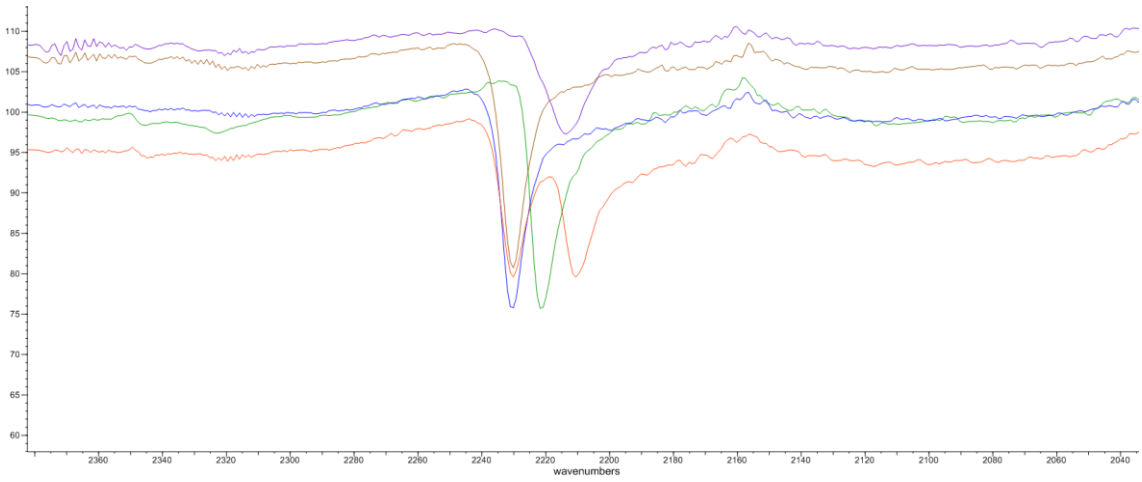


***Figure 4.10*** *FTIR spectra of a number of ROY polymorphs and a combination thereof, focused around the peaks at a wavenumber of approximately 2220cm$^{-1}$.*

The spectra displayed in Figure 4.10 are of polymorphs of ROY which were obtained by evaporation from different solvents. The reference wavenumbers for which Table 4.3 below compares the products of screening to determine indication of significant intermolecular interaction are derived from the spectra in Figure 4.10. Unfortunately, the identity of the polymorph for each of these spectra is not known. The polymorph samples were produced in small quantities by solvent evaporation and analysed immediately by FTIR as access to PXRD was not available at the time. It has not been possible to recreate all forms experimentally, neither has identification the polymorphs solely by their IR spectra as this is not available in the literature. The utility of the polymorph spectra for comparison to those of the screen products is not diminished though as they still allow the identification of ROY polymorphism regardless of the polymorph.

***Table 4.3*** *Wavelengths of infrared absorption peak maxima obtained from the products of the ROY co-crystal screen listed by co-former rank and including results from each of the repeats with different solvents (acetone, ethanol and hexane).*

| Co-former | ~3300 peak (acetone) | ~2220 peak (acetone) | ~3300 peak (ethanol) | ~2220 peak (ethanol) | ~3300 peak (hexane) | ~2220 peak (hexane) |
|---|---|---|---|---|---|---|
| Pentafluorophenol | 3280 | 2209+2230 | 3280 | 2229 | 3303+3281 | 2210+2230 |
| Acesulfame | 3280 | 2209+2230 | 3280 | 2210+2230 | 3280 | 2210+2230 |
| Oxalic acid | 3282+3302 | 2209+2230 | 3279 | 2228 | 3281 | 2221+2230 |
| Quercetin | 3280 | 2230 | 3279 | 2230 | 3280 | 2222+2230 |
| Sulfamic acid | 3280 | 2229 | 3280 | 2229 | 3283 | 2221 |
| 3,5-Dinitrobenzoic acid | 3280 | 2210+2229 | 3280 | 2230 | 3281 | 2223+2229 |
| 1,2,3-Trihydroxybenzene | 3278 | 2229 | 3279 | 2229 | 3280 | 2230 |
| 2,4-Dihydroxybenzoic acid | 3280 | 2229 | 3280 | 2230 | 3282 | 2222+2230 |
| 5-Nitroisophthalic acid | 3278 | 2229 | 3278 | 2229 | 3281+3300 | 2210+2230 |
| Gallic acid | 3277 | 2209+2229 | 3276 | 2228 | 3278 | 2209+2230 |
| *tert*-Butylhydroquinone | 3280 | 2230 | 3279 | 2229 | 3281 | 2211+2230 |
| 1-Hydroxy-2-naphthoic acid | 3279 | 2230 | 3282+3300 | 2209+2230 | 3280 | 2216+2230 |
| Catechol | 3278 | 2229 | 3279 | 2230 | 3282 | 2218+2230 |
| 4-Hexylresorcinol | 3280 | 2229 | 3281 | 2226 | 3334 | 2223 |
| 5-Chlorosalicylic acid | 3278 | 2229 | 3278 | 2229 | 3281 | 2222 |
| Resorcinol | 3277 | 2209+2229 | 3279 | 2230 | 3306 | 2227 |
| 3,5-Dihydroxybenzoic acid | 3278 | 2209+2229 | 3279 | 2230 | 3281 | 2210+2230 |
| Orcinol | 3279 | 2229 | 3279 | 2229 | 3292 | 2221 |
| 2,5-Dihydroxybenzoic acid | 3278 | 2229 | 3280 | 2210+2230 | 3280 | 2230 |
| *o*-Cresol | 3280 | 2229 | 3278 | 2229 | 3283 | 2222 |
| 3,4-Dihydroxybenzoic acid | 3280 | 2230 | 3278 | 2229 | 3281 | 2229 |
| Thymol | 3279 | 2229 | 3279 | 2229 | 3282 | 2222 |
| Phenol | 3280 | 2229 | 3281 | 2230 | 3280 | 2221+2230 |
| Trimesic acid | 3280 | 2210+2230 | 3280 | 2229 | 3280 | 2222+2230 |
| Indole | 3279 | 2229 | 3300 | 2218 | 3297 | 2217 |
| 3-Hydroxy-2-naphthoic acid | 3279 | 2229 | 3280 | 2230 | 3280 | 2210+2229 |
| 2,5-Xylenol | 3280 | 2229 | 3279 | 2229 | 3280 | 2230 |
| Salicylic acid | 3280 | 2230 | 3279 | 2229 | 3280 | 2210+2222+2229 |
| *m*-Nitrobenzoic acid | 3282 | 2215+2229 | 3295 | 2215+2230 | 3295 | 2215 |
| Skatole | 3278 | 2229 | 3280 | 2216+2230 | 3289 | 2216 |
| Hydroquinone | 3279 | 2229 | 3279 | 2210+2229 | 3280 | 2223+2230 |
| Fumaric acid | 3279 | 2229 | 3280 | 2209+2230 | 3279 | 2229 |
| Methyl gallate | 3280 | 2230 | 3280 | 2230 | 3281+3303 | 2209+2230 |
| *p*-Cresol | 3279 | 2229 | 3281 | 2209+2230 | 3279+3303 | 2210+2229 |
| Methanesulfonic acid | 3279 | 2229 | 3282+3301 | 2209+2230 | 3280 | 2230 |
| *p*-Ethylphenol | 3280 | 2210+2230 | 3281 | 2229 | 3280 | 2230 |
| 3-Hydroxybenzoic acid | 3280 | 2230 | 3278 | 2229 | 3281 | 2222+2230 |
| 6-Hydroxy-2-naphthoic acid | 3280 | 2230 | 3294 | 2218 | 3281 | 2222+2230 |
| Ethanesulfonic acid | 3280 | 2229 | 3282+3301 | 2210+2223 | 3274 | 2214+2226 |
| Allocitric acid | 3279 | 2230 | 3280 | 2229 | 3280 | 2222+2230 |
| *p-tert*-butylphenol | 3280 | 2210+2230 | 3279 | 2209+2229 | 3280+3303 | 2210+2230 |
| 3,4-Xylenol | 3280 | 2230 | 3279 | 2209+2230 | 3280 | 2230 |
| 2,6-Xylenol | 3281+3301 | 2209+2230 | 3284+3302 | 2209+2230 | 3279+3301 | 2209+2229 |
| Citric acid | 3280 | 2210+2230 | 3280 | 2211+2229 | 3278 | 2223+2229 |
| Etidronic acid | 3279 | 2228 | 3279 | 2229 | 3279 | 2229 |
| 4-Hydroxybenzoic acid | 3280 | 2229 | 3281 | 2211+2229 | 3281 | 2219 |
| *o*-Phenylphenol | 3279 | 2211+2229 | 3279 | 2229 | 3303 | 2208 |
| 2-Oxo-3-phenylpropionic acid | 3279 | 2229 | 3278 | 2229 | 3281 | 2215+2229 |

Based on the analysis of the FTIR spectra, the screen applied to ROY found no evidence of the formation of co-crystals. This was not the desired outcome in relation to progress of the project but also not surprising as a degree of excess enthalpy from prediction is no guarantee of co-crystallisation *in vitro*, due to lack of consideration of the purported lattice in the adopted computational approach. As this was the first time the optimised co-crystal screen had been

applied to a real candidate for co-crystallisation in full, investigation of the negative result was undertaken to prove robustness of the method.

## 4.4 Further investigations of the top 10 predicted co-formers

Further efforts to produce co-crystals of ROY from the top 10 predicted co-formers were undertaken. This involved applying different methods of manufacture: liquid assisted grinding (LAG), evaporative crystallisation and reaction crystallisation, which have previously been shown in the literature to be robust screening tools.[145,146,147]

### 4.4.1 Methods

#### 4.4.1.1 Liquid assisted grinding

Approximately 50mg of ROY was weighed out, and with an equimolar equivalent of potential co-former, placed in a mortar. An addition of 25µl of acetone occurred before grinding by hand with a pestle for 5 minutes. This process was repeated for each of the top 10 predicted potential co-formers for ROY. The products were analysed by FTIR.

#### 4.4.1.2 Evaporative crystallisation

Saturated solutions in acetonitrile of each of the top 10 predicted potential co-formers for ROY were produced and 1ml of each placed in 10 vials. To each of these 1 ml of a saturated solution of ROY in acetonitrile was added. The vials were shaken and left to allow evaporation of the solvent. The products were analysed by PXRD.

#### 4.4.1.3 Reaction crystallisation

Saturated solutions in acetonitrile of each of the top 10 predicted potential co-formers for ROY were produced and 1ml of each placed in 10 vials. Solid ROY was added to each vial until no further dissolution occurred and the contents of the vial left stirring. The vials were inspected periodically and to those where complete dissolution had occurred, more solid ROY was added. This continued for 10 days at which point all vials had visible solid material present and further dissolution did not occur. The remaining liquid was removed by pipette, and the material left for residual solvent to evaporate before analysis by PXRD.

## 4.4.2 Analysis

### 4.4.2.1 FTIR spectroscopy

FTIR analysis of the samples produced by LAG was carried out as for the products of the original screen and the results displayed in Table 4.4. A full set of spectra can be found in Appendix 4.3. With the exception of the ROY:pentafluorophenol sample, the results of the FTIR analysis of the products of LAG again showed no evidence of the formation of co-crystals as the position of the peaks were all accounted for in the spectra of the parent compounds or one or more of the polymorphs of ROY. The peak maximum of 2240cm$^{-1}$ measured for the product of LAG of ROY and pentafluorophenol is slightly higher than that seen in any of the measured polymorphs. It is possible that it is due to the formation of a polymorph of ROY of which the IR spectrum was not available due to the similarity in peak profile, however as there is no evidence of this, the result would count as a hit in term of screening and further investigation would be warranted.

In addition to the peaks listed, the product of LAG of ROY and oxalic acid displayed an IR absorption peak not present in the spectra of either of the two parent compounds. It was determined by comparison of the spectra of oxalic acid as received, after hydration during a DVS experiment and after LAG with ROY, that the explanation of the presence of this peak was due to hydration of oxalic acid during the manufacture of the sample (see Appendix 4.3 for IR spectra).

***Table 4.4*** *Wavenumber of IR absorption peaks associated with bonds affected by hydrogen bonding within ROY polymorphs measured in the product of LAG of ROY and the top ten predicted co-formers.*

| **Potential co-former** | **Wavenumber of peaks associated with bonds affected by hydrogen bonding within ROY polymorphs** | |
|---|---|---|
| | **~3300 peak** | **~2220 peak** |
| Pentafluorophenol | 3281 | 2230+2240 |
| Acesulfame | 3281 | 2230 |
| Oxalic acid | 3280 | 2229 |
| Quercetin | 3281 | 2230 |
| Sulfamic acid | 3280 | 2230 |
| 3,5-Dinitrobenzoic acid | 3281 | 2230 |
| Pyrogallol | 3279 | 2230 |
| 2,4-Dihydroxybenzoic acid | 3279 | 2230 |
| 5-Nitroisophthalic acid | 3280 | 2230 |
| Gallic acid | 3279 | 2230 |

### 4.4.2.2 Powder X-ray diffractometry

For the reaction crystallisation experiments, comparatively large quantities of ROY were required to be added to the solutions over the 10 days of stirring while dissolution continued, possibly multiple times that of the co-former in solution depending on the co-former's solubility in acetonitrile. Were any of these binary systems to form a co-crystal, the procedure implemented would have given plenty of opportunity for the solution to access the required space of the ternary phase diagram for co-crystal formation before the precipitation of ROY. As co-crystalline material did not form, as inferred from the PXRD analysis (Table 4.5), and due to the excess quantity of ROY used, this lead to the main constituent of the analysed material being ROY, effectively formed from an acetonitrile slurry. When carried out at room temperature, it is known that polymorph Y will be produced by a solution-mediated (i.e. slurry) conversion from any other form of ROY,[141] hence the ubiquity of the Y polymorph powder pattern in the reaction crystallisation results.

***Table 4.5*** *Summary of PXRD analysis of samples from the evaporative and reaction crystallisation experiments.*

| Potential co-former | Polymorph(s) of ROY detected in PXRD analysis | | Peaks not associated with either ROY or pure co-former | |
|---|---|---|---|---|
| | Reaction crystallisation | Evaporative crystallisation | Reaction crystallisation | Evaporative crystallisation |
| Acesulfame | Y | Y | No | No |
| Oxalic acid | Y | ON | No | No |
| Quercetin | Y | ON | No | No |
| Sulfamic acid | Y | R | No | No |
| 3,5-Dinitrobenzoic acid | Y | ON | No | No |
| Pyrogallol | Y | ON | No | Yes |
| 2,4-Dihydroxybenzoic acid | Y | ON | No | Yes |
| 5-Nitroisophthalic acid | Y | ON | No | No |
| Gallic acid | Y | Y | No | No |

Pentafluorophenol melts slightly above room temperature and it was impossible to obtain an accurate diffractogram without a variable temperature stage. Pentafluorophenol was therefore excluded from the reaction and evaporative crystallisation experiments due to the lack of a means of comparison for which to analyse the experimental samples against. The full set of PXRD patterns for the reaction and evaporative crystallisation experiments can be found in Appendix 4.4 and a summary of the results is presented in Table 4.5.

Many of the experimentally obtained PXRD patterns vary very slightly from the calculated ROY patterns for example small peak shifts to higher 2θ (approximately 0.1°) and occasionally comparatively larger peaks than those in the calculated pattern. These discrepancies can be explained in all cases by the effects of zero-point error of the diffractometer and preferred orientation. The diffractograms for the samples from the evaporative crystallisation of ROY with pyrogallol and 2,4-dihydroxybenzoic acid contain peaks at positions not observed in either parent material which signifies the presence of a new form. In the case of ROY and pyrogallol, the new peaks were found to match those of pyrogallol tetartohydrate (pattern calculated from CSD entry QQQBKD02) as shown in Figure 4.11.

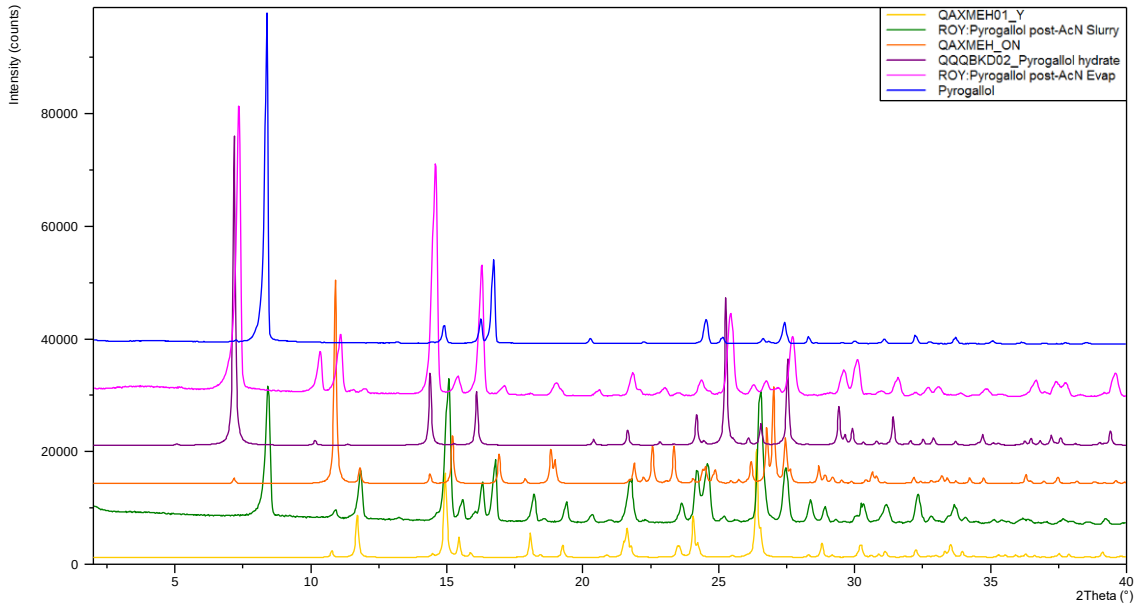


***Figure 4.11*** *PXRD patterns of the experimental samples of ROY and pyrogallol from reaction crystallisation (green) and evaporative crystallisation (pink), pyrogallol (blue), along with the calculated patterns of ROY polymorphs: Y (yellow) and ON (orange) and pyrogallol tetartohydrate (purple) for comparison.*

The new peaks in the powder pattern of the evaporative crystallisation product of ROY and 2,4-dihydroxybenzoic partially match those of polymorph ON of ROY however there are two unexplained peaks between 8 and 10° 2θ (Figure 4.12) which render this a hit from a co-crystal screen perspective.

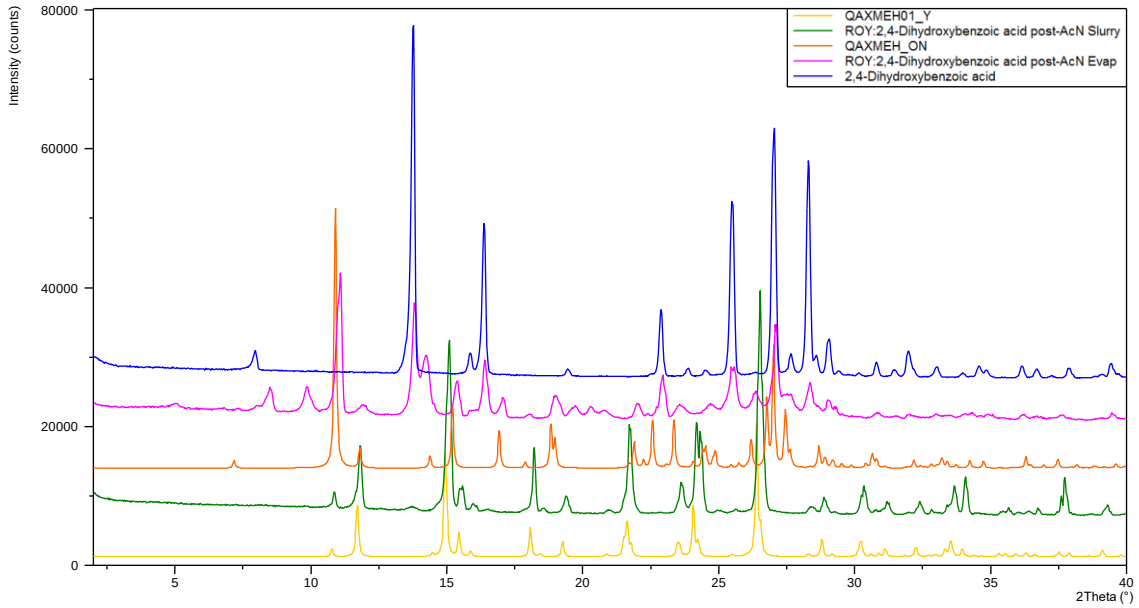


***Figure 4.12*** *PXRD patterns of the experimental samples of ROY and 2,4-dihydroxybenzoic acid from reaction crystallisation (green) and evaporative crystallisation (pink), 2,4-dihydroxybenzoic acid (blue), along with the calculated patterns of ROY polymorphs: Y (yellow) and ON (orange) for comparison.*

### 4.4.2.3 Differential scanning calorimetry

In addition to IR analysis, the products of LAG were also analysed by DSC employing the standard heat/cool/heat method detailed in Chapter 2. Nine of the 10 products of LAG displayed unremarkable thermal recrystallization behaviour, however the LAG product of ROY and pyrogallol stood out. Pure ROY and pyrogallol both show poor amorphous stability. Pyrogallol crystallises on cooling from melt and ROY crystallises during the second heating cycle (class (I-A) and class (II) materials following the classification system as described by Baird *et al.*[148] respectively), the product of the grind of both materials does not crystallise and remains in amorphous form throughout the temperature range tested. This suggests that an amorphous form was produced on cooling and this remained stable until at least 150°C resulting in a material categorised as class (III); producing a co-amorphous material.[149] The second heating cycles for the two parent components and the product of the 1:1 molar ratio grind are shown in Figure 4.13. (See Appendix 4.5 for a full set of plots of initial heating, cooling and second heating cycles for all ROY:co-former pairs). This behaviour differs from all other ROY:co-former combinations, as they all crystallise either on cooling (class (I)), on the second heating phase (class (II)), or in one case both, as shown in Table 4.6.

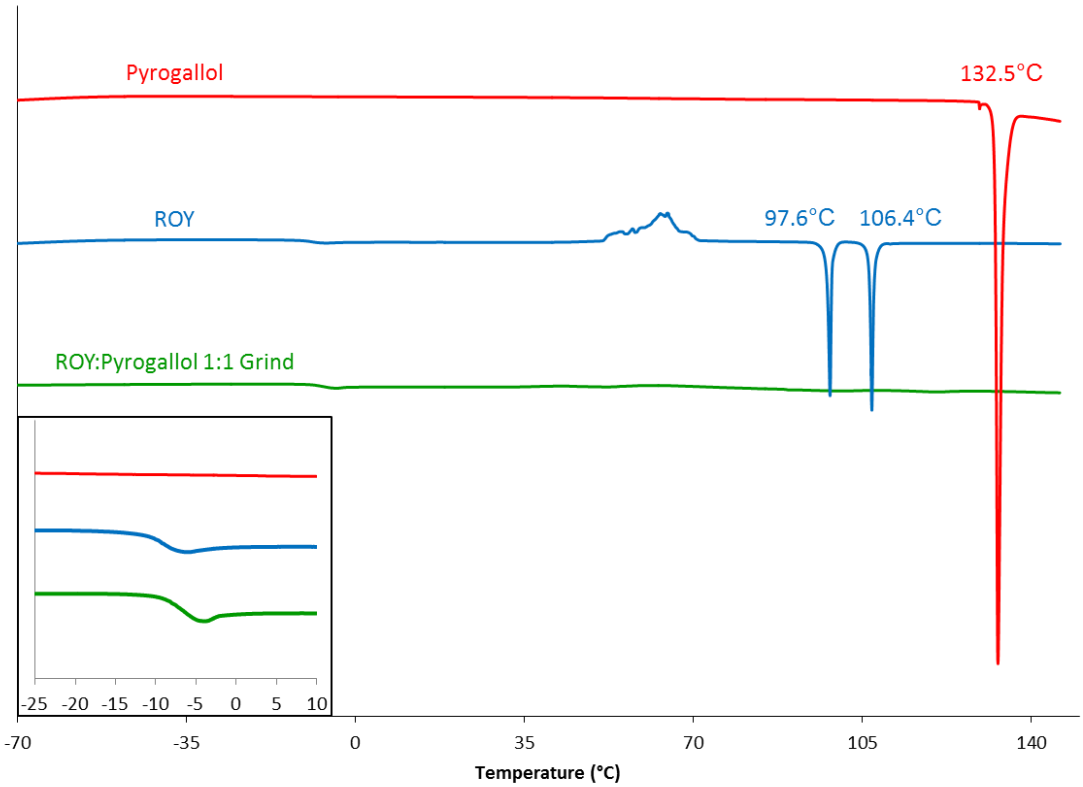


***Figure 4.13*** *Second heating phase DSC curves of pyrogallol (red), ROY (blue) and ROY:pyrogallol 1:1 grind (green). Peak onset temperatures displayed. Presence of $T_g$ highlighted in inset.*

***Table 4.6*** *Summary of the crystallisation behaviour of pairs of ROY and the top 10 predicted co-formers.*

| Potential co-former | Cycle in which crystallisation occurs during DSC of the grind of the respective co-former with ROY |
|---|---|
| Pentafluorophenol | Second heating |
| Acesulfame | Cooling |
| Oxalic acid | Cooling |
| Quercetin | Second heating |
| Sulfamic acid | Cooling |
| 3,5-Dinitrobenzoic acid | Cooling |
| Pyrogallol | None |
| 2,4-Dihydroxybenzoic acid | Cooling and second heating |
| 5-Nitroisophthalic acid | Cooling |
| Gallic acid | Cooling |

### 4.4.3 Summary

After much more thorough screening of the top ten predicted co-formers for ROY, only two potential hits were encountered – pentafluorophenol using LAG and 2,4-dihydroxybenzoic acid with evaporative crystallisation. With the high-throughput nature of the original co-crystal screen and the significant extra effort required by employing three less time-efficient methods, it would be unreasonable to expect to incorporate this level of extensive investigation into the co-crystal screening process. Given that the optimised co-crystal screen passed validation testing by identifying form change in all of the test samples (Chapter 3) and later found 23 hits in a co-crystal screen of ornidazole (Chapter 6), and that to the best of the author's knowledge there are no known co-crystals of ROY, it is suggested that the optimised screen is fit for purpose and that the resources required to find a co-crystal of ROY, vast (with the caveat of serendipity). Lack of access to an X-ray diffractometer at the time of analysis of the LAG experiment prevented immediate follow up of the hit, and interest in the ROY:pyrogallol thermal behaviour led to focus on this system for further investigation.

## 4.5 ROY:pyrogallol investigations

As a unique behaviour compared to all other tested co-formers was detected in the ROY-pyrogallol pairing, work to further examine this interaction was undertaken.

### 4.5.1 Hot-stage microscopy – Kofler technique

One further experiment was carried out to confirm that a co-crystal of ROY and pyrogallol would not form from the melt. A method for using hot-stage microscopy to probe for co-crystalline forms, perhaps best known as the Kofler technique, was employed. The component with the higher melting point, in this case pyrogallol was first melted and allowed to cool and solidify on a glass microscope slide. The second component (ROY) was then placed on the other side of the slide and heated above its melting point but below that of the first component. This allowed the molten ROY to come into contact with the solid pyrogallol causing solubilisation of a small portion of the solid component and in doing so creating a zone of mixing. Within this zone of mixing a concentration gradient is formed with the concentration of each component decreasing as the distance from its original position towards the other component increases. The slide with both components on was placed on a hot-stage and viewed using cross polarised light microscopy (with photomicrographs captured every 20 second) while cooling until all of the material had crystallised and then heating following the method listed in Table 4.7.

***Table 4.7*** *Details of the hot-stage method implemented.*

| Method section | Temperature | Rate | Terminating at | Purpose |
|---|---|---|---|---|
| 1 | Increasing | 10°C/min | 50°C | Allowed time to ensure complete crystallisation had occurred before beginning temperature ramp. |
| 2 | Decreasing | 1°C/min | 35°C | |
| 3 | Increasing | 1°C/min | 160°C | Slow increase of temperature to above melting points to detect melting of separate phases. |

Figure 4.14 contains eight photomicrographs (labelled A to H), each depicting a snapshot of the experiment at key points. In all of the photomicrographs the blue coloured crystalline material is pyrogallol, the orange-red coloured is ROY, and any black area is molten material, either ROY or pyrogallol due to viewing under cross polarised light. Due to the microscope slide being moved directly from a hot plate to the hot-stage, the temperature recorded for the first three (A-C) micrographs may be inaccurate as the slide may have been hotter than the stage at this point.

In micrograph A, there is solid pyrogallol (blue area) and molten ROY (black area); the orange-green area at the interface of the two phases is where the molten ROY had caused solubilisation of the pyrogallol and a zone of mixing had formed. Micrograph B shows the point at which ROY began to crystallise from the melt, nucleating from the solid material at the edge of the zone of mixing. By micrograph C, most of the molten ROY had crystallised and between C and D, complete crystallisation occurred and the hot-stage began increasing the temperature at 1°C/min from 35°C. At around 90°C ROY began to melt from the zone of mixing outward (E), and by approximately 103°C it had almost completely melted (F). During this time, the pyrogallol also started to melt, again, from the zone of mixing outwards (G) and by 132°C it too had completely melted (H). Were co-crystalline material present, it would be expected that it would be observable, between the time of micrographs E and G, as a separate phase of crystalline material bordered by molten liquid. This was not observed and as such indicates that a co-crystal of ROY and pyrogallol is not readily obtainable from the melt.

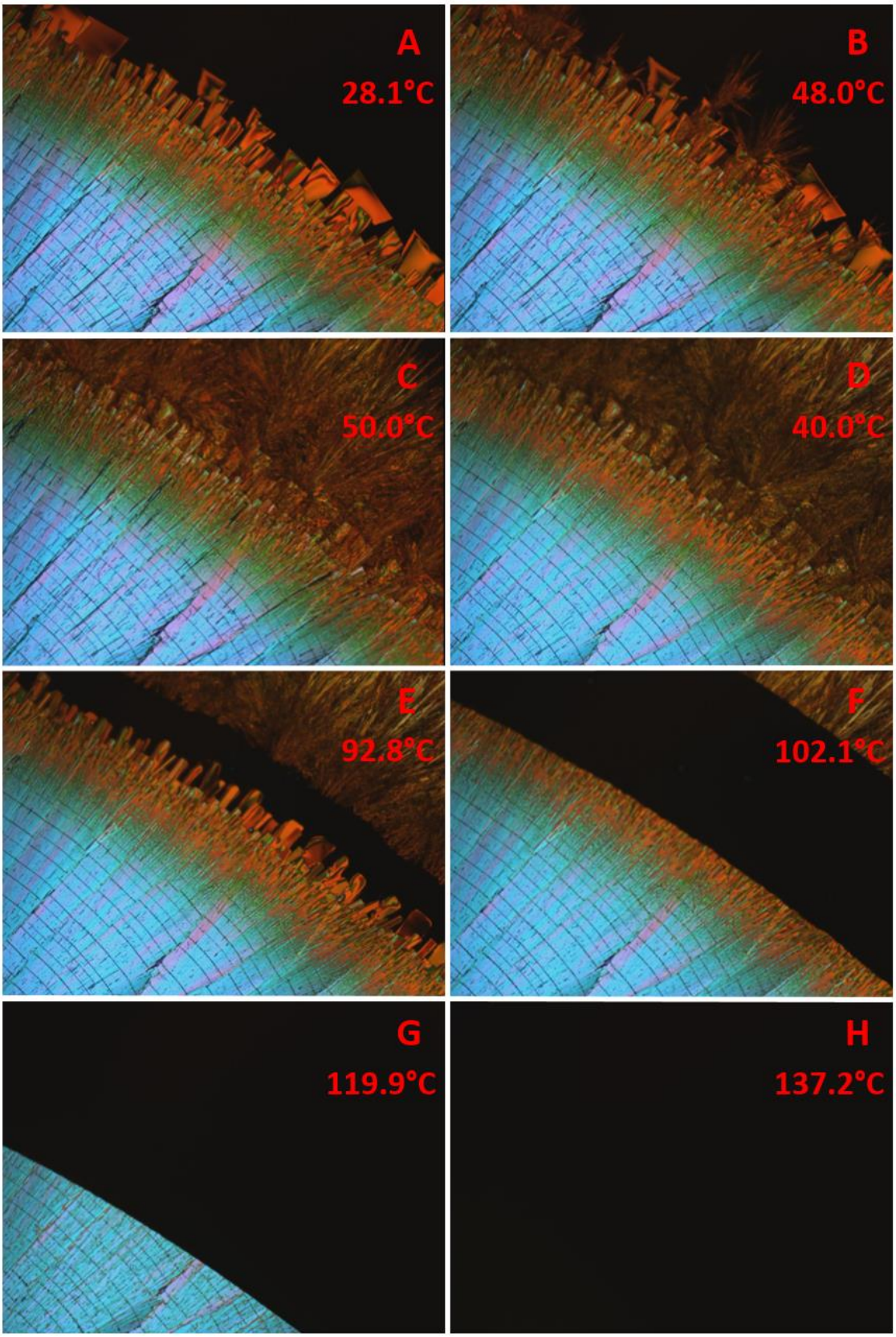


***Figure 4.14*** *Micrographs of ROY and pyrogallol under cross polarised light over the course of the Kofler technique experiment.*

### 4.5.2 Amorphous stability

Having determined that co-crystallisation of ROY and pyrogallol is not readily achievable but that presence of pyrogallol leads to the stabilisation of ROY in the amorphous form, further investigation into the nature of this interaction commenced.

The glass transition temperatures for ROY and for the ROY:pyrogallol 1:1 grind, shown in Figure 4.13 and in more detail in Appendix 4.6, vary by less than 4°C, and as such suggest that a change in molecular mobility great enough to affect molecular translational ability is not caused by the presence of pyrogallol. Three samples of ROY:pyrogallol grind were produced with varying pyrogallol content to see if smaller quantities of pyrogallol could still improve amorphous stability, potentially indicating nucleation inhibition as the source of the phenomenon. The samples were produced by grinding the following ratios of ROY and pyrogallol: 1:1 molar ratio, 10% w/w and 1% w/w pyrogallol. The initial heating DSC traces for these samples are displayed in Figure 4.15 and it is worth noting that an endothermic melting peak at around 88.5°C is present in all three samples, with decreasing intensity as the pyrogallol content is reduced. The cooling and second heating cycles for the three samples are in Appendix 4.7 and show that the ROY:pyrogallol grinds containing 10%w/w and 1%w/w pyrogallol display similar behaviour to the 1:1 grind in that crystallisation does not occur during the cooling cycle and that glass transitions are observed. During the second heating phase, exothermic events occur for the two samples with lower pyrogallol content indicating that complete stabilisation of the amorphous phase did not occur.

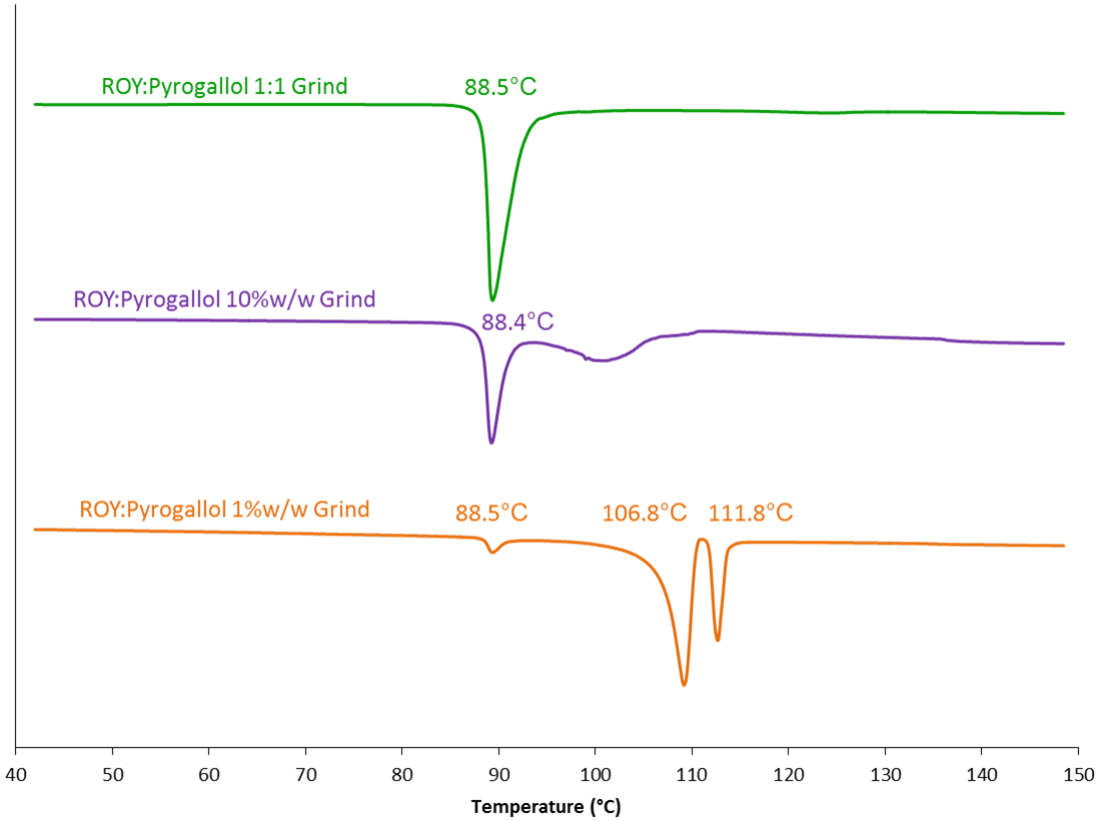


***Figure 4.15*** *Initial melting points for grinds of varying ratio of ROY:pyrogallol content.*

With the presence of smaller quantities of pyrogallol failing to prevent crystallisation from the amorphous phase and having a proportional effect on the initial endothermic peak, the significance of its relative content in the system is clear. To determine whether the amorphous stability elicited by the presence of the pyrogallol was related to its stoichiometric ratio with ROY, further ROY:pyrogallol samples were produced at 5% w/w increments from 0% to 100%, representative thermograms of the second heating cycle are shown in Figure 4.16. The initial melting point varies very little over the range 5% to 95% w/w pyrogallol (Figure 4.17) and therefore indicate that this is not a eutectic system, as, if it were, a single lower melting point at the eutectic composition would be expected.[74]

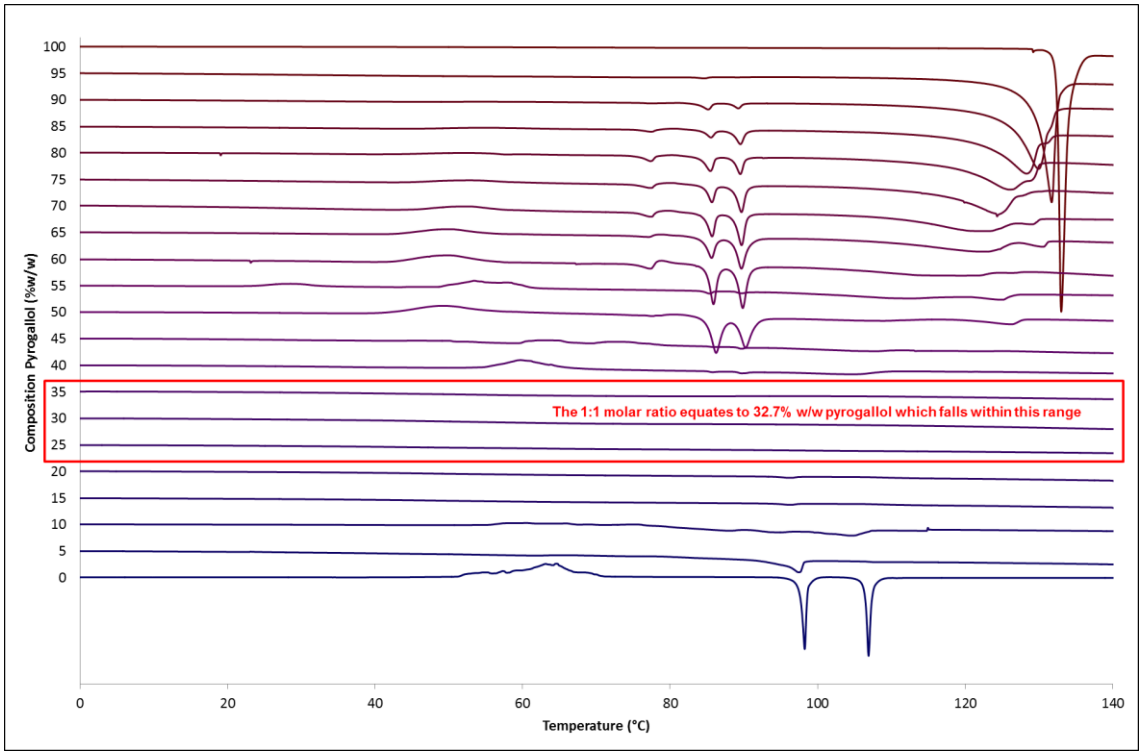


***Figure 4.16*** *Second heating phase DSC curves of ROY (0%), pyrogallol (100%) and varying compositions of ROY:pyrogallol in 5% w/w increments. The red box highlights the range of compositions in which the amorphous form is stabilised. This equates to 1:1 stoichiometry.*

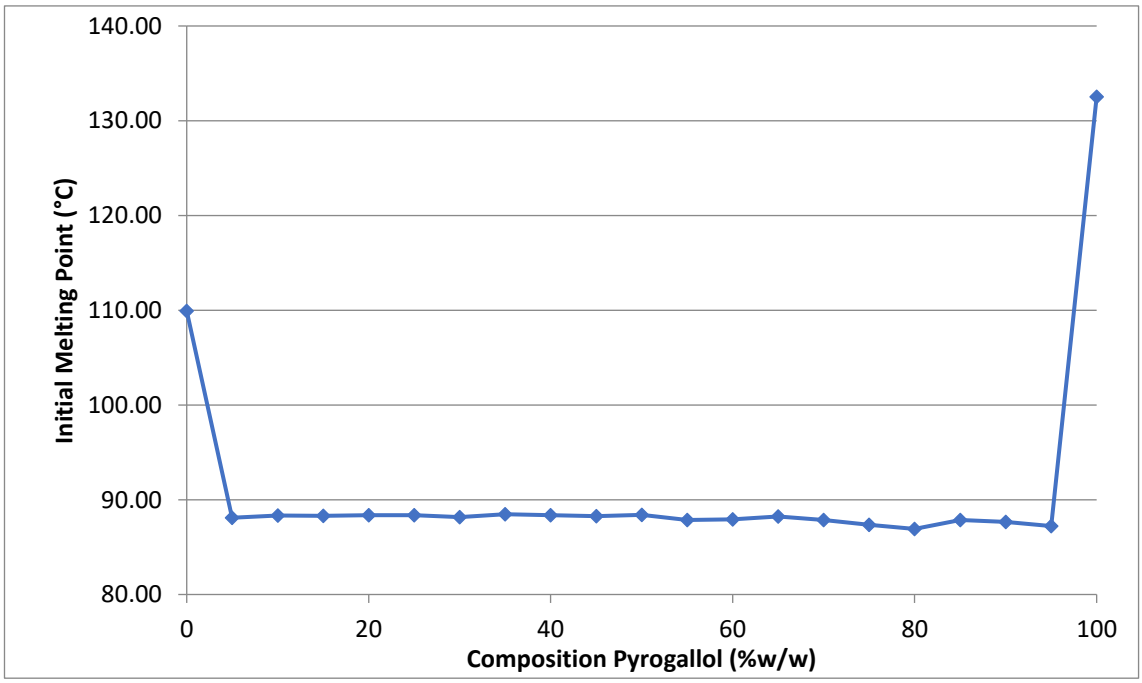


***Figure 4.17*** *Initial melting points for grinds of varying ratios of ROY:pyrogallol content. Melting points range between 86.9 to 88.5°C for 5-95% w/w pyrogallol.*

When looking at the second heating cycle (Figure 4.16) at the 1:1 composition the lack of any endothermic or exothermic events in the given temperature range suggest the 1:1 stabilisation rather than a small amount of pyrogallol inhibiting the crystallisation of ROY. The approximate boundaries of this range (25% to 35% w/w pyrogallol content) equate to molar ratios (in the form 1 ROY to X pyrogallol) of 0.69 and 1.11 respectively. These data suggest that with a lower ratio of pyrogallol to ROY, there is excess ROY behaving as pure ROY and uninfluenced by the presence of pyrogallol. The formation of intermolecular interactions between individual molecules of ROY and pyrogallol in a one to one manner would give rise to such behaviour.

## 4.5.3 Timescale of amorphous stability

The timescale of the stability of the ROY:pyrogallol mix was also investigated by DSC and PXRD.

### 4.5.3.1 Differential scanning calorimetry

The DSC traces involved in this investigation are presented in Figure 4.18, where the blue DSC trace is of the initial ground sample of 1:1 ROY:pyrogallol, which was sealed within a standard DSC pan and subjected to the same heat-cool-heat method as previous samples. This sample was left sealed at RT for approximately 65 hours and then a cool-heat method (cool at 10°C/min from 25°C to -90°C then heat at 10°C/min to 150°C) which gave the green DSC trace. As is evident, no crystallisation has occurred and the sample remains in the amorphous state. Another ground sample of 1:1 ROY:pyrogallol was placed in an open Tzero aluminium DSC pan (no lid added) and the heat-cool-heat method run giving rise to the red trace. This sample was placed in a 75% relative humidity environment and was visually seen to crystallise immediately, with the purple trace generated around 18 hours later (cool-heat method). This evidence suggests that crystallisation from the amorphous phase is mediated by an increased humidity presumed to be due to the plasticising effect of water.[149,150]

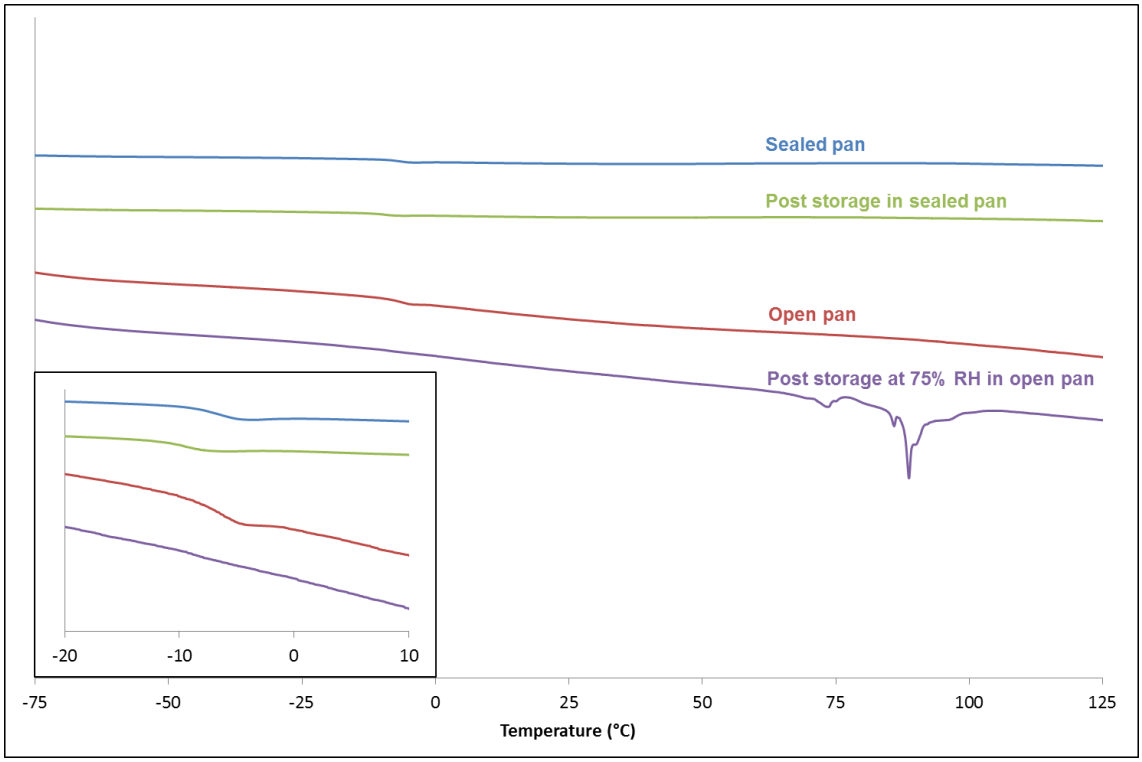


***Figure 4.18*** *Heating phase DSC curves of ROY:pyrogallol 1:1 grind: in sealed DSC pan (blue), after storage in sealed DSC pan for approximately 65 hours (green), in an open DSC pan (red) and after storage at 75% RH in an open DSC pan (purple). Presence of $T_g$ in all samples except that stored at 75% RH (purple) are highlighted in the inset.*

### 4.5.3.2 Powder X-ray diffractometry

Samples were also prepared of ROY and the 1:1 co-amorphous mixture and stored at ambient conditions and monitored for crystallinity by PXRD, the results of which are displayed in Figures 4.19 and 4.20.

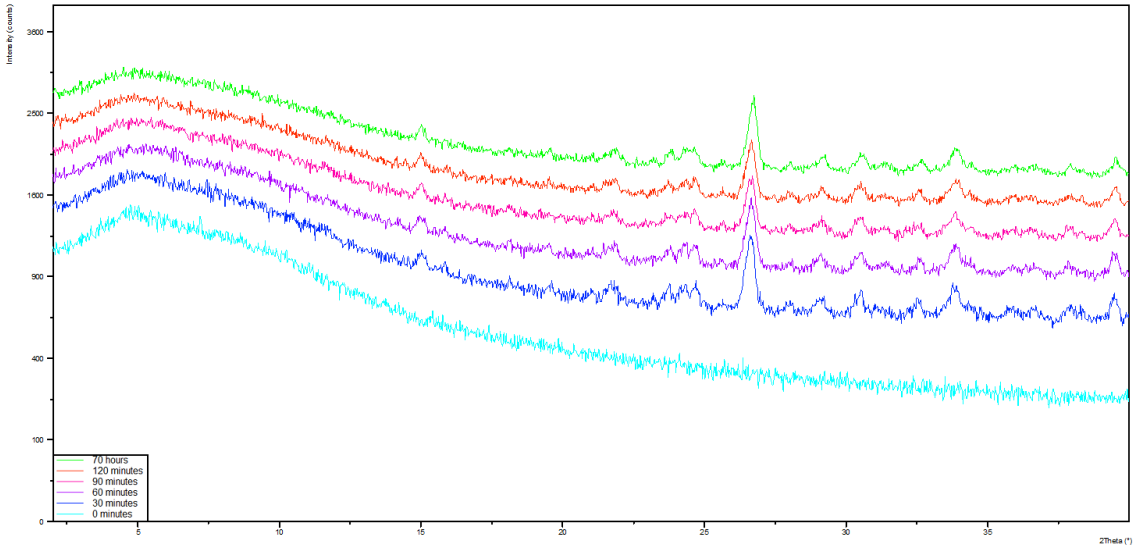


***Figure 4.19*** *Evolution of crystallinity over a 70-hour period from an amorphous droplet of pure ROY, scan lengths of approximately 10 minutes at 30 minute intervals for two hours and a final scan after 70 hours.*

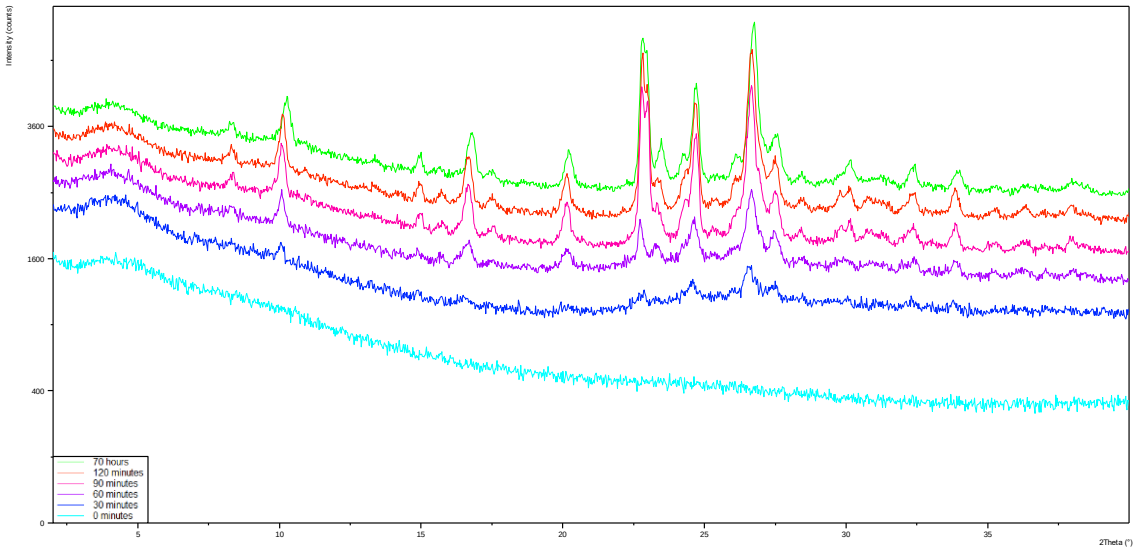


***Figure 4.20*** *Evolution of crystallinity over a 70-hour period from an amorphous droplet of ROY:pyrogallol 1:1 grind, scan lengths of approximately 10 minutes at 30 minute intervals for two hours and a final scan after 70 hours.*

In this case, crystallisation appears to have occurred earlier in the ROY sample than the co-amorphous mixture. In the ROY sample, crystallinity is seen at 15 minutes with no change in crystallinity at 70 hours, as seen by the lack of change in patterns between these times. In contrast, the ROY:pyrogallol data suggests a gradual increase in crystallinity from the 15-minute scan to at least 90 minutes.

#### 4.5.3.3 Summary

The stability of the co-amorphous ROY:pyrogallol material was seen to be highly dependent on atmospheric moisture conditions. Indeed, samples stored under dry nitrogen flow, or in a lidded DSC pan were seen to be stable for up to 65 hours. It was not possible to verify this through vapour sorption study due to the fast recrystallization that was seen on the instrument, but storage at 75% RH 25°C showed immediate visual recrystallization, which was confirmed by DSC at 18 hours (Figure 4.18). However, samples exposed to atmospheric conditions were only stable for around 30 minutes, as determined by PXRD analysis (Figure 4.20) and compared to pure ROY this is a significant improvement, as complete recrystallization from the amorphous form was seen after 15 minutes (Figure 4.19).

### 4.5.4 Intermolecular interaction investigation

Having determined that intermolecular interactions between individual molecules of ROY and pyrogallol in a one to one manner are likely to be the cause of the stabilisation seen in the co-amorphous material, further investigation into the interaction was undertaken. This involved the use of both computational and physical methods.

#### 4.5.4.1 Computational

In order to explore the nature of the interactions between ROY and pyrogallol in the amorphous form, hydrogen bond propensity prediction and an amorphous cell were produced, with the assistance of Dr David Berry (Durham University). The hydrogen bonding propensity of ROY, with the addition of aromatic hydroxyl to represent the potential pyrogallol interaction, was calculated using the logit hydrogen bonding propensity (LHP) model.[151] The calculations resulted in an area under ROC curve of 0.86. (See Appendix 4.8), and predicted strong hydrogen bonds between molecules of ROY only (Table 4.8).

***Table 4.8*** *Summary of predicted hydrogen bonding.*

| Type of interaction | Donor | Acceptor | Propensity |
|---|---|---|---|
| Intermolecular | N1 of sec amine 1 | N3 of cyano | 0.31 |
| Intermolecular | N1 of sec amine 1 | O2 of ar nitro | 0.25 |
| Intermolecular | N1 of sec amine 1 | O1 of ar nitro | 0.19 |
| Intermolecular | N1 of sec amine 1 | S1 of cyclic thioester | 0.01 |
| Intramolecular | N1 | O1 | 0.89 |
| Intramolecular | N1 | O2 | 0.89 |
| Intramolecular | N1 | N3 | 0.09 |

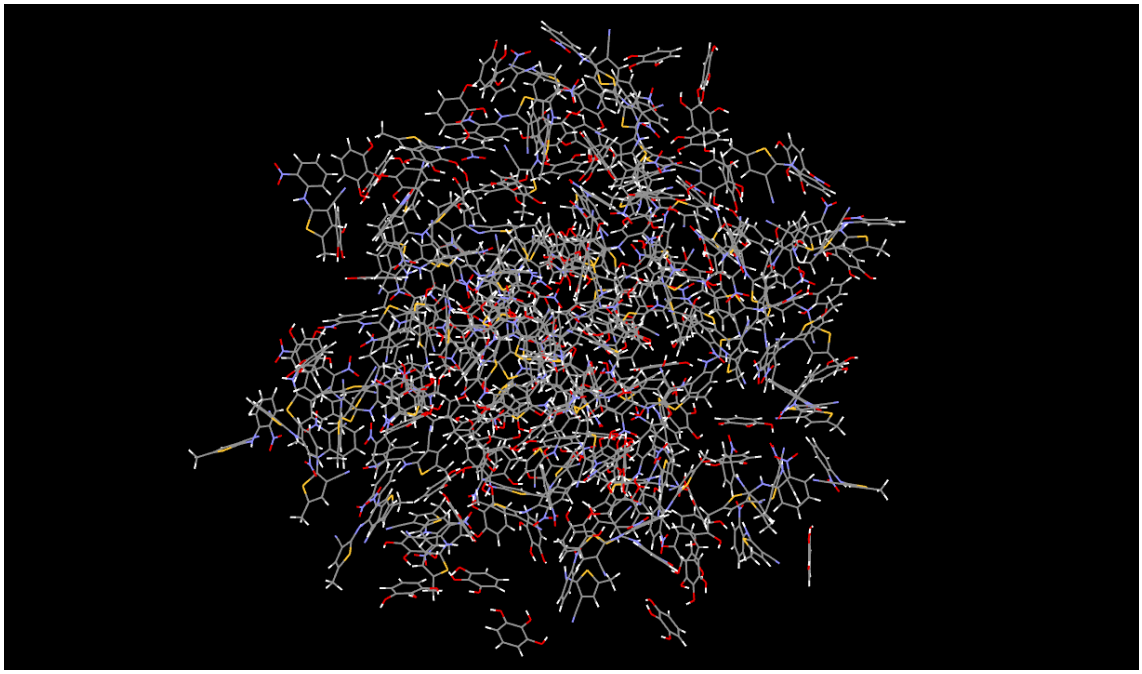

***Figure 4.21*** *Amorphous cell displaying all 200 molecules made up of 100 pyrogallol and 100 ROY molecules.*

Further modelling utilised a 200-molecule amorphous cell, generated in Materials Studio (Dassault Systemes, BIOVIA Ltd.). The cell of 100 of each molecule (1:1 ratio ROY and pyrogallol) was produced with charges defined by Gasteiger, utilising a Dreiding forcefield with molecular conformations taken from the entries in the CSD. This was allowed to minimise yielding the amorphous cell displayed in Figure 4.21, which displayed no change to the N-H bond of ROY, but changes to the environment around it. The hydrogen bonding observed within the amorphous cell is shown in Appendix 4.9 and is summarised in Table 4.9.

***Table 4.9*** *Number of strong H-bond contacts in the amorphous cell between molecules.*
**The interactions between ROY and pyrogallol were supported by a total of 44 pyrogallol molecules, i.e. some molecules supported more than one interaction. A further 32 pyrogallol molecules bonding self:self and 24 taking no part in any strong hydrogen bonding.*

| Molecule (group) 1 | Molecule (group) 2 | Number |
|---|---|---|
| ROY (nitro) | ROY (amine) | 100 (all) intramolecular bond |
| Pyrogallol (OH) | Pyrogallol (OH) | 32 |
| ROY (nitro) | Pyrogallol (OH)* | 20 |
| ROY (cyano) | Pyrogallol (OH)* | 32 |
| ROY (amine) | Pyrogallol (OH)* | 4 |
| ROY (sulfur) | Pyrogallol (OH)* | 8 |

These results correlate with the H-bond propensity prediction, as all ROY molecules possess the characteristic intra-molecular bond (propensity) and pyrogallol would be expected to alter the environment of this through its interaction.

### 4.5.4.2 FTIR spectroscopy

FTIR analysis was carried out using the standard method detailed in Chapter 2 and the spectra obtained for ROY and the ROY:pyrogallol 1:1 grind, in both amorphous and crystalline forms are displayed in Figure 4.22.

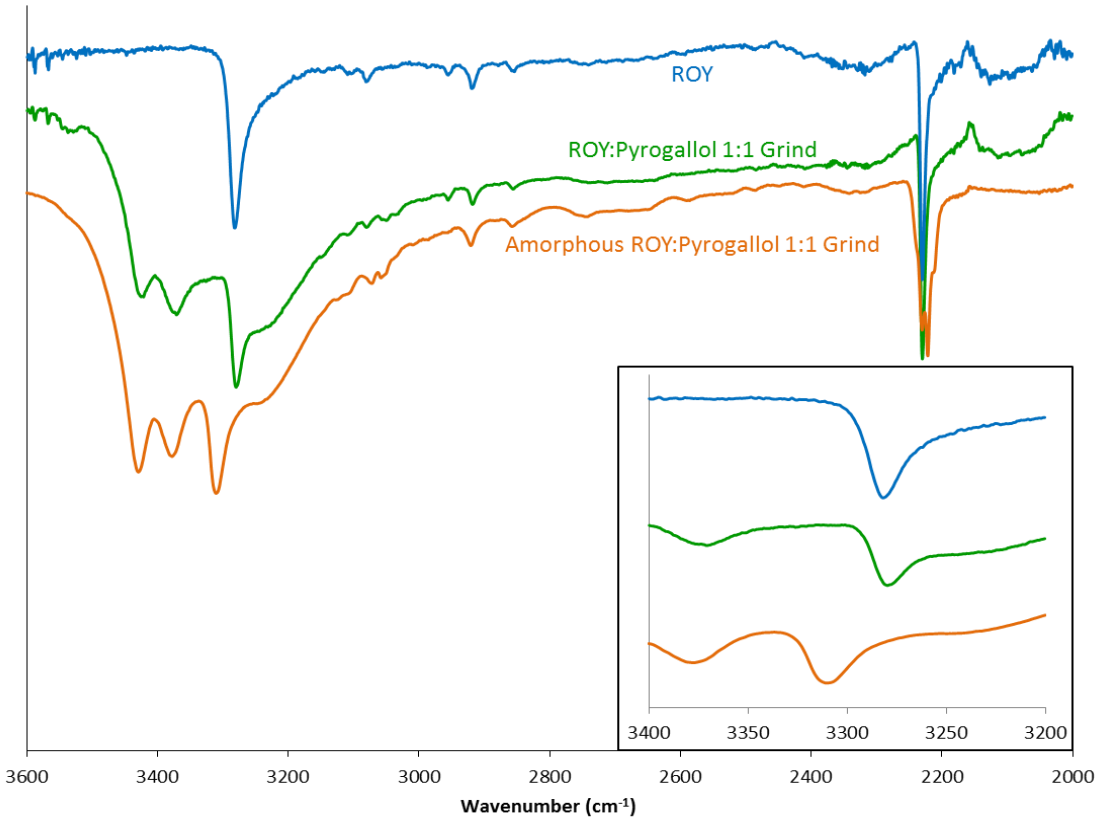


***Figure 4.22*** *FTIR spectra of ROY (blue), ROY:pyrogallol 1:1 grind (green) and amorphous ROY:pyrogallol 1:1 grind (orange). Focused area of wavenumbers 3200-3400 $cm^{-1}$ shown in inset.*

Figure 4.22 displays the FTIR spectra of an amorphous sample of the ROY:pyrogallol 1:1 grind and a peak shift corresponding to the N-H bond in ROY is apparent. A possible rationale, supported by the amorphous cell prediction, could be that of pyrogallol forming intermolecular bonds in proximity to the N-H bond of ROY causing the slight alteration in environment of the N-H bond. Such interactions in co-amorphous materials have previously been reported.[64] Polymers such as PVP, PVPVA and HPMC are often used for stabilising the amorphous API,[54] however this can lead to certain issues, for example side effects and limited drug loading of the formulation.[61] With ROY being the model API, a comparison between a traditional polymer stabilisation of the amorphous API using PVP was compared to the use of the small molecule, pyrogallol, as the stabilising agent, with the aim of addressing these issues.

### 4.5.5 Polymer comparison

Having discovered the co-amorphous nature of the ROY:pyrogallol system, exploration of its possible utility was considered. Due to the inherent improvement in solubility of the amorphous form of drugs, development of formulations utilising amorphous API has been of interest for poorly soluble drugs.[54,55] Often these formulations require the inclusion of stabilising agents to prevent the crystallisation of the API within a timescale which would prevent adequate shelf life of the product.[152]

#### 4.5.5.1 Method

In order to compare the pyrogallol-stabilised amorphous ROY form to a more traditional polymer stabilised form, a grind of ROY with polyvinylpyrrolidone (PVP) was created. This was at both a typical 10%w/w drug loading, with regards to ROY, and also at a 1:1 molar ratio, based on the molecular weight of the PVP monomer. These samples were analysed by DSC employing the standard heat/cool/heat method and PVP and pyrogallol were analysed by DVS, again employing the standard method, both detailed in Chapter 2.

#### 4.5.5.2 Differential scanning calorimetry

Both of these ROY:PVP ratios led to stabilised amorphous forms being produced. The second heating cycle DSC traces are shown in Figure 4.23 and the lack of any exothermic peaks, having also been none in the previous two cycles (Appendix 4.10), is indicative of the stabilised amorphous form. The similarity of the ROY:pyrogallol sample to the behaviour seen with the ROY:PVP grind adds further evidence to the possibility of replacing polymer with small molecule stabilising agents in some situations.

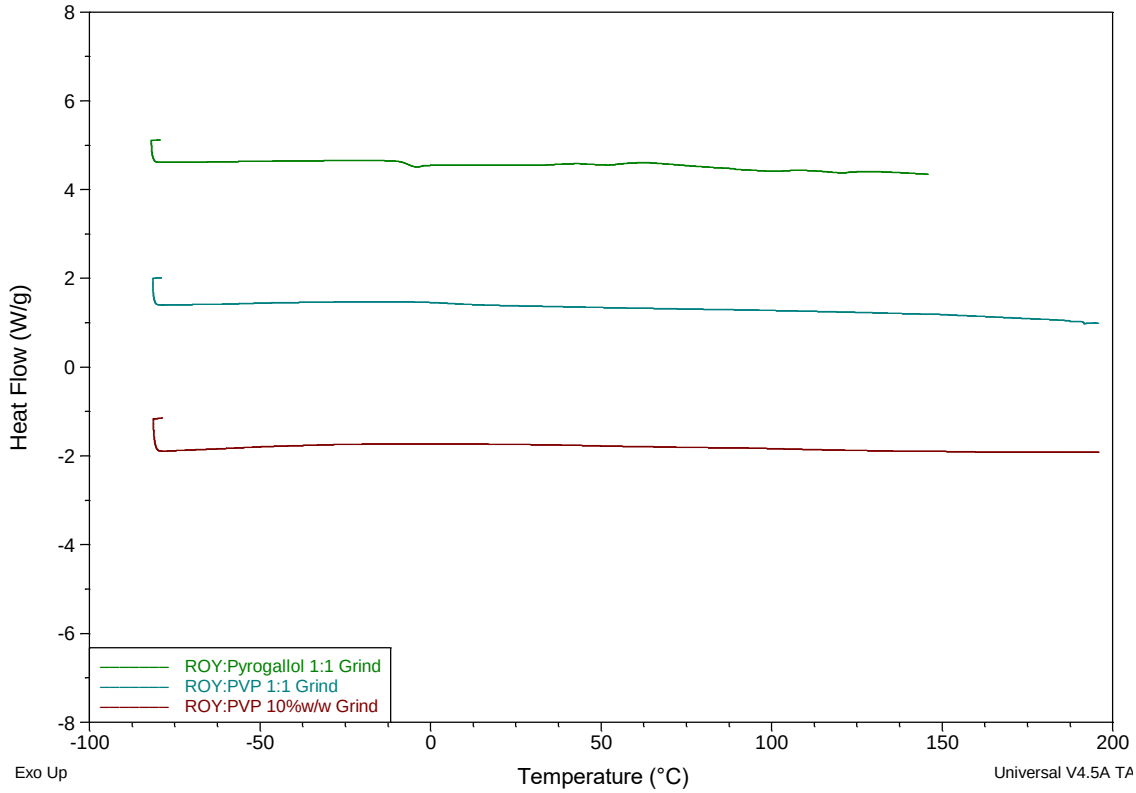


***Figure 4.23*** *Second heating phase DSC curves of ROY:pyrogallol 1:1 grind (green), ROY:PVP 1:1 grind (teal) and ROY:PVP 10%w/w grind (maroon).*

### 4.5.5.3 Dynamic vapour sorption

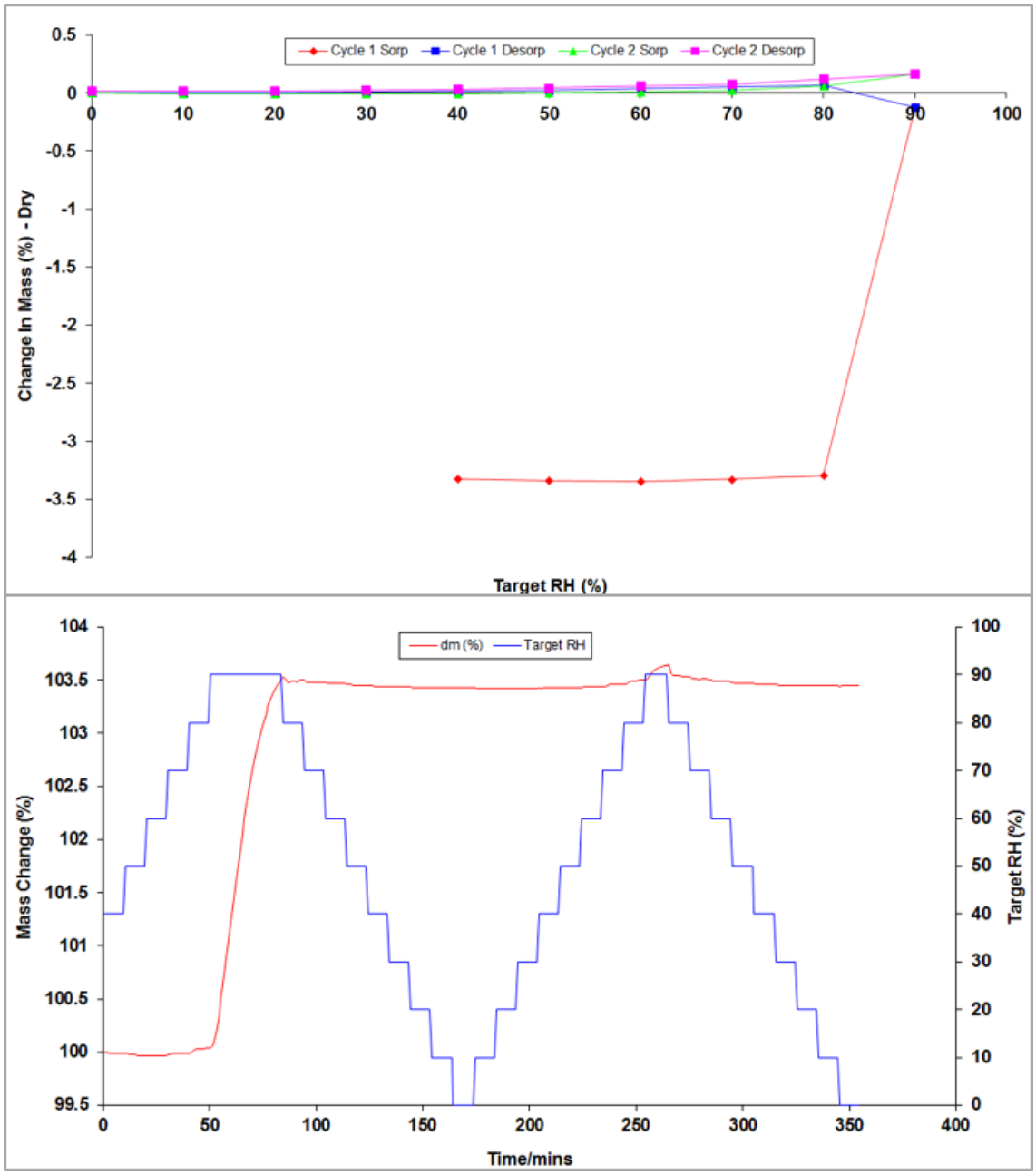


***Figure 4.24*** *Isotherms (top) and change in mass plot (bottom) for pyrogallol. N.B. see scale.*

In the initial sorption cycle, relative humidity above 80% displays moisture uptake indicative of an absorption of ¼ mole of water seen in Figure 4.24, this is followed by very little change against humidity in the following desorption/sorption cycles. This indicates that the pyrogallol sample hydrated from its initial form. In this case, there is approximately 3.3% change in mass correlating to the tetartohydrate being formed.[153,154]

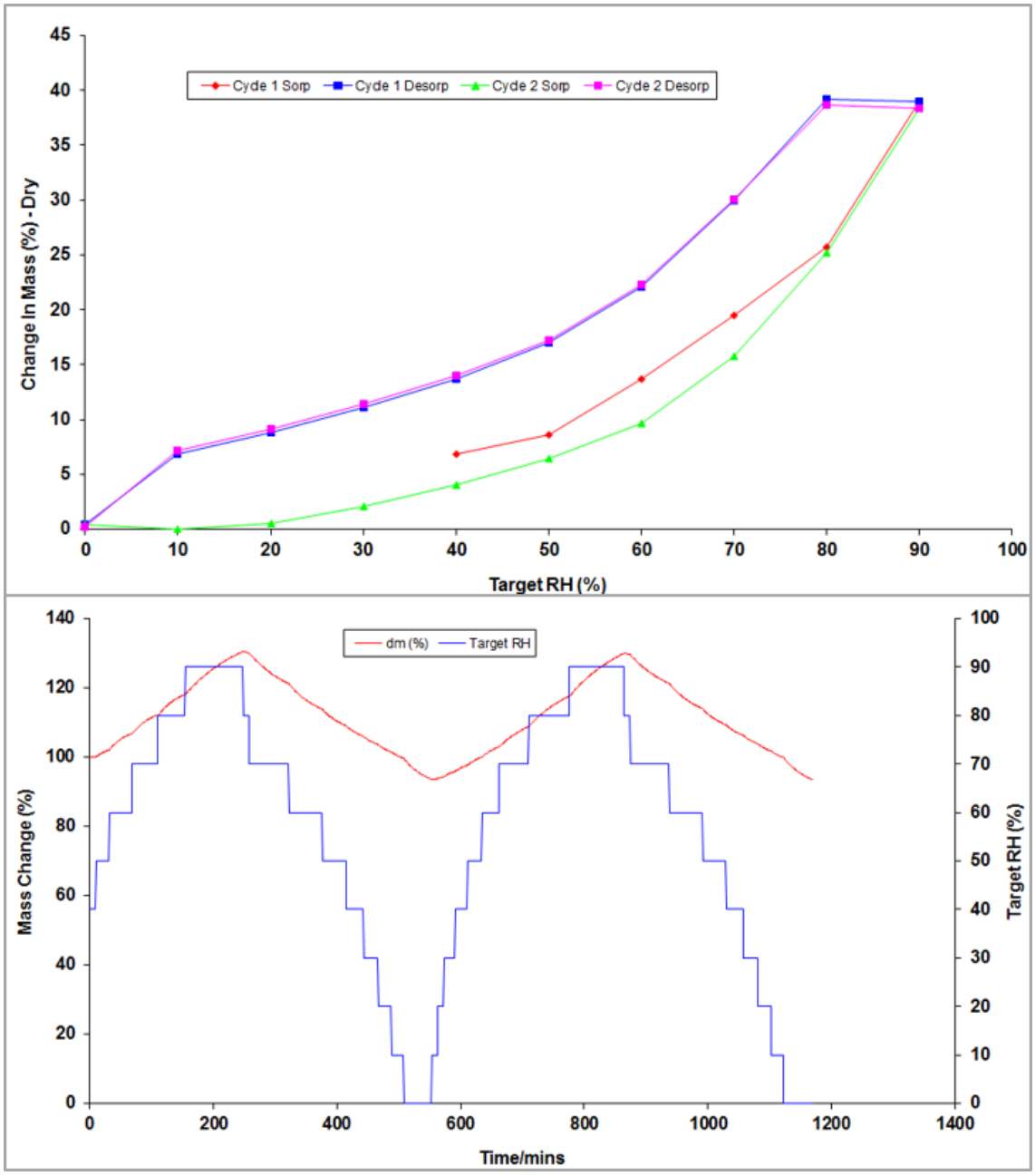


***Figure 4.25*** *Isotherms (top) and change in mass plot (bottom) for PVP. N.B. see scale.*

PVP displays much greater hygroscopicity across the humidity range tested (Figure 4.25) than that of pyrogallol. Use of a material which displays greater resistance to moisture uptake, such as pyrogallol, especially at lower humidity levels, may prove beneficial for use as an amorphous stabilising agent where the uptake of water can negatively impact the stability of the phase.

#### 4.5.5.4 Summary

The possibility of replacing polymer with small molecule stabilising agents when developing formulations with amorphous API could potentially allow greater drug loading and the use of compounds with more suitable side effect profiles. With the example of pyrogallol showing reduced moisture uptake in comparison to PVP, the possibility of further reducing the chance of crystallisation from the amorphous form by careful selection of co-former is highlighted.

## 4.6 Conclusions

In this work, the application of an optimised co-crystal screen, utilising computational tools to predict the most energetically favourable co-formers, has led to the discovery of no co-crystals, but has highlighted a 1:1 interaction between ROY and pyrogallol. This interaction stabilises ROY in the amorphous form, although this stability is moisture dependent. Although predictive technology exists for single component amorphous phases,[155] currently no predictive method for co-amorphous phases has been suggested and all screening is by trial and error. The discovery of this behaviour stemmed from a screen of 342 co-formers, in three stoichiometries, in which predicted interaction had been ranked highly in the gas phase. This suggests that co-crystal screening approaches can be modified to enable study into co-amorphous phases and that 'negative' co-crystal hits should be investigated for alternative utility as co-amorphous materials. Such an approach would enable a broader palate of pharmaceutical development options and improve process efficiency.

# Chapter 5 – Investigation into co-amorphous interactions

## 5.1 Introduction

Having made the discovery of the co-amorphous behaviour of the combination of ROY and pyrogallol in the previous chapter, further work to better understand this behaviour, and its applicability beyond pyrogallol, was explored and will be presented in this chapter. To aid in understanding of the interactions leading to the stabilisation of the amorphous material, experiments employing analogous compounds to pyrogallol were combined with ROY in the same manner. These compounds included other trihydroxybenzenes (1,2,4-benzenetriol and phloroglucinol) as well as dihydroxybenzenes (resorcinol, catechol and hydroquinone) to investigate the effect of position of the hydroxy functional group and two dihydroxycylohexanes (1,2- and 1,4-cyclohexanediol) to probe the effect due to the presence or lack of aromaticity in the co-former.

To summarise the steps of the investigation; after producing the ROY:co-former grinds using the same method as that for ROY:pyrogallol in Chapter 4, the materials were first analysed by PXRD to check for co-crystallisation or other form change. The ROY:co-former samples as well as the pure compounds were analysed by DSC to allow comparison between their thermal behaviour and that seen in the ROY:pyrogallol system. Consideration of the structure of the pyrogallol analogues and the outcome of the DSC experiments allowed conclusions relating the structure to the stabilisation interactions. A brief comparison of stability of the co-amorphous systems was also conducted.

## 5.2 Production and analysis of ROY:co-former pairs

### 5.2.1 Method

The required amount of ROY to achieve 25mg of a 1:1 molar ratio with each specific co-former was weighed out, and with the equimolar equivalent of potential co-former, placed in a mortar before grinding by hand with a pestle for five minutes. The resultant materials were characterised as described below.

## 5.2.2 Characterisation

### 5.2.2.1 Powder X-ray diffractometry

Before using thermal techniques to investigate the amorphous stabilisation behaviour of the ground ROY:co-former materials, they were first analysed by PXRD to confirm that in their current form they consisted of a physical mixture of the two parent compounds and no form change had taken place during the grinding process. Figure 5.1 is an example PXRD pattern comparison between the patterns of pure ROY (red), pure co-former, in this case 1,2,4-benzenetriol (blue) and the 1:1 molar ratio grind of these two compounds (green). The comparison shown is representative of all but one of the other co-formers in that all of the peaks observed are present in either of the parent components and therefore not indicative of form change. The only exception is that of the comparison of ROY and phloroglucinol, in which either a new peak has been detected or a peak shift occurred and there is a lack of presence of relatively small but still significant peaks which feature in the PXRD pattern of pure phloroglucinol (Figure 5.2, peaks at 17.25° 2θ, green pattern and 14.15 and 19.80° 2θ blue pattern). These differences in PXRD patterns indicate the formation of a new form, which is discussed in the TGA section below. A full set of PXRD patterns is presented in Appendix 5.

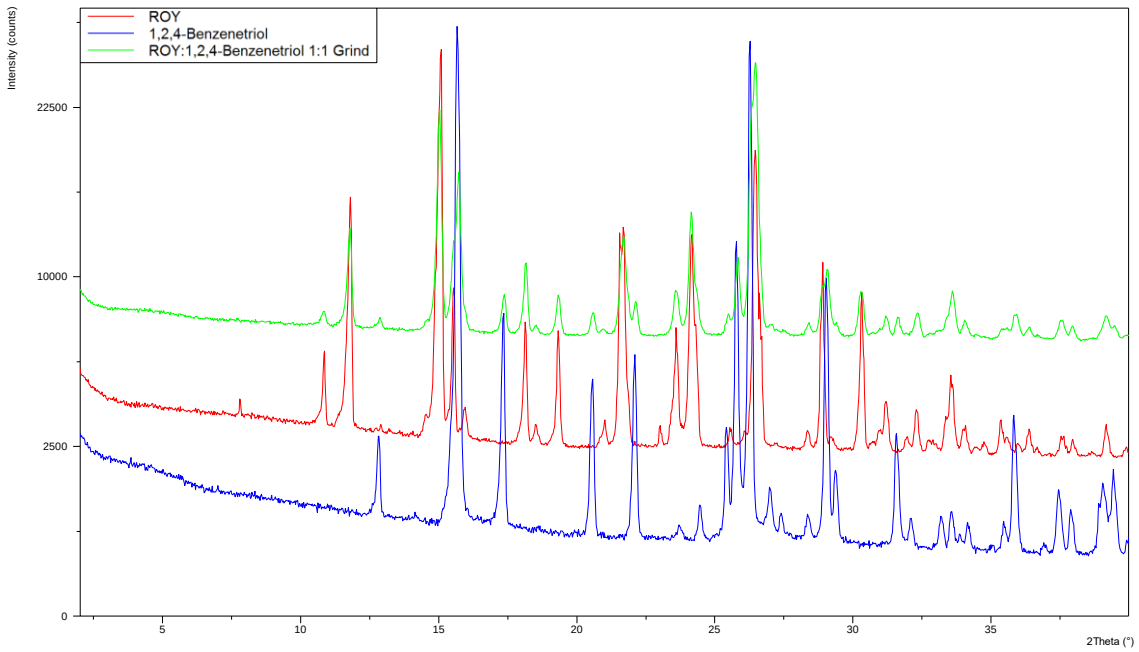


***Figure 5.1*** *PXRD patterns for ROY (red), 1,2,4-benzenetriol (blue) and the product of the grind of a 1:1 molar ratio of these two compounds (green).*

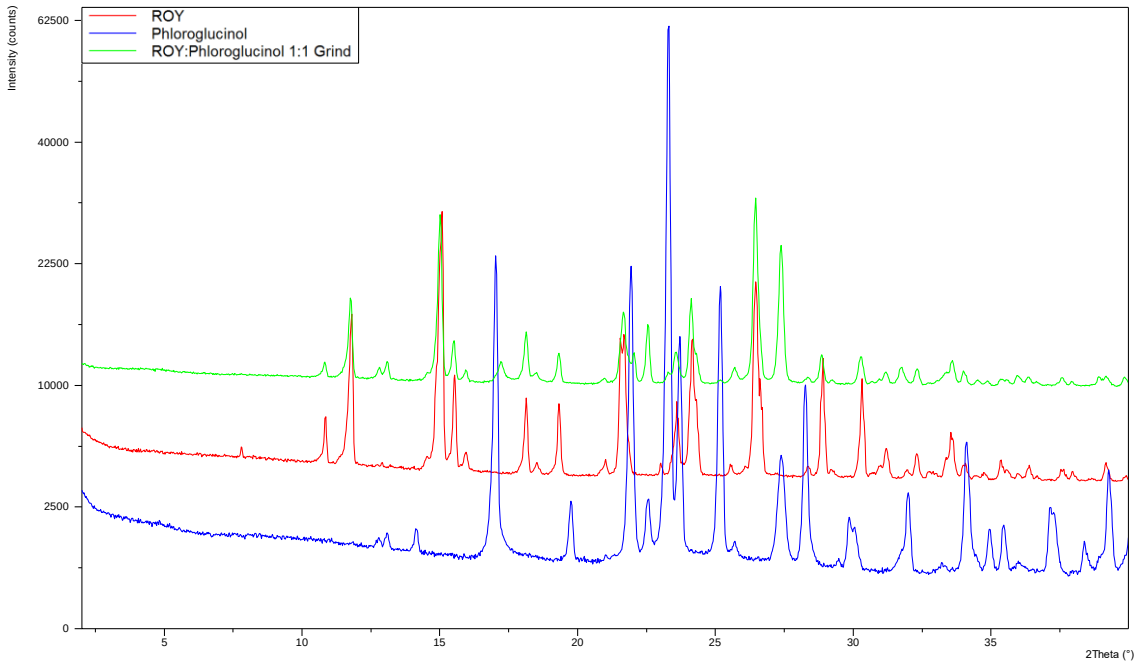


***Figure 5.2*** *PXRD patterns for ROY (red), phloroglucinol (blue) and the product of the grind of a 1:1 molar ratio of these two compounds (green).*

Figure 5.3 compares the experimentally measured PXRD patterns of phloroglucinol and the product of the grind of a 1:1 molar ratio of ROY and phloroglucinol to a predicted pattern of anhydrous phloroglucinol and a predicted pattern of phloroglucinol dihydrate.[156] The predicted patterns were produced using Mercury software and are based on the CIF files of the CSD entries for phloroglucinol (PHGLOL) and phloroglucinol dihydrate (PHGLOH04) as these were the only structures determined from a room temperature experiment. The experimental phloroglucinol pattern is very similar to that of the predicted anhydrous phloroglucinol pattern but clearly also contains peaks specific to the dihydrate, for example the two peaks at around 13° 2θ. The presence of these peaks indicates that there is some amount of phloroglucinol dihydrate impurity within the phloroglucinol sample. The pattern for the product of the grind of a 1:1 molar ratio of ROY and phloroglucinol obviously additionally contains peaks caused by the presence of ROY. However, the phloroglucinol dihydrate characteristic peaks are also more prominent in this sample than those of the experimental phloroglucinol sample, suggesting greater conversion to phloroglucinol dihydrate than in the phloroglucinol sample. The more prominent phloroglucinol dihydrate peaks may potentially be causing peak overlap at around 17.25° 2θ explaining the presence of this peak which is not present in either of the pure ROY or phloroglucinol samples.

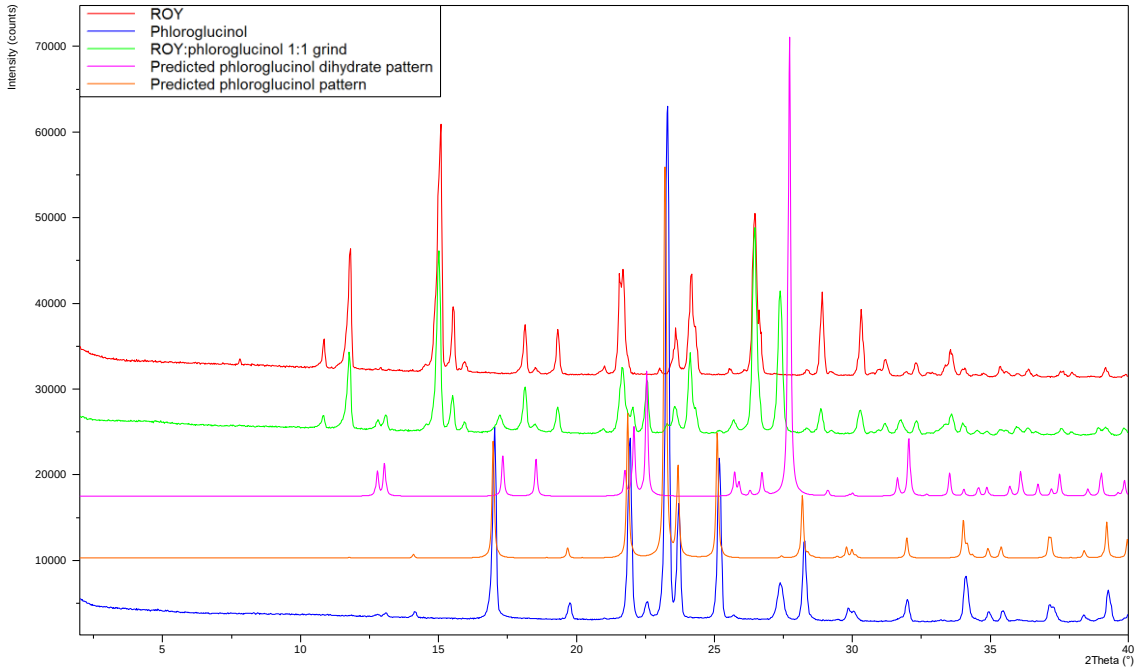


***Figure 5.3*** *PXRD patterns for phloroglucinol (blue), ROY (red), the product of the grind of a 1:1 molar ratio of ROY and phloroglucinol (green), a predicted pattern of phloroglucinol (orange) and a predicted pattern of phloroglucinol dihydrate (pink).*

### 5.2.2.2 Dynamic vapour sorption analysis of phloroglucinol

Due to the presence of the hydrated form of phloroglucinol being detected by PXRD, a sample was analysed by DVS following the standard method detailed in Chapter 2, in order to better understand its hydration behaviour in relation to the investigations with ROY.

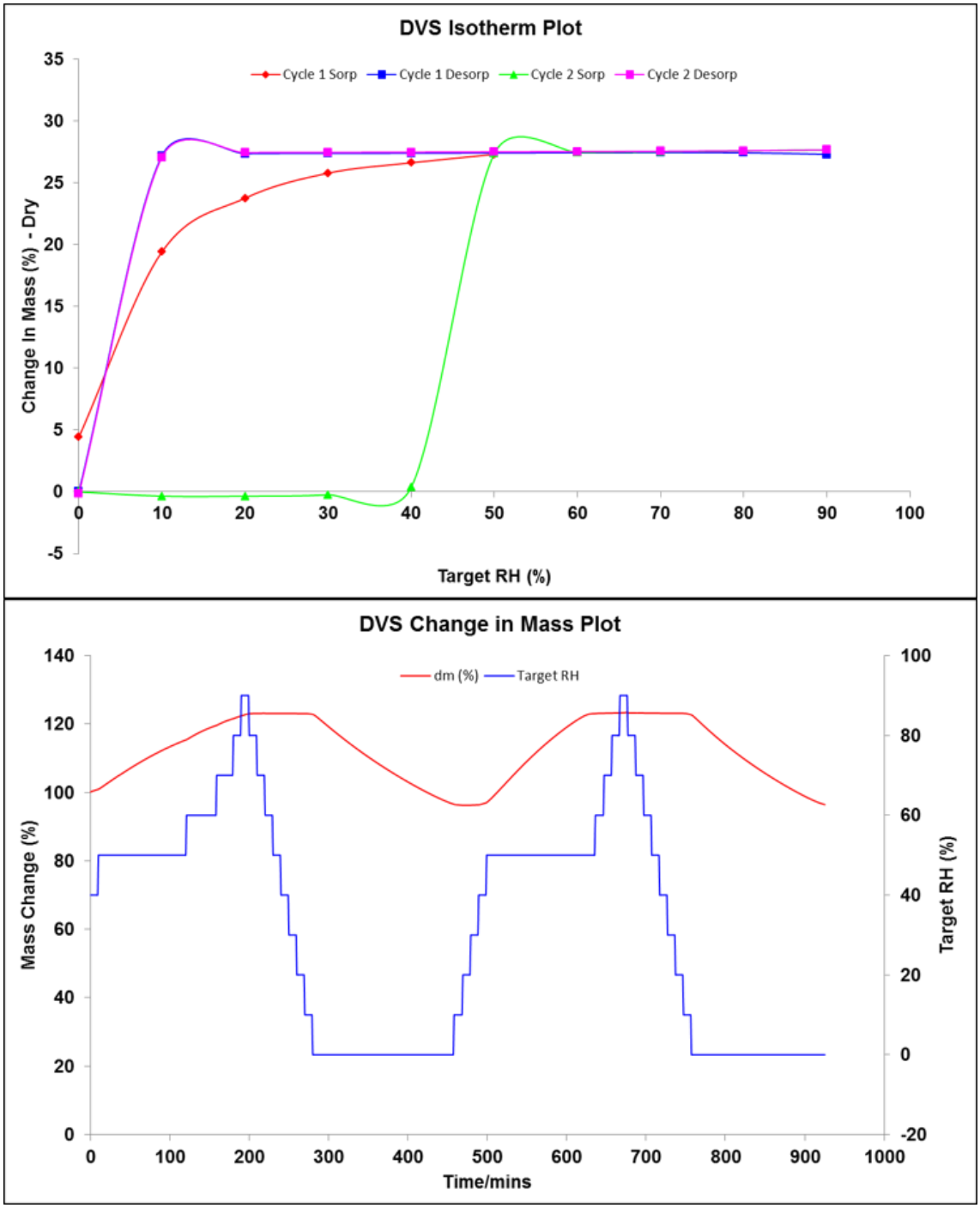


***Figure 5.4*** *Isotherms (top) and change in mass plot (bottom) for phloroglucinol.*

The percentage mass gain and loss during the sorption and desorption cycles of the DVS isotherm plot for phloroglucinol (Figure 5.4) is consistent with the formation of the dihydrate from anhydrous phloroglucinol. The relative humidity range over which the transition between anhydrous and dihydrate occurs is within that often measured in the laboratory, however dehydration is not seen above approximately 20% relative humidity. Due to the low RH required for dehydration from the dihydrate to occur this is very unlikely to have taken place in the laboratory. These findings are in line with the analysis from PXRD and TGA.

### 5.2.2.3 Thermogravimetric analysis of phloroglucinol samples

TGA profiles were recorded following the standard TGA method detailed in Chapter 2 for phloroglucinol and the product of the grind of the 1:1 molar ratio of ROY and phloroglucinol due to the suspected presence of a hydrated form of phloroglucinol from the PXRD and DVS analysis.

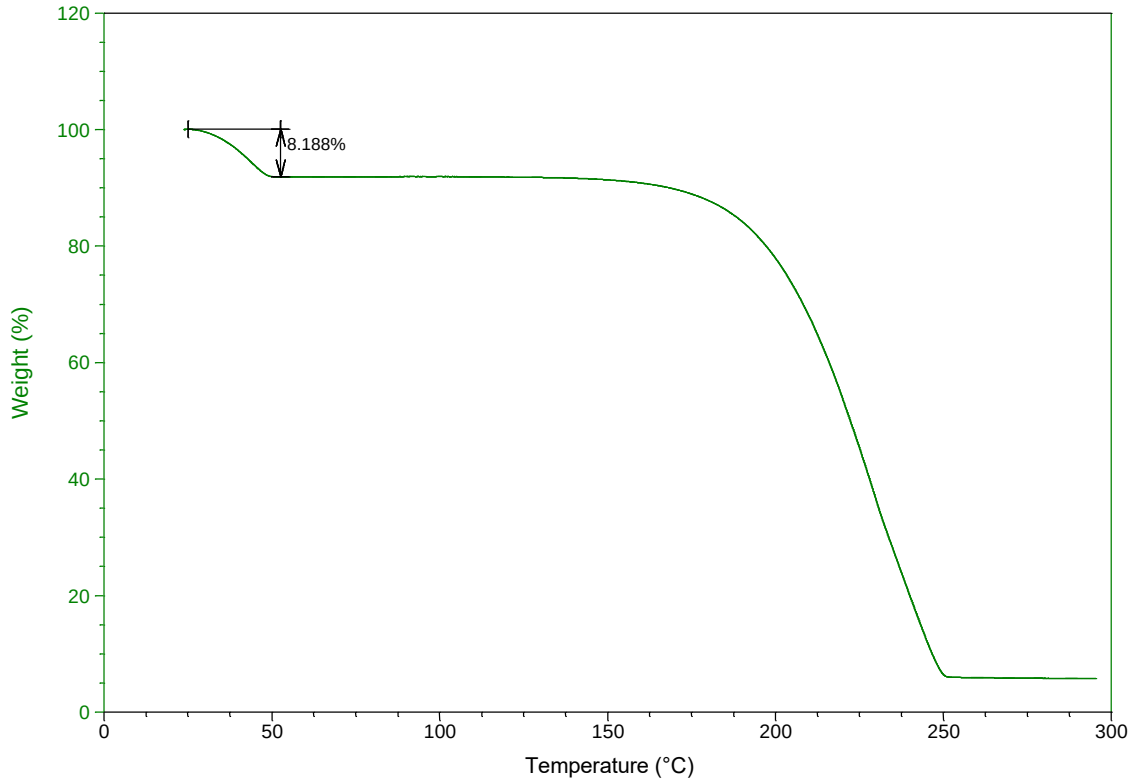


***Figure 5.5*** *TGA profile for the product of the grind of the 1:1 molar ratio of ROY and phloroglucinol.*

Figure 5.5 shows the TGA profile for the product of the grind of the 1:1 molar ratio of ROY and phloroglucinol. A mass loss of 8.188% occurs over the temperature range of approximately 25°C to 50°C. This equates to a molecular mass of 31.56 for each pair of ROY and phloroglucinol molecules, or 126.22 for every four pairs. The molecular weight of water is 18.02 and given that the grinding of materials occurred in a standard laboratory where relative humidity often falls within a 20 to 60% range it is possible from this evidence that a 4:4:7 ROY:phloroglucinol:water hydrate has formed. A potentially more likely scenario is that the dihydrate of phloroglucinol had formed leaving a small amount of anhydrous phloroglucinol which would explain the ratio of water molecules calculated from the mass loss being closer to seven than eight per four ROY and phloroglucinol molecules. The endothermic event in the DSC trace is however not consistent with this, and it is possible that, as necessarily a different sample must be used, as that in the TGA will be destroyed, the samples may have varying amounts of hydrated phloroglucinol present.

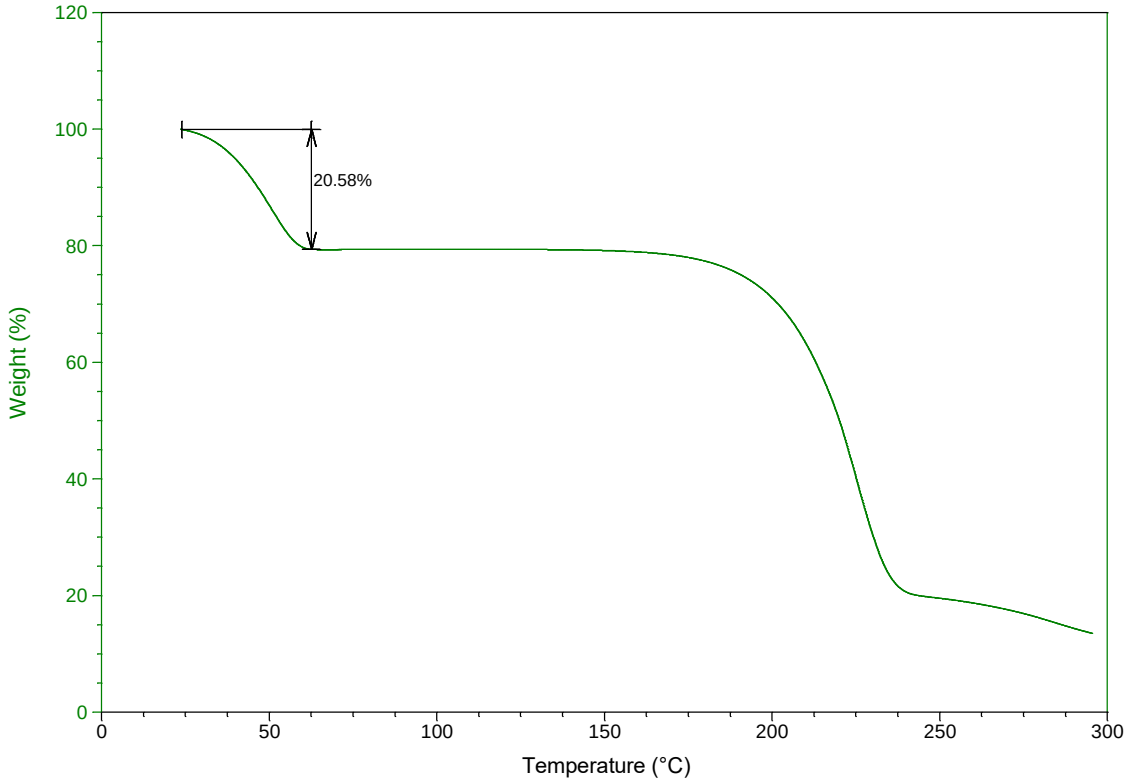


***Figure 5.6*** *TGA profile for phloroglucinol.*

The TGA profile for phloroglucinol (Figure 5.6) shows a mass loss of 20.58% which is lower than expected if the sample was the dihydrate form (22.22%), but obviously more than if it were the anhydrous form. Given the results from PXRD and DVS it is likely that due to RH in the laboratory fluctuating within a range encompassing that in which hydration of anhydrous phloroglucinol occurs, partial hydration of the sample led to the intermediate mass loss during the TGA experiment. This would also explain the extra PXRD peaks observed and thereby indicate that co-crystalline material was not formed.

### 5.2.2.4 Differential scanning calorimetry

The pure co-formers and the products of the grind of a 1:1 molar ratio of ROY and the co-formers were analysed by DSC employing the standard heat/cool/heat method detailed in Chapter 2. This analysis was undertaken to allow comparison between their thermal behaviour and that seen in the ROY:pyrogallol system. Where necessary the sample was prepared by light grinding by hand to achieve a more uniform particle size, in the case of these samples this was only done for 1,2-cyclohexanediol. The maximum temperature for the DSC method was set slightly above the melting point for the sample based on the literature values for the pure co-formers and for the products of grinding with ROY, where this was not suitable due to degradation occurring, a repeat DSC analysis was carried out with the maximum temperature set in excess of the melting

point observed in the original analysis but below the temperature where degradation occurred. The samples which required the repeated analysis (and the maximum temperature set for the DSC method) were: ROY:hydroquinone (110°C), ROY:1,2-cyclohexanediol (120°C), ROY: 1,4-cyclohexanediol (110°C) and ROY:phloroglucinol (120°C).

The figures below group the DSC traces into pure co-formers (Figures 5.7-5.9) and products of the grind of a 1:1 molar ratio of ROY and the co-formers (Figures 5.10-5.12). These are further arranged by the cycle of the DSC method and the traces for pure ROY are included in all figures for comparison. i.e. Figure 5.7 shows the first heating cycle, Figure 5.8 cooling etc.

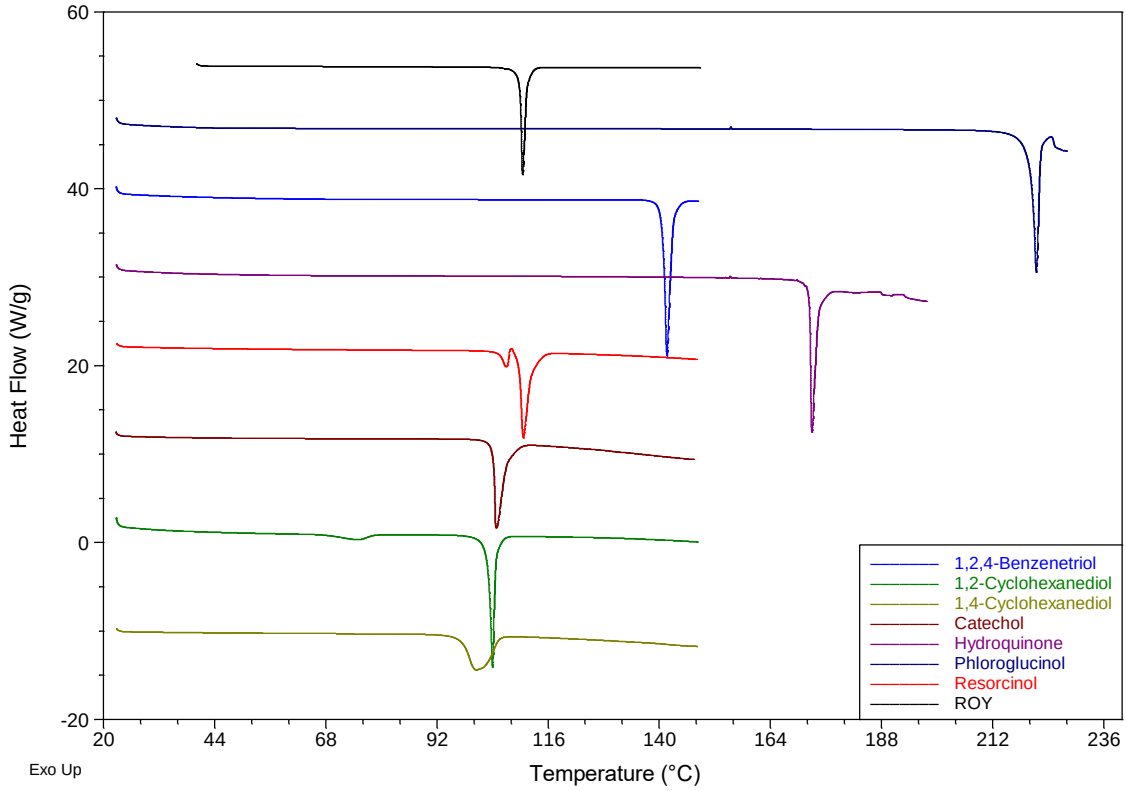


***Figure 5.7*** *DSC traces for the initial heating cycle of pure ROY (black) and pure co-formers: phloroglucinol (dark blue), 1,2,4-benzenetriol (blue), hydroquinone (purple), resorcinol (red), catechol (brown), 1,2-cyclohexanediol (green) and 1,4-cyclohexanediol (olive).*

The DSC trace for resorcinol displays a small endothermic peak just before a much larger one. There are two polymorphs of resorcinol[157] and it is possible that a small amount of the polymorph with the lower melting point was present in the sample leading to the initial melting peak. It is also possible that there was a larger amount of the lower melting point polymorph which melted while simultaneously some of the now molten resorcinol crystallised as the higher melting point polymorph before melting again at a higher temperature thereby leading to a smaller endothermic peak at the lower melting point temperature. Varying the heating rate

would be required to better separate the endothermic events. The minor endotherm in the initial heating cycle of 1,2-cyclohexanediol (Figure 5.7) is possibly due to a phase transition, evidence of which has been previously reported.[158] The second endothermic peak in the second heating cycle of 1,2-cyclohexanediol (Figure 5.9) appears to be an artefact in the measurement due to the shape of the trace.

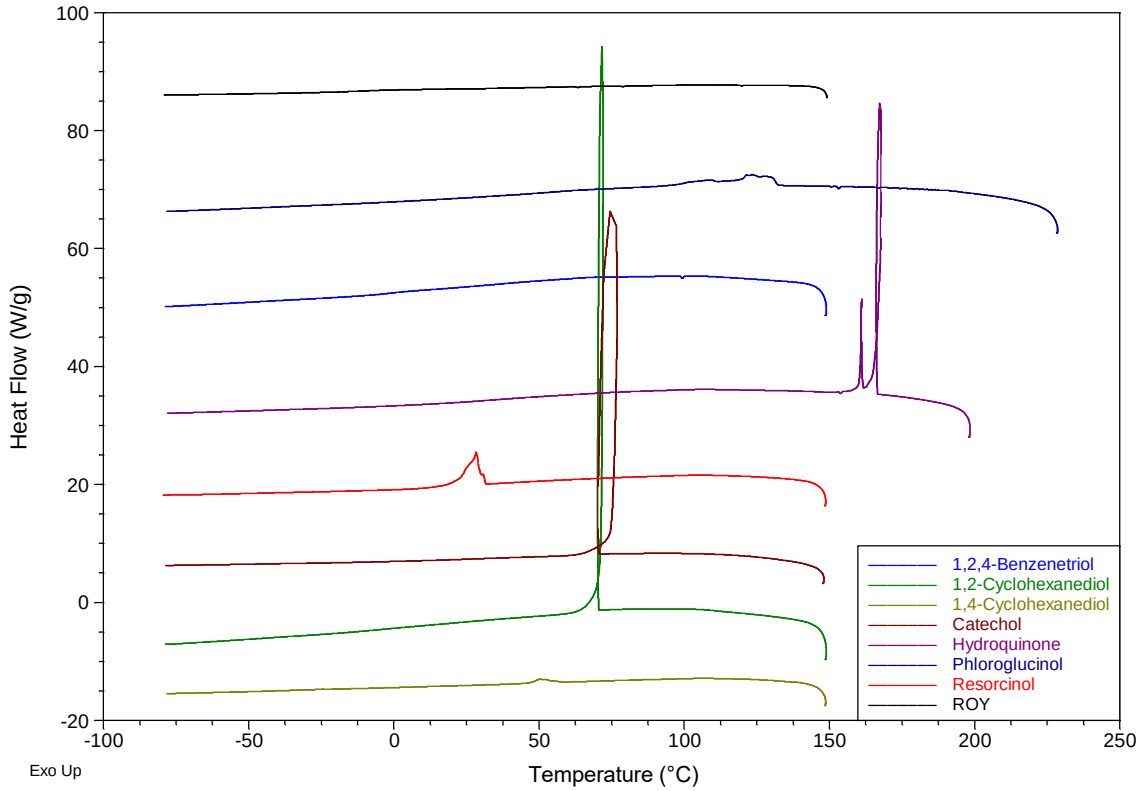


***Figure 5.8*** *DSC traces for the cooling cycle of pure ROY (black) and pure co-formers: phloroglucinol (dark blue), 1,2,4-benzenetriol (blue), hydroquinone (purple), resorcinol (red), catechol (brown), 1,2-cyclohexanediol (green) and 1,4-cyclohexanediol (olive).*

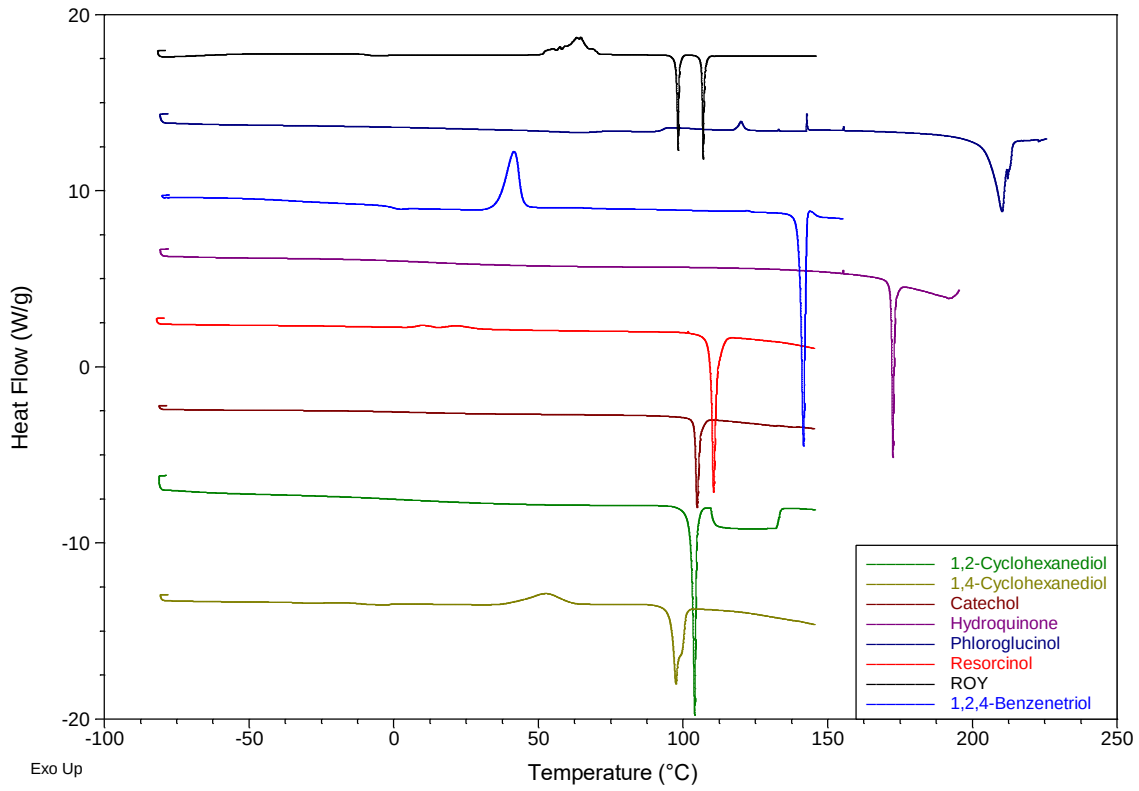


***Figure 5.9*** *DSC traces for the second heating cycle of pure ROY (black) and pure co-formers: phloroglucinol (dark blue), 1,2,4-benzenetriol (blue), hydroquinone (purple), resorcinol (red), catechol (brown), 1,2-cyclohexanediol (green) and 1,4-cyclohexanediol (olive).*

***Table 5.1*** *Data obtained from DSC analysis of the pure co-formers recording the temperature and type of events observed in the thermograms and the corresponding class of material. Pure ROY and pyrogallol data are included for comparison.*

| **Material** | **Observations in cycle (Endo/Exo/$T_g$ at temperature (°C))** | | | **Class** |
|---|---|---|---|---|
| | **Initial heating** | **Cooling** | **Second heating** | |
| ROY | Endo 109.9 | - | $T_g$ -9.4, Exo 58.5, Endo 97.6, Endo 106.4 | II |
| Pyrogallol | Endo 132.5 | Exo 100.4 | Endo 132.5 | I |
| 1,2,4-Benzenetriol | Endo 140.9 | - | $T_g$ -0.2, Exo 35.9, Endo 140.4 | II |
| Phloroglucinol | Endo 220.3 | Exo 132.1 | Endo 205.1 | I |
| Catechol | Endo 104.3 | Exo 74.4 | Endo 104.0 | I |
| Resorcinol | Endo 105.4, Endo 109.7 | Exo 29.6 | Exo 6.3, Exo 16.7, Endo 109.6 | I |
| Hydroquinone | Endo 172.5 | Exo 167.2, Exo 161.2 | Endo 171.9 | I |
| 1,2-Cyclohexanediol | Endo 67.7, Endo 103.2 | Exo 71.2 | Endo 102.9, 110.2 | I |
| 1,4-Cyclohexanediol | Endo 97.3 | Exo 55.1 | Exo 40.2, Endo 95.7 | I |

The data in Table 5.1 was obtained using TA Instruments Universal Analysis 2000 software (version 4.5A) and temperatures listed are the onset temperatures of peaks determined by integration were possible, or of peak maxima where integration was not possible for example superheating of samples in some of the cooling cycles giving rise to loops in the traces. The temperature reported for the glass transitions is the inflection point. The classes listed in Table 5.1 refer to the classification of materials based their crystallisation tendency from the undercooled melt, following the classification system introduced by Baird *et al*.[148] The same experiments were repeated for the products of the grind of a 1:1 molar ratio of ROY and the co-formers and the resultant DSC traces shown in Figures 5.10 to 5.12 and summarised in Table 5.2.

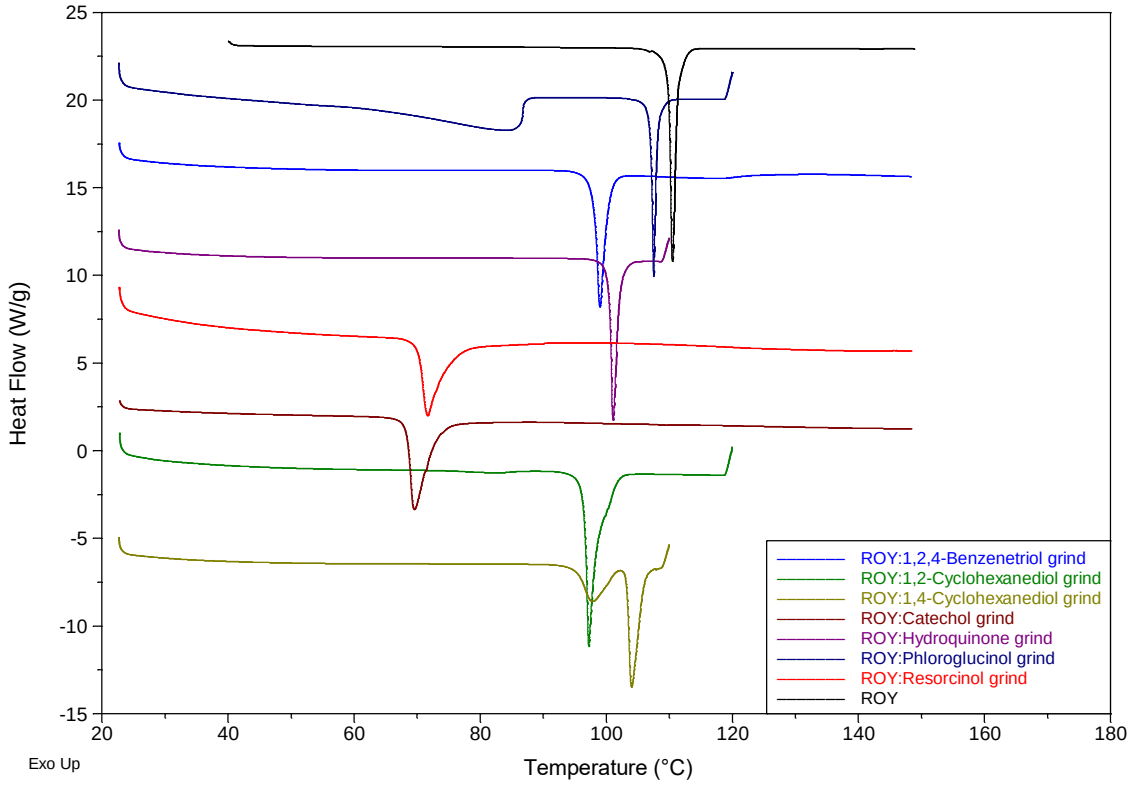


***Figure 5.10*** *DSC traces for the initial heating cycle of the products of the grind of a 1:1 molar ratio of ROY and the co-formers: 1,2,4-benzenetriol (blue), hydroquinone (purple), resorcinol (red), catechol (brown), 1,2-cyclohexanediol (green) and 1,4-cyclohexanediol (olive); and pure ROY (black) for comparison.*

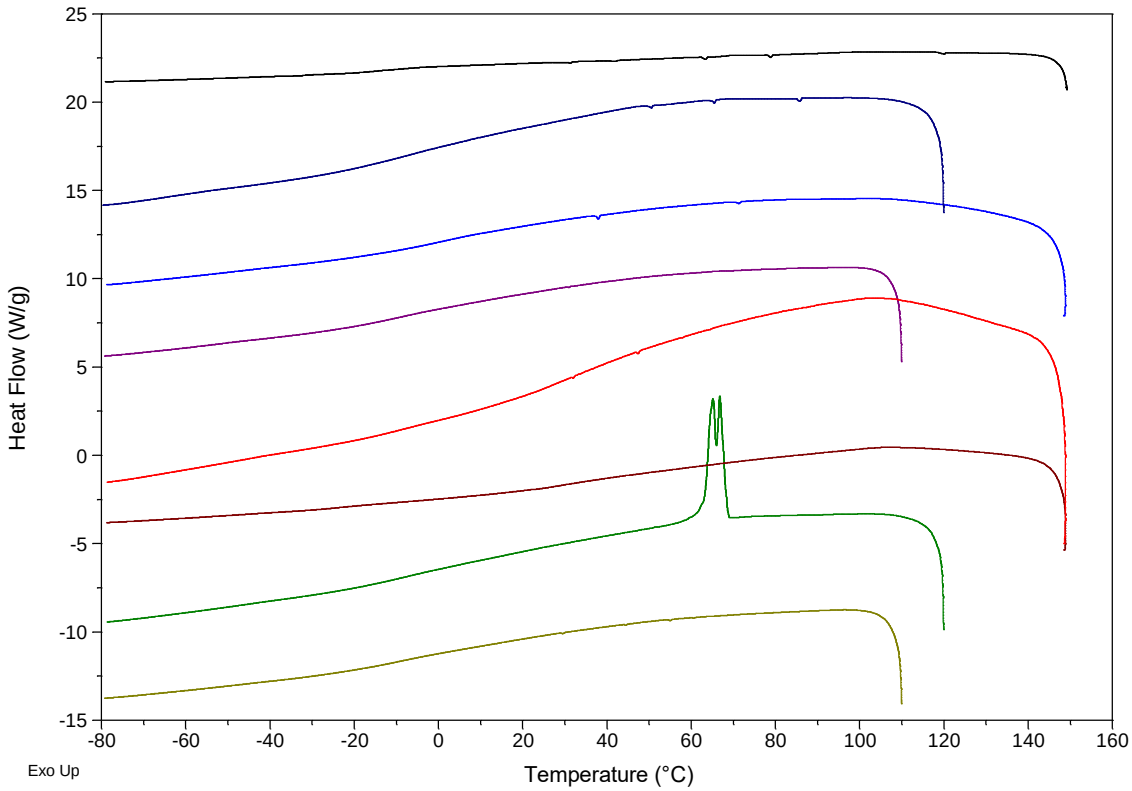


***Figure 5.11*** *DSC traces for the cooling cycle of the products of the grind of a 1:1 molar ratio of ROY and the co-formers and pure ROY for comparison. Traces are coloured as in Figure 5.10.*

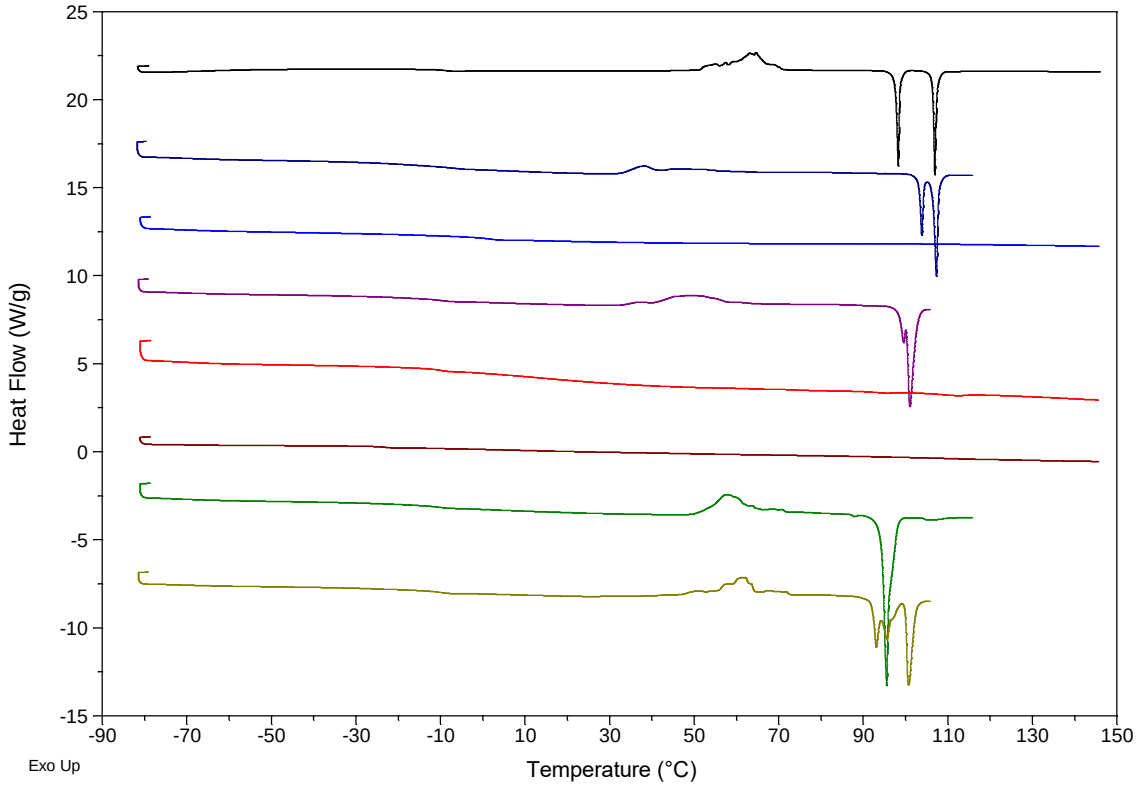


***Figure 5.12*** *DSC traces for the second heating cycle of the products of the grind of a 1:1 molar ratio of ROY and the co-formers and pure ROY for comparison. Traces are coloured as in Figure 5.10.*

***Table 5.2*** *Data obtained from DSC analysis of the products of the grind of a 1:1 molar ratio of ROY and the co-formers, recording the temperature and type of events observed in the thermograms and the corresponding class of material. Pure ROY and ROY:pyrogallol data are included for comparison.*

| Material | Observations in cycle (Endo/Exo/$T_g$ at temperature (°C)) | | | Class |
|---|---|---|---|---|
| | Initial heating | Cooling | Second heating | |
| ROY | Endo 109.9 | - | $T_g$ -9.4, Exo 58.5, Endo 97.6, Endo 106.4 | II |
| ROY:pyrogallol | Endo 88.5 | - | $T_g$ -6.3 | III |
| ROY:1,2,4-benzenetriol | Endo 98.1 | - | $T_g$ 1.75 | III |
| ROY:phloroglucinol | Endo 91.9, Endo 107.0 | - | $T_g$ -6.2, Exo 33.3, Endo 103.3, Endo 106.5 | II |
| ROY:catechol | Endo 68.3 | - | $T_g$ -23.0 | III |
| ROY:resorcinol | Endo 70.1 | - | $T_g$ -10.0 | III |
| ROY:hydroquinone | Endo 100.6 | - | $T_g$ -9.4, Exo 33.0, Exo 41.4, Endo 99.5, Endo 100.3 | II |
| ROY:1,2-cyclohexanediol | Endo 96.5 | Exo 68.3, Exo 65.7 | $T_g$ -10.7, Exo 57.6, Endo 94.4 | I |
| ROY:1,4-cyclohexanediol | Endo 95.2, Endo 103.3 | - | $T_g$ -9.8, Exo 62.1, Endo 93.0, Endo 94.5, Endo 100.0 | II |

The broad endothermic peak observed in the initial heating cycle of ROY:phloroglucinol (Figure 5.10) is typical of dehydration, likely caused by hydration of the phloroglucinol to form the dihydrate to some extent, as discussed in the initial characterisation section. The multiple melting endotherms seen in the second heating phase of this sample and that of ROY:1,4-cyclohexanediol, around 90-110°C is likely due to different polymorphs of ROY having crystallised and the interaction with the co-former present in the sample causing adjustment to the temperature at which melting occurs compared to that of the pure ROY polymorphs.

### 5.2.3 Summary

A summary of the amorphous behaviour of the ROY:co-former samples compared to the pure parent components is shown in Table 5.3, which lists the outcome, in terms of improvement in amorphous stability, based on DSC analysis of the 1:1 ROY:co-former grinds. The co-formers are listed by those affording the co-amorphous material with greatest increase in glass transition temperature compared to pure ROY.

***Table 5.3*** *Summary of co-amorphous behaviour of ROY:co-former pairs as determined by DSC.*

| Co-former | Class co-former | Class ROY:co-former grind | Improvement in amorphous stability compared to | | $T_g$ shift compared to ROY (°C) |
|---|---|---|---|---|---|
| | | | ROY | Co-former | |
| 1,2,4-Benzenetriol | II | III | Yes | Yes | +11.2 |
| 1,3,5-Benzenetriol (phloroglucinol) | I | II | No | Yes | +3.2 |
| 1,2,3-Benzentriol (pyrogallol) | I | III | Yes | Yes | +3.1 |
| 1,4-Dihydroxybenzene (hydroquinone) | I | II | No | Yes | 0.0 |
| 1,4-Cyclohexanediol | I | II | No | Yes | -0.4 |
| 1,3-Dihydroxybenzene (resorcinol) | I | III | Yes | Yes | -0.6 |
| 1,2-Cyclohexanediol | I | I | No | No | -1.3 |
| 1,2-Dihydroxybenzene (Catechol) | I | III | Yes | Yes | -13.6 |

Although the amorphous stability of the, in this case, model, API is of most concern, it is interesting to note that the presence of ROY improves the amorphous stability in relation to the co-former in all but the case of 1,2-cyclohexanediol. As the API component of a co-crystal is only determined by its medicinal use, and it is quite possible to use a drug as a co-former,[65,159,160,161] the overall high rate of improvement in amorphous stability is promising as applying to a large range of compounds. There does not appear to be a clear correlation between the shift in glass transition temperature and improved stability in relation to ROY. In both cases where large shifts in $T_g$ were measured, improved amorphous stability in relation to ROY and the co-former were observed, however improved stability was also seen with smaller shifts in $T_g$, for example with resorcinol. There does appear to be a correlation between the structure of the co-former and the shift in $T_g$ however, with benzenetriols causing a positive shift, and the dihydroxybenzenes and cyclohexanediols producing a neutral or negative shift. The presence of a third hydroxy group in the co-former molecule potentially altering the environment of the intermolecular bonding to produce the observed increased glass transition temperature as compared to the co-formers with two OH groups.

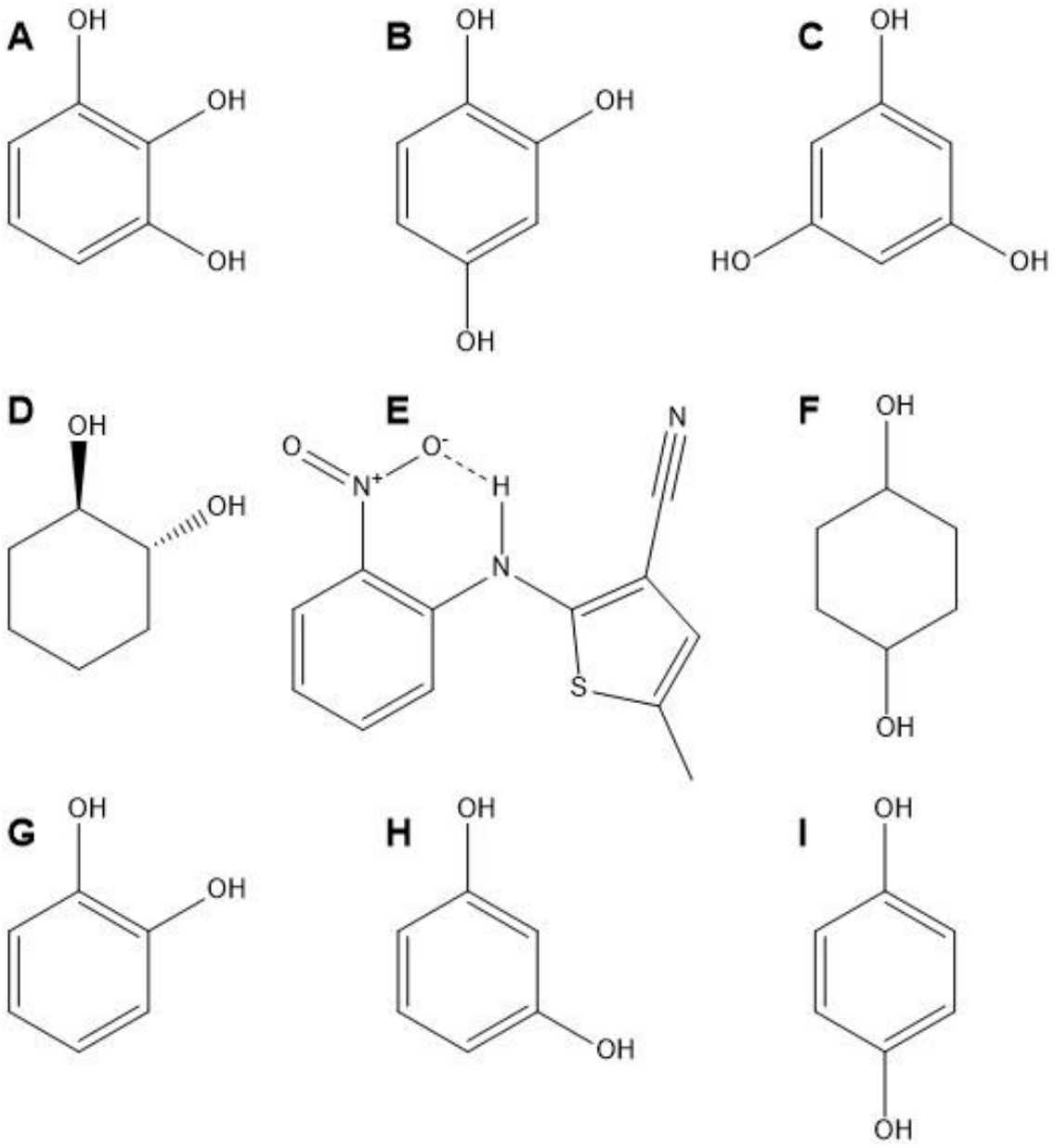


***Figure 5.13*** *Structures of the eight co-formers investigated and that of ROY. A. pyrogallol, B. 1,2,4-benzenetriol, C. phloroglucinol, D. trans-1,2-cyclohexanediol, E. ROY, F. 1,4-cyclohexanediol, G. catechol, H. resorcinol and I. hydroquinone.*

The structures of the compounds (Figure 5.13) which do and do not improve the amorphous stability of ROY, suggest that aromaticity of the ring is necessary for the interactions involved in stabilisation of the amorphous form. This is apparent as neither *trans*-1,2-cyclohexanediol nor the racemic 1,4-cyclohexanediol cause an increase in amorphous stability compared to ROY and in all co-amorphous materials where stability is improved, the co-former is a benzene derivative. The position of the hydroxy group also appears to influence the interactions involved in stabilisation, as although the amorphous stability of all three dihydroxybenzenes are improved

when ground in a 1:1 molar ratio with ROY compared to co-former alone, only catechol and resorcinol also further stabilise the amorphous form in comparison to pure ROY. As these dihydroxybenzene isomers differ only in the position of their OH groups, the location must be of influence in the stabilisation of the co-amorphous material.

In order to test the predictability of the co-amorphous behaviour in these ROY:co-former systems, COSMOtherm calculations were performed as for the ROY co-crystal screen (see Chapter 4, section 4.3.3.1), replacing the standard list of co-formers with the pyrogallol analogues used in this chapter. Preliminary data is displayed in Table 5.4, with the co-formers listed by excess enthalpy and an indication of whether an improvement in amorphous stability compared to ROY was seen experimentally. With the exception of phloroglucinol, all co-formers which led to excess enthalpy being calculated to be less than -0.5kJ.mol$^{-1}$ resulted in an experimentally observed improvement in amorphous stability compared to ROY and those which led to excess enthalpy being calculated to be greater than -0.5kJ.mol$^{-1}$ resulted in no experimentally observed improvement. The results in these ROY:co-former systems lend further evidence to the feasibility of predicting co-amorphous behaviour and show the potential for the possibility of ranking co-formers based on likelihood of co-amorphous material formation.

***Table 5.4*** *Summary of COSMOtherm calculations for the co-formers paired with ROY. List ranked based on calculated excess enthalpy.*

| Co-former | Improvement in amorphous stability compared to ROY | Calculated excess enthalpy ($\Delta H$/kJ.mol$^{-1}$) |
|---|---|---|
| 1,2,3-Benzentriol (pyrogallol) | Yes | -1.237 |
| 1,2-Dihydroxybenzene (Catechol) | Yes | -0.795 |
| 1,2,4-Benzenetriol | Yes | -0.738 |
| 1,3,5-Benzenetriol (phloroglucinol) | No | -0.694 |
| 1,3-Dihydroxybenzene (resorcinol) | Yes | -0.504 |
| 1,4-Dihydroxybenzene (hydroquinone) | No | -0.334 |
| 1,2-Cyclohexanediol | No | -0.033 |
| 1,4-Cyclohexanediol | No | 0.634 |

## 5.3 Further investigation of materials displaying co-amorphous behaviour

The timescale of the stability of the ROY:1,2,4-benzenetriol material was also investigated and compared to that previously measured for ROY:pyrogallol.

### 5.3.1 Method

To produce these results a molten drop of both samples was allowed to fall onto a silicon sample disc. The discs were immediately transferred to the X-ray diffractometer and measurements collected using the same source and slit parameters as the standard PXRD method (Chapter 2) but shortening the scan time to one minute and repeating the method continuously for 100 scans.

### 5.3.2 Powder X-ray diffractometry

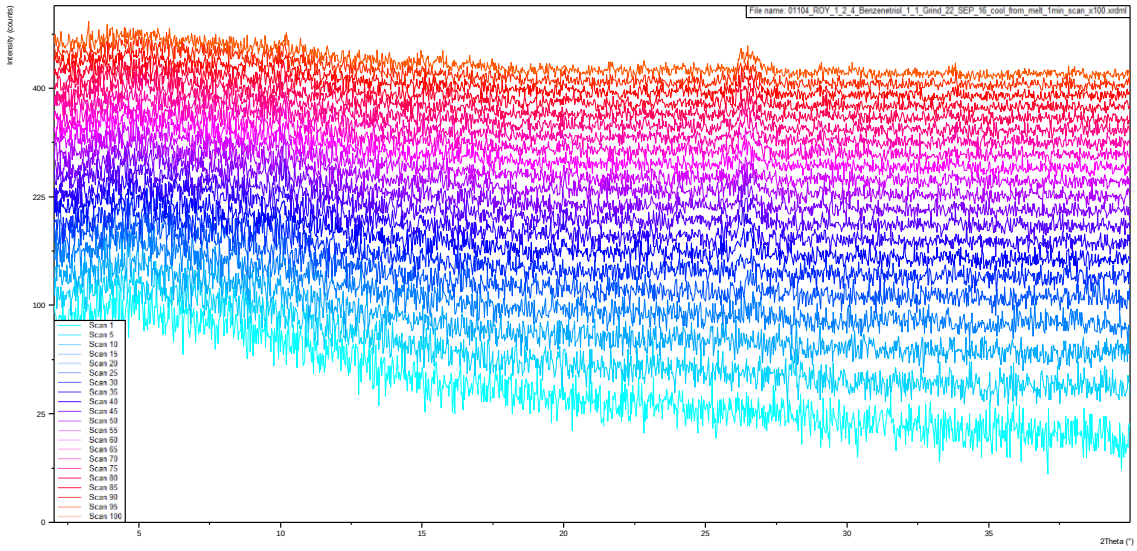


***Figure 5.14*** *Evolution of crystallinity over a 100-minute period from an amorphous droplet of ROY:1,2,4-benzenetriol 1:1 grind, scan lengths of approximately one minute repeating continuously for 100 minutes.*

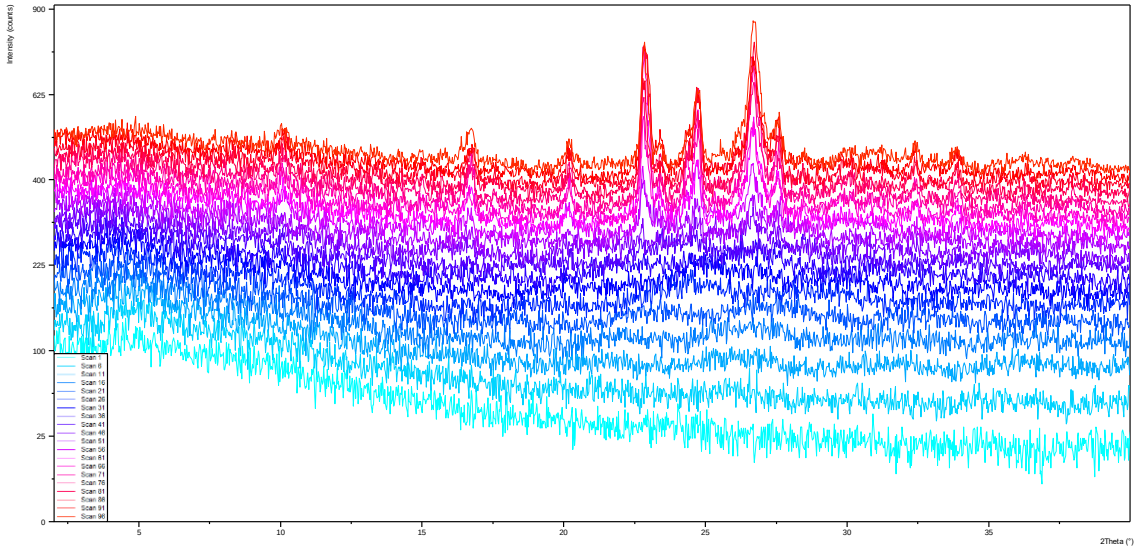


***Figure 5.15*** *Evolution of crystallinity over a 100-minute period from an amorphous droplet of ROY:pyrogallol 1:1 grind, scan lengths of approximately one minute repeating continuously for 100 minutes.*

Figures 5.14 and 5.15 compare the evolution of crystallinity from a molten droplet of ROY:1,2,4-benzenetriol 1:1 grind with that of ROY:pyrogallol 1:1 grind. With the ROY:pyrogallol 1:1 grind sample there is clearly significant crystalline material present after 100 minutes as evidenced by the multiple defined peaks present in the powder pattern at that time point. In comparison, the powder pattern for the ROY:1,2,4-benzenetriol 1:1 grind sample at 100 minutes contains only very slight peaks above the limit of detection, for example at around 22° 2θ, indicating a much lower level of crystallisation. The time point at which a peak above the limit of detection is observable is difficult to determine due to the short measuring time for each scan, however appears to be around 30 minutes for both samples suggesting a similar retardation time of crystallisation in both materials. The slight shifting of peak position over time, seen especially in the ROY:1,2,4-benzenetriol 1:1 grind sample, is likely due to the progressive change in shape of the droplet of sample as crystallisation occurred varying the overall height of the sample.

## 5.4 Conclusions

By producing materials, combining ROY and co-formers in the same manner as in the previous chapters, but replacing pyrogallol with different co-formers with similar molecular structures, it has been possible to identify certain structural properties which influence the co-amorphous behaviours observed in some of these materials. The aromaticity of the ring structure along with the position of the hydroxy groups both play a part in determining whether intermolecular interactions sufficient to stabilise the amorphous form are formed. The results from the PXRD experiment investigating crystallisation from a molten drop of material suggests that pairing 1,2,4-benzenetriol with ROY may afford an improvement in amorphous stabilisation compared to pyrogallol. It was also noted that even though the co-former may have poor amorphous stability itself, it may still bring about improved amorphous stability in combination with the API, and that the discovery of these stabilised co-amorphous systems stemmed from computational prediction of gas-phase interactions suggests that co-amorphous material formation may be predicable.

# Chapter 6 – Analysis of a co-crystal screen of ornidazole

## 6.1 Introduction

Many techniques have been reported for the analysis of co-crystals, ranging from simple detection of form change from starting components using PXRD to much more in-depth analysis of the physical properties of co-crystals.[47,146,162] Techniques for investigating properties necessarily depend upon the properties being investigated and include for example DSC and TGA for probing thermal behaviour, DVS for looking at moisture sensitivity as an example and HPLC as an option for solubility determination. Improvements in chemical stability such as reduced photodegradation could also require HPLC for sample content determination,[163] and the implementation of other techniques such as IR and NMR spectroscopy to analyse molecular changes. For immediate analysis of a physical co-crystal screen the main aim, especially in high-throughput screening, is efficient identification of any API:co-former pairs which have interacted in a way leading to a form change from the parent materials. This allows further investigations, which require the investment of resources, to be limited to only those substances which may have potentially formed a co-crystalline material. For this reason, a technique that can quickly identify changes in physical form from a small quantity sample is needed. Raman and IR spectroscopy and PXRD are all examples of suitable techniques.[29,121,164,165]

Infrared spectroscopy was used as the initial analytical technique for the ROY co-crystal screen and was a suitable method, as due to the nature of infrared spectroscopy, form changes could be identified from small samples and the process was relatively quick. Although PXRD can require longer analysis times than vibrational spectroscopy, especially with small sample sizes,[29] it is a better technique for detecting changes in solid form as needed for co-crystal screening. The quantity of API and co-former used per well in the co-crystal screening undertaken was specifically chosen to allow adequate material to be recovered for analysis and so PXRD was used for the initial analysis of the ornidazole co-crystal screen presented in this chapter. PXRD is the standard technique for solid form identification (inferior to single crystal X-ray diffraction, however this is usually saved for structure determination due to its many drawbacks) and is a more sensitive technique for the task of hit identification.

Once the hits from the screen have been identified, further characterisation of these materials are undertaken to better understand their nature. This may require the production of a larger scale of the materials for further characterisation to be feasible. Finally, the best co-crystal based on the material with the most desirable properties for the intended application will be identified for possible future development. In pharmaceutical terms, this would usually be an improvement in one or more properties that were identified as substandard for progressing an API further through development into a marketable product. For example: low solubility and ultimately bioavailability, high hygroscopicity or lack of crystallinity, preventing efficient or even feasible processing, or poor physical stability precluding the required shelf life from being achieved.

Analysis from the co-crystal screen of ROY can be found in Chapter 4, a conclusion from this is the highlighting of the potential for analysis from a 'failed' co-crystal screen to lead to other discoveries related to the behaviour of the materials under investigation relevant to the desired outcome. Ornidazole was chosen as the API for this second co-crystal screen as it crystallises with Z' = 3 (i.e., there are three molecules in the crystallographic asymmetric unit) and because it has been hypothesised that molecules which crystallise with Z' > 1 in their pure form, are more likely to form co-crystals than those which do not.[166,167]

## 6.2 Ornidazole co-crystal screen

### 6.2.1 Method

The ornidazole co-crystal screen was conducted using the same methods as that for the ROY co-crystal screen for the computational pre-screen and the physical screen with some variations. The same COSMOtherm method was used to produce a ranked list of potential co-formers and a slight alteration was made to include two co-formers not ranked in the top 48 as positive controls for this screen (C1 and C2 in Table 6.1). The two compounds were 3,5-dinitrobenzoic acid and 4-aminobenzoic acid (PABA) which had both previously been reported in the literature to form co-crystals with ornidazole.[166,168] PABA was ranked (before duplicates were removed, as detailed below) at position 109 with a minimum excess enthalpy of -0.22341 $\Delta H$/kJ.mol$^{-1}$ at a 1:1 stoichiometric ratio, whereas 3,5-dinitrobenzoic acid did not feature in the list of potential co-formers.

The full list of potential co-formers used to create the ranked list consisted of 314 compounds which is less than that used for the ROY calculations. This discrepancy was due to the list being

continuously updated as more compounds are added by the researchers at AZ. The calculations for the ornidazole pre-screen were performed before those for the ROY pre-screen, hence the lower number of compounds. Some duplicates existed in the list and were removed by sorting the list of co-formers alphabetically and deleting any obvious duplicates found next to each other. The chemical structures of all of the co-formers ranking in the top 48 were also checked to remove any which were listed under multiple names, for example 2,5-dihydroxybenzoic acid and gentisic acid.

From the top 48 of the ranked list, three were removed due to duplication and one excluded due to lack of availability (#18 *p*-vinylphenol). The contents of the list were moved accordingly and the original numbers 49 to 52 were consequently included. The two compounds being used as positive controls were substituted in place of two compounds at the lower end of the top 48 ranked list. Isoquinoline (position 46) and pyruvic acid (position 48) were substituted with 3,5-dinitrobenzoic and 4-aminobenzoic acid and respectively. Isoquinoline rather than succinic acid (position 47) was chosen for substitution due to the easier handling of the latter and at such a low position in the ranked list the differences in calculated excess enthalpy are small enough to be insignificant for practical purposes. The final list of the top 46 ranked co-formers and two controls, after amendments, is presented in Table 6.1 below and the full list is presented in Appendix 6.1.

***Table 6.1*** *Co-formers used for the physical co-crystal screen listed by rank based on calculated excess enthalpy and with positive controls highlighted.*

| Rank | Well | Co-former | Calculated excess enthalpy ($\Delta H$/kJ.mol$^{-1}$) |
|---|---|---|---|
| 1 | A1 | Oxalic acid | -2.202 |
| 2 | A2 | Sulfamic acid | -1.957 |
| 3 | A3 | Acesulfame | -1.919 |
| 4 | A4 | 5-Nitroisophthalic acid | -1.654 |
| 5 | A5 | Isocitric acid | -1.591 |
| 6 | A6 | Piperazine | -1.540 |
| 7 | A7 | 2,4-Dihydroxybenzoic acid | -1.432 |
| 8 | A8 | tert-Butylhydroquinone | -1.345 |
| 9 | B1 | Trimesic acid | -1.337 |
| 10 | B2 | 4-Hexylresorcinol | -1.328 |
| 11 | B3 | 3,5-Dihydroxybenzoic acid | -1.327 |
| 12 | B4 | Citric acid | -1.319 |
| 13 | B5 | Etidronic acid | -1.289 |
| 14 | B6 | Resorcinol | -1.283 |
| 15 | B7 | Carnitine | -1.245 |
| 16 | B8 | 1-Hydroxy-2-naphthoic acid | -1.220 |
| 17 | C1 | Fumaric acid | -1.202 |
| 18 | C2 | 2,5-Dihydroxybenzoic acid | -1.155 |
| 19 | C3 | 5-Chlorosalicylic acid | -1.147 |
| 20 | C4 | Aconitic acid | -1.127 |
| 21 | C5 | 3,4-Dihydroxybenzoic acid | -1.016 |
| 22 | C6 | Ketoglutaric acid | -0.995 |
| 23 | C7 | 4,4-Bipyridine | -0.973 |
| 24 | C8 | m-Nitrobenzoic acid | -0.960 |
| 25 | D1 | o-Cresol | -0.938 |
| 26 | D2 | Malonic acid | -0.934 |
| 27 | D3 | Phenol | -0.920 |
| 28 | D4 | Tartaric acid | -0.897 |
| 29 | D5 | Salicylic acid | -0.896 |
| 30 | D6 | Methyl gallate | -0.892 |
| 31 | D7 | 3-Hydroxybenzoic acid | -0.881 |
| 32 | D8 | 3-Hydroxy-2-naphthoic acid | -0.876 |
| 33 | E1 | Octadecylamine | -0.870 |
| 34 | E2 | Thymol | -0.846 |
| 35 | E3 | Maleic acid | -0.832 |
| 36 | E4 | 6-Hydroxy-2-naphthoic acid | -0.816 |
| 37 | E5 | 2,5-Xylenol | -0.802 |
| 38 | E6 | 4-Hydroxybenzoic acid | -0.779 |
| 39 | E7 | 2,6-Dimethylpyrazine | -0.772 |
| 40 | E8 | 2-Oxo-3-phenylpropionic acid | -0.734 |
| 41 | F1 | p-Cresol | -0.724 |

***Table 6.1*** *(Continued)*

| Rank | Well | Co-former | Calculated excess enthalpy ($\Delta H$/kJ.mol$^{-1}$) |
|---|---|---|---|
| 42 | F2 | L-Lysine | -0.707 |
| 43 | F3 | DL-Valine | -0.704 |
| 44 | F4 | 3-Methyl-2-oxobutanoic acid | -0.701 |
| 45 | F5 | p-Ethylphenol | -0.684 |
| 46 | F7 | Succinic acid | -0.669 |
| C1 | F6 | 3,5-Dinitrobenzoic acid | -1.765 |
| C2 | F8 | 4-Aminobenzoic acid | -0.223 |

As 3,5-dinitrobenzoic acid did not feature in the original list of co-formers for the computational pre-screen, a directly comparable value was not determined at the time of COSMOtherm calculations. Access to software which performs similar calculations but on sigma surfaces of predetermined fragments of molecules (COSMOquick) rather than requiring the full molecule sigma surface to be determined ad hoc, and therefore much quicker but potentially less accurate,[169,170] allowed at least a guide value to be calculated (at 1:1 stoichiometry) which is highlighted in Table 6.1.

The physical screening followed the same method as that of the ROY screen except that the 48 co-formers were only screened with ornidazole using acetone as the solvent as there were not repeats with the other solvents as there were for the ROY co-crystal screen. The follow-up analysis for the screen with acetone took priority over repeating with other solvents in this case, as the focus on characterisation of hits from this screen allowed the second optimisation experiment to be undertaken (presented in Chapter 3). The method was thus, 1.25g of ornidazole was dissolved in a DCM solution at a concentration of 100mg/ml. A 250µl aliquot equating to 25mg of ornidazole was added to an equimolar amount of solid, previously weighed, potential co-former in 48 wells of a borosilicate glass 96-well plate. After leaving the initial solvent to evaporate, 50µl of acetone was added to eight wells and the 8-tips of the ultrasonic probe were placed in these wells and sonicated at 50% power for 10 minutes using a Sonics Vibra Cell 130W 20kHz ultrasonic processor. This process was repeated for the remaining wells, one row of eight at a time. In Figure 6.1 the co-formers which had been weighed out and transferred to the wells can be seen in the photograph on the left. The photograph in the middle shows the material in the wells after ornidazole in DCM solution had been added and given time to dry, and the photograph on the right, after the addition of acetone and sonication.

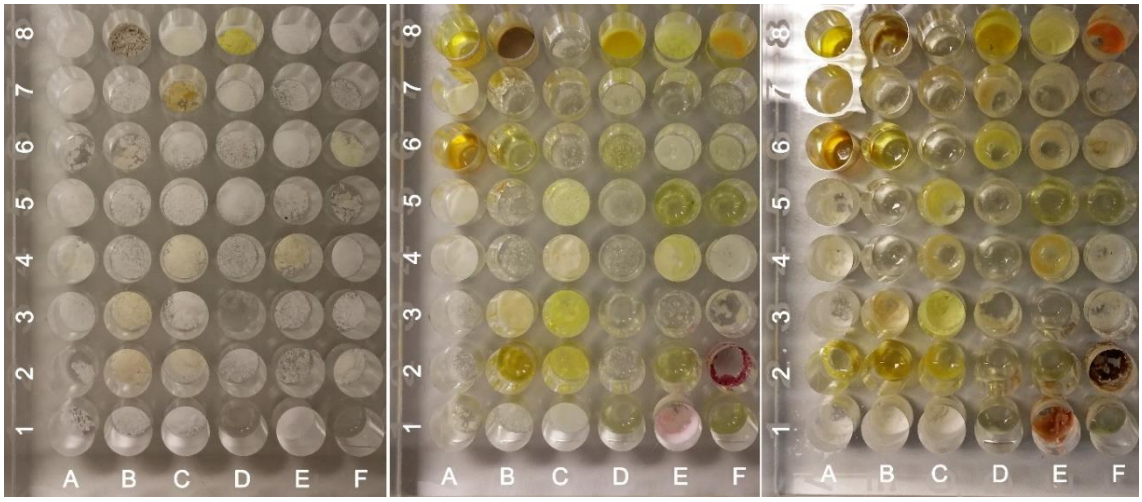


***Figure 6.1*** *Three photographs showing, on the left, the pure co-formers which had been weighed out and transferred into the wells, in the middle, the same plate after the addition of 25mg of ornidazole via a 100mg/ml solution of DCM to each well and being left 14 hours for the solvent to evaporate, and on the right, after sonication.*

Both after the addition of DCM and the subsequent time for solvent evaporation, and after sonication of the wells, it was observed that many of the wells contained material which did not appear crystalline.

## 6.2.2 Analysis of the screen by powder X-ray diffractometry

X-ray diffraction is the 'gold standard' for solid state form identification and would ideally be used for analysis of all co-crystal screening products. Due to limited access to X-ray diffraction resources, previous screens have had to be analysed by FTIR and, if a hit detected, further analysis by PXRD would be warranted. For the ornidazole co-crystal screen analysis was entirely by PXRD rather than FTIR.

When attempting to extract the material from the wells to enable preparation for PXRD analysis, it became apparent that in the wells where the material did not appear crystalline, it tended to be sticky and likely amorphous. Initially only the material from wells where crystalline material was present was removed from the plate for analysis. The rest of the wells were left for up to three months, giving chance for crystallisation to occur.

The plots below (Figures 6.2 – 6.4) are examples of the three types of result that were obtained from the PXRD analysis of the co-crystal screen products. The first, shown in Figure 6.2, is a hit and is identified as such because there is at least one new peak detected that is not present in either of the parent components PXRD patterns. In this case, there are multiple new peaks, the most obvious of which is positioned at 9.7° 2θ, where there are clearly no peaks in the patterns of either of the parent compounds: ornidazole or 5-nitroisophthalic acid.

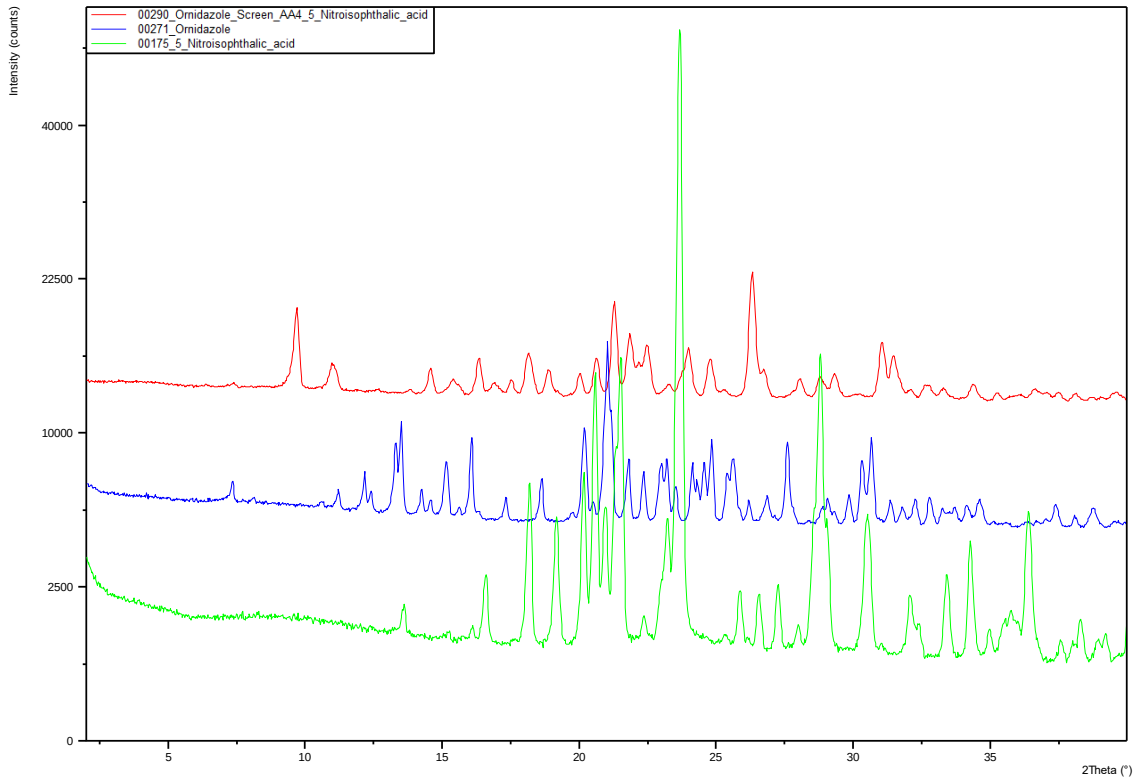


***Figure 6.2*** *PXRD patterns for 5-nitroisophthalic acid (green), ornidazole (blue) and the product of the screen for these two compounds (red).*

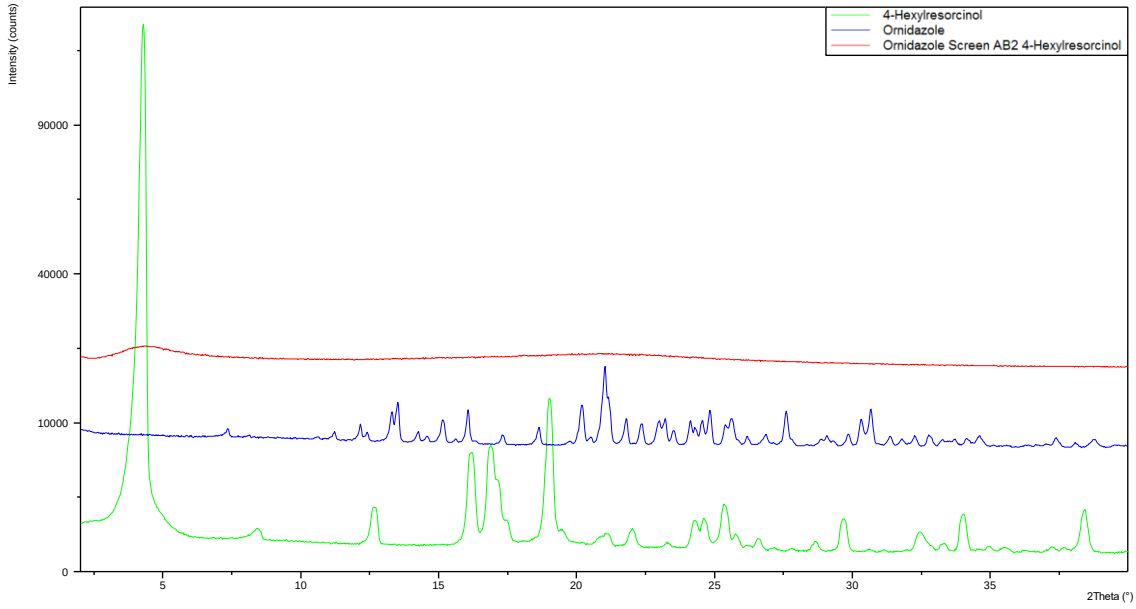


***Figure 6.3*** *PXRD patterns for 4-hexylresorcinol (green), ornidazole (blue) and the product of the screen for these two compounds (red).*

The second two examples are of screen products which were not counted as hits, the first, that of ornidazole and 4-hexylresorcinol shown in Figure 6.3, displays an almost flat line devoid of peaks which is typical of an amorphous material. This material, if left would likely eventually crystallise, and as stated above, where amorphous material was found in wells it was left for a significant period of time before analysis. The available timescale of the experiment meant that waiting longer was not possible and as the time before crystallisation occurs could be potentially limitless, such screen products featuring characteristic amorphous PXRD patterns were counted as fails. The final example is ornidazole and acesulfame potassium and is presented in Figure 6.4. The PXRD patterns here are an example of a product of the screen where crystalline material is produced, but which shares all of its peaks with those present in either of the parent compounds, thereby indicating that no new solid form has been produced and that the product is merely a physical combination of the two starting components.

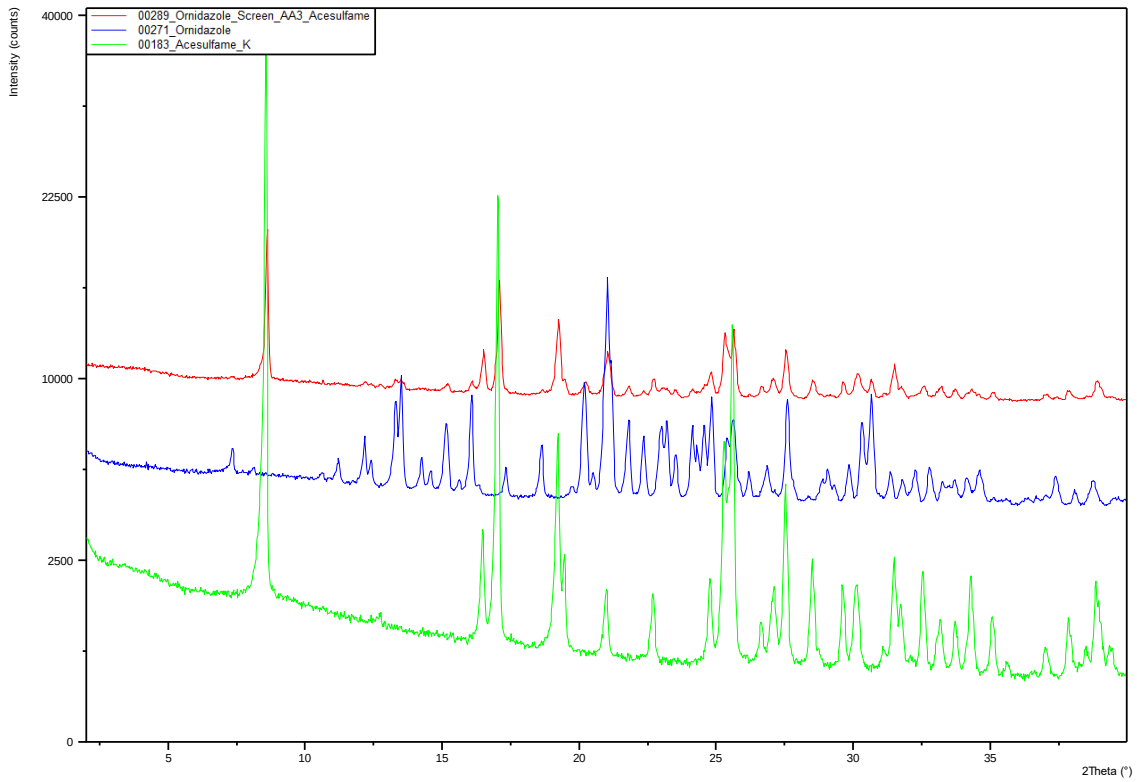


***Figure 6.4*** *PXRD patterns for acesulfame potassium (green), ornidazole (blue) and the product of the screen for these two compounds (red).*

## 6.2.3 Results

Based on the PXRD analysis where a sample was considered a hit if a new peak, not present in either of the parent components PXRD patterns, was detected, a total of 23 hits were observed. The figures above are examples of the types of results observed and a full set of PXRD patterns are recorded in Appendix 6.2. Given that the potential co-formers were ranked based on their calculated propensity to co-crystallise with ornidazole, it might be expected that the hits would be gathered more towards the start of the list. This was not the case however, with a relatively even spread of hits throughout the range of co-formers screened, as displayed in Figure 6.5 below.

| | 1 | 2 | 3 | 4 | 5 | 6 | 7 | 8 |
|---|---|---|---|---|---|---|---|---|
| A | **1 Cryst. -2.2019** | 2 Cryst./Am. -1.9570 | 3 Cryst. -1.9194 | **4 Cryst. -1.6545** | 5 Cryst. -1.5914 | 6 Am. -1.5401 | **7 Cryst./Am. -1.4322** | 8 Cryst./Am. -1.3452 |
| B | **9 Cryst. -1.3367** | 10 Am. -1.3280 | **11 Cryst. -1.3268** | 12 Cryst./Am. -1.3187 | 13 Cryst./Am. -1.2885 | 14 Am. -1.2826 | 15 Cryst. -1.2448 | **16 Cryst. -1.2198** |
| C | **17 Cryst. -1.2018** | **18 Cryst. -1.1547** | **19 Cryst. -1.1470** | 20 Cryst./Am. -1.1273 | **21 Cryst./Am. -1.0162** | 22 Am. -0.9947 | 23 Cryst./Am. -0.9727 | **24 Cryst./Am. -0.9604** |
| D | 25 Cryst. -0.9382 | 26 Am. -0.9345 | 27 Cryst. -0.9205 | 28 Cryst./Am. -0.8971 | **29 Cryst./Am. -0.8960** | 30 Cryst. -0.8919 | **31 Cryst. -0.8807** | **32 Cryst. -0.8760** |
| E | **33 Cryst./Am. -0.8700** | **34 Cryst. -0.8460** | 35 Cryst./Am. -0.8315 | 36 Cryst./Am. -0.8163 | **37 Cryst. -0.8020** | **38 Cryst./Am. -0.7790** | 39 Cryst. -0.7717 | **40 Cryst. -0.7343** |
| F | **41 Cryst./Am. -0.7241** | 42 Cryst./Am. -0.7073 | 43 Cryst. -0.7041 | **44 Cryst. -0.7009** | 45 Cryst./Am. -0.6841 | **C1 Cryst. -1.765** | 46 Cryst. -0.6689 | **C2 Cryst. -0.2234** |

***Figure 6.5*** *Diagrammatic representation of the results laid out in the format of the plate. Bold purple numbers represent hits and the two bold blue numbers represent the positive controls, also hits. Values in each 'well' refer to rank of co-former, whether the sample was identified as crystalline (Cryst.), amorphous (Am.) or a combination of both (Cryst./Am.) as determined by PXRD analysis, and the excess enthalpy (given in ΔH/kJ.mol$^{-1}$) as calculated by COSMOtherm (with the exception of C1 (well F6) which was calculated by COSMOquick).*

The results in bold purple represent hits and the two bold blue results represent the positive controls, also hits. The initial value is the rank of co-former based on the excess enthalpy calculated by COSMOtherm which is the third value in each set. Based on analysis of the powder patterns obtained for the sample from the screen, they were identified as crystalline (where a

flat baseline with characteristic narrow peaks were present), amorphous (where no diffraction peaks were evident) or a combination of crystalline and amorphous where characteristic of both crystalline and amorphous patterns were identified. This last category ranged from one or two sharp peaks (indicating the presence of at least some crystalline material) in a pattern otherwise devoid of an peaks except for an amorphous halo, to a pattern consiting of many peaks typical of a crystalline sample but with relatively high very low 2θ counts and a halo, both characteristic of amorphous content within the sample. The counts at very low 2θ is common to all samples on a given diffractometer and is due to the X-ray source and detector being almost linear (i.e. pointing at each other) which leads to a greater amount of diffuse scattered X-rays being detected than at higher angles. The reason this is more often noticed in largly amorphous samples is that in relative terms, compared to the intensity of the highest peak in the full range of the scan, these low 2θ counts will constitute a larger ratio than in highly crystalline samples and due to scaling of the pattern, will appear more obvious.

It is interesting to note that all five of the samples in which no crystallisation occurred within the given timeframe were ranked within the top 26 co-formers. It is possible that intermolecular interaction between the co-formers and ornidazole are leading to stabilisation of the amorphous phase, as seen with ROY and pyrogallol (Chapter 4), resulting in a co-amorphous material less prone to crystallising than either component individually. This would fit theoretically with the single molecule gas phase COSMOtherm calculations, as the interactions predicted are valid in any physical state. That lattice parameters are not taken into account in the calculations could explain the lack of crystallisation in the amorphous samples where predicted interactions may still be present leading to stabilisation of the phase.

### 6.2.4 Summary

Out of the 48 co-formers screened, 23 were detected as hits with ornidazole by PXRD, including the two positive controls. There were 25 co-formers which were not identified as hits, however that does not mean that under no circumstances will a co-crystal of ornidazole and any of these co-former never be obtainable. Many of the materials produced by the combination of ornidazole and these co-formers were amorphous and thus identified only as such by PXRD. Had these materials been left for even longer periods of time or crystallisation induced by some means, it is quite possible that co-crystalline material would have resulted from some if not many of these combinations. For the practical purposes of conducting a high-throughput screen in an efficient and timely manner, those ornidazole and co-former pairs which did not yield material with great enough crystallinity two be identified as containing a new form by PXRD

were treated as a fail. Crystallisation tendency is an important attribute, especially when selecting potential forms for further development; poor crystallisation tendency would hamper processing and therefore be a less suitable candidate, making the failure status from the screen appropriate in terms of form selection for drug development.

## 6.3 Further investigations into co-crystal screen hits (materials in which form change was detected)

As previously stated, detecting a hit from PXRD analysis of the products of the co-crystal screen, only indicates that form change has occurred. This could be caused by a number of possibilities such as polymorphic transition, degradation of either component or formation of a solvate or hydrate. Hence it is necessary to further analyse the material subsequent to it being identified as a hit. DSC and TGA were employed to examine the thermal behaviour of the materials recovered from the screen procedure and evaporative crystallisation was attempted for some of these ornidazole co-former pairs. The crystallisation was attempted to determine whether similar results would be achieved for the co-crystal screen by evaporative methods, i.e. removing the requirement for sonication, and additionally to ascertain a suitable method for scaled up production of the materials. Only the very first materials which were analysed by PXRD, i.e. those observed to be crystalline upon initial appearance immediately after the screening procedure, were subjected to the attempted evaporative crystallisation.

### 6.3.1 Differential scanning calorimetry

DSC thermograms were recorded for the material recovered from the 96-well plate for those determined to be hits, following the standard DSC ramp method detailed in Chapter 2. Figure 6.6 shows the DSC traces for two of the materials analysed, the products of the ornidazole screen with 5-nitroisophthalic acid and 3,5-dihydroxybenzoic acid. These are examples of the two main results (a full set of which can be found in Appendix 6.3 and a summary in Table 6.2 below): a single endothermic peak at the melting point (ornidazole:5-nitroisophthalic acid) and a trace in which multiple endothermic events are observed (ornidazole:3,5-dihydroxybenzoic acid). In these samples, at temperatures greater than around 200°C, decomposition may occur giving rise to variation in heat flow and artefacts in the traces. The presence of multiple endothermic events suggests that the sample does not consist purely of a co-crystal, and in the case of ornidazole:3,5-dihydroxybenzoic acid the initial peak with an onset of 50.9°C is due to the presence of solvent as determined by the analysis of TGA data below.

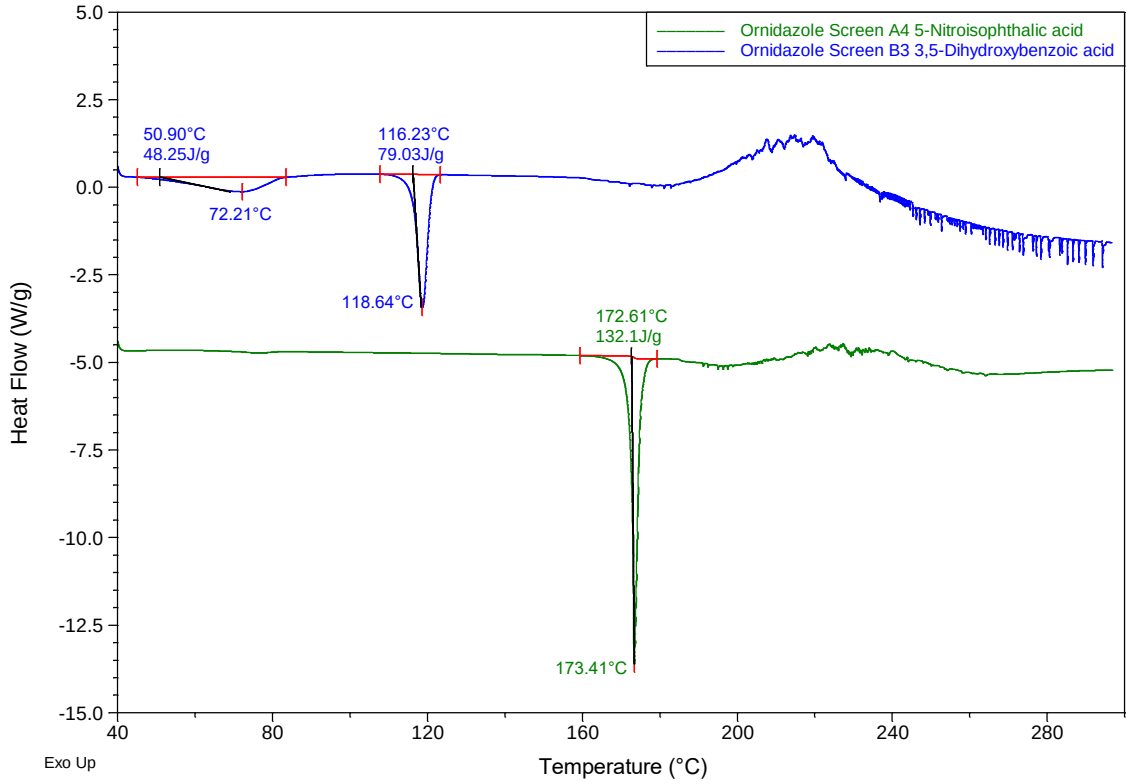


***Figure 6.6*** *DSC profiles of the products of the ornidazole screen with 5-nitroisophthalic acid (green) and 3,5-dihydroxybenzoic acid (blue). The peak onset and peak maximum temperatures are displayed by the traces.*

The DSC traces for the product of the ornidazole screen with 5-nitroisophthalic acid is plotted in Figure 6.7 with those for pure ornidazole and 5-nitroisophthalic acid. Again, at higher temperatures decomposition causes variation in heat flow and artefacts in the traces. Each of the traces features a single endothermic peak indicative of melting of the sample. The onset temperatures of those peaks of 87.31°C, 172.61°C and 258.39°C for ornidazole, ornidazole:5-nitroisophthalic acid and 5-nitroisophthalic acid respectively, establish that the melting point of the product of ornidazole and 5-nitroisophthalic acid is between that of the parent components.

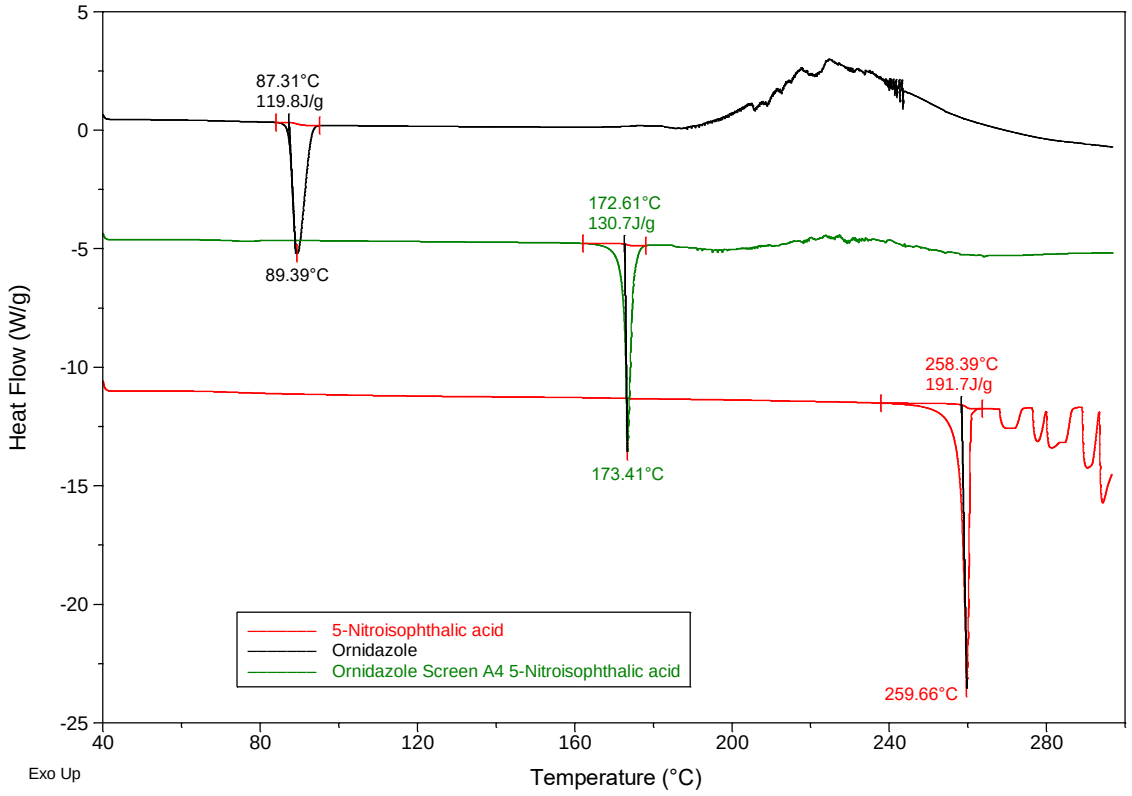


***Figure 6.7*** *DSC profiles of the product of the ornidazole screen with 5-nitroisophthalic acid (green), ornidazole (black) and 5-nitroisophthalic acid (red). The peak onset and peak maximum temperatures are display by the traces.*

## 6.3.2 Thermogravimetric analysis

TGA profiles were recorded following the standard TGA method detailed in Chapter 2 for all materials which underwent DSC analysis. The TGA profile for the product of the ornidazole screen with 5-nitroisophthalic acid is presented in Figure 6.8 and shows no significant mass change until degradation of the sample above about 175°C. This is commensurate with the DSC trace for this material as the effects of degradation are seen at the same temperatures in both. Figure 6.9 shows the TGA profile for the product of the ornidazole screen with 3,5-dihydroxybenzoic acid and displays a different sample behaviour. A mass loss of 3.1% occurs over the temperature range of approximately 45°C to 75°C. This could be due to residual solvent present in the sample, however the mass loss equates to a molecular mass of 11.586 for each pair of ornidazole and 3,5-dihydroxybenzoic acid molecules, or 57.93 for every five pairs. The molecular weight of acetone is 58.079 and given that acetone was used in the LAG step of the co-crystal screen it is possible from this evidence that a 5:5:1 ornidazole:3,5-dihydroxybenzoic acid:acetone solvate has formed. The endothermic event in the DSC trace is also consistent with this, occurring over the same temperature range as the mass loss seen in the TGA profile.

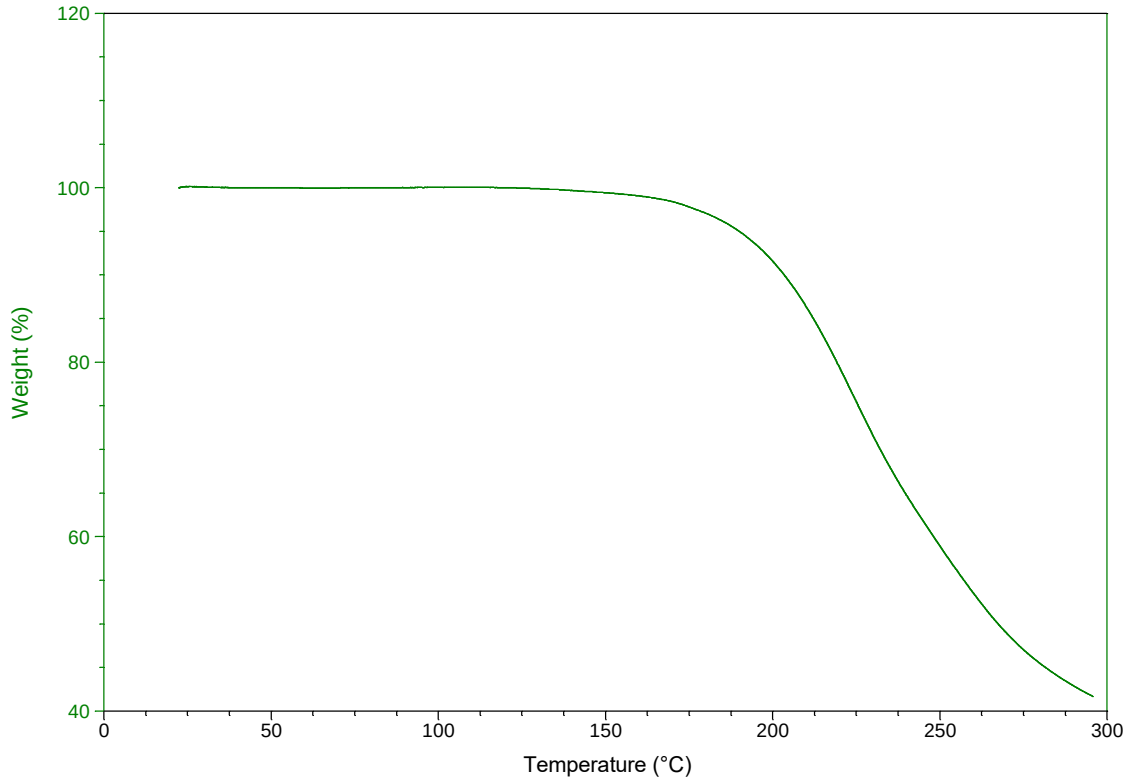


***Figure 6.8*** *TGA profile of the product of the ornidazole screen with 5-nitroisophthalic acid showing no significant mass change until degradation of the sample above about 175°C.*

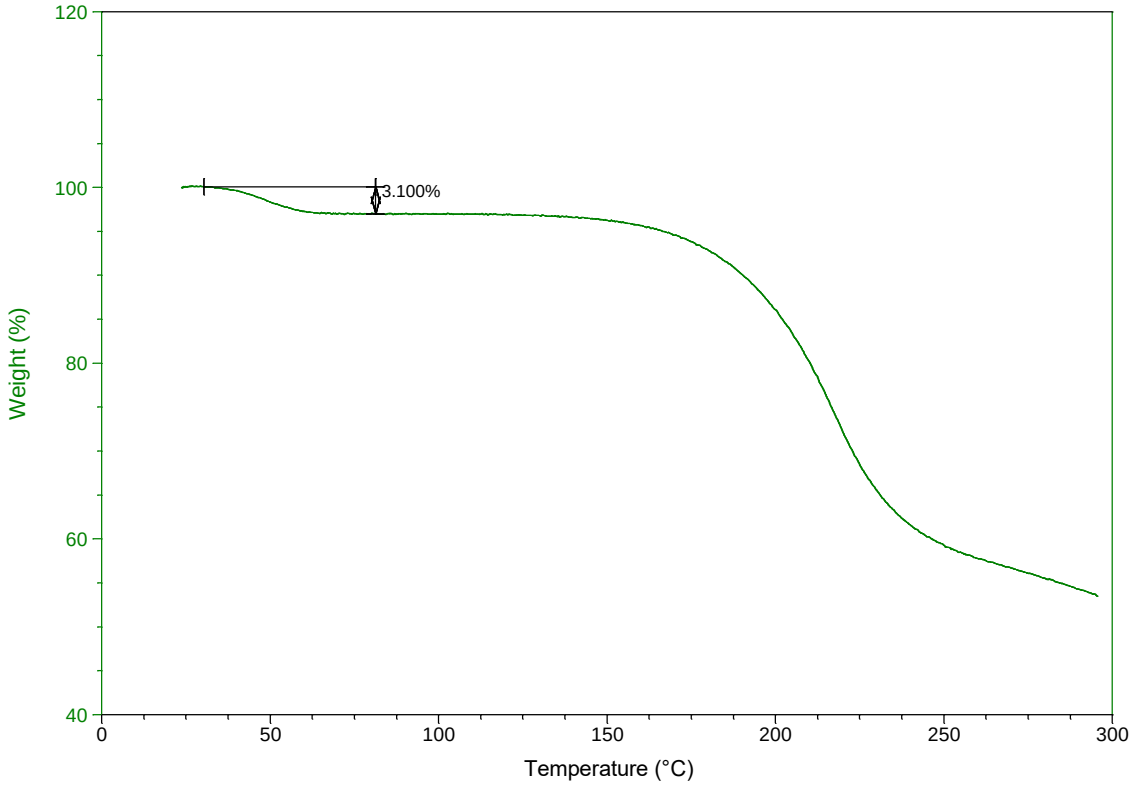


***Figure 6.9*** *TGA profile of the product of the ornidazole screen with 3,5-dihydroxybenzoic acid showing mass change over the temperature range of approximately 45°C to 75°C, followed by mass loss due to degradation above around 150°C.*

***Table 6.2*** *Summary of the results from DSC and TGA analysis of materials from the ornidazole co-crystal screen which were identified as hits. In relation to the literature melting point, (s) and (d) refer to sublimation and decomposition respectively.*

| Co-former | Literature melting point (°C) | Number of endothermic peaks | Onset of major endothermic peak (°C) | Melting point compared to parent materials | Significant mass loss |
|---|---|---|---|---|---|
| Oxalic acid | 189.5 (d) | 2 | 53.3 | Lower | Yes |
| **5-Nitroisophthalic acid** | **259-261** | **1** | **172.6** | **Mid** | **No** |
| 2,4-Dihydroxybenzoic acid | 208-211 (d) | 2 | 150.3 | Mid | No |
| **Trimesic acid** | **>300** | **1** | **143.7** | **Mid** | **No** |
| 3,5-Dihydroxybenzoic acid | 236-238 (d) | 2 | 116.2 | Mid | Yes |
| **1-Hydroxy-2-naphthoic acid** | **195-200 (d)** | **1** | **95.9** | **Mid** | **No** |
| Fumaric acid | 298-300 (s) | 2 | 125.4 | Mid | No |
| **2,5-Dihydroxybenzoic acid** | **204-208** | **1** | **86.7** | **Lower** | **No** |
| **5-Chlorosalicylic acid** | **171-172** | **1** | **94.8** | **Mid** | **No** |
| 3,4-Dihydroxybenzoic acid | 197-200 (d) | 2 | 60.3 | Lower | Yes |
| *m*-Nitrobenzoic acid | 139-141 | 2 | 78.0 | Lower | No |
| Salicylic acid | 158-161 | 2 | 85.6 | Lower | No |
| 3-Hydroxybenzoic acid | 200-203 | 2 | 91.9 | Mid | No |
| **3-Hydroxy-2-naphthoic acid** | **218-221** | **1** | **127.2** | **Mid** | **No** |
| Octadecylamine | 52-55 | 2 | 50.6 | Lower | Yes |
| Thymol | 48-51 | 2 | 86.2 | Mid | No |
| 2,5-Xylenol | 73-78 | 1 | 83.6 | Mid | Yes |
| 4-Hydroxybenzoic acid | 213-217 | 2 | 113.3 | Mid | No |
| 2-Oxo-3-phenylpropionic acid | 150-154 | 2 | 84.7 | Lower | Yes |
| *p*-Cresol | 32-34 | 2 | 74.5 | Mid | Yes |
| 3-Methyl-2-oxobutanoic acid sodium salt | 220-230 (d) | 3 | 86.8 | Lower | Yes |
| **3,5-Dinitrobenzoic acid** | **236-238 (d)** | **1** | **130.3** | **Mid** | **No** |
| **4-Aminobenzoic acid** | **187-189** | **1** | **134.0** | **Mid** | **No** |

The results from DSC and TGA of the materials investigated are summarised in Table 6.2. The melting points for the co-formers are those listed by the supplier and that of 3-methyl-2-oxobutanoic acid sodium salt is given as it was the chemical used in place of 3-methyl-2-oxobutanoic acid as discussed in Chapter 2. The number of endothermic peaks present in the

DSC trace other than those at higher temperatures caused by degradation, and very small peaks possibly due to the melting of a slight excess of ornidazole, are listed and the temperature of onset of the most prominent of these also listed. It is this temperature that is used to determine the position of the melting point of the material in relation to the parent components. This relationship in melting points is of most value where only one endothermic peak and likely co-crystalline material are present and where there is no mass loss, again, not due to degradation, present in the TGA profile, which is also listed in the table. Samples matching this description are highlighted in bold in Table 6.2. If complete conversion from starting materials to co-crystal had occurred, a single endothermic peak would be expected in the DSC trace and no mass loss should be seen in the TGA thermogram; an exception could be a small quantity of trapped non-structural solvent which would lead to a very small mass loss.

A survey of 50 co-crystalline samples conducted by Schultheiss and Newman found that 52% of the co-crystals had melting points between those of parent components, 39% were lower than either, 6% higher and 4% the same as either API of co-former.[47] When considering all 23 hits from the co-crystal screen, the results correlate well with those previously published, 34.8% displaying a lower melting point than either API or co-former and 65.2% a melting point between the two. Narrowing the range to only those hits which met the thermal behaviour requirements set out above (materials highlighted in bold in Table 6.2) results in a greater percentage of materials displaying a melting point between those of the parent components (87.5%).

This combination of DSC and TGA results is observed for only eight of the 23 materials from the co-crystal screen which were hits, allowing for very slight mass loss, a very small peak possibly due a slight excess of ornidazole and not considering anything above the temperature in which degradation of the material is apparent. The co-former constituents of these eight materials were: 5-nitroisophthalic acid, trimesic acid, 1-hydroxy-2-naphthoic acid, 2,5-dihydroxybenzoic acid, 5-chlorosalicylic acid, 3-hydroxy-2-naphthoic acid, 3,5-dinitrobenzoic acid and 4-aminobenzoic acid. Of these, all had melting points between ornidazole and the co-former except ornidazole:2,5-dihydroxybenzoic acid which had a peak onset temperature of 86.7°C, just below ornidazole's melting point of 87.3°C. The DSC trace for this sample (Figure 6.10) however, displayed signs of degradation from a relatively low temperature, around 150°C, which with the broad shape of its endothermic peak suggest that this was not a melting event of a pure co-crystal.

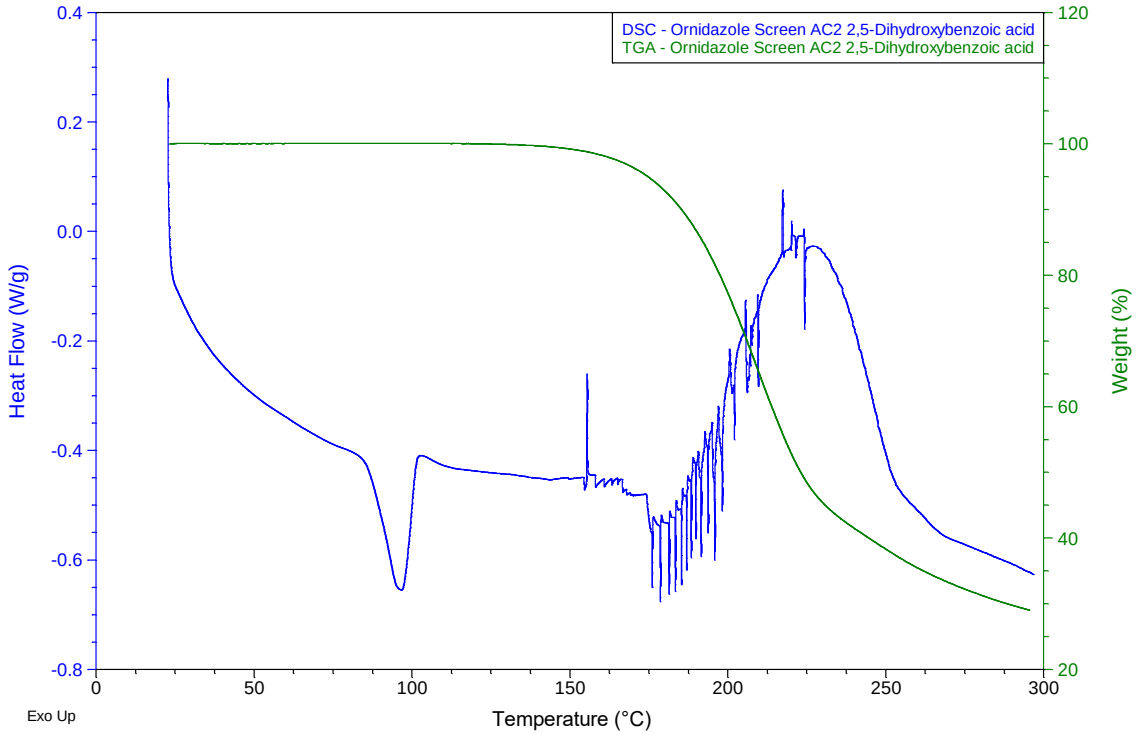


***Figure 6.10*** *DSC and TGA overlay plot for ornidazole:2,5-dihydroxybenzoic acid.*

Many of the samples have multiple endothermic peaks suggesting multiple phases present in the sample or that transformation occurs during the DSC measurement. These points do not mean that co-crystallisation did not occur, but that possibly complete conversion did not take place or a co-crystal of a stoichiometry other than 1:1 formed. Either of these situations would lead to excess of one or both of the starting materials which could lead to multiple endothermic peaks in the DSC trace unless eutectic mixtures were formed. In case of the formation of a eutectic mixture, a single lower melting peak would be expected, however this would not have given rise to a distinct PXRD pattern.

Another explanation which lead to a new phase being detected by PXRD but not necessarily the formation of co-crystalline material may be that a solvate or hydrate of either of the materials (more likely the co-former otherwise it would be expected to be observed more frequently if it was the API) formed and desolvation gives rise to an initial endothermic peak prior to any melting events. This is the likely explanation for the occurrence of multiple endothermic peaks in the DSC trace (Figure 6.11) for the ornidazole:4-hydroxbenzoic acid sample, as an account of a similar DSC profile with a desolvation peak at around 67°C for 4-hydroxybenzoic monohydrate has previously been reported.[171] The TGA profile for this material does not correlate with this explanation however as there is no mass loss seen which would occur with desolvation. There is

the possibility that desolvation occurred in the sample which underwent TGA analysis but not in that of the DSC sample due to the natural variation in ambient temperature and relative humidity within the laboratory. The article referenced suggested some degree of stability for the monohydrated form of 4-hydroxybenzoic acid, but without further analysis by DVS, ruling out the given explanation would not be possible.

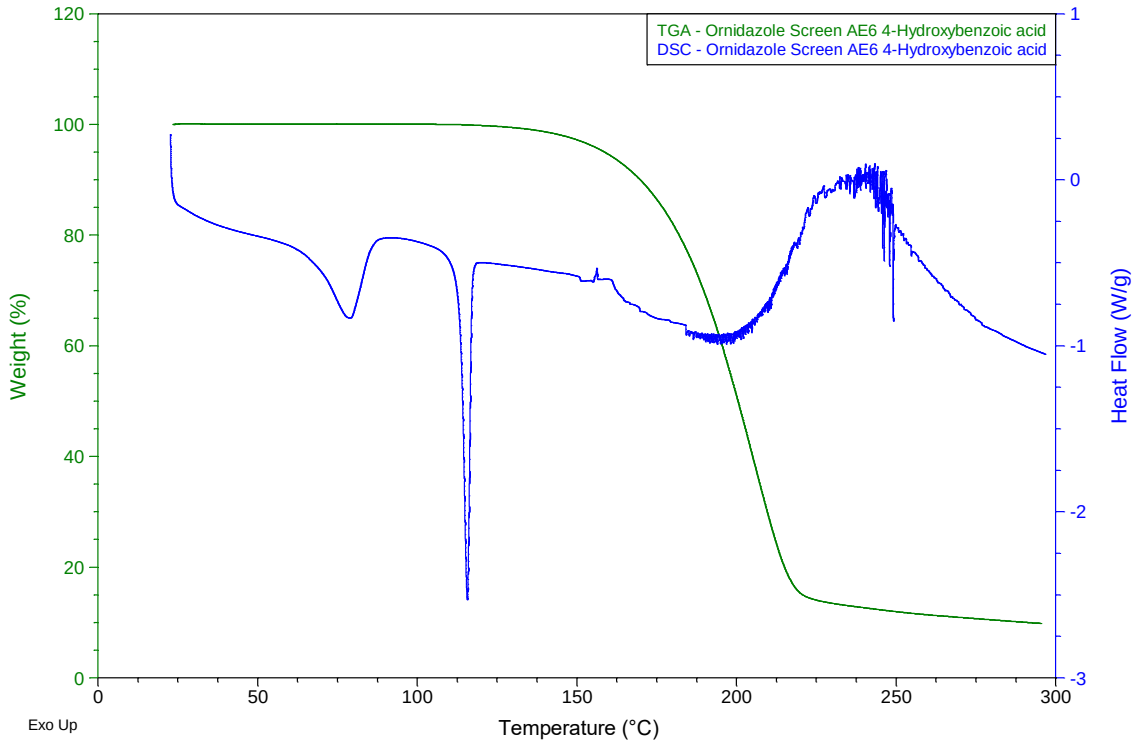


***Figure 6.11*** *DSC and TGA overlay plot for ornidazole:4-hydroxybenzoic acid.*

Individual analysis of each material from the screen would be required to determine its nature (i.e. co-crystal or otherwise) and due to the focus of this project being on screening, resources were limited to only thoroughly characterising one hit from the co-crystal screen. As such, DSC and TGA plots for all materials identified as hits from the co-crystal screen are presented in Appendix 6.3 and the results summarised in Table 6.2, in depth analysis for each material was not performed but several examples are used in the preceding discussions.

### 6.3.3 Evaporative crystallisation from DCM solution

Only five co-formers were selected for attempted evaporative crystallisation with ornidazole and all were chosen as they had been identified as hits from PXRD analysis and had been of the first materials to crystallise after the co-crystal screening procedure. These co-formers were: 5-nitroisophthalic acid, trimesic acid, 3,5-dihydroxybenzoic acid, fumaric acid and 2-oxo-3-phenylpropionic acid (phenylpyruvic acid).

Ornidazole and 5-nitroisophthalic acid from DCM gives a PXRD pattern very similar to that from the screen as can be seen in Figure 6.12. Where there are any small peaks that are not the same, they appear at positions in which either of the parent materials has a peak suggesting that the sample is not pure and that some of the starting materials are present as well as the ornidazole:5-nitroisophthalic acid, i.e. full conversion did not occur. The same goes for the PXRD analysis of ornidazole and 3,5-dihydroxybenzoic acid from DCM, the plot of which can be found in Appendix 6.4 which contains the full set of results, a summary of which is presented in Table 6.3.

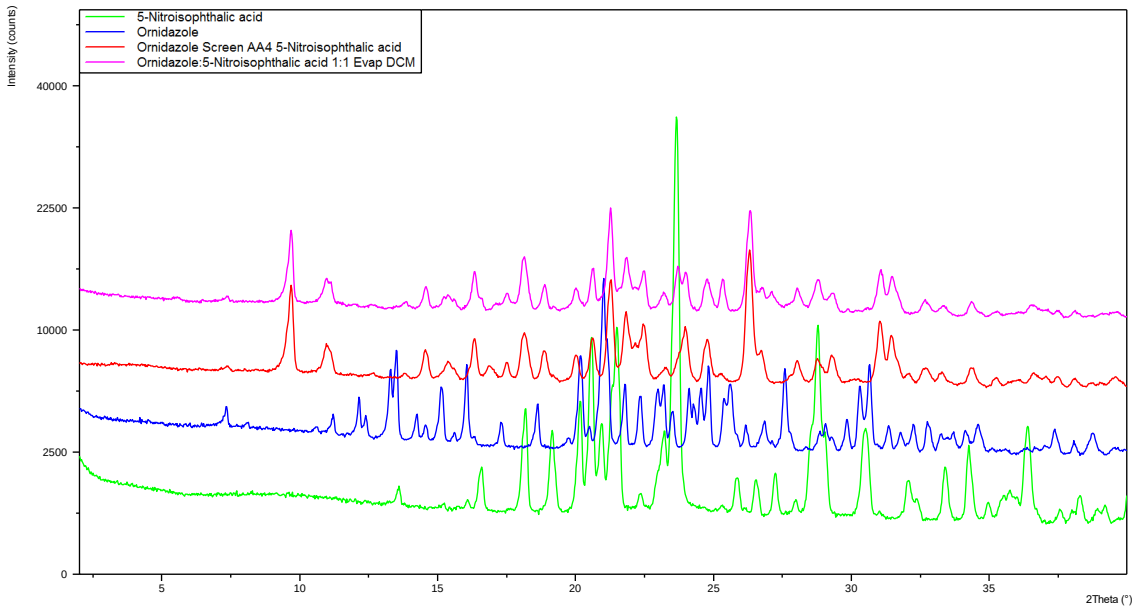


***Figure 6.12*** *PXRD patterns for 5-nitroisophthalic acid (green), ornidazole (blue), the product of the screen for these two compounds (red) and the material produced by evaporative crystallisation of a 1:1 molar ratio of the two components from DCM (pink). Note the similarity of the red and pink patterns.*

The PXRD patterns of the product of evaporative crystallisation for ornidazole and fumaric acid (Figure 6.13) and ornidazole and trimesic acid show new peaks at positions which none of the respective parent materials nor the respective products of the screen have peaks. This is indicative of new forms and would be considered a hit for screening purposes but produces a different form to that which the screening method applied gave.

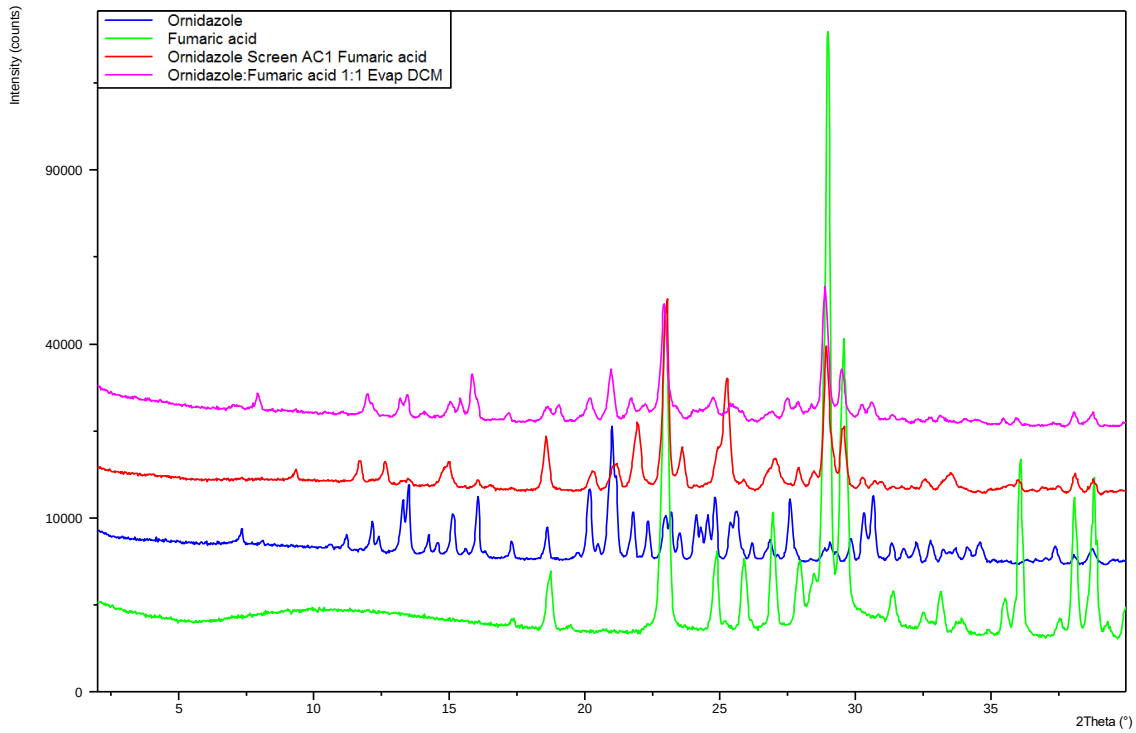


***Figure 6.13*** *PXRD patterns for fumaric acid (green), ornidazole (blue), the product of the screen for these two compounds (red) and the material produced by evaporative crystallisation of a 1:1 molar ratio of the two components from DCM (pink). Note the difference between the red and pink patterns.*

The evaporative crystallisation of ornidazole and phenylpyruvic acid from a DCM solution produces a PXRD pattern which matches that of the product of the screen of these two materials i.e. the possible co-crystal. The evaporative crystallisation method would indicate a hit for screening purposes and produces the same form to that which the screening method applied gave (Figure 6.14).

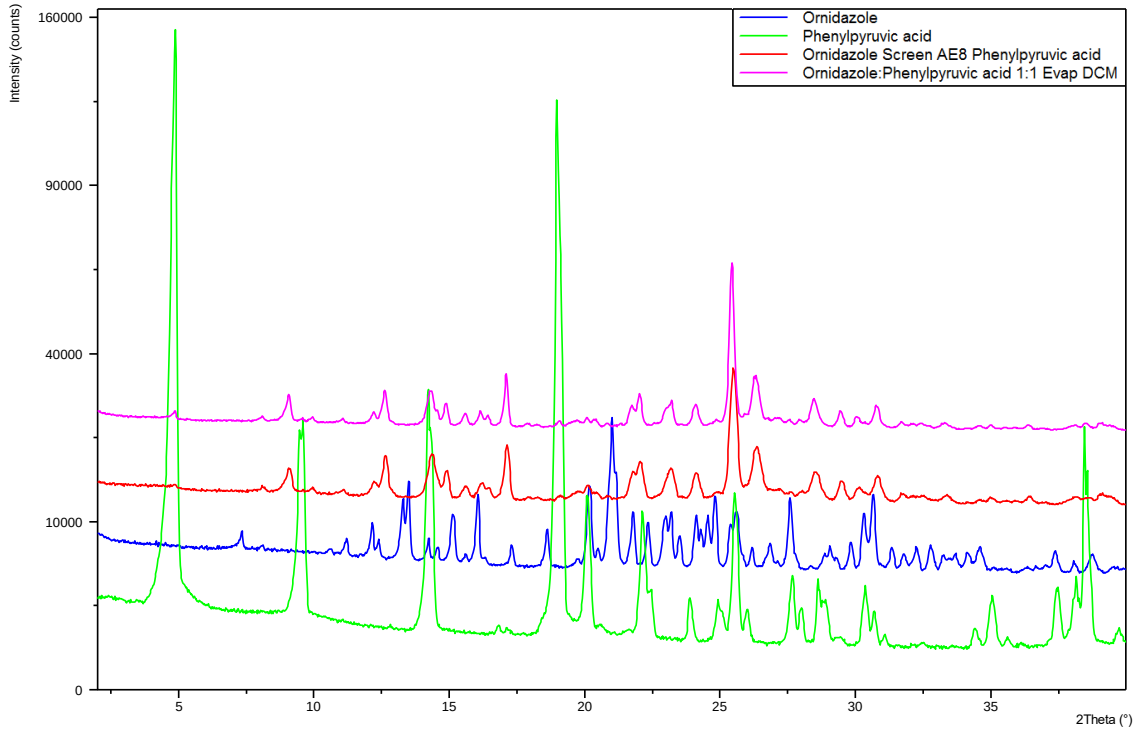


***Figure 6.14*** *PXRD patterns for phenylpyruvic acid (green), ornidazole (blue), the product of the screen for these two compounds (red) and the material produced by evaporative crystallisation of a 1:1 molar ratio of the two components from DCM (pink). Note the equivalence of the red and pink patterns.*

***Table 6.3*** *Summary of the results from the evaporative crystallisation from DCM.*

| Co-former | 'Hit' from evaporative crystallisation? | Same form as from co-crystal screen? |
|---|---|---|
| 5-Nitroisophthalic acid | Yes | Yes – not full conversion |
| Trimesic acid | Yes | No |
| 3,5-Dihydroxybenzoic acid | Yes | Yes – not full conversion |
| Fumaric acid | Yes | No |
| Phenylpyruvic acid | Yes | Yes |

## 6.3.4 Summary

All five ornidazole:co-former pairs chosen for the evaporative crystallisation experiments resulted in form change detected by PXRD, however this was not always the same pattern as for the product of the co-crystal screen. These results suggest that the combination of ornidazole and these co-formers will routinely lead to the production of a new form, whether co-crystal or otherwise, but consideration should be given to the method of production when trying to reproduce a given material due to the variability seen in these PXRD patterns between the products of the ultrasonication based process and the evaporative crystallisation method.

Of all the further investigated hits from the screen, ornidazole:5-nitroisophthalic acid stood out as having a very clear characteristic peak in its PXRD pattern, along with a clean DSC thermogram with a single melting point and TGA thermogram showing no mass loss over a large temperature range until degradation. Few other of the hits had such qualities in their results and none had all of them, ornidazole:5-nitroisophthalic acid was also among the first 'batch'/'set' of wells to crystallise, making it a clear choice for further characterisation. The melting point for the ornidazole:5-nitroisophthalic acid material, as determined by DSC is 172.6°C which lies between that of both parent components, with ornidazole having a melting point of 87.3°C and 5-nitroisophthalic acid 258.4°C. It is normal for the melting point of the co-crystal to fall between that of the two pure components, with the majority following this trend.[47,21] A specific example is the 1:1 co-crystal of a sodium channel blocker (2-[4-(4chloro-2-fluorophenoxy)phenyl]pyrimidine-4-carboxamide) and glutaric acid in which the co-crystal melts at 142°C and the API and co-former melt at temperatures either side of this at 206°C and 97.5°C respectively.[50]

## 6.4 Further investigation into ornidazole:5-nitroisophthalic acid

### 6.4.1 Production of material

In order to carry out further experimentation on the ornidazole:5-nitroisophthalic acid system, a larger quantity of the material needed to be produced as that recovered from the screen had been depleted by the analyses already undertaken. An initial attempt by dry grinding a 1:1 molar ratio of the two components proved unsuccessful, as determined by PXRD (Figure 6.15, black pattern). Using acetone as a solvent drop, LAG using the same material achieved conversion to the form obtained from the screen, again as determined by PXRD (Figure 6.15, pink pattern).

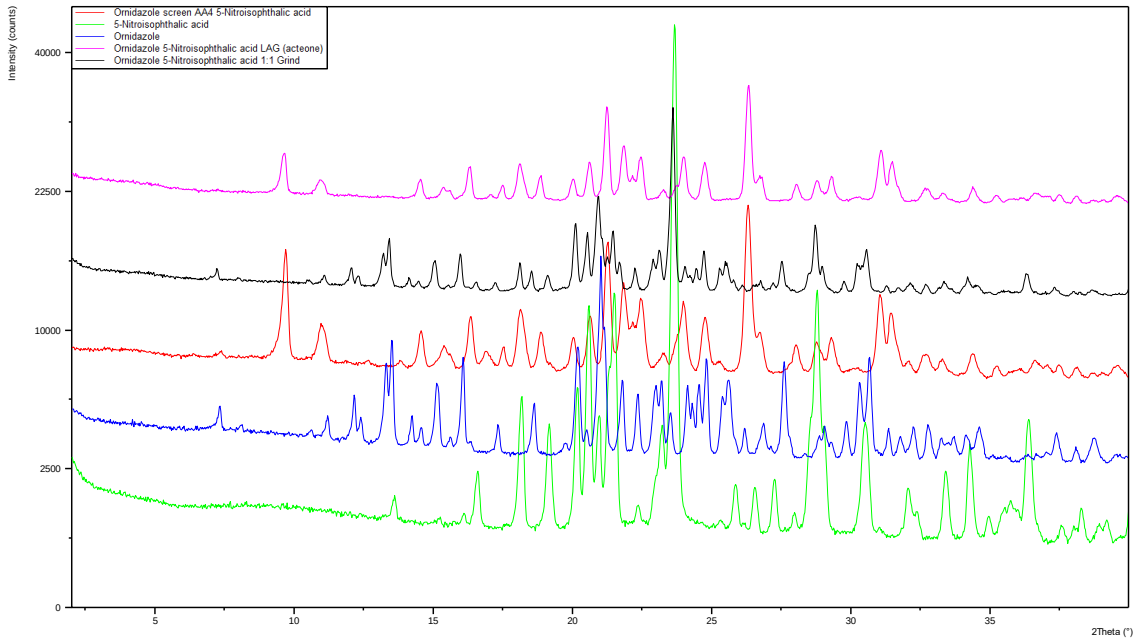


***Figure 6.15*** *PXRD patterns for 5-nitroisophthalic acid (green), ornidazole (blue), the product of the screen for these two compounds (red), the material produced by grinding a 1:1 molar ratio of the two components (black) and the material produced by LAG of that ground material using acetone as the solvent drop (pink). Note the equivalence of the red and pink patterns.*

## 6.4.2 Structure determination using single crystal X-ray diffraction

### 6.4.2.1 Method

Solid ornidazole was added to 1ml of acetone in a small sample vial until saturated at which point a little more acetone was added to ensure full dissolution of the ornidazole. To this, solid 5-nitroisophthalic acid was added, again until saturation occurred and more acetone added to dissolve any remaining solid. The solution was covered with parafilm which was pierced and left to evaporate slowly. After approximately one month, crystalline material was visible in the vial and suitable single crystals were observed by polarised light microscopy (Figure 6.16).

***Figure 6.16*** *Micrograph of a single crystal of ornidazole:5-nitroisophthalic acid (circled) on a larger crystalline mass viewed under cross polarised light.*

Single crystal X-ray diffraction was carried out in the Chemistry department at Durham University by Dr Katharina Edkins, following the procedure below.

Experimental

Single clear colourless block-shaped crystals of ornidazole:5-nitroisophthalic acid were obtained by recrystallisation from acetone. A suitable crystal (0.49×0.40×0.26) $mm^3$ was selected and mounted on an Xcalibur, Sapphire3 diffractometer. The crystal was kept at T = 120K during data collection. Using Olex2,[172] the structure was solved with the olex2.solve[173] structure solution program, using the Charge Flipping solution method. The model was refined with a version of olex2.refine[173] using Gauss-Newton minimisation.

### 6.4.2.2 Analysis

Crystal Data

$C_{15}H_{15}ClN_4O_9$, $M_r$ = 430.76, orthorhombic, $P2_12_12_1$ (No. 19), a = 6.04078(15)Å, b = 16.2494(4)Å, c = 18.5511(7)Å, $\alpha = \beta = \gamma = 90°$, $V$ = 1820.96(9)Å$^3$, T = 120K, Z = 4, Z' = 1, $\mu$(Mo $K_\alpha$) = 0.270, 16703 reflections measured, 3578 unique ($R_{int}$ = 0.0597) which were used in all calculations. The final $wR_2$ was 0.1430 (all data) and R1 was 0.0490 (I≥σ(I)).

The asymmetric unit of the determined crystal structure is displayed in Figure 6.17 and confirms the 1:1 stoichiometric ratio of the crystal but certainty over its nature as a co-crystal or salt is not confirmed. It is unclear if the hydrogen bond between the OH of the carboxylic acid of 5-nitroisophthalic acid and the N of the ring of ornidazole has proton transfer associated with it. The hydrogen bond distance (2.634Å) is within normal range[174] and there is nothing to suggest that proton transfer has occurred. Aakeröy *et al.* reported on a method to sort over 80 compounds synthesised from carboxylic acids and N-heterocycles between salts and co-crystals by examining the ratio of the two C–O bond lengths of the carboxylic acid and the endocyclic bond angles of the most basic nitrogen atom.[175] Applying this method to the ornidazole:5-nitroisophthalic acid structure results in identification as a co-crystal rather than a salt based on a ratio of 1.093Å for the C–O bond lengths of the carboxylic acid which is much more in line with the average for co-crystals (1.081Å) than salts (1.027Å). As further evidence of its co-crystalline nature, the increased endocyclic C–N–C bond angle only observed in the protonated examples in the referenced study is not present in the imidazole ring of ornidazole in the ornidazole:5-nitroisophthalic acid binary system.

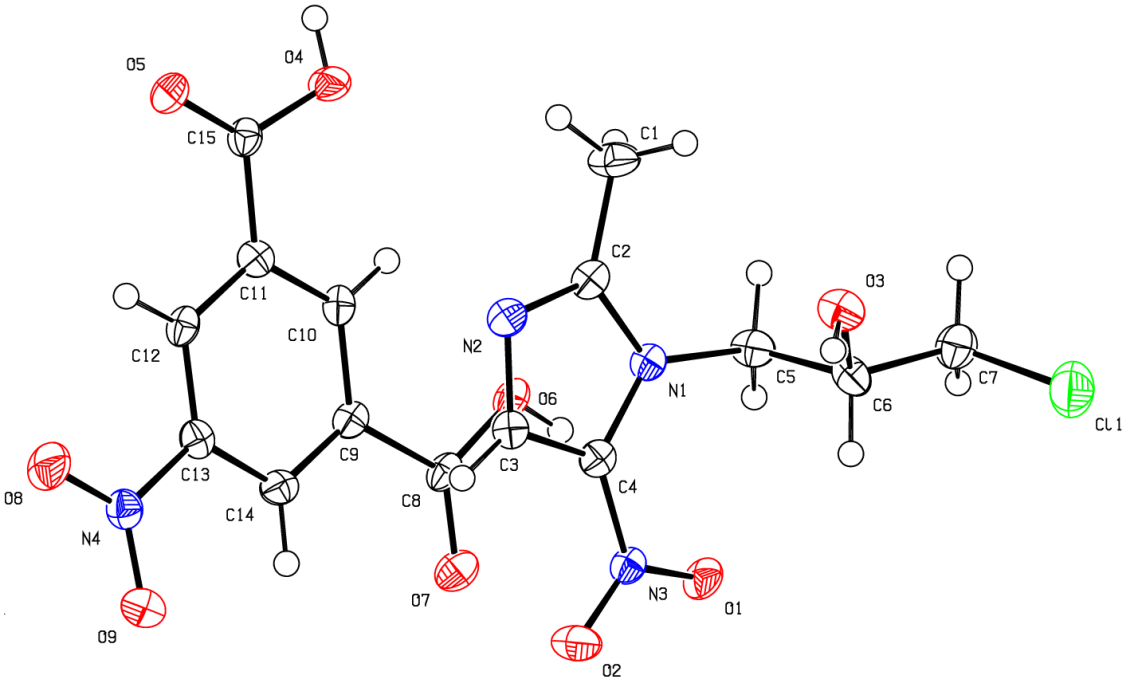


***Figure 6.17*** *Asymmetric unit of the crystal structure of the ornidazole:5-nitroisophathlic acid crystal as determined by single crystal X-ray diffraction.*

Using the crystallographic information file (CIF) produced from the single crystal X-ray diffraction analysis for ornidazole:5-nitroisophthalic acid, and those from the CSD entries for ornidazole and 5-nitroisophthalic acid, the crystal structures were visualised in Mercury and the images in Figures 6.18 to 6.20 obtained displaying packing and hydrogen bonding within the respective crystal structures.

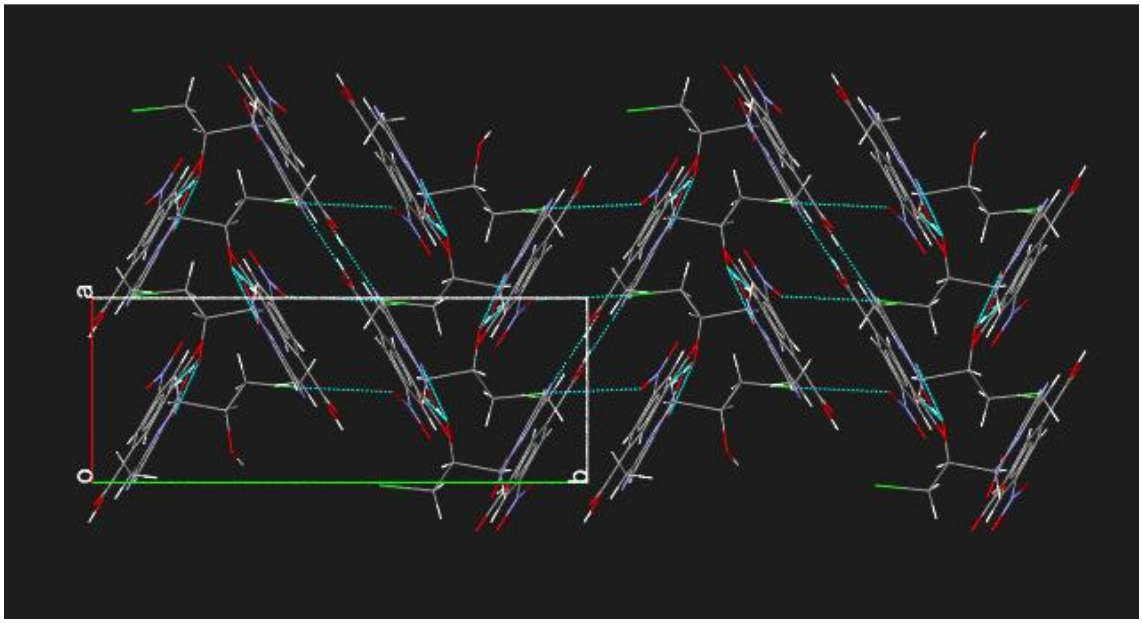


***Figure 6.18*** *Packing and hydrogen bonding within the ornidazole:5-nitroisophthalic acid crystal structure.*

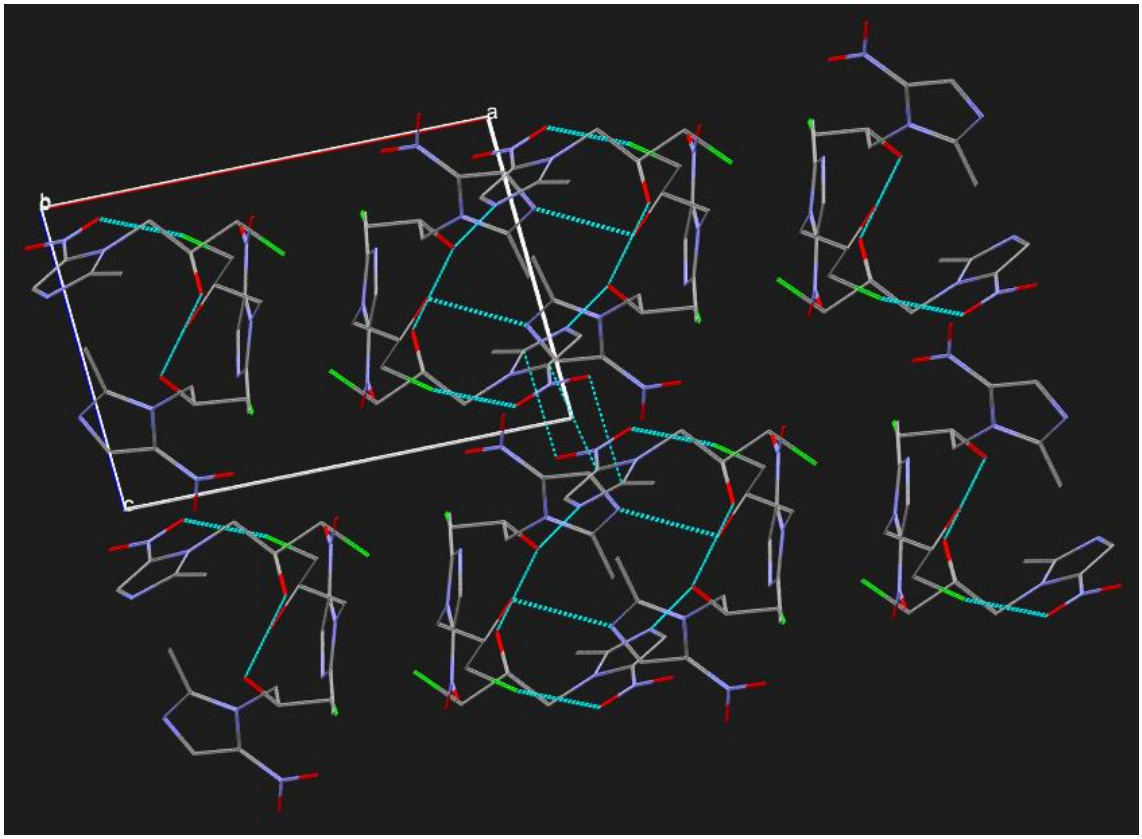


***Figure 6.19*** *Packing and hydrogen bonding within the ornidazole crystal structure.*

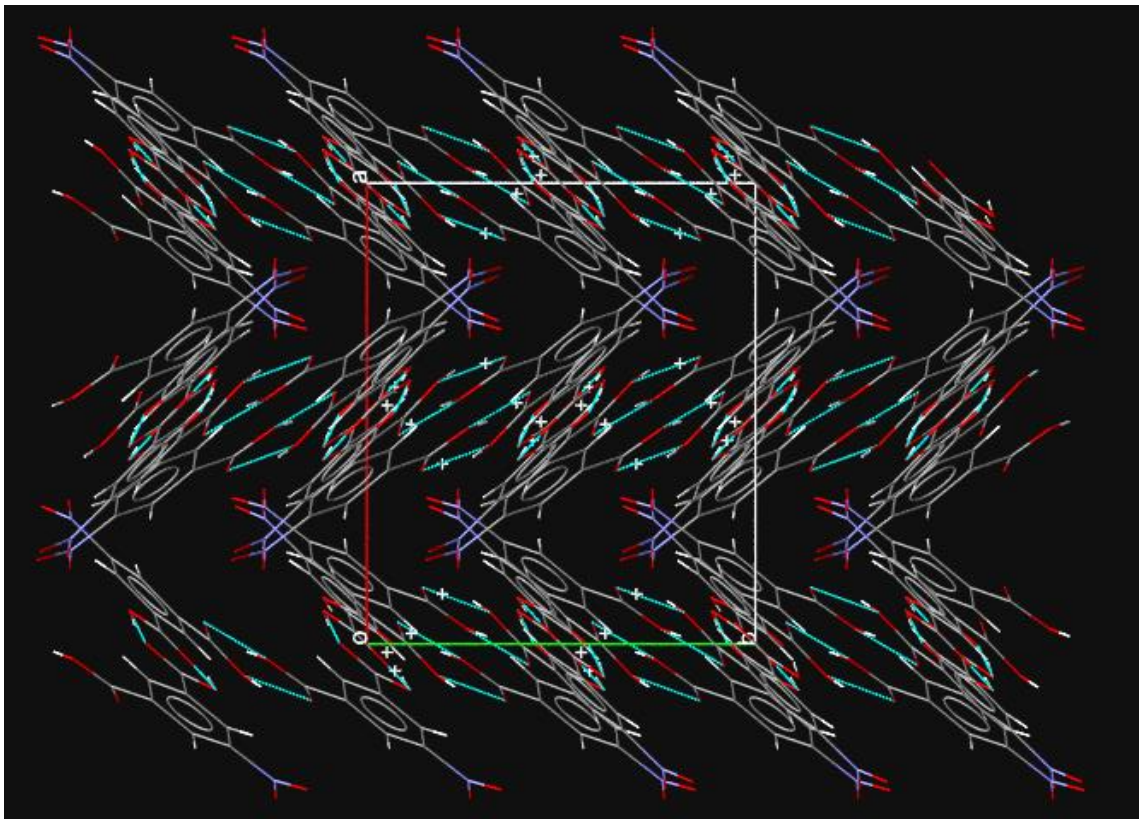


***Figure 6.20*** *Packing and hydrogen bonding within the 5-nitroisophthalic acid crystal structure.*

The packing seen in both 5-nitroisophthalic acid and ornidazole:5-nitroisophthalic acid (Figures 6.18 and 6.20) is very similar featuring a herringbone shape and hydrogen bonding occurring between planes of the molecules. The crystal structure of ornidazole differs significantly from that of 5-nitroisophthalic acid and the co-crystal, with hydrogen bonding between groups of molecules leading to a completely different packing arrangement. Due to the nature of this molecular arrangement, there are planes within the structure in which hydrogen bonding is not present and although further examination of the structure would be required to substantiate the theory, it is possible that these could be identified as slip planes.

### 6.4.3 Compression and hardness testing

Approximately 20mg of pure compound was weighed out and compressed with a maximum load setting of 200kg using a Gamlen tablet press with a 3mm die size. The tablet was ejected, its width measured using digital callipers and its hardness tested using a Sotax HT-1 hardness tester calibrated to 1N. This was repeated for each material to produce multiple tablets and the measurements recorded (Table 6.4). Production of tablets of reasonable integrity from the pure compounds was not straightforward and required multiple adjustments of the maximum load before a number of suitable tables could be formed. Measuring hardness in the normal manner across the diameter of the tablet also proved problematic in terms of obtaining reproducible results and so the hardness was measured across the height of the tablet (thickness). This precluded the calculation of tensile strength of the tablets, however led to more meaningful results, if still more varied than ideally desired.

***Table 6.4*** *Measurements of the produced tablets of ornidazole (O), 5-nitroisophathlic acid (N) and ornidazole:5-nitroisophathlic acid (ON).*

| Sample | Mass (mg) | Compression force (MPa) | Thickness (mm) | Hardness (N) |
|---|---|---|---|---|
| O1 | 18.3 | 333.02 | 1.74 | 184 |
| O2 | 17.2 | 307.99 | 1.61 | 196 |
| O3 | 20 | 302.68 | 1.17 | 93 |
| **Av (mean)** | **18.5** | **314.57** | **1.51** | **158** |
| sd | 1.152 | 13.230 | 0.244 | 45.988 |
| | | | | |
| N1 | 19.5 | 300.45 | 1.75 | 126 |
| N2 | 20.9 | 296.72 | 1.87 | 89 |
| N3 | 20.5 | 296.88 | 1.94 | 93 |
| **Av (mean)** | **20.3** | **298.02** | **1.85** | **103** |
| sd | 0.589 | 1.721 | 0.078 | 16.580 |
| | | | | |
| ON1 | 20.5 | 289.43 | 1.74 | 109 |
| ON2 | 20.7 | 286.62 | 1.84 | 117 |
| ON3 | 22.5 | 286.55 | 1.91 | 107 |
| **Av (mean)** | **21.2** | **287.53** | **1.83** | **111** |
| sd | 0.899 | 1.344 | 0.070 | 4.320 |

The results are presented in Table 6.4 and with the exception of those for the ornidazole:5-nitroisophathlic acid tablets, were somewhat inconsistent. There are still some clear outcomes from these results though, namely that the ornidazole tablets had a far greater hardness than the tablets of the other two materials, and that although similar, the ornidazole:5-nitroisophathlic acid tablets had less variability and a slight advantage in hardness. Taking the findings from the analysis of crystal packing of these materials into consideration, the possible presence of slip planes in the crystal structure of ornidazole, allowing better compaction, and lack thereof in 5-nitroisophthalic acid and ornidazole:5-nitroisophthalic acid, resulting in lower hardness, fits well with these results. It is well known that the presence of slip planes in a crystal structure can lead to greater plastic deformation and in turn, better compaction, this is exemplified by the superiority of form II of paracetamol in comparison to form I in this respect.[176]

## 6.4.4 Dynamic vapour sorption

DVS analysis was undertaken for the ornidazole, 5-nitroisophthalic acid and ornidazole:5-nitroisophthalic acid, following the standard DVS method detailed in Chapter 2. The resulting isotherm and change in mass plots are shown in Figures 6.21 to 6.23 below.

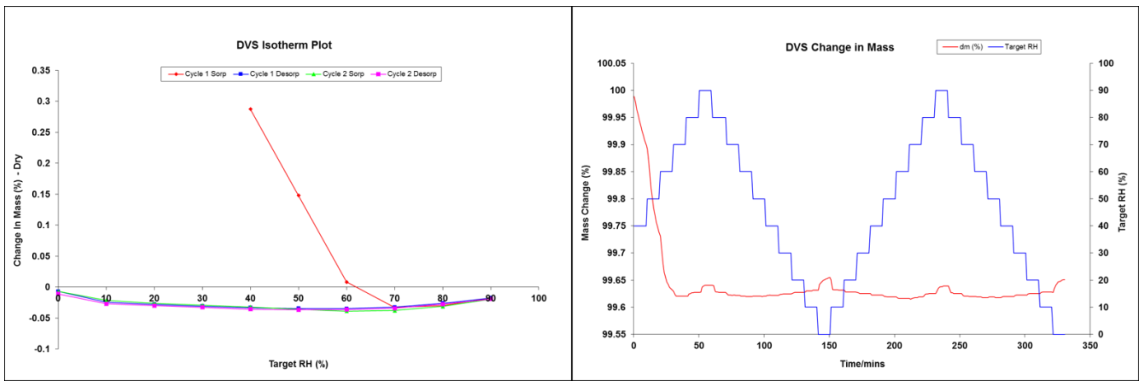


***Figure 6.21*** *Isotherm plot from DVS analysis of ornidazole (left) and plot showing percentage change in mass versus the target relative humidity over time (right).*

During the initial sorption cycle for ornidazole, as relative humidity is increased to 70%, mass reduces slightly before stabilising and varying by less than 0.05% for the rest of the sorption and desorption cycles. This is likely caused by the sample containing a very small amount of amorphous ornidazole; as the relative humidity is increased water is taken up by this amorphous material, causing plasticisation and increasing molecular mobility to the point that induces crystallisation in the remaining amorphous material. The mass loss seen is due to the loss of the water molecules from the sample as this small amount of amorphous material crystallises. Once the sample is fully crystalline, by 70% relative humidity of the initial cycle, any further mass change is negligible.

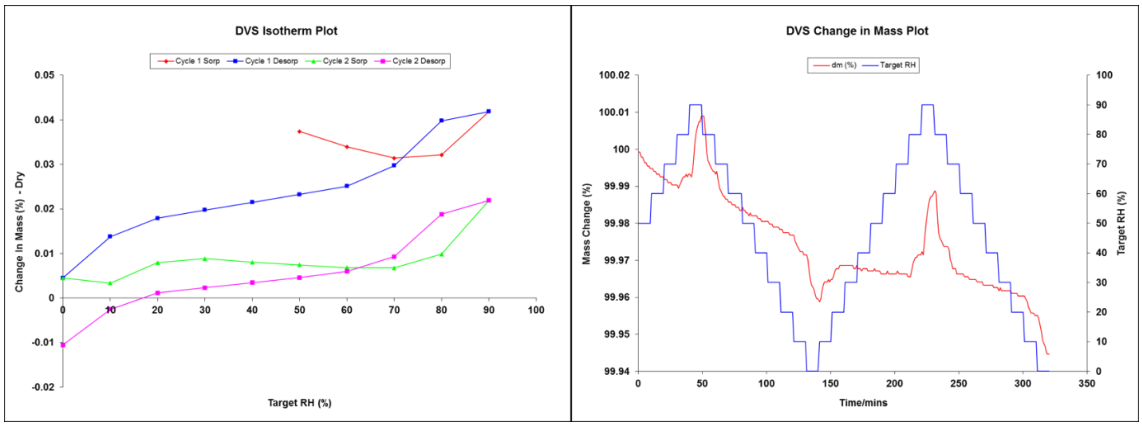


***Figure 6.22*** *Isotherm plot from DVS analysis of 5-nitroisophthalic acid (left) and plot showing percentage change in mass versus the target relative humidity over time (right).*

For 5-nitroisophthalic acid all changes in mass measured during the two sorption and desorption cycles are within an approximate 0.05% range (note scale of y-axis Figure 6.22) and as such are likely explained by surface adsorption and desorption of water.

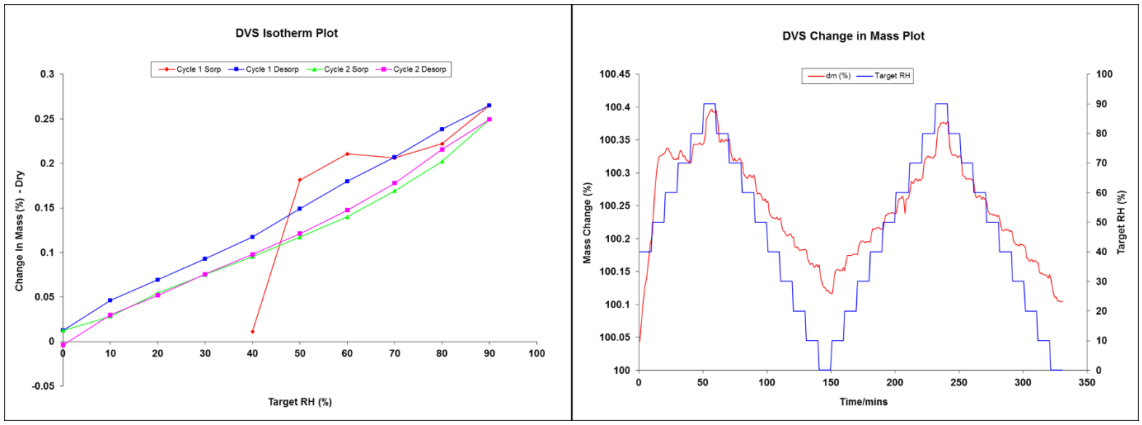


***Figure 6.23*** *Isotherm plot from DVS analysis of ornidazole:5-nitroisophthalic acid (left) and plot showing percentage change in mass versus the target relative humidity over time (right).*

Results from the DVS analysis of ornidazole:5-nitroisophthalic acid are presented in Figure 6.23 and again, taking note of the scale of the y-axis, all changes in mass are likely due to surface adsorption and desorption of water, with less than 0.3% mass change.

## 6.4.5 Intrinsic dissolution testing

### 6.4.5.1 Method

The Sirius surface dissolution imager (SDI) equipment was used to determine the intrinsic dissolution rate for ornidazole, 5-nitroisophthalic acid and the ornidazole:5-nitroisophthalic acid co-crystal. The SDI is a flow through cell approach that uses a laminar flow cell to determine intrinsic dissolution from a UV sensor array. FaSSIF-v2 is a biorelevant media produced (and purchased from) biorelevant.com, which simulates the intestinal fluid in the fasted state. It was chosen as the dissolution medium for this experiment to improve the biorelevance of the results compared to a simple buffer and was used at 37°C throughout and UV absorbance was measured at a wavelength of 280nm. The flow rates used were 0.8ml/min for 10 minutes and 0.2ml/min for 10 minutes, which are the standard flow rates nominally equivalent to the fed and fasted states respectively, based on the Apparatus 4 volumetric rates when factored for flow cell volume. Intrinsic dissolution rate is calculated by the SDI software and requires the molar extinction coefficient for the compound being tested for this calculation. To determine the molar extinction coefficient (also called the molar absorptivity or molar attenuation coefficient) UV calibration curves were produced for each of the three compounds (ornidazole, 5-nitroisophthalic acid and the ornidazole:5-nitroisophthalic co-crystal).

### 6.4.5.2 UV calibration curve preparation

To produce the UV calibration standards, the pure substances were dissolved in a 20% ethanol 80% acetonitrile mixture to give 400µg/ml stock solutions. Aliquots from these stock solutions were diluted with the appropriate amount of FaSSIF-v2 to produce the calibration standards at concentrations of 100, 50, 20, 10 and 5µg/ml. UV absorbance was measured using an Agilent Technologies Cary 100 UV-Vis spectrophotometer, the measurements listed in Table 6.5, and the calibration curves presented in Figure 6.24 below.

***Table 6.5*** *UV absorbance measurements for the calibration standards of ornidazole, 5-nitroisophthalic acid and ornidazole:5-nitroisophthalic acid.*

| Concentration (µg/ml) | Absorbance at 280nm | | |
|---|---|---|---|
| | Ornidazole | 5-Nitroisophthalic acid | Ornidazole:5-Nitroisophthalic acid |
| 5 | 0.0768 | 0.1777 | 0.1327 |
| 10 | 0.1382 | 0.2450 | 0.2262 |
| 20 | 0.2542 | 0.5050 | 0.3793 |
| 50 | 0.5741 | 1.2020 | 0.9434 |
| 100 | 1.1303 | 2.1150 | 1.7819 |

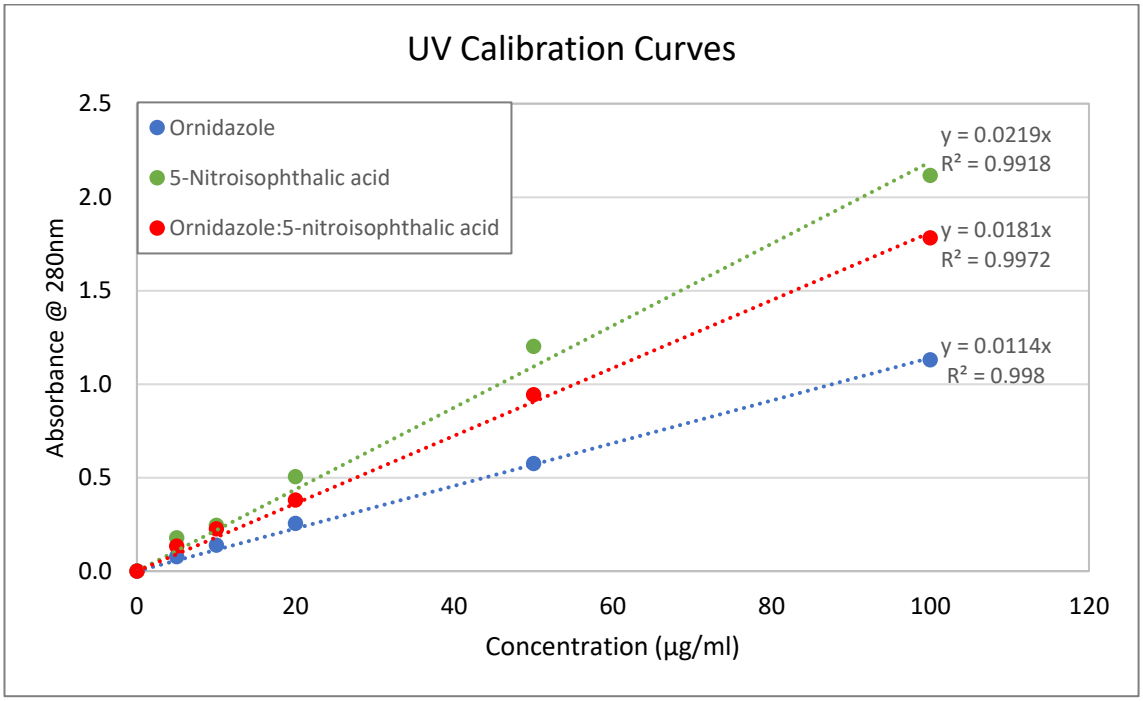


***Figure 6.24*** *UV calibration curves for ornidazole, 5-nitroisophthalic acid and ornidazole:5-nitroisophthalic acid in FaSSIF-v2 at 280nm.*

The trend lines for all three UV calibration curves gave equations with $R^2$ values of greater than 0.99 and are thus acceptable for use in the determination of intrinsic dissolution rate. The figure above was plotted with concentration in the units of µg/ml, however by plotting the same graph with molar concentrations the value for the gradient of the trend lines gives the molar extinction

coefficient. The values obtained for the molar extinction coefficients for each material are reported in Table 6.6.

***Table 6.6*** *Molar extinction coefficients determined from UV calibration curves.*

| Material | Molar extinction coefficient ($M^{-1}cm^{-1}$) |
|---|---|
| Ornidazole | 2505.5 |
| 5-Nitroisophthalic acid | 4620.4 |
| Ornidazole:5-Nitroisophthalic acid | 7800.7 |

### 6.4.5.3 Analysis

The intrinsic dissolution testing was carried out as stated and the measurements recorded by the SDI software. Full results are reported in Appendix 6.5 and a selection of results at the two different flow rates have been consolidated in Table 6.5. The average intrinsic dissolution rate and surface concentration in one-minute segments were calculated throughout the experiments. The results for one-minute sections taken in the middle of the runs for both flow rates (5-6 minutes and 15-16 minutes for 0.2ml/min and 0.8ml/min flow rates respectively) are listed in Table 6.7 for each material. The full results set shows a relatively high consistency throughout the measurements within each flow rate for all three materials. At the start and end of each section (whenever the flow rate changes) higher variation is seen in IDR, which is the reason the segments chosen to include in the consolidated results table were from the middle of the time ranges. The main exceptions are the IDR for 5-nitroisophthalic acid at 0.2ml/min flow rate where there is a larger variation throughout that section of the experiment, and the surface concentration of ornidazole:5-nitroisophthalic acid which increased greatly during the 0.8ml/min flow rate section.

***Table 6.7*** *Consolidated results for the intrinsic dissolution testing of ornidazole, 5-nitroisophthalic acid and ornidazole:5-nitroisophthalic acid in FaSSIF-v2.*

| Material | Time period (mins) | Flow Rate (ml/min) | Surface concentration (mg/ml) | IDR ($\mu g/min/cm^2$) | Standard deviation |
|---|---|---|---|---|---|
| Ornidazole | 5-6 | 0.2 | 222.63 | 190.18 | 4.80 |
| | 15-6 | 0.8 | 162.18 | 275.47 | 8.16 |
| 5-Nitroisophthalic acid | 5-6 | 0.2 | 195.29 | 322.31 | 17.37 |
| | 15-16 | 0.8 | 161.51 | 269.45 | 3.64 |
| Ornidazole:5-Nitroisophthalic acid | 5-6 | 0.2 | 102.09 | 59.17 | 1.13 |
| | 15-16 | 0.8 | 6.80 | 41.45 | 0.86 |

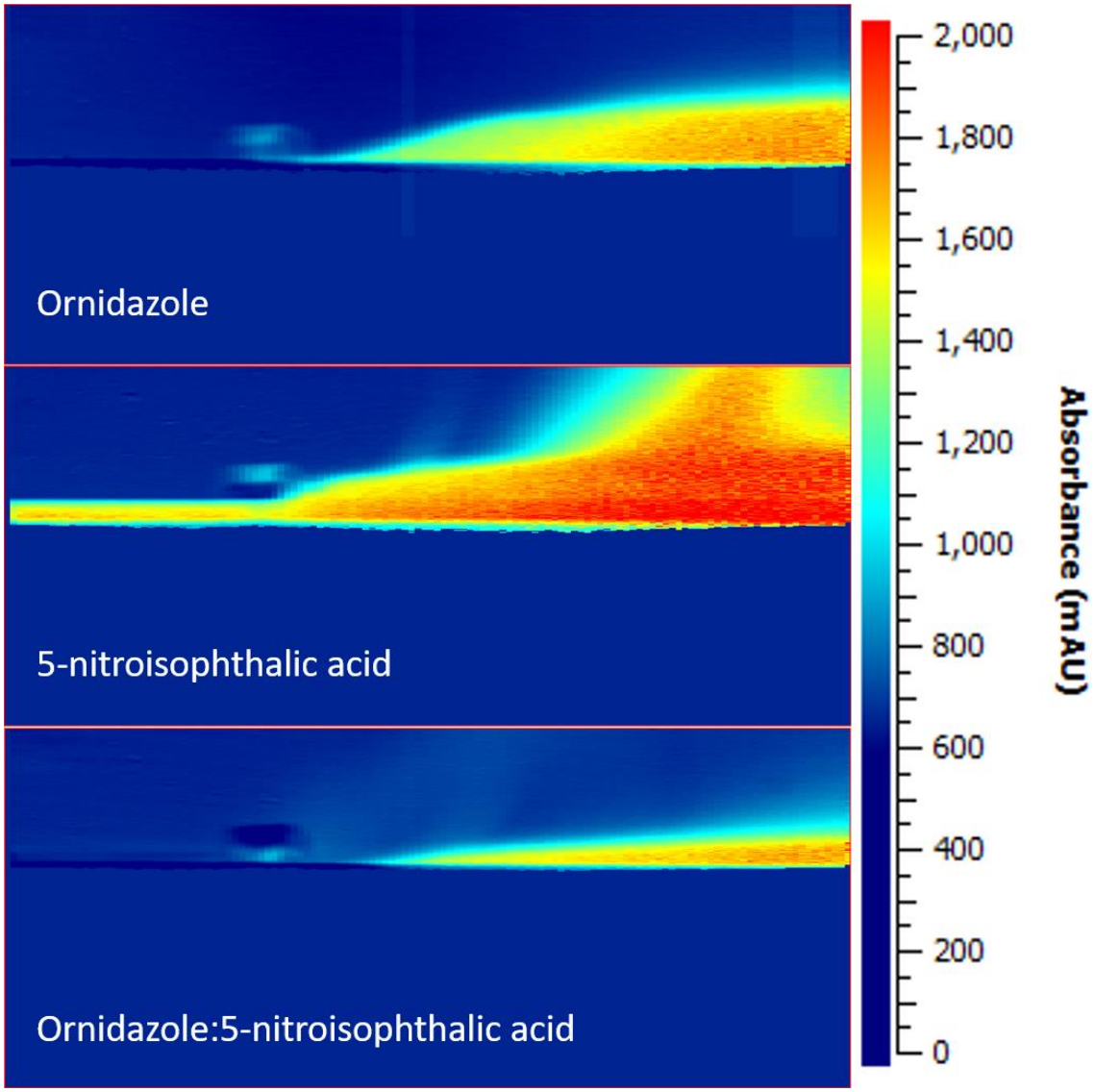


***Figure 6.25*** *False colour snapshots of the measurements from the UV detector array at the midpoint (5 minutes) of the 0.2ml/min flow rate section of the experiment for ornidazole (top), 5-nitroisophthalic acid (middle) and ornidazole:5-nitroisophthalic acid (bottom).*

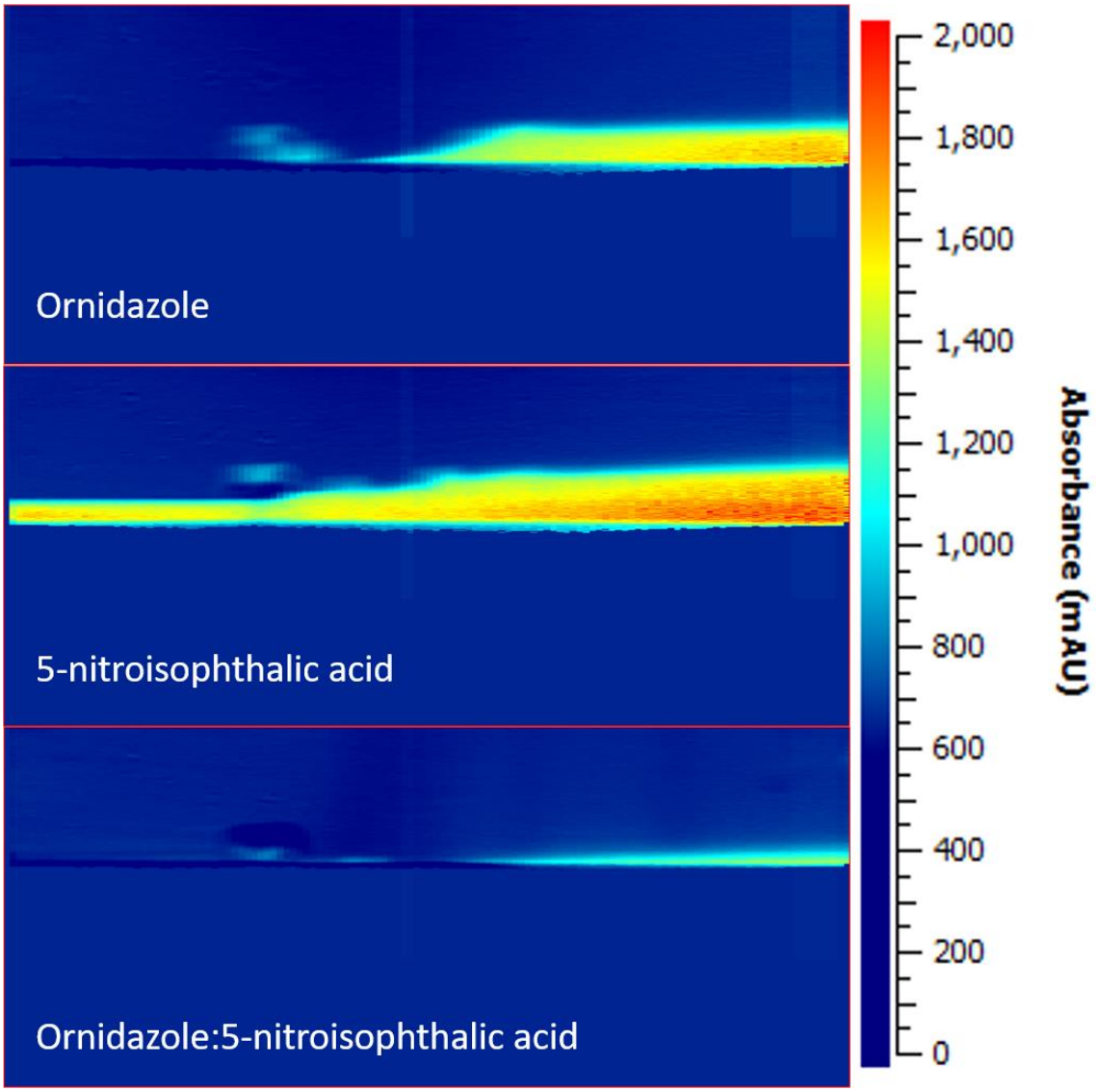


***Figure 6.26*** *False colour snapshots of the measurements from the UV detector array at the midpoint (15 minutes) of the 0.8ml/min flow rate section of the experiment for ornidazole (top), 5-nitroisophthalic acid (middle) and ornidazole:5-nitroisophthalic acid (bottom).*

Figures 6.25 and 6.26 show false colour images produced from the measurements from the UV detector array at a specific point during the experiments for each material. Figure 6.25 is at the 5 minute timepoint of the experiment which is the midpoint for the 0.2ml/min flow rate section and Figure 6.26 is at the 15 minute timepoint, the midpoint for the 0.2ml/min flow rate section. These images give a visual representation of the concentration of each material throughout the flow cell, with higher absorbance values displayed in red and reducing to dark blue where no absorbance is occurring. In general, the images in Figures 6.25 and 6.26 match the calculated IDR results in that at the given flow rate, the material with the higher IDR value can be seen to have a greater area of high concentration.

The sample is situated in the centre of the image and flow of the dissolution media is from left to right. In the 5-nitroisophthalic image in Figure 6.25 there is an area of high concentration in the top right, above where it would be expected from looking at the rest of the concentration profile. A possible explanation for this would be that some material broke away from the compacted sample and allowed a greater surface area for dissolution. The production of this 'front' which moved with the flow out of the flow cell could be the cause of the higher variation in IDR recorded for 0.2ml/min flow rate section of the experiment and would explain the higher IDR also seen throughout the middle section of the experiment in Figure 6.27.

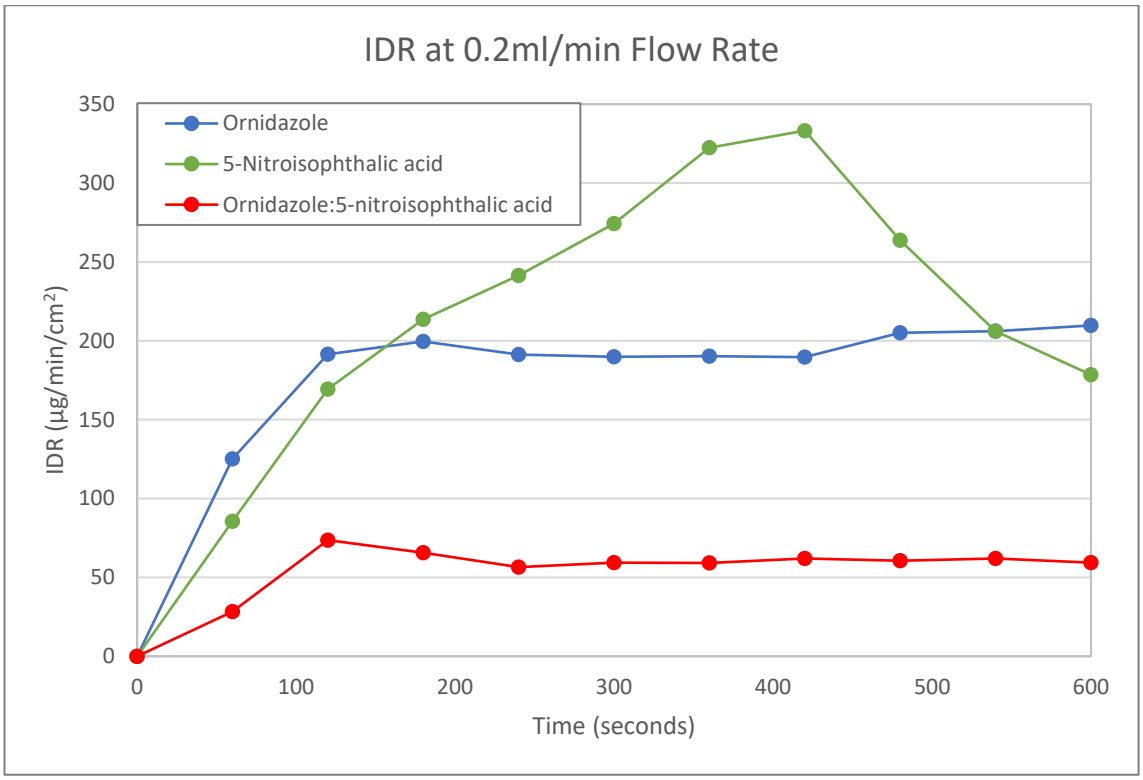


***Figure 6.27*** *Intrinsic dissolution rate of ornidazole, 5-nitroisophthalic acid and ornidazole:5-nitroisophthalic acid in FaSSIF-v2 at a flow rate of 0.2ml/min over 10 minutes (n=1).*

Figures 6.27 and 6.28 show the IDR plotted over the course of the full experiment, with a single average value plotted for the preceding 60 seconds. These results are split between the first 10 minutes at 0.2ml/min and the second 10minutes at 0.8ml/min flow rates. The unusually high measurement at the start of the 0.8ml/min experiments is due to the change in flow rate as these measurements followed directly from the 0.2ml/min experiment. Once the flow rate had stabilised it is clear that IDR is consistent throughout the remaining experiment run time.

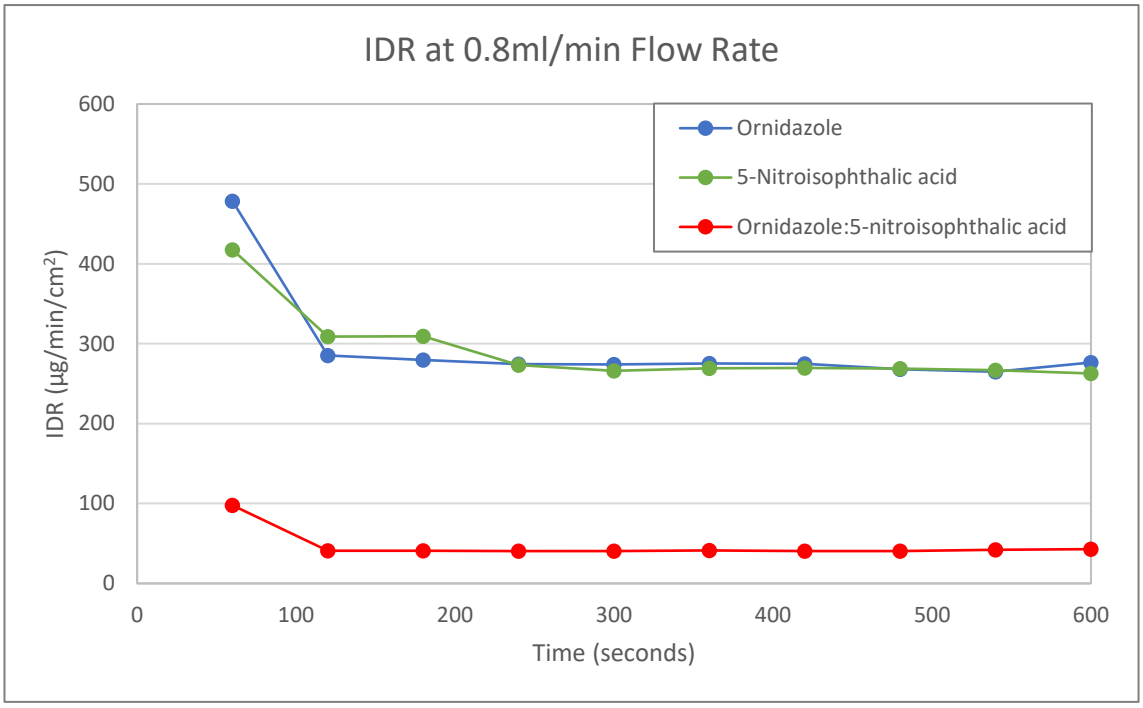


***Figure 6.28*** *Intrinsic dissolution rate of ornidazole, 5-nitroisophthalic acid and ornidazole:5-nitroisophthalic acid in FaSSIF-v2 at a flow rate of 0.8ml/min over 10 minutes (n=1).*

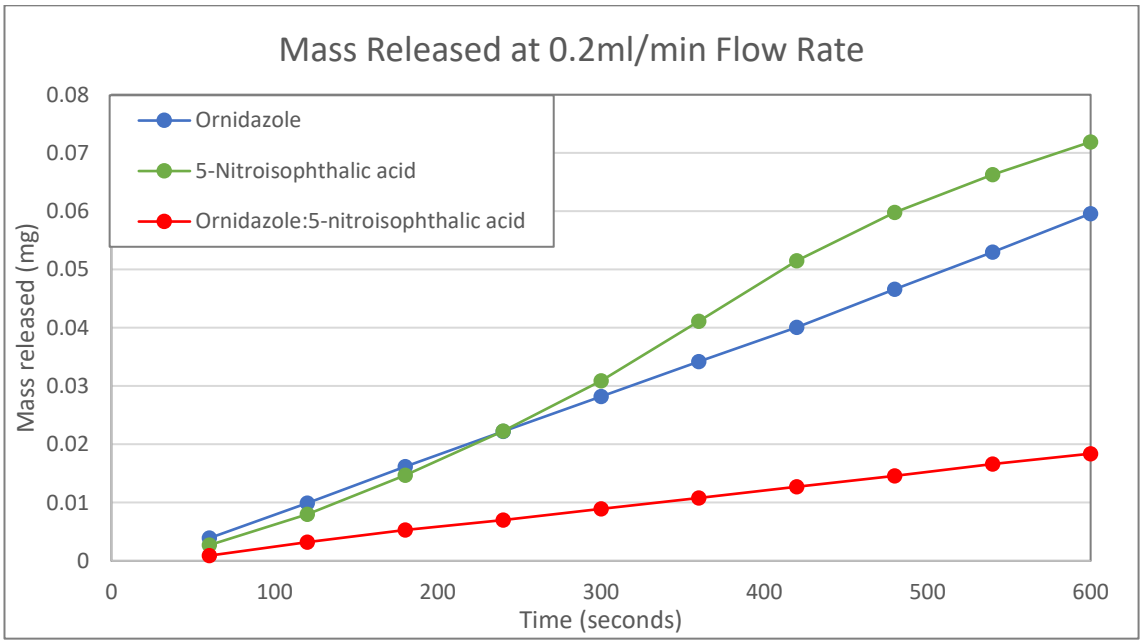


***Figure 6.29*** *Cumulative mass of ornidazole, 5-nitroisophthalic acid and ornidazole:5-nitroisophthalic acid released over 10 minutes in FaSSIF-v2 at a flow rate of 0.2ml/min (n=1).*

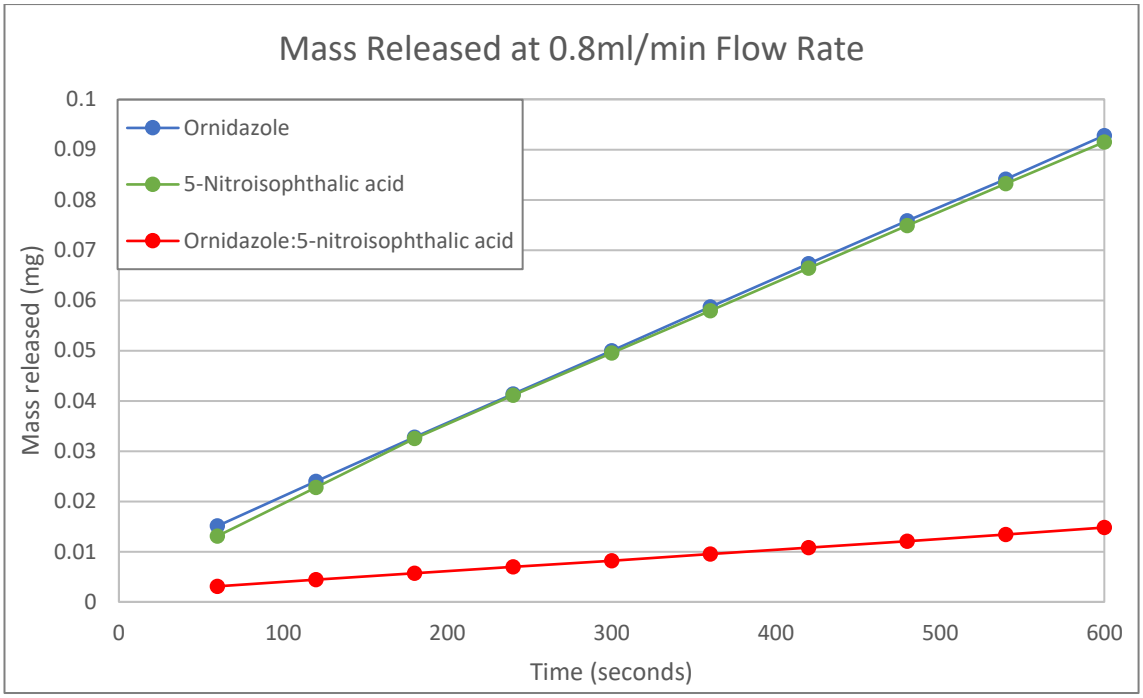


***Figure 6.30*** *Cumulative mass of ornidazole, 5-nitroisophthalic acid and ornidazole:5-nitroisophthalic acid released over 10 minutes in FaSSIF-v2 at a flow rate of 0.8ml/min (n=1).*

The cumulative mass released from the samples at the 0.2ml/min and 0.8ml/min flow rates are shown in Figures 6.29 and 6.30 respectively. These correspond well with the IDR plots, with both ornidazole and 5-nitroisophthalic acid displaying much greater sample release over the equivalent period of time as the ornidazole:5-nitroisophthalic acid co-crystal at both flow rates.

## 6.4.6 Summary

Further investigation into the ornidazole:5-nitroisophthalic acid system by single crystal X-ray diffraction led to the determination of its crystal structure, which has been identified as a 1:1 co-crystal. Analysis of the crystal structure in structure in comparison of those of pure 5-nitroisophthalic acid and ornidazole showed greater similarity between the co-crystal and 5-nitroisophthalic acid than with ornidazole, especially in terms of the presence of potential slip planes. Relating this to the outcome of the compression and hardness testing, it is likely that greater plastic deformation occurs in ornidazole than either 5-nitroisophthalic acid or the co-crystal due to the features of the packing within the crystal structures, i.e. potential slip planes, and results in the greater hardness measured in the ornidazole tablets.

DVS analysis showed very little difference in water sorption between the three compounds, with no hydration occurring in any of the samples. The intrinsic dissolution experiments however, resulted in an unexpected outcome; the IDR measured for the co-crystal was lower than that of either parent component. Intrinsic dissolution rate has been shown to correlate with solubility in many systems,[177,178] hence this outcome is unusual as co-crystals normally have a solubility between that of the parent materials,[21] with more soluble co-formers leading to more soluble co-crystals.[49,179] There are numerous examples of co-crystals in which intrinsic dissolution rate is improved compared to the parent drug for example flufenamic acid:theophylline[159] and nitazoxanide:*p*-aminosalicylic acid.[180]

The melting point of the ornidazole:5-nitroisophthalic acid co-crystal is between that of ornidazole and 5-nitroisophthalic acid, providing no suggestion of a lower IDR before the measurement. Although increasing the solubility and release rate of the parent API by co-crystallisation is often the aim, the lower IDR measured for the co-crystal in this case shows the potential for co-crystal use in the development of a slow-release formulations. Such use of co-crystals has previously been postulated,[181] and examples of co-crystal of ribavirin with reduced release rates reported.[182]

## 6.5 Conclusions

The work presented in this chapter has served as further validation of the optimised co-crystal screening method as developed in Chapter 3 by proving its utility, applying the method to ornidazole as a model API and resulting in 23 hits of out the top 46 computationally predicted co-formers for the API and importantly including the two positive controls. Further investigation in the form of DSC and TGA analysis of the hits found that many of these materials were not pure co-crystal. Production of pure co-crystal phases is certainly not an expectation for a co-crystal screen, and many new phases were correctly detected by the screening process. The evaporative crystallisation experiments showed that for potential future scaled up production, the method of manufacture would require further consideration as the materials produced did not always match those produced by the initial ultrasonication based co-crystal screening method.

The ornidazole:5-nitrisophthalic acid system was identified for more thorough characterisation and was found to differ from the norm regarding its lower IDR compared to both parent components, but which does not correlate with its melting point which, like the majority of co-

crystals, falls between those of both its parent materials. The lower dissolution rate is the opposite of the intention of most rationales for developing co-crystals however the ornidazole:5-nitroisophthalic acid co-crystal was found to crystallise much more readily than ornidazole alone. Although normally a reduction in solubility may negatively outweigh any benefits, in some cases such as with relatively soluble drugs (such as ornidazole) in which a slight reduction in solubility wouldn't have as negative an impact on bioavailability, the improvement in crystallisation kinetics and crystallinity may be worth the solubility hit for the vast improvement in processing ability.

# Chapter 7 – Formulation and performance of zafirlukast:piperazine co-crystals

## 7.1 Introduction

This thesis, up until now has mainly focused on the processes involved in screening for and producing co-crystals/binary materials and has looked in depth at the properties of only one of these new forms – ornidazole:5-nitroisothalic acid in Chapter 6. This chapter therefore concerns the measurement of performance of the co-crystals in terms of properties relevant to the oral bioavailability of the form if it were to be administered to a patient.

Areas of study which are important when considering the performance of a medicine to be administered to a patient include pharmacokinetics and pharmacodynamics, and stability (both chemical and physical) when thinking about storage and shelf life. When looking at different forms of the same drug, the aim is to improve the pharmacokinetics of the drug, specifically the efficiency of absorption processes. These can be broken down into a number of semi-independent steps which include improving solubility of the drug and dissolution rate of the form, and permeability of the drug. Permeability is not something that is readily altered and generally requires chemical modification of the API or the addition of permeability enhances to the formulation.

The work presented in this chapter has been to determine robust methods for the measurement and characterisation for an API (zafirlukast), and three stoichiometric co-crystals of this drug and piperazine.[183] These co-crystal forms were discovered by Dr Rafel Prohens (CIRCE) as part of an AZ project and our group became involved to carry out further characterisation work. Zafirlukast is a leukotriene receptor antagonist and is used as an oral treatment for asthma.[184] The original crystalline tablet formulation of zafirlukast used during development and early clinical trials resulted in unacceptably low bioavailability and was replaced by an amorphous formulation which is the form of the marketed product.[185,186] Zafirlukast is a perfect candidate for co-crystallisation then, as the solubility and hence bioavailability may be improved compared to the crystalline pure drug. Additionally, potential improvements to the ease of manufacturing compared to the amorphous form may be achieved and having a thermodynamically stable co-crystalline form negates the concerns of crystallisation from an amorphous form with regard to physical stability and shelf life of the product.

## 7.2 Production of co-crystals

Small samples of three co-crystals of zafirlukast and piperazine (1:1, 2:1 and a toluene solvate of a 1:1 co-crystal) in addition to a larger supply of pure zafirlukast were provided by AZ for this work. The quantity received was sufficient to carry out a number of characterisation and property determination experiments which will be presented within this chapter, however for more robust dissolution and *in vivo* experiments a greater supply was required. This necessitated the production of a greater quantity of the co-crystals in-house and this was mostly successfully achieved by scaling up the method used to produce the original batches by AZ. The original documented methods are presented in Appendix 7.1. The methods detailed below are adapted only by the quantity of material necessary to scale up and some of the timings. The only exception to this was the zafirlukast:piperazine co-crystal (2:1) Form A which required further modification to the method in order for robust scale up to be achieved.

### 7.2.1 Zafirlukast:piperazine co-crystal (2:1) Form A

Obtained by slurry in acetonitrile at room temperature after initial slow crystallization from a solution of zafirlukast:piperazine (1:1) in ethanol. Zafirlukast (2.0242 g) and piperazine (312.7 mg), molar ratio 1:1, were dissolved in ethanol (500 mL) at 60-70°C. The solution was left to cool down to room temperature and the liquid evaporate.

PXRD analysis, detailed below, showed that this process did not achieve production of the co-crystal; a small sample of the material was removed and the rest of the material was then slurried in approximately 15ml ethanol at room temperature for 71 hours. This yielded (2:1) Form A (m.p. of product 220.6°C). Net amount of product after drying = 1.1421g (Yield = 52.5%)

### 7.2.2 Zafirlukast:piperazine co-crystal (1:1) Form D

Obtained by slurry in acetonitrile at room temperature. Zafirlukast (2.0246 g) and piperazine (438.9 mg), molar ratio 1:1.5, were slurred in acetonitrile (40 mL) at room temperature for 64 hours. The solid was filtered and dried under vacuum for 48 hours. (m.p. of product 181.0°C). Net amount of product after drying = 1.9686g (Yield = 84.6%)

### 7.2.3 Zafirlukast:piperazine co-crystal (1:1) toluene solvate Form E

Obtained by slurry in toluene at room temperature. Zafirlukast (1.9993 g) and piperazine (444.9 mg), molar ratio 1:1.5, were slurred in toluene (40 mL) at room temperature for 29 hours. The solid was filtered and dried under vacuum for 42 hours. (m.p. of product 119.2°C). Net amount of product after drying = 2.2356g (Yield = 89.0%)

## 7.3 Characterisation of co-crystals

### 7.3.1 Powder X-ray diffractometry

PXRD patterns were recorded for the produced co-crystals, following the standard XRPD method detailed in Chapter 2, and compared to those of the reference patterns of the co-crystals to confirm equivalence. These consistent PXRD patterns are displayed in Figure 7.1 and details of the different batches are presented in Table 7.1.

***Table 7.1*** *Details of zafirlukast:piperazine co-crystals.*

| Material | Batch | Origin |
|---|---|---|
| Zafirlukast:piperazine 2:1 co-crystal | Bx37b, Bx42, Bx45 | Received from CIRCE/AZ |
| | ZP21CC | Produced at Durham University |
| Zafirlukast:piperazine 1:1 co-crystal | Bx24, Bx43 | Received from CIRCE/AZ |
| | ZP11CC | Produced at Durham University |
| Zafirlukast:piperazine co-crystal toluene solvate (3:3:2) | Bx26b, Bx44 | Received from CIRCE/AZ |
| | ZPTSCC | Produced at Durham University |

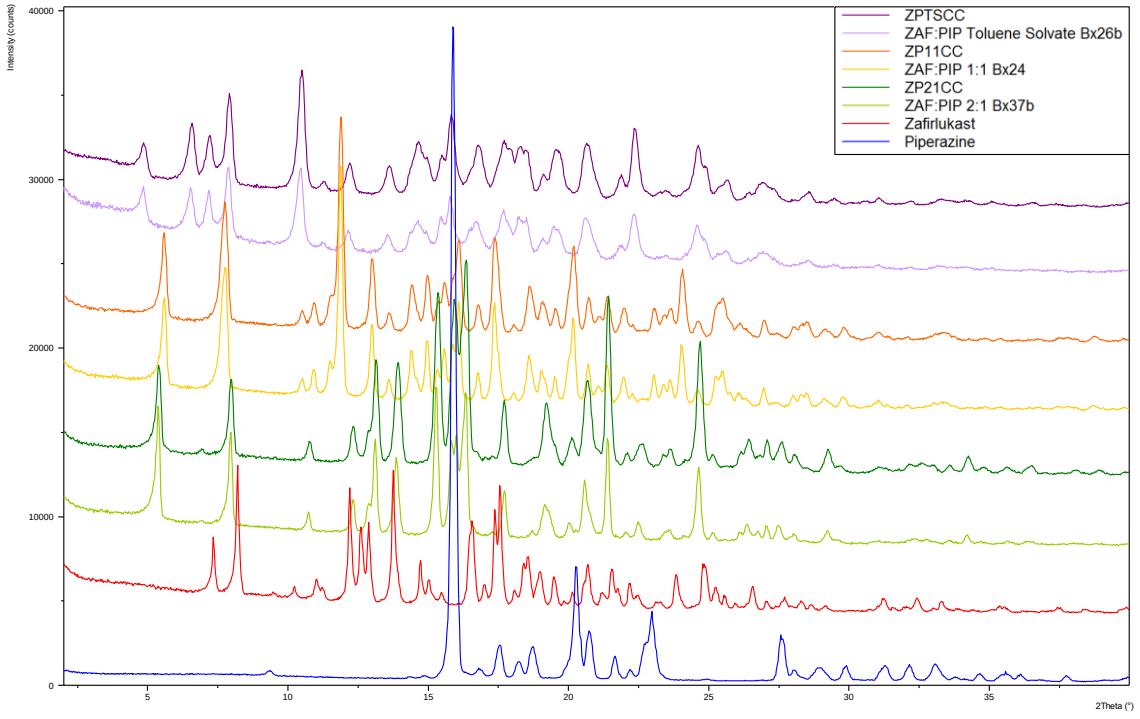


***Figure 7.1*** *PXRD patterns of zafirlukast (red) and piperazine (blue) with those of the original co-crystals produced by AZ/CIRCE: 2:1 (light green), 1:1 (yellow) and toluene solvate (lilac), and those produced in-house: 2:1 (ZP21CC, dark green), 1:1 (ZP11CC, orange) and toluene solvate (ZPTSCC, purple).*

Each of the pairs of PXRD patterns for the co-crystals match, which confirms that the correct forms were produced in each case. PXRD patterns of a sample from the intermediate material produced after the initial attempt to produce the 2:1 co-crystal, along with those of the reference sample and parent components are shown in Figure 7.2. The presence of the peak at 5.5° 2θ suggest that some conversion to the co-crystal has occurred but extra peaks, for example those at 11.3° and 17.1° 2θ, are evidence that the sample still contains some impurities, i.e. starting material. This analysis led to the application of the alternative slurry method to produce the desired co-crystal form displayed as the dark green pattern which is consistent with the reference 2:1 co-crystal pattern (light green, Figure 7.2).

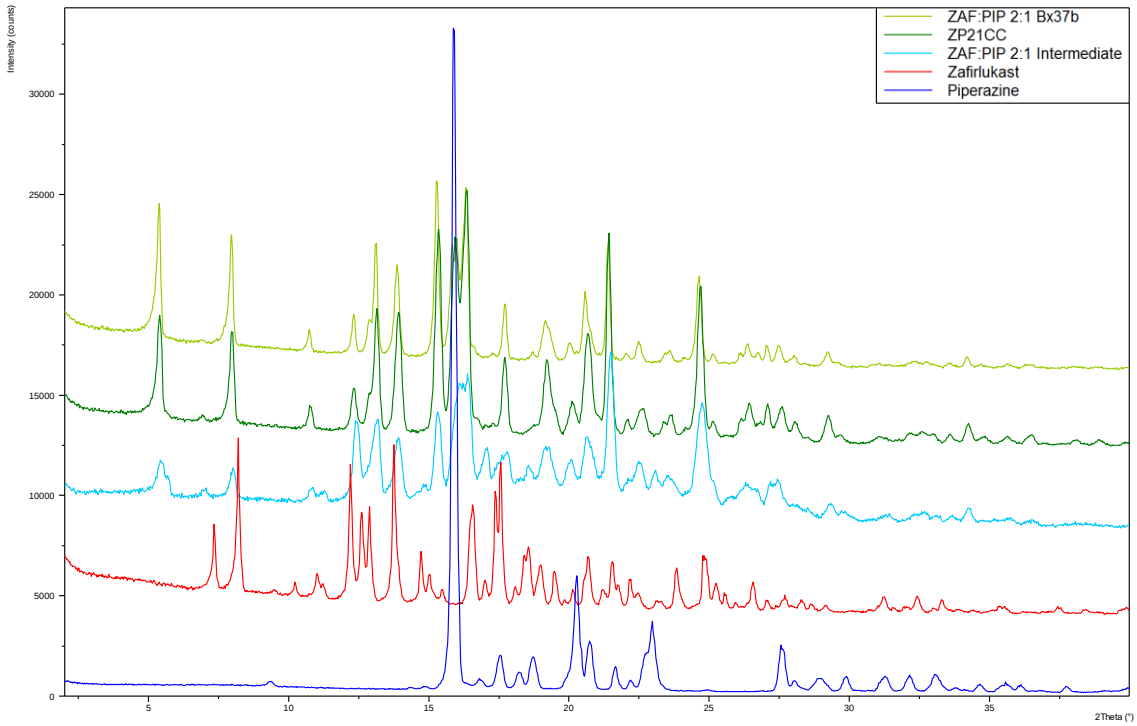


***Figure 7.2*** *PXRD patterns of the intermediate material produced after the initial attempt to produce the 2:1 co-crystal (light blue), with those of the starting materials: zafirlukast (red) and piperazine (blue); the original 2:1 co-crystal produced by AZ/CIRCE (light green), and the 2:1 co-crystal produced from the intermediate (ZP21CC, dark green).*

## 7.3.2 Differential scanning calorimetry

DSC thermograms were recorded for the produced co-crystals, following the standard DSC ramp method detailed in Chapter 2. The DSC traces displayed in Figure 7.3 were obtained from samples of co-crystals received from CIRCE/AZ (Bx24, Bx26b and Bx42) and those in Figure 7.4 from the co-crystals produced in-house and of zafirlukast and piperazine as received. The DSC traces for ZP11CC and ZP21CC correspond well with and display very similar melting points to

those of the reference materials. Together with the matching powder patterns shown above (Figure 7.1), this would be sufficient evidence to prove to a regulator that these were the same form for batch release. The profile for ZPTSCC has a lower onset temperature for the endothermic peak, compared to the reference material and could indicate a slight difference in desolvation behaviour which is also apparent in the TGA profiles of the two materials.

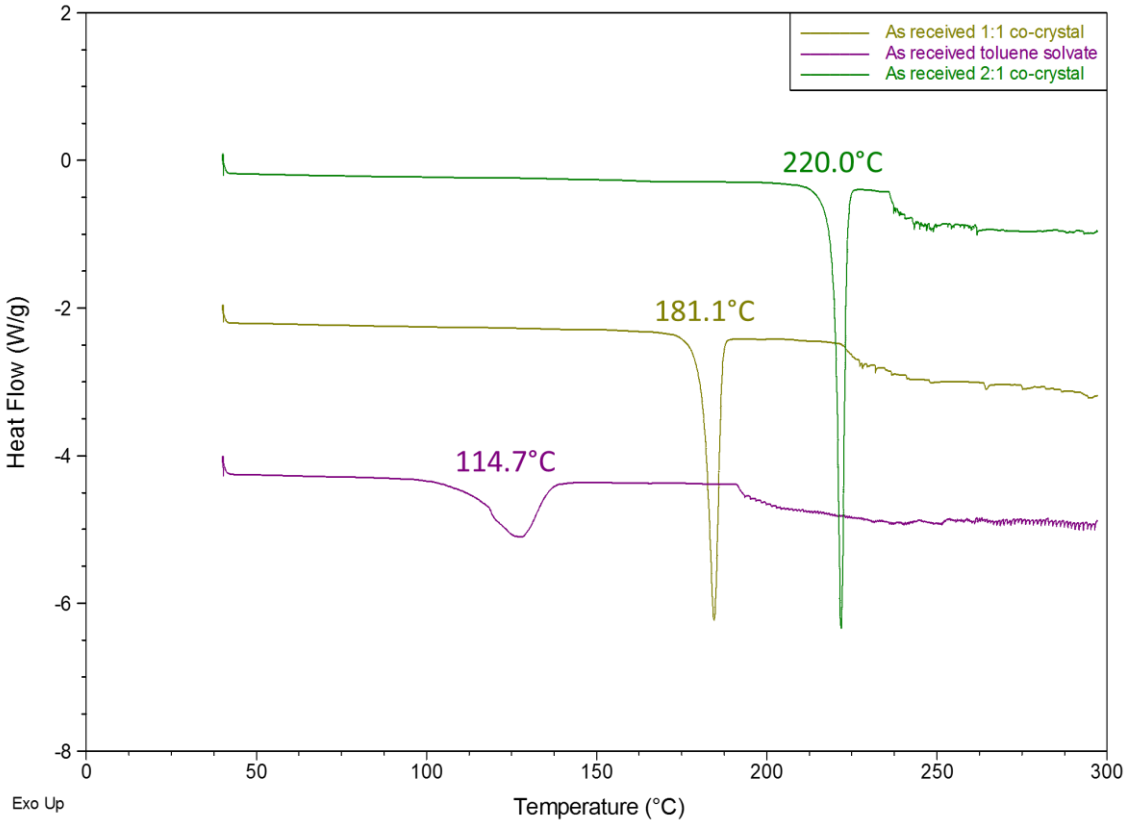


***Figure 7.3*** *DSC profiles of the 1:1 (olive), 2:1 (green) and toluene solvate (purple) zafirlukast:piperazine co-crystals received from CIRCE/AZ. The peak onset temperatures are displayed by the traces.*

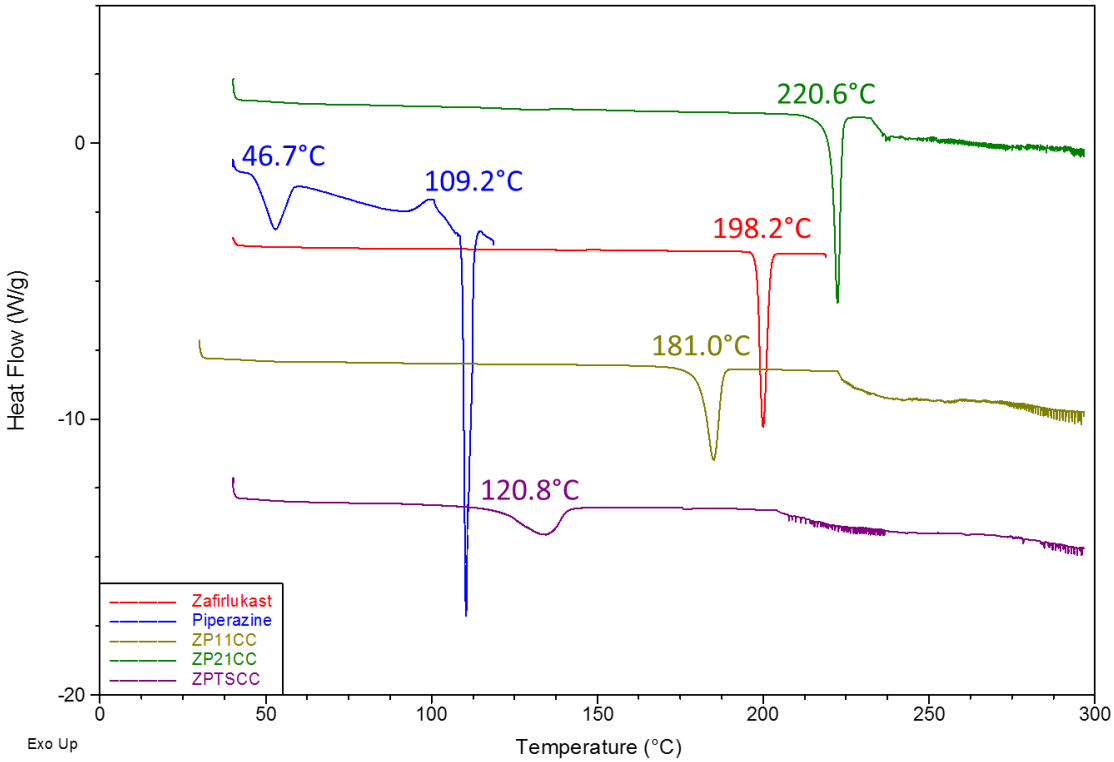


***Figure 7.4*** *DSC profiles of Zafirlukast (red), piperazine (blue) and the produced co-crystals: ZP11CC (olive), ZP21CC (green) and ZPTSCC (purple). The peak onset temperatures are displayed by the traces.*

The DSC trace of zafirlukast shows a single melting peak, as expected, at 198.2°C, however the profile for piperazine has a lower, broad, endothermic peak at 46.7°C followed by a much sharper peak at 109.2°C. Figure 7.5 shows the DCS traces for a full heat-cool-heat method for the same piperazine sample with the cycles separated. It is most likely that a hydrate of piperazine had formed causing this lower endothermic peak. The hexahydrate form has been previously reported featuring a melting point matching that of the initial peak observed in Figure 7.5.[187] On second heating, once dehydrated, the melting point of the now anhydrous sample, matches that of the second endothermic peak of the initial cycle and literature value (listed by the supplier) for the melting point of piperazine of 109-112°C.

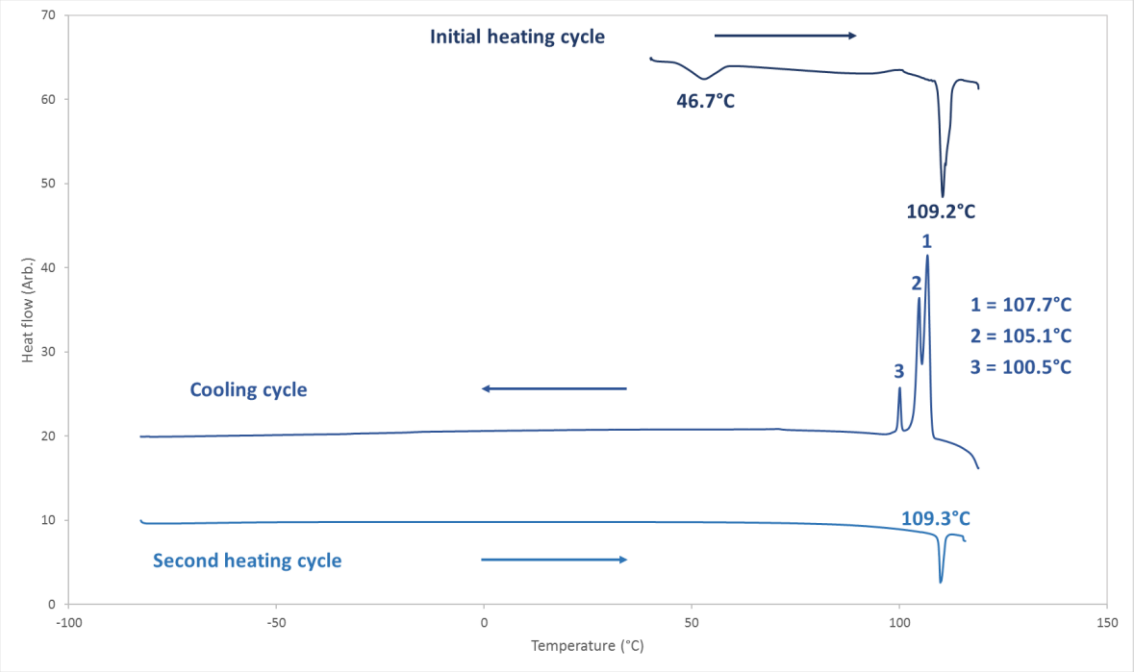


***Figure 7.5*** *Separated DSC traces for piperazine showing initial heating, cooling and second heating cycles. (Exo. up)*

In addition to being used for identification purposes, the melting point information obtained from the DSC experiments is interesting in understanding the modifications co-crystal formation has on the properties of the parent drug. The melting points observed for the co-crystals differ significantly from pure zafirlukast but also from each other. The peak onset temperature for piperazine, once dehydrated, is 109.3°C. The melting point of two of the co-crystals therefore fall between those of co-former and API and one, the 2:1 co-crystal, is higher than either of the components of the co-crystal. This is a less common outcome than a melting point for the co-crystal being between those of the two parent compounds, however is also not novel having been observed previously.[47]

## 7.3.3 Thermogravimetric analysis

TGA profiles were recorded for both the newly produced and original co-crystals, following the standard TGA method detailed in Chapter 2. A full set of DSC and TGA plots are presented in Appendix 7.2 and show good similarity between the received and produced 1:1 and 2:1 zafirlukast:piperazine co-crystals. The TGA analysis of the produced and received toluene solvates however have a discrepancy which is highlighted in Figure 7.6.

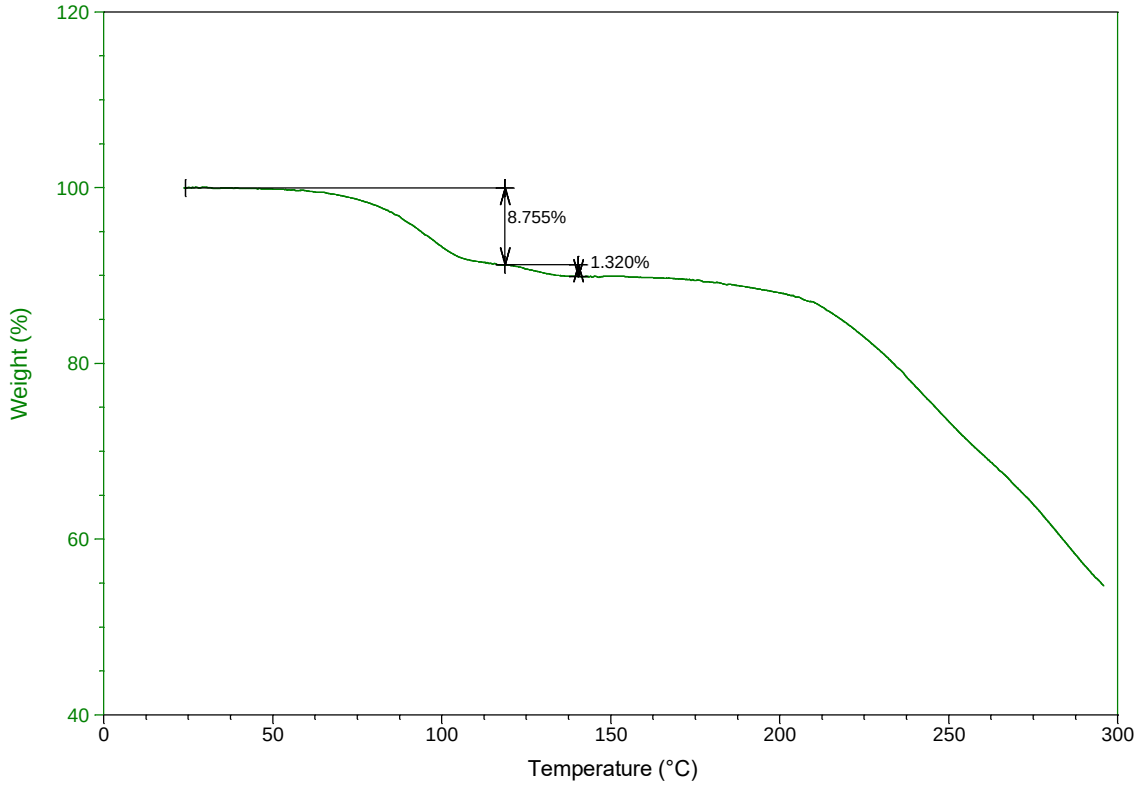


***Figure 7.6*** *TGA profile of the produced zafirlukast:piperazine co-crystal toluene solvate showing mass change over the temperature range of approximately 50°C to 150°C.*

The calculated percentage mass loss based on the 3:3:2 zafirlukast:piperazine:toluene ratio should be 8.49%. The intermediate step in the TGA profile equates to an 8.755% weight loss and is more commensurate with the calculated value, suggesting that a large constituent of the sample is the expected co-crystal toluene solvate. A possible explanation for the observation of two mass losses is the presence of a second solvated form of the co-crystal, which is left after desolvation of the expected solvate form. For example, it is possible that a small amount of an isomorphic 3:3:1 co-crystal toluene solvate formed, which could explain the identical PXRD patterns but which could also give rise to the recorded TGA profile and account for the slight disparity in mass loss given the exact content of each solvated form remains unknown.

## 7.3.4 Dynamic vapour sorption analysis

DVS analysis was undertaken for the original co-crystals, following the standard DVS method detailed in Chapter 2. The scale of the y-axis should be borne in mind when comparing between the compounds' DVS plots in Figures 7.7 to 7.11.

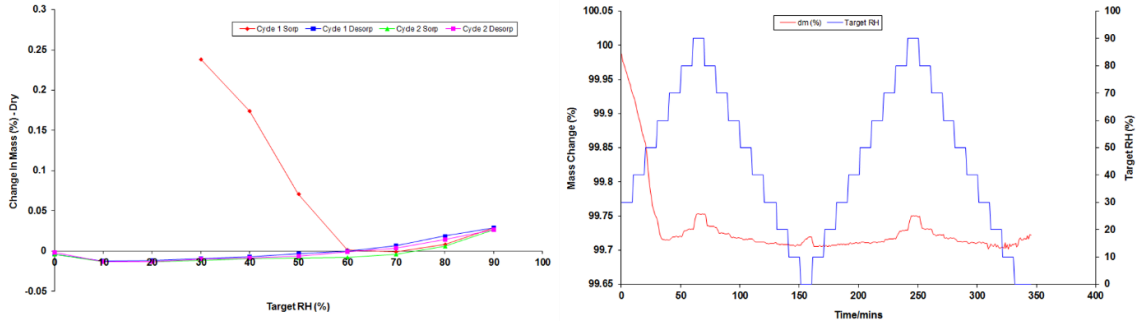


***Figure 7.7*** *Isotherm plot from DVS analysis of zafirlukast (left) and plot showing percentage change in mass versus the target relative humidity over time (right).*

The zafirlukast sample demonstrates practically no change in mass over the 0-90% RH range measured other than for the initial decrease during the first sorption cycle (Figure 7.7). This is likely caused by the sample containing a very small amount of amorphous zafirlukast. The increasing relative humidity above ambient conditions causes plasticisation and increased molecular mobility as water is taken up by this amorphous material. Crystallisation is thus induced leading to the expulsion of water molecules and consequently a decrease in mass is observed. By 60% relative humidity of the initial cycle, no amorphous material remains and any further mass change over the course of the measurement is negligible. The same initial decrease in mass due to the presence of small quantities of amorphous material is seen in the 1:1 and 2:1 zafirlukast:piperazine co-crystals (Figures 7.8 and 7.9).

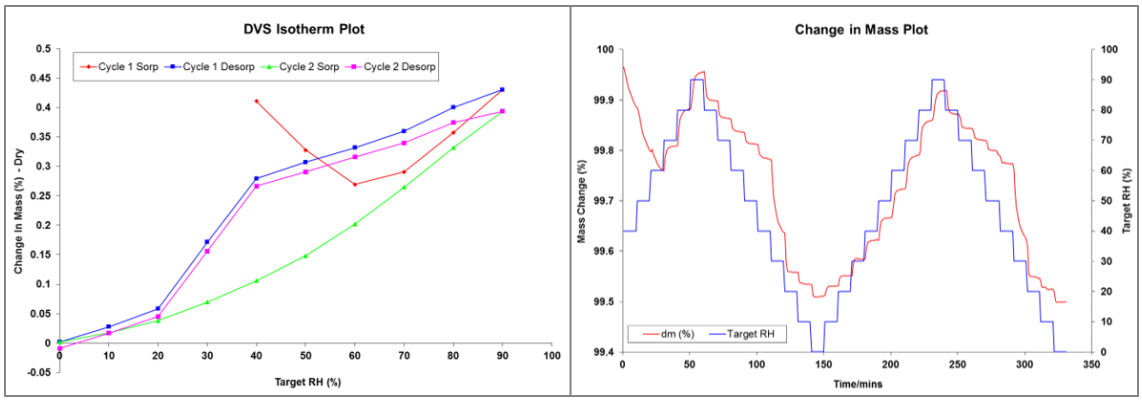


***Figure 7.8*** *Isotherm plot from DVS analysis of the zafirlukast:piperazine 1:1 co-crystal (left) and plot showing percentage change in mass versus the target relative humidity over time (right).*

In the isotherm plot for the 1:1 co-crystal (Figure 7.8) the presence of hysteresis suggests that a structure change is occurring however taking into consideration the percentage mass changes measured, it is unlikely that it is a stoichiometric hydrate.

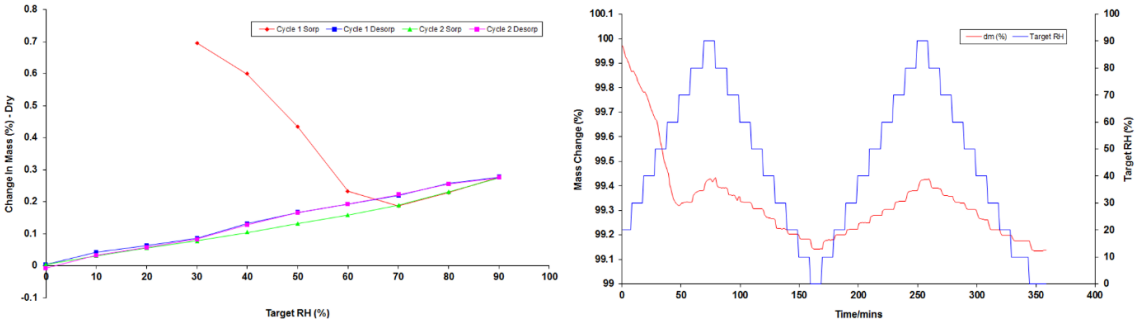


***Figure 7.9*** *Isotherm plot from DVS analysis of the zafirlukast:piperazine 2:1 co-crystal (left) and plot showing percentage change in mass versus the target relative humidity over time (right).*

After the initial decrease in mass in the first sorption cycle, the 2:1 co-crystal displays a very minor increase in mass during sorption cycles and decrease during desorption cycles, this is very likely due to surface adsorption and desorption of water.

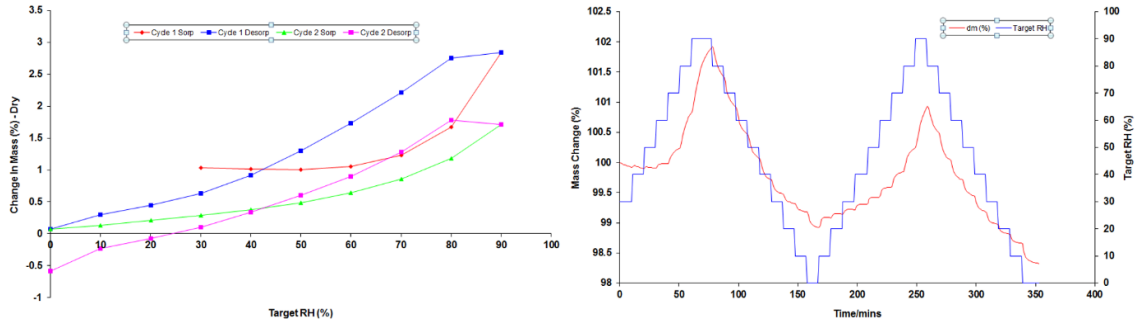


***Figure 7.10*** *Isotherm plot from DVS analysis of the zafirlukast:piperazine 1:1 co-crystal toluene solvate (left) and plot showing percentage change in mass versus the target relative humidity over time (right).*

The isotherm plot for the zafirlukast:piperazine co-crystal toluene solvate (Figure 7.10) is interesting as it shows that by the end of the first desorption cycle the total mass is lower than the initial sample mass. Mass increases with RH again in the second sorption cycle, but again ends at a lower mass than at the beginning of the second cycle. A potential cause of the observed behaviour would be that the uptake of water molecules disrupts the solvate crystal structure leading to the partial release of toluene from the sample, repeating with a less significant loss of toluene seen in the second cycle.

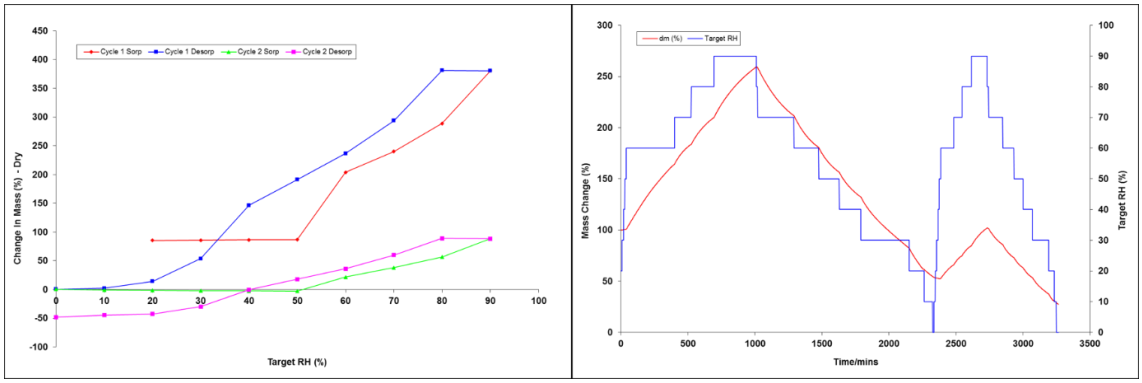


***Figure 7.11*** *Isotherm plot from DVS analysis of piperazine (left) and plot showing percentage change in mass versus the target relative humidity over time (right).*

DVS analysis of piperazine resulted in large variations in sample mass during the first cycle and similar patterns of variation but proportionally less mass change in the second. Similarly to in the case of the toluene solvate, the mass of the sample after analysis was less than at the beginning. Piperazine is known to be deliquescent,[188] justifying the very large percentage mass increase observed, and volatile,[189] potentially the cause of sample loss.

Zafirlukast and the 2:1 co-crystal show very little moisture sensitivity, however the 1:1 co-crystal does exhibit a small degree of hygroscopicity. Both piperazine and the zafirlukast:piperazine co-crystal toluene solvate display sample loss, though likely through different mechanisms. Overall the introduction of secondary components to the zafirlukast crystal structure introduces varying levels of moisture sorption tendencies. With the 2:1 co-crystal this is limited to surface adsorption and would likely not pose a problem in terms of physical stability, however with the 1:1 co-crystal and toluene solvate, this could not be guaranteed.

## 7.3.5 Compression and hardness testing

Approximately 50mg of pure compound was weighed out and compressed with a maximum load setting of 400kg using a Gamlen tablet press with a 6mm die size. The tablet was ejected and its hardness tested using a Sotax HT-1 hardness tester calibrated to 1N. This was repeated to produce three tablets for zafirlukast, piperazine and each of the three co-crystals and the measurements recorded (Table 7.2).

***Table 7.2*** *Measurements of the produced tablets of zafirlukast (ZAF), piperazine (PIP), the 1:1 (1:1CC), 2:1 (2:1CC) and toluene solvate (TSCC) zafirlukast:piperazine co-crystals.*

| Sample | Sample mass (mg) | Compression force (MPa) | Hardness (N) |
|---|---|---|---|
| ZAF 1 | 49.0 | 150.56 | 13 |
| ZAF 2 | 49.6 | 150.09 | 16 |
| ZAF 3 | 50.2 | 150.13 | 12 |
| **Av. (mean)** | **49.6** | **150.26** | **13.7** |
| s.d. | 0.490 | 0.210 | 1.700 |
| | | | |
| PIP 1 | 48.7 | 151.09 | 48 |
| PIP 2 | 48.9 | 155.76 | 41 |
| PIP 3 | 50.6 | 153.25 | 44 |
| **Av. (mean)** | **49.4** | **153.37** | **44.3** |
| s.d. | 0.85 | 1.91 | 2.87 |
| | | | |
| 2:1CC 1 | 50.5 | 145.18 | 16 |
| 2:1CC 2 | 50.3 | 145.12 | 12 |
| 2:1CC 3 | 47.7 | 145.33 | 12 |
| **Av. (mean)** | **49.5** | **145.21** | **13.3** |
| s.d. | 1.275 | 0.086 | 1.886 |
| | | | |
| 1:1CC 1 | 50.8 | 146.64 | 28 |
| 1:1CC 2 | 51.1 | 146.19 | 28 |
| 1:1CC 3 | 50.3 | 146.55 | 28 |
| **Av. (mean)** | **50.7** | **146.46** | **28.0** |
| s.d. | 0.330 | 0.194 | 0.000 |
| | | | |
| TSCC 1 | 52.4 | 144.84 | 67 |
| TSCC 2 | 50.0 | 145.00 | 61 |
| TSCC 3 | 51.8 | 144.21 | 46 |
| **Av. (mean)** | **51.4** | **144.69** | **58.0** |
| s.d. | 1.020 | 0.341 | 8.832 |

Large differences in hardness were measured between the tables of pure zafirlukast and piperazine and the co-crystals. Both the zafirlukast and the 2:1 co-crystal tablets displayed similarly low hardness with an average around 13N, piperazine tablets had much greater hardness with an average of 44.3N and the 1:1 co-crystal fell between these values with a measurement of 28N. The toluene solvate tablets displayed a far greater hardness than the other co-crystals and even more than that of piperazine at an average of 58N.

The large variation in hardness of the tablets of the co-crystals suggest differences in the crystal structures of these materials leading to improved compaction and thus increased hardness.

Unfortunately not all crystal structures are available for the materials under investigation, however those of pure zafirlukast and the 2:1 zafirlukast:piperazine co-crystal have been reported by Llinas *et al.*[183] and that of piperazine by Parkin *et al*.[190] The packing and hydrogen bonding within these structures are displayed in Figures 7.12 to 7.14 below. The crystal structure of zafirlukast (Figure 7.12) contains intermolecular hydrogen bonds between amide groups forming ribbons of zafirlukast molecules. The structure of the co-crystal differs significantly from that of pure zafirlukast, with zafirlukast molecules forming chains and piperazine molecules occupying a cavity formed by four zafirlukast molecules and participating in hydrogen bonding (Figure 7.13). Although notably different, possible similarities between these two crystal structures, such as a potential lack of slip planes could lead to both materials possessing poor compressibility which would cause the low hardness observed. It is likely that features of the crystal structure of the zafirlukast:piperazine co-crystal toluene solvate support significant compressibility resulting in a comparably very high hardness of the material as measured.

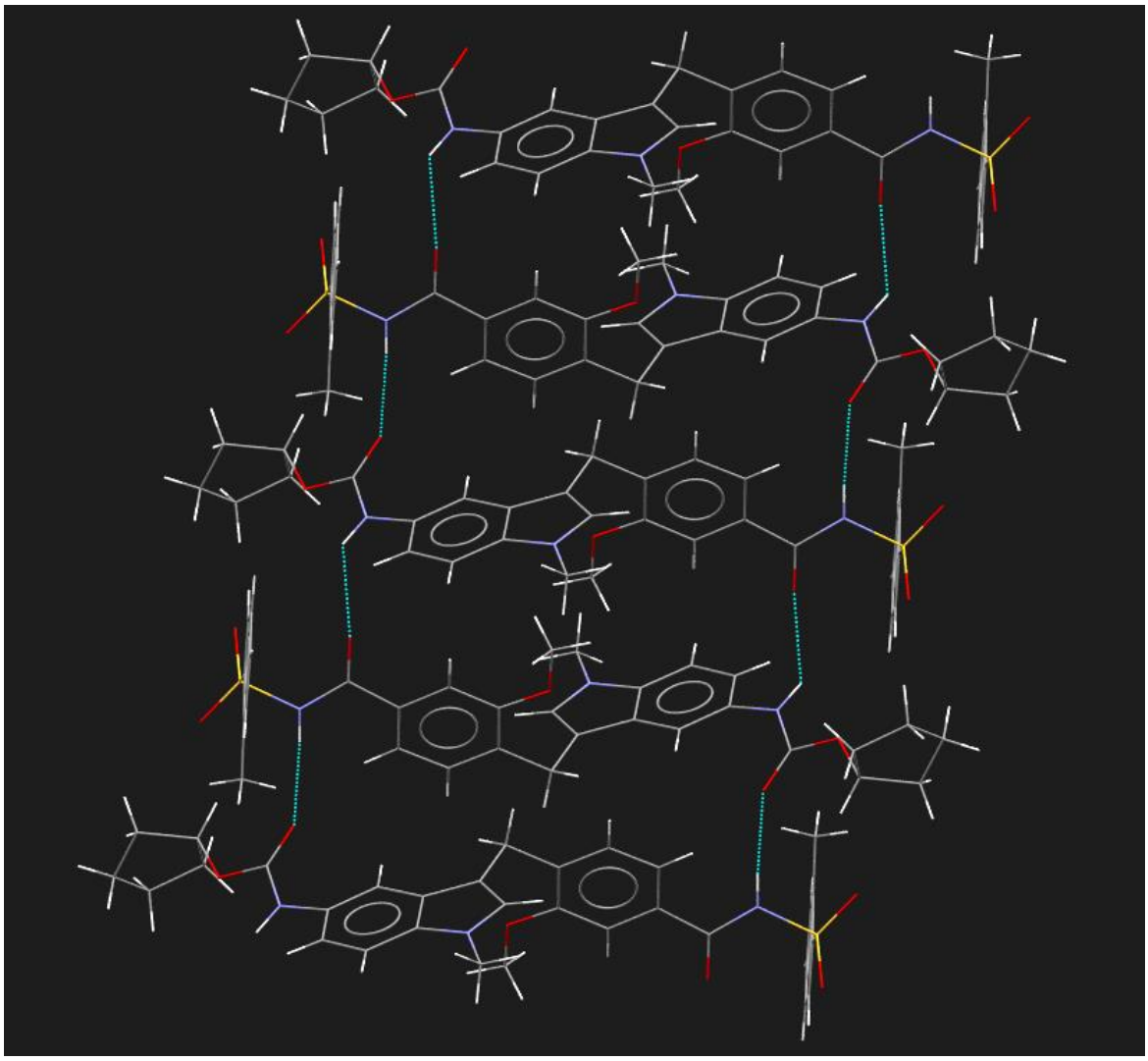

***Figure 7.12*** *Packing and hydrogen bonding within the zafirlukast crystal structure.*

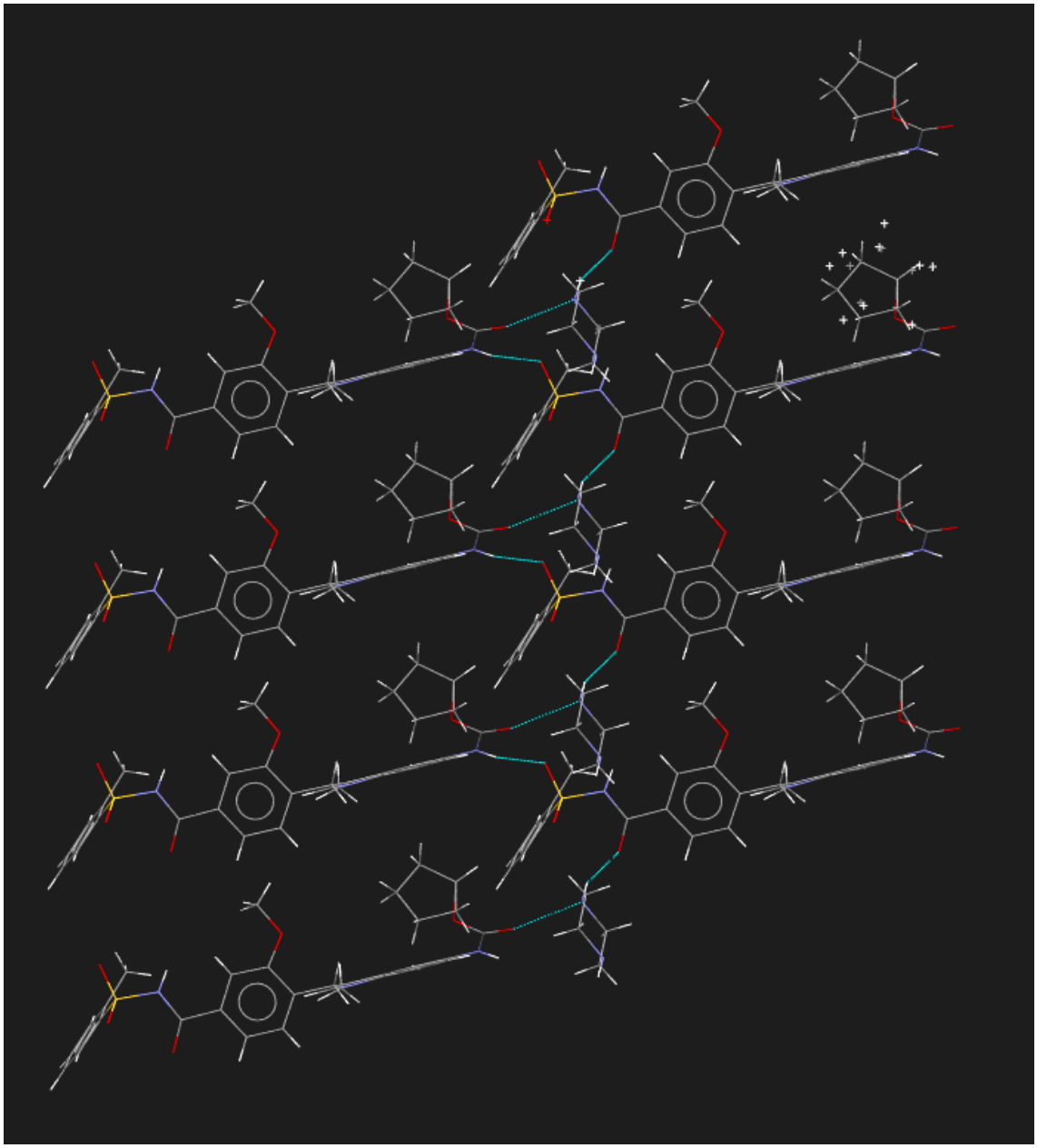

***Figure 7.13*** *Packing and hydrogen bonding within the 2:1 zafirlukast:piperazine crystal structure.*

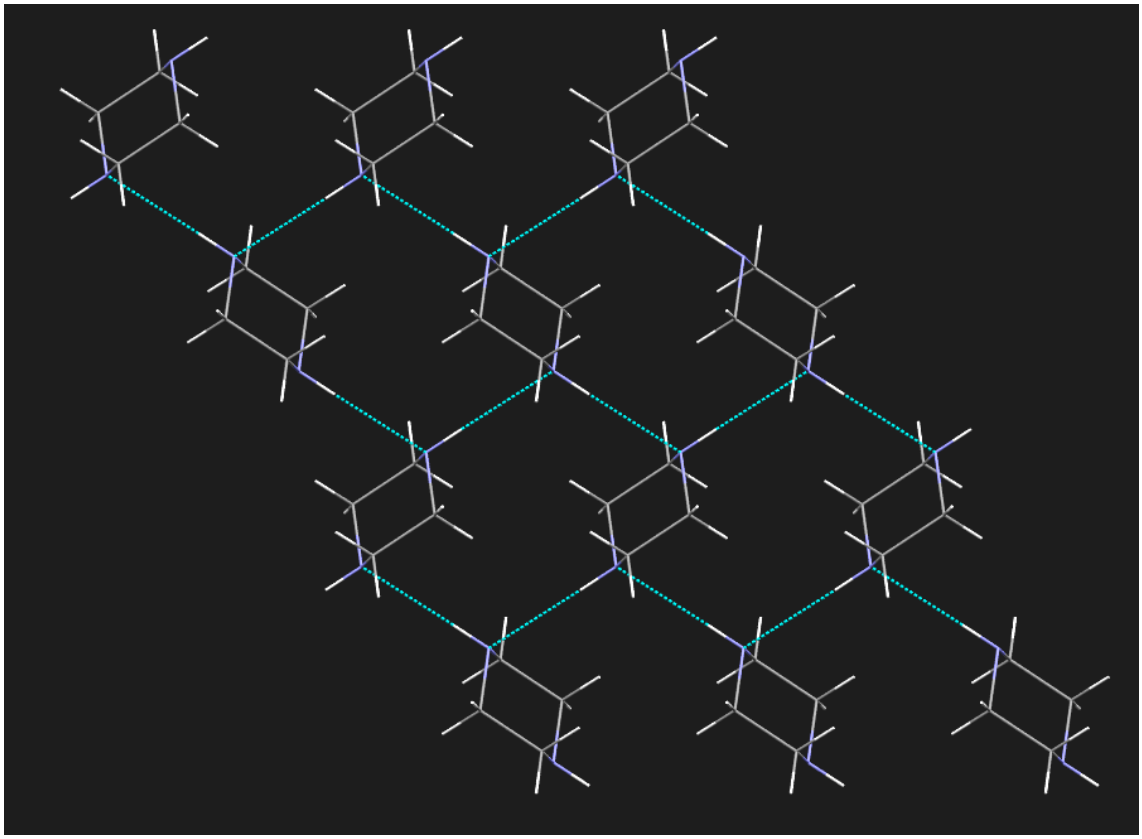

***Figure 7.14*** *Packing and hydrogen bonding within the piperazine crystal structure.*

## 7.4 Solubility and dissolution determination

### 7.4.1 Preliminary work

HPLC was chosen as the analytical technique for solubility and dissolution determination as only the concentration of zafirlukast was sought, but as the dissolution of co-crystals produces a solution containing two solutes (API and co-former) chromatography would allow the separation and measurement of the concentration of the API alone.

#### 7.4.1.1 HPLC method development

An HPLC method for the detection of zafirlukast was found to have been previously reported,[191] and after further development resulted in the following method which was used in this work.

HPLC analyses were performed using an Agilent 1260 Infinity fitted with an Agilent Eclipse Plus C18 reverse-phase column (3.5µm particle size, 4.6 x 100mm). The mobile phase used was a 30:70 ratio solution of pH 3.5 0.01M $KH_2PO_4$ buffer and acetonitrile. Injection volume was 100µl and elution of the sample constituents occurred over 6 minutes at a flow rate of 1ml/min, with column temperature set at 22-25°C. The detector used was an Agilent 1260 VWD spectrophotometer set at a wavelength of 223nm.

### 7.4.1.2 NMR investigation into potential degradation of zafirlukast

Preliminary dissolution testing had produced dissolution profiles similar to those seen in Figure 7.17 and an initial concern was that degradation of zafirlukast may be responsible for the reduction in concentration measured during the dissolution test. Given that the zafirlukast molecule contains amide functionality, and is therefore potentially liable to hydrolysis occurring, its stability in aqueous media was examined. Two samples of zafirlukast were prepared for NMR analysis one simply by dissolving in deuterated DMSO and the other by first leaving in water at 37°C for approximately 12 hours, much in excess of the timescale of the dissolution experiments, filtering and drying. The spectra obtained by NMR analysis of the two samples are shown in Figures 7.15 and 7.16 for the unprocessed zafirlukast and the zafirlukast from aqueous solution samples respectively. As can be seen, there is no observable difference between the spectra, indicating that, at least within the timescale and temperature range investigated, zafirlukast remains stable in aqueous media and that degradation was not responsible for the irregular results obtained from the dissolution testing.

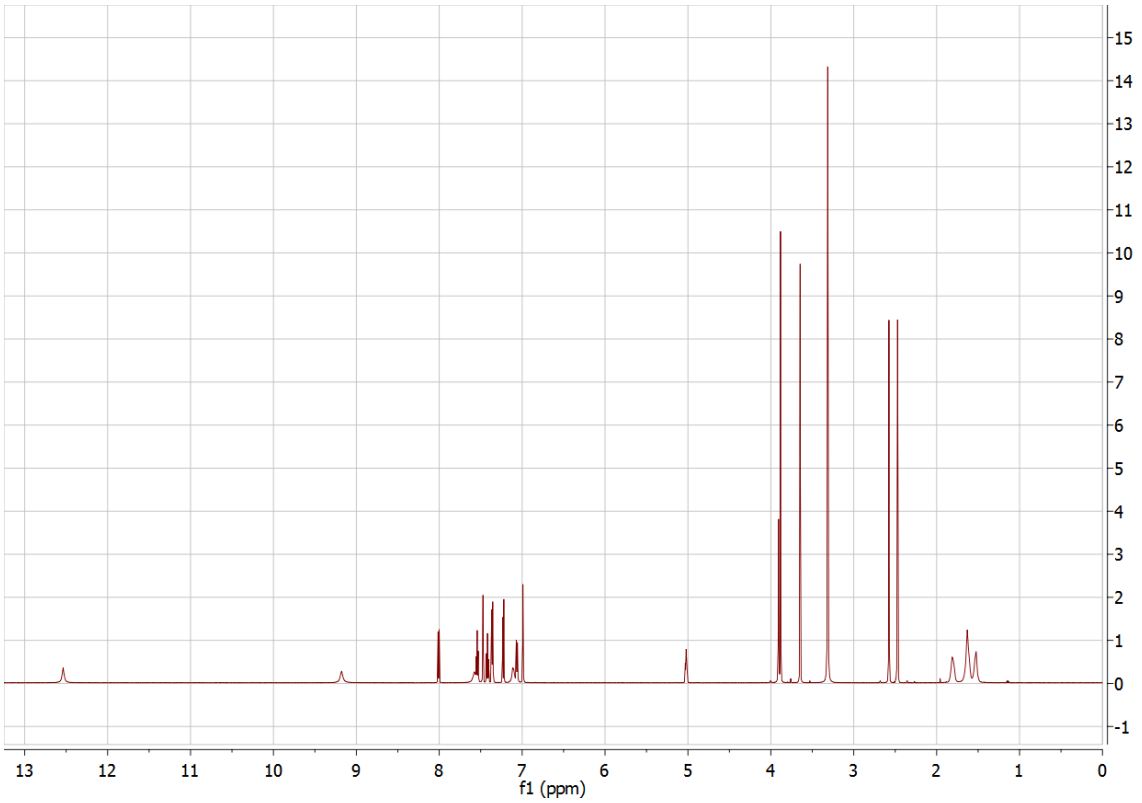


***Figure 7.15*** *$^{1}$H NMR spectrum of a sample of pure zafirlukast.*

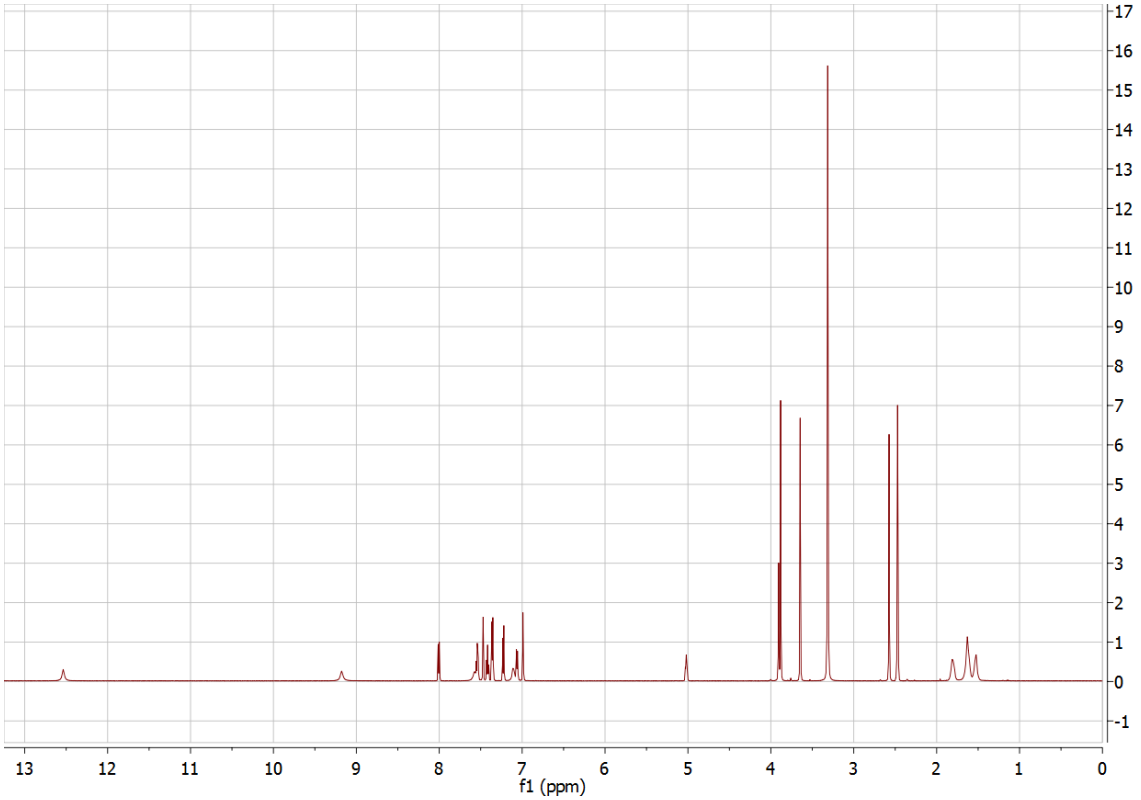


***Figure 7.16*** *$^{1}$H NMR spectrum of a sample of zafirlukast which had been stirred in water at 37°C for approximately 12 hours prior to drying and analysis. Note the near identicality to the spectrum of pure zafirlukast (Figure 7.15).*

## 7.4.2 Solubility measurement

Solubility of crystalline zafirlukast and the three co-crystals was measure in purified water at room temperature (20°C) by adding an excess amount of each material to a vial of purified water which was left stirring for approximately 24 hours. The solution was filtered, 1ml of each solution was diluted with 9ml of mobile phase and analysed by HPLC resulting in the concentrations listed in Table 7.3 below (accounting for the dilution).

***Table 7.3*** *Solubility measurements for zafirlukast and the three zafirlukast:piperazine co-crystals.*

| Material | Solubility in water at 20°C as measured by HPLC (µg/ml) |
|---|---|
| Zafirlukast | 3.018 |
| Zafirlukast:piperazine 2:1 co-crystal | 4.957 |
| Zafirlukast:piperazine 1:1 co-crystal | 42.805 |
| Zafirlukast:piperazine 1:1 co-crystal toluene solvate | 293.0568 |

## 7.4.3 Dissolution testing with developed method

### 7.4.3.1 Experimental details

Calibration standards were produced from a 1mg/ml zafirlukast in acetonitrile stock solution by diluting with mobile phase to double the concentration required. These solutions were diluted with an equal volume of SGF to produce the calibration standards used.

The mobile phase used was a 30:70 ratio solution of pH 3.5 0.01M $KH_2PO_4$ buffer and acetonitrile. Samples from dissolution testing were taken using an Agilent 850-DS auto sampler and diluted with an equal volume of mobile phase (400µl) before analysing by HPLC. The HPLC run parameters were as follows: 100µl injection volume, 6-minute run time, 1ml/min pump speed and 22°C column temperature.

The samples used for dissolution testing were four capsules per vessel, three vessels for each material. The capsules contained the lactose blends of the four APIs and contained approximately 75mg (zafirlukast), 86mg (ZP11CC), 81mg (ZP21CC) and 94mg (ZPTSCC) per capsule, equating to approximately 30mg of zafirlukast per dissolution vessel. USP2 apparatus was used, with each vessel containing 600ml SGF dissolution medium at 37°C and the paddle speed was 150rpm throughout the 120-minute run time.

### 7.4.3.2 Dissolution results

The available results from the experiment are displayed below in Figure 7.17. Results for a repeat of the experiment substituting SGF for FaSSIF are not shown as every single sample from the dissolution test failed to produce a detectable zafirlukast peak in HPLC analysis. The four plots in Figure 7.17 are of the mean percentage dissolution (n=3, error bars showing standard error) calculated based on the dose of zafirlukast, taking into account per vessel capsule content mass but not the content uniformity of the powder blend i.e. the assumed content of the API may/will be different from actuality. A calibration curve for the HPLC analysis of zafirlukast can be found in Appendix 7.3.

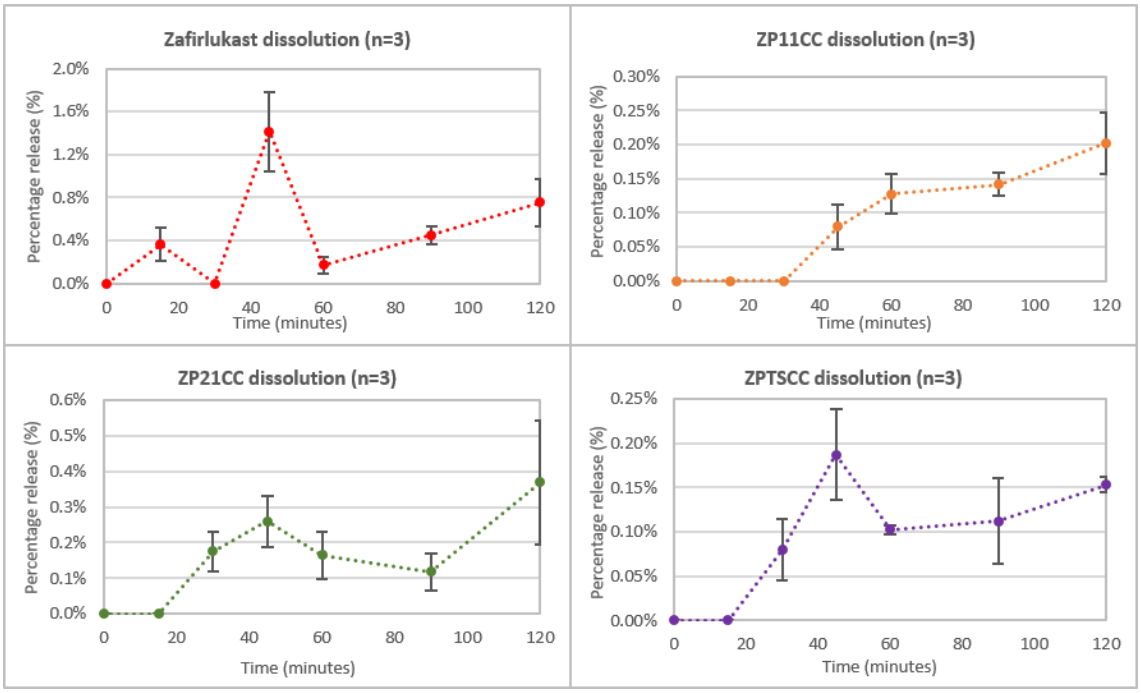


***Figure 7.17*** *Dissolution profiles for, clockwise from top left: zafirlukast (red), ZP11CC (orange), ZP21CC (green) and ZPTSCC (purple), formulated as capsules of API:lactose blends (n=3).*

A possible explanation for the reduction in zafirlukast concentration seen in the ZP21CC and ZPTSCC co-crystal results could be that the co-crystals possess higher aqueous solubility than that of zafirlukast resulting in zafirlukast crystallising from a supersaturated solution after dissociating from piperazine as the co-crystal dissolves. This reduction in concentration is not seen in the ZP11CC co-crystal but is seen in the pure zafirlukast results which casts doubt on the above explanation. The considerable variability apparent in the results, in terms of inconsistent trend and large error within most samples, suggests that the measured concentrations are not reliable. Observations from the dissolution experiments led to the conclusion that the most likely cause of the poor quality of data was the severe lack of wetting of the powder samples. Figure 7.18 shows a photograph of the content of one of the capsules taken 33 minutes after the start of the dissolution test and the mass of undispersed powder can be seen still inside the capsule sinker.

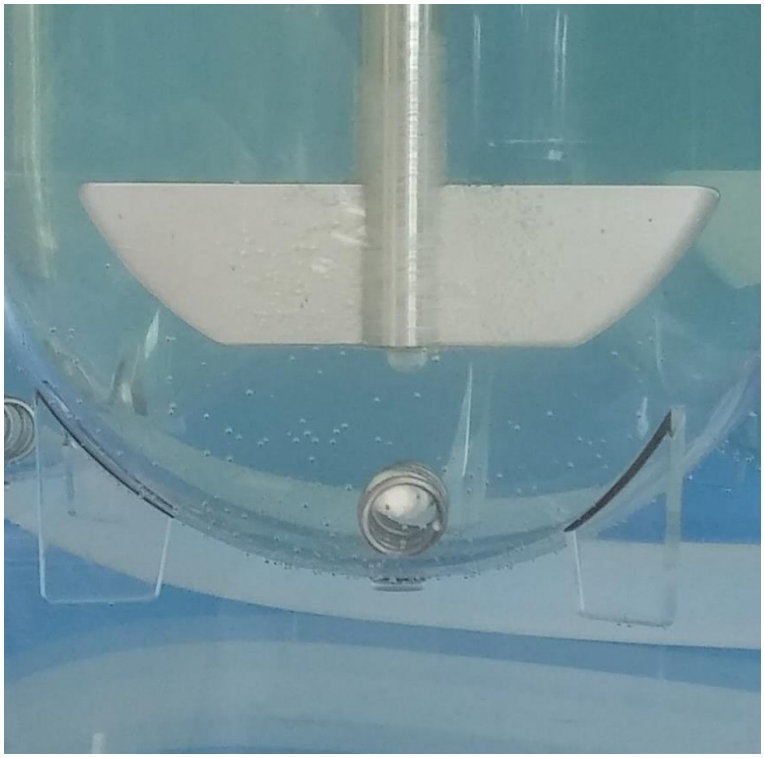

***Figure 7.18*** *Photograph of undispersed powder still inside the capsule sinker 33 minutes after the start of the experiment.*

#### 7.4.3.3 Summary

The results from the dissolution testing are clearly erroneous showing unexpected profiles and large error. These results come after much method development and indicate that the method employed is unsuitable for the materials under investigation. This is believed to be due to difficulty to achieve representative dissolution caused by a lack of wetting of the powder based formulation. For this reason, intrinsic dissolution testing was employed to measure the dissolution of these materials without need for further formulation.

### 7.4.4 Intrinsic dissolution testing

The Sirius surface dissolution imager (SDI) equipment was used to for the intrinsic dissolution testing of zafirlukast and the three zafirlukast:piperazine co-crystals. The experiment used FaSSIF-v2 as the dissolution media at 37°C throughout and UV absorbance was measured at a wavelength of 280nm. Due to the very low solubility of zafirlukast in the aqueous medium used a very low flow rate was necessary which led to the IDR being unreliably calculated by the software. A second method for measuring the solubility/dissolution rate was devised using a mode in the software whereby detection zones can be manually set. A zone at the 6mm position was set, which can be identified in Figure 7.19 as the orange rectangle, slightly to the right of the centre of each image.

The concentration within the pre-defined zone was measured throughout the experiment. This required the molar extinction coefficient of the combine component, determined by producing a calibration curve for each of the co-crystals and zafirlukast independently using the same method as described in Chapter 6 (Section 6.4.5.2). The calibration curves and determined molar extinction coefficients are presented in Appendix 7.4. The use of calibration curves of each co-crystal provided well-fitting linear trend lines appropriate for the application of the Beer-Lambert law and was deemed suitable to use for this purpose given the complication added by the negative correlation of concentration to absorbance observed in the piperazine calibration curve. Table 7.4 lists the highest peak concentration recorded within the pre-defined zone throughout the experiment for each of the materials and a visual representation of the dissolution at the midpoint of the experiment is provided by the false colour images in Figure 7.19.

***Table 7.4*** *Highest peak concentration detected for each of the three co-crystals and pure zafirlukast at different measurement points manually selected using the IDT analysis software (n=1).*

| Material | Highest peak concentration at 6mm X-axis outlet (µg/ml) |
|---|---|
| Zafirlukast | 97.6844 |
| ZP11CC | 195.507 |
| ZP21CC | 97.9169 |
| ZPTSCC | 182.993 |

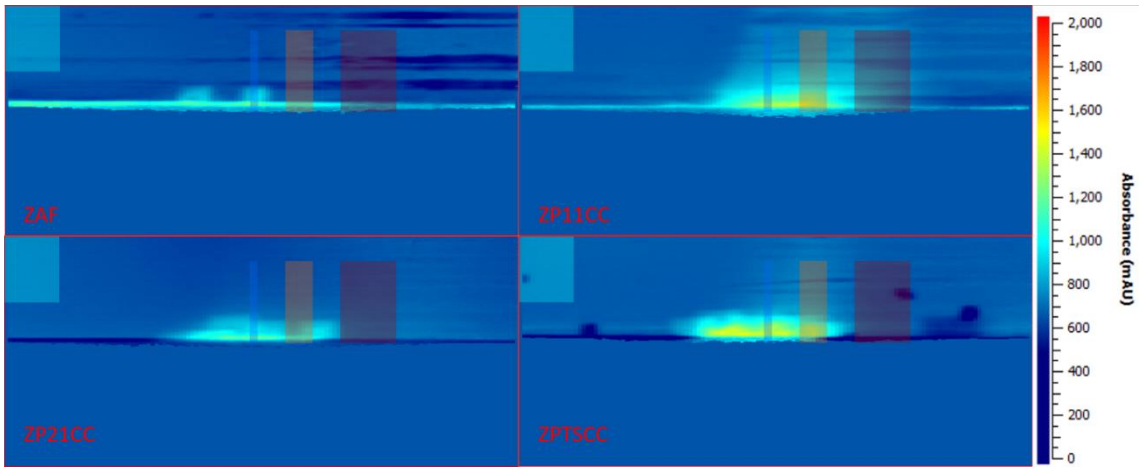


***Figure 7.19*** *False colour images from the UV detector array showing the release of the four samples at the same time point within the respective experiments. Clockwise from top left: zafirlukast, ZP11CC, ZP21CC and ZPTSCC.*

As the concentration recorded takes into account the co-former and is not purely based on the concentration of zafirlukast it is not directly comparable with the solubility measurements.

However, it is clear to see from the images in Figure 7.19 and the measured peak concentrations in Table 4 that both co-crystals provide an increase in solubility and dissolution rate compared to zafirlukast and that the improvement is far more significant in the 1:1 co-crystal.

## *7.5 In vivo* study

To accurately assess the effect of co-crystallisation on bioavailability, which is a much more important metric than simple solubility or *in vitro* dissolution profiles for determining the improvement a co-crystal product could have in the clinic, *in vivo* investigation is required. Neither the facility, nor ethical approval for this to take place on site at Durham was available, however through collaboration with AZ on this project it was possible to organise this testing to take place externally. The involvement of the author in this work was to formulate and characterise the dosage units to be used in the study.

### 7.5.1 Formulation of capsules for *in vivo* study

In order to enable a robust comparison of the co-crystals to the parent drug in the animal model study, the materials were formulated as capsules. Using a formulation common in early studies, such as a solution or suspension, is not representative of the typical use co-crystals are lauded for, which is oral solid dosage forms (due to the improvements in physical properties that can be achieved). By using a solution for example, barring any solubility enhancement in solution of the co-former and API, possible benefits of the co-crystalline form would be negated before the administration of the dose. The characterisation of the formulation in terms of content uniformity of the powder blend was necessary to ensure that the formulation is of an acceptable quality. This also serves to ensure differences seen in the results of the study are due to inherent differences between the APIs/co-crystals and not due to significant differences between the formulations.

#### 7.5.1.1 Powder blend and capsule production

Excess amounts of zafirlukast, zafirlukast:piperazine co-crystal (2:1) Form A and zafirlukast:piperazine co-crystal (1:1) Form D were sieved to obtain the particle size fraction between 38 µm and 75 µm. Zafirlukast:piperazine co-crystal (1:1) toluene solvate Form E was not suitable for sieving and instead optical microscopy was employed to determine an approximate particle size of the material. A Leica DM 2700P with attached QImaging QICAM was used to take micrographs at 500x magnification of four samples from the material and a total of 74 particles were measured manually. The mean diameter recorded was 8.5 µm with a standard

deviation of 3.39. Grades of lactose were selected with a similar particle size to the APIs, thus Zafirlukast, the 1:1 and the 2:1 co-crystals were blended in a 1:9 ratio by mass with Granulac 70 and the 1:1 co-crystal toluene solvate was blended with Sorbolac 400 at the same ratio. Mixing was by Turbula mixer (WAB, Type T2F) and for at least 30 minutes for each blend. The resultant powder was weighed out into three size 9 capsules per material and the mass recorded.

***Table 7.5*** *Details of the powder blends produced, showing for each compound: molecular weight (per molecule of zafirlukast) (MW), number of moles required (nmol), the equivalent weight in milligrams, the mass of API used in the powder blend, the calculated mass of lactose required for a 1:9 API:lactose ratio, the actual mass of lactose used, the resulting API:lactose ratio and the calculated mass of powder blend required per capsule.*

| Compound | MW | nmol | Weight (mg) | Powder blend | | | | |
|---|---|---|---|---|---|---|---|---|
| | | | | Mass used (mg) | Lactose required (mg) | Lactose used (mg) | API to lactose ratio (mg/mg) | Mass required per capsule (mg) |
| Zafirlukast | 575.68 | 2.171 | 1.250 | 10.357 | 93.215 | 93.21 | 0.10001 | 12.499 |
| ZP11CC | 661.82 | 2.171 | 1.437 | 12.560 | 113.036 | 113.06 | 0.09998 | 14.371 |
| ZP21CC | 618.75 | 2.171 | 1.343 | 13.627 | 122.641 | 122.69 | 0.09996 | 13.438 |
| ZPTSCC | 723.24 | 2.171 | 1.570 | 7.845 | 70.606 | 70.58 | 0.10003 | 15.696 |

***Table 7.6*** *Details of the capsule content.*

| API | Capsule | Mass of full capsule (mg) | Mass of empty capsule (mg) | Mass of blend used (mg) | API (mg) | % of stated dose |
|---|---|---|---|---|---|---|
| **ZAF** | 1 | 22.45 | 9.9 | 12.55 | 1.255058 | 100.405% |
| | 2 | 23.71 | 11.31 | 12.4 | 1.240057 | 99.205% |
| | 3 | 23.4 | 10.95 | 12.45 | 1.245058 | 99.605% |
| | | | | **Av (mean)** | **1.246724** | **99.738%** |
| | | | | **sd** | 0.006236 | |
| **1:1 CC** | 1 | 24.81 | 10.49 | 14.32 | 1.431721 | 99.646% |
| | 2 | 24.75 | 10.33 | 14.42 | 1.441719 | 100.342% |
| | 3 | 24.5 | 10.12 | 14.38 | 1.437720 | 100.064% |
| | | | | **Av (mean)** | **1.437053** | **100.018%** |
| | | | | **sd** | 0.004109 | |
| **2:1 CC** | 1 | 24.28 | 10.94 | 13.34 | 1.333522 | 99.272% |
| | 2 | 23.84 | 10.26 | 13.58 | 1.357514 | 101.058% |
| | 3 | 24.02 | 10.41 | 13.61 | 1.360513 | 101.281% |
| | | | | **Av (mean)** | **1.350516** | **100.537%** |
| | | | | **sd** | 0.012079 | |
| **Tol. Sol.** | 1 | 26.24 | 10.35 | 15.89 | 1.589525 | 101.237% |
| | 2 | 26.21 | 10.62 | 15.59 | 1.559515 | 99.326% |
| | 3 | 26.19 | 10.32 | 15.87 | 1.587524 | 101.110% |
| | | | | **Av (mean)** | **1.578855** | **100.558%** |
| | | | | **sd** | 0.013700 | |

### 7.5.1.2 Uniformity of content determination

For each of the four powder blends produced, three samples were taken for analysis. This was accomplished by first pouring the powder out of its container into a line on a sheet of clean paper. The three samples were taken approximately equidistantly along the line. The samples which were approximately 5-40 mg were weighed and the accurate mass recorded. To this 1.5 ml of solvent was added and sonication used to aid dissolution. A 1 in 100 dilution was performed and the resultant solution analysed by HPLC. The concentration of Zafirlukast of each sample solution was determined and compared to the calculated expected mass for each material taking into account the differences in stoichiometry.

***Table 7.7*** *Results of the uniformity of content determination.*

| Sample | Mass of Zafirlukast as analysed by HPLC (mg) | Calculated mass of zafirlukast (mg) | Zafirlukast content (as % of calculated) | Mean | Standard deviation |
|---|---|---|---|---|---|
| ZAF 1 | 0.7106 | 0.8815 | 80.60% | | |
| ZAF 2 | 0.7783 | 0.9575 | 81.28% | **ZAF** | |
| ZAF 3 | 0.3915 | 0.4500 | 87.01% | **82.96%** | 3.52% |
| ZP11CC 1 | 0.6163 | 0.6427 | 95.90% | | |
| ZP11CC 2 | 0.6581 | 0.7758 | 84.84% | **ZP11CC** | |
| ZP11CC 3 | 1.0299 | 1.1119 | 92.63% | **91.12%** | 5.68% |
| ZP21CC 1 | 0.7916 | 0.9435 | 83.89% | | |
| ZP21CC 2 | 0.7435 | 0.8808 | 84.42% | **ZP21CC** | |
| ZP21CC 3 | 0.7403 | 0.7919 | 93.48% | **87.27%** | 5.39% |
| ZPTSCC 1 | 0.2600 | 0.3269 | 79.54% | | |
| ZPTSCC 2 | 0.4940 | 0.4682 | 105.51% | **ZPTSCC** | |
| ZPTSCC 3 | 0.2614 | 0.2843 | 91.95% | **92.33%** | 12.98% |

## 7.5.2 Pharmacokinetic study

### 7.5.2.1 Details

The capsules were sent to Pharmaron (China) for dosing to male Wistar Han rats. The *in vivo* study was performed with the specifications listed in Table 7.8 and full details of the method are given in Appendix 7.5. A limited number of rats were available for this study and as such it is likely not statistically significant. Ideally a larger number of rats would have been used, sufficient to meet that determined by a power analysis but not in excess, to prevent unnecessary and unethical waste of animals. This study therefore should be thought of as a pilot and the results potentially indicative of the modification of properties between the solid forms but with the caveat of variability between the rats and doses with such a small sample size introducing unavoidable limitations to the study as performed.

***Table 7.8*** *Tabulated in vivo study details.*

| Material (API/CC) | Route | Dose | Number of rats | Time points (hours) |
|---|---|---|---|---|
| Zafirlukast | IV | 1 mg/kg | 2 | 0, 0.033, 0.083, 0.167, 0.5, 1, 2, 4, 8, 24 |
| Zafirlukast | PO | 5 mg/kg | 2 | 0, 0.25, 0.5, 1, 1.5, 2, 3, 4, 8, 24 |
| Zaf:pip (1:1) | PO | 5 mg/kg | 2 | 0, 0.25, 0.5, 1, 1.5, 2, 3, 4, 8, 24 |
| Zaf:pip (2:1) | PO | 5 mg/kg | 2 | 0, 0.25, 0.5, 1, 1.5, 2, 3, 4, 8, 24 |
| Zaf:pip:tol (3:3:2) | PO | 5 mg/kg | 2 | 0, 0.25, 0.5, 1, 1.5, 2, 3, 4, 8, 24 |

### 7.5.2.2 Results

Figure 7.20 shows the plasma concentration over time for the three co-crystals and pure zafirlukast, plots showing individual profiles versus the IV dose can be found in Appendix 7.6. Table 7.9 contains a summary of the results from the *in vivo* study and Table 7.10 details the measured pharmacokinetic parameters.

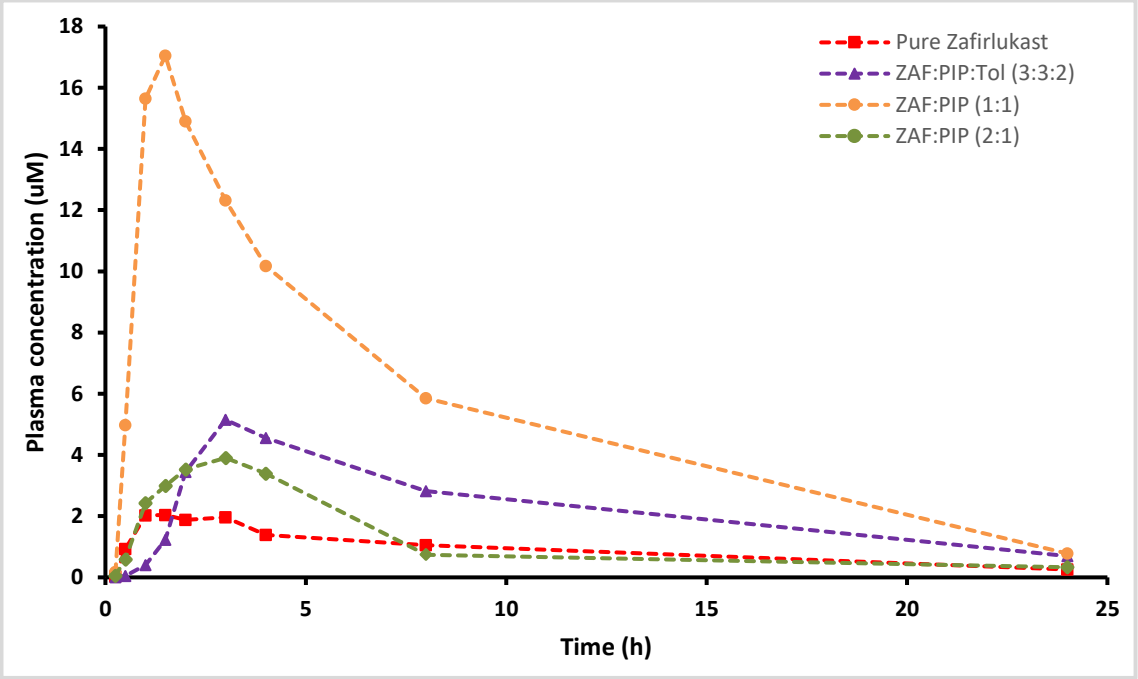


***Figure 7.20*** *Plasma concentration of zafirlukast vs time profile for pure zafirlukast and the three zafirlukast:piperazine co-crystals (n=2).*

***Table 7.9*** *Summary of results of the in vivo study showing for each compound: the stated weight of API per capsule, dose in mg/kg, route of administration – either intravenous (IV) or oral (PO), area under the curve for the duration of the experiment measured for zafirlukast, and for piperazine and the calculated percentage oral bioavailability of zafirlukast (F% zafirlukast).*

| Compound | Weight of API contained within capsule (mg) | Dose (mg/Kg) | Route | $AUC_{0\text{-}t}$ zafirlukast (h*µmol/L) | $AUC_{0\text{-}t}$ piperazine (h*µmol/L) | *F* (%) Zafirlukast |
|---|---|---|---|---|---|---|
| Zafirlukast | - | 1 | IV | 39.4 | NA | NA |
| | 1.250 | 5 | PO | 21.8 | NA | 11.1 |
| ZP11CC | 1.437 | 5 | PO | 132 | 2.4 | 67.0 |
| ZP21CC | 1.343 | 5 | PO | 28.1 | 1.12 | 14.3 |
| ZPTSCC | 1.570 | 5 | PO | 53.8 | 2.1 | 27.3 |

***Table 7.10*** *Measured pharmacokinetic parameters of zafirlukast and the zafirlukast:piperazine co-crystals.*

| **Pharmacokinetic Parameter** | **IV (mean, n=2)** | **PO (mean, n=2)** | | | |
|---|---|---|---|---|---|
| | **Zafirlukast** | **Zafirlukast** | **ZP11CC** | **ZP21CC** | **ZPTSCC** |
| CL (mL/min/Kg) | 0.69 ± 0.19 | - | - | - | - |
| $V_{ss}$ (L/Kg) | 0.35 ± 0.08 | - | - | - | - |
| $V_z$ (L/Kg) | 0.50 ± 0.11 | - | - | - | - |
| $T_{1/2}$ (h) | 8.55 ± 0.44 | 8.2 ± 0.8 | 5.4 ± 0.5 | 7.1 ± 0.7 | 7 ± 2 |
| F (%) | - | 11.3 ± 0.3 | 63 ± 8 | 14± 3 | 28 ± 6 |
| $C_{max}$ (µM) | 35 ± 4 | 2.3 ± 0.0 | 19 ± 4 | 3.9 ± 0.9 | 5 ± 2 |
| $T_{max}$ (h) | 0.0333 ± 0.00 | 1.5 ± 0.7 | 1.2 ± 0.3 | 3.0 ± 0.0 | 3.5 ± 0.7 |
| AUC (µM*h) | 44 ± 12 | 24.9 ± 0.8 | 138 ± 17 | 32 ± 7 | 62 ± 13 |
| $AUC_{0\text{-}24}$ (µM*h) | 39 ± 10 | 21.8 ± 0.2 | 132 ± 15 | 28 ± 6 | 54 ± 7 |

A significant improvement in absorption compared to zafirlukast was seen with all three co-crystals. The 1:1 co-crystal showed the largest improvement of 5.6 times the bioavailability of the free drug, broadly comparable to that seen in the commercial amorphous form,[185] with the 2:1 co-crystal attaining a 1.2 times increase. This matches the *in vitro* solubility and dissolution measurements almost exactly and is an indicator of the potential ability to rank the *in vivo* performance of different stoichiometries of co-crystal based on their *in vitro* measurements. The co-crystal toluene solvate also shows an improvement in bioavailability compared to zafirlukast but not to the same extent as the improvement seen in the *in vitro* measurements. The presence of a third component as well as a slightly lower particle size range in the formulation are potential factors for causing variability of the toluene solvate performance compared to the other materials.

## 7.6 Conclusions

In this work, the formulation and characterisation of a poorly soluble drug and its co-crystal derivatives have allowed robust *in vitro* and *in vivo* performance comparisons of these materials to be undertaken. The significant characterisation of the formulation was necessary to achieve the robust comparison of the co-crystal performance to that of the API and characterisation to a similar extent is seen in few comparable studies.[21,192] The improvements seen between the 1:1 and 2:1 co-crystals and zafirlukast *in vitro* have been found to be mimicked *in vivo* which suggests that future prediction of the performance of multiply stoichiometric co-crystals may be possible. Should this be achievable, a reduction in the amount of animal studies required would be possible by utilising *in vitro* observations as a predictive means to enable form selection.

# Chapter 8 – Conclusions and future work

## 8.1 Introduction

This chapter is split into sections which draw conclusions from, and propose potential future work relating to, each of the aims set out in Chapter 1. The sections are further apportioned by some of the objectives devised to address the aims.

## 8.2 Production of co-crystals

### 8.2.1 Optimisation of co-crystal screening

The computational pre-screening element of the screening process was shown to be of value by, where interactions between API and co-former occurred, consistently having ranked these compounds highly, i.e. leading to hit detection. It was noted though, that exact values calculated for excess enthalpy differences are not enough by themselves for prediction of co-formers that will form co-crystals with any API. This is seen in the outcomes of the ROY and ornidazole co-crystal screen where significant differences in excess enthalpy calculations did not match the experimental outcomes in terms of co-crystalline material forming. The excess enthalpy calculated for a number of co-formers which were hits from the ornidazole screen would have ranked very highly for the ROY screen, yet no hits were detected in the initial ROY screen.

The optimisation presented in Chapter 3 resulted in a process and set of parameters which have been shown to successfully perform co-crystal screening as indicated by the outcome of the ornidazole co-crystal screen. Further optimisation is likely unnecessary for the current process, however inclusion of additional steps within the process may be warranted under certain circumstances. An example would be where potential co-amorphous material is produced from the screen, as was the case for many of the ornidazole:co-former pairs, but crystalline material is required. A potential solution to this could be to add a crystallisation inducement step at the end of the current process, for example by cycling humidity of the plate before analysis with PXRD. If any extra stages to the screening procedure were to be added, then optimisation before their implementation would be worthy of consideration.

### 8.2.2 Implementation of co-crystal screen

Two co-crystal screens were undertaken within this work, that of ROY presented in Chapter 4 and that of ornidazole, Chapter 6. The screen applied to ROY did not find any co-crystals which does not reflect poorly on the screening method as not every compound will necessarily form

co-crystals, or at least not using a reasonable amount of resources to probe for co-crystal formation. Further screening of the top 10 predicted co-formers was nonetheless undertaken to ensure the robustness of the screen and this led to the discovery of the co-amorphous form of ROY and pyrogallol. The ornidazole co-crystal screen proved more successful in the traditional sense for a co-crystal screen, detecting 23 hits, including the two co-formers included as positive controls.

Further co-crystal screening would be required in future work in order to efficiently discover a larger number of co-crystals for analysis and ultimate structure-property determination. Use of a robotics platform for which the screening method is optimised for would be necessary to achieve the required efficiency.

### 8.2.3 Analysis of co-crystal screen products

The initial analysis of the products of a co-crystal screen is purely to detect form change in the sample, i.e. a hit. In the co-crystal screens undertaken in this work both FTIR and PXRD analysis have been employed. Although FTIR analysis is less time consuming, PXRD analysis is preferred due to the more definitive conclusions as to form change which can be determined. Automated (96-well plate reader) Raman spectrometers are more readily available than the equivalent powder diffractometers and as such future work would be to compare the quality of hit detection between these platforms to see if the screening method could be further automated and available to a wider audience.

## 8.3 Characterisation of co-crystals

Identification of the product of a co-crystal screen hit follows from the initial analysis of the screen products for form change and was demonstrated in this thesis in Chapters 4 and 6. The thermal methods employed allowed the determination of the ROY:pyrogallol co-amorphous material and the shortlisting of the screen products most likely to be co-crystals from the 23 hits of the ornidazole screen. One of these products, ornidazole:5-nitroisophthalic acid, was further characterised using single crystal X-ray diffraction and confirmed to be a 1:1 co-crystal of these components. Other than the two positive controls and one further co-former (4-hydroxybenzoic acid) for which a co-crystal with ornidazole has previously been reported,[168] that leaves 19 hits from the screen which are potential ornidazole co-crystals which could be further investigated in future work.

## 8.4 Measurement of co-crystal properties

### 8.4.1 Properties closely related to bioavailability

In Chapter 6 the intrinsic dissolution rates of ornidazole, 5-nitroisophthalic acid and the co-crystal of these two components were measured, allowing a comparison between the co-crystal and the pure API. Both the solubility and intrinsic dissolution were investigated for zafirlukast and its three co-crystals with piperazine, again allowing comparison of property improvement in the co-crystalline forms compared to the drug alone. The absorption, and oral bioavailability compared to an IV dose of zafirlukast, were also measured for zafirlukast and the co-crystals in an *in vivo* study.

### 8.4.2 Properties related to processing

Compression and hardness testing was conducted on samples of ornidazole co-crystal and parent components and of the zafirlukast co-crystals and parent components in Chapters 6 and 7 respectively. In both cases variation in the hardness measured for the compressed tablets of each material was observed. The presence of certain features in the crystal structures of some but not all of the materials are thought to contribute to the differences in compressibility and the measured hardness. These findings highlighted the potential for a co-crystal to enable improved formulation by more efficient tabletting. It was noted during the ornidazole co-crystal screen that some of the products, including the 5-nitroisophthalic acid co-crystal, crystallise more readily than pure ornidazole. In some cases, this improvement in processing ability may outweigh potential reductions in other properties, such as solubility, as long as they are not severe enough to reduce the utility of the product.

The measurement of properties both relating to bioavailability and processing, of further co-crystals and parent components, are of continued importance to build a large enough dataset to be able to determine robust relationships between parent and co-crystal properties. Future work would include collecting data on many more co-crystal systems to move towards this goal.

## 8.5 Predictability of property modification

In Chapter 4 it was shown that although no co-crystals of ROY were found, the computational pre-screen had ranked pyrogallol at a high position, indicating a likelihood for molecules of ROY and pyrogallol to display intermolecular interaction, based on calculation of interaction in the gas phase. The hit rate of 21 out of 46 (discounting the positive controls) seen in the ornidazole co-crystal screen presented in Chapter 6 also agrees with reports in the literature[103] that support the use of computational pre-screening for shortlisting potential co-formers. From the work in

Chapter 7, a correlation between the *in vitro* and *in vivo* performance between the 1:1 and 2:1 co-crystals and the pure API was apparent. This is promising for the future predictability of not only of improved properties compared to the parent drug but also of the effect of differing stoichiometry of the co-crystal forms.

The idea of being able to accurately predict the physical properties and *in vivo* performance of a co-crystal simply by knowing the structure of the parent components and having measured some of their properties is still currently unattainable. It is hoped that this work has demonstrated that current research is progressing towards that goal and that such prediction, restricted to a specific co-crystal system, is certainly a possibility. Future work to achieve this goal would require the study of many more co-crystal systems, using the methods employed and developed within this work, to build a large dataset and, in combination with further data in the literature allow the construction of widely applicable structure-property relationships for future co-crystal systems.

## 8.6 Summary

Although the work presented in this thesis has used multiple model compounds between chapters, most of the steps for taking an API, with identified potentially unsatisfactory properties, through the drug development process, are covered. Chapters 3, 4 and 6 deal with screening for a co-crystalline form of the API with potentially improved properties; Chapter 5 looks at how substitution with a similar co-former may be able to further modify properties of interest in binary materials, in this case co-amorphous rather than co-crystalline. Improvements in physical properties of the co-crystal compared to the pure API are investigated in Chapter 6 and 7, and the formulation and *in vivo* testing of a potential co-crystalline product are explored in Chapter 7. The utility of co-crystals, or co-amorphous material, has been highlighted at each stage of drug development covered in this work and the need for further research to be able to predict the properties of co-crystals based on those of their parent components realised.

In summary, a robust multi-step co-crystal screening method has been optimised which demonstrates utility to efficiently identify co-crystals and co-amorphous materials. The feasibility to predict those co-formers likely to form binary compounds with an API and the potential to use *in vitro* results to inform expected *in vivo* improvements in the systems studied have also been demonstrated.

# References


(1) Mullin, J. W. *Crystallization*, Third.; Butterworth Heinemann: Oxford, 2000.

(2) Aitipamula, S.; Banerjee, R.; Bansal, A. K.; Biradha, K.; Cheney, M. L.; Choudhury, A. R.; Desiraju, G. R.; Dikundwar, A. G.; Dubey, R.; Duggirala, N.; et al. Polymorphs, Salts, and Cocrystals: What's in a Name? *Cryst. Growth Des.* **2012**, *12* (5), 2147–2152.

(3) Zaworotko, M. J. Molecules to Crystals, Crystals to Molecules ... and Back Again? *Cryst. Growth Des.* **2007**, *7* (1), 4–9.

(4) Vishweshwar, P.; Mcmahon, J. Pharmaceutical Co-Crystals. *J. Pharm. Sci.* **2006**, *95* (3), 499–516.

(5) Bond, A. D. What Is a Co-Crystal? *CrystEngComm* **2007**, *9* (9), 833.

(6) U.S. Department of Health and Human Services: Food and Drug Administration: Centre for Drug Evaluation and Research. *Guidance for Industry: Regulatory Classification of Pharmaceutical Co-Crystals*; 2013.

(7) Steed, J. W. The Role of Co-Crystals in Pharmaceutical Design. *Trends Pharmacol. Sci.* **2013**, *34* (3), 185–193.

(8) Cheney, M. L.; McManus, G. J.; Perman, J. A.; Wang, Z.; Zaworotko, M. J. The Role of Cocrystals in Solid-State Synthesis: Cocrystal-Controlled Solid-State Synthesis of Imides. *Cryst. Growth Des.* **2007**, *7* (4), 616–617.

(9) Sokolov, A. N.; Friscić, T.; MacGillivray, L. R. Enforced Face-to-Face Stacking of Organic Semiconductor Building Blocks within Hydrogen-Bonded Molecular Cocrystals. *J. Am. Chem. Soc.* **2006**, *128* (9), 2806–2807.

(10) Yan, D.; Delori, A.; Lloyd, G. O.; Friščić, T.; Day, G. M.; Jones, W.; Lu, J.; Wei, M.; Evans, D. G.; Duan, X. A Cocrystal Strategy to Tune the Luminescent Properties of Stilbene-Type Organic Solid-State Materials. *Angew. Chem. Int. Ed. Engl.* **2011**, *50* (52), 12483–12486.

(11) Landenberger, K. B.; Matzger, A. J. Cocrystal Engineering of a Prototype Energetic Material: Supramolecular Chemistry of 2,4,6-Trinitrotoluene. *Cryst. Growth Des.* **2010**, *10* (12), 5341–5347.

(12) Bolton, O.; Simke, L. R.; Pagoria, P. F.; Matzger, A. J. High Power Explosive with Good Sensitivity: A 2:1 Cocrystal of CL-20:HMX. *Cryst. Growth Des.* **2012**, *12* (9), 4311–4314.

(13) Shen, J. P.; Duan, X. H.; Luo, Q. P.; Zhou, Y.; Bao, Q.; Ma, Y. J.; Pei, C. H. Preparation and Characterization of a Novel Cocrystal Explosive. *Cryst. Growth Des.* **2011**, *11* (5), 1759–1765.

(14) Berry, D. J. Pharmaceutical Co-Crystals; Design, Discovery and Behaviour, University of Bradford, 2009.

(15) Greet, R. J.; Turnbull, D. Glass Transition in O-Terphenyl. *J. Chem. Phys.* **1967**, *46* (4), 1243–1251.

(16) Hatase, M.; Hanaya, M.; Oguni, M. Studies of Homogeneous-Nucleation-Based Crystal Growth: Significant Role of Phenyl Ring in the Structure Formation. *J. Non. Cryst. Solids* **2004**, *333* (2), 129–136.

(17) Musumeci, D.; Powell, C. T.; Ediger, M. D.; Yu, L. Termination of Solid-State Crystal Growth in Molecular Glasses by Fluidity. *J. Phys. Chem. Lett.* **2014**, *5* (10), 1705–1710.

(18) Sun, Y.; Xi, H.; Chen, S.; Ediger, M. D.; Yu, L. Crystallization near Glass Transition: Transition from Diffusion-Controlled to Diffusionless Crystal Growth Studied with Seven Polymorphs. *J. Phys. Chem. B* **2008**, *112* (18), 5594–5601.

(19) Sun, Y.; Xi, H.; Ediger, M. D.; Richert, R.; Yu, L. Diffusion-Controlled And "diffusionless" crystal Growth near the Glass Transition Temperature: Relation between Liquid Dynamics and Growth

Kinetics of Seven ROY Polymorphs. *J. Chem. Phys.* **2009**, *131* (7).

(20) Sun, Y.; Xi, H.; Ediger, M. D.; Yu, L. Diffusionless Crystal Growth from Glass Has Precursor in Equilibrium Liquid. *J. Phys. Chem. B* **2008**, *112* (3), 661–664.

(21) Berry, D. J.; Steed, J. W. Pharmaceutical Cocrystals, Salts and Multicomponent Systems; Intermolecular Interactions and Property Based Design. *Adv. Drug Deliv. Rev.* **2017**.

(22) Chiarella, R.; Davey, R.; Peterson, M. Making Co-Crystals the Utility of Ternary Phase Diagrams. *Cryst. Growth Des.* **2007**, *7* (7), 1223–1226.

(23) Desiraju, G. R.; Vittal, J. J.; Ramanan, A. *Crystal Engineering: A Textbook*; 2011.

(24) Rodríguez-Hornedo, N. Cocrystals: Molecular Design of Pharmaceutical Materials. *Mol. Pharm.* **2007**, *4* (3), 299–300.

(25) Steed, J. W.; Atwood, J. L. *Supramolecular Chemistry*; 2009.

(26) Desiraju, G. Supramolecular Synthons in Crystal Engineering—a New Organic Synthesis. *Angew. Chemie Int. Ed. …* **1995**, *34*, 2311–2327.

(27) Thakuria, R.; Delori, A.; Jones, W.; Lipert, M. P.; Roy, L.; Rodríguez-Hornedo, N. Pharmaceutical Cocrystals and Poorly Soluble Drugs. *Int. J. Pharm.* **2013**, *453* (1), 101–125.

(28) Fábián, L. Cambridge Structural Database Analysis of Molecular Complementarity in Cocrystals. *Cryst. Growth Des.* **2009**, *9* (3), 1436–1443.

(29) Morissette, S. L.; Almarsson, O.; Peterson, M. L.; Remenar, J. F.; Read, M. J.; Lemmo, A. V; Ellis, S.; Cima, M. J.; Gardner, C. R. High-Throughput Crystallization: Polymorphs, Salts, Co-Crystals and Solvates of Pharmaceutical Solids. *Adv. Drug Deliv. Rev.* **2004**, *56* (3), 275–300.

(30) Luu, V.; Jona, J.; Stanton, M. K.; Peterson, M. L.; Morrison, H. G.; Nagapudi, K.; Tan, H. High-Throughput 96-Well Solvent Mediated Sonic Blending Synthesis and on-Plate Solid/solution Stability Characterization of Pharmaceutical Cocrystals. *Int. J. Pharm.* **2013**, *441* (1–2), 356–364.

(31) Nehm, S. J.; Rodriguez-Spong, B.; Rodriguez-Hornedo, N. Phase Solubility Diagrams of Cocrystals Are Explained by Solubility Product and Solution Complexation. *Cryst. Growth Des.* **2006**, *6* (2), 592–600.

(32) Rodríguez-Hornedo, N.; Nehm, S. J.; Seefeldt, K. F.; Pagan-Torres, Y.; Falkiewicz, C. J. Reaction Crystallization of Pharmaceutical Molecular Complexes. *Mol. Pharm.* **2006**, *3* (3), 362–367.

(33) Jayasankar, A.; Good, D. J.; Rodríguez-Hornedo, N. Mechanisms by Which Moisture Generates Cocrystals. *Mol. Pharm.* **2007**, *4* (3), 360–372.

(34) Friščić, T.; Childs, S.; Rizvi, S.; Jones, W. The Role of Solvent in Mechanochemical and Sonochemical Cocrystal Formation: A Solubility-Based Approach for Predicting Cocrystallisation Outcome. *CrystEngComm* **2009**, *11* (3), 418–426.

(35) Friscic, T.; Jones, W. Recent Advances in Understanding the Mechanism of Cocrystal Formation via Grinding. *Cryst. Growth Des.* **2009**, *9* (3), 1621–1637.

(36) Trask, A. V; Jones, W. Crystal Engineering of Organic Cocrystals by the Solid-State Grinding Approach. *Top. Curr. Chem.* **2005**, *254*, 41–70.

(37) Jones, W.; Motherwell, W. D. S.; Trask, A. V. Pharmaceutical Cocrystals : An Emerging Approach to Physical Property Enhancement. *MRS Bull.* **2006**, *31* (November), 875–879.

(38) Berry, D.; Seaton, C. Applying Hot-Stage Microscopy to Co-Crystal Screening: A Study of Nicotinamide with Seven Active Pharmaceutical Ingredients. *Cryst. Growth Des.* **2008**, *8* (5), 1697–1712.

(39) Eddleston, M. D.; Patel, B.; Day, G. M.; Jones, W. Cocrystallization by Freeze-Drying: Preparation of Novel Multicomponent Crystal Forms. *Cryst. Growth Des.* **2013**, *13* (10), 4599–4606.

(40) Alhalaweh, A.; Velaga, S. P. Formation of Cocrystals from Stoichiometric Solutions of Incongruently Saturating Systems by Spray Drying. *Cryst. Growth Des.* **2010**, *10* (8), 3302–3305.

(41) Padrela, L.; Rodrigues, M. a; Velaga, S. P.; Matos, H. a; de Azevedo, E. G. Formation of Indomethacin-Saccharin Cocrystals Using Supercritical Fluid Technology. *Eur. J. Pharm. Sci.* **2009**, *38* (1), 9–17.

(42) Kelly, A. L.; Gough, T.; Dhumal, R. S.; Halsey, S. A.; Paradkar, A. Monitoring Ibuprofen-Nicotinamide Cocrystal Formation during Solvent Free Continuous Cocrystallization (SFCC) Using near Infrared Spectroscopy as a PAT Tool. *Int. J. Pharm.* **2012**, *426* (1–2), 15–20.

(43) Pagire, S.; Korde, S.; Ambardekar, R.; Deshmukh, S.; Dash, R. C.; Dhumal, R.; Paradkar, A. Microwave Assisted Synthesis of Caffeine/maleic Acid Co-Crystals: The Role of the Dielectric and Physicochemical Properties of the Solvent. *CrystEngComm* **2013**, *15* (18), 3705.

(44) Bernstein, J. *Polymorphism in Molecular Crystals*; Oxford University Press: New York, 2002.

(45) Eddleston, M. D.; Sivachelvam, S.; Jones, W. Screening for Polymorphs of Cocrystals: A Case Study. *CrystEngComm* **2013**, *15* (1), 175.

(46) Lemmerer, A.; Adsmond, D. a.; Esterhuysen, C.; Bernstein, J. Polymorphic Co-Crystals from Polymorphic Co-Crystal Formers: Competition between Carboxylic Acid···Pyridine and Phenol···Pyridine Hydrogen Bonds. *Cryst. Growth Des.* **2013**, *13* (9), 3935–3952.

(47) Schultheiss, N.; Newman, A. Pharmaceutical Cocrystals and Their Physicochemical Properties. *Cryst. Growth Des.* **2009**, *9* (6), 2950–2967.

(48) Babu, N. J.; Nangia, A. Solubility Advantage of Amorphous Drugs and Pharmaceutical Cocrystals. *Cryst. Growth Des.* **2011**, *11*, 2662–2679.

(49) Good, D. J.; Rodríguez-Hornedo, N. Solubility Advantage of Pharmaceutical Cocrystals. *Cryst. Growth Des.* **2009**, *9* (5), 2252–2264.

(50) McNamara, D. P.; Childs, S. L.; Giordano, J.; Iarriccio, A.; Cassidy, J.; Shet, M. S.; Mannion, R.; O'Donnell, E.; Park, A. Use of a Glutaric Acid Cocrystal to Improve Oral Bioavailability of a Low Solubility API. *Pharm. Res.* **2006**, *23* (8), 1888–1897.

(51) Trask, A. V.; Motherwell, W. D. S.; Jones, W. Pharmaceutical Cocrystallization: Engineering a Remedy for Caffeine Hydration. *Cryst. Growth Des.* **2005**, *5* (3), 1013–1021.

(52) Vangala, V. R.; Chow, P. S.; Tan, R. B. H. Characterization, Physicochemical and Photo-Stability of a Co-Crystal Involving an Antibiotic Drug, Nitrofurantoin, and 4-Hydroxybenzoic Acid. *CrystEngComm* **2011**, *13* (3), 759.

(53) Khankari, R. K.; Grant, D. J. W. Pharmaceutical Hydrayes. *Thermochim. Acta* **1995**, *248*, 61–79.

(54) Van Den Mooter, G. The Use of Amorphous Solid Dispersions: A Formulation Strategy to Overcome Poor Solubility and Dissolution Rate. *Drug Discov. Today Technol.* **2012**, *9* (2), e79–e85.

(55) Sotthivirat, S.; McKelvey, C.; Moser, J.; Rege, B.; Xu, W.; Zhang, D. Development of Amorphous Solid Dispersion Formulations of a Poorly Water-Soluble Drug, MK-0364. *Int. J. Pharm.* **2013**, *452* (1–2), 73–81.

(56) Alonzo, D. E.; Gao, Y.; Zhou, D.; Mo, H.; Zhang, G. G. Z.; Taylor, L. S. Dissolution and Precipitation Behavior of Amorphous Solid Dispersions. *J. Pharm. Sci.* **2010**, *100* (8), 3316–3331.

(57) Hancock, B. C.; Zografi, G. Characteristics and Significance of the Amorphous State in Pharmaceutical Systems. *J. Pharm. Sci.* **1997**, *86* (1), 1–12.

(58) Vasconcelos, T.; Sarmento, B.; Costa, P. Solid Dispersions as Strategy to Improve Oral Bioavailability of Poor Water Soluble Drugs. *Drug Discov. Today* **2007**, *12* (23–24), 1068–1075.

(59) Janssens, S.; Van den Mooter, G. Review: Physical Chemistry of Solid Dispersions. *J. Pharm. Pharmacol.* **2009**, *61* (12), 1571–1586.

(60) Mahieu, A.; Willart, J. F.; Dudognon, E.; Daneìde, F.; Descamps, M. A New Protocol to Determine the Solubility of Drugs into Polymer Matrixes. *Mol. Pharm.* **2013**, *10* (2), 560–566.

(61) Tian, Y.; Booth, J.; Meehan, E.; Jones, D. S.; Li, S.; Andrews, G. P. Construction of Drug-Polymer Thermodynamic Phase Diagrams Using Flory-Huggins Interaction Theory: Identifying the Relevance of Temperature and Drug Weight Fraction to Phase Separation within Solid Dispersions. *Mol. Pharm.* **2013**, *10*, 236–248.

(62) Rumondor, A. C.; Taylor, L. S. Effect of Polymer Hygroscopicity on the Phase Behavior of Amorphous Solid Dispersions in the Presence of Moisture. *Mol. Pharm.* **2010**, *7* (2), 477–490.

(63) CIR Expert Panel. Final Report on the Safety Assessment of H Ydroxyethylcellulose , H Yd Roxy pro Py Ice1 I U Lose , Met H Ylcellu Lose , H Yd Roxy pro Pyl Methylcellulose , and Cellulose Gum. *Int. J. Toxicol.* **1986**, *5* (3), 1–59.

(64) Dengale, S. J.; Grohganz, H.; Rades, T.; L??bmann, K. Recent Advances in Co-Amorphous Drug Formulations. *Adv. Drug Deliv. Rev.* **2016**, *100*, 116–125.

(65) Chieng, N.; Aaltonen, J.; Saville, D.; Rades, T. Physical Characterization and Stability of Amorphous Indomethacin and Ranitidine Hydrochloride Binary Systems Prepared by Mechanical Activation. *Eur. J. Pharm. Biopharm.* **2009**, *71* (1), 47–54.

(66) Laitinen, R.; Lo̊mann, K.; Strachan, C. J.; Grohganz, H.; Rades, T. Emerging Trends in the Stabilization of Amorphous Drugs. *Int. J. Pharm.* **2013**, *453* (1), 65–79.

(67) Aakeröy, C. B.; Forbes, S.; Desper, J. Using Cocrystals to Systematically Modulate Aqueous Solubility and Melting Behavior of an Anticancer Drug. *J. Am. Chem. Soc.* **2009**, *131* (47), 17048–17049.

(68) Chan, H. C. S.; Kendrick, J.; Neumann, M. a.; Leusen, F. J. J. Towards Ab Initio Screening of Co-Crystal Formation through Lattice Energy Calculations and Crystal Structure Prediction of Nicotinamide, Isonicotinamide, Picolinamide and Paracetamol Multi-Component Crystals. *CrystEngComm* **2013**, *15* (19), 3799.

(69) Issa, N.; Karamertzanis, P. G.; Welch, G. W. a.; Price, S. L. Can the Formation of Pharmaceutical Cocrystals Be Computationally Predicted? I. Comparison of Lattice Energies. *Cryst. Growth Des.* **2009**, *9* (1), 442–453.

(70) Blagden, N.; Coles, S. J.; Berry, D. J. Pharmaceutical Co-Crystals - Are We There Yet? *CrystEngComm* **2014**.

(71) Höhne, G.; Hemminger, W. F.; Flammersheim, H.-J. *Differential Scanning Calorimetry*, Second Ed.; Springer, 2003.

(72) Haines, P. J. Introduction. In *Principles of Thermal Analysis and Calorimetry*; Haines, P. J., Ed.; The Royal Society of Chemistry: Cambridge, 2002.

(73) Laye, P. G. Differential Thermal Analysis and Differential Scanning Calorimetry. In *Principles of Thermal Analysis and Calorimetry*; Haines, P. J., Ed.; The Royal Society of Chemistry: Cambridge, 2002.

(74) Cherukuvada, S.; Nangia, A. Eutectics as Improved Pharmaceutical Materials: Design, Properties and Characterization. *Chem. Commun.* **2014**, *50* (8), 906–923.

(75) Mackenzie, R. C. Nomenclature in Thermal Analysis. In *Treatise on Analytical Chemistry*; Elving, P. J., Kolthoff, I. M., Eds.; John Wiley & Sons, Ltd: New York, 1983.

(76) Heal, G. R. Thermogravimetry and Derivative Thermogravimetry. In *Principles of Thermal Analysis and Calorimetry*; The Royal Society of Chemistry: Cambridge, 2002.

(77) Warrington, S. B. Simultaneous Thermal Analysis Techniques. In *Principles of Thermal Analysis and Calorimetry*; Haines, P. J., Ed.; The Royal Society of Chemistry: Cambridge, 2002.

(78) Jenkins, R.; Snyder, R. L. *Introduction to X-Ray Powder Diffractometry*; John Wiley & Sons, Ltd: New York, 1996.

(79) Massa, W. *Crystal Structure Determination*, Second Ed.; Springer: Berlin, 2004.

(80) Giacovazzo, C. The Diffraction of X-Rays by Crystals. In *Fundamentals of Crystallography*; Giacovazzo, C., Ed.; Oxford University Press: Oxford, 1992.

(81) Fultz, B.; Howe, J. *Transmission Electron Microscopy and Diffractometry of Materials*, Fourth Ed.; Springer-Verlag: Berlin, 2013.

(82) Bragg, W. L. The Diffraction of Short Electromagnetic Waves by a Crystal. *Proc. Camb. Philol. Soc.* **1912**, *17* (1), 43–57.

(83) Ewald, P. P. Zur Theorie Der Interferenzen Der Röntgentstrahlen in Kristallen. *Phys. Z.* **1913**, *14*, 465–472.

(84) Wittering, K. E. Multi-Component Crystallisation in the Continuous Flow Environment, University of Bath, 2015.

(85) Blake, A. J.; Clegg, W.; Gould, R. O.; Main, P. *Crystal Structure Analysis: Principles and Practice*, Second Ed.; Oxford University Press: Oxford, 2001.

(86) Clegg, W. *Crystal Structure Determination*; Oxford University Press: Oxford, 1998.

(87) Kealey, D.; Haines, P. J. *Analytical Chemistry*; BIOS Scientific Publishers Limited: Oxford, 2002.

(88) Hollas, J. M. *Modern Spectroscopy*, Fourth Ed.; John Wiley & Sons, Ltd: Chichester, 2004.

(89) Willard, H. H.; Merrit, L. L.; Dean, J. A.; Settle, F. A. *Instrumental Methods of Aanalysis*, Seventh Ed.; Wadsworth Publishing Company: Belmont, CA, 1988.

(90) Schrader, B. General Survey of Vibrational Spectroscopy. In *Infrared and Raman Spectroscopy: Methods and Applications*; Schrader, B., Ed.; VCH Publishers, Inc.: New York, 1995.

(91) Buckton, G. Solid-State Properties. In *Aulton's Pharmaceutics: The Design and Manufacture of Medicines*; Aulton, M. E., Ed.; Churchill Livingston: London, 2007.

(92) Sheokand, S.; Modi, S. R.; Bansal, A. K. Quantification of Low Levels of Amorphous Content in Crystalline Celecoxib Using Dynamic Vapor Sorption (DVS). *Eur. J. Pharm. Biopharm.* **2016**, *102*, 77–86.

(93) Wells, J. I. *Pharmaceutical Preformulation: The Physicochemical Properties of Drug Substances*; Taylor & Francis: London, 1988.

(94) Aulton, M. E. Dissolution and Solubility. In *Aulton's Pharmaceutics: The Design and Manufacture of Medicines*; Aulton, M. E., Ed.; Churchill Livingston: London, 2007.

(95) Wells, J. I.; Aulton, M. E. Pharmaceutical Preformulation. In *Aulton's Pharmaceutics: The Design and Manufacture of Medicines*; Aulton, M. E., Ed.; Churchill Livingston: London, 2007.

(96) Eckert, F.; Klamt, A. Fast Solvent Screening via Quantum Chemistry: COSMO-RS Approach. *AIChE J.* **2002**, *48* (2), 369–385.

(97) Klamt, A. Conductor-like Screening Model for Real Solvents: A New Approach to the Quantitative Calculation of Solvation Phenomena. *J. Phys. Chem.* **1995**, *99* (7), 2224–2235.

(98) Klamt, A.; Schüürmann, G. COSMO: A New Approach to Dielectric Screening in Solvents with Explicit Expressions for the Screening Energy and Its Gradient. *J. Chem. Soc., Perkin Trans. 2* **1993**, No. 5, 799–805.

(99) COSMOlogic. COSMOtherm Reference Manual. COSMOlogic GmbH & Co. KG: Leverkusen 2015.

(100) COSMOlogic. COSMOthermX: A Graphical User Interface to the COSMOtherm Program. User Guide. COSMOlogic GmbH & Co. KG: Leverkusen 2015.

(101) Abramov, Y.; Loschen, C.; Klamt, A. Rational Coformer or Solvent Selection for Pharmaceutical Cocrystallization or Desolvation. *J. Pharm. Sci.* **2012**, *101* (10), 3687–3697.

(102) Musumeci, D.; Hunter, C. A.; Prohens, R.; Scuderi, S.; McCabe, J. F. Virtual Cocrystal Screening. *Chem. Sci.* **2011**, *2* (5), 883–890.

(103) Grecu, T.; Hunter, C. A.; Gardiner, E. J.; McCabe, J. F. Validation of a Computational Cocrystal Prediction Tool: Comparison of Virtual and Experimental Cocrystal Screening Results. *Cryst. Growth Des.* **2014**, *14* (1), 165–171.

(104) Grecu, T.; Adams, H.; Hunter, C. A.; McCabe, J. F.; Portell, A.; Prohens, R. Virtual Screening Identifies New Cocrystals of Nalidixic Acid. *Cryst. Growth Des.* **2014**, *14*, 1749–1755.

(105) Fisher, R. A. *Design of Experiments*; Oliver & Boyd: Edinburgh, 1935.

(106) Montgomery, D. C. *Design and Analysis of Experiments*, Ninth Ed.; John Wiley & Sons, Ltd: Hoboken, NJ, 2012.

(107) Vicente, G.; Coteron, A.; Martinez, M.; Aracil, J. Application of the Factorial Design of Experiments and Response Surface Methodology to Optimize Biodiesel Production. *Ind. Crops Prod.* **1998**, *8*, 29–35.

(108) Franceschini, G.; Macchietto, S. Model-Based Design of Experiments for Parameter Precision: State of the Art. *Chem. Eng. Sci.* **2008**, *63* (19), 4846–4872.

(109) Klous, M. G.; Nuijen, B.; Brink, W. Van Den; Ree, J. M. Van; Beijnen, J. H. Process Characterisation, Optimisation and Validation of Production of Diacetylmorphine/caffeine Sachets: A Design of Experiments Approach. *Int. J. Pharm.* **2004**, *285* (1–2), 65–75.

(110) Cox, D. R.; Reid, N. *The Theory of the Design of Experiments*; Chapman & Hall/CRC: Boca Raton, FL, 2000.

(111) Eriksson, L.; Johansson, E.; Kettaneh-Wold, N.; Wilstrom, C.; Wold, S. *Design of Experiments: Principles and Applications*, Third Ed.; Umetrics AB: Umeå, 2008.

(112) Blagden, N.; Coles, S. J.; Berry, D. J. Pharmaceutical Co-Crystals – Are We There Yet? *CrystEngComm* **2014**, *16*, 5753–5761.

(113) Morrison, H.; Mrozek-Morrison, M.; Toschi, J.; Luu, V.; Tan, H.; Daurio, D. High Throughput Bench-Top Co-Crystal Screening via a Floating Foam Rack/Sonic Bath Method. *Org. Process Res. Dev.* **2013**, *17* (3), 533–539.

(114) Childs, S. L.; Rodríguez-Hornedo, N.; Reddy, L. S.; Jayasankar, A.; Maheshwari, C.; McCausland, L.; Shipplett, R.; Stahly, B. C. Screening Strategies Based on Solubility and Solution Composition Generate Pharmaceutically Acceptable Cocrystals of Carbamazepine. *CrystEngComm* **2008**, *10* (7), 856–864.

(115) Karamertzanis, P. G.; Kazantsev, A. V.; Issa, N.; Welch, G. W. a.; Adjiman, C. S.; Pantelides, C. C.; Price, S. L. Can the Formation of Pharmaceutical Cocrystals Be Computationally Predicted? 2. Crystal Structure Prediction. *J. Chem. Theory Comput.* **2009**, *5* (5), 1432–1448.

(116) Stahl, P. H.; Wermuth, C. G. *Handbook of Pharmaceutical Salts: Properties, Selection, and Use*, Second Ed.; VHCA and Wiley-VCH: Zürich and Weinheim, 2011.

(117) Trask, A. V. An Overview of Pharmaceutical Cocrystals as Intellectual Property. *Mol. Pharm.* **2007**, *4* (3), 301–309.

(118) FDA. GRAS substances (SCOGS) database

http://www.accessdata.fda.gov/scripts/fdcc/?set=SCOGS (accessed Mar 23, 2017).

(119) FDA. Everything Added to Food in the United States (EAFUS) List https://www.accessdata.fda.gov/scripts/fcn/fcnNavigation.cfm?rpt=eafuslisting (accessed Mar 23, 2017).

(120) Trask, A. V.; Motherwell, W. D. S.; Jones, W.; Samuel, W. D.; Jones, W. Solvent-Drop Grinding: Green Polymorph Control of Cocrystallisation. *Chem. Commun.* **2004**, No. 7, 890–891.

(121) Childs, S. L.; Hardcastle, K. I. Cocrystals of Piroxicam with Carboxylic Acids. *Cryst. Growth Des.* **2007**, *7* (7), 1291–1304.

(122) Karki, S.; Friscić, T.; Jones, W.; Motherwell, W. D. S. Screening for Pharmaceutical Cocrystal Hydrates via Neat and Liquid-Assisted Grinding. *Mol. Pharm.* **2007**, *4* (3), 347–354.

(123) Rubin, A. E.; Tummala, S.; Both, D. A.; Wang, C.; Delaney, E. J. Emerging Technologies Supporting Chemical Process R and D and Their Increasing Impact on Productivity in the Pharmaceutical Industry. *Chem. Rev.* **2006**, *106* (7), 2794–2810.

(124) Nartowski, K. P.; Khimyak, Y. Z.; Berry, D. J. Tuning the Spontaneous Formation Kinetics of Caffeine : Malonic Acid Co-Crystals. *CrystEngComm* **2016**, *18* (15), 2617–2620.

(125) Ibrahim, A. Y.; Forbes, R. T.; Blagden, N. Spontaneous Crystal Growth of Co-Crystals: The Contribution of Particle Size Reduction and Convection Mixing of the Co-Formers. *CrystEngComm* **2011**, *13* (4), 1141.

(126) Salari, A.; Young, R. E. Application of Attenuated Total Reflectance FTIR Spectroscopy to the Analysis of Mixtures of Pharmaceutical Polymorphs. *Int. J. Pharm.* **1998**, *163* (1–2), 157–166.

(127) Patel, a D.; Luner, P. E.; Kemper, M. S. Quantitative Analysis of Polymorphs in Binary and Multi-Component Powder Mixtures by near-Infrared Reflectance Spectroscopy. *Int. J. Pharm.* **2001**, *212* (2), 295.

(128) Jayasankar, A.; Somwangthanaroj, A.; Shao, Z. J.; Rodríguez-Hornedo, N. Cocrystal Formation during Cogrinding and Storage Is Mediated by Amorphous Phase. *Pharm. Res.* **2006**, *23* (10), 2381–2392.

(129) Stuart, B. H. *Infrared Spectroscopy: Fundamentals and Applications*; John Wiley & Sons, Ltd, 2004.

(130) MKS Umetrics. User Guide to MODDE. MKS Umetrics AB 2014.

(131) Wang, I.-C.; Lee, M.-J.; Sim, S.-J.; Kim, W.-S.; Chun, N.-H.; Choi, G. J. Anti-Solvent Co-Crystallization of Carbamazepine and Saccharin. *Int. J. Pharm.* **2013**, *450* (1–2), 311–322.

(132) Yu, L. Polymorphism in Molecular Solids: An Extraordinary System of Red, Orange, and Yellow Crystals. *Acc. Chem. Res.* **2010**, *43* (9), 1257–1266.

(133) López-Mejías, V.; Kampf, J. W.; Matzger, A. J. Nonamorphism in Flufenamic Acid and a New Record for a Polymorphic Compound with Solved Structures. *J. Am. Chem. Soc.* **2012**, *134* (24), 9872–9875.

(134) Zeidan, T. A.; Trotta, J. T.; Tilak, P. A.; Oliveira, M. A.; Chiarella, R. A.; Foxman, B. M.; Almarsson, O.; Hickey, M. B. An Unprecedented Case of Dodecamorphism: The Twelfth Polymorph of Aripiprazole Formed by Seeding with Its Active Metabolite. *CrystEngComm* **2016**, *18* (9), 1486–1488.

(135) Allen, F. H. The Cambridge Structural Database: A Quarter of a Million Crystal Structures and Rising. *Acta Crystallogr. Sect. B Struct. Sci.* **2002**, *58*, 380–388.

(136) Goyal, S.; Thorson, M. R.; Zhang, G. G. Z.; Gong, Y.; Kenis, P. J. A. Microfluidic Approach to Cocrystal Screening of Pharmaceutical Parent Compounds. *Cryst. Growth Des.* **2012**, *12* (12), 6023–6034.

(137) Blagden, N. Controlling Crystallisation: The Utilisation of Micro Channels. In *Industrial Group Autumn Meeting: Cracking Challenging Crystals*; BCA Industrial Group, 2015.

(138) Chakrabarti, J. K.; Hotten, T. M.; Tupper, D. E. Pharmaceutical Compounds - EP 0454436 B1. 0454436B1, September 13, 1995.

(139) Sekhar, C. B. Synthesis and Characterization of Novel Anti-Lipidemic Agents; Studies in the Synthesis of Montelukast, Olanzapine and Diltiazem, Jawaharlal Nehru Technological University, 2012.

(140) Hartwig, J.; Ceylan, S.; Kupracz, L.; Coutable, L.; Kirschning, A. Heating under High-Frequency Inductive Conditions: Application to the Continuous Synthesis of the Neurolepticum Olanzapine (Zyprexa). *Angew. Chemie - Int. Ed.* **2013**, *52* (37), 9813–9817.

(141) Yu, L.; Stephenson, G. A.; Mitchell, C. A.; Bunnell, C. A.; Snorek, S. V.; Bowyer, J. J.; Borchardt, T. B.; Stowell, J. G.; Bryn, S. R. Thermochemistry and Conformational Polymorphism of a Hexamorphic Crystal System. *J. Am. Chem. Soc.* **2000**, *122* (4), 585–591.

(142) Macrae, C. F.; Edgington, P. R.; McCabe, P.; Pidcock, E.; Shields, G. P.; Taylor, R.; Towler, M.; Van De Streek, J. Mercury: Visualization and Analysis of Crystal Structures. *J. Appl. Crystallogr.* **2006**, *39* (3), 453–457.

(143) Kourkoumelis, N. PowDLL, a Reusable .NET Component for Interconverting Powder Diffraction Data: Recent Developments. In *ICDD Annual Spring Meetings, Powder Diffraction, 28*; O'Neill, L., Ed.; 2013; pp 137–148.

(144) Bernstein, J. *Polymorphism in Molecular Crystals*; Oxford University Press, 2002.

(145) Newman, A. Specialized Solid Form Screening Techniques. *Org. Process Res. Dev.* **2013**, *17* (3), 457–471.

(146) Alhalaweh, A.; George, S.; Basavoju, S.; Childs, S. L.; Rizvi, S. A. A.; Velaga, S. P. Pharmaceutical Cocrystals of Nitrofurantoin: Screening, Characterization and Crystal Structure Analysis. *CrystEngComm* **2012**, *14* (15), 5078–5088.

(147) Rahim, S. A.; Hammond, R. B.; Sheikh, A. Y.; Roberts, K. J. A Comparative Assessment of the Influence of Different Crystallization Screening Methodologies on the Solid Forms of Carbamazepine Co-Crystals. *CrystEngComm* **2013**, *15* (19), 3862–3873.

(148) Baird, J. A.; Eerdenbrugh, B. Van; Taylor, L. S. A Classification System to Assess the Crystallization Tendency of Organic Molecules from Undercooled Melts. *J. Pharm. Sci.* **2010**, *99* (9), 3787–3806.

(149) Grohganz, H.; Löbmann, K.; Priemel, P.; Tarp Jensen, K.; Graeser, K.; Strachan, C.; Rades, T. Amorphous Drugs and Dosage Forms. *J. Drug Deliv. Sci. Technol.* **2013**, *23* (4), 403–408.

(150) Knopp, M. M.; Löbmann, K.; Elder, D. P.; Rades, T.; Holm, R. Recent Advances and Potential Applications of Modulated Differential Scanning Calorimetry (mDSC) in Drug Development. *Eur. J. Pharm. Sci.* **2016**, *87*, 164–173.

(151) Wood, P. A.; Feeder, N.; Furlow, M.; Galek, P. T. A.; Groom, C. R.; Pidcock, E. Knowledge-Based Approaches to Co-Crystal Design. *CrystEngComm* **2014**, *16* (26), 5839.

(152) Sun, Y.; Zhu, L.; Wu, T.; Cai, T.; Gunn, E. M.; Yu, L. Stability of Amorphous Pharmaceutical Solids: Crystal Growth Mechanisms and Effect of Polymer Additives. *AAPS J.* **2012**, *14* (3), 380–388.

(153) Thakuria, R.; Cherukuvada, S.; Nangia, A. Crystal Structures of Pyrogallol, Its Hydrate, and Stable Multiple Z' Cocrystals with N-Heterocycles Containing Metastable Conformers of Pyrogallol. *Cryst. Growth Des.* **2012**, *12*, 3944–3953.

(154) Braun, D. E.; Bhardwaj, R. M.; Arlin, J. B.; Florence, A. J.; Kahlenberg, V.; Griesser, U. J.; Tocher, D. A.; Price, S. L. Absorbing a Little Water: The Structural, Thermodynamic, and Kinetic Relationship between Pyrogallol and Its Tetarto-Hydrate. *Cryst. Growth Des.* **2013**, *13* (9), 4071–4083.

(155) Mahlin, D.; Ponnambalam, S.; Höckerfelt, M. H.; Bergström, C. A. S. Toward in Silico Prediction of Glass-Forming Ability from Molecular Structure Alone: A Screening Tool in Early Drug Development. *Mol. Pharm.* **2011**, *8* (2), 498–506.

(156) Braun, D. E.; Tocher, D. A.; Price, S. L.; Griesser, U. J. The Complexity of Hydration of Phloroglucinol: A Comprehensive Structural and Thermodynamic Characterization. *J. Phys. Chem. B* **2012**, *116* (13), 3961–3972.

(157) Robertson, J. M.; Ubbelohde, A. R. A New Form of Resorcinol. II. Thermodynamic Properties in Relation to Structure. *Proc. R. Soc. Lond. A. Math. Phys. Sci.* **1938**, *167*, 136–147.

(158) Maria, T. M. R.; Costa, F. S.; Leitão, M. L. P.; Redinha, J. S. A Calorimetric Study of Phase Transitions for Some Cyclohexanediols. *Thermochim. Acta* **1995**, *269–270*, 405–413.

(159) Aitipamula, S.; Wong, A. B. H.; Chow, P. S.; Tan, R. B. H. Cocrystallization with Flufenamic Acid: Comparison of Physicochemical Properties of Two Pharmaceutical Cocrystals. *CrystEngComm* **2014**, *16* (26), 5793.

(160) Thipparaboina, R.; Kumar, D.; Chavan, R. B.; Shastri, N. R. Multidrug Co-Crystals: Towards the Development of Effective Therapeutic Hybrids. *Drug Discov. Today* **2016**, *21* (3), 481–490.

(161) Sekhon, B. Drug-Drug Co-Crystals. *DARU J. Pharm. Sci.* **2012**, *20* (1), 45.

(162) Qiao, N.; Li, M.; Schlindwein, W.; Malek, N.; Davies, A.; Trappitt, G. Pharmaceutical Cocrystals: An Overview. *Int. J. Pharm.* **2011**, *419* (1–2), 1–11.

(163) Zhu, B.; Wang, J. R.; Zhang, Q.; Mei, X. Improving Dissolution and Photostability of Vitamin K3 via Cocrystallization with Naphthoic Acids and Sulfamerazine. *Cryst. Growth Des.* **2016**, *16* (1), 483–492.

(164) Lee, E. H. A Practical Guide to Pharmaceutical Polymorph Screening & Selection. *Asian J. Pharm. Sci.* **2014**, *9* (4), 163–175.

(165) Fuliaş, A.; Vlase, G.; Vlase, T.; Şuta, L. M.; Şoica, C.; Ledeţi, I. Screening and Characterization of Cocrystal Formation between Carbamazepine and Succinic Acid. *J. Therm. Anal. Calorim.* **2015**, *121* (3), 1081–1086.

(166) Anderson, K. M.; Probert, M. R.; Whiteley, C. N.; Rowland, A. M.; Goeta, A. E.; Steed, J. W. Designing Co-Crystals of Pharmaceutically Relevant Compounds That Crystallize with Z ' > 1. *Cryst. Growth Des.* **2009**, *9* (2), 1082–1087.

(167) Lehmler, H. J.; Robertson, L. W.; Parkin, S.; Brock, C. P. Z' = 4 Structure without Obvious Pseudosymmetry: Implications for the Formation of Solid-State Compounds. *Acta Crystallogr. Sect. B Struct. Sci.* **2002**, *58* (1), 140–147.

(168) Prasad, K. D.; Cherukuvada, S.; Devaraj Stephen, L.; Guru Row, T. N. Effect of Inductive Effect on the Formation of Cocrystals and Eutectics. *CrystEngComm* **2014**, *16* (42), 9930–9938.

(169) Loschen, C.; Klamt, A. COSMO Quick: A Novel Interface for Fast σ-Profile Composition and Its Application to COSMO-RS Solvent Screening Using Multiple Reference Solvents. *Ind. Eng. Chem. Res.* **2012**, *51* (43), 14303–14308.

(170) Hornig, M.; Klamt, A. COSMOfrag : A Novel Tool for High-Throughput ADME Property Prediction and Similarity Screening Based on Quantum Chemistry. *J. Chem. Inf. Model.* **2005**, *45* (5), 1169–1177.

(171) Nordström, F. L.; Rasmuson, Å. C. Phase Equilibria and Thermodynamics of P-Hydroxybenzoic Acid. *J. Pharm. Sci.* **2006**, *95* (4), 748–760.

(172) Dolomanov, O. V.; Bourhis, L. J.; Gildea, R. J.; Howard, J. A. K.; Puschmann, H. OLEX2: A Complete Structure Solution, Refinement and Analysis Program. *J. Appl. Crystallogr.* **2009**, *42* (2), 339–341.

(173) Bourhis, L. J.; Dolomanov, O. V.; Gildea, R. J.; Howard, J. A. K.; Puschmann, H. The Anatomy of a

Comprehensive Constrained, Restrained Refinement Program for the Modern Computing Environment - Olex2 Dissected. *Acta Crystallogr. Sect. A Found. Crystallogr.* **2015**, *71* (1), 59–75.

(174) Jeffrey, G. A. *An Introduction to Hydrogen Bonding*; Oxford University Press, 1997.

(175) Aakeröy, C. B.; Fasulo, M. E.; Desper, J. Cocrystal or Salt : Does It Really Matter ? *Mol. Pharm.* **2007**, *4* (3), 317–322.

(176) Nichols, G.; Frampton, C. S. Physicochemical Characterization of the Orthorhombic Polymorph of Paracetamol Crystallized from Solution. *J. Pharm. Sci.* **1998**, *87* (6), 684–693.

(177) Yu, L. X.; Carlin, A. S.; Amidon, G. L.; Hussain, A. S. Feasibility Studies of Utilizing Disk Intrinsic Dissolution Rate to Classify Drugs. *Int. J. Pharm.* **2004**, *270* (1–2), 221–227.

(178) Dezani, A. B.; Pereira, T. M.; Caffaro, A. M.; Reis, J. M.; Serra, C. H. dos R. Equilibrium Solubility versus Intrinsic Dissolution: Characterization of Lamivudine, Stavudine and Zidovudine for BCS Classification. *Brazilian J. Pharm. Sci.* **2013**, *49* (4), 853–863.

(179) Hunter, C. A.; Prohens, R. Solid Form and Solubility. *CrystEngComm* **2016**, *19* (December), 1–4.

(180) Suresh, K.; Mannava, M. K. C.; Nangia, A. Cocrystals and Alloys of Nitazoxanide: Enhanced Pharmacokinetics. *Chem. Commun.* **2016**, *52* (22), 4223–4226.

(181) Tiekink, E. R. T.; Vittal, J.; Zaworotko, M. J. *Organic Crystal Cngineering: Frontiers in Crystal Engineering*; Wiley, 2010.

(182) Chen, J. M.; Li, S.; Lu, T. B. Pharmaceutical Cocrystals of Ribavirin with Reduced Release Rates. *Cryst. Growth Des.* **2014**, *14* (12), 6399–6408.

(183) Llinas, A.; Barbas, R.; Font-Bardia, M.; Quayle, M. J.; Velaga, S.; Prohens, R. Two New Polymorphic Cocrystals of Zafirlukast: Preparation, Crystal Structure, and Stability Relations. *Cryst. Growth Des.* **2015**, *15* (8), 4162–4169.

(184) Joint Formulary Committe. *British National Formulary*, 61st Ed.; BMJ Group & Pharmaceutical Press: London, 2011.

(185) Holohan, J. J.; Edwards, I. J.; Timko, R. J.; Bradway, R. J.; Clements, A. Pharmaceutical Agents Useful as Leukotriene Antagonists. 5482963, 1996.

(186) Goldring, D.; Botoshansky, M.; Khalfin, R. L.; Pertsikov, B.; Nisnevitch, G.; Ponomarev, V.; Zaltzman, I.; Gutman, A.; Kaftory, M. Solvates of Zafirlukast. *Acta Crystallogr. Sect. C Cryst. Struct. Commun.* **2004**, *60* (12).

(187) Schwarzenbach, D. Structure of Piperazine Hexahydrate. *J. Chem. Phys.* **1968**, *48* (9), 4134–4140.

(188) NPCS Board. *Detailed Project Profiles On Chemical Industries Vol II*, Second Ed.; NIIR Project Consultancy Services, 2012.

(189) Cohen, R. D.; Liu, Y.; Gong, X. Analysis of Volatile Bases by High Performance Liquid Chromatography with Aerosol-Based Detection. *J. Chromatogr. A* **2012**, *1229*, 172–179.

(190) Parkin, A.; Oswald, I. D. H.; Parsons, S. Structures of Piperazine, Piperidine and Morpholine. *Acta Crystallogr. Sect. B Struct. Sci.* **2004**, *60* (2), 219–227.

(191) Radhakrishna, T.; Satyanarayana, J.; Satyanarayana, A. Determination of Zafirlukast by Stability Indicating LC and Derivative Spectrophotometry. *J. Pharm. Biomed. Anal.* **2002**, *30* (3), 695–703.

(192) Shan, N.; Perry, M. L.; Weyna, D. R.; Zaworotko, M. J. Impact of Pharmaceutical Cocrystals: The Effects on Drug Pharmacokinetics. *Expert Opin. Drug Metab. Toxicol.* **2014**, *10* (9), 1255–1271.

# Appendix 1

Research papers published from work in this thesis

1. P. A. Corner, J. J. Harburn, J. W. Steed, J. F. McCabe and D. Berry, *Stabilisation of an amorphous form of ROY through a predicted co-former interaction.* Chem. Commun., 2016, 52, 6537.

*2.* Philip Corner, David Berry, James McCabe, Rafael Barbas, Rafel Prohens, Hongwen Du, Hongyu Zhou and Antonio Llinas, *Property Prediction and Pharmacokinetic Evaluation of Mixed Stoichiometry Cocrystals of Zafirlukast, a Drug Delivery Case Study.*

3. Andrea Perrin, Melissa J. Goodwin, Osama M. Musa, David J. Berry, Philip Corner, Katharina Edkins, Dmitry S. Yufit, and Jonathan W. Steed, *Hydration Behavior of Polylactam Clathrate Hydrate Inhibitors and Their Small-Molecule Model Compounds.* Cryst. Growth Des., 2017.

# Appendix 2

Conference abstracts for oral presentations

1. An Optimised Co-crystal Screen, presented at the Academy of Pharmaceutical Sciences (APS) PharmSci 2014, University of Hertfordshire, Hatfield, UK.

   Page 212.

2. Applying an Optimised Co-crystal Screen Utilising Ultrasonication to Active Pharmaceutical Ingredients, presented at the British Crystallographic Association (BCA) Spring Meeting 2016, University of Nottingham, Nottingham, UK.

   Pages 213-214.

# Optimised High-throughput Co-crystal Screen Utilising Ultrasonication Applied to Ornidazole

Philip A. Corner,[a] David J. Berry,[a*] J. Jonathan Harburn,[a] Jonathan W. Steed[b] and James F. McCabe[c]
[a] Durham University, Division of Pharmacy, Wolfson Building, Queen's Campus, Stockton on Tees, TS17 6BH, UK.
[b] Department of Chemistry, Durham University, University Science Laboratories, South Road, Durham DH1 3LE, UK.
[c] Pharmaceutical Development, AstraZeneca Macclesfield, SK11 2SN, UK.

*Abstract* – **In order to allow efficient screening for pharmaceutical co-crystals, a proven method of high-throughput screening was adapted and the parameters are to be optimised using DOE. We anticipate that this will provide a suitable, cost effective process for future screening of potential co-formers for multiple APIs, initially applying it to the chemotherapeutic agent ornidazole. The development of this screening method is being undertaken as part of a larger project aiming to determine a structure property relationship between co-formers and the co-crystals they form.**

## INTRODUCTION

Interest in the utility of co-crystals within the pharmaceutical field has been significant in recent years, with many studies bringing to light the numerous benefits co-crystallisation can afford pharmaceutical products [1]. Due to the potential to improve several characteristics of active pharmaceutical ingredients (APIs) with sub-optimal properties, numerous methods have been developed to screen for co-crystals. One such method is high-throughput screening of potential co-formers with the desired API using ultrasonication. The feasibility of this method has been proven with researchers employing variations such as SonicSlurry™ and sonic bath processes to introduce the sonic energy to the samples in 96-well plates [2][3].
This project aims to optimise key parameters for well plate screening with the desire to achieve a robust, cost effective process for future screening of potential co-formers for multiple APIs. The development of such a screening methodology is paramount to achieving the broader goal of the project – to determine a structure property relationship between co-formers and the co-crystals they form. In light of this a Design of Experiments (DOE) optimisation has been planned.

## MATERIALS AND METHODS

Umetrics MODDE DOE software has been used to design an optimisation experiment employing the following factors (variables): ultrasonication time, ultrasonication power, solvent drying time and temperature. The response to be measured is percentage conversion to co-crystal, and will be determined by comparing FTIR data to a predetermined set of reference data.

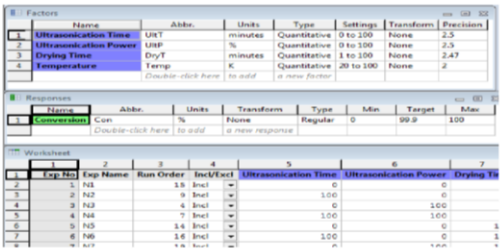


**Fig. 1.** Excerpt of experimental plan for DOE optimisation experiment.

## RESULTS AND DISCUSSION

The measurements taken from the optimisation experiment will be analysed using Umetrics SIMCA software to provide results detailing the optimal parameters in this context to employ for efficient screening of potential co-formers. These parameters will then be applied to a co-crystal screen of ornidazole, employing potential co-formers which have been computationally predicted to be most likely to co-crystallise with the API. By first applying computational prediction, the requirement for physical screening and therefore the associated costs can be reduced [4].

## CONCLUSIONS

We anticipate the use of DOE to reduce the overall experiment optimisation time and provide an efficient process for future screening of potential co-formers.

## ACKNOWLEDGMENTS
We are thankful to AstraZeneca for providing funding for this research.

## REFERENCES

[1] R. Thakuria, A. Delori, W. Jones, M.P. Lipert, L. Roy and N. Rodríguez-Hornedo, "Pharmaceutical cocrystals and poorly soluble drugs" *Int. J. Pharm.*, **453** ( 2013) 101–125.

[2] V. Luu, J. Jona, M.K. Stanton, M.L. Peterson, H.G. Morrison, K. Nagapudi, *et al.*, "High-throughput 96-well solvent mediated sonic blending synthesis and on-plate solid/solution stability characterization of pharmaceutical cocrystals" *Int. J. Pharm.***441** (2013) 356–364.

[3] S.L. Childs, N. Rodríguez-Hornedo, L.S. Reddy, A. Jayasankar, C. Maheshwari, L. McCausland, *et al.*, "Screening strategies based on solubility and solution composition generate pharmaceutically acceptable cocrystals of carbamazepine" *CrystEngComm* **10** (2008) 856–864.

[4] N. Blagden, S.J. Coles and D.J. Berry, "Pharmaceutical co-crystals – are we there yet?" *CrystEngComm* (2014) DOI: 10.1039/C4CE00127C

# Applying an Optimised Co-crystal Screen Utilising Ultrasonication to Active Pharmaceutical Ingredients

Philip A. Corner,[a] David J. Berry,[a*] J. Jonathan Harburn,[a] Jonathan W. Steed and James F. McCabe
[a] Durham University, Division of Pharmacy, Wolfson Building, Queen's Campus, Stockton on Tees, TS17 6BH, UK.

## INTRODUCTION

Interest in pharmaceutical co-crystals has been significant recently, with many studies highlighting the benefits of co-crystals.[1,2] Without extensive screening it is not currently possible to know with certainty which co-formers, if any, will form a co-crystal with a given active pharmaceutical ingredient (API) and what effects the introduction of the co-former into the crystal structure would have in terms of physical and chemical properties. Having optimised key parameters for co-crystal screening to achieve a robust, cost effective process, this project aims to allow the defining of co-crystal structure property relationships.

## MATERIALS AND METHODS

The design of experiments (DOE) approach was used to determine optimal settings for key parameters of the process, which was then applied to the screening of potential co-formers with model APIs.

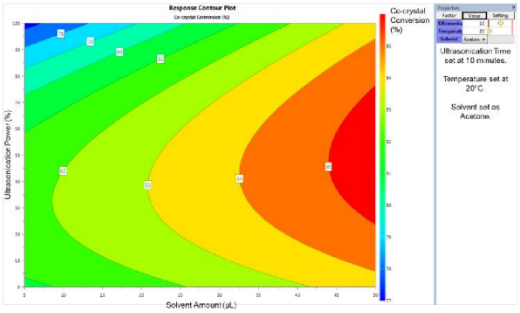


*Figure 1. A contour plot showing the relationship between ultrasonication power and solvent amount on the conversion of starting material to co-crystal with all other parameters fixed at their optimum levels, showing the best possible response in the plot area.*

Infra-red spectroscopy (FTIR) was used to initially identify any form changes in the samples from the co-crystal screen and further analysis with PXRD was carried out when indicated.

## RESULTS AND DISCUSSION

The co-crystal screen for ROY resulted in no indication of co-crystal formation, only of polymorphic conversion of ROY. Further investigation into some of the predicted API:co-former pairs led to the discovery of a 'co-former' stabilised amorphous form of ROY as explained in Figure 2.

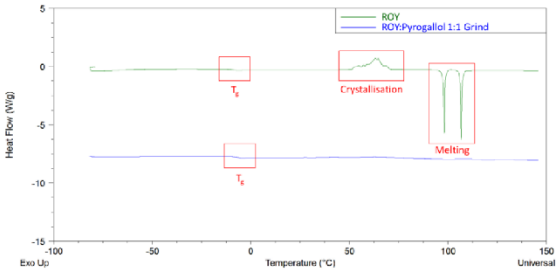


*Figure 2. DSC curves of the heating cycle after the amorphous form has been achieved by fast cooling from the melt. ROY alone (green) first crystallises on heating and then melts, the addition of pyrogallol in the form of a grind of a 1:1 molar ratio of the two components (blue) does not crystallise, indicating stabilisation of the amorphous form, compared to ROY alone.*

Initial results from further APIs appear more promising in terms of co-crystal formation. Samples from these screens in which the FTIR analysis was suggestive of the formation of a co-crystal underwent crystallographic analysis using PXRD. An example result from one screen in which co-crystals were identified is shown in Figure 3. Subsequent screens will include known co-crystals co-formers with the APIs as positive controls. Should co-crystals be identified, attempts to grow single crystals of these will follow.

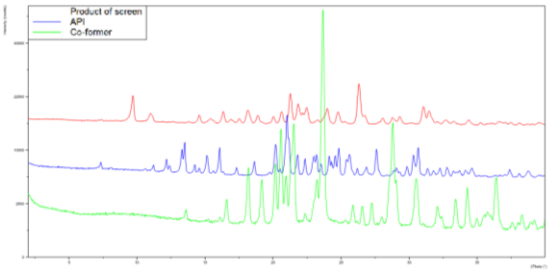


*Figure 3. PXRD patterns showing one result from a screen in which a co-crystal was identified. The co-crystal PXRD pattern (red) is compared with the pure API (blue) and pure co-former (green).*

## CONCLUSIONS

We anticipate the use of the optimised screening method for potential co-crystals together with crystallographic analysis of the resulting material to allow an efficient and cost-effective process for co-crystal discovery to progress the project towards its wider goal of structure-property relationship determination.

## REFERENCES

1. J. W. Steed, *Trends Pharmacol. Sci.*, 2013, **34**, 185–93.
2. R. Thakuria, A. Delori, W. Jones, M. P. Lipert, L. Roy, and N. Rodríguez-Hornedo, *Int. J. Pharm.*, 2013, **453**, 101–25.

# Appendix 3

## 3.1 IR Spectra of caffeine, malonic acid and the calibration standards

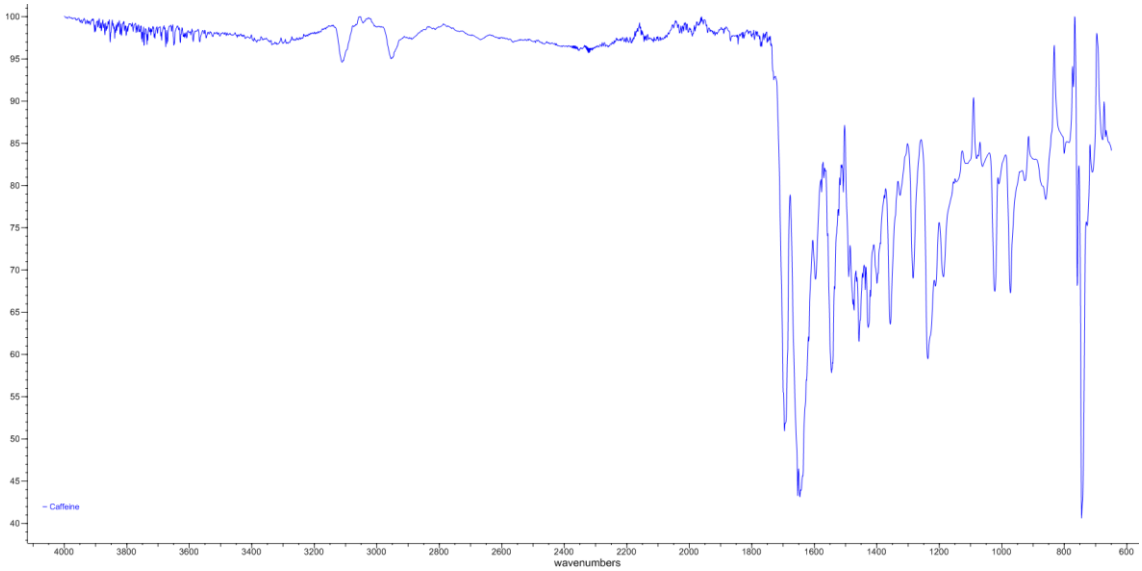


*Figure 1. Infrared spectrum of caffeine.*


*Figure 2. Infrared spectrum of malonic acid.*

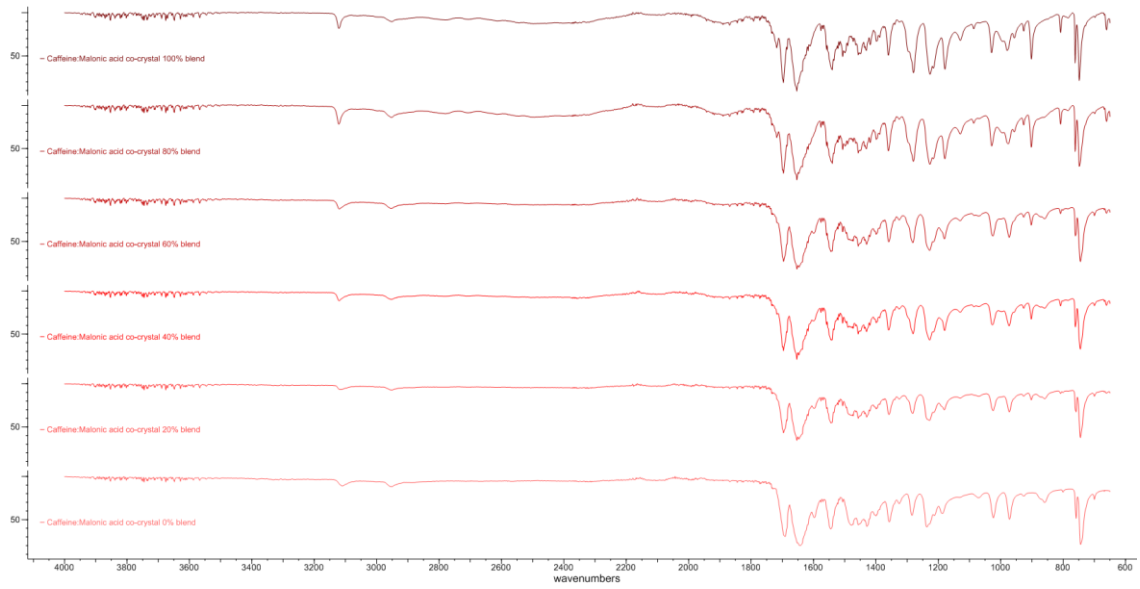


*Figure 3. Infrared spectra of the calibration standards from 0% (bottom) to 100% co-crystal content (top) in 20% increments.*

## 3.2 IR spectra of DOE optimisation experiment samples

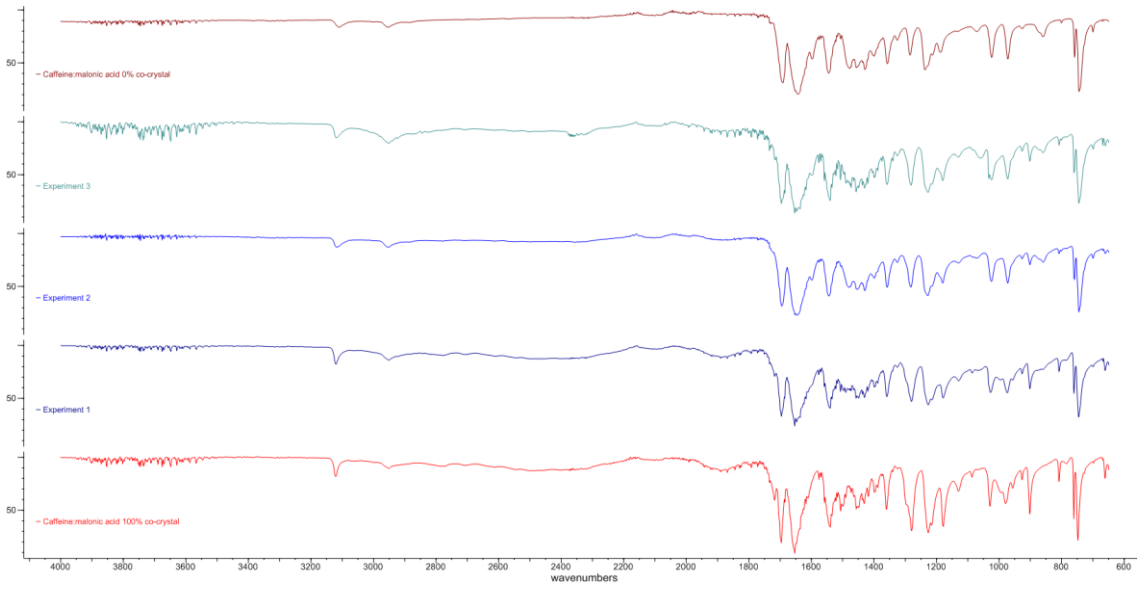


*Figure 4. Measured IR spectra of samples from experiments: 1 (dark blue), 2 (blue) and 3 (teal), with spectra of caffeine:malonic acid standards containing: 0% co-crystal (brown) and 100% co-crystal (red), for reference.*

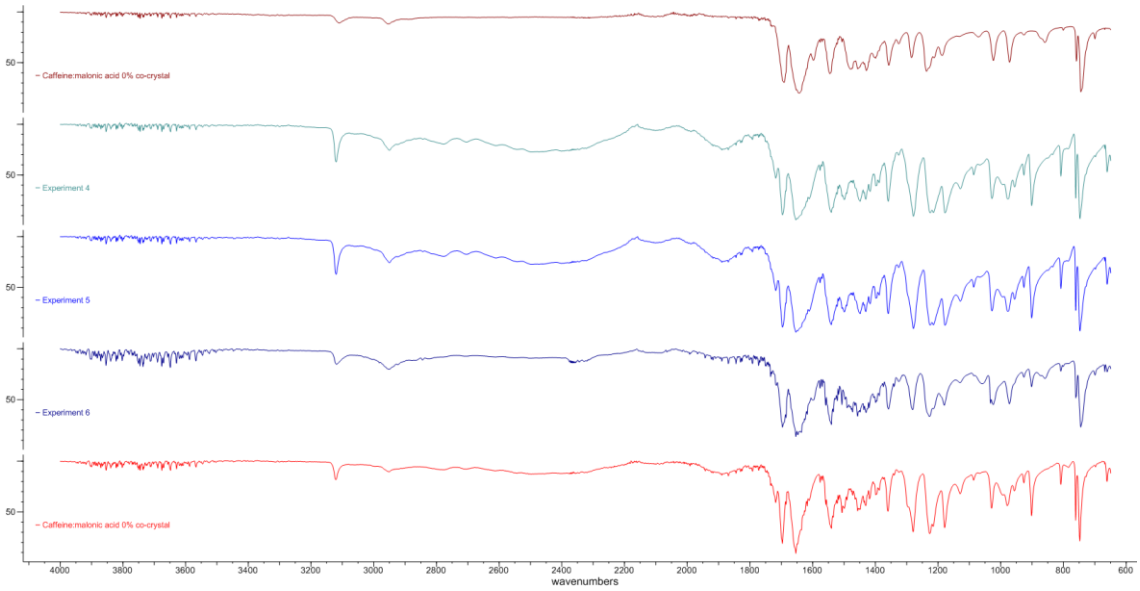


*Figure 5. Measured IR spectra of samples from experiments: 4 (dark blue), 5 (blue) and 6 (teal), with spectra of caffeine:malonic acid standards containing: 0% co-crystal (brown) and 100% co-crystal (red), for reference.*

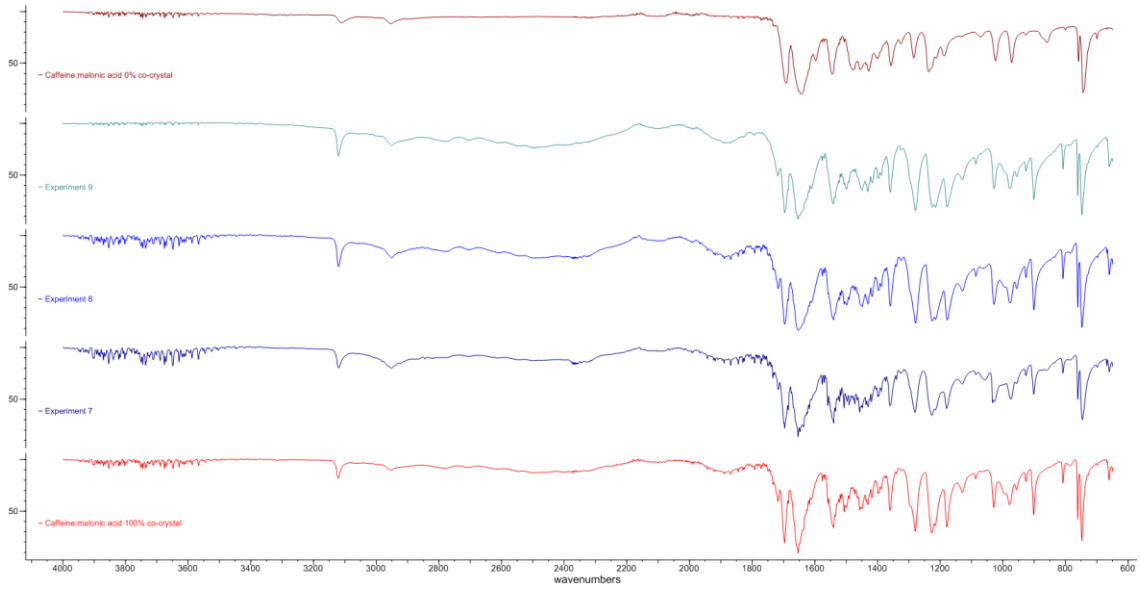


*Figure 6. Measured IR spectra of samples from experiments: 7 (dark blue), 8 (blue) and 9 (teal), with spectra of caffeine:malonic acid standards containing: 0% co-crystal (brown) and 100% co-crystal (red), for reference.*

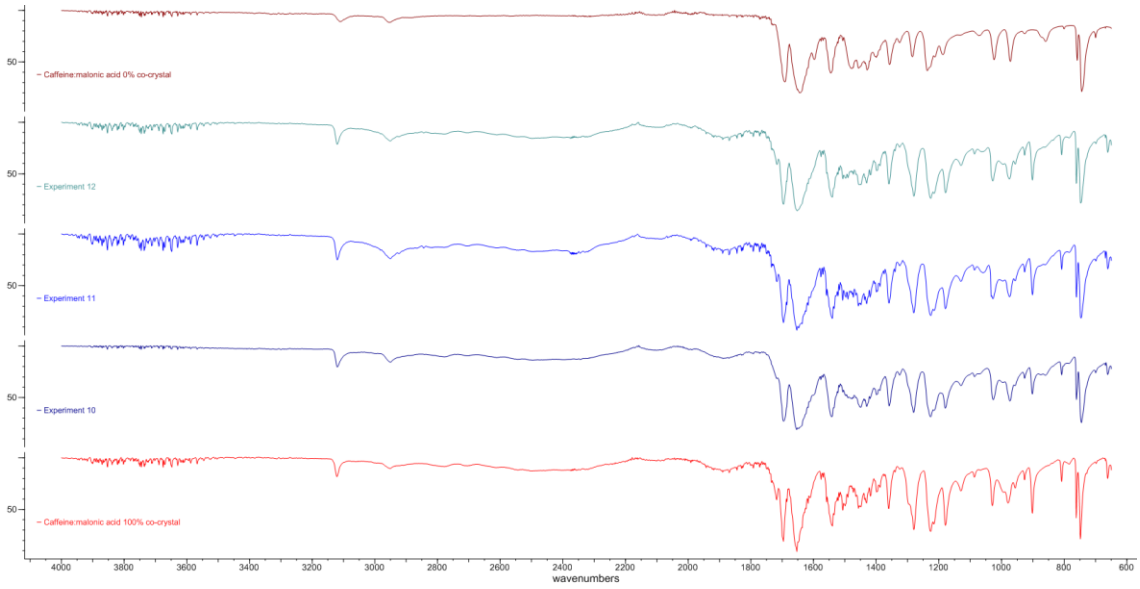


*Figure 7. Measured IR spectra of samples from experiments: 10 (dark blue), 11 (blue) and 12 (teal), with spectra of caffeine:malonic acid standards containing: 0% co-crystal (brown) and 100% co-crystal (red), for reference.*

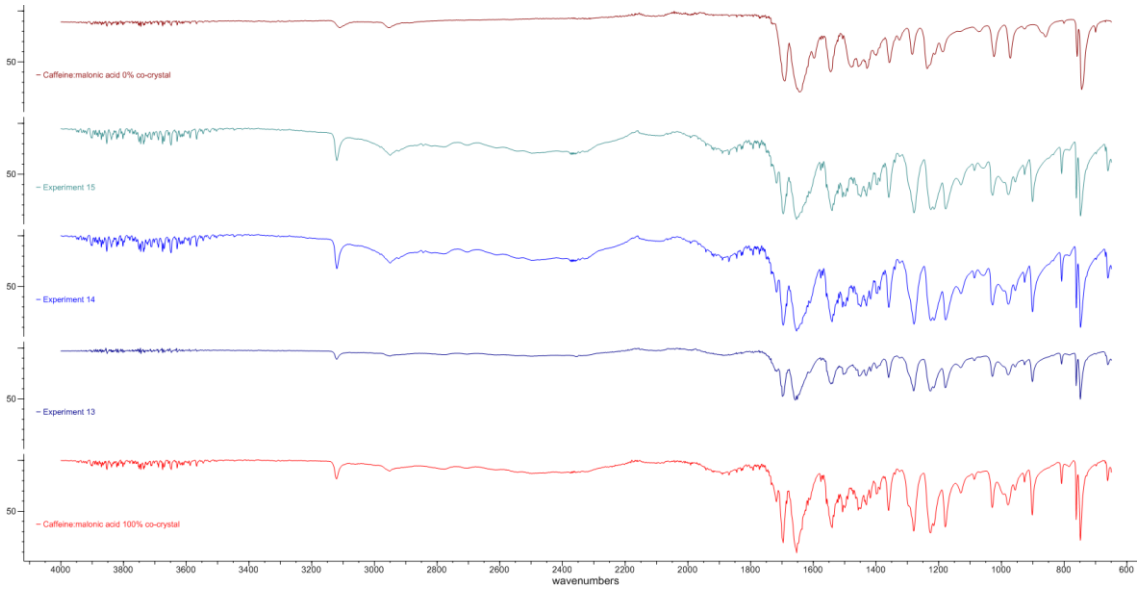


*Figure 8. Measured IR spectra of samples from experiments: 13 (dark blue), 14 (blue) and 15 (teal), with spectra of caffeine:malonic acid standards containing: 0% co-crystal (brown) and 100% co-crystal (red), for reference.*

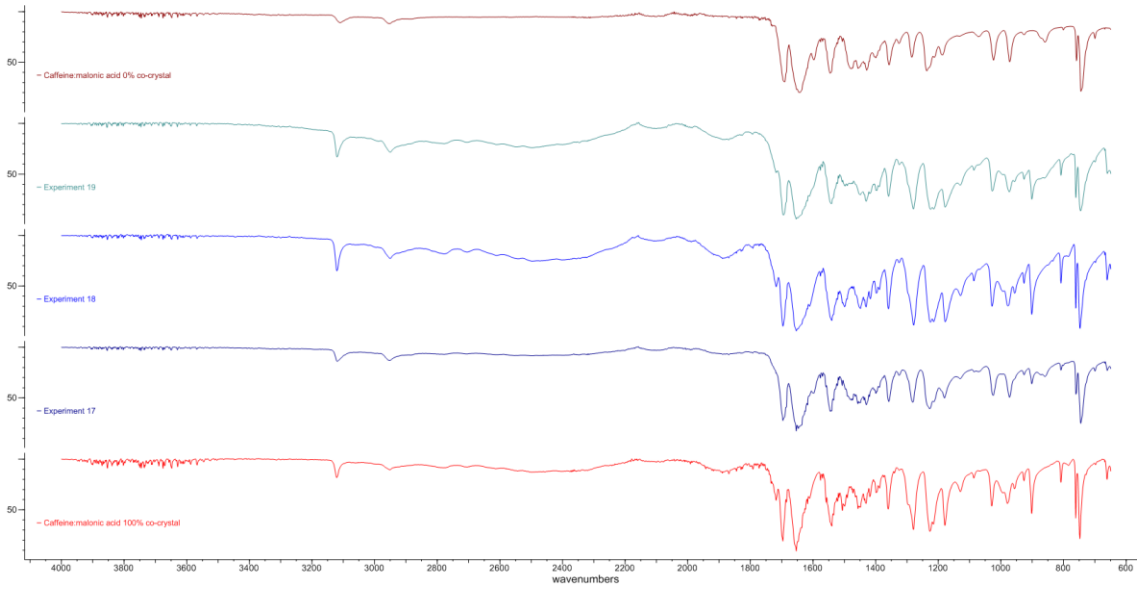


*Figure 9. Measured IR spectra of samples from experiments: 17 (dark blue), 18 (blue) and 19 (teal), with spectra of caffeine:malonic acid standards containing: 0% co-crystal (brown) and 100% co-crystal (red), for reference.*

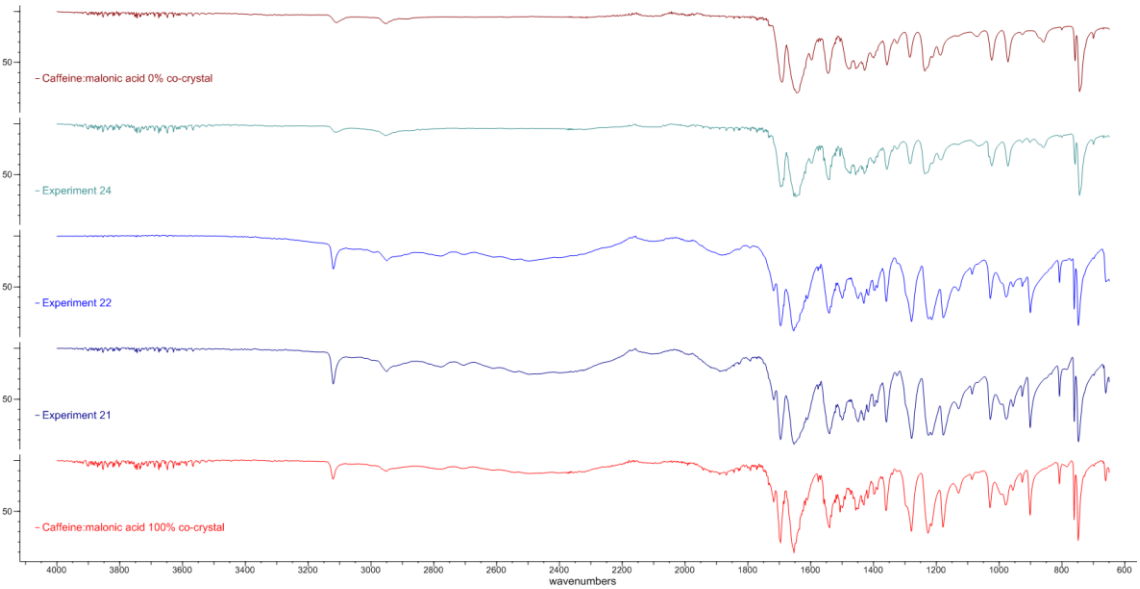


*Figure 10. Measured IR spectra of samples from experiments: 21 (dark blue), 22 (blue) and 24 (teal), with spectra of caffeine:malonic acid standards containing: 0% co-crystal (brown) and 100% co-crystal (red), for reference.*

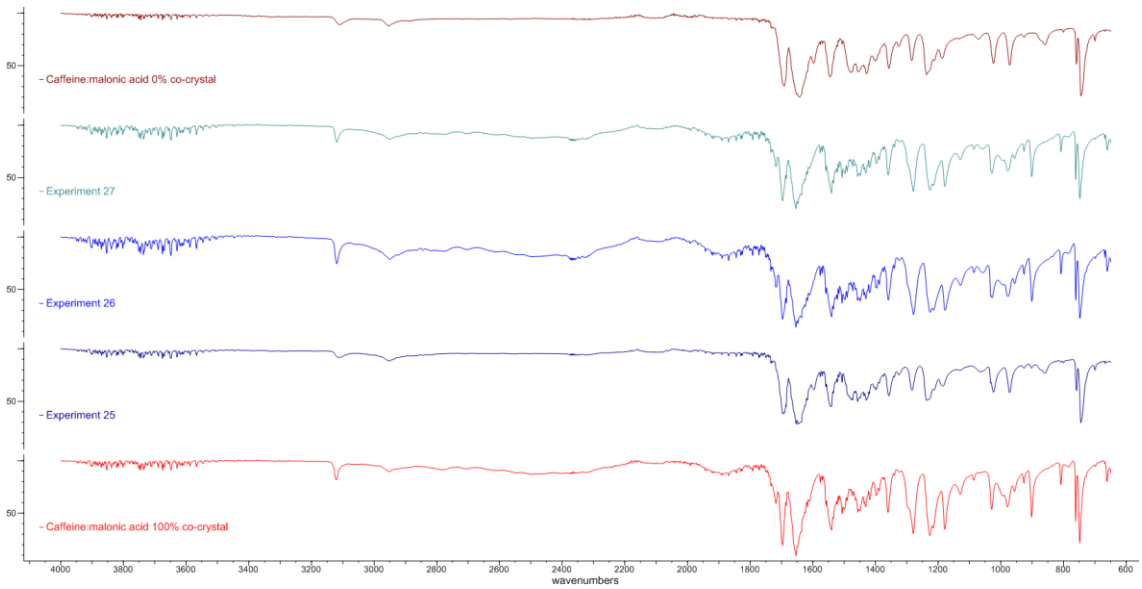


*Figure 11. Measured IR spectra of samples from experiments: 25 (dark blue), 26 (blue) and 27 (teal), with spectra of caffeine:malonic acid standards containing: 0% co-crystal (brown) and 100% co-crystal (red), for reference.*

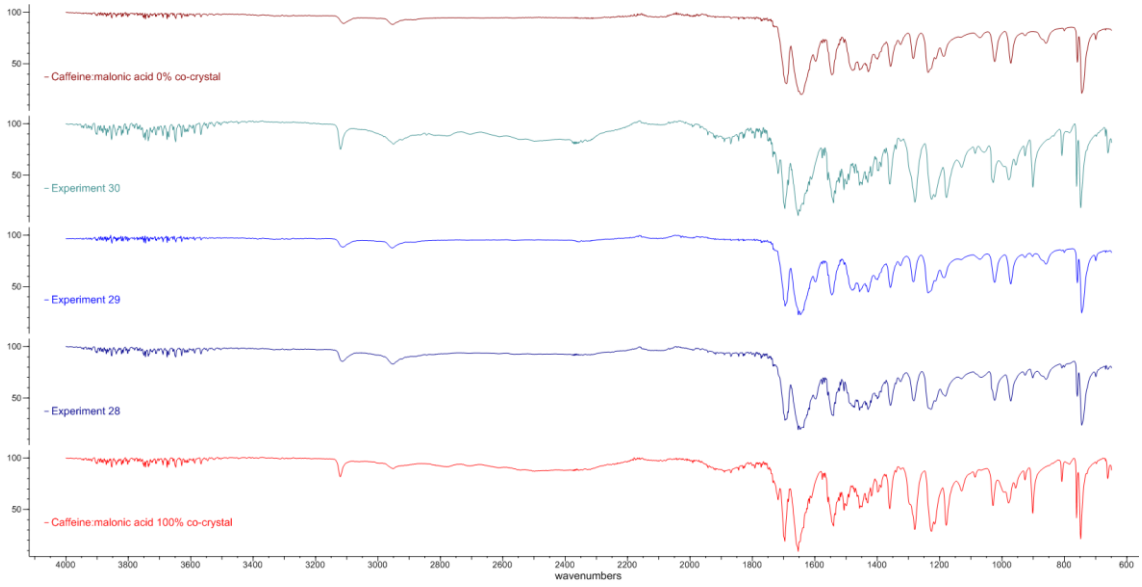


*Figure 12. Measured IR spectra of samples from experiments: 28 (dark blue), 29 (blue) and 30 (teal), with spectra of caffeine:malonic acid standards containing: 0% co-crystal (brown) and 100% co-crystal (red), for reference.*

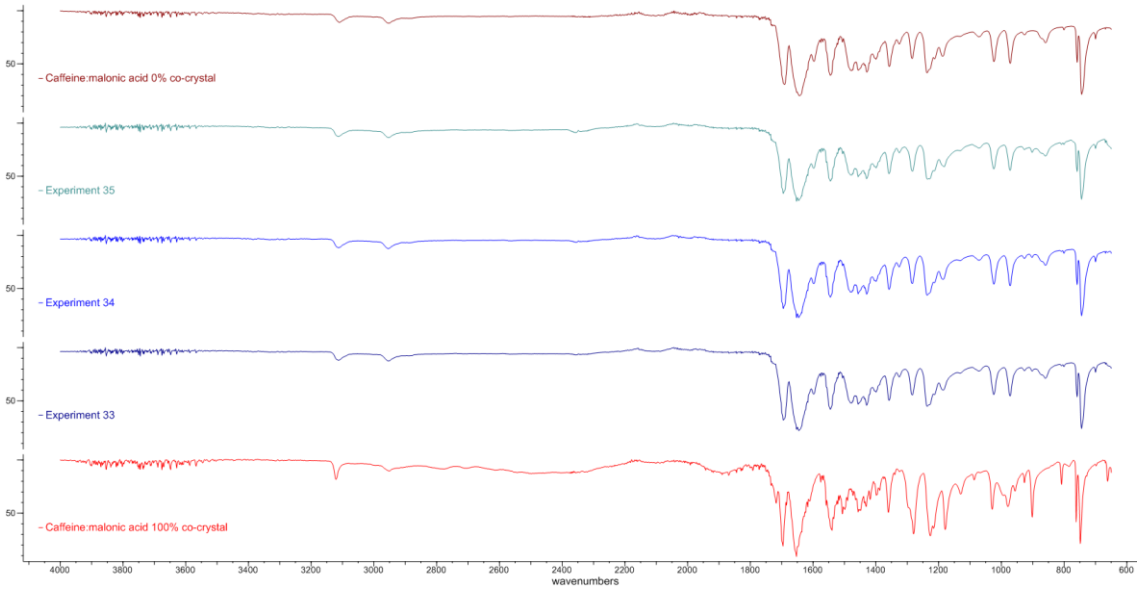


*Figure 13. Measured IR spectra of samples from experiments: 33 (dark blue), 34 (blue) and 35 (teal), with spectra of caffeine:malonic acid standards containing: 0% co-crystal (brown) and 100% co-crystal (red), for reference.*

## 3.3 DOE contour plots

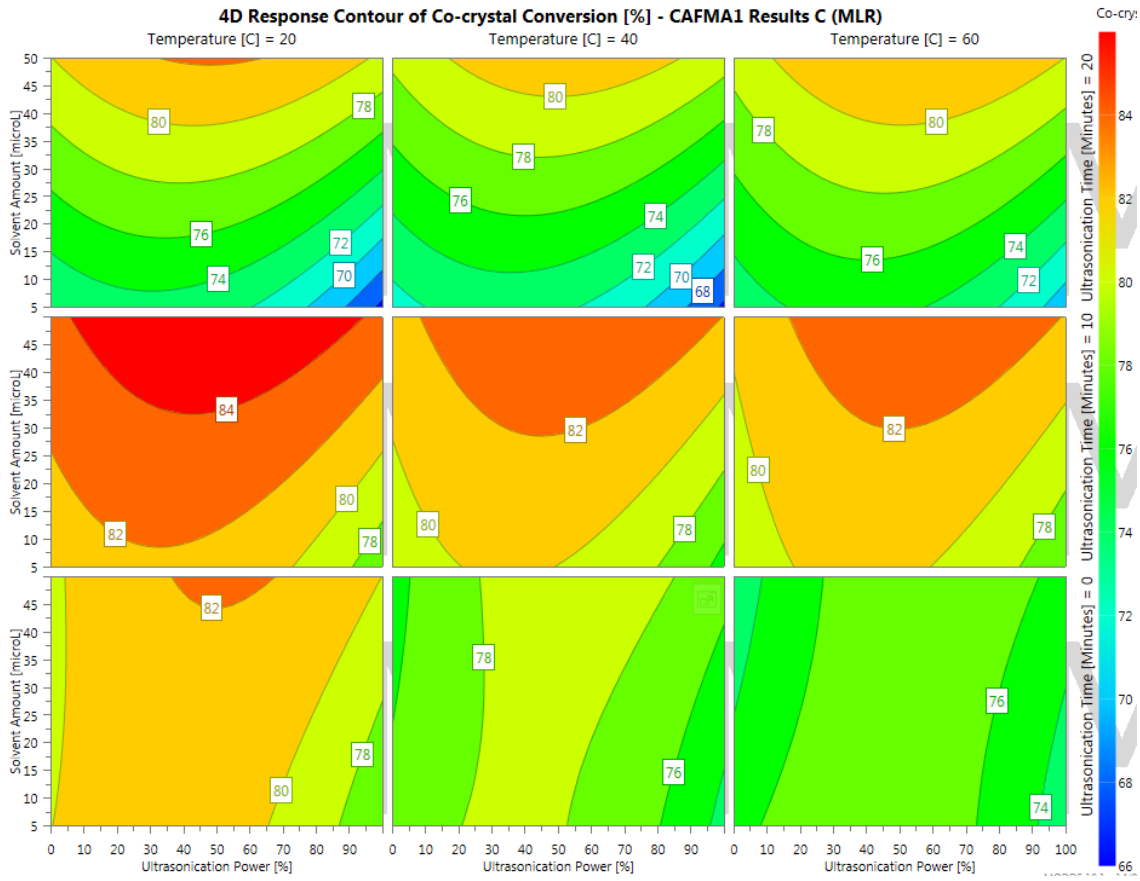


*Figure 14. A 4D contour plot showing the relationship between temperature, solvent amount, ultrasonication power and time, on the conversion of starting material to co-crystal, with the acetone as the solvent.*

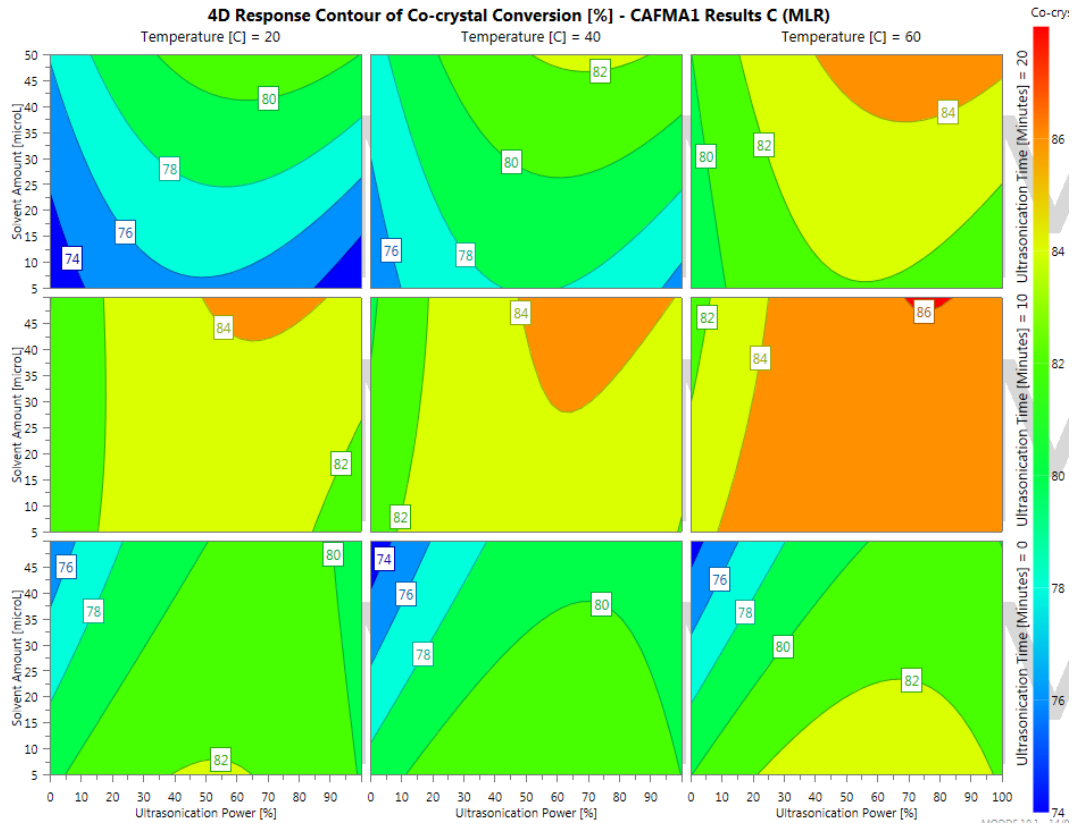


*Figure 15. A 4D contour plot showing the relationship between temperature, solvent amount, ultrasonication power and time, on the conversion of starting material to co-crystal, with the ethanol as the solvent.*

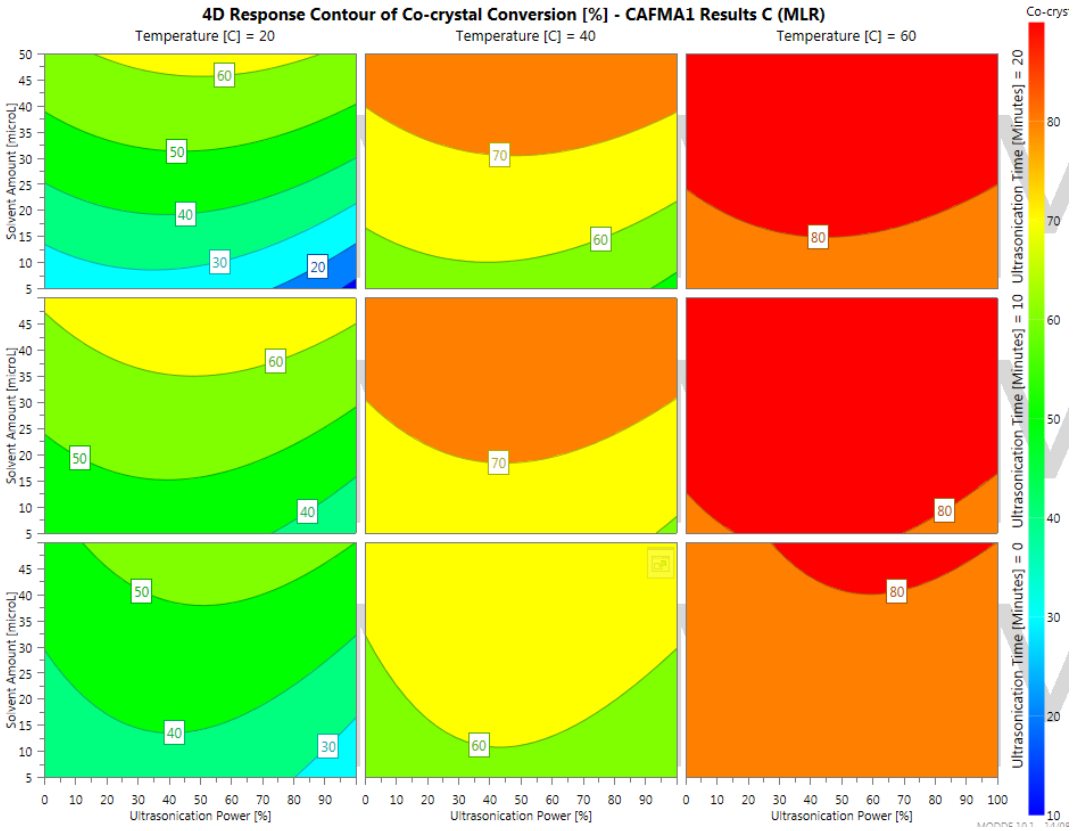


*Figure 16. A 4D contour plot showing the relationship between temperature, solvent amount, ultrasonication power and time, on the conversion of starting material to co-crystal, with the hexane as the solvent.*

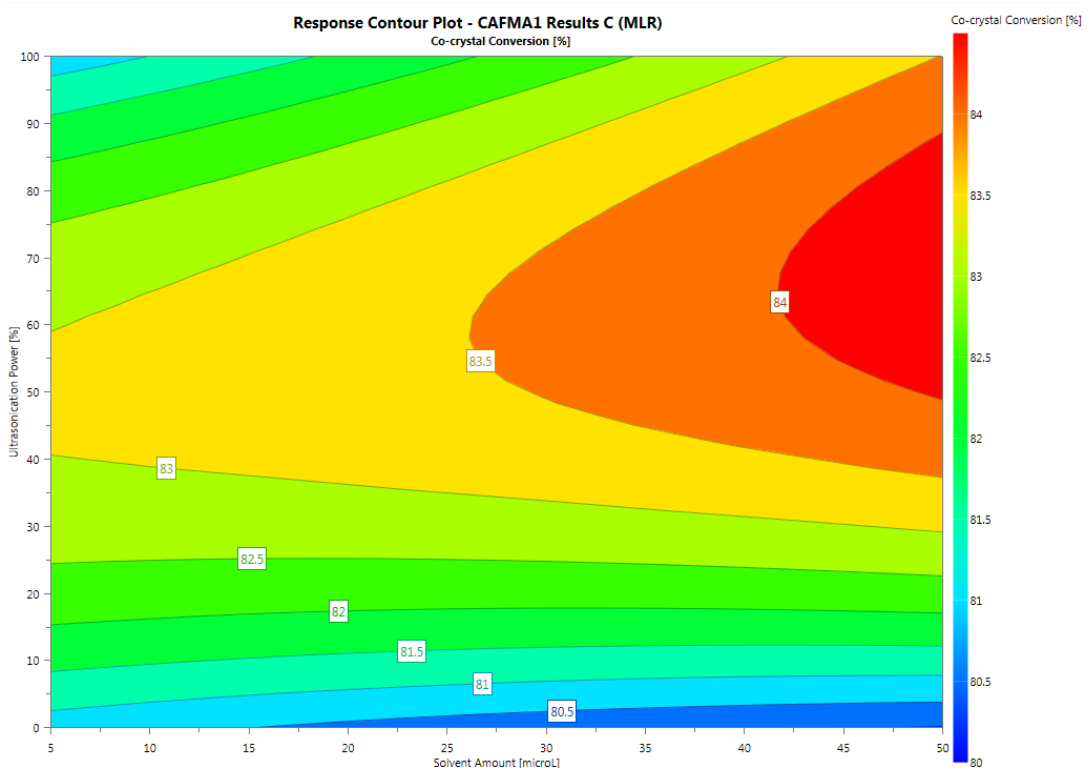


*Figure 17. A contour plot showing the relationship between ultrasonication power and solvent amount on the conversion of starting material to co-crystal when using ethanol as the solvent, with all other parameters fixed at their optimum levels, showing the best possible response in the plot area. Ultrasonication time: 10 minutes, Temperature: 20°C, Solvent: ethanol.*

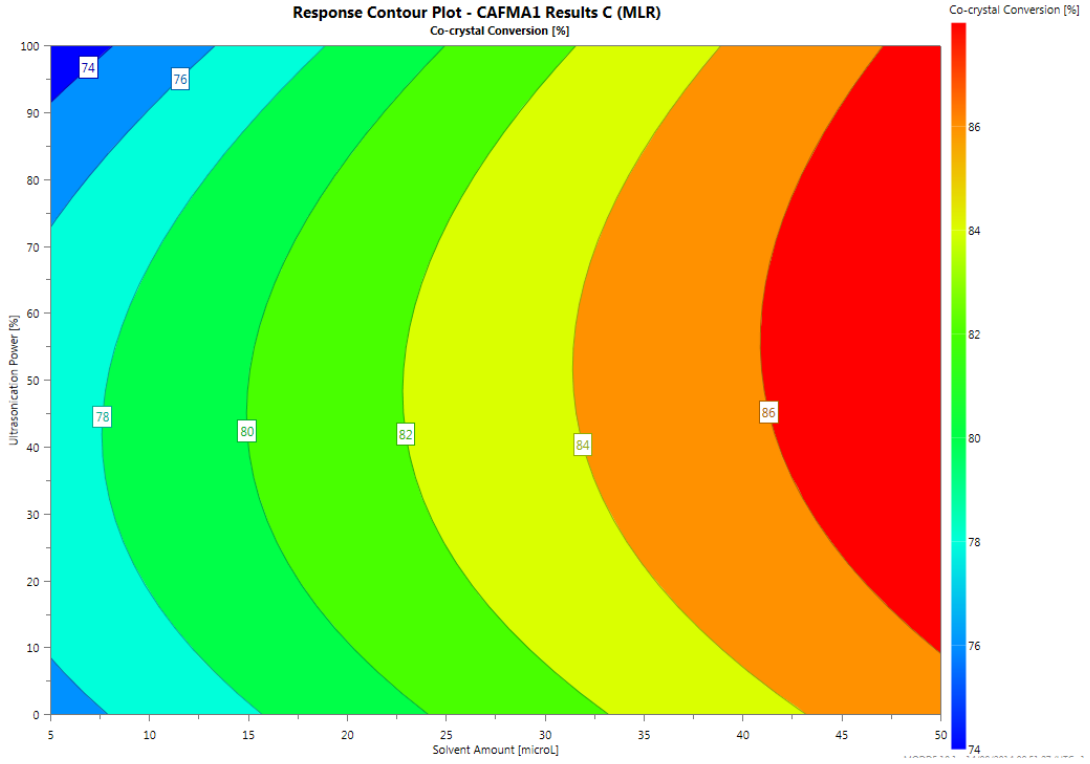


*Figure 18. A contour plot showing the relationship between ultrasonication power and solvent amount on the conversion of starting material to co-crystal when using hexane as the solvent, with all other parameters fixed at their optimum levels, showing the best possible response in the plot area. Ultrasonication time: 20 minutes, Temperature: 60°C, Solvent: hexane.*

## 3.4 List of previously determined co-crystal systems and production methods.

Unpublished work supplied by Dr David Berry, Durham University.

*Table 1. Confirmed co-crystal production by different methods of manufacture.*

| API | Co-former | Reaction Crystallisation | Liquid assisted grinding | Crystallisation from melt | Liquid assisted sonication |
|---|---|---|---|---|---|
| Caffeine | Oxalic Acid | Y | Y | Y | Y |
| Caffeine | Maleic Acid | Y | Y | Y | Y |
| Caffeine | Malonic Acid | Y | Y | N | Y |
| Caffeine | Glutaric Acid | Y | Y | ? | Y |
| Sulfamethazine | Aspirin | Y | Y | N | Y |
| Sulfamethazine | Benzoic Acid | Y | Y | N | Y |
| Trimethoprim | Sulfamethoxypyridazine | Y | N | N | Y |
| Carbamazepine | Saccharin | Y | Y | N | Y |
| Carbamazepine | Nicotinamide | Y | Y | Y | Y |
| Paracetamol | 4,4-bipyridyl | Y | Y | Y | Y |
| Aspirin | 4,4-bipyridyl | Y | Y | N | Y |
| Ibuprofen | 4,4-bipyridyl | Y | Y | Y | Y |
| Ibuprofen | Nicotinamide | ? | Y | ? | Y |

## 3.5 IR spectra of validation APIs, co-formers and experimental samples

Each figure shows the spectra of the API (red), the co-former (green), the product of applying the optimised physical screening process to a 1:1 molar ratio of the two components (blue) and 2:1 molar ratio (purple), where applicable. The figures are labelled by API and co-former.

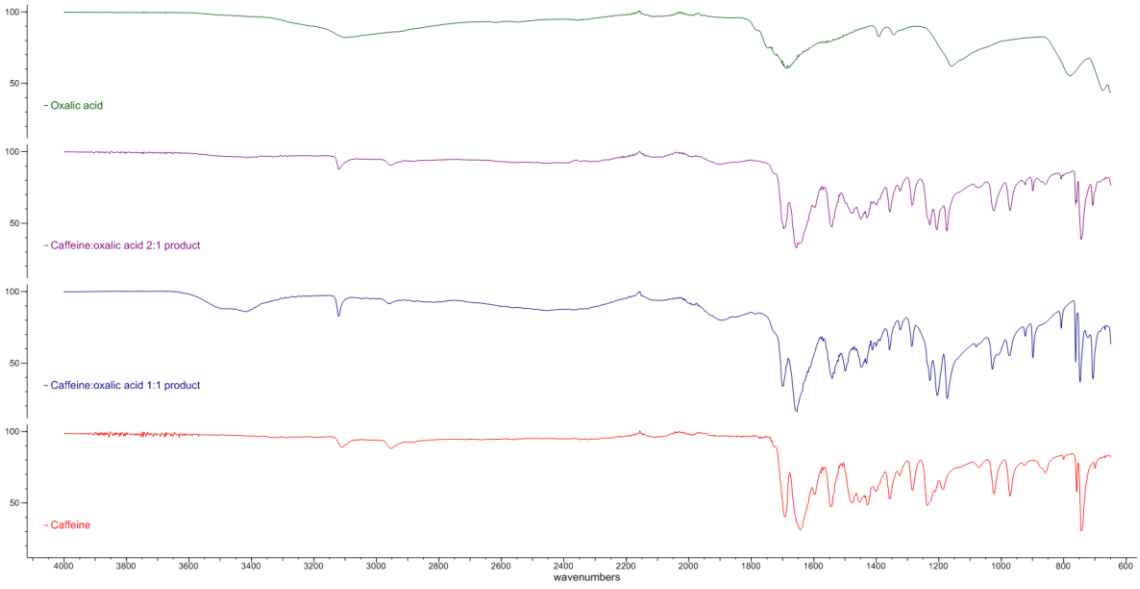


*Figure 19. Caffeine and oxalic acid.*

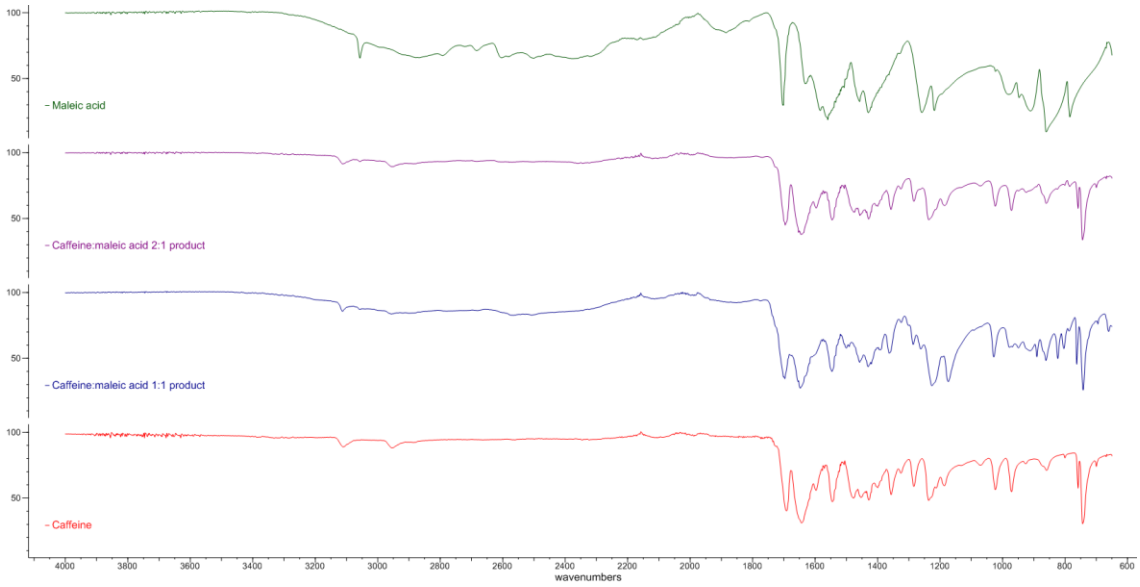


*Figure 20. Caffeine and maleic acid.*

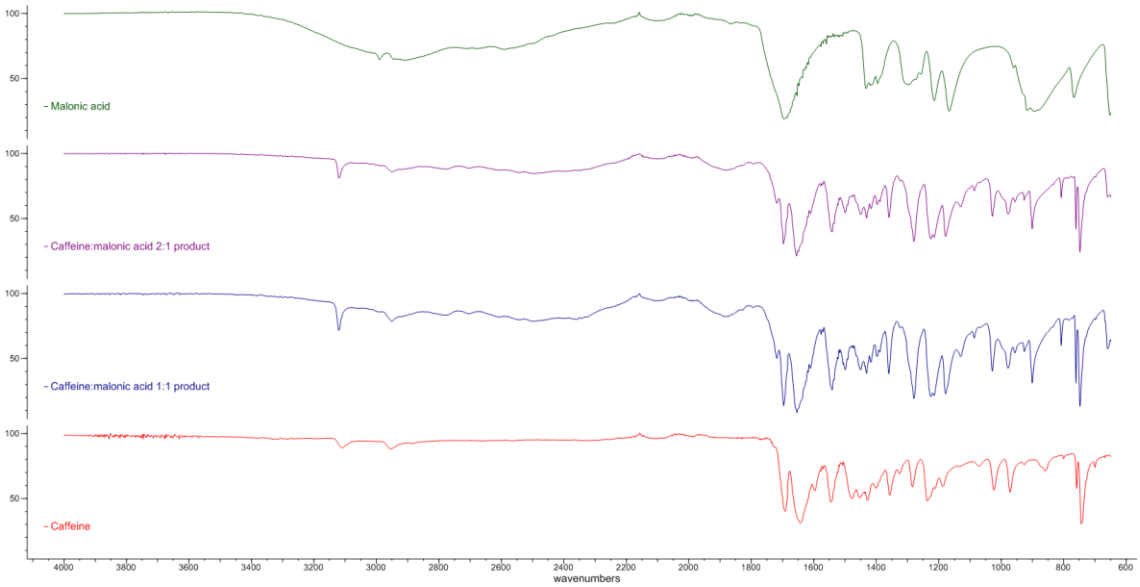


*Figure 21. Caffeine and malonic acid.*

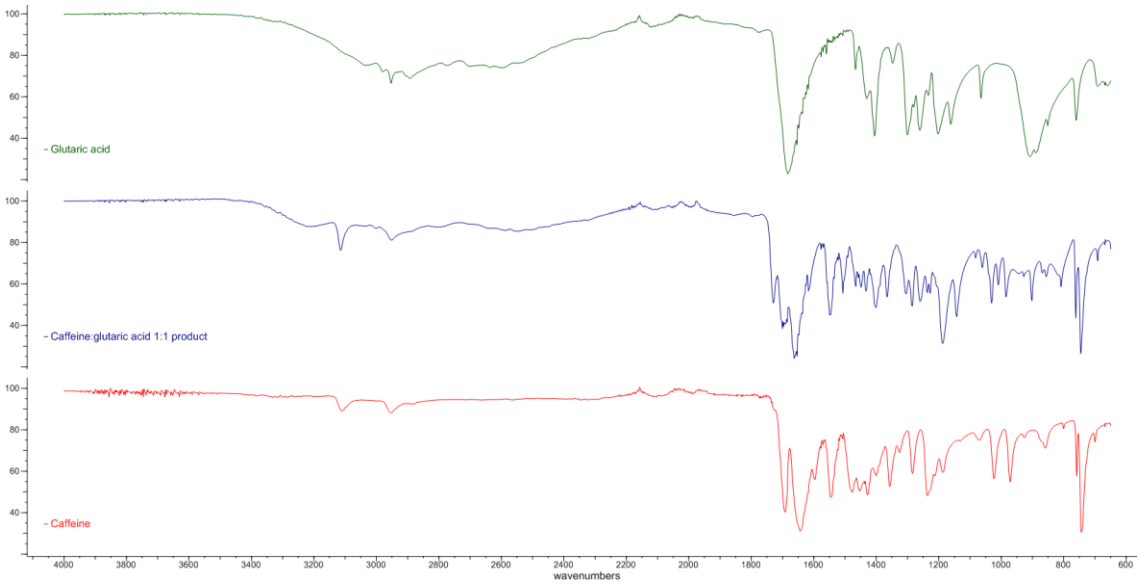


*Figure 22. Caffeine and glutaric acid.*

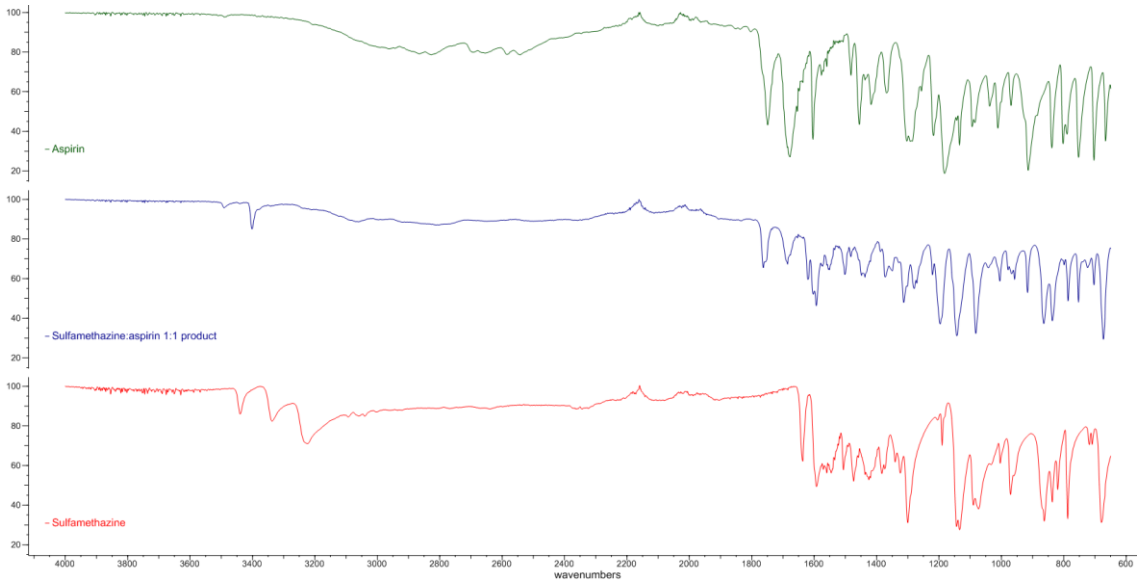


*Figure 23. Sulfamethazine and aspirin.*

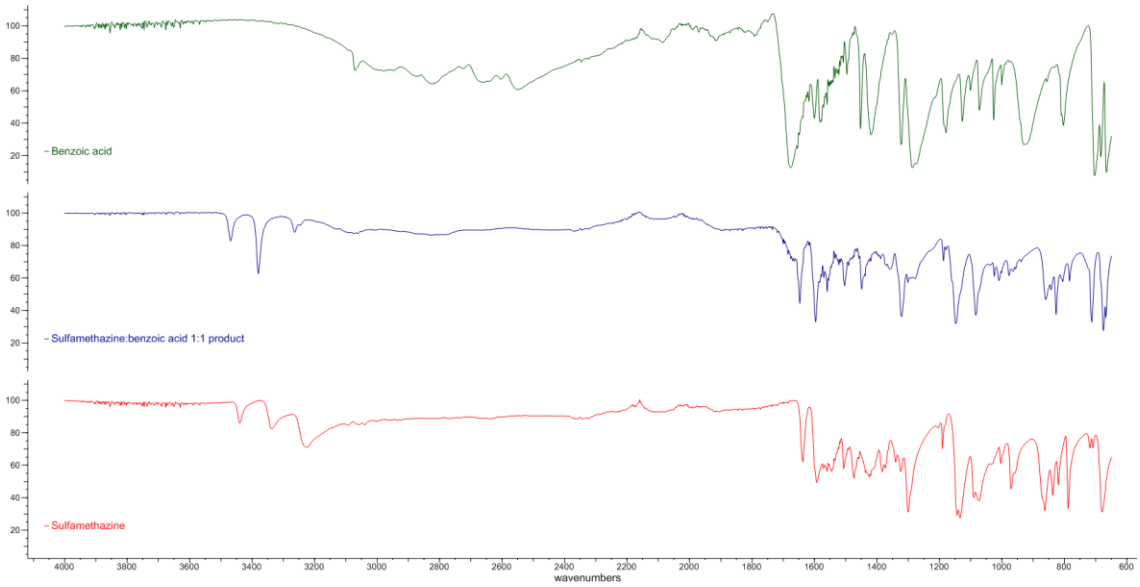


*Figure 24. Sulfamethazine and benzoic acid.*

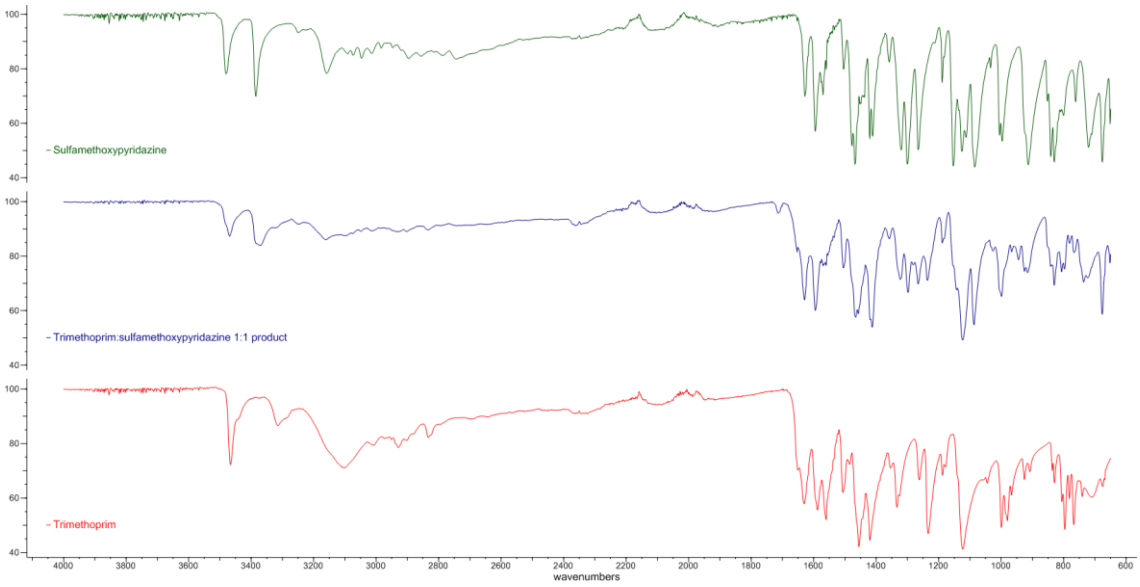


*Figure 25. Trimethoprim and sulfamethoxypyridazine.*

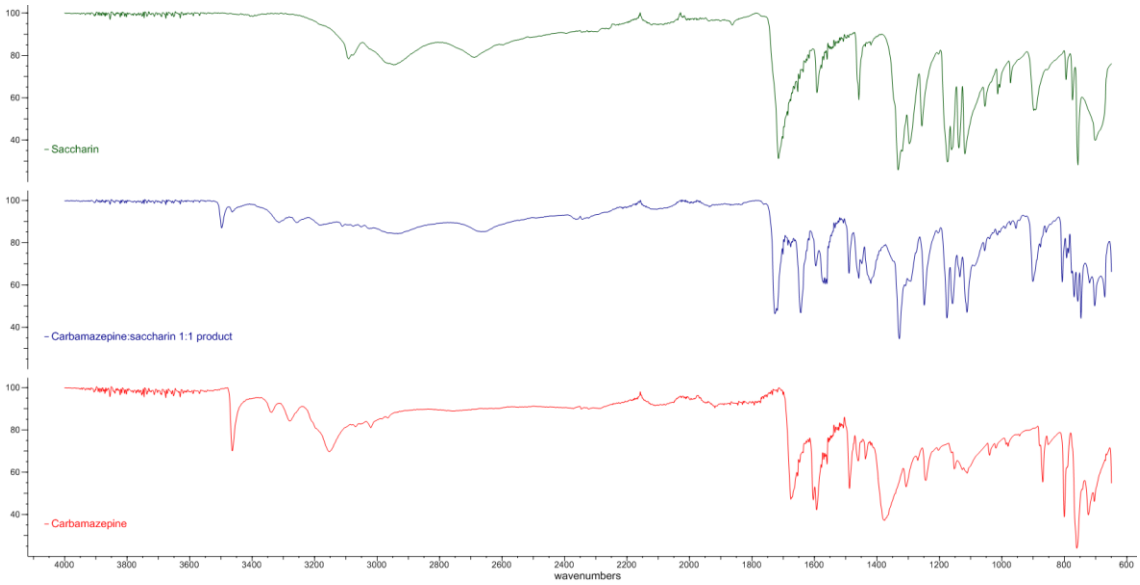


*Figure 26. Carbamazepine and saccharin.*

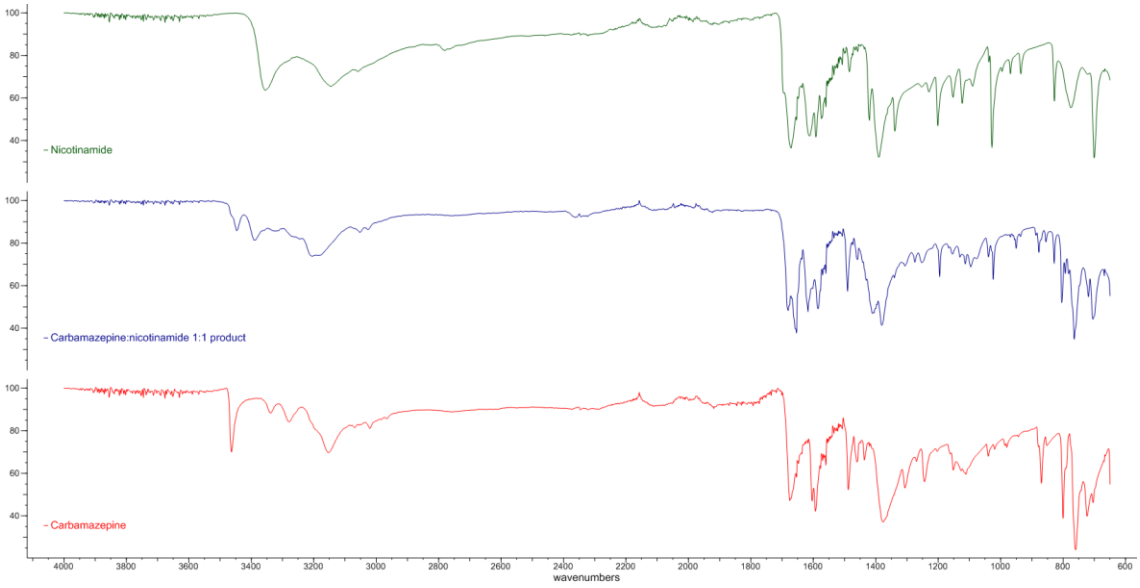


*Figure 27. Carbamazepine and nicotinamide.*

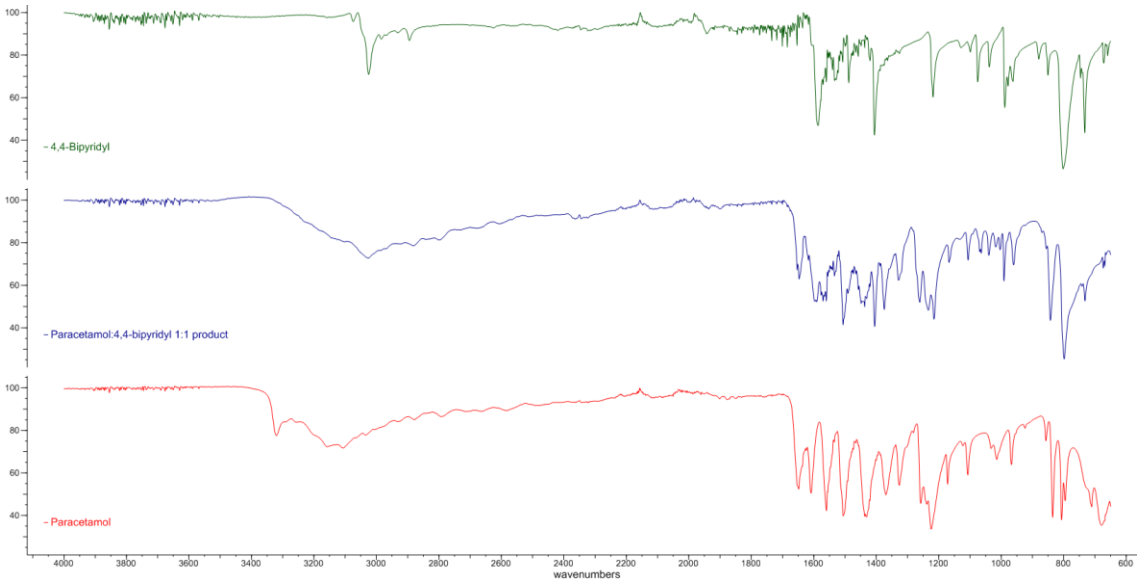


*Figure 28. Paracetamol and 4,4-bipyridine.*

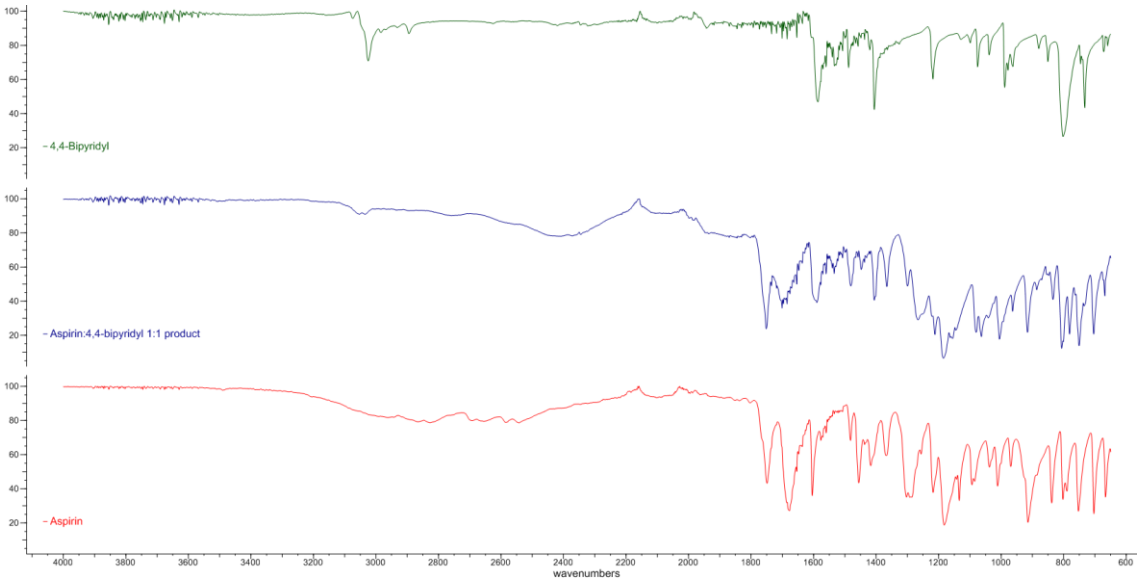


*Figure 29. Aspirin and 4,4-bipyridine.*

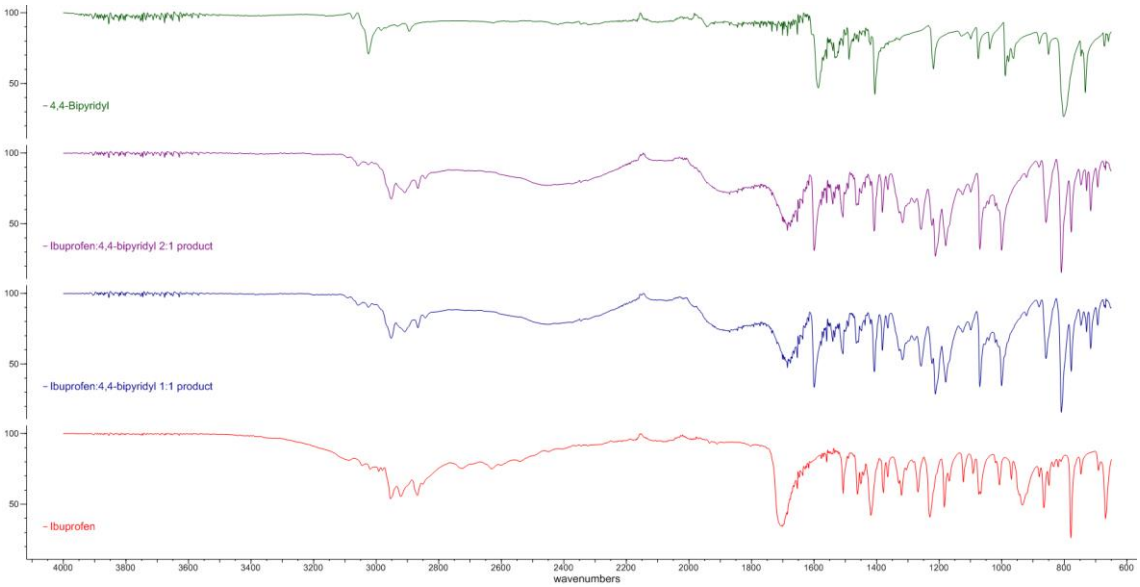


*Figure 30. Ibuprofen and 4,4-bipyridine.*

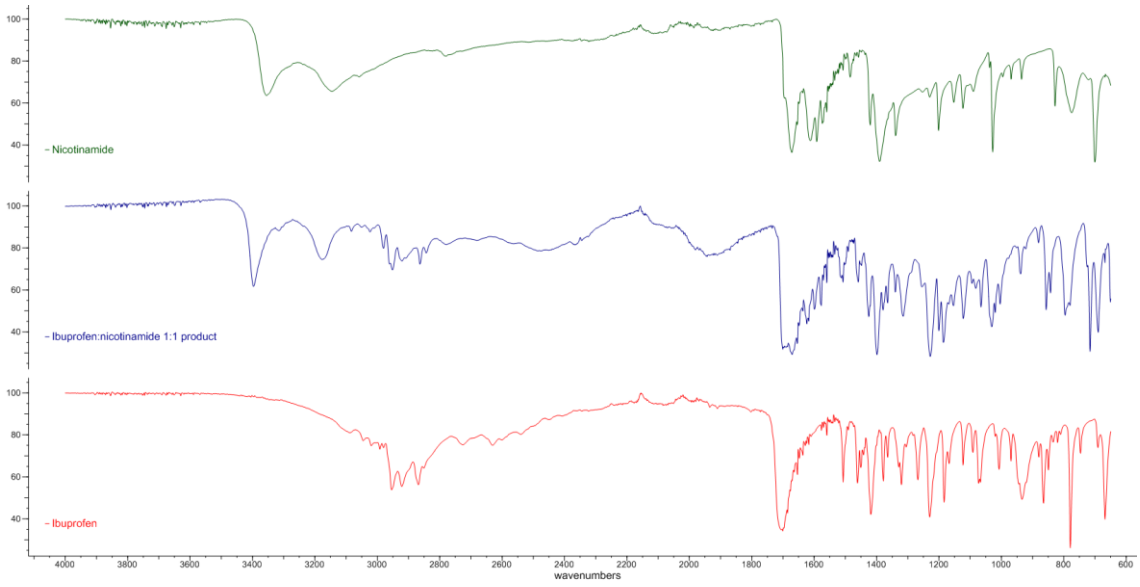


*Figure 31. Ibuprofen and nicotinamide.*

## 3.6 PXRD patterns of ornidazole, select co-formers and samples from the second DOE optimisation experiment

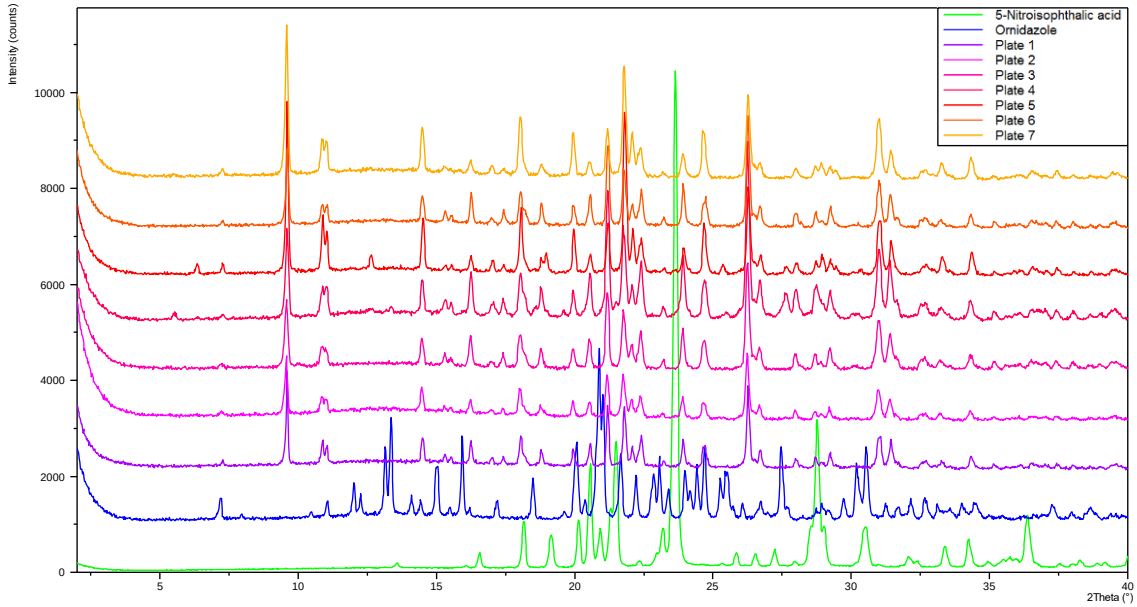


*Figure 32. PXRD patterns of ornidazole, 5-nitroisophthalic acid and the experimental samples from Well A1 of Plates 1 to 7 (co-former: 5-nitroisothalic acid; solvent: acetonitrile).*

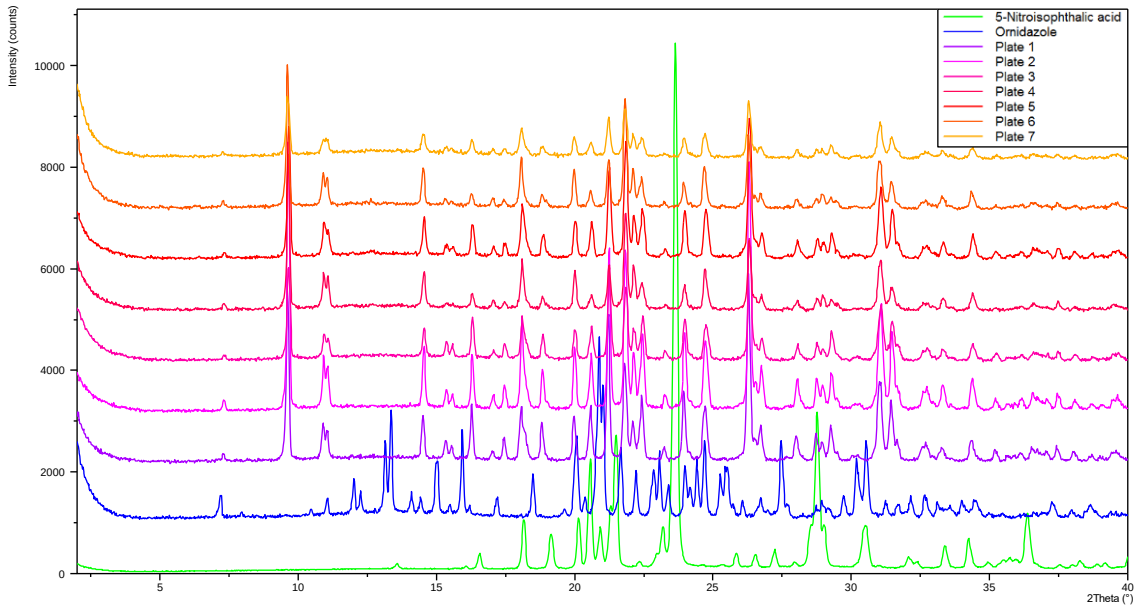


*Figure 33. PXRD patterns of ornidazole, 5-nitroisophthalic acid and the experimental samples from Well B1 of Plates 1 to 7 (co-former: 5-nitroisothalic acid; solvent: ethanol).*

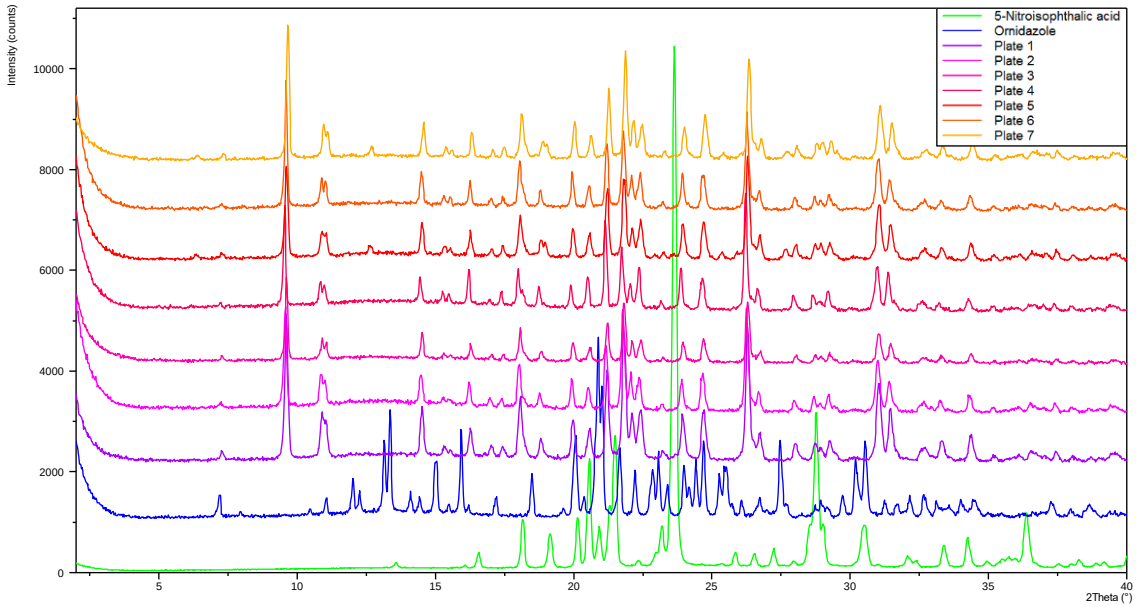


*Figure 34. PXRD patterns of ornidazole, 5-nitroisophthalic acid and the experimental samples from Well A2 of Plates 1 to 7 (co-former: 5-nitroisothalic acid; solvent: THF).*

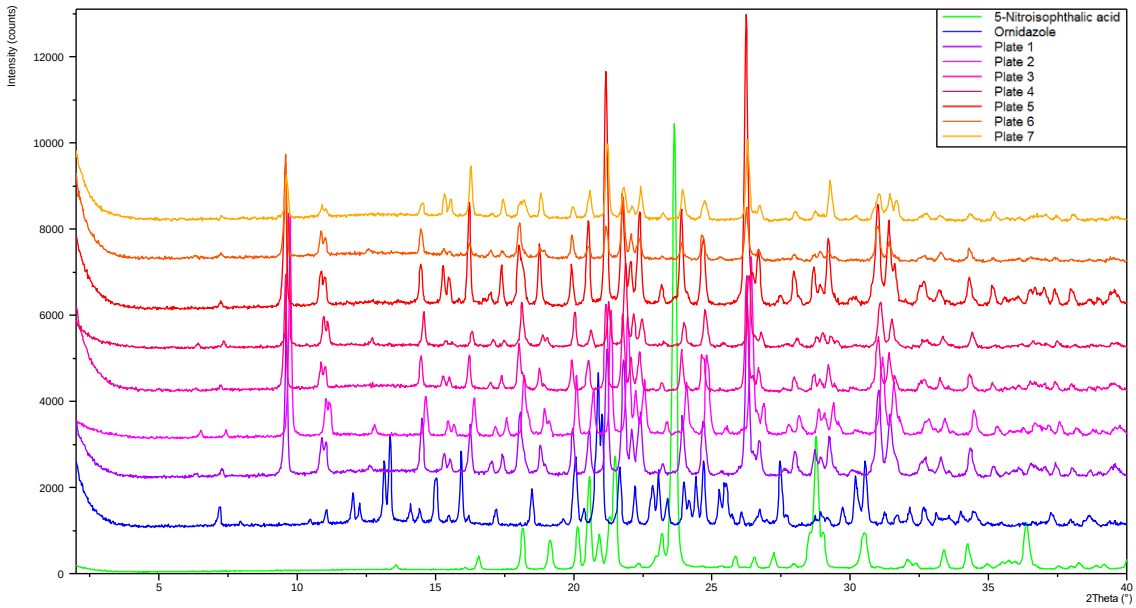


*Figure 35. PXRD patterns of ornidazole, 5-nitroisophthalic acid and the experimental samples from Well B2 of Plates 1 to 7 (co-former: 5-nitroisothalic acid; solvent: toluene).*

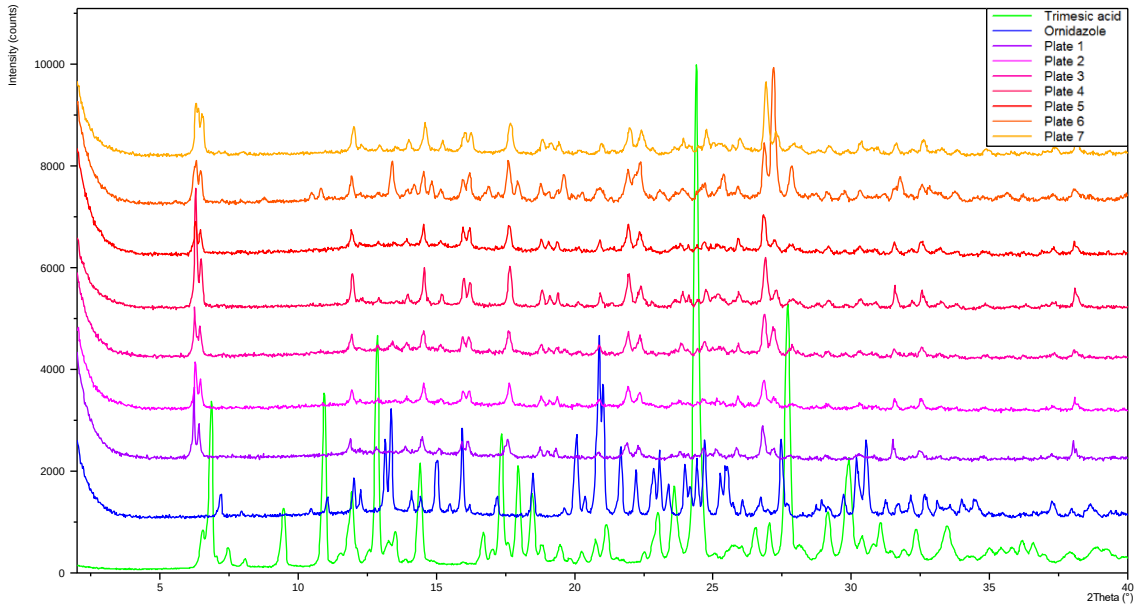


*Figure 36. PXRD patterns of ornidazole, trimesic acid and the experimental samples from Well G1 of Plates 1 to 7 (co-former: trimesic acid; solvent: acetonitrile).*

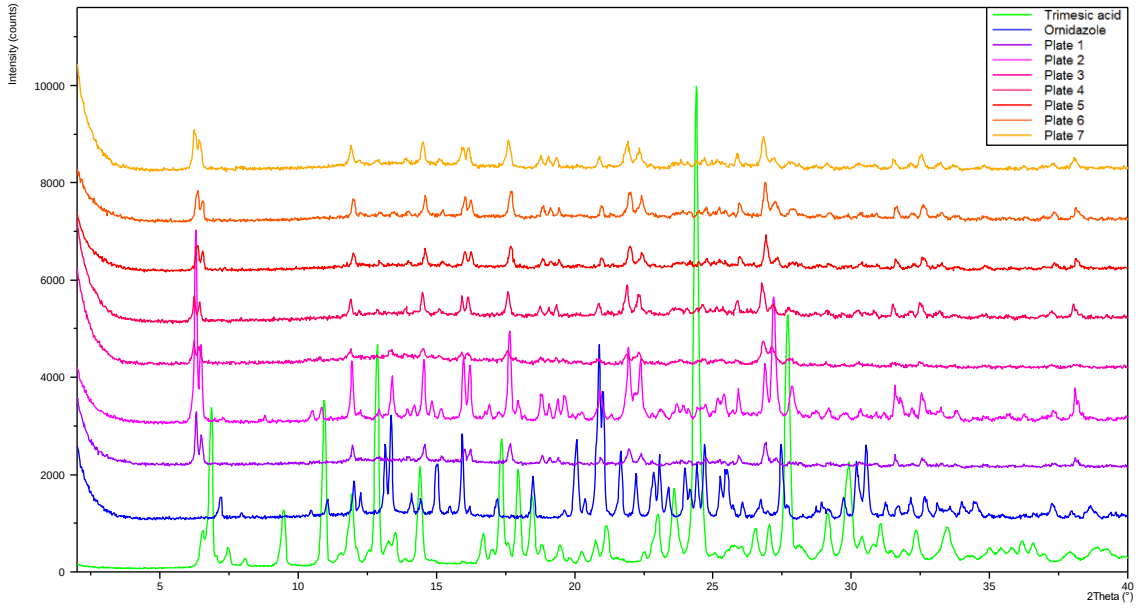


*Figure 37. PXRD patterns of ornidazole, trimesic acid and the experimental samples from Well H1 of Plates 1 to 7 (co-former: trimesic acid; solvent: ethanol).*

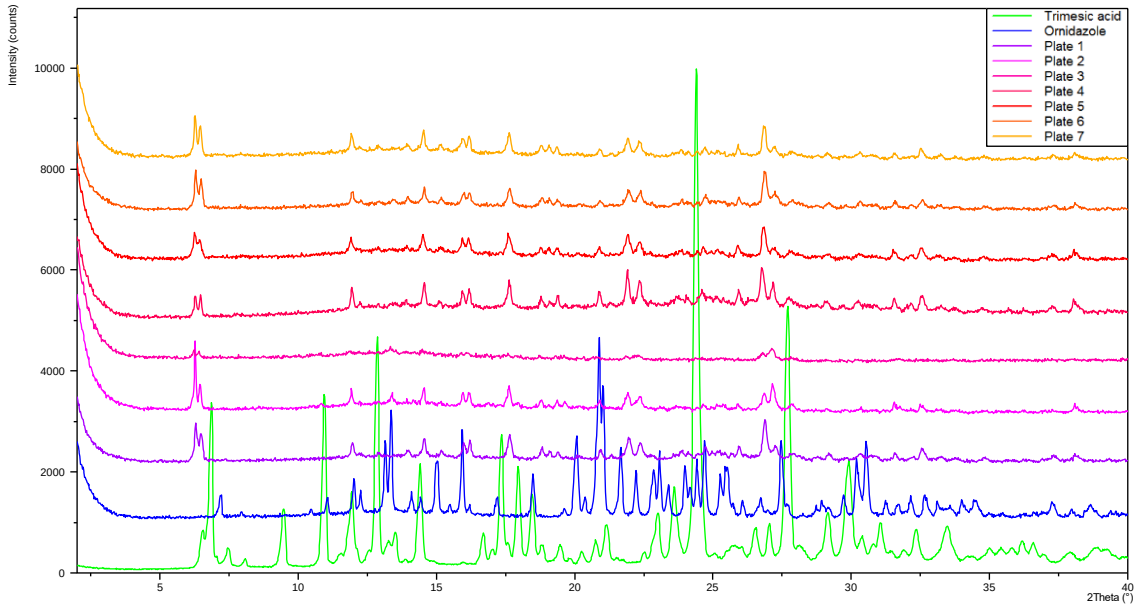


*Figure 38. PXRD patterns of ornidazole, trimesic acid and the experimental samples from Well G2 of Plates 1 to 7 (co-former: trimesic acid; solvent: THF).*

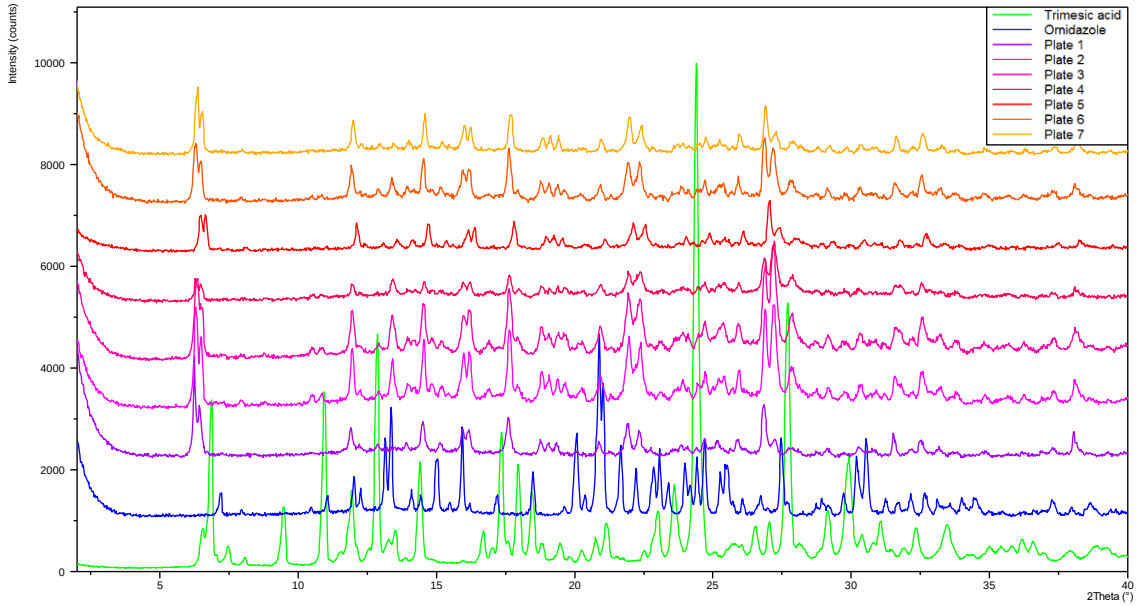


*Figure 39. PXRD patterns of ornidazole, trimesic acid and the experimental samples from Well H2 of Plates 1 to 7 (co-former: trimesic acid; solvent: toluene).*

## 3.7 DOE model summary plots

Model summaries for ornidazole:5-nitroisophthalic acid and ornidazole:trimesic acid data based on measured responses: FWHM, net peak height and calculated FWHM:peak height value. One model for each response for both co-formers, six summaries in total, each as follows: Clockwise from top left: Replicates (results of repeated experiments shown by blue squares), summary of fit ($R^2$ (green), $Q^2$ (dark blue), model validity (yellow) and reproducibility (light blue)), residuals and coefficients.

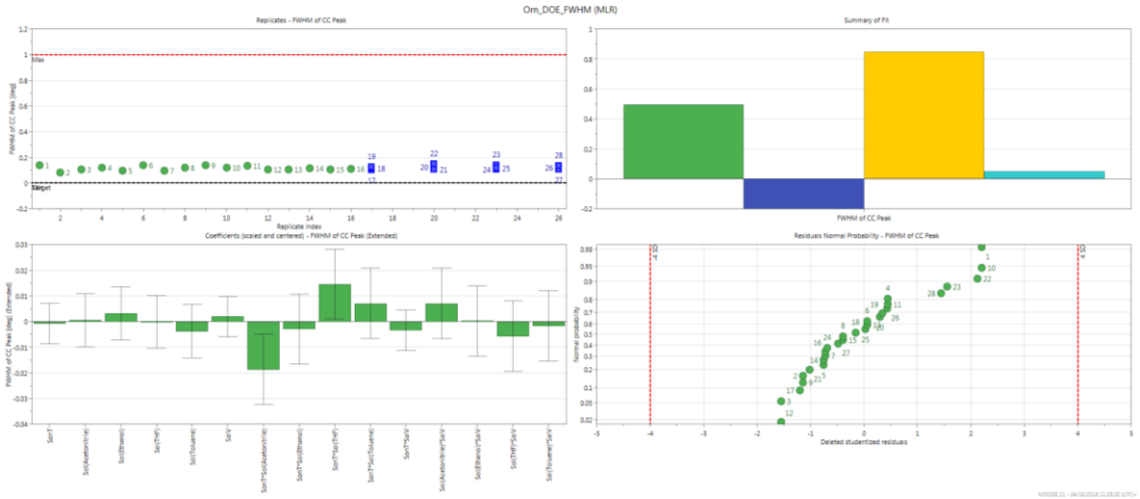


*Figure 40. Model summary for ornidazole:5-nitroisophthalic acid based on measured FWHM.*

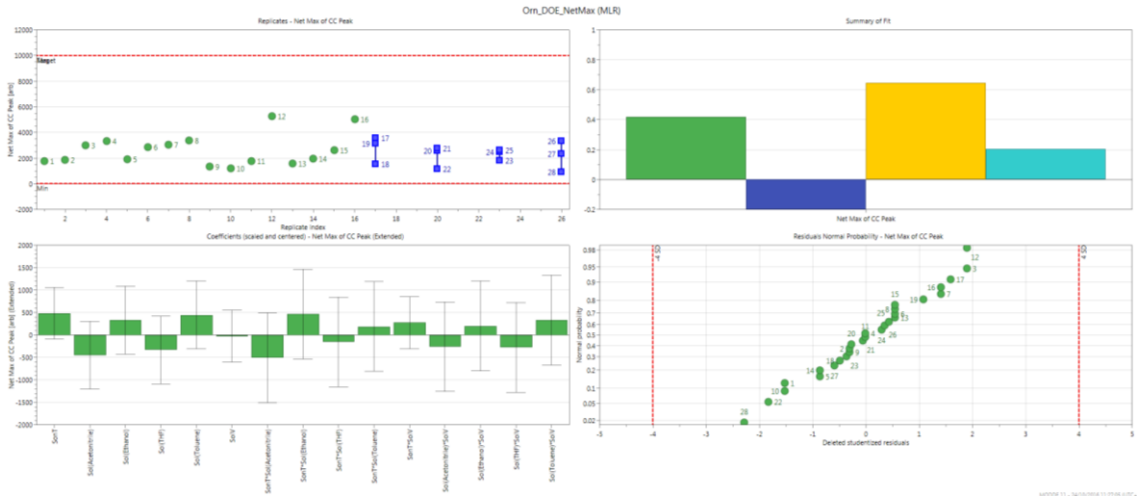


*Figure 41. Model summary for ornidazole:5-nitroisophthalic acid based on measured net peak height.*

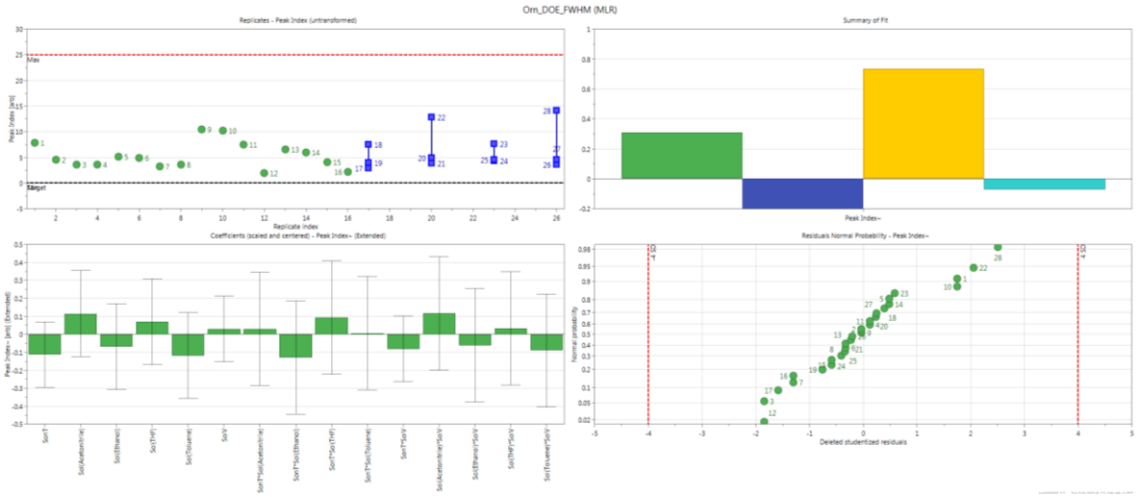


*Figure 42. Model summary for ornidazole:5-nitroisophthalic acid based on calculated FWHM:peak value.*

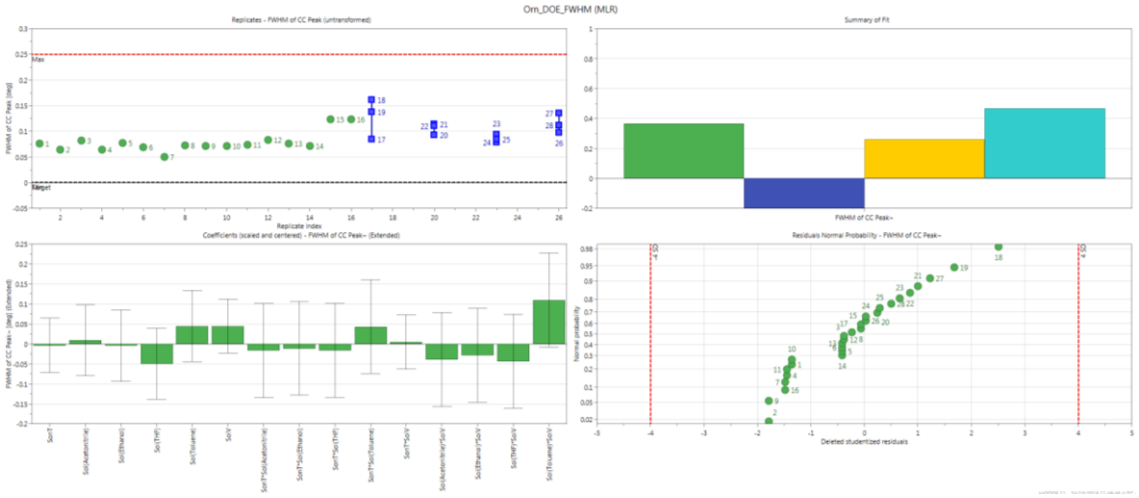


*Figure 43. Model summary for ornidazole:trimesic acid based on measured FWHM.*

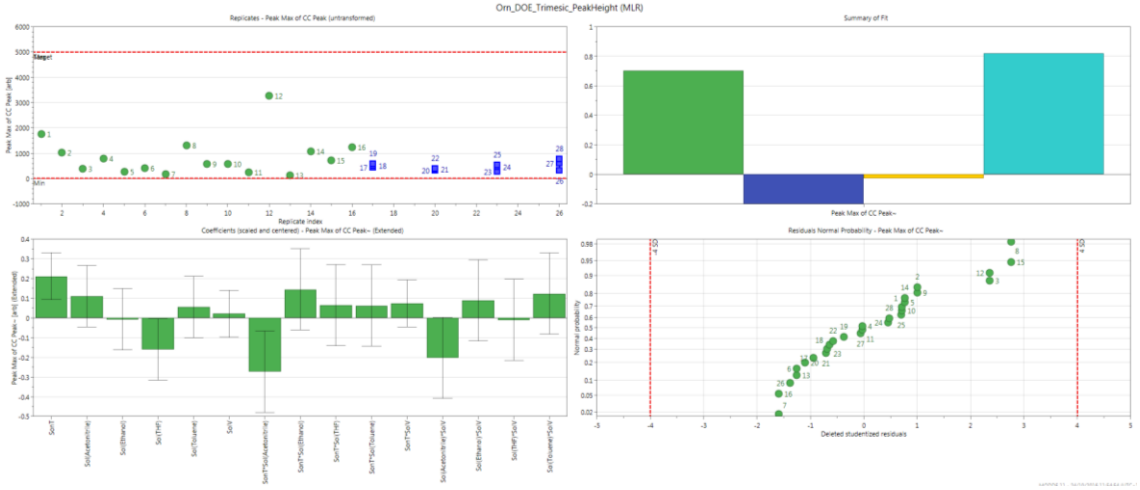


*Figure 44. Model summary for ornidazole:trimesic acid based on measured net peak height.*

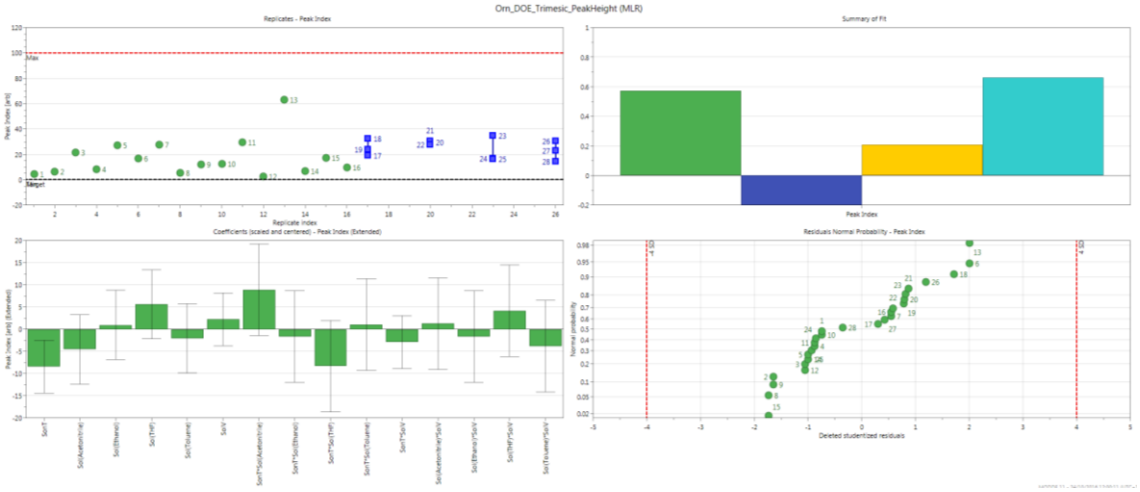


*Figure 45. Model summary for ornidazole:trimesic acid based on calculated FWHM:peak height value.*

# Appendix 4

## 4.1 Full list co-formers from the computational pre-screen for ROY

*Table 1. List of co-formers with excess enthalpy calculated for the given stoichiometry with ROY as produced by COSMOtherm.*

| Co-Former Name | ΔH / kJ.mol$^{-1}$ | Stoichiometry |
|---|---|---|
| Pentafluorophenol_c0 | -1.95304667 | "1:2" |
| Pentafluorophenol_c0 | -1.83812 | "1:1" |
| Acesulfame | -1.508955 | "1:1" |
| Acesulfame | -1.38306667 | "1:2" |
| Pentafluorophenol_c0 | -1.37965333 | "2:1" |
| OXALIC_ACID | -1.345755 | "1:1" |
| Quercetin | -1.296365 | "1:1" |
| Quercetin | -1.29356 | "2:1" |
| Acesulfame | -1.26151667 | "2:1" |
| OXALIC_ACID | -1.22758 | "2:1" |
| SULFAMIC_ACID | -1.22224 | "1:1" |
| 3_5_Dinitrobenzoic_Acid | -1.19337 | "1:1" |
| OXALIC_ACID | -1.1712 | "1:2" |
| 1,2,3-Trihydroxybenzene | -1.144635 | "1:1" |
| SULFAMIC_ACID | -1.12732333 | "2:1" |
| SULFAMIC_ACID | -1.08531667 | "1:2" |
| 3_5_Dinitrobenzoic_Acid | -1.06875333 | "1:2" |
| 2,4-dihydroxybenzoic_acid | -1.04422 | "1:1" |
| 3_5_Dinitrobenzoic_Acid | -1.04109333 | "2:1" |
| 5-nitroisophthalic_acid | -1.036695 | "1:1" |
| Quercetin | -1.03450333 | "1:2" |
| Gallic_acid | -1.031715 | "1:1" |
| 1,2,3-Trihydroxybenzene | -1.03138333 | "2:1" |
| TERT-BUTYLHYDROQUINONE | -1.02651 | "1:1" |
| 5-nitroisophthalic_acid | -0.99448 | "2:1" |
| 1-hydroxy-2-naphthoic_acid | -0.99384 | "1:1" |
| Catechol | -0.98762 | "1:1" |
| 1,2,3-Trihydroxybenzene | -0.98737 | "1:2" |
| 4-Hexylresorcinol | -0.98664 | "1:1" |
| 1-hydroxy-2-naphthoic_acid | -0.95433 | "1:2" |
| 2,4-dihydroxybenzoic_acid | -0.95418667 | "2:1" |
| TERT-BUTYLHYDROQUINONE | -0.94342 | "1:2" |
| Gallic_acid | -0.942 | "2:1" |
| Catechol | -0.92858667 | "1:2" |
| 2,4-dihydroxybenzoic_acid | -0.90741 | "1:2" |
| 4-Hexylresorcinol | -0.90391667 | "1:2" |

| | | |
|---|---|---|
| 5-chlorosalicylic_acid | -0.902455 | "1:1" |
| Gallic_acid | -0.90101667 | "1:2" |
| RESORCINOL | -0.897925 | "1:1" |
| P-VINYLPHENOL_c0 | -0.89657 | "1:1" |
| P-VINYLPHENOL_c0 | -0.89029333 | "1:2" |
| TERT-BUTYLHYDROQUINONE | -0.87088 | "2:1" |
| 3,5-dihydroxybenzoic_acid | -0.86552 | "1:1" |
| 5-nitroisophthalic_acid | -0.86511 | "1:2" |
| 4-Hexylresorcinol | -0.84925667 | "2:1" |
| RESORCINOL | -0.83844 | "1:2" |
| 5-chlorosalicylic_acid | -0.8336 | "1:2" |
| Catechol | -0.82803667 | "2:1" |
| 3,5-dihydroxybenzoic_acid | -0.81828667 | "2:1" |
| 1-hydroxy-2-naphthoic_acid | -0.81693333 | "2:1" |
| RESORCINOL | -0.77271 | "2:1" |
| 5-chlorosalicylic_acid | -0.76804333 | "2:1" |
| Orcinol | -0.768 | "1:1" |
| 2,5-dihydroxybenzoic_acid | -0.762985 | "1:1" |
| gentisic_acid | -0.756395 | "1:1" |
| 3,5-dihydroxybenzoic_acid | -0.74557667 | "1:2" |
| P-VINYLPHENOL_c0 | -0.71876667 | "2:1" |
| Orcinol | -0.71534333 | "1:2" |
| 2,5-dihydroxybenzoic_acid | -0.69776667 | "2:1" |
| gentisic_acid | -0.69399333 | "2:1" |
| O-CRESOL | -0.68783 | "1:1" |
| O-CRESOL | -0.67925 | "1:2" |
| 3_4-DIHYDROXYBENZOIC_acid | -0.675945 | "1:1" |
| 2,5-dihydroxybenzoic_acid | -0.67136333 | "1:2" |
| THYMOL | -0.66492 | "1:1" |
| gentisic_acid | -0.66227333 | "1:2" |
| Orcinol | -0.66176333 | "2:1" |
| THYMOL | -0.66030667 | "1:2" |
| PHENOL_c0 | -0.65244 | "1:2" |
| trimesic_acid | -0.64779667 | "2:1" |
| PHENOL_c0 | -0.645445 | "1:1" |
| trimesic_acid | -0.625265 | "1:1" |
| 3_4-DIHYDROXYBENZOIC_acid | -0.61500667 | "2:1" |
| INDOLE_c0 | -0.598635 | "1:1" |
| INDOLE_c0 | -0.59816 | "1:2" |
| 3_4-DIHYDROXYBENZOIC_acid | -0.59177333 | "1:2" |
| 3-hydroxy-2-naphthoic_acid | -0.58607 | "1:1" |
| 2,5-Xylenol | -0.582905 | "1:1" |
| 2_5-XYLENOL | -0.58251 | "1:1" |
| 2,5-Xylenol | -0.57731 | "1:2" |

| | | |
|---|---|---|
| 2_5-XYLENOL | -0.57632333 | "1:2" |
| salicylic_acid | -0.569225 | "1:1" |
| m-nitrobenzoic_acid | -0.566095 | "1:1" |
| SKATOLE_c0 | -0.55596 | "1:2" |
| O-CRESOL | -0.55326 | "2:1" |
| SKATOLE_c0 | -0.552105 | "1:1" |
| Hydroquinone_c0 | -0.552085 | "1:1" |
| FUMARIC_ACID | -0.549575 | "1:1" |
| 3-hydroxy-2-naphthoic_acid | -0.53992 | "1:2" |
| Hydroquinone_c0 | -0.53467333 | "1:2" |
| FUMARIC_ACID | -0.53440667 | "2:1" |
| THYMOL | -0.52590333 | "2:1" |
| methylgallate | -0.524405 | "1:1" |
| salicylic_acid | -0.5235 | "1:2" |
| PHENOL_c0 | -0.51339333 | "2:1" |
| m-nitrobenzoic_acid | -0.50407667 | "2:1" |
| 3-hydroxy-2-naphthoic_acid | -0.50406 | "2:1" |
| m-nitrobenzoic_acid | -0.50092 | "1:2" |
| trimesic_acid | -0.49986667 | "1:2" |
| P-CRESOL | -0.49931333 | "1:2" |
| salicylic_acid | -0.48972 | "2:1" |
| P-CRESOL | -0.4879 | "1:1" |
| Methanesulfonic | -0.482445 | "1:1" |
| Methanesulfonic | -0.47865333 | "2:1" |
| INDOLE_c0 | -0.47527333 | "2:1" |
| methylgallate | -0.47443667 | "1:2" |
| P-ETHYLPHENOL_c0 | -0.47219333 | "1:2" |
| 3-HYDROXYBENZOIC_ACID | -0.469155 | "1:1" |
| 2_5-XYLENOL | -0.46777333 | "2:1" |
| 2,5-Xylenol | -0.46765333 | "2:1" |
| FUMARIC_ACID | -0.46547667 | "1:2" |
| methylgallate | -0.46515667 | "2:1" |
| Hydroquinone_c0 | -0.46011333 | "2:1" |
| P-ETHYLPHENOL_c0 | -0.459365 | "1:1" |
| 6-hydroxy-2-naphthoic_acid | -0.449685 | "1:1" |
| Ethanesulfonic_acid | -0.448055 | "1:1" |
| SKATOLE_c0 | -0.43566 | "2:1" |
| Ethanesulfonic_acid | -0.43312667 | "2:1" |
| 3-HYDROXYBENZOIC_ACID | -0.43194 | "2:1" |
| ALLOCITRIC_ACID | -0.42774 | "1:1" |
| p-tButyl-PHENOL_c0 | -0.42679333 | "1:2" |
| 3,4-Xylenol_c0 | -0.41840667 | "1:2" |
| ISOCITRIC_ACID | -0.41742 | "1:1" |
| 3_4-xylenol_c0 | -0.41659667 | "1:2" |

| | | |
|---|---|---|
| 3-HYDROXYBENZOIC_ACID | -0.4129 | "1:2" |
| p-tButyl-PHENOL_c0 | -0.40929 | "1:1" |
| 6-hydroxy-2-naphthoic_acid | -0.40685333 | "2:1" |
| ALLOCITRIC_ACID | -0.40594333 | "1:2" |
| 3,4-Xylenol_c0 | -0.40526 | "1:1" |
| 3_4-xylenol_c0 | -0.40316 | "1:1" |
| 6-hydroxy-2-naphthoic_acid | -0.39945667 | "1:2" |
| 2_6-xylenol_c0 | -0.39238333 | "1:2" |
| P-CRESOL | -0.38472667 | "2:1" |
| ISOCITRIC_ACID | -0.38090667 | "2:1" |
| 2_6-xylenol_c0 | -0.3799 | "1:1" |
| ISOCITRIC_ACID | -0.37862 | "1:2" |
| Methanesulfonic | -0.37413667 | "1:2" |
| citric_acid | -0.373535 | "1:1" |
| Etidronic_acid | -0.36914333 | "1:2" |
| 4-HYDROXYBENZOIC_ACID | -0.367105 | "1:1" |
| ALLOCITRIC_ACID | -0.36153 | "2:1" |
| P-ETHYLPHENOL_c0 | -0.36051333 | "2:1" |
| O-PHENYLPHENOL | -0.35926 | "1:1" |
| Ethanesulfonic_acid | -0.3506 | "1:2" |
| Etidronic_acid | -0.350515 | "1:1" |
| citric_acid | -0.34377333 | "1:2" |
| O-PHENYLPHENOL | -0.33863 | "1:2" |
| citric_acid | -0.33800667 | "2:1" |
| 4-HYDROXYBENZOIC_ACID | -0.33745667 | "1:2" |
| 4-HYDROXYBENZOIC_ACID | -0.32179333 | "2:1" |
| 2-OXO-3-PHENYLPROPIONIC_ACID | -0.32097 | "1:1" |
| 3,4-Xylenol_c0 | -0.31694667 | "2:1" |
| p-tButyl-PHENOL_c0 | -0.31617667 | "2:1" |
| 3_4-xylenol_c0 | -0.31507667 | "2:1" |
| O-PHENYLPHENOL | -0.30168333 | "2:1" |
| 2_6-xylenol_c0 | -0.29408 | "2:1" |
| 2-OXO-3-PHENYLPROPIONIC_ACID | -0.28822667 | "1:2" |
| 2-OXO-3-PHENYLPROPIONIC_ACID | -0.28083667 | "2:1" |

## 4.2 IR spectra of samples from the ROY co-crystal screen

Each figure shows the spectra of ROY (red), the co-former (brown) and the three experimental samples (one from each screen with acetone (dark blue), ethanol (blue) and hexane (teal) as the solvent). The figures are labelled by co-former.

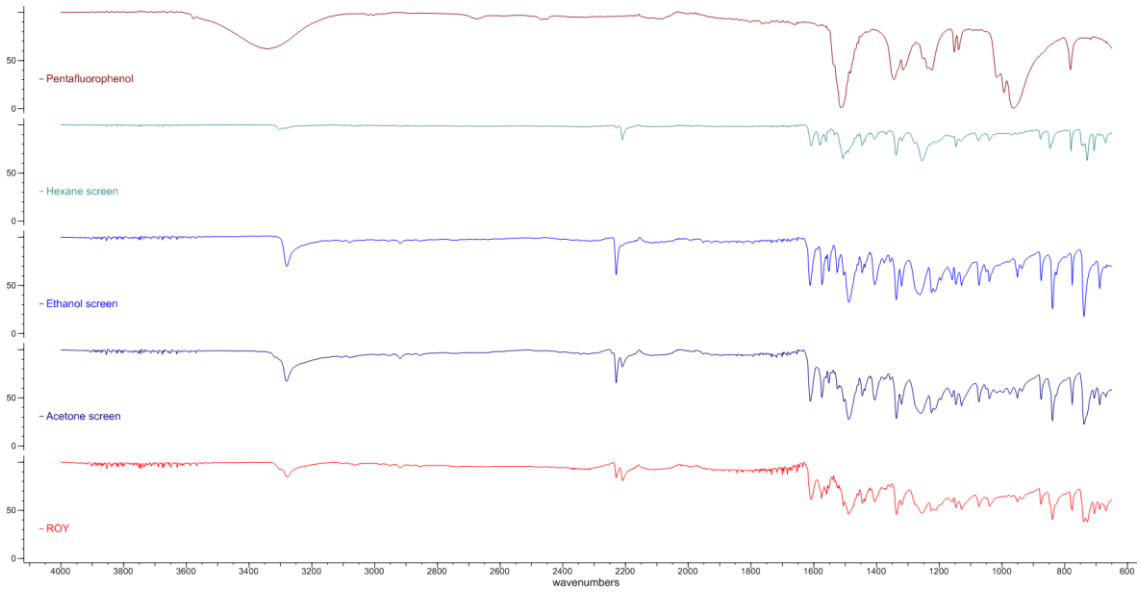


*Figure 1. Pentafluorophenol.*

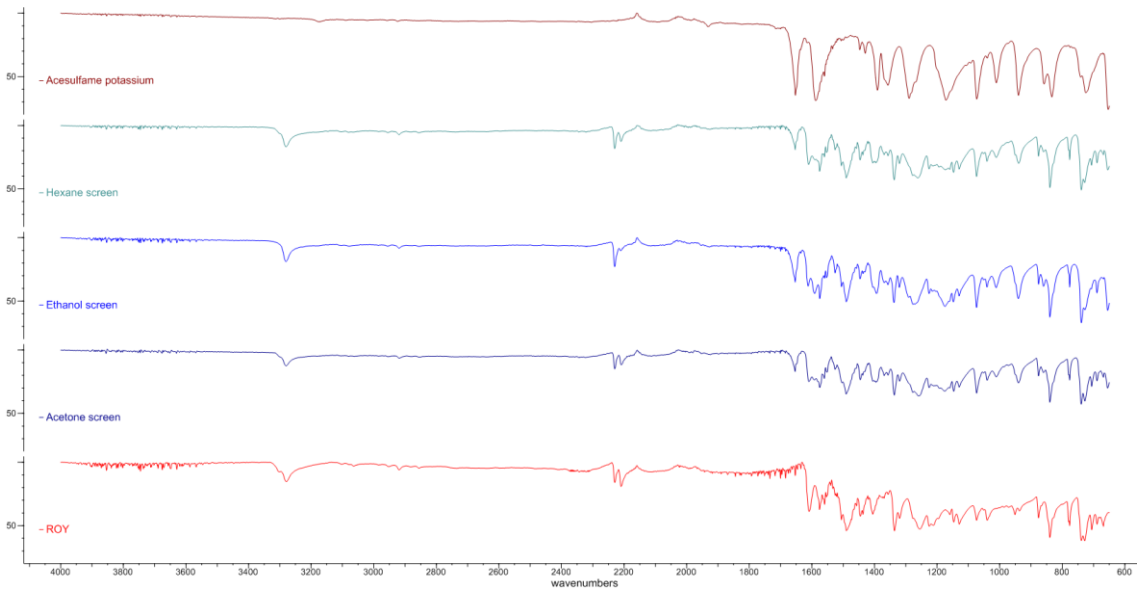


*Figure 2. Acesulfame potassium.*

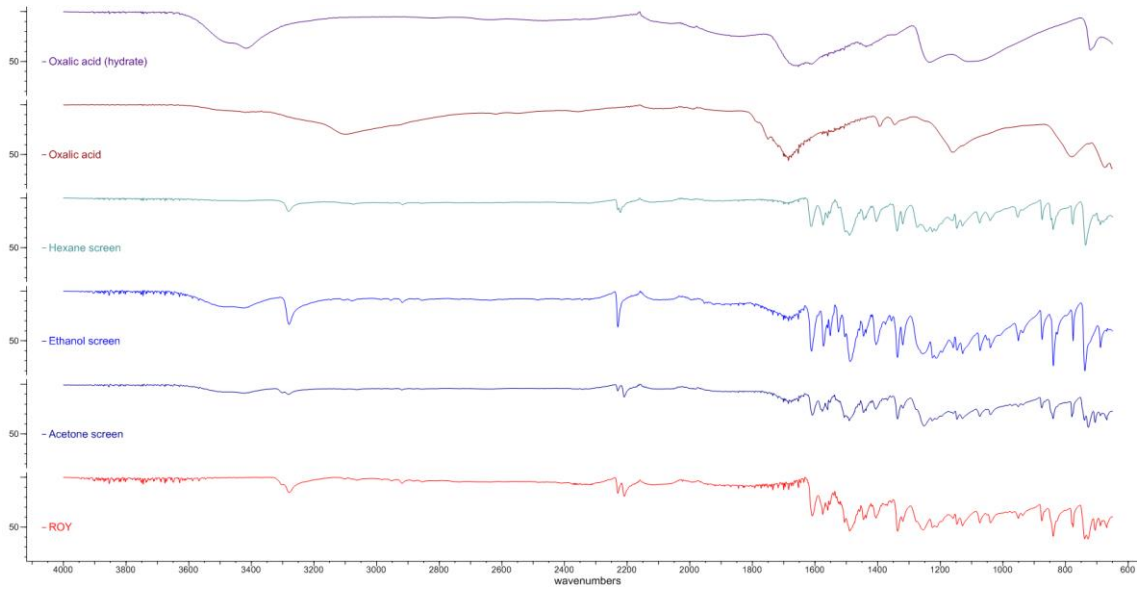


*Figure 3. Oxalic acid. Hydrate of oxalic acid (purple) is included for comparison.*

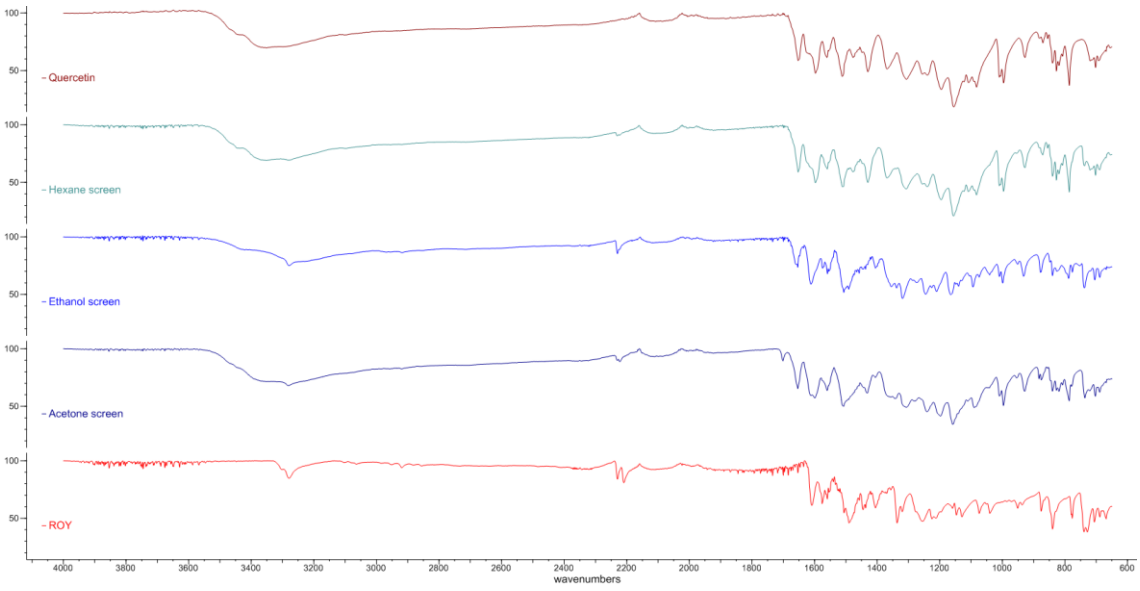


*Figure 4. Quercetin.*

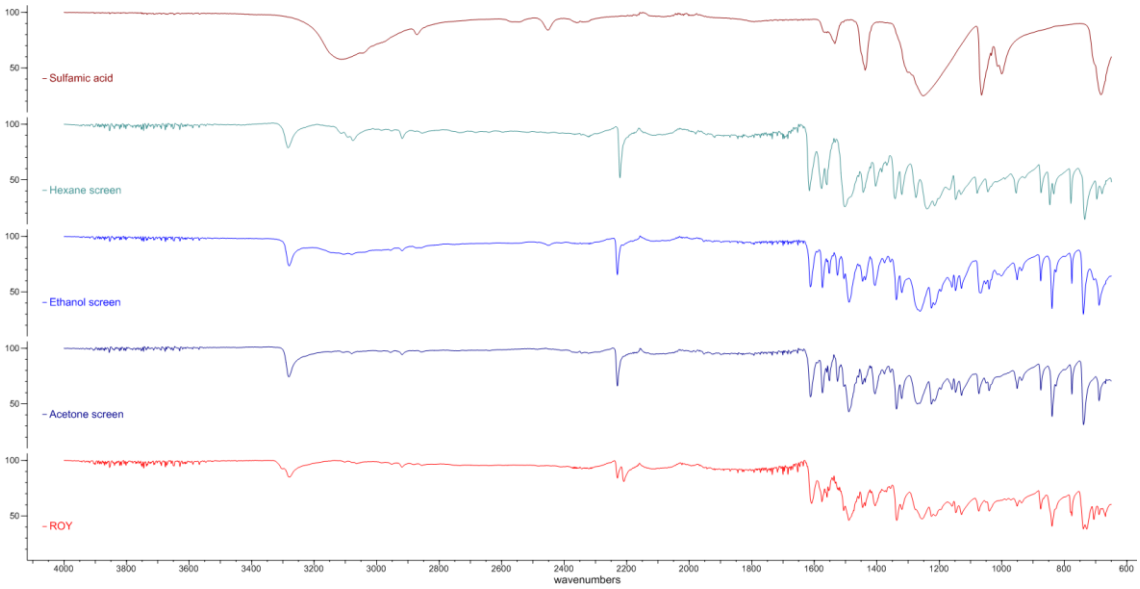


*Figure 5. Sulfamic acid.*

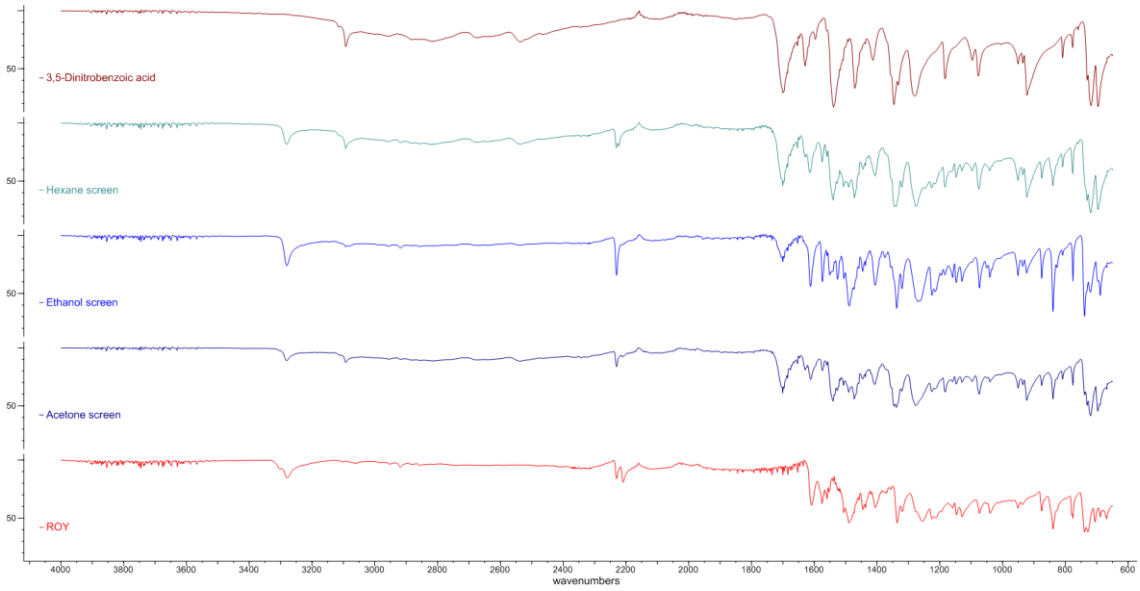


*Figure 6. 3,5-Dinitrobenzoic acid.*

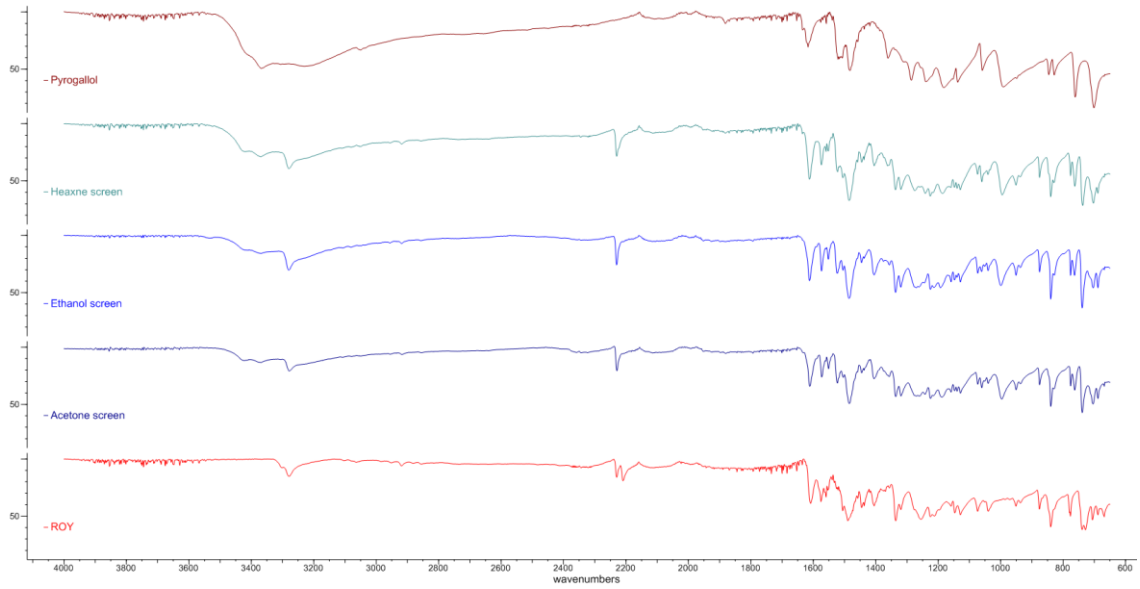


*Figure 7. Pyrogallol.*

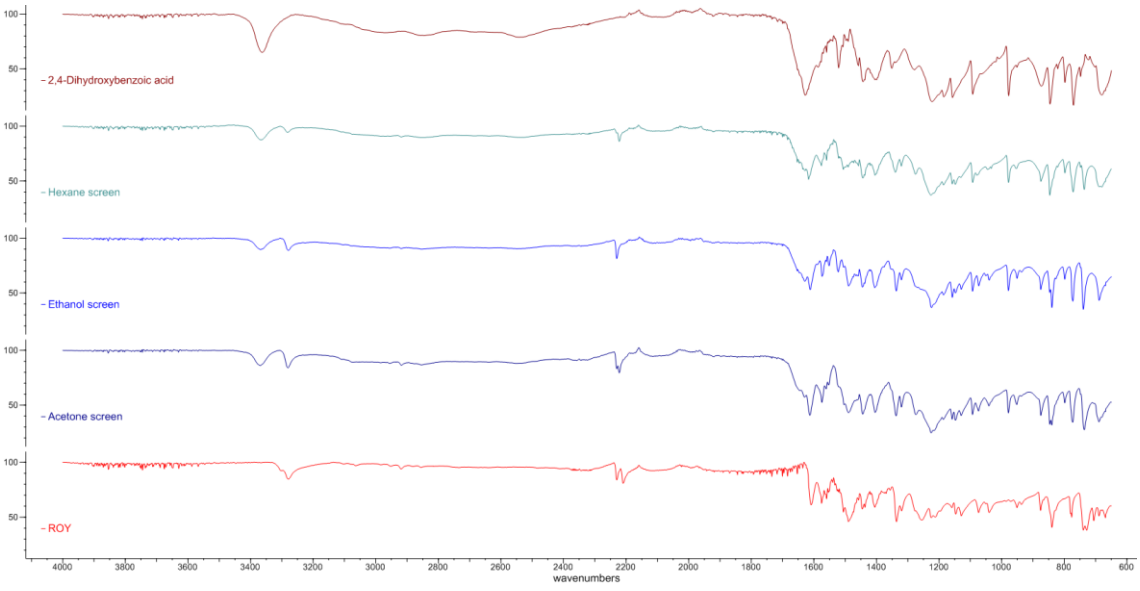


*Figure 8. 2,4-Dihydroxybenzoic acid.*

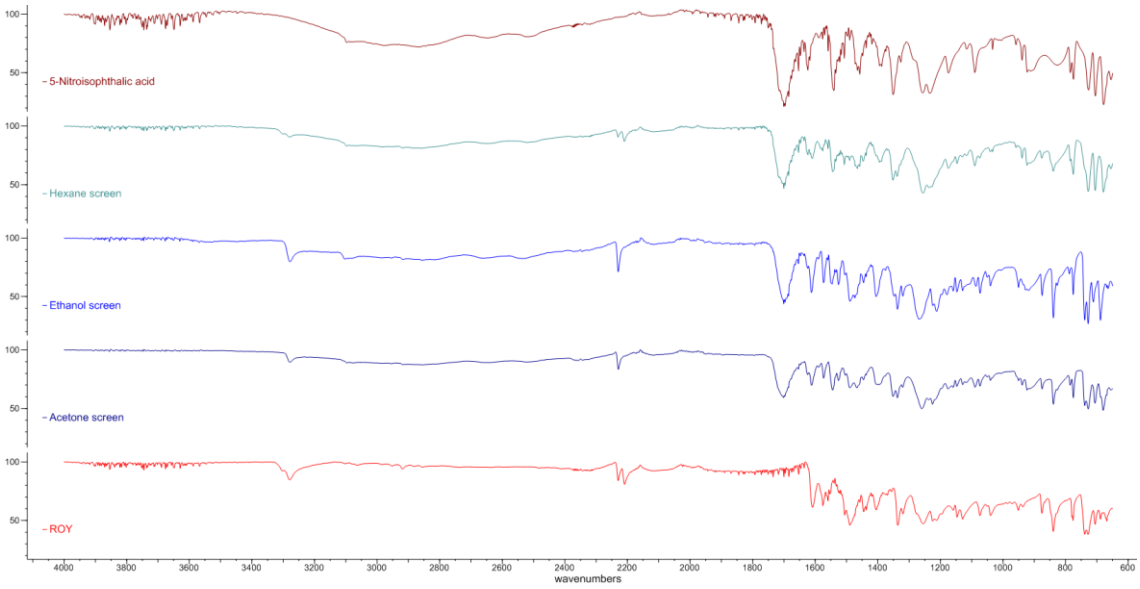


*Figure 9. 5-Nitroisophthalic acid.*

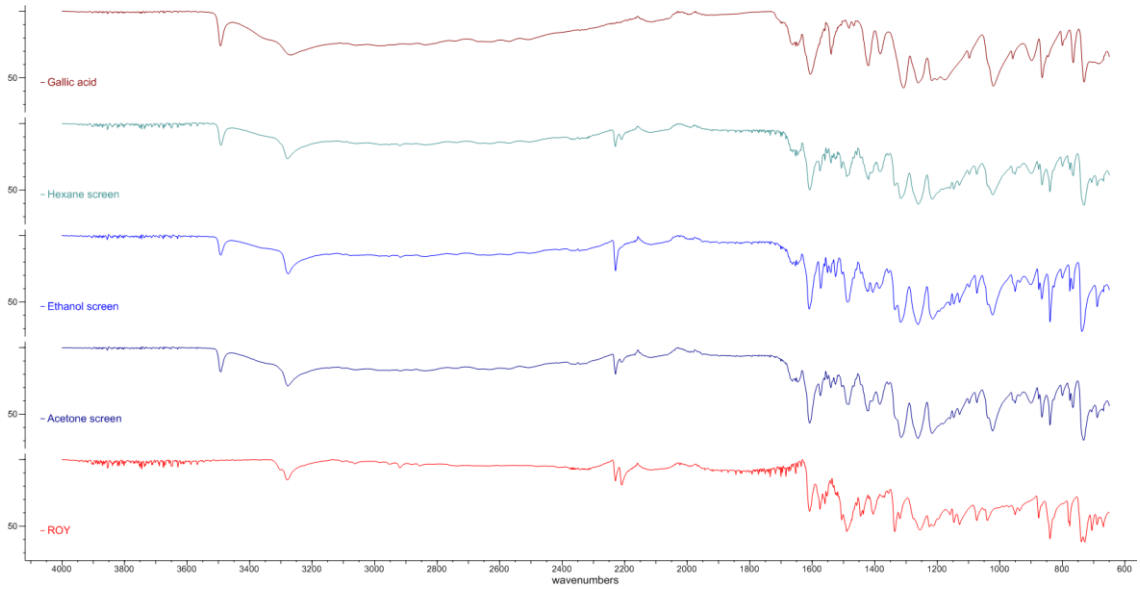


*Figure 10. Gallic acid.*

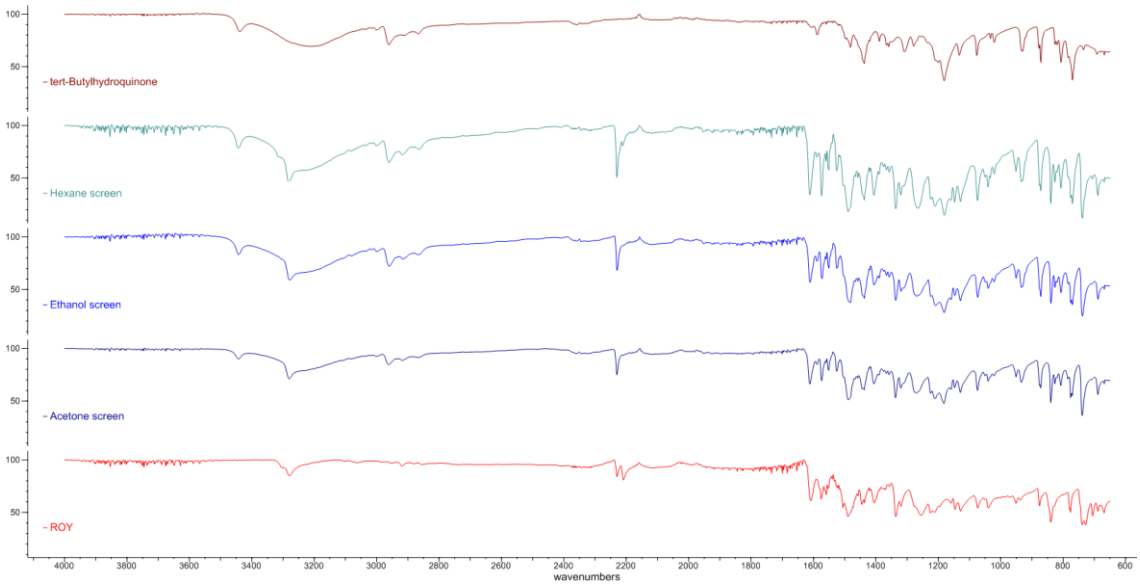


*Figure 11. tert-Butylhydroquinone.*

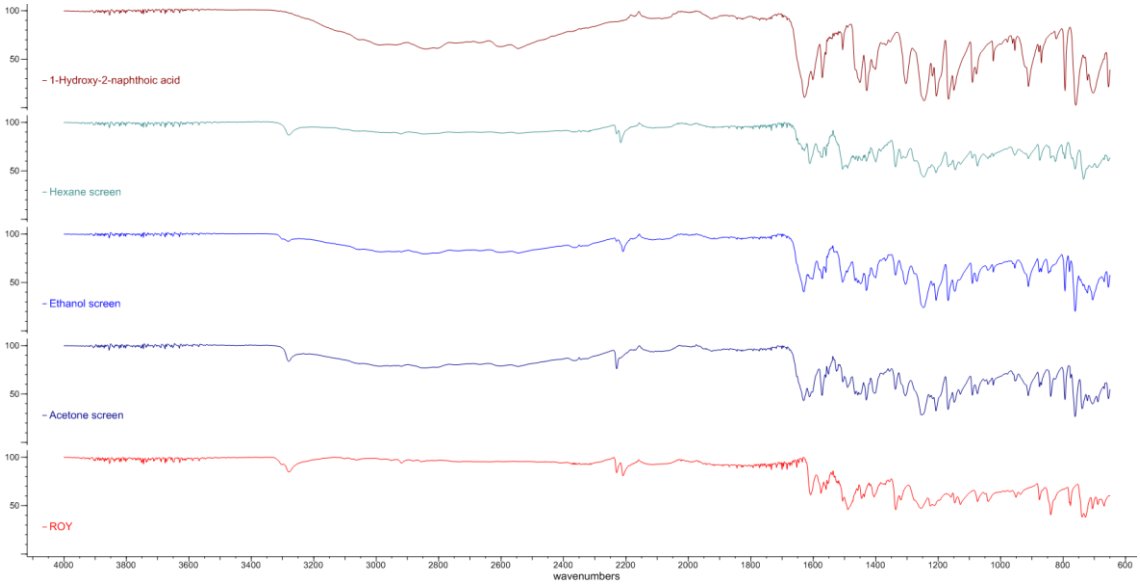


*Figure 12. 1-Hydroxy-2-naphthoic acid.*

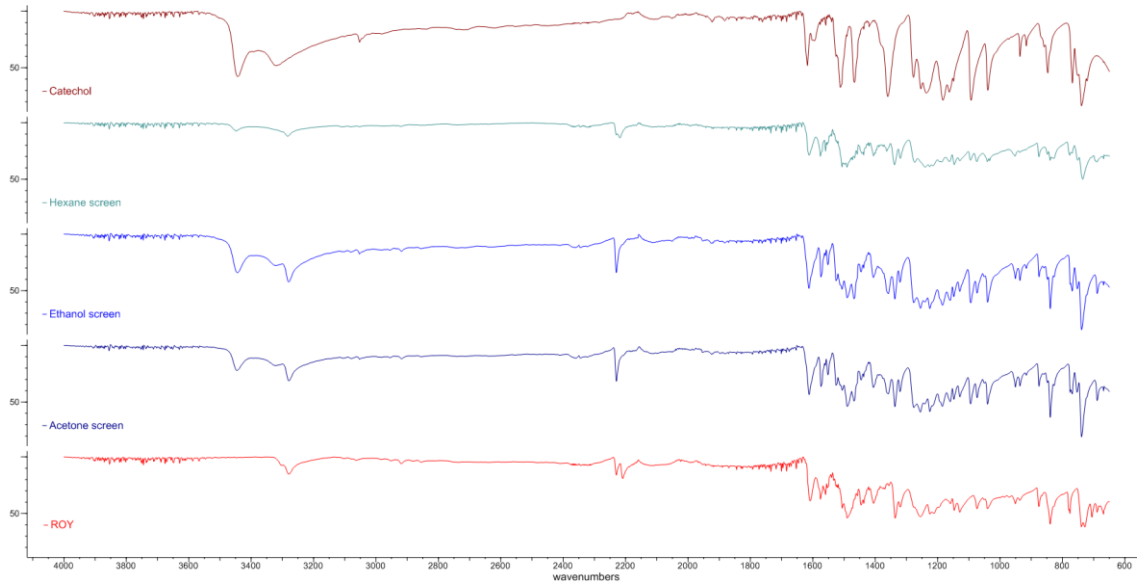


*Figure 13. Catechol.*

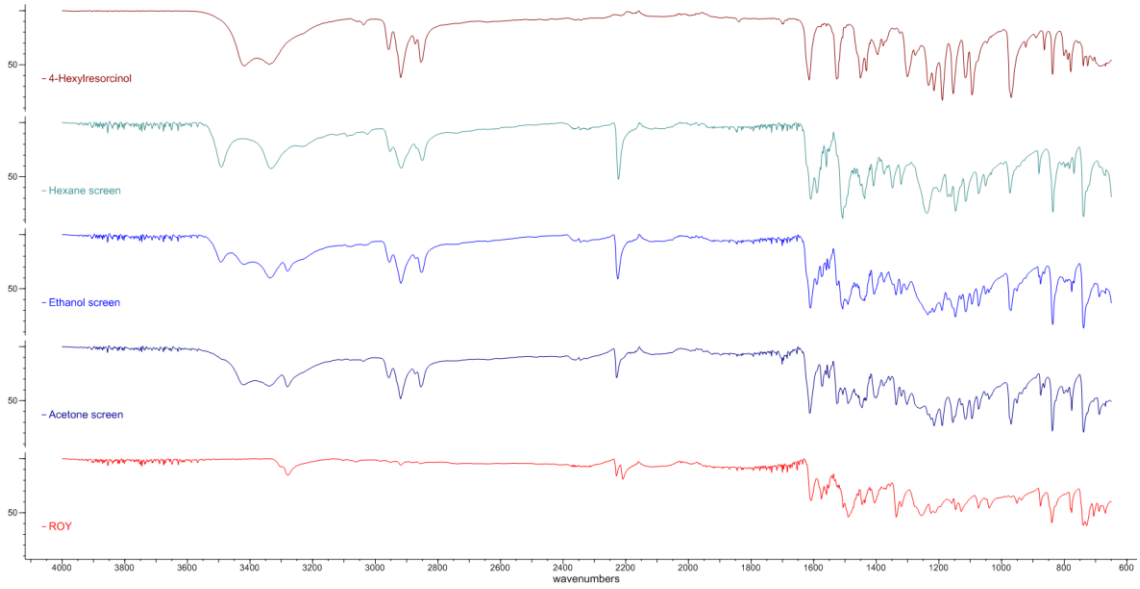


*Figure 14. 4-Hexylresorcinol.*

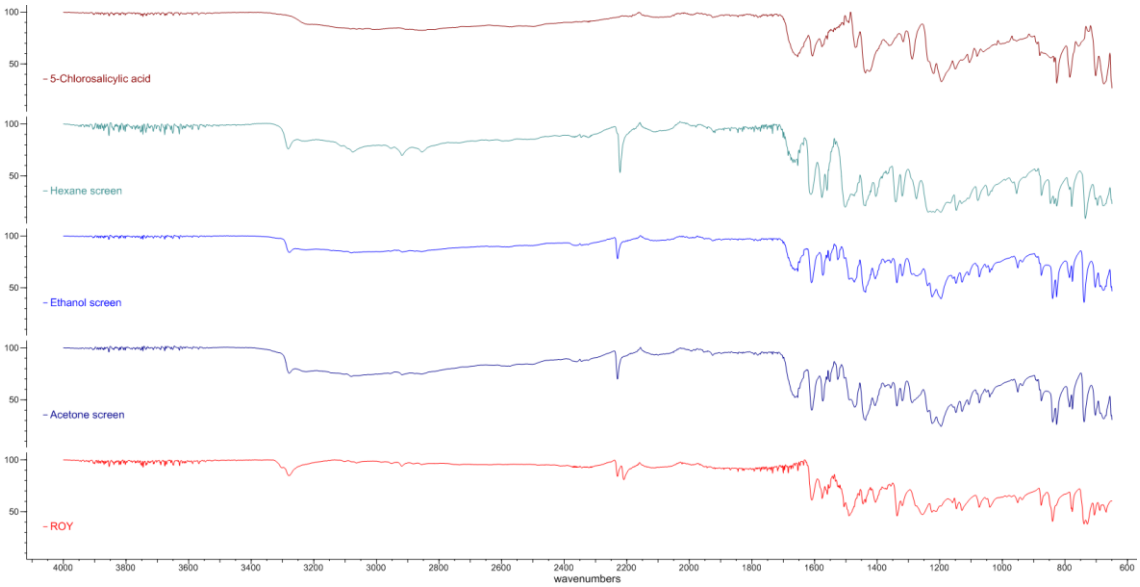


*Figure 15. 5-Chlorosalicylic acid.*

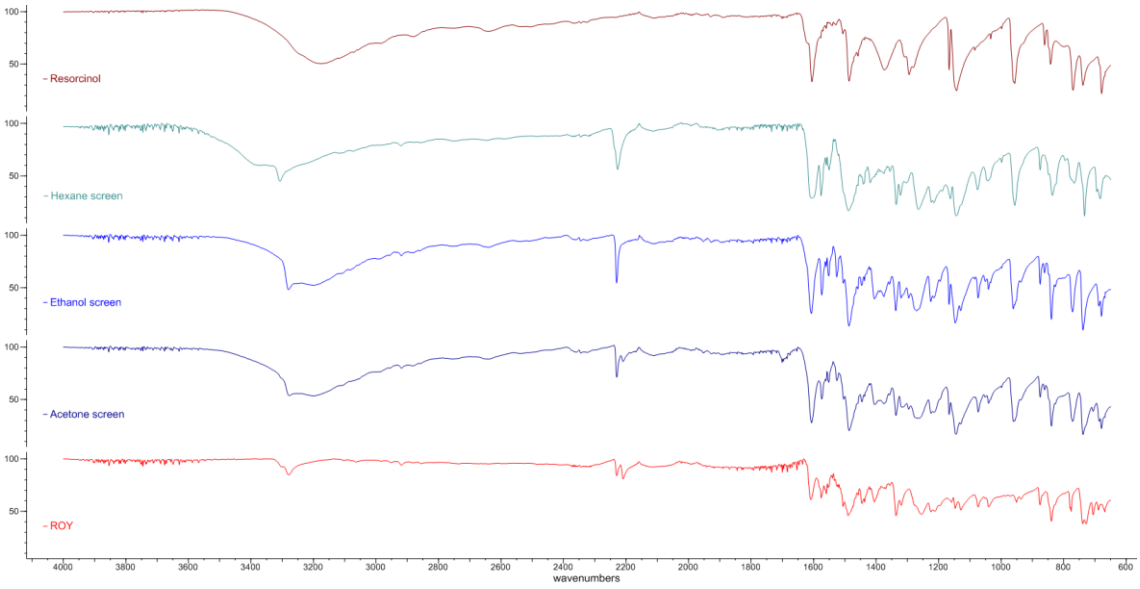


*Figure 16. Resorcinol.*

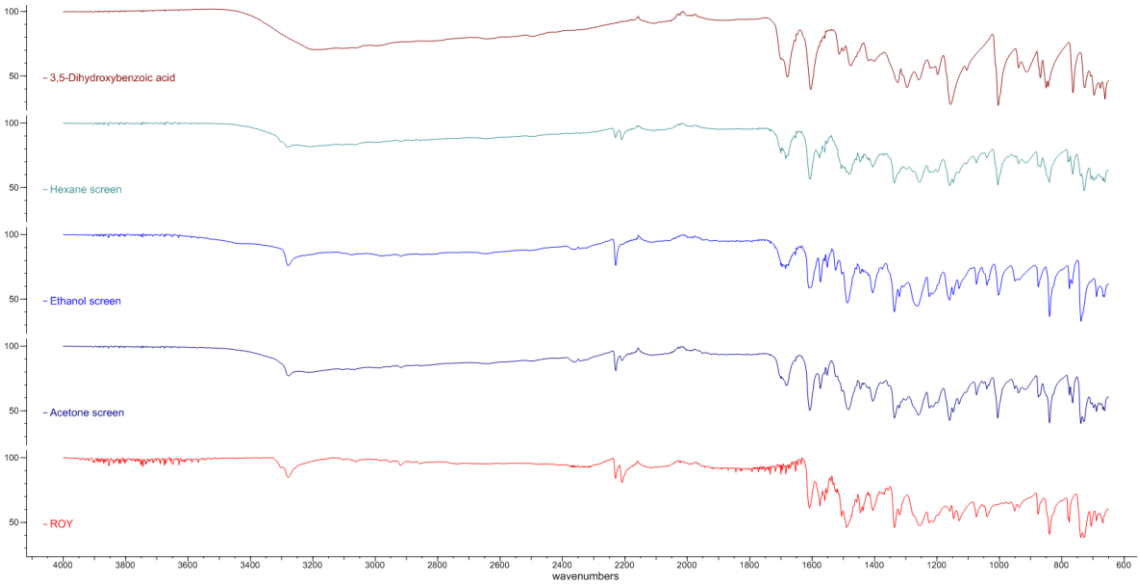


*Figure 17. 3,5-Dihydroxybenzoic acid.*

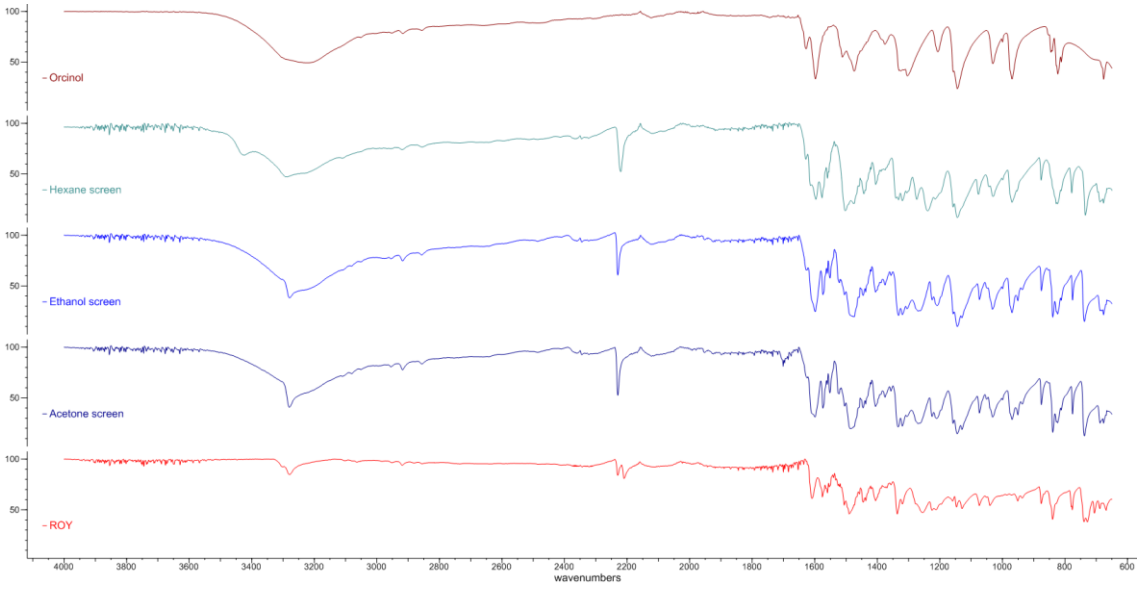


*Figure 18. Orcinol.*

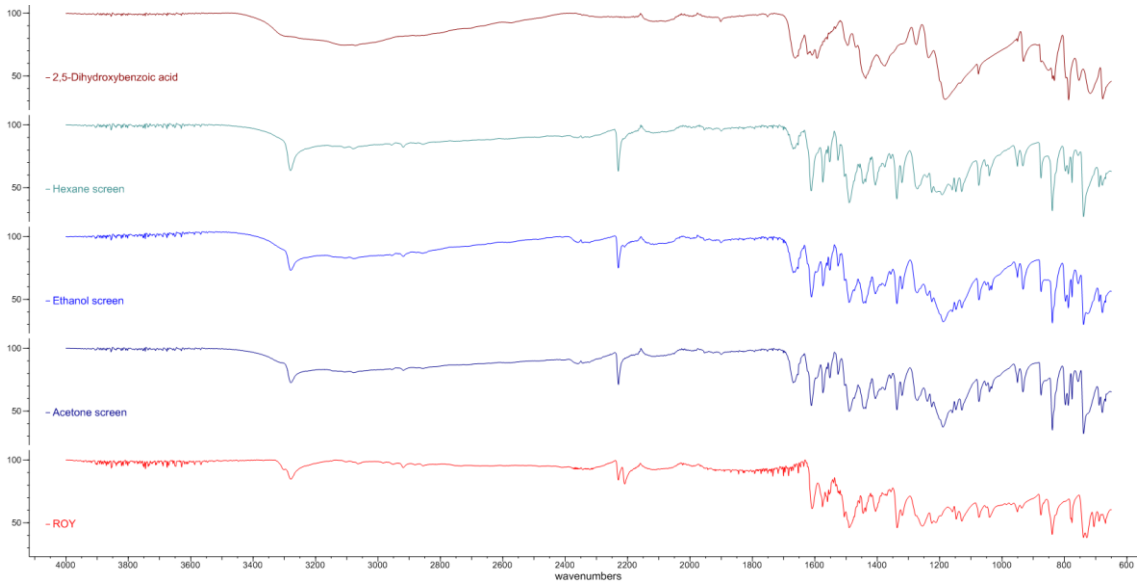


*Figure 19. 2,5-Dihydroxybenzoic acid.*

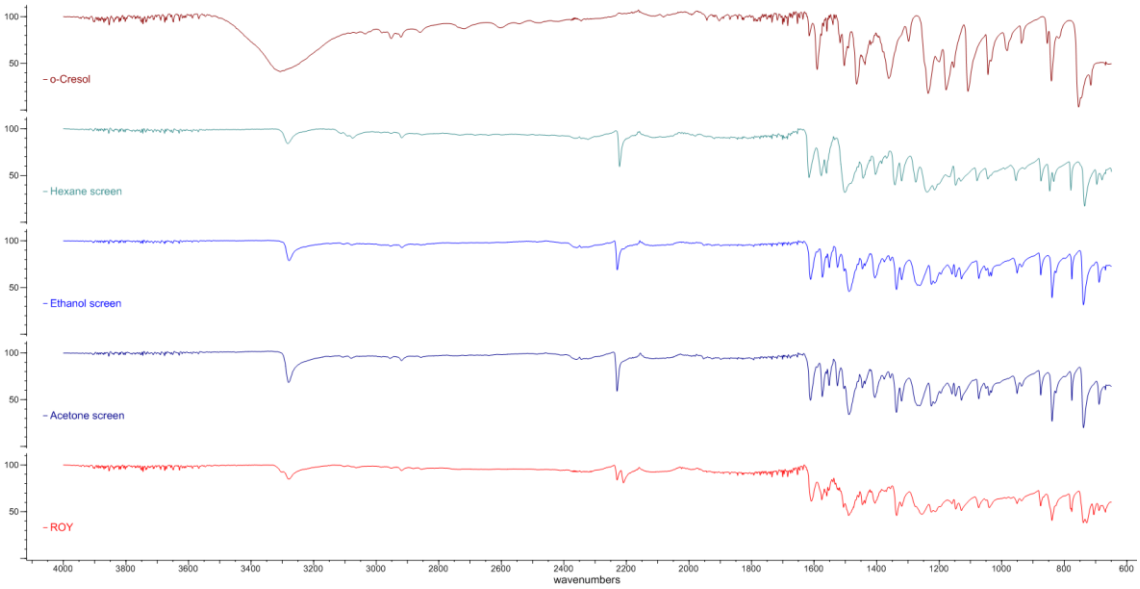


*Figure 20. o-Cresol.*

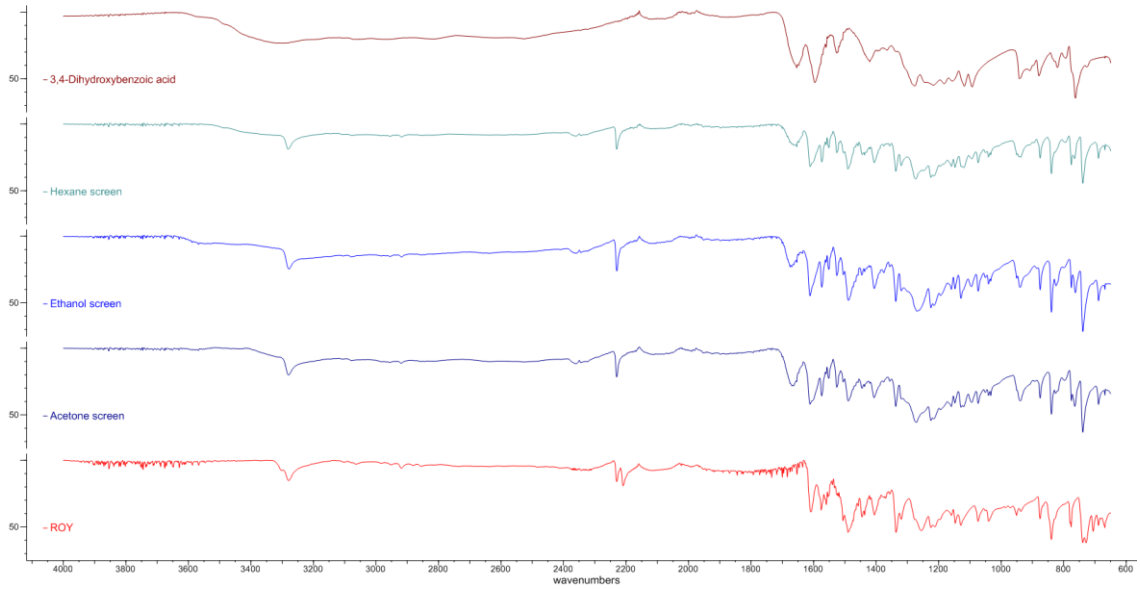


*Figure 21. 3,4-Dihydroxybenzoic acid.*

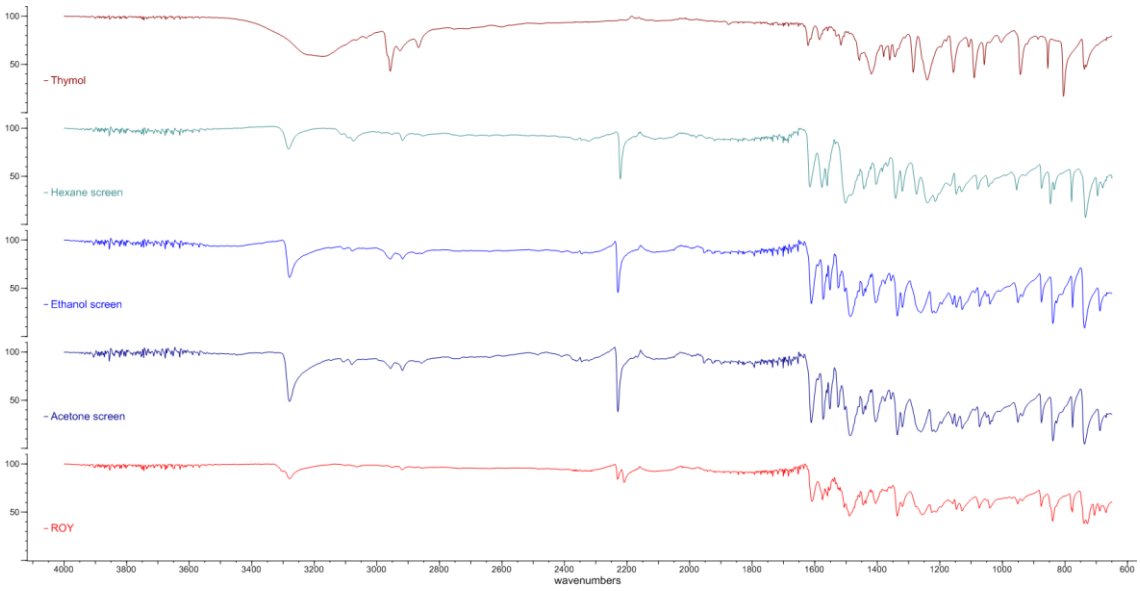


*Figure 22. Thymol.*

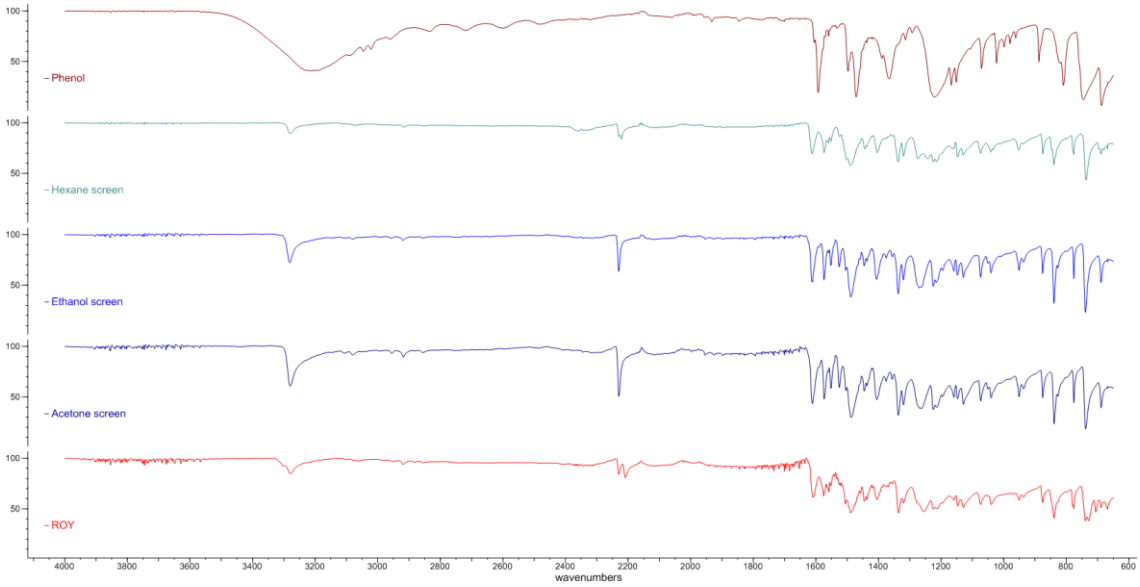


*Figure 23. Phenol.*

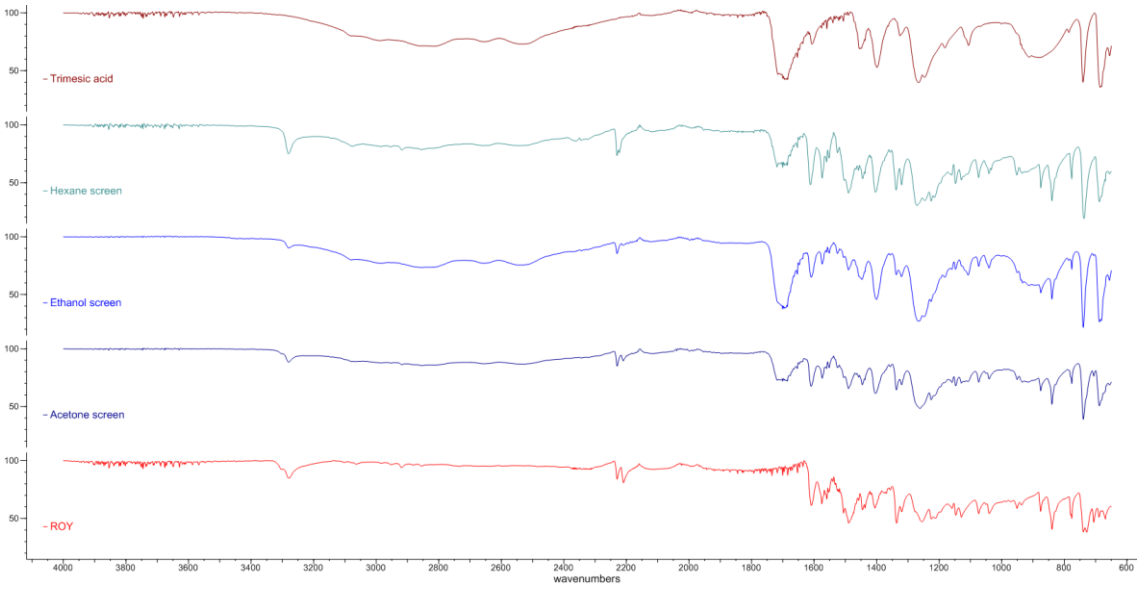


*Figure 24. Trimesic acid.*

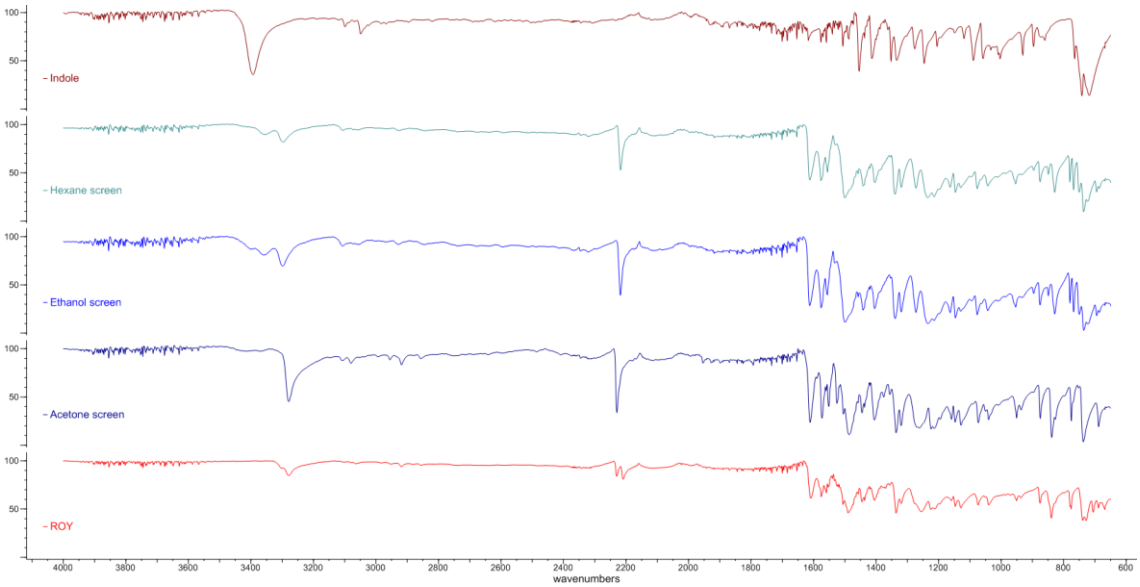


*Figure 25. Indole.*

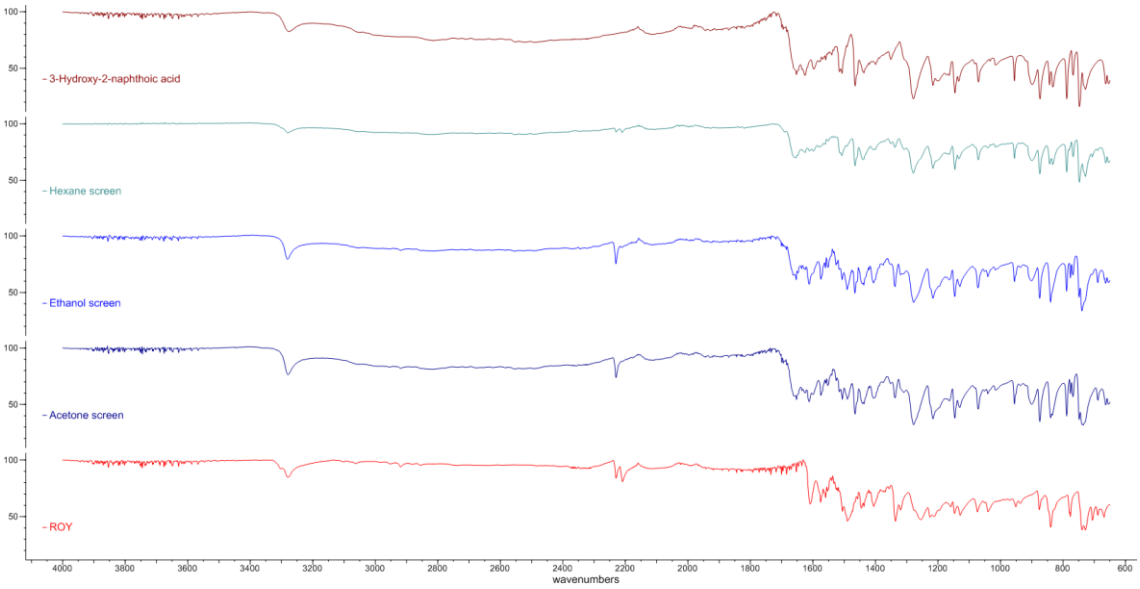


*Figure 26. 3-Hydroxy-2-naphthoic acid.*

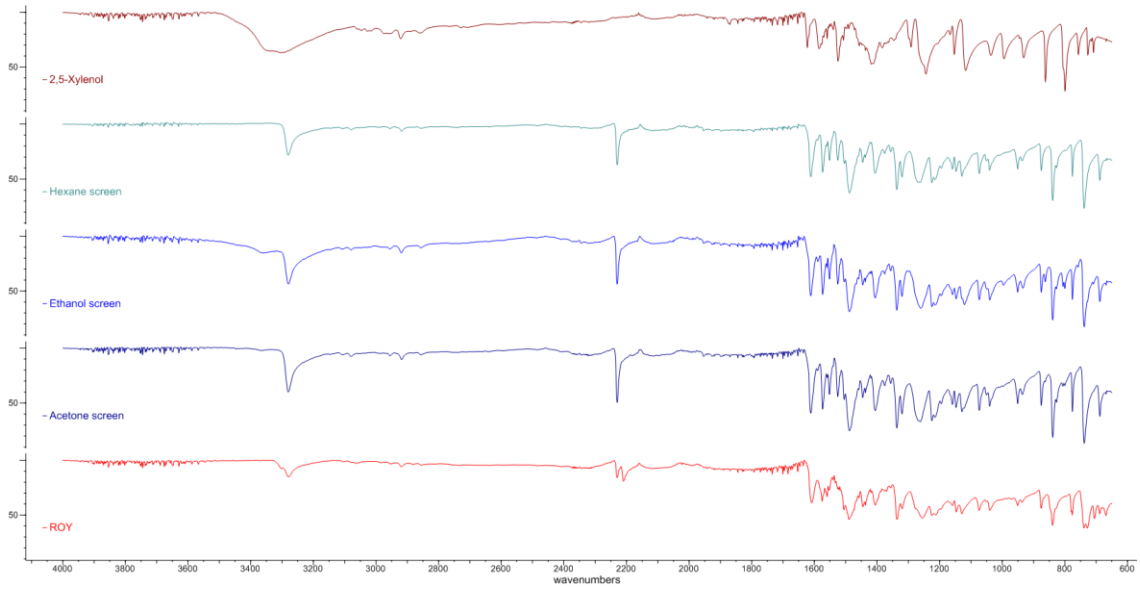


*Figure 27, 2,5-Xylenol.*

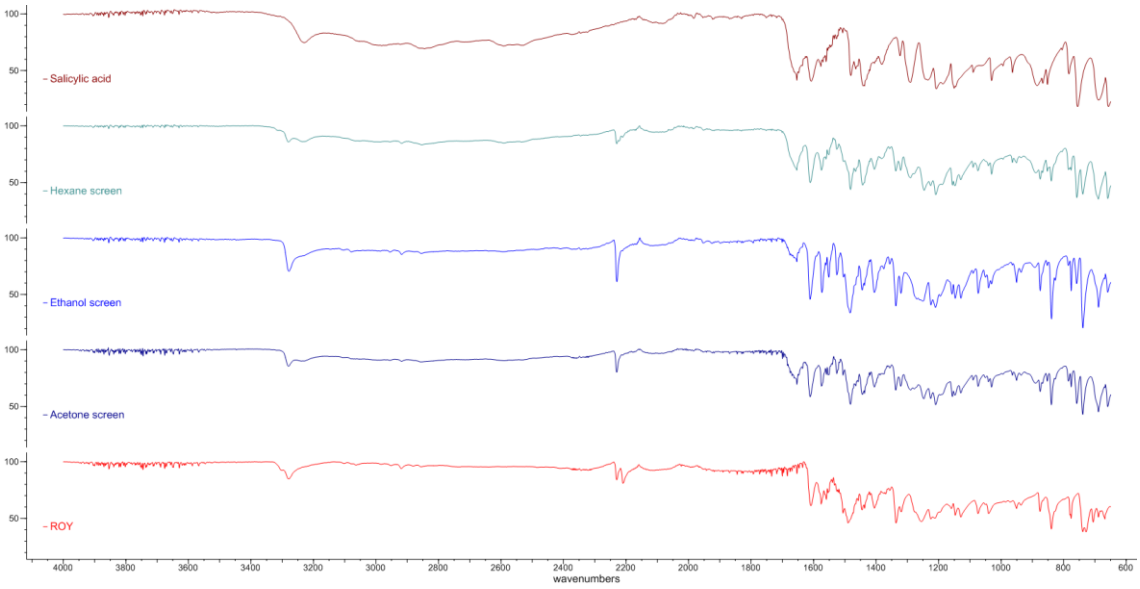


*Figure 28. Salicylic acid.*

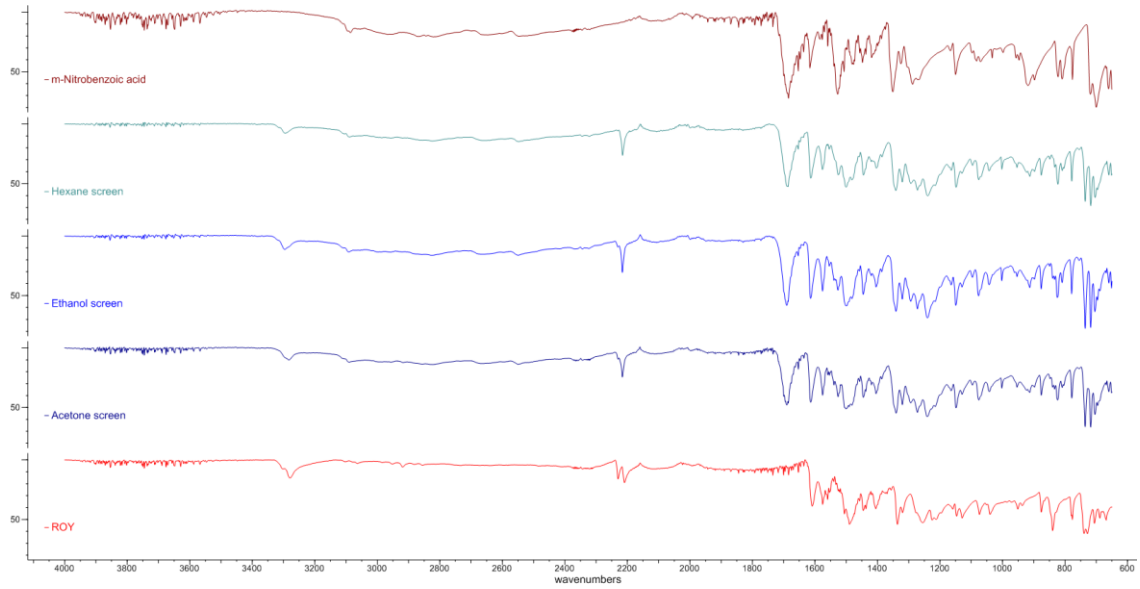


*Figure 29. m-Nitrobenzoic acid.*

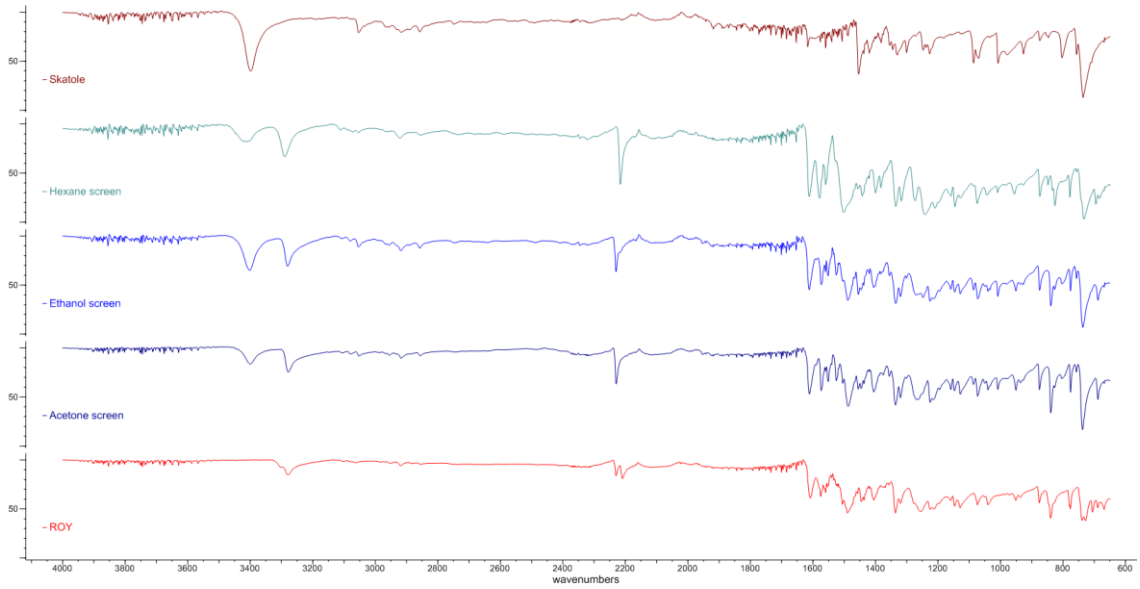


*Figure 30. Skatole.*

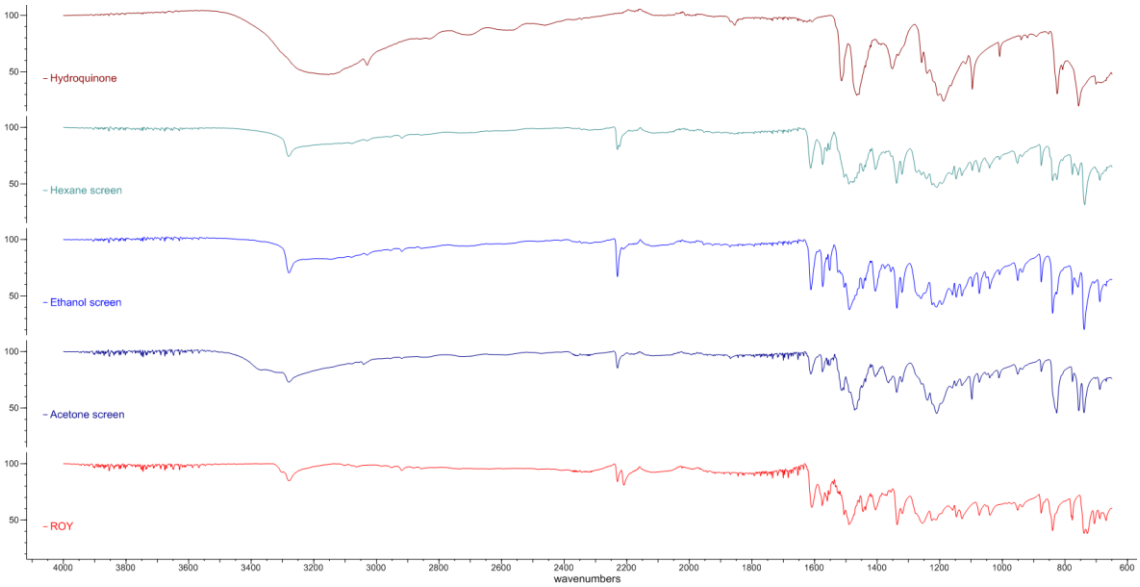


*Figure 31. Hydroquinone.*

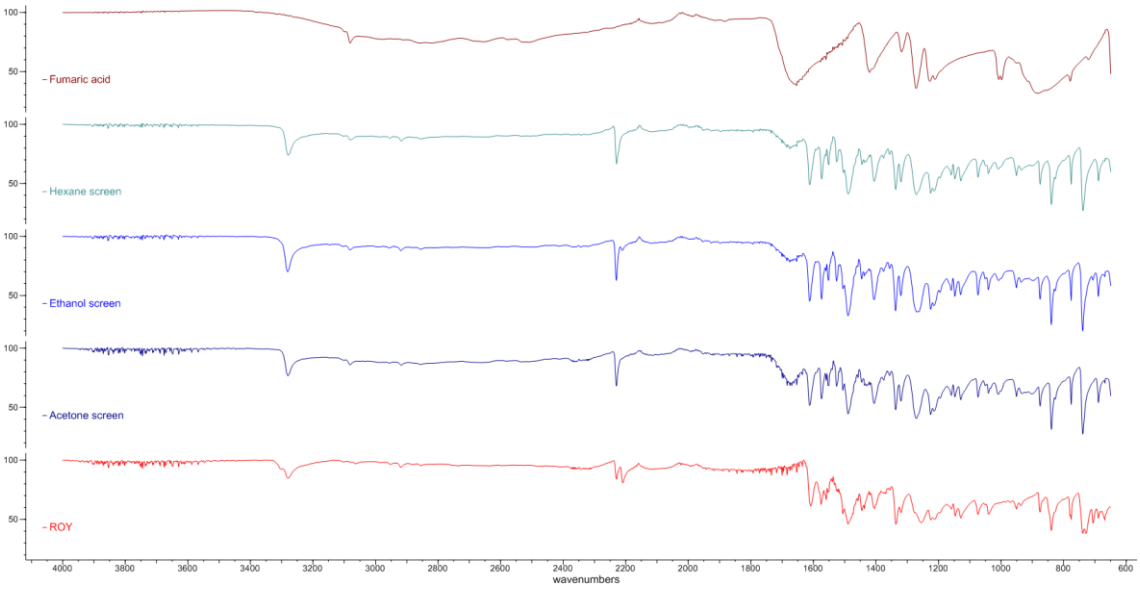


*Figure 32. Fumaric acid.*

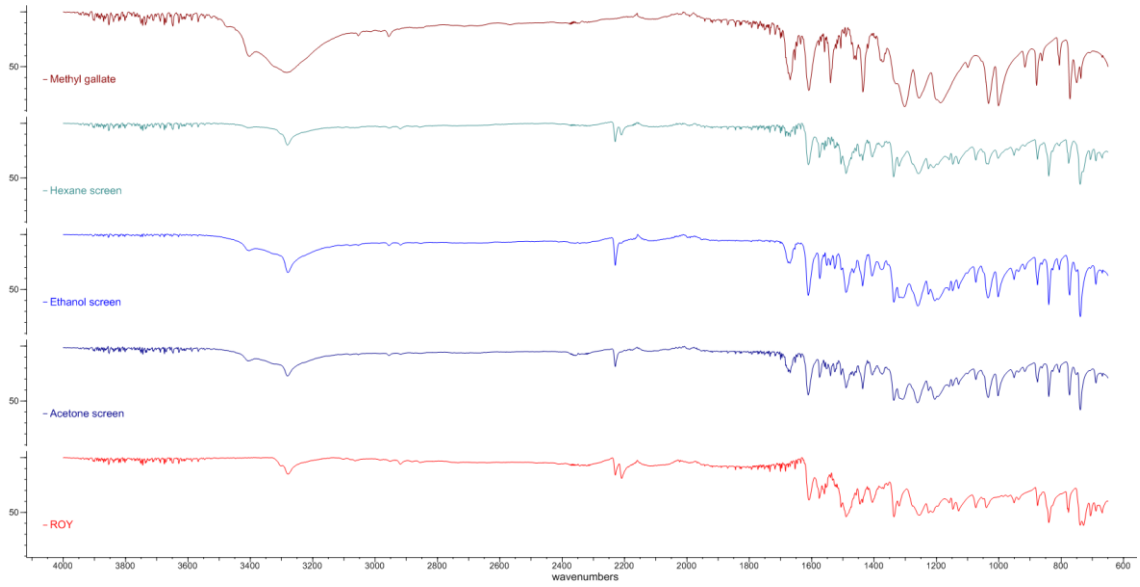


*Figure 33. Methyl gallate.*

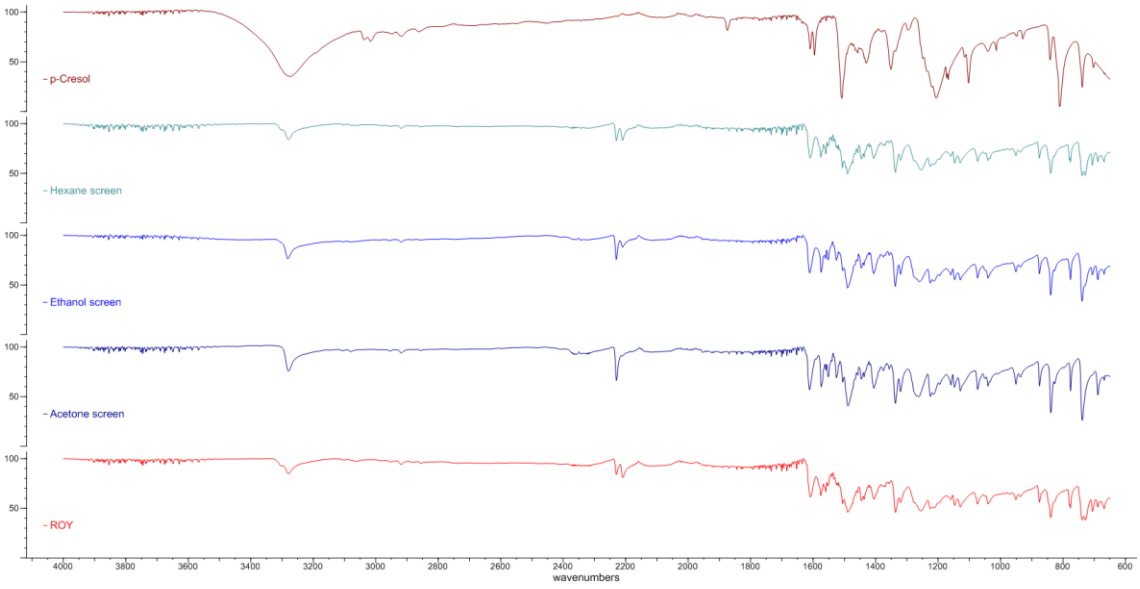


*Figure 34. p-Cresol.*

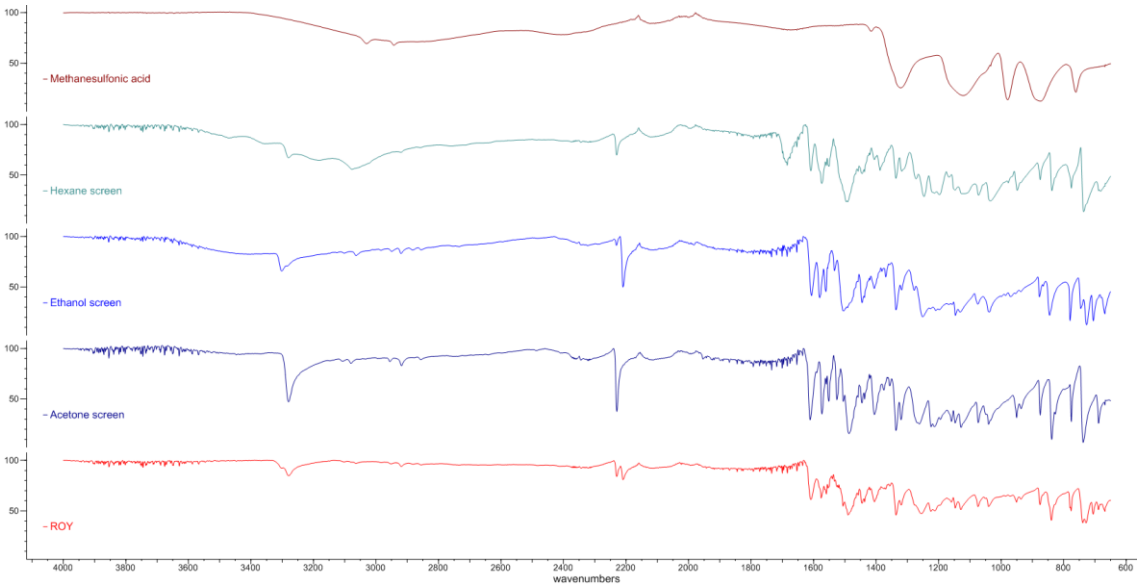


*Figure 35. Methanesulfonic acid.*

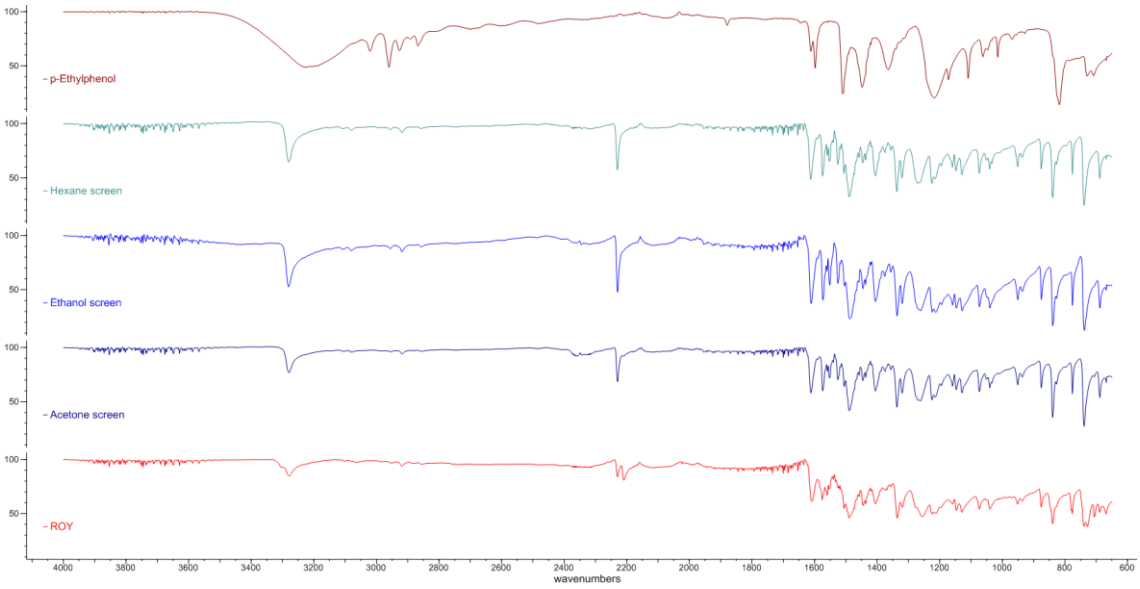


*Figure 36. p-Ethylphenol.*

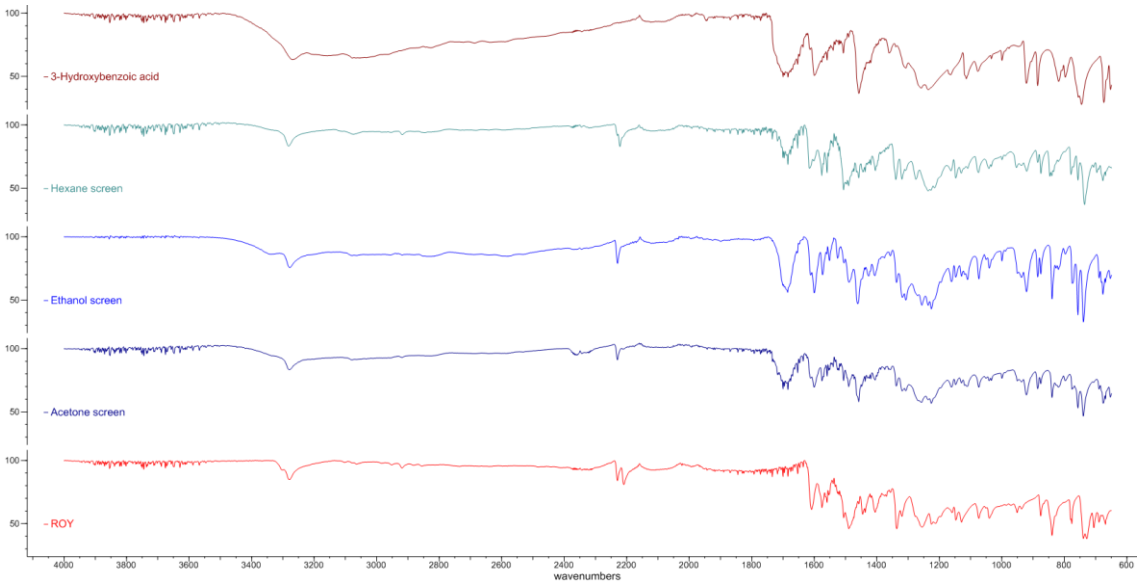


*Figure 37. 3-Hydroxybenzoic acid.*

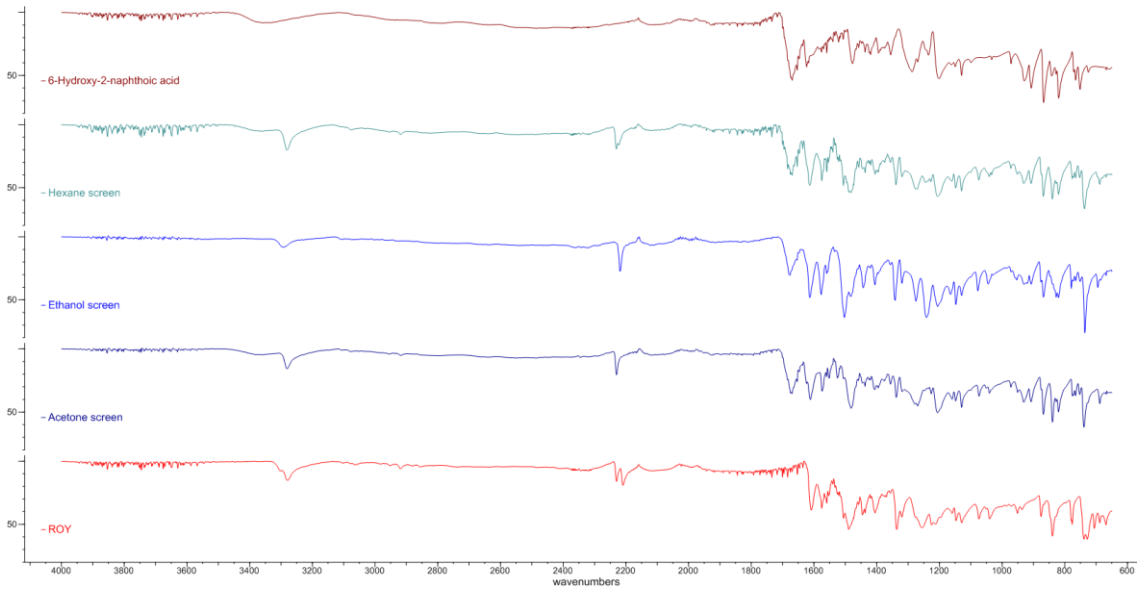


*Figure 38. 6-Hydroxy-2-naphthoic acid.*

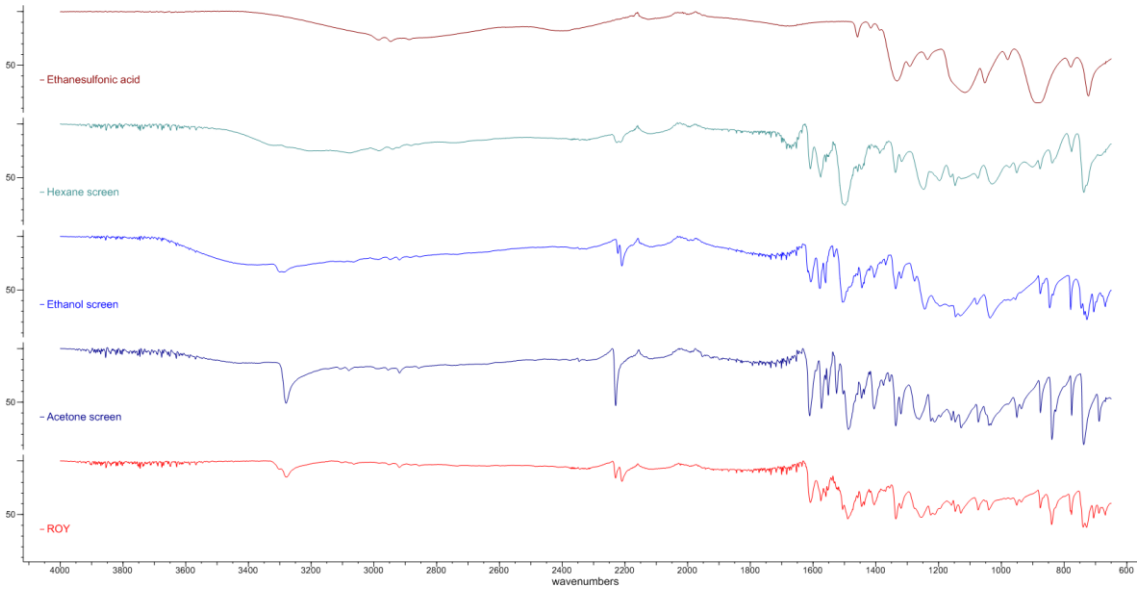


*Figure 39. Ethanesulfonic acid.*

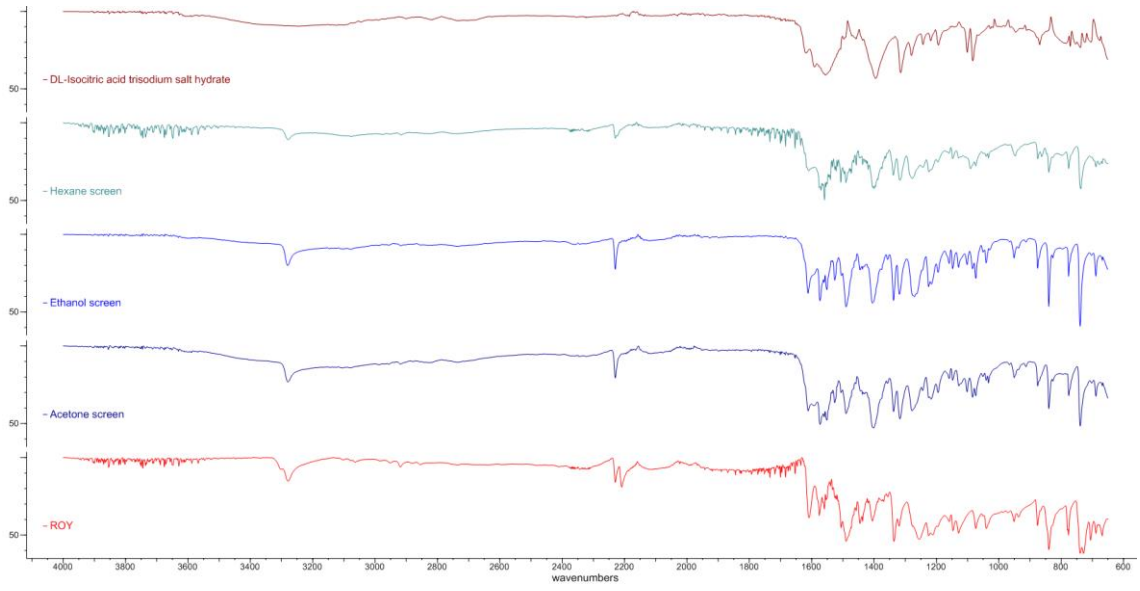


*Figure 40. Isocitric acid trisodium salt hydrate.*

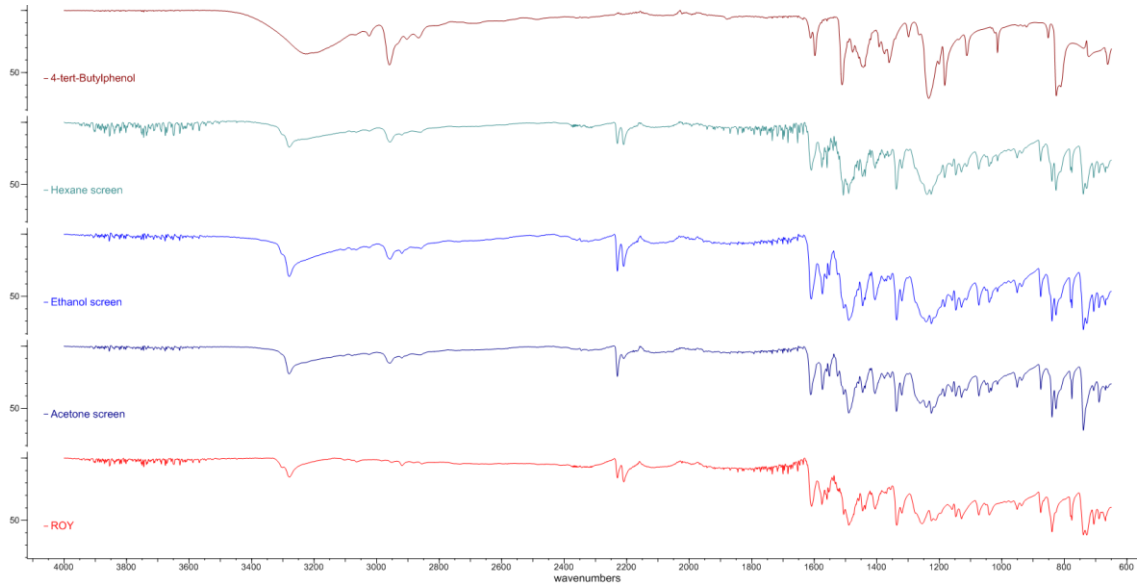


*Figure 41. p-tert-Butylphenol.*

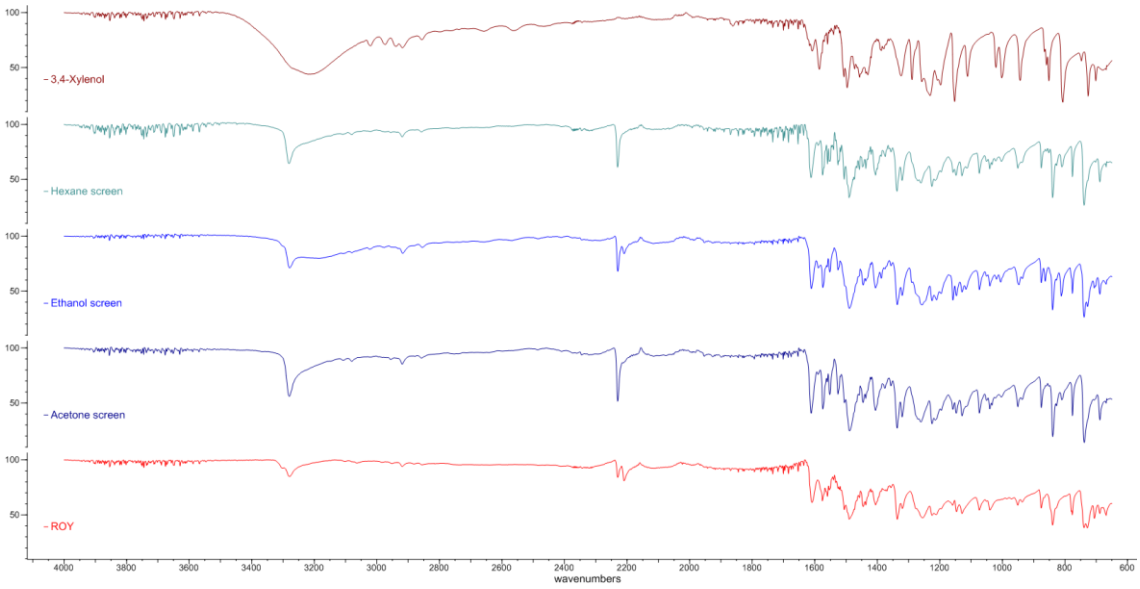


*Figure 42. 3,4-Xylenol.*

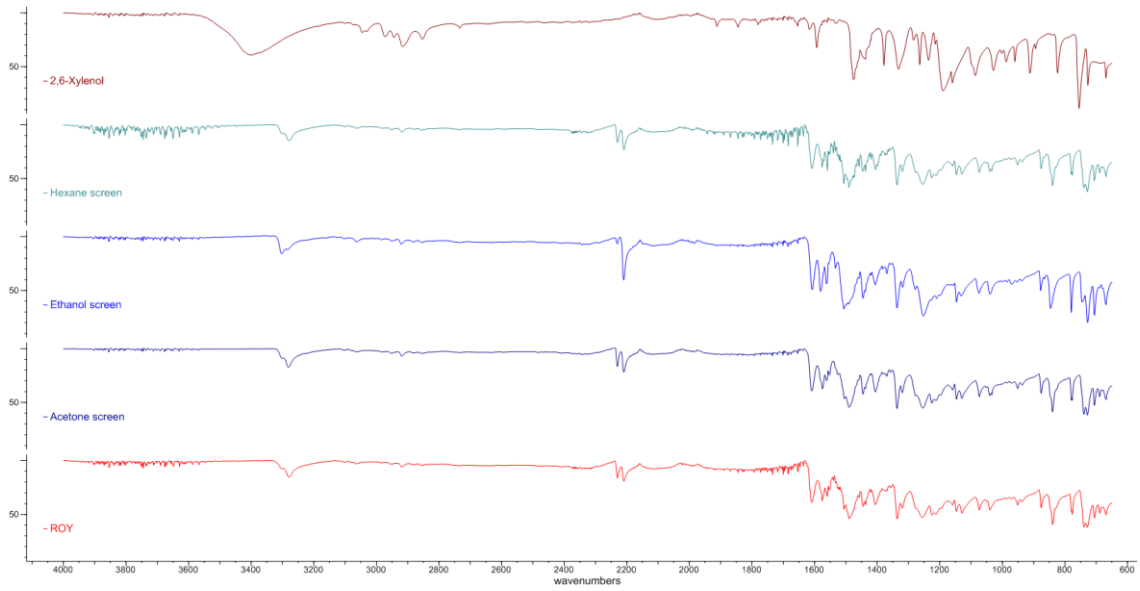


*Figure 43. 2,6-Xylenol.*

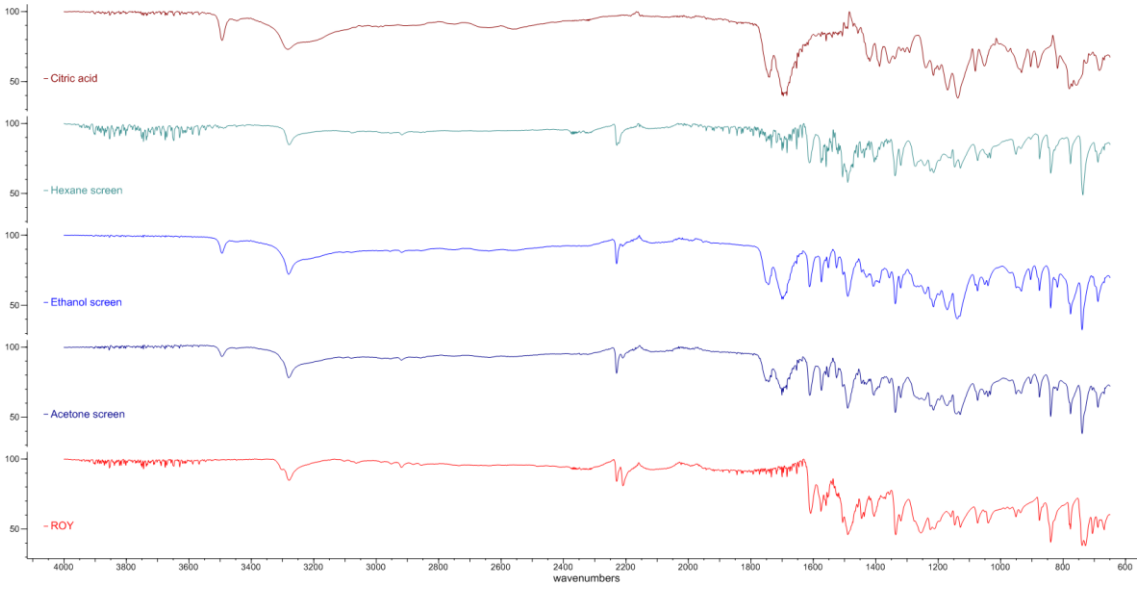


*Figure 44. Citric acid.*

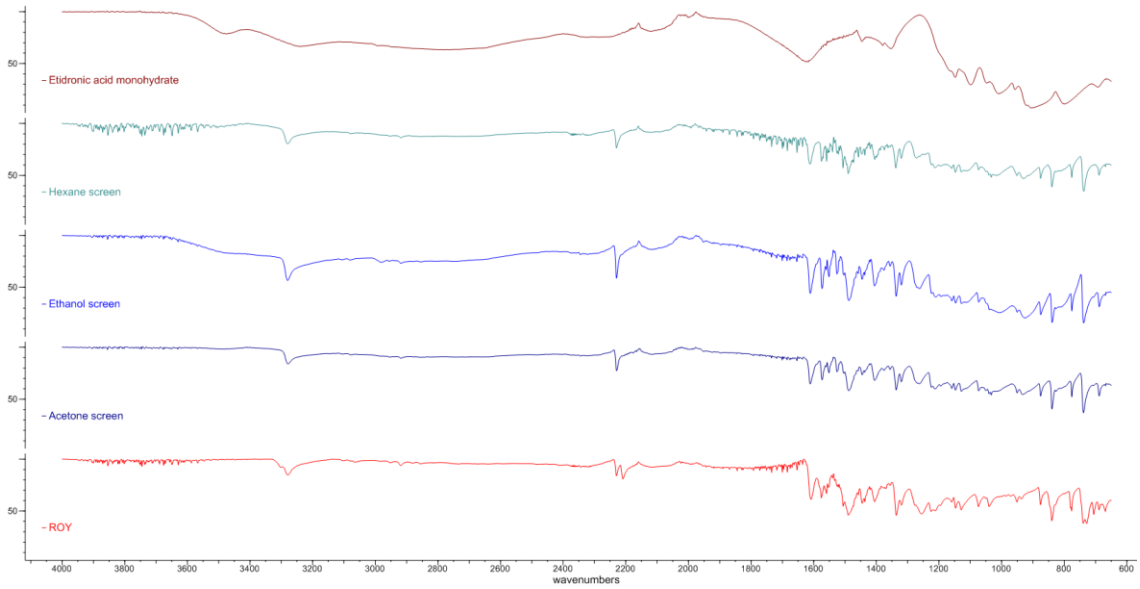


*Figure 45. Etidronic acid monohydrate.*

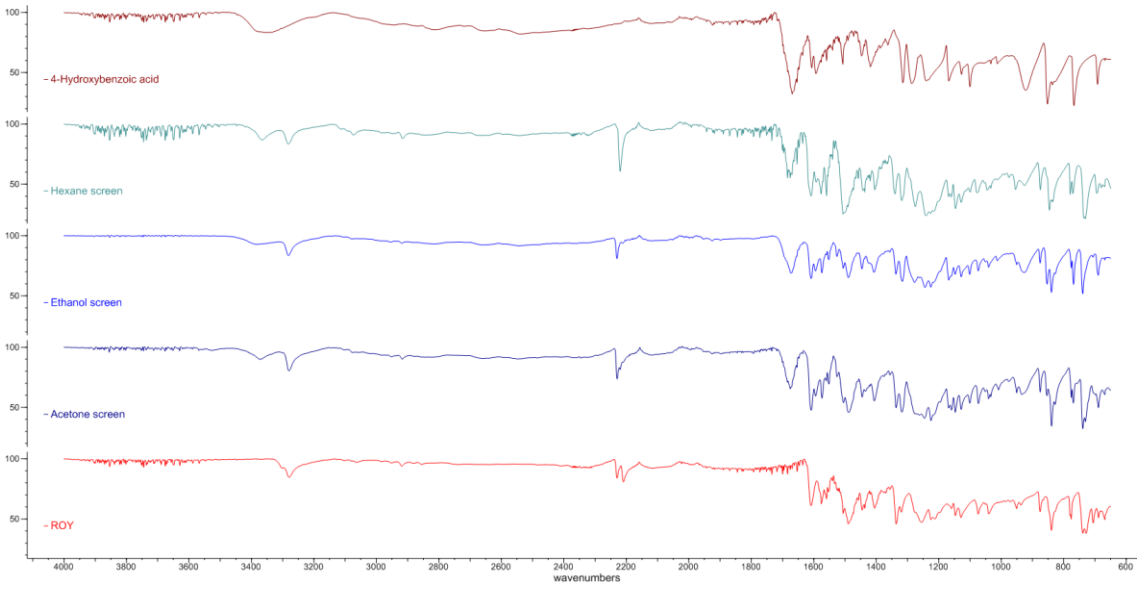


*Figure 46. 4-Hydroxybenzoic acid.*

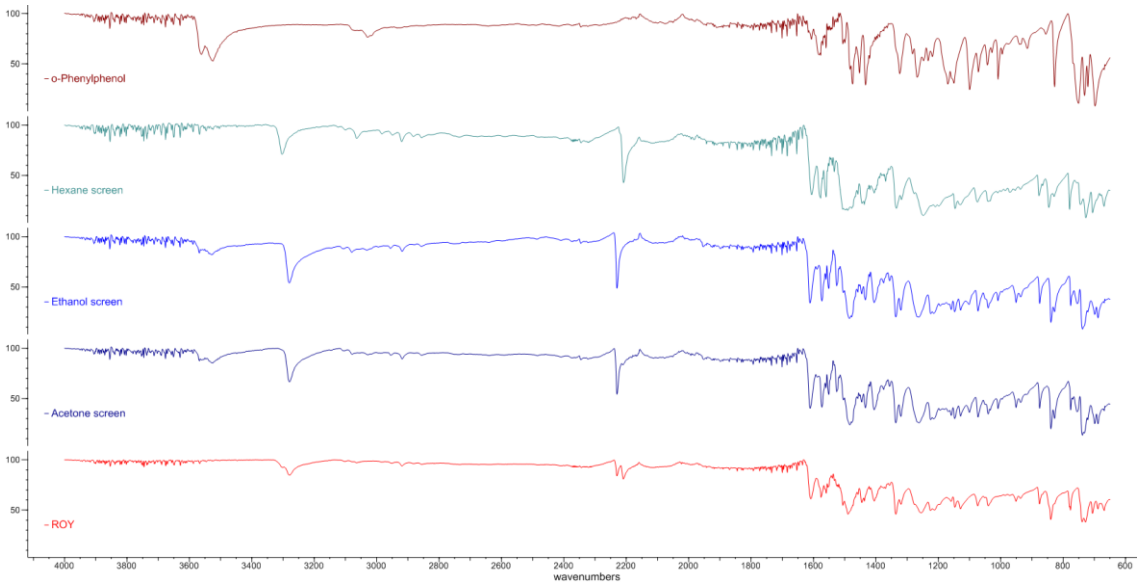


*Figure 47. o-Phenylphenol.*

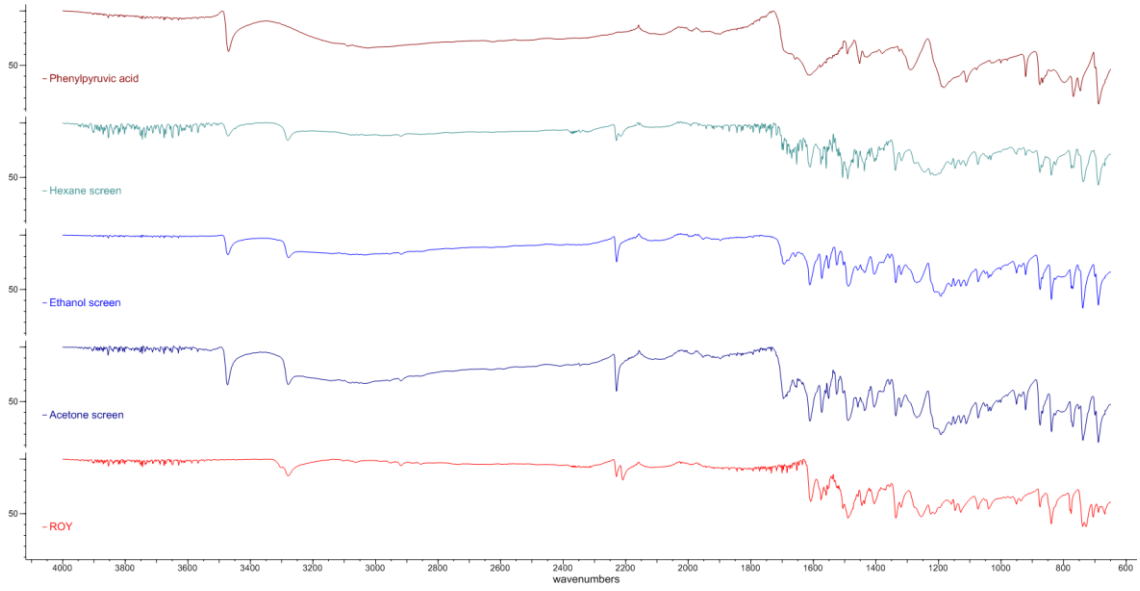


*Figure 48. Phenylpyruvic acid.*

## 4.3 IR spectra of samples from the LAG experiments

Each figure shows the spectra of ROY (red), the co-former (brown) and the product of LAG of a 1:1 molar mixture of these two components (LAG, blue). The figures are labelled by co-former.

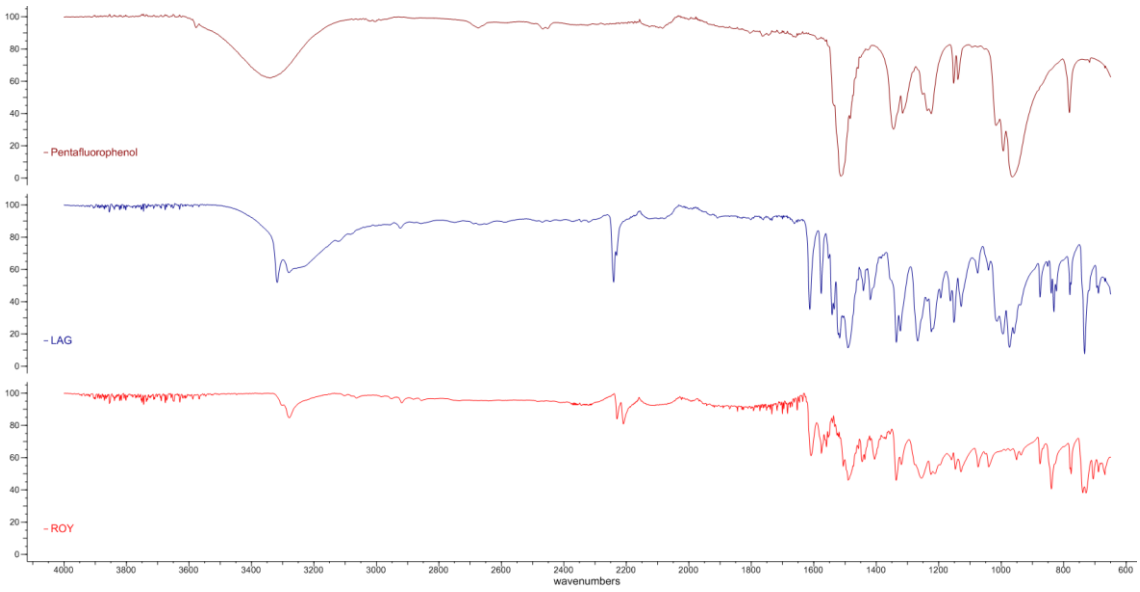


*Figure 49. Pentafluorophenol.*

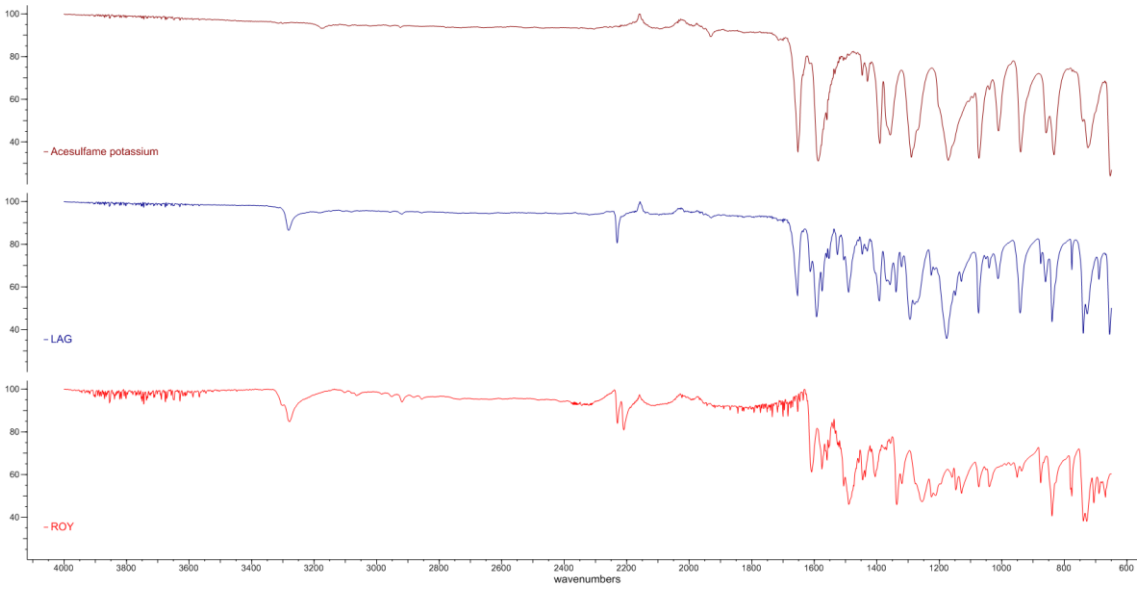


*Figure 50. Acesulfame potassium.*

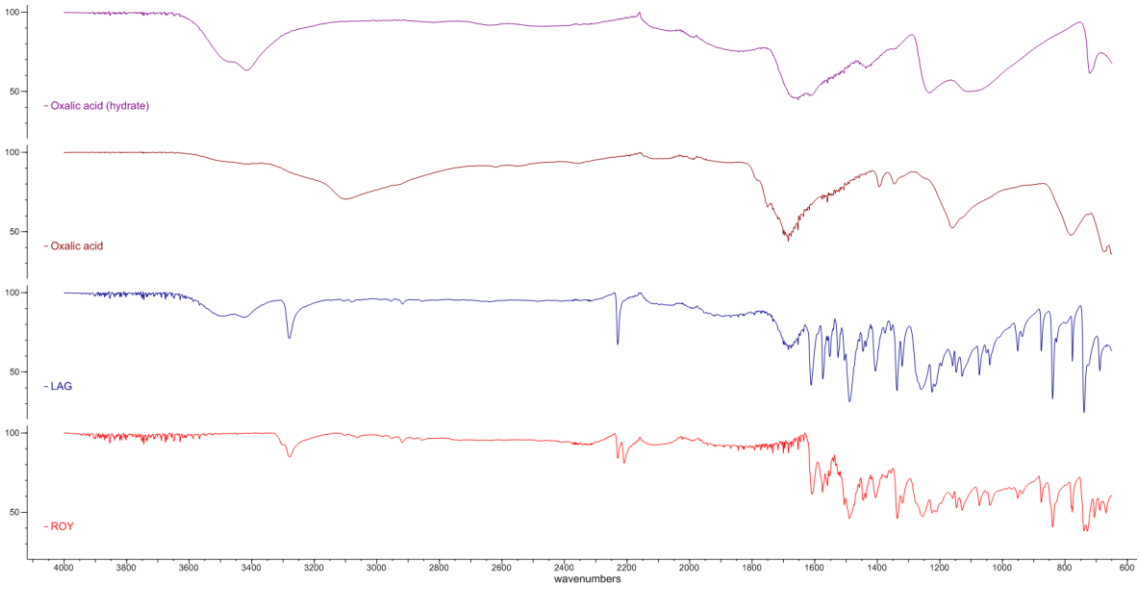


*Figure 51. Oxalic acid. Hydrate of oxalic acid (purple) is included for comparison.*

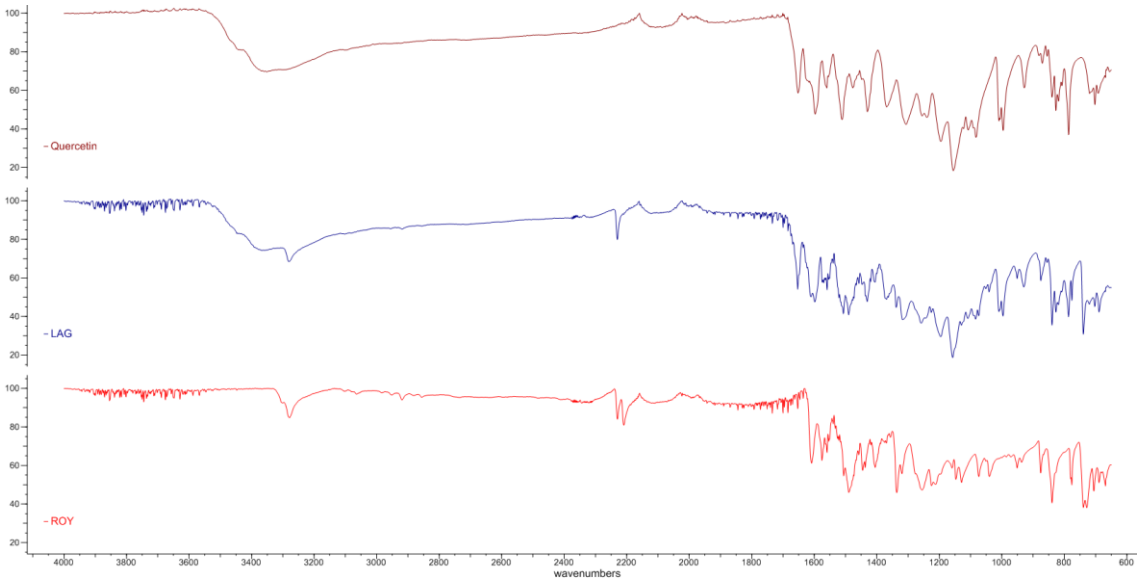


*Figure 52. Quercetin.*

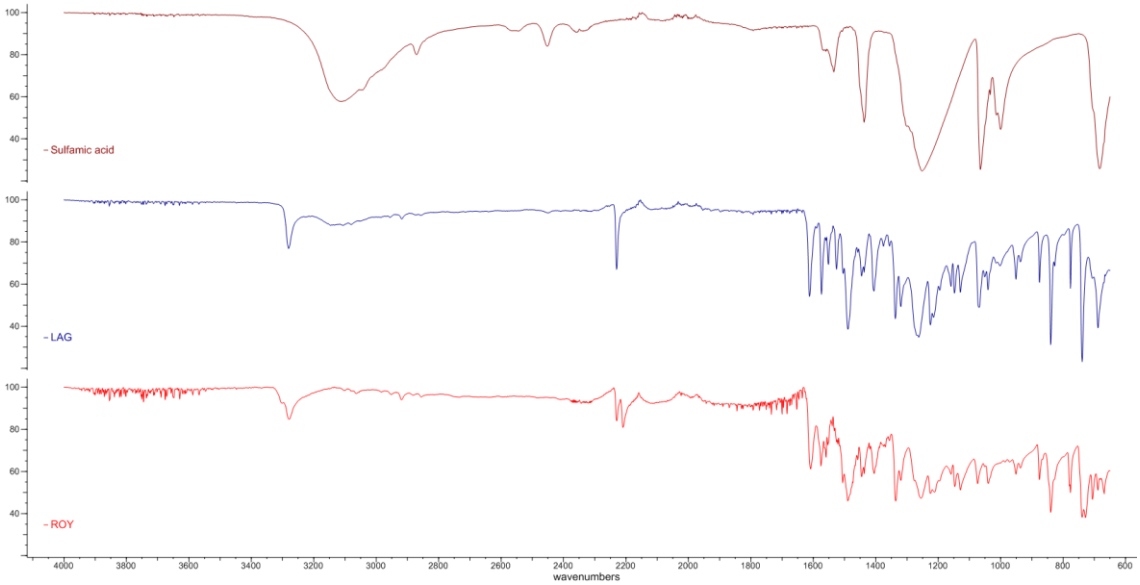


*Figure 53. Sulfamic acid.*

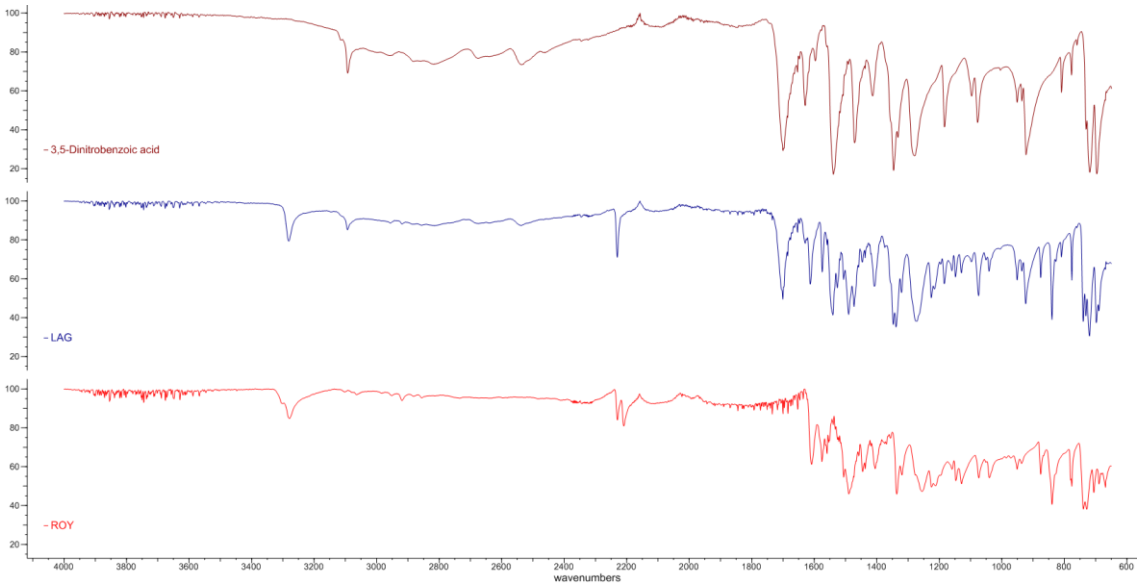


*Figure 54. 3,5-Dinitrobenzoic acid.*

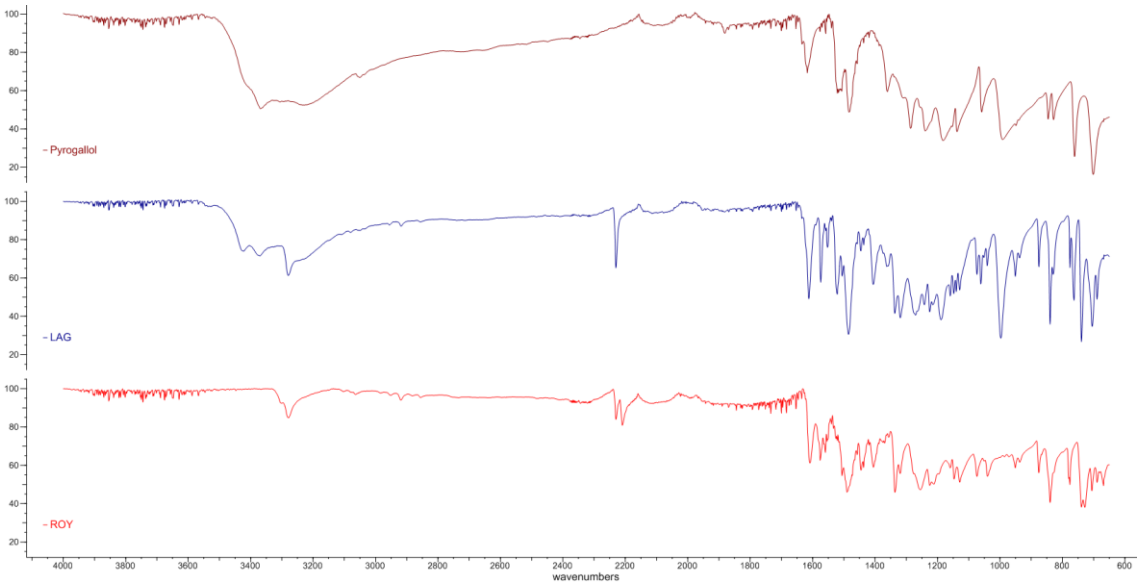


*Figure 55. Pyrogallol.*

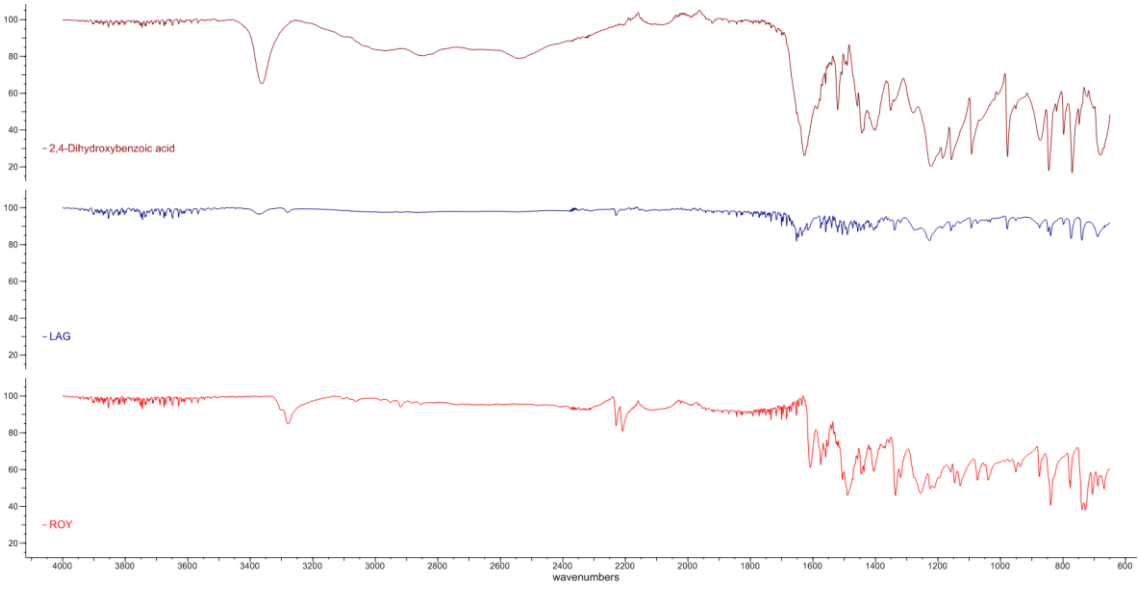


*Figure 56. 2,4-Dihydroxybenzoic acid.*

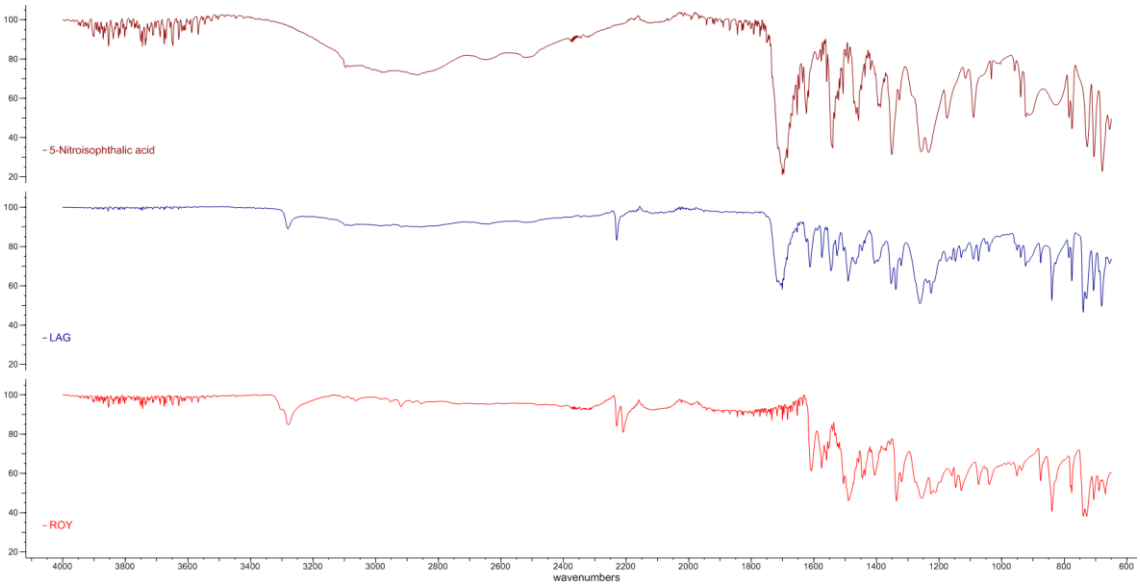


*Figure 57. 5-Nitroisophthalic acid.*

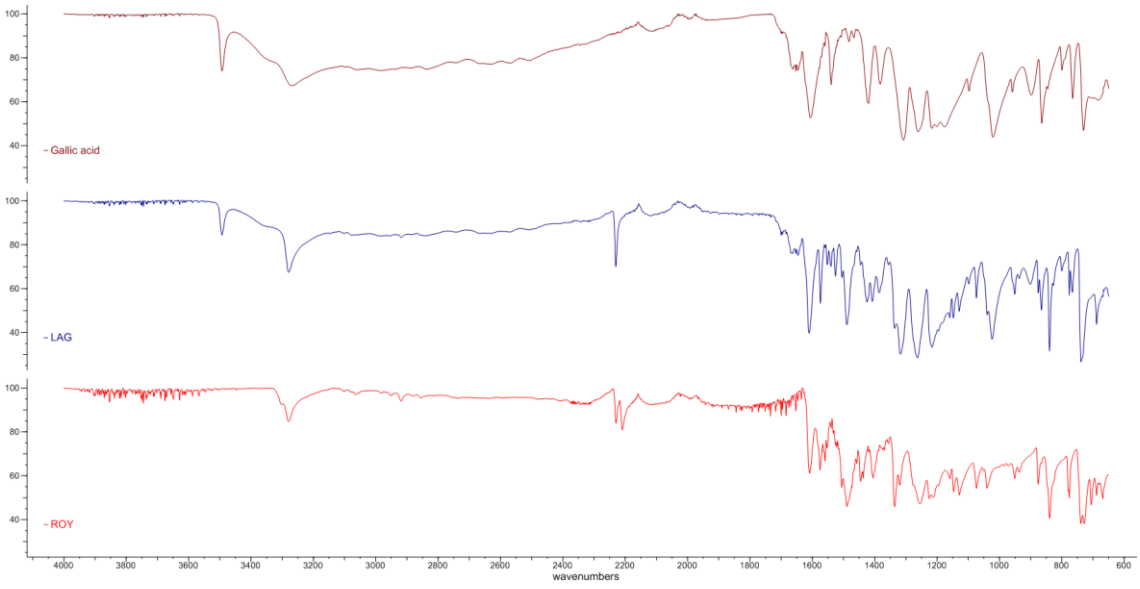


*Figure 58. Gallic acid.*

## 4.4 PXRD patterns from the evaporative and reaction crystallisation experiments

PXRD patterns comparing the co-formers (blue patterns) with the product of the reaction crystallisation ('slurry') (green patterns) and evaporative crystallisation experiments (pink patterns). The PXRD patterns of the product of the reaction and evaporative crystallisation experiments were compared to those of the ROY polymorphs that have patterns available (i.e. the seven which have a CSD entry). The patterns of the ROY polymorphs present are displayed in the plots and are coloured by polymorph colour. The plots are labelled by co-former.

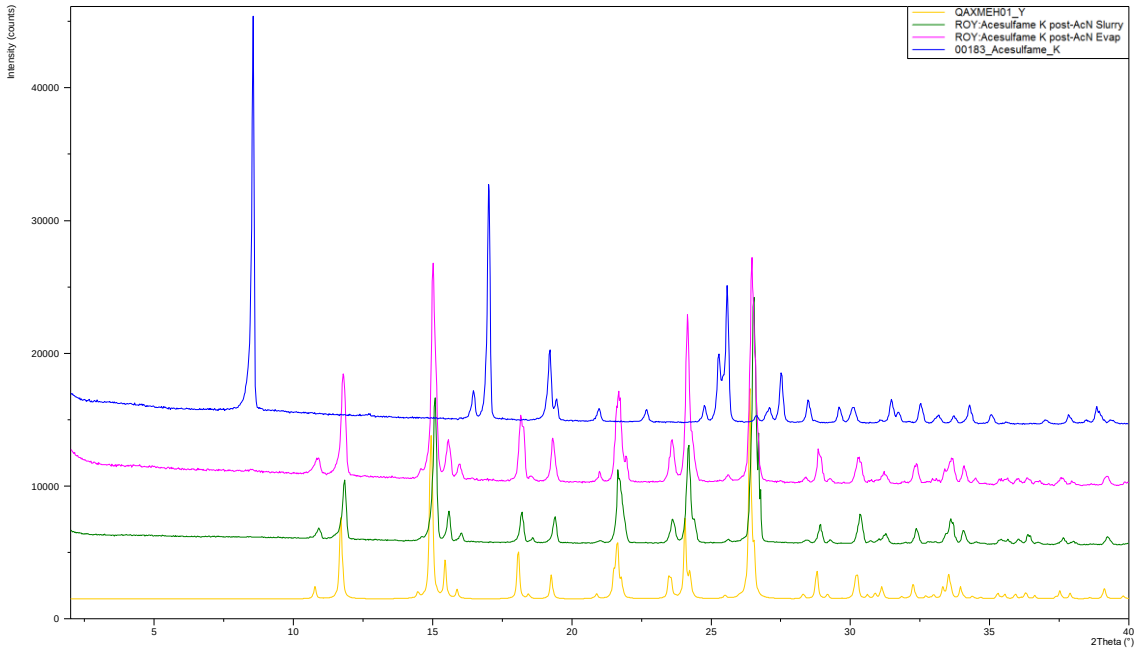


*Figure 59. Acesulfame potassium.*

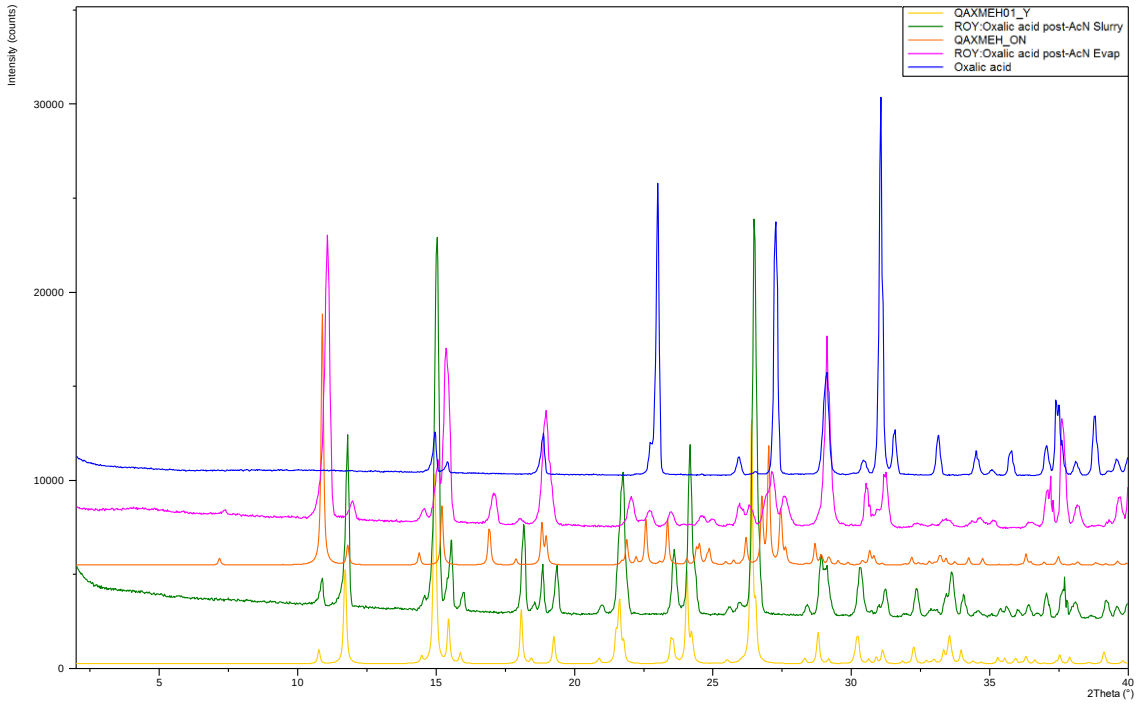


*Figure 60. Oxalic acid.*

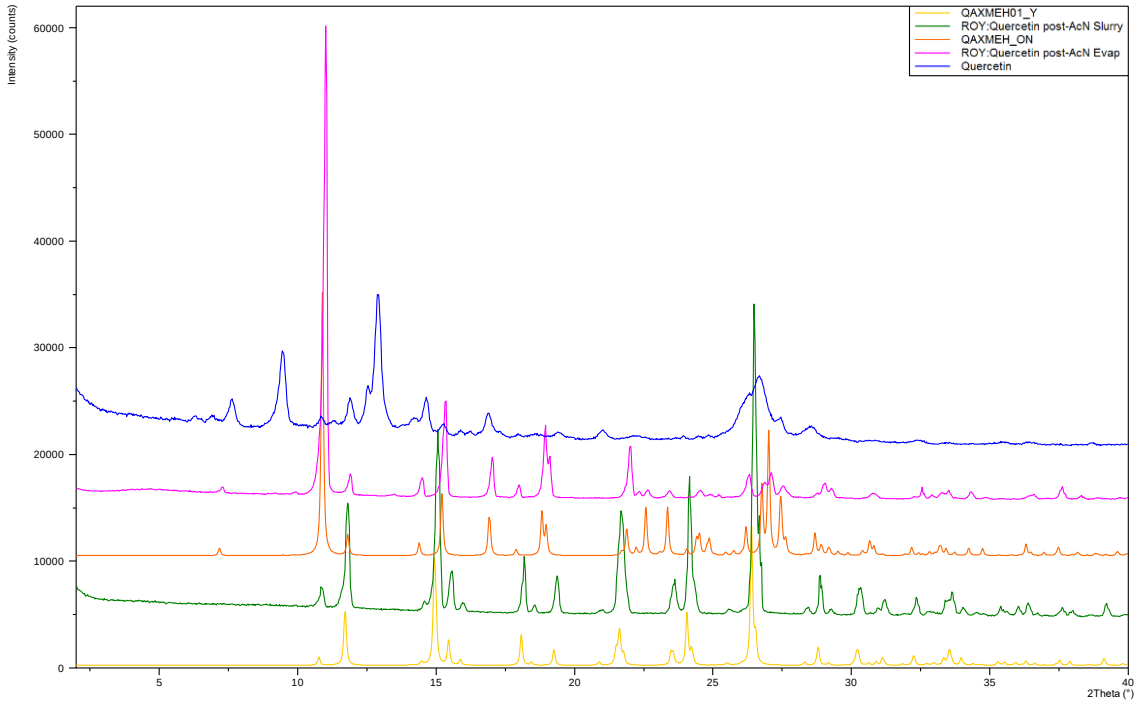


*Figure 61. Quercetin.*

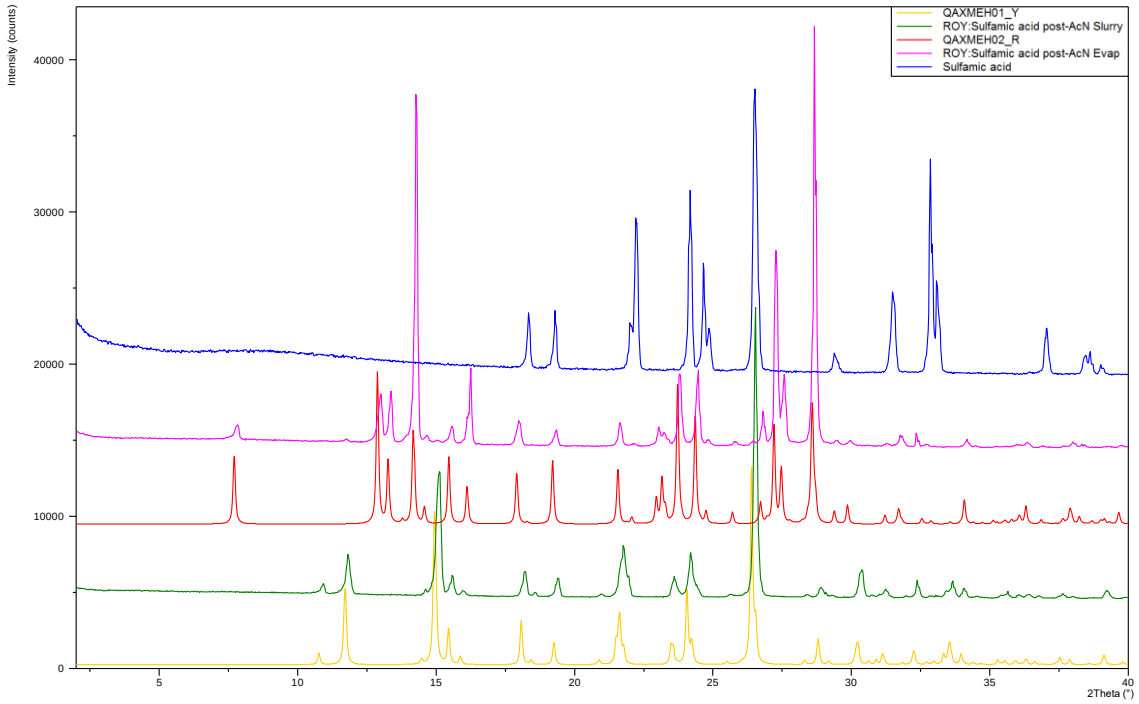


*Figure 62. Sulfamic acid.*

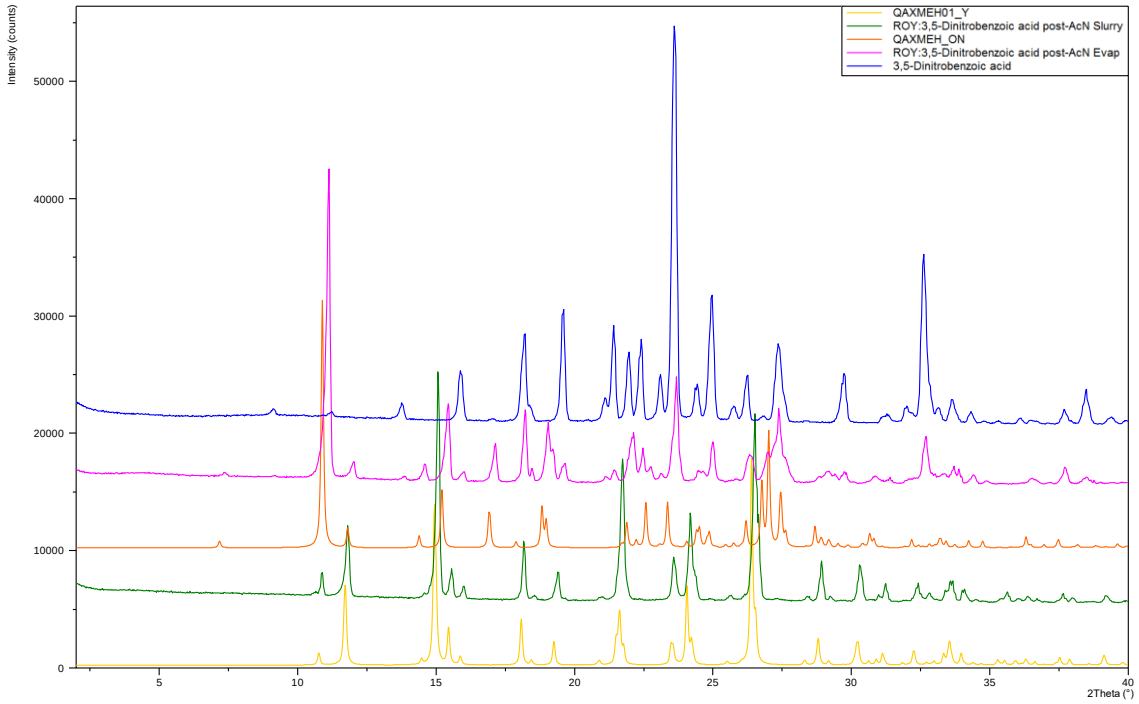


*Figure 63. 3,5-Dinitrobenzoic acid.*

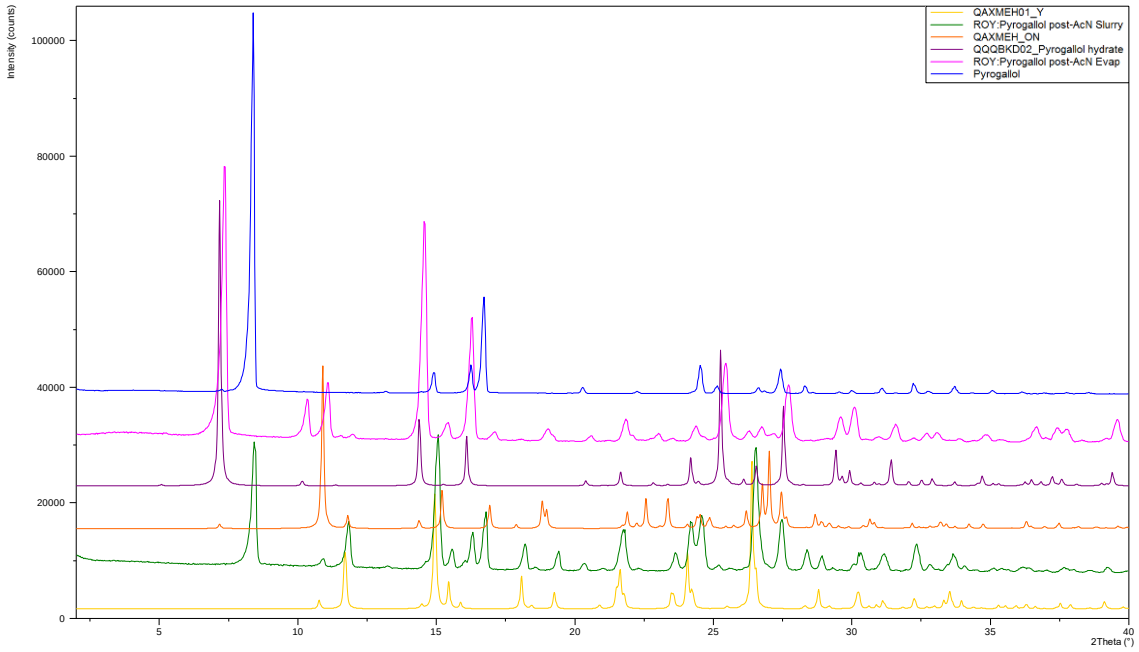


*Figure 64. Pyrogallol.*

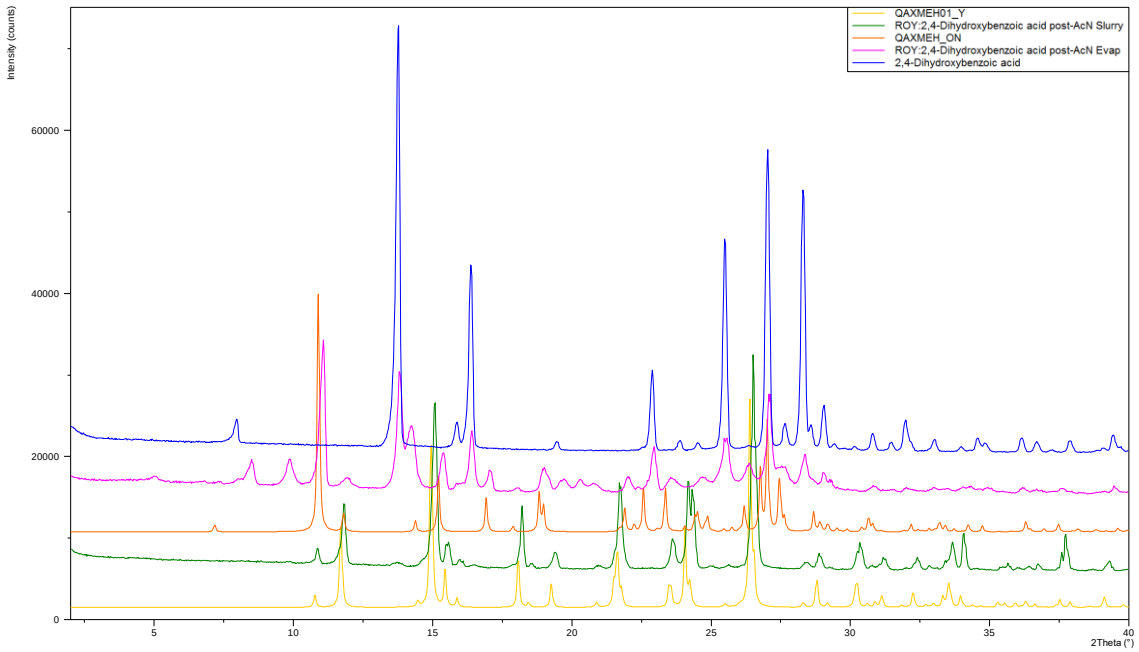


*Figure 65. 2,4-Dihydroxybenzoic acid.*

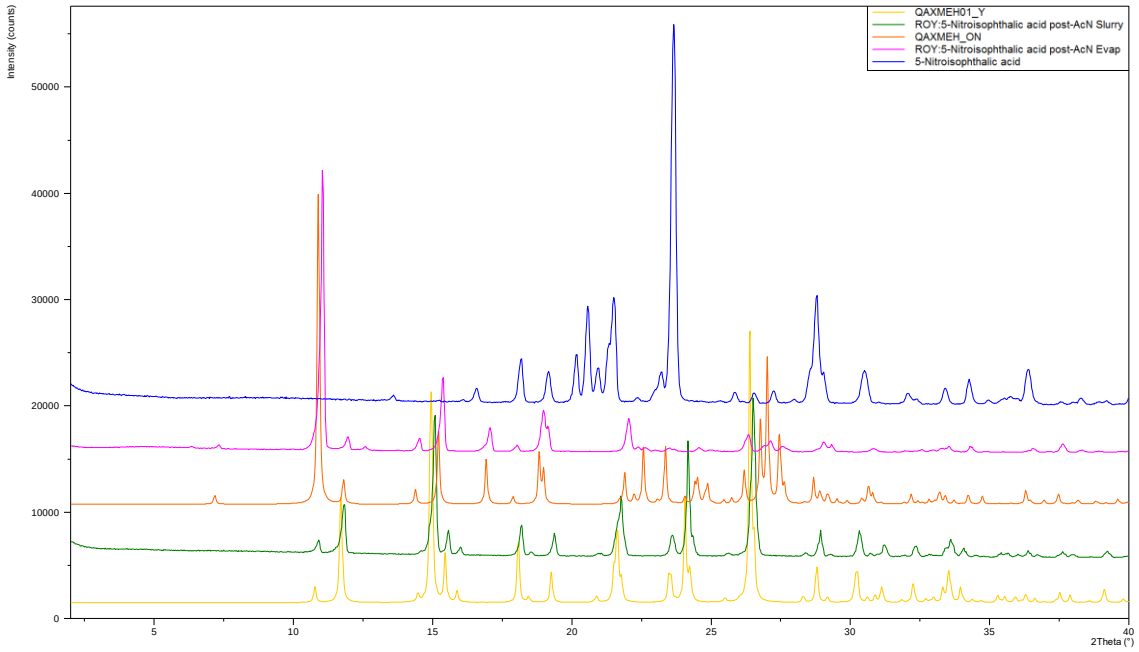


*Figure 66. 5-Nitroisophthalic acid.*

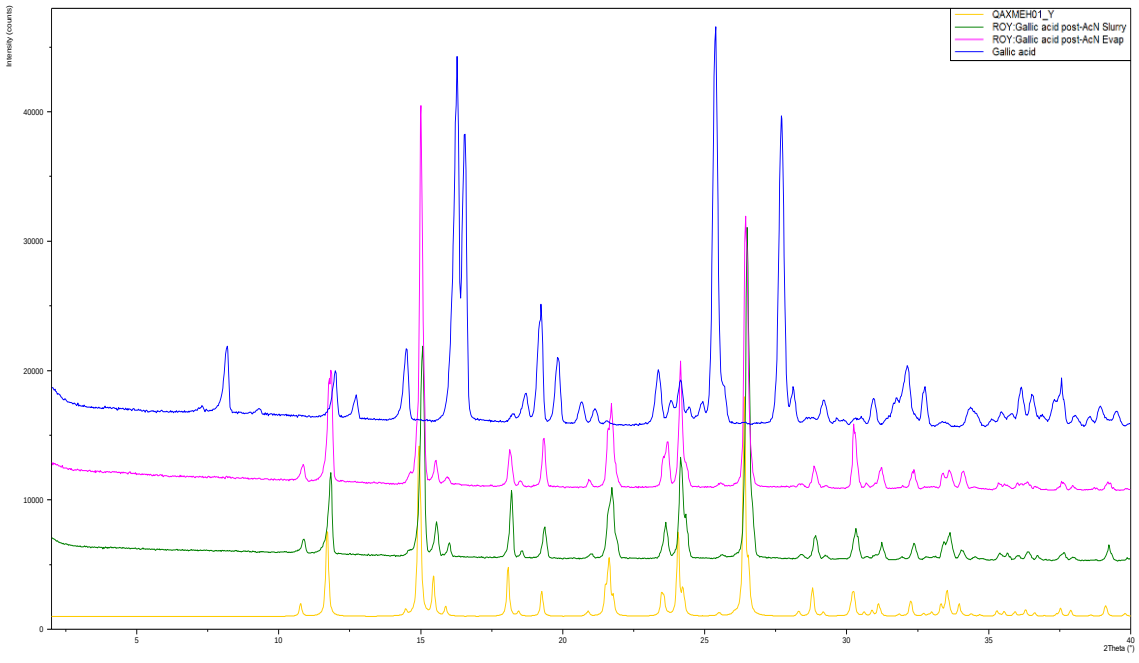


*Figure 67. Gallic acid.*

## 4.5 DSC thermograms of samples from the LAG experiments

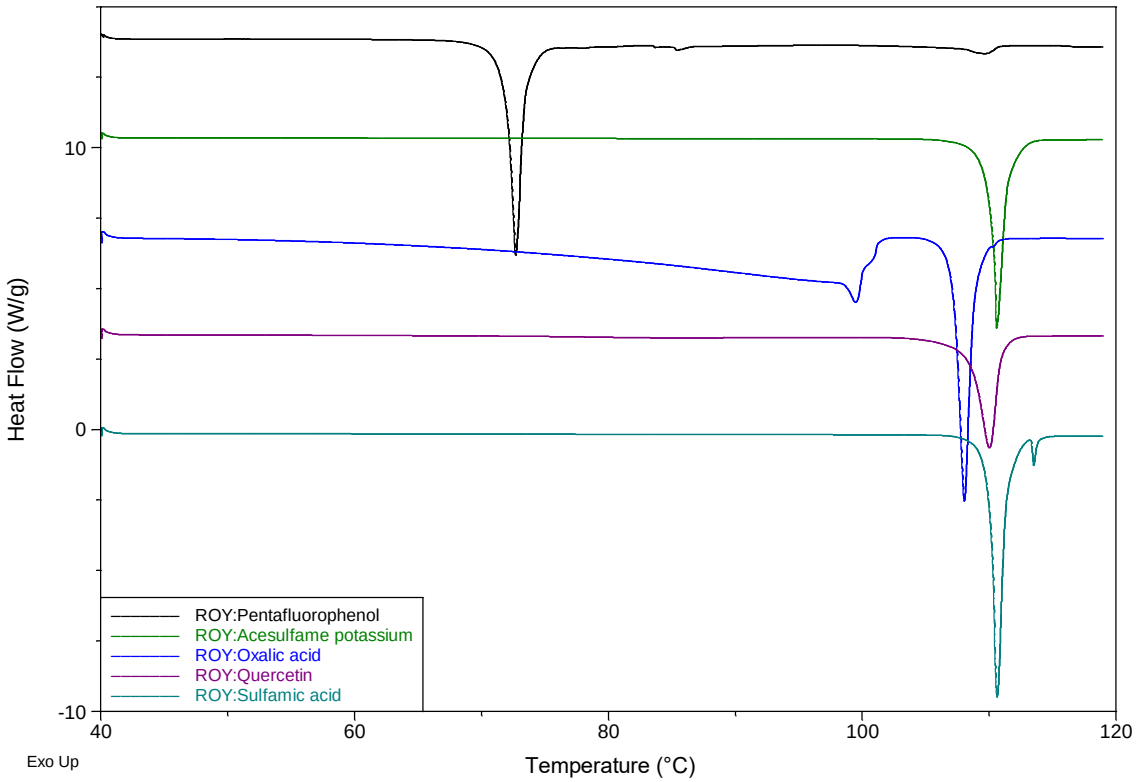


*Figure 68. DSC traces for the initial heating cycle of the products of LAG of ROY and co-formers: pentafluorophenol (black), acesulfame potassium (green), oxalic acid (blue), quercetin (purple) and sulfamic acid (teal).*

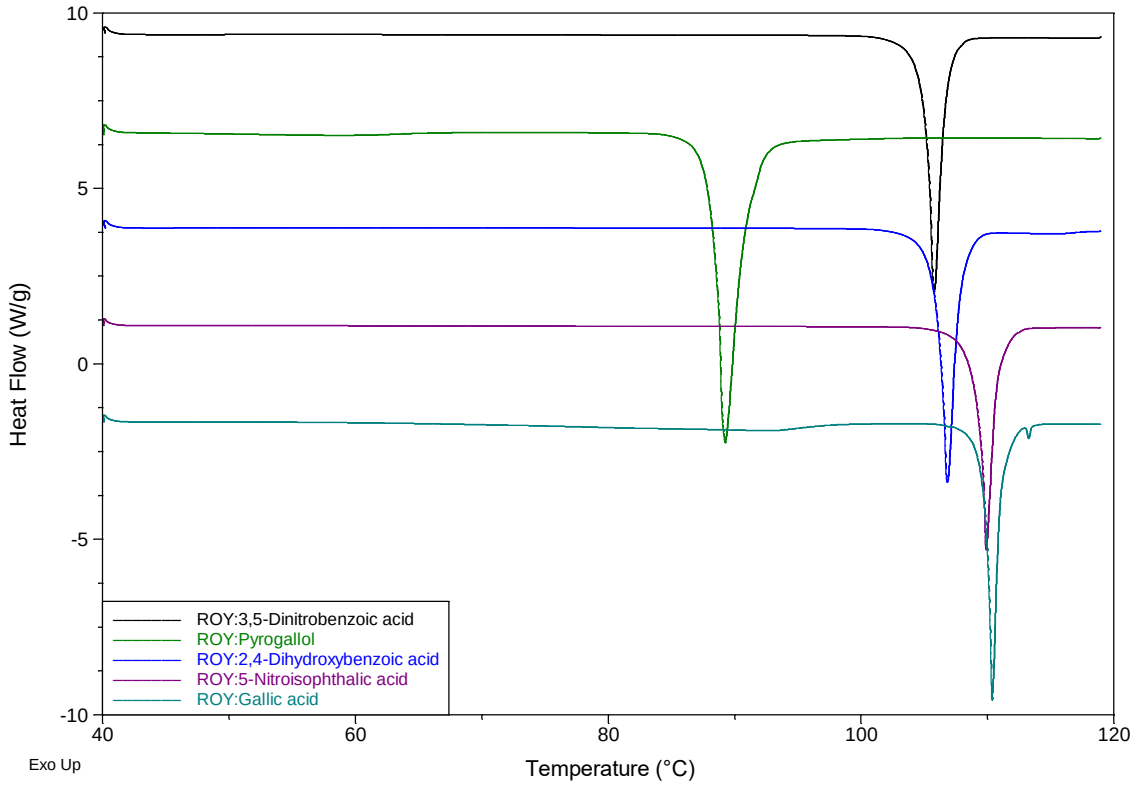


*Figure 69. DSC traces for the initial heating cycle of the products of LAG of ROY and co-formers: 3,5-dinitrobenzoic acid (black), pyrogallol (green), 2,4-dihydroxybenzoic acid (blue), 5-nitroisophthalic acid (purple) and gallic acid (teal).*

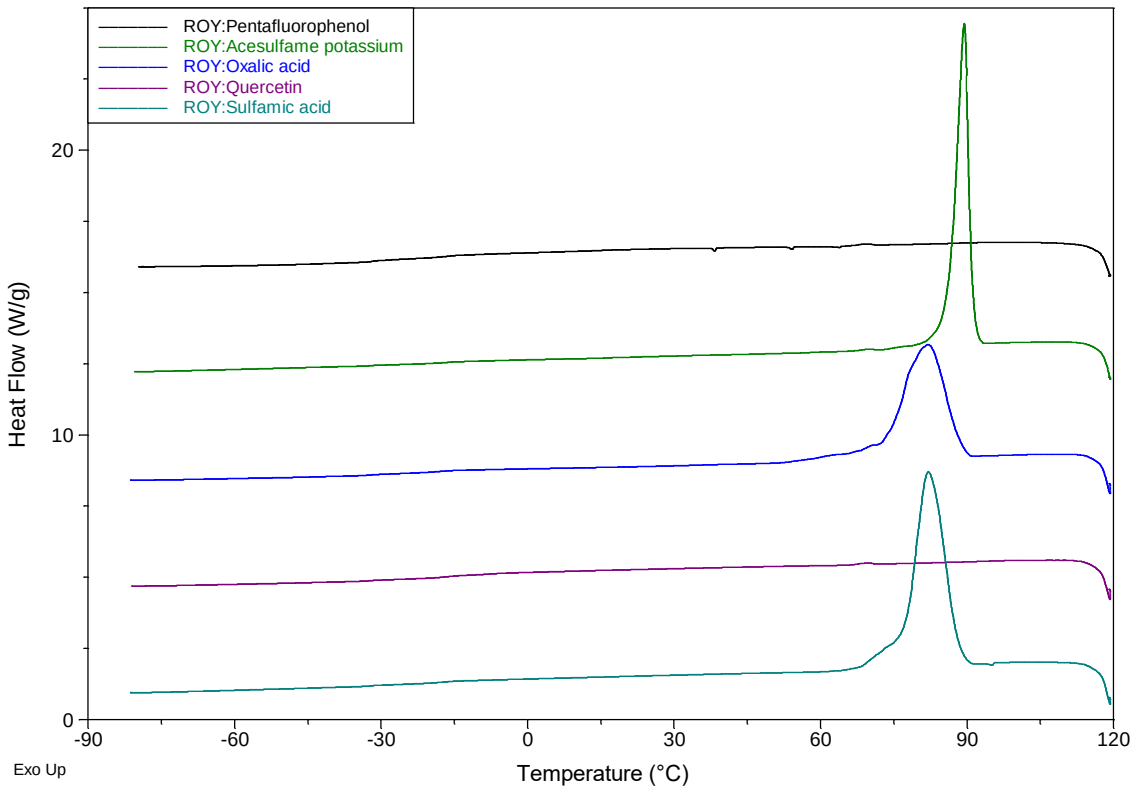


*Figure 70. DSC traces for the cooling cycle of the products of LAG of ROY and co-formers: pentafluorophenol (black), acesulfame potassium (green), oxalic acid (blue), quercetin (purple) and sulfamic acid (teal).*

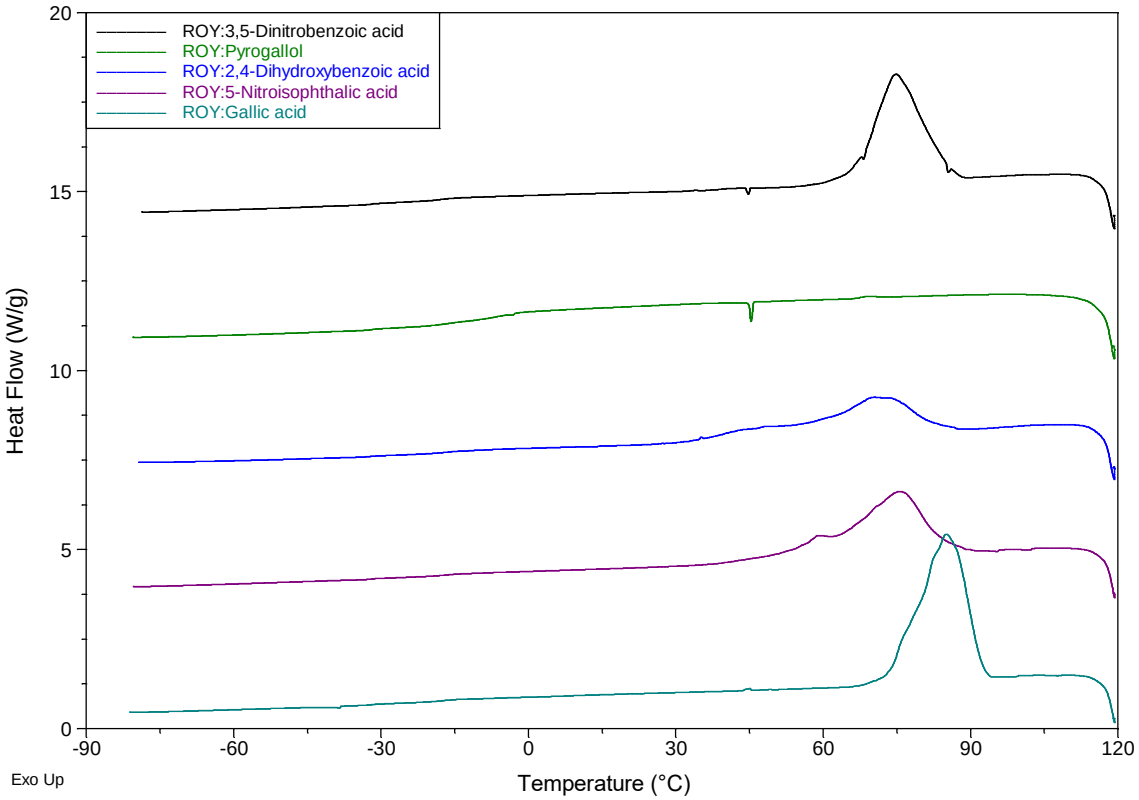


*Figure 71. DSC traces for the cooling cycle of the products of LAG of ROY and co-formers: 3,5-dinitrobenzoic acid (black), pyrogallol (green), 2,4-dihydroxybenzoic acid (blue), 5-nitroisophthalic acid (purple) and gallic acid (teal).*

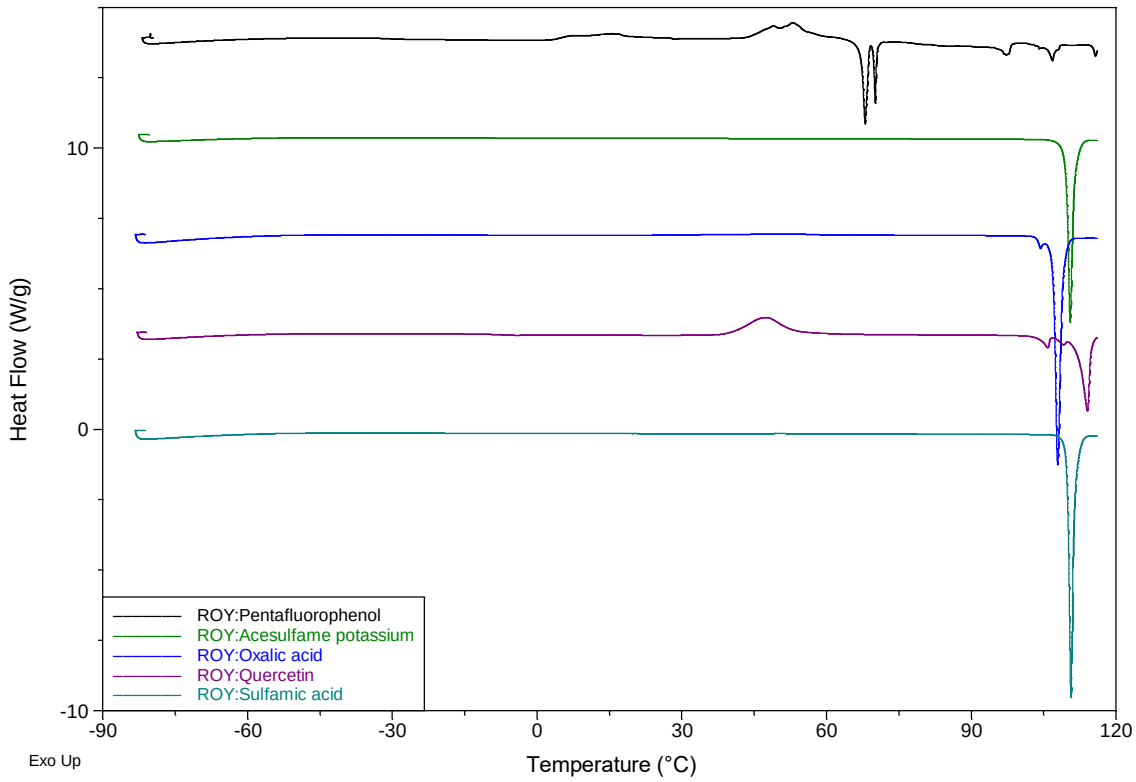


*Figure 72. DSC traces for the second heating cycle of the products of LAG of ROY and co-formers: pentafluorophenol (black), acesulfame potassium (green), oxalic acid (blue), quercetin (purple) and sulfamic acid (teal).*

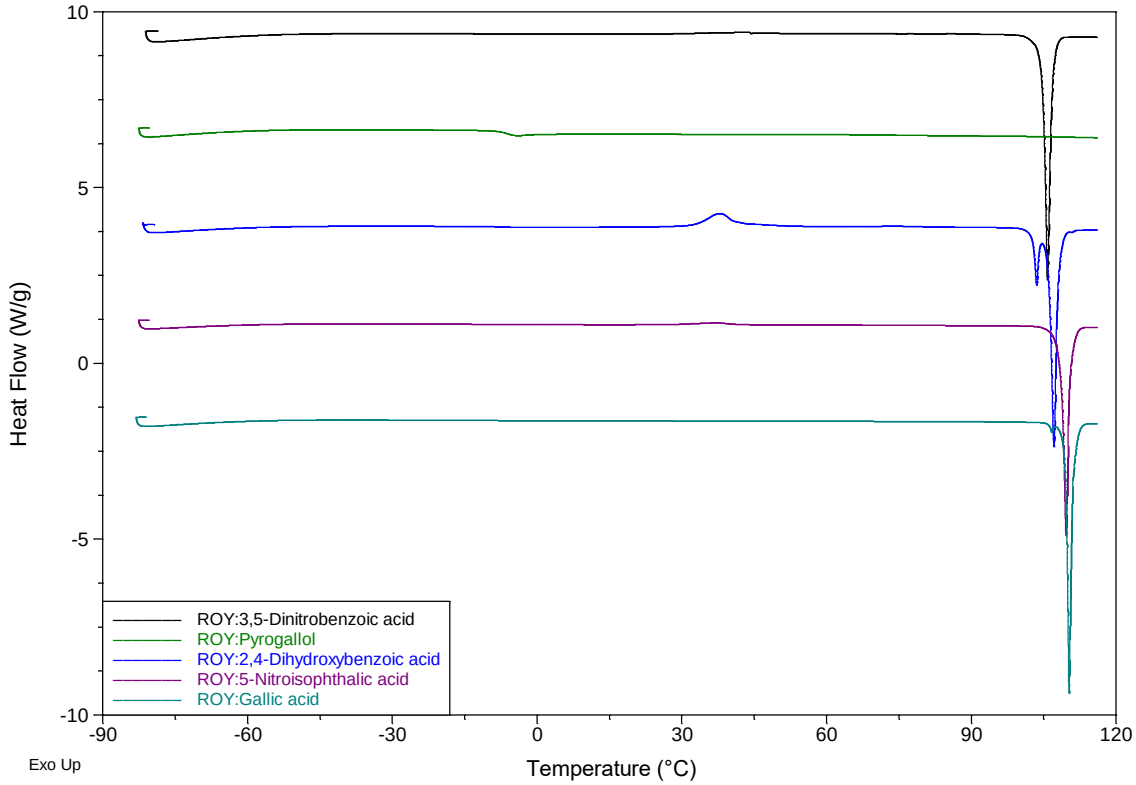


*Figure 73. DSC traces for the second heating cycle of the products of LAG of ROY and co-formers: 3,5-dinitrobenzoic acid (black), pyrogallol (green), 2,4-dihydroxybenzoic acid (blue), 5-nitroisophthalic acid (purple) and gallic acid (teal).*

## 4.6 DSC thermograms of ROY, pyrogallol and the product of their 1:1 molar ratio grind

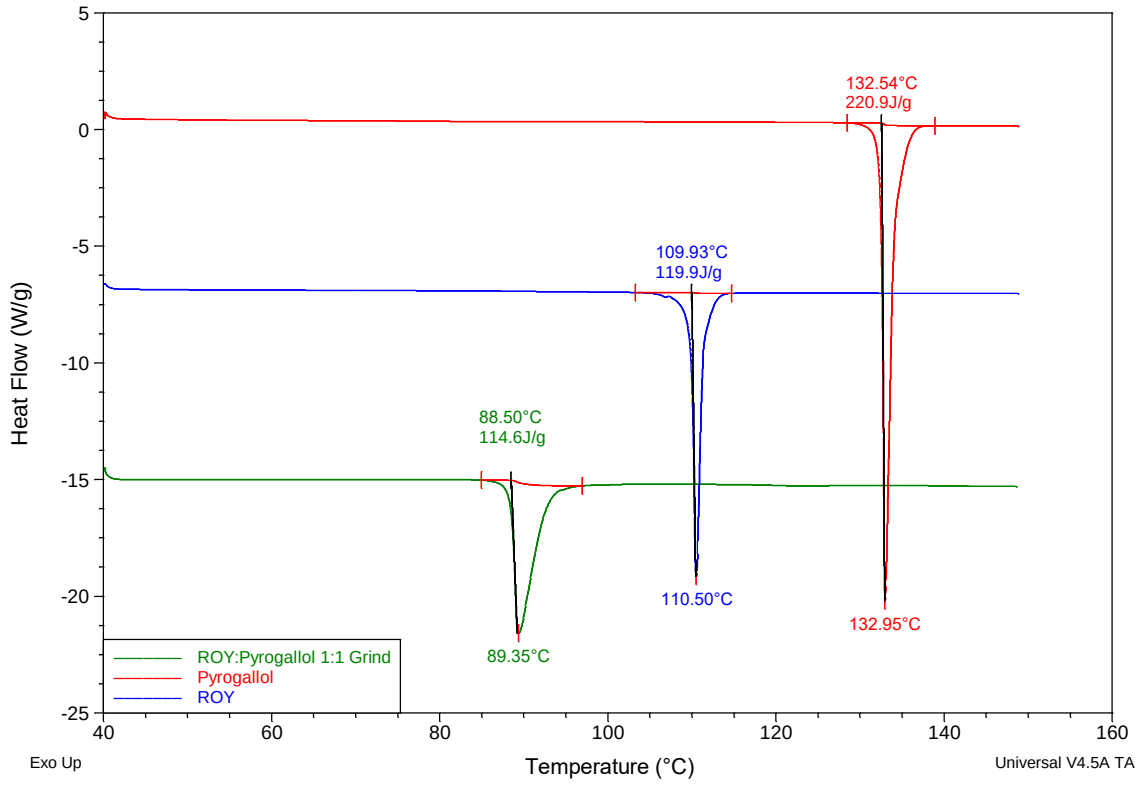


*Figure 74. Initial heating phase DSC curves of pyrogallol (red), ROY (blue) and ROY:pyrogallol 1:1 grind (green).*

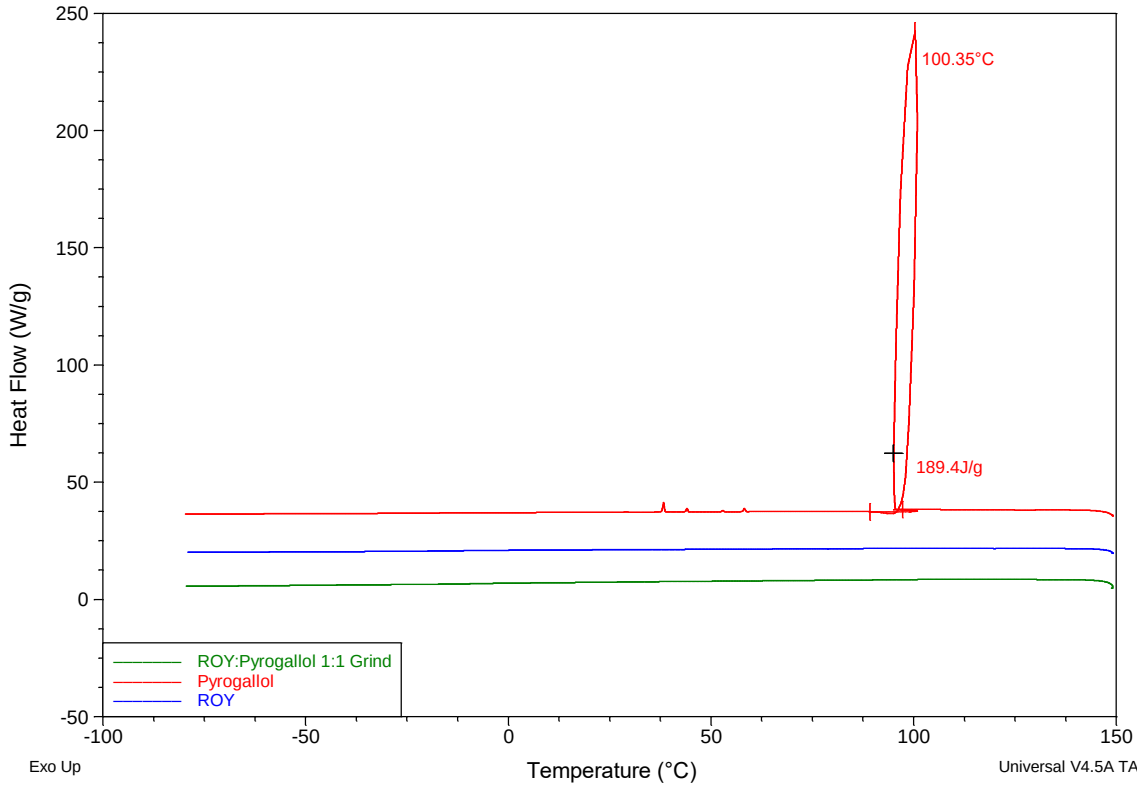


*Figure 75. Cooling phase DSC curves of pyrogallol (red), ROY (blue) and ROY:pyrogallol 1:1 grind (green).*

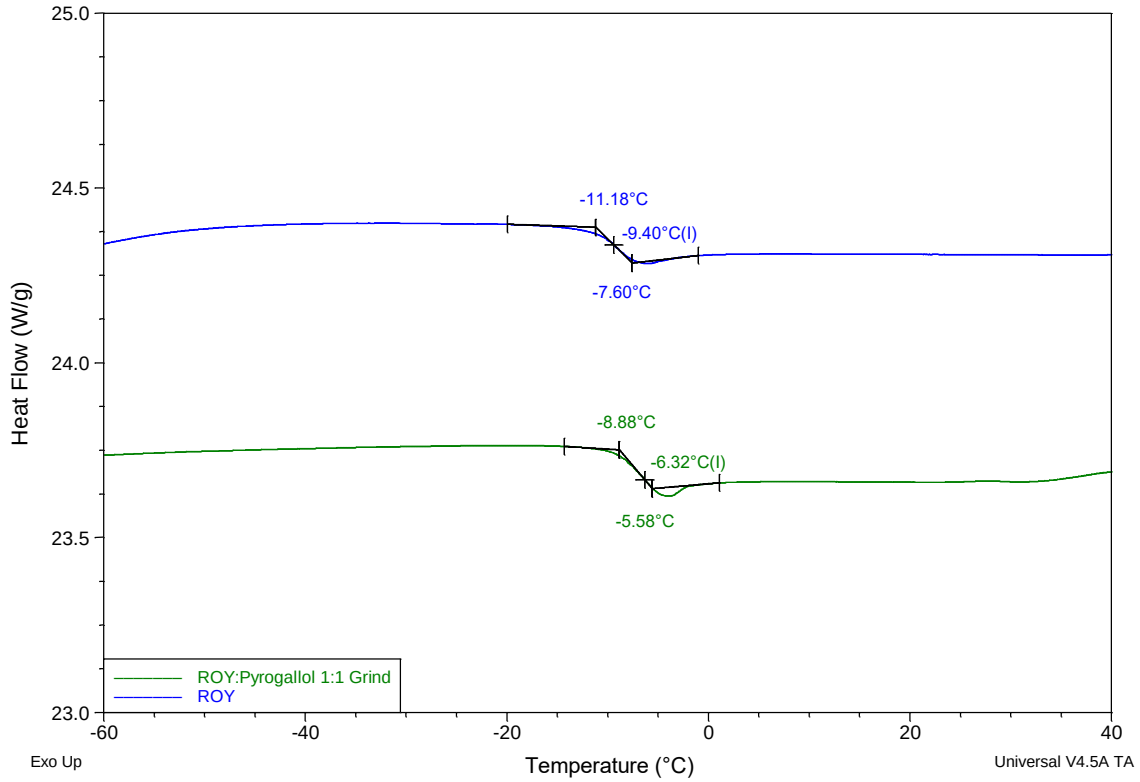


*Figure 76. Focused area of second heating cycle DSC curves of ROY (blue) and ROY:pyrogallol 1:1 grind (green) showing glass transitions.*

## 4.7 DSC thermograms of grinds of ROY and pyrogallol in varying molar ratios

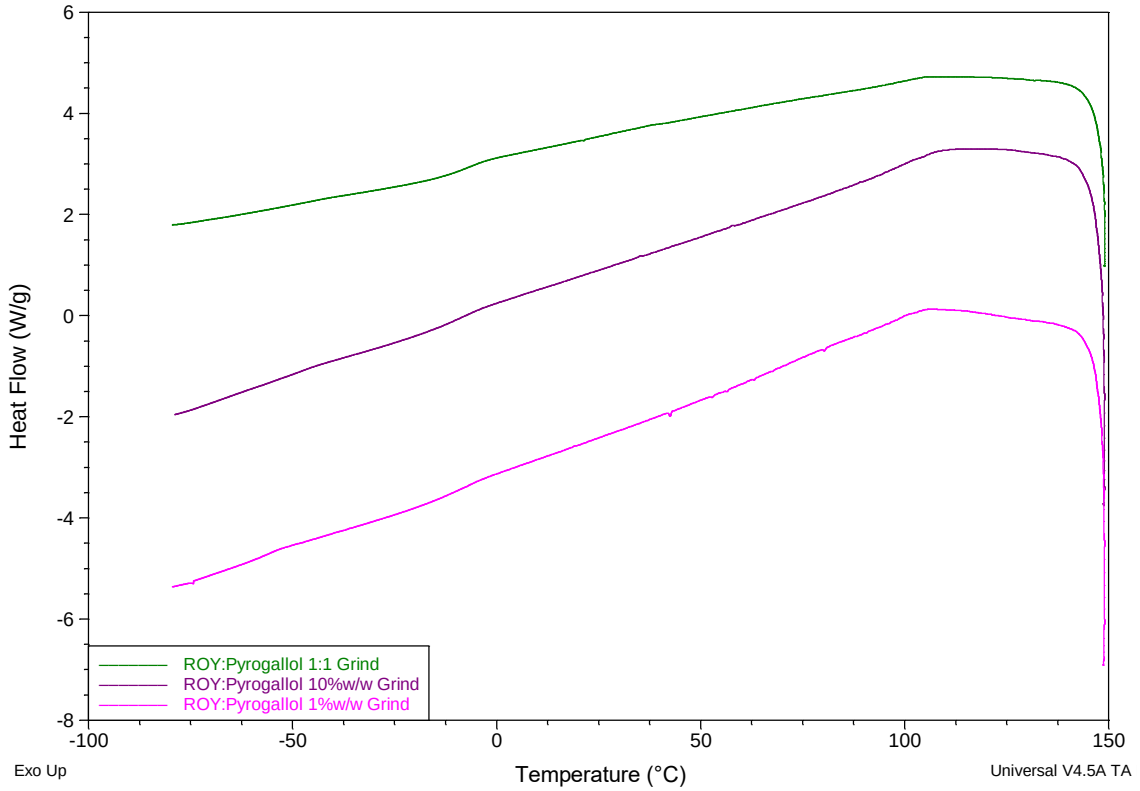


*Figure 77. Cooling phase DSC curves of ROY:pyrogallol: 1:1 grind (green), 10%w/w (purple) and 1%w/w (pink).*

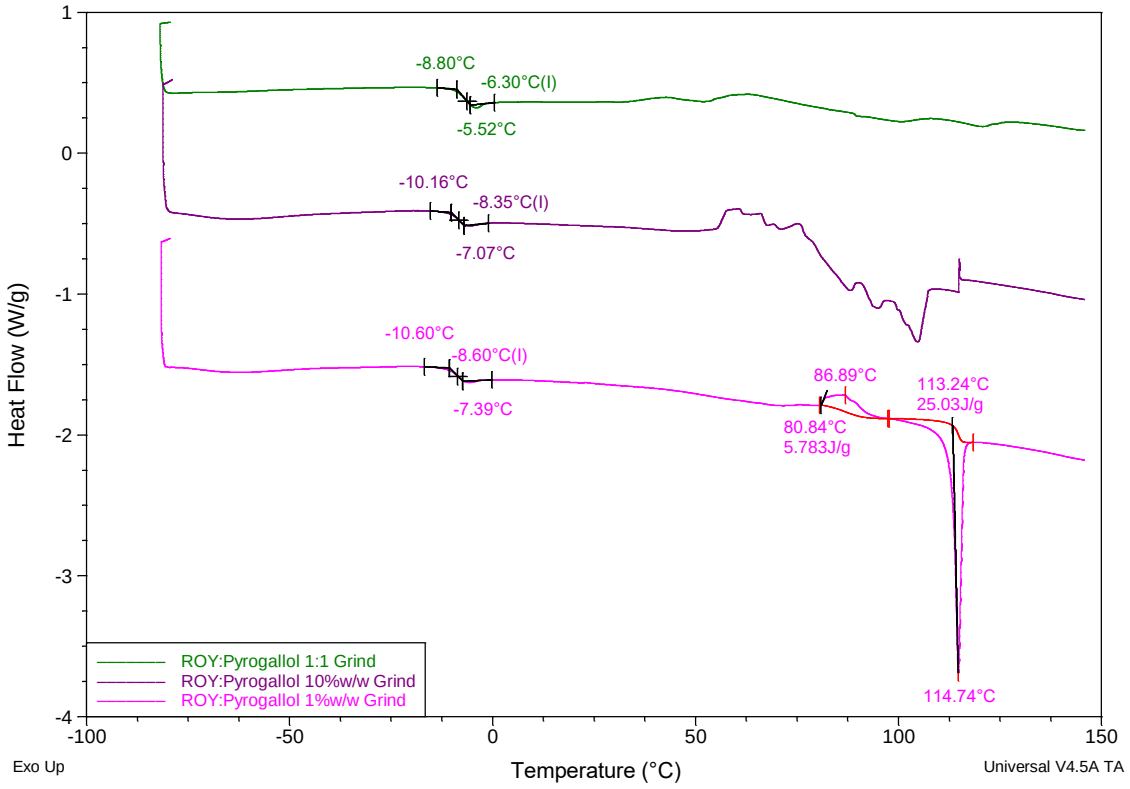


*Figure 78. Second heating phase DSC curves of ROY:pyrogallol 1:1 grind (green), 10%w/w (purple) and 1%w/w (pink) including glass transitions.*

## 4.8 Full data set from hydrogen bonding propensity prediction

*Table 2. Coefficients for logit_model_1 applied to ROY (QAXMEH01).*

| Coefficients: | Estimate | Std.Error | Z value | Pr(>\|z\|) | Significance code | Lower Bound | Upper Bound |
|---|---|---|---|---|---|---|---|
| (Intercept) | **0.633** | 0.234 | 2.709 | 0.00675519 | ** | 0.165 | 1.083 |
| Donoratom_2 of ar_hydroxy | **-0.391** | 0.074 | -5.258 | 1.45444e-07 | *** | -0.537 | -0.246 |
| Donorother | **0.611** | 0.066 | 9.221 | 2.9478e-20 | *** | 0.482 | 0.742 |
| Acceptoratom_2(3) of ar_nitro | **2.242** | 0.195 | 11.519 | 1.06424e-30 | *** | 1.874 | 2.639 |
| Acceptoratom_2 of ar_hydroxy | **1.883** | 0.193 | 9.756 | 1.73657e-22 | *** | 1.519 | 2.277 |
| Acceptoratom_2 of cyano | **2.361** | 0.196 | 12.017 | 2.89222e-33 | *** | 1.989 | 2.761 |
| Acceptorother | **4.313** | 0.183 | 23.549 | 1.28037e-122 | *** | 3.969 | 4.689 |
| competition | **-0.086** | 0.005 | -17.931 | 6.78803e-72 | *** | -0.096 | -0.077 |
| Donor_steric_density | **-0.023** | 0.002 | -12.486 | 8.87143e-36 | *** | -0.027 | -0.019 |
| Acceptor_steric_density | **-0.045** | 0.002 | -20.515 | 1.58124e-93 | *** | -0.050 | -0.041 |
| Donor_aromaticity | **-0.805** | 0.177 | -4.545 | 5.49985e-06 | *** | -1.154 | -0.459 |
| Acceptor_aromaticity | **-0.529** | 0.164 | -3.228 | 0.00124467 | ** | -0.850 | -0.208 |
| Donoratom_0 of sec_amine_1 | **0.000** | N/A | N/A | N/A | N/A | N/A | N/A |
| Acceptoratom_1 of cyclic_thioether | **0.000** | N/A | N/A | N/A | N/A | N/A | N/A |

*Table 3. Goodness of fit.*

| | |
|---|---|
| **Log Likelihood** | -5207.380 |
| **Area under ROC curve** | 0.860968 |
| **Akaike Information Criterion (AIC)** | 10438.8 |
| **Null deviance** | 15325.3 on 11218 degrees of freedom |
| **Residual deviance** | 10414.8 on 11207 degrees of freedom |

*Table 4. Predicted inter-molecular hydrogen bond propensities.*

| Donor | Acceptor | Competition | Donor steric density | Acceptor steric density | Donor aromaticity | Acceptor aromaticity | Propensity | Lower bound | Upper bound | Frequency |
|---|---|---|---|---|---|---|---|---|---|---|
| N1 of sec amine 1 | N3 of cyano | 4.00 | 62.75 | 27.57 | 0.58 | 0.58 | **0.31** | 0.22 | 0.42 | 36.8 |
| N1 of sec amine 1 | O2 of ar_nitro | 4.00 | 62.75 | 31.19 | 0.58 | 0.58 | **0.25** | 0.17 | 0.35 | 11.7 |
| N1 of sec amine 1 | O1 of ar_nitro | 8.00 | 62.75 | 31.19 | 0.58 | 0.58 | **0.19** | 0.13 | 0.28 | 18.2 |
| N1 of sec amine 1 | S1 of cyclic thioether | 8.00 | 62.75 | 62.75 | 0.58 | 0.58 | **0.01** | 0.01 | 0.01 | 1.1 |

*Table 5. Predicted intra-molecular hydrogen bond propensities.*

| Donor | Acceptor | Donor sybyl atom type | DA Pair constrained connectivity | DA Pair path string | Donor count | Propensity | Lower bound | Upper bound |
|---|---|---|---|---|---|---|---|---|
| N1 | O1 | N.pl3 | 1 | 0 | 1 | **0.890416** | 0.890416 | 0.890416 |
| N1 | O2 | N.pl3 | 1 | 0 | 1 | **0.890416** | 0.890416 | 0.890416 |
| N1 | N3 | N.pl3 | 1 | 0 | 1 | **0.0918711** | 0.0918711 | 0.0918711 |

4.9 Hydrogen bonding within the ROY:pyrogallol amorphous cell

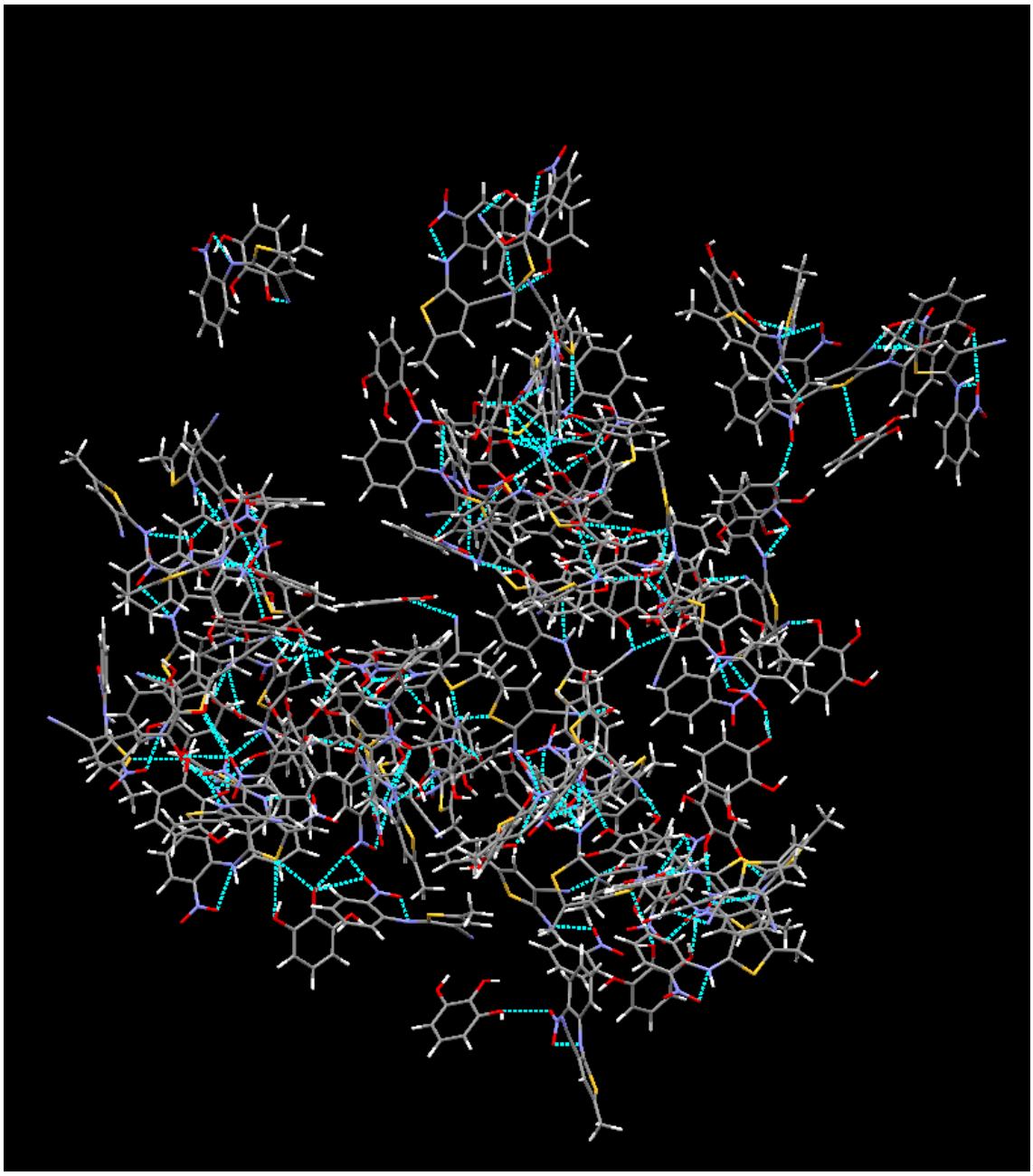

*Figure 79. Amorphous cell displaying strong hydrogen bond contacts between ROY and pyrogallol. N.B. All non-bonded molecules and those containing ROY:ROY contacts and pyrogallol:pyrogallol interactions have been removed for clarity.*

## 4.10 DSC thermograms of grinds of ROY and PVP in varying molar ratios

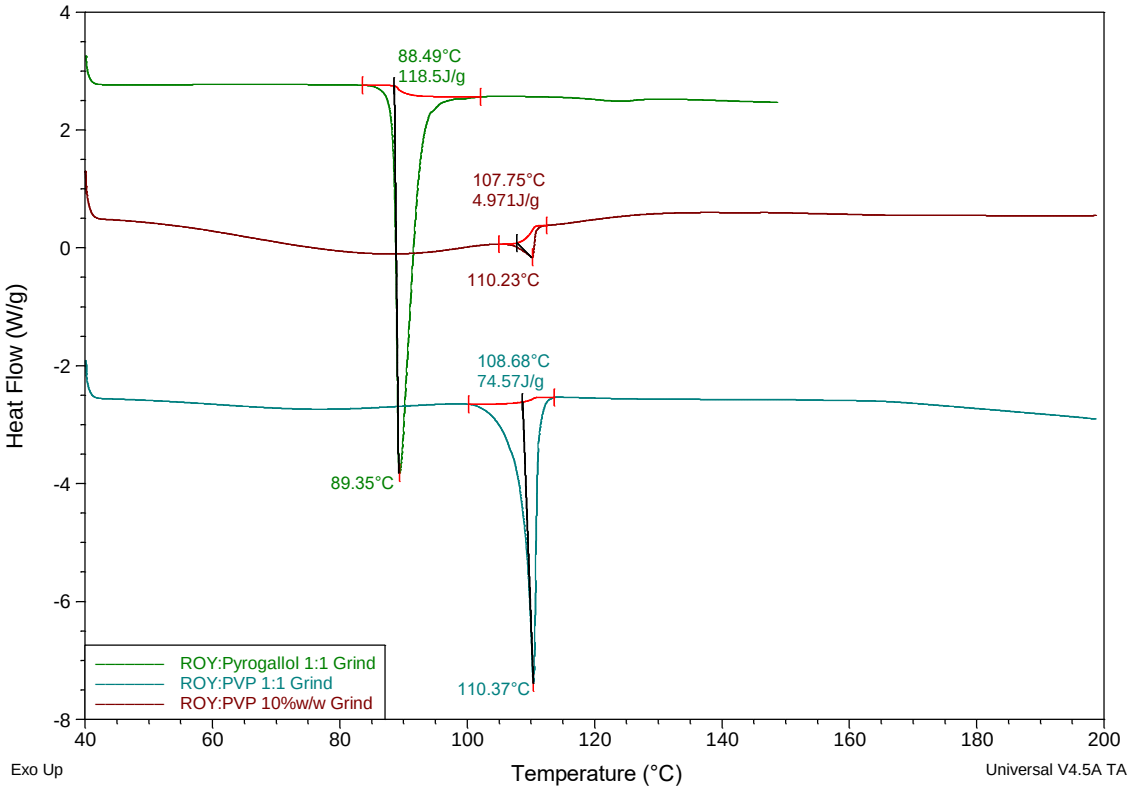


*Figure 80. Initial heating phase DSC curves of ROY:pyrogallol 1:1 grind (green), ROY:PVP 1:1 grind (teal) and ROY:PVP 10%w/w grind (maroon).*

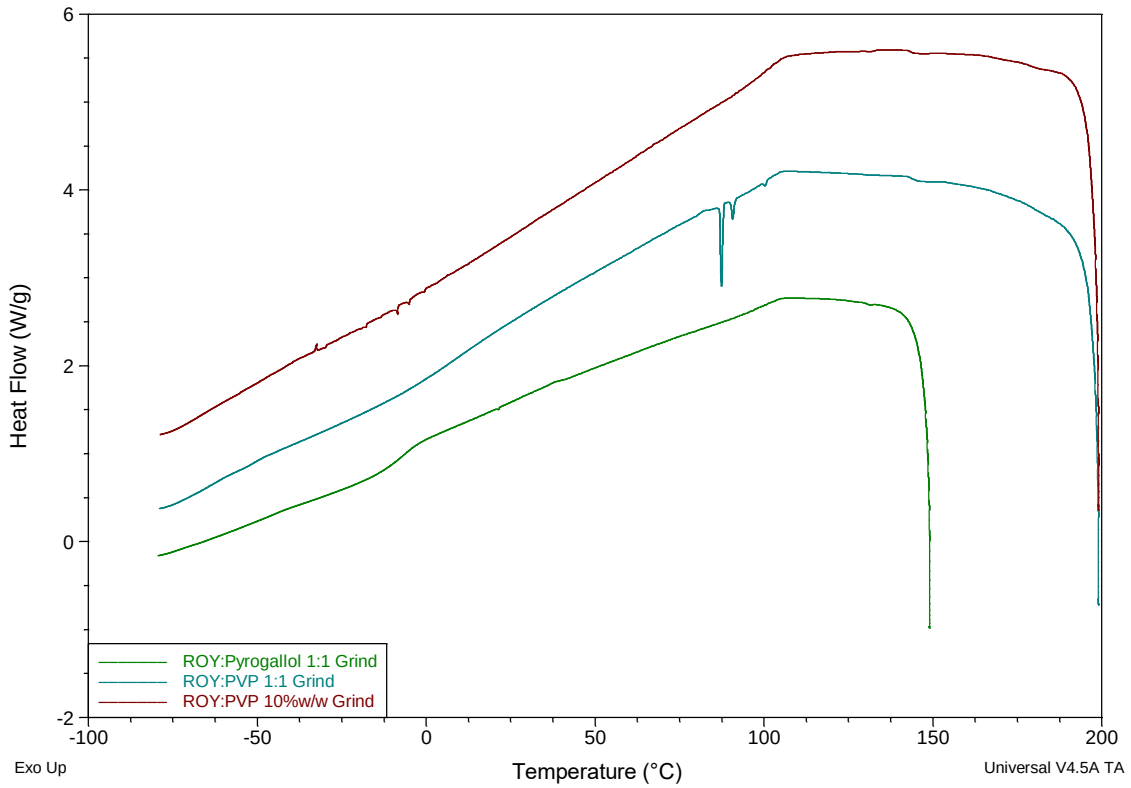


*Figure 81. Cooling phase DSC curves of ROY:pyrogallol 1:1 grind (green), ROY:PVP 1:1 grind (teal) and ROY:PVP 10%w/w grind (maroon).*

# Appendix 5

PXRD patterns of ROY, co-formers and the product of the 1:1 grinds of these components

PXRD patterns comparing the pure parent components: ROY (red patterns) and co-formers (blue patterns), with the 1:1 molar ratio grind of the two compounds (green patterns). The figures are labelled by co-former.

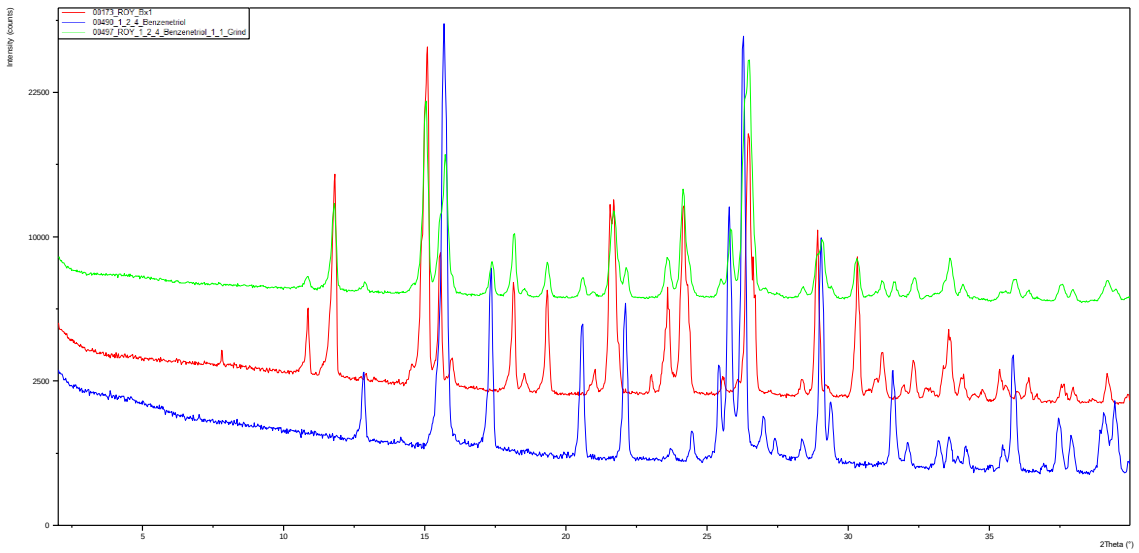


*Figure 1. 1,2,4-benzenetriol.*

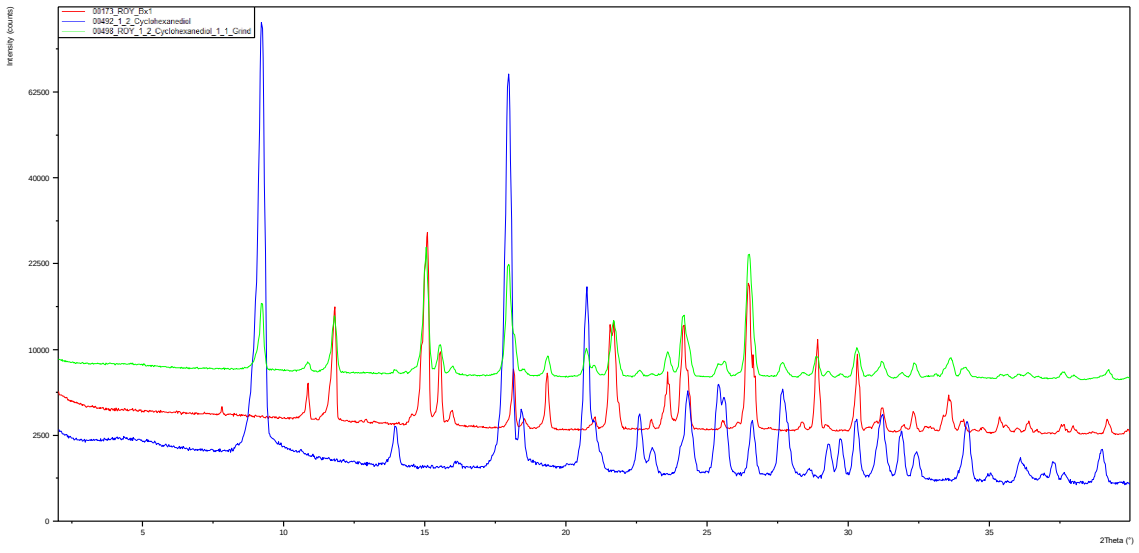


*Figure 2. 1,2-cyclohexanediol.*

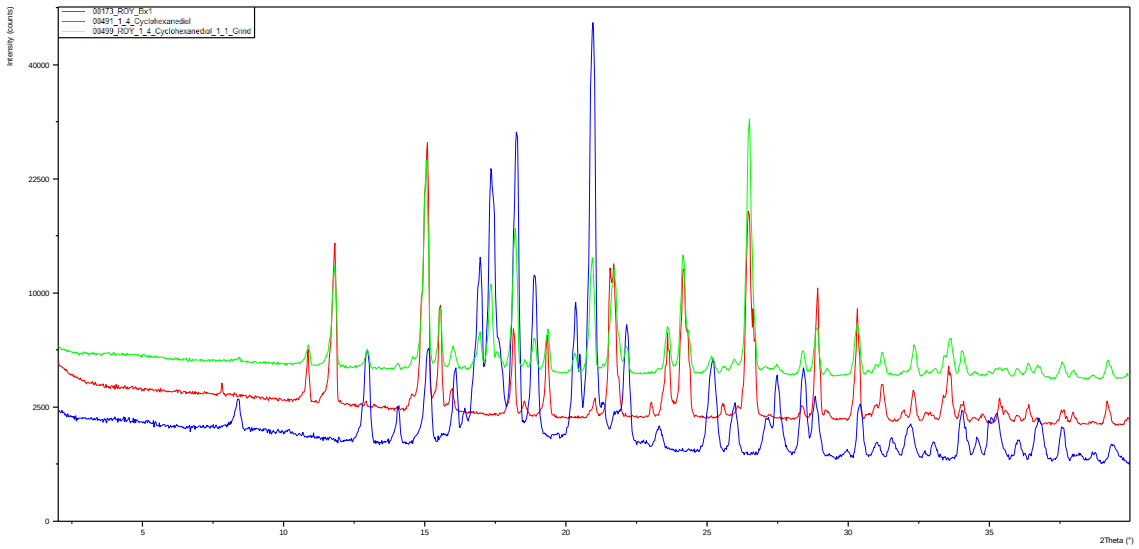


*Figure 3. 1,4-cyclohexanediol.*

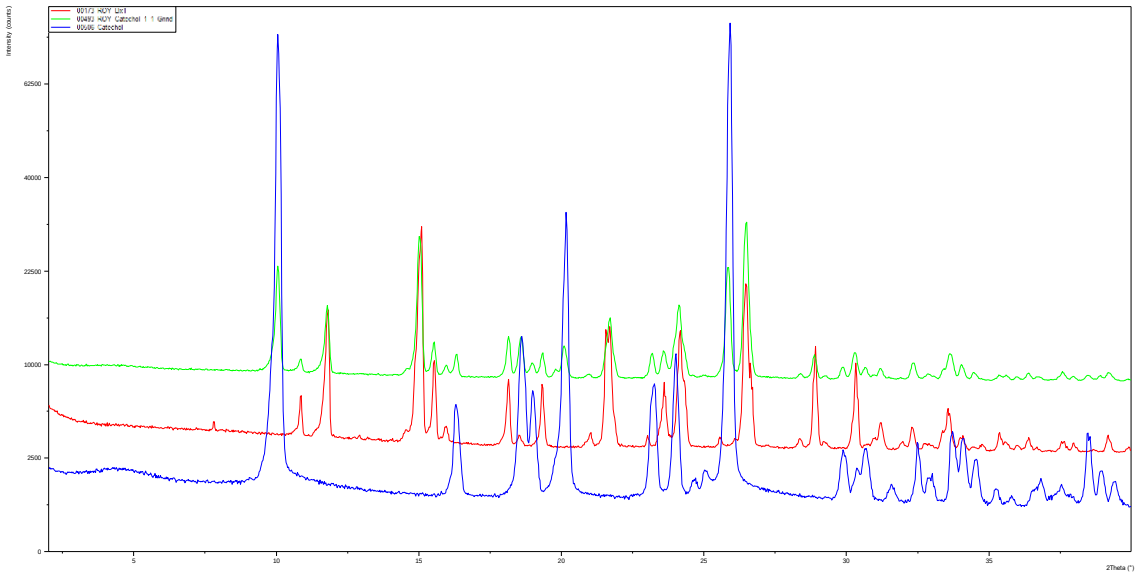


*Figure 4. Catechol.*

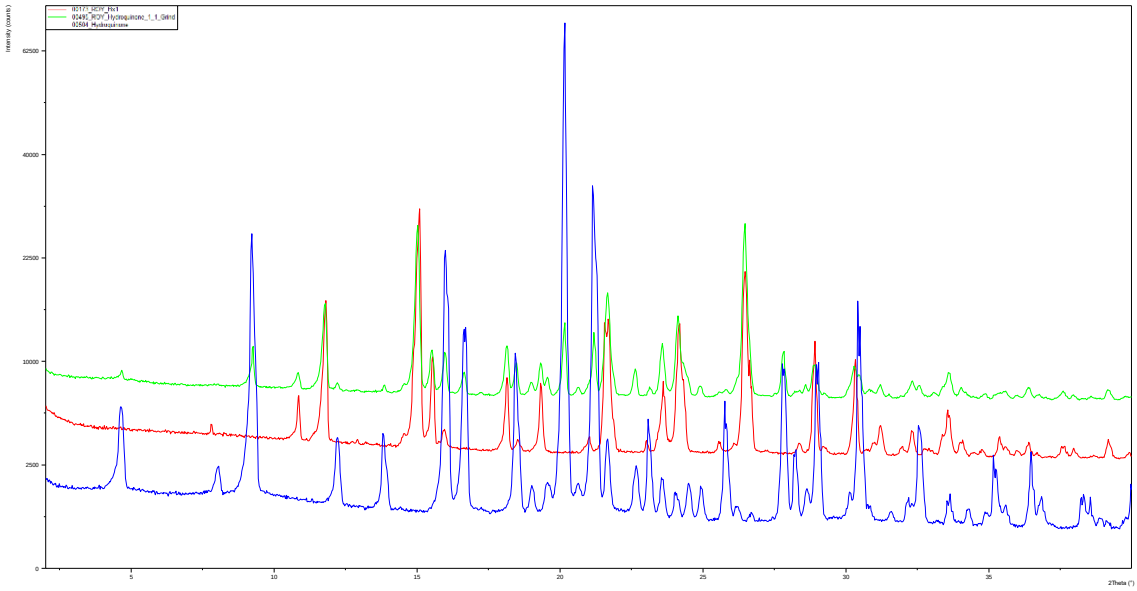

*Figure 5. Hydroquinone.*

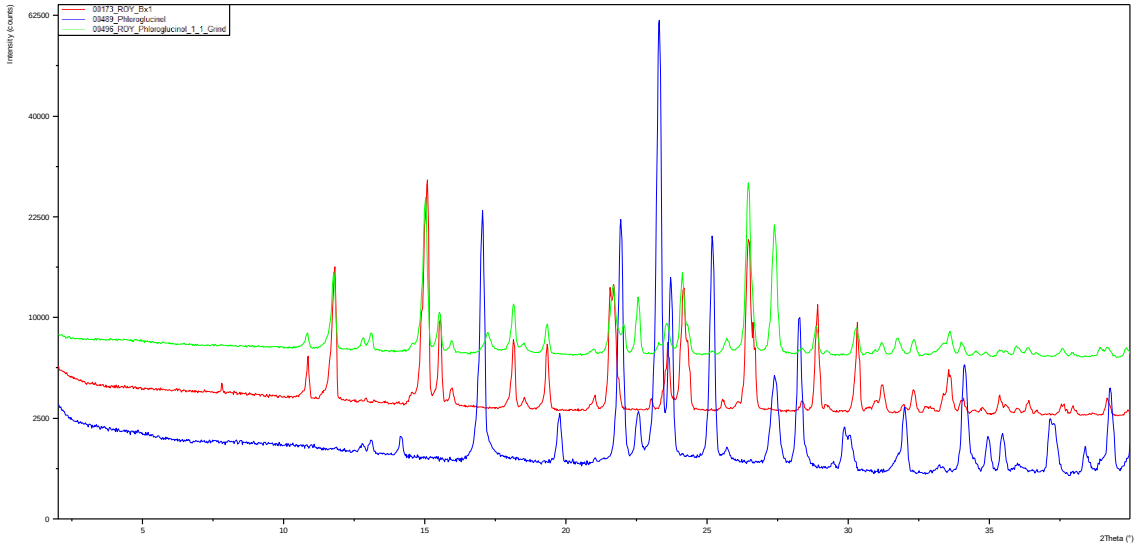


*Figure 6. Phloroglucinol.*

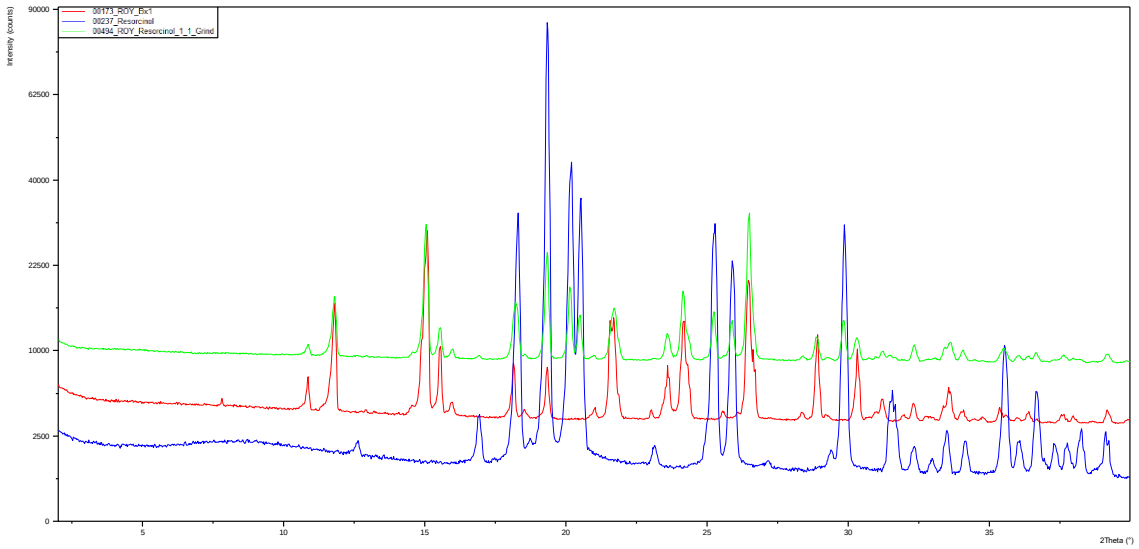


*Figure 7. Resorcinol.*

# Appendix 6

## 6.1 COSMOtherm ranked co-former list for ornidazole co-crystal computational pre-screen

*Table 1. List of co-formers with excess enthalpy calculated for three stoichiometric ratios with ornidazole as produced by COSMOtherm.*

| Co-former | Calculated ΔH / kJ.mol$^{-1}$ | | | |
|---|---|---|---|---|
| | Stoichiometric ratio | | | (Ranked by) Minimum |
| | 1:1 | 2:1 | 1:2 | |
| OXALIC_ACID | -2.2019 | -1.8773 | -2.1114 | -2.2019 |
| SULFAMIC_ACID | -1.9570 | -1.7648 | -1.7619 | -1.9570 |
| Acesulfame | -1.9194 | -1.7157 | -1.6617 | -1.9194 |
| 5-nitroisophthalic_acid | -1.6533 | -1.3260 | -1.6545 | -1.6545 |
| ISOCITRIC_ACID | -1.5488 | -1.2633 | -1.5914 | -1.5914 |
| piperazine | -1.5401 | -1.2682 | -1.4240 | -1.5401 |
| 2,4-dihydroxybenzoic_acid | -1.4322 | -1.1597 | -1.4167 | -1.4322 |
| 2_4-DIHYDROXYBENZOIC_acid | -1.4274 | -1.1597 | -1.4094 | -1.4274 |
| TERT-BUTYLHYDROQUINONE | -1.3452 | -1.1881 | -1.2083 | -1.3452 |
| trimesic_acid | -1.2152 | -0.9117 | -1.3367 | -1.3367 |
| 4-Hexylresorcinol | -1.3280 | -1.1757 | -1.2041 | -1.3280 |
| 3,5-dihydroxybenzoic_acid | -1.2627 | -0.9875 | -1.3268 | -1.3268 |
| citric_acid | -1.3187 | -1.1098 | -1.2907 | -1.3187 |
| Etidronic_acid | -1.2885 | -1.0996 | -1.2727 | -1.2885 |
| RESORCINOL | -1.2826 | -1.1166 | -1.1933 | -1.2826 |
| CARNITINE | -1.2429 | -1.0127 | -1.2448 | -1.2448 |
| 1-hydroxy-2-naphthoic_acid | -1.2198 | -1.1163 | -1.0466 | -1.2198 |
| FUMARIC_ACID | -1.1847 | -0.9511 | -1.2018 | -1.2018 |
| ALLOCITRIC_ACID | -1.1788 | -1.0042 | -1.0940 | -1.1788 |
| P-VINYLPHENOL_c0 | -1.1598 | -1.1165 | -0.9601 | -1.1598 |
| gentisic_acid | -1.1519 | -0.9233 | -1.1547 | -1.1547 |
| 5-chlorosalicylic_acid | -1.1470 | -1.0059 | -1.0199 | -1.1470 |
| ACONITIC_Acid | -1.1224 | -0.9178 | -1.1273 | -1.1273 |
| 3_4-DIHYDROXYBENZOIC_acid | -0.9570 | -0.7301 | -1.0162 | -1.0162 |
| Keto_glutaric_acid | -0.9878 | -0.8023 | -0.9947 | -0.9947 |
| 4_4-bipyridine | -0.9727 | -0.8480 | -0.8719 | -0.9727 |
| m-nitrobenzoic_acid | -0.9604 | -0.8242 | -0.8695 | -0.9604 |
| O-CRESOL | -0.9382 | -0.8964 | -0.7780 | -0.9382 |
| Malonic_acid | -0.9345 | -0.8235 | -0.8710 | -0.9345 |
| PHENOL_c0 | -0.9205 | -0.8801 | -0.7687 | -0.9205 |
| TARTARIC_ACID | -0.8712 | -0.7347 | -0.8971 | -0.8971 |
| salicylic_acid | -0.8960 | -0.7679 | -0.8117 | -0.8960 |
| methylgallate | -0.8764 | -0.6987 | -0.8919 | -0.8919 |

| | | | | |
|---|---|---|---|---|
| 3-HYDROXYBENZOIC_ACID | -0.8566 | -0.6706 | -0.8807 | -0.8807 |
| 3-hydroxy-2-naphthoic_acid | -0.8760 | -0.7527 | -0.7947 | -0.8760 |
| OCTADECYLAMINE | -0.8143 | -0.8700 | -0.5269 | -0.8700 |
| THYMOL | -0.8460 | -0.8217 | -0.6839 | -0.8460 |
| Maleic_acid | -0.8315 | -0.7199 | -0.7710 | -0.8315 |
| 6-hydroxy-2-naphthoic_acid | -0.7959 | -0.6260 | -0.8163 | -0.8163 |
| 2_5-XYLENOL | -0.8020 | -0.7671 | -0.6636 | -0.8020 |
| 4-HYDROXYBENZOIC_ACID | -0.7523 | -0.5869 | -0.7790 | -0.7790 |
| 2-6-DIMETHYLPYRAZINE_c0 | -0.7717 | -0.7256 | -0.6476 | -0.7717 |
| 2_6-DIMETHYLPYRAZINE_c0 | -0.7717 | -0.7256 | -0.6476 | -0.7717 |
| 2-OXO-3-PHENYLPROPIONIC_ACID | -0.7343 | -0.6332 | -0.6692 | -0.7343 |
| P-CRESOL | -0.7241 | -0.6905 | -0.6069 | -0.7241 |
| L-LYSINE | -0.6694 | -0.5186 | -0.7073 | -0.7073 |
| DL-VALINE | -0.7041 | -0.6490 | -0.6026 | -0.7041 |
| 3-METHYL-2-OXOBUTANOIC_ACID | -0.7009 | -0.6153 | -0.6287 | -0.7009 |
| P-ETHYLPHENOL_c0 | -0.6841 | -0.6548 | -0.5713 | -0.6841 |
| ISOQUINOLINE_c0 | -0.6722 | -0.6637 | -0.5375 | -0.6722 |
| SUCCINIC_ACID | -0.6567 | -0.5301 | -0.6689 | -0.6689 |
| PYRUVIC_ACID | -0.6649 | -0.6005 | -0.5828 | -0.6649 |
| PROPYL_GALLATE | -0.5934 | -0.4437 | -0.6450 | -0.6450 |
| THIODIPROPIONIC_ACID | -0.5903 | -0.4438 | -0.6364 | -0.6364 |
| 3-HYDROXY-2-OXOPROPIONIC_ACID | -0.6291 | -0.5330 | -0.6020 | -0.6291 |
| MALIC_ACID | -0.6244 | -0.5216 | -0.6124 | -0.6244 |
| 3_4-xylenol_c0 | -0.6214 | -0.5925 | -0.5206 | -0.6214 |
| p-tButyl-PHENOL_c0 | -0.6207 | -0.6010 | -0.5122 | -0.6207 |
| PHENOXYACETIC_ACID | -0.6198 | -0.5094 | -0.5885 | -0.6198 |
| ALPHA-KETOBUTYRIC_ACID | -0.5988 | -0.5370 | -0.5267 | -0.5988 |
| PYRAZINE_c0 | -0.5712 | -0.5314 | -0.4845 | -0.5712 |
| CAPROLACTAM_c0 | -0.5684 | -0.4957 | -0.5280 | -0.5684 |
| OCTYL_GALLATE | -0.5231 | -0.4113 | -0.5475 | -0.5475 |
| O-PHENYLPHENOL | -0.5354 | -0.4706 | -0.4785 | -0.5354 |
| Mandelic_acid | -0.5276 | -0.4271 | -0.5124 | -0.5276 |
| Glutaric_acid | -0.4728 | -0.3681 | -0.4972 | -0.4972 |
| METHYL_NICOTINATE_c0 | -0.4834 | -0.4590 | -0.4032 | -0.4834 |
| PIPERINE_c0 | -0.4803 | -0.3991 | -0.4548 | -0.4803 |
| DIHYDROXYACETOPHENONE_c0 | -0.4705 | -0.3831 | -0.4486 | -0.4705 |
| 4-5-DIMETHYLTHIAZOLE_c0 | -0.4693 | -0.4685 | -0.3724 | -0.4693 |
| M-METHOXYBENZOIC_ACID | -0.4599 | -0.3771 | -0.4334 | -0.4599 |
| INDOLE_c0 | -0.4572 | -0.4471 | -0.3675 | -0.4572 |
| ERYTHORBIC_ACID | -0.4312 | -0.3540 | -0.4407 | -0.4407 |
| 2_6-xylenol_c0 | -0.4250 | -0.4399 | -0.3279 | -0.4399 |
| adipic_acid | -0.4129 | -0.3167 | -0.4392 | -0.4392 |
| BENZOIC_ACID | -0.4204 | -0.3392 | -0.4005 | -0.4204 |

| | | | | |
|---|---|---|---|---|
| ASCORBIC_ACID | -0.3919 | -0.3221 | -0.4036 | -0.4036 |
| D-ISOASCORBIC_ACID | -0.3919 | -0.3221 | -0.4036 | -0.4036 |
| HYDROQUINONE_MONOETHYL_ETHER_c0 | -0.3904 | -0.3383 | -0.3519 | -0.3904 |
| NOOTKATONE | -0.3851 | -0.3562 | -0.3255 | -0.3851 |
| PHENYLACETIC_ACID | -0.3803 | -0.3124 | -0.3598 | -0.3803 |
| CAFFEINE_c0 | -0.3789 | -0.3114 | -0.3660 | -0.3789 |
| SKATOLE_c0 | -0.3772 | -0.3712 | -0.3009 | -0.3772 |
| METHYL_P-HYDROXYBENZOATE_c0 | -0.3740 | -0.2947 | -0.3681 | -0.3740 |
| methyl-4-hydroxy_benzoate_c0 | -0.3740 | -0.2947 | -0.3681 | -0.3740 |
| Homovanillic_ACID | -0.3598 | -0.2780 | -0.3677 | -0.3677 |
| 3-PHENYLPROPIONIC_ACID | -0.3477 | -0.2846 | -0.3288 | -0.3477 |
| Hydrocinnamic_acid | -0.3477 | -0.2846 | -0.3288 | -0.3477 |
| camphoric_acid | -0.2647 | -0.1674 | -0.3244 | -0.3244 |
| P-METHOXYBENZOIC_ACID | -0.3193 | -0.2596 | -0.3042 | -0.3193 |
| MALTOL_PROPIONATE | -0.3137 | -0.2666 | -0.2917 | -0.3137 |
| PIPERITONE | -0.3105 | -0.2984 | -0.2541 | -0.3105 |
| P-METHOXYCINNAMALDEHYDE | -0.3087 | -0.2649 | -0.2813 | -0.3087 |
| ethyl-4-hydroxy_benzoate | -0.2941 | -0.2240 | -0.2970 | -0.2970 |
| CIS-2-HEXENAL | -0.2798 | -0.2636 | -0.2338 | -0.2798 |
| Rubenamin | -0.2683 | -0.2095 | -0.2778 | -0.2778 |
| 2-METHOXY-4-VINYLPHENOL | -0.2681 | -0.2703 | -0.2134 | -0.2703 |
| 5-METHYLQUINOXALINE_c0 | -0.2699 | -0.2622 | -0.2201 | -0.2699 |
| Propionic_acid | -0.2651 | -0.2158 | -0.2542 | -0.2651 |
| O-METHOXYCINNAMALDEHYDE | -0.2596 | -0.2273 | -0.2318 | -0.2596 |
| 4-PHENYL-3-BUTEN-2-ONE | -0.2591 | -0.2286 | -0.2295 | -0.2591 |
| LEVULINIC_ACID | -0.2583 | -0.2278 | -0.2316 | -0.2583 |
| CINNAMIC_ACID | -0.2531 | -0.2009 | -0.2462 | -0.2531 |
| P-METHYLCINNAMALDEHYDE | -0.2452 | -0.2153 | -0.2178 | -0.2452 |
| VERATRALDEHYDE | -0.2448 | -0.2050 | -0.2272 | -0.2448 |
| PROPYL_P-HYDROXYBENZOATE | -0.2342 | -0.1722 | -0.2426 | -0.2426 |
| 4-2-FURYL-3-BUTEN-2-ONE | -0.2288 | -0.1975 | -0.2075 | -0.2288 |
| LACTIC_ACID | -0.2171 | -0.1662 | -0.2250 | -0.2250 |
| P-AMINOBENZOIC_ACID | -0.2234 | -0.1916 | -0.2080 | -0.2234 |
| ACETYLPYRAZINE | -0.2204 | -0.1989 | -0.1931 | -0.2204 |
| butyric_acid | -0.2116 | -0.1627 | -0.2108 | -0.2116 |
| ACETANISOLE_c0 | -0.2036 | -0.1786 | -0.1808 | -0.2036 |
| METHYL_ANISATE_c0 | -0.2036 | -0.1786 | -0.1808 | -0.2036 |
| P-METOXYACETOPHENONE_c0 | -0.2036 | -0.1786 | -0.1808 | -0.2036 |
| 3-2-FURYL_ACROLEIN | -0.1988 | -0.1687 | -0.1830 | -0.1988 |
| BUTYL_P-HYDROXIBENZOATE | -0.1865 | -0.1317 | -0.1981 | -0.1981 |
| L-PROLINE | -0.1824 | -0.1606 | -0.1659 | -0.1824 |
| glycolic_acid | -0.1564 | -0.1118 | -0.1811 | -0.1811 |
| 3-METHYLCROTONIC_ACID | -0.1764 | -0.1339 | -0.1761 | -0.1764 |

| | | | | |
|---|---|---|---|---|
| VANILLYL_ALCOHOL | -0.1756 | -0.1424 | -0.1715 | -0.1756 |
| 5-ETHYL-3-HYDROXY-4-METHYL-2_5H-FURANONE | -0.1733 | -0.1558 | -0.1516 | -0.1733 |
| SORBIC_ACID | -0.1637 | -0.1275 | -0.1628 | -0.1637 |
| 4-HYDROXY-3-5-DIMETHOXYBENZALDEHYDE | -0.1627 | -0.1471 | -0.1420 | -0.1627 |
| THEOBROMINE_c0 | -0.1621 | -0.1343 | -0.1571 | -0.1621 |
| O-METHOXYBENZOIC_ACID | -0.1601 | -0.1421 | -0.1453 | -0.1601 |
| 5-OXOOCTANOIC_ACID | -0.1579 | -0.1381 | -0.1427 | -0.1579 |
| TRANS-2-METHYL-2-BUTENOIC_ACID | -0.1484 | -0.1074 | -0.1544 | -0.1544 |
| GUAIACOL | -0.1486 | -0.1515 | -0.1165 | -0.1515 |
| 2-FURYL_METHYL_KETONE | -0.1492 | -0.1291 | -0.1339 | -0.1492 |
| 4-_P-HYDROXYPHENYL-2-BUTANONE | -0.1477 | -0.1199 | -0.1430 | -0.1477 |
| 4-METHYLACETOPHENONE_c0 | -0.1411 | -0.1284 | -0.1205 | -0.1411 |
| Vanillin | -0.1396 | -0.1247 | -0.1237 | -0.1396 |
| 6-METHYLCOUMARIN_c0 | -0.1348 | -0.1116 | -0.1246 | -0.1348 |
| TRANS-2-HEXENOIC_ACID | -0.1244 | -0.0872 | -0.1325 | -0.1325 |
| trans-2-hexanoic_acid | -0.1244 | -0.0872 | -0.1325 | -0.1325 |
| 4-HYDROXY-2_5-DIMETHYL-3_2H-FURANONE | -0.1277 | -0.1186 | -0.1091 | -0.1277 |
| L-HISTIDINE | -0.1146 | -0.0878 | -0.1193 | -0.1193 |
| MALTOL | -0.1123 | -0.1014 | -0.0987 | -0.1123 |
| O-METHOXYBENZALDEHYDE | -0.1123 | -0.0960 | -0.1005 | -0.1123 |
| 4-HYDROXY-5-METHYL-3_2H-FURANONE | -0.1079 | -0.0998 | -0.0926 | -0.1079 |
| 4-HYDROXYBENZYL_ALCOHOL | -0.1069 | -0.0877 | -0.1072 | -0.1072 |
| hippuric_acid | -0.0994 | -0.0723 | -0.1071 | -0.1071 |
| N-ETHYL-2_2-DIISOPROPYLBUTANAMIDE | -0.1047 | -0.1066 | -0.0811 | -0.1066 |
| nicotinic_acid | -0.1055 | -0.0868 | -0.0996 | -0.1055 |
| 3-ethoxy-4-hydroxy_benzaldehyde | -0.1053 | -0.0954 | -0.0924 | -0.1053 |
| METHYLCYCLOPENTENOLONE_c0 | -0.1053 | -0.0826 | -0.0997 | -0.1053 |
| 2-METHYL-2-PENTENOIC_ACID | -0.0876 | -0.0509 | -0.1023 | -0.1023 |
| METHYLCYCLOPENTENOLONE_tautomer | -0.1019 | -0.1004 | -0.0826 | -0.1019 |
| PHTHALIDE_c0 | -0.1016 | -0.0802 | -0.0971 | -0.1016 |
| D-GLUCONIC_ACID | -0.0990 | -0.0923 | -0.0983 | -0.0990 |
| 5-OXODECANOIC_ACID | -0.0961 | -0.0853 | -0.0846 | -0.0961 |
| saccharin_c0 | -0.0925 | -0.0738 | -0.0909 | -0.0925 |
| L-ARGININE | -0.0642 | -0.0535 | -0.0863 | -0.0863 |
| HEPTYLPARABEN | -0.0727 | -0.0401 | -0.0858 | -0.0858 |
| PIPERONAL_c0 | -0.0855 | -0.0679 | -0.0812 | -0.0855 |
| CAMPHOR_c0 | -0.0795 | -0.0855 | -0.0553 | -0.0855 |
| Imidazole_c0 | -0.0677 | -0.0375 | -0.0837 | -0.0837 |
| pyroglutamic_acid | -0.0790 | -0.0713 | -0.0730 | -0.0790 |
| CYCLOHEXANECARBOXYLIC_ACID | -0.0561 | -0.0196 | -0.0765 | -0.0765 |
| VANILLIN_ACETATE | -0.0656 | -0.0388 | -0.0749 | -0.0749 |
| N-ACETYL-L-METHIONINE | -0.0736 | -0.0706 | -0.0600 | -0.0736 |
| 2-ACETYL-2-THIAZOLINE_c0 | -0.0733 | -0.0579 | -0.0683 | -0.0733 |

| | | | | |
|---|---|---|---|---|
| GLUCOSE_PENTAACETATE | -0.0357 | -0.0029 | -0.0653 | -0.0653 |
| BUTYLATED_HYDROXYTOLUENE | 0.0687 | -0.0599 | 0.1431 | -0.0599 |
| SUCRALOSE | -0.0396 | -0.0277 | -0.0513 | -0.0513 |
| Piperonylacetone | -0.0486 | -0.0317 | -0.0512 | -0.0512 |
| VITAMIN_K3_c0 | -0.0447 | -0.0233 | -0.0502 | -0.0502 |
| NEOTAME | -0.0386 | -0.0225 | -0.0478 | -0.0478 |
| 2-CYCLOHEXYL_ACETIC_ACID | -0.0139 | 0.0180 | -0.0390 | -0.0390 |
| L-TYROSINE | -0.0310 | -0.0179 | -0.0386 | -0.0386 |
| ZINGERONE | -0.0364 | -0.0338 | -0.0309 | -0.0364 |
| METHYL_BETA-NAPHTHYL_KETONE_c0 | -0.0328 | -0.0215 | -0.0330 | -0.0330 |
| METHYL_PHENYLACETATE | -0.0260 | -0.0110 | -0.0302 | -0.0302 |
| Benzoin | -0.0282 | -0.0190 | -0.0291 | -0.0291 |
| 5-OXODODECANOIC_ACID | -0.0249 | -0.0263 | -0.0162 | -0.0263 |
| PROPENYLGUAETHOL | -0.0151 | -0.0255 | -0.0046 | -0.0255 |
| BIOTIN | -0.0151 | -0.0131 | -0.0148 | -0.0151 |
| 10-UNDECENOIC_ACID | -0.0053 | 0.0087 | -0.0133 | -0.0133 |
| 2-6-DIMETHOXYPHENOL | -0.0115 | -0.0110 | -0.0097 | -0.0115 |
| 2_6-DIMETHOXYPHENOL | -0.0115 | -0.0110 | -0.0097 | -0.0115 |
| ASPARTAME | 0.0049 | 0.0120 | -0.0086 | -0.0086 |
| LEVULOSE | 0.0002 | -0.0082 | 0.0059 | -0.0082 |
| METHYL_CINNAMATE | 0.0054 | 0.0191 | -0.0044 | -0.0044 |
| SCLAREOLIDE_c0 | 0.0032 | 0.0035 | 0.0081 | 0.0032 |
| 2-HYDROXY-4-METHOXYBENZALDEHYDE_c0 | 0.0195 | 0.0324 | 0.0077 | 0.0077 |
| BENZOPHENONE_c0 | 0.0321 | 0.0419 | 0.0203 | 0.0203 |
| L-HYDROXYPROLINE | 0.0318 | 0.0216 | 0.0341 | 0.0216 |
| ISOEUGENYL_METHYL_ETHER | 0.0378 | 0.0407 | 0.0304 | 0.0304 |
| METHYL_2-PYRROLYL_KETONE | 0.0378 | 0.0366 | 0.0308 | 0.0308 |
| GUAIACYL_ACETATE | 0.0594 | 0.0747 | 0.0383 | 0.0383 |
| ISOEUGENYL_ETHYL_ETHER | 0.0485 | 0.0440 | 0.0451 | 0.0440 |
| P-TOLYL_ACETATE_c0 | 0.0586 | 0.0657 | 0.0444 | 0.0444 |
| 2-HYDROXY-4-METHYLBENZALDEHYDE | 0.0659 | 0.0753 | 0.0481 | 0.0481 |
| METHYL_ANTHRANILATE | 0.0644 | 0.0655 | 0.0508 | 0.0508 |
| 2-HYDROXY-5-METHYLACETOPHENONE_c0 | 0.0724 | 0.0796 | 0.0552 | 0.0552 |
| ACETAMIDE_c0 | 0.0915 | 0.1028 | 0.0554 | 0.0554 |
| DL-PHENYLALANINE | 0.0763 | 0.0760 | 0.0600 | 0.0600 |
| L-ISOLEUCINE | 0.0835 | 0.0837 | 0.0643 | 0.0643 |
| DL-ALANINE | 0.0810 | 0.0786 | 0.0647 | 0.0647 |
| METHIONINE | 0.0807 | 0.0786 | 0.0653 | 0.0653 |
| 1_3-DIPHENYL-2-PROPANONE | 0.0879 | 0.0969 | 0.0662 | 0.0662 |
| 2-PROPIONYLPYRROLE | 0.0824 | 0.0791 | 0.0682 | 0.0682 |
| Nicotinamide_c0 | 0.1002 | 0.1029 | 0.0740 | 0.0740 |
| D-RIBOSE | 0.0907 | 0.0765 | 0.0834 | 0.0765 |
| Xylose | 0.0907 | 0.0765 | 0.0834 | 0.0765 |

| | | | | |
|---|---|---|---|---|
| NIACINAMIDE_c0 | 0.1041 | 0.1068 | 0.0773 | 0.0773 |
| ALPHA_ALPHA-DIMETHYLPHENETHYL_ALCOHOL | 0.0901 | 0.0823 | 0.0784 | 0.0784 |
| Cinnamyl-BETA-D-GLUCOPYRANOSIDE | 0.0938 | 0.0794 | 0.0861 | 0.0794 |
| Aspartic_acid_c0 | 0.1857 | 0.0832 | 0.2297 | 0.0832 |
| Cysteine | 0.0984 | 0.0921 | 0.0833 | 0.0833 |
| 2-NAPHTHALENTHIOL_c0 | 0.1322 | 0.1607 | 0.0910 | 0.0910 |
| L-LEUCINE | 0.1173 | 0.1142 | 0.0942 | 0.0942 |
| DIHYDROXYACETONE | 0.1158 | 0.1099 | 0.0962 | 0.0962 |
| PYRIDOXINE | 0.1134 | 0.1045 | 0.0963 | 0.0963 |
| TYRAMINE | 0.1153 | 0.1017 | 0.1053 | 0.1017 |
| GLUCONO-DELTA_LACTONE | 0.1369 | 0.1286 | 0.1030 | 0.1030 |
| ISOEUGENYL_ACETATE_c0 | 0.1365 | 0.1446 | 0.1057 | 0.1057 |
| BUTYRAMIDE_c0 | 0.1542 | 0.1635 | 0.1085 | 0.1085 |
| Barbital_c0 | 0.1235 | 0.1101 | 0.1088 | 0.1088 |
| P-DIMETHOXYBENZENE_c0 | 0.1481 | 0.1626 | 0.1112 | 0.1112 |
| ALLYL_ANTHRANILATE | 0.1396 | 0.1428 | 0.1116 | 0.1116 |
| SORBOSE | 0.1326 | 0.1121 | 0.1228 | 0.1121 |
| RIBOFLAVIN | 0.1365 | 0.1126 | 0.1317 | 0.1126 |
| METHYL_ISOTHIOCYANATE_c0 | 0.1629 | 0.1936 | 0.1154 | 0.1154 |
| UNDECANOIC_ACID | 0.1395 | 0.1355 | 0.1183 | 0.1183 |
| FOLIC_ACID | 0.1520 | 0.1256 | 0.1434 | 0.1256 |
| BENZYL_CINNAMATE | 0.1600 | 0.1634 | 0.1277 | 0.1277 |
| BENZYLCINNAMATE | 0.1630 | 0.1663 | 0.1302 | 0.1302 |
| OMEGA-PENTADECALACTONE_c0 | 0.1647 | 0.1338 | 0.1684 | 0.1338 |
| 3-amino-1_2-propanediol | 0.2087 | 0.2318 | 0.1353 | 0.1353 |
| L-TRYPTOPHAN | 0.1580 | 0.1394 | 0.1426 | 0.1394 |
| 2-TRIDECANONE | 0.1918 | 0.1411 | 0.2064 | 0.1411 |
| GLYCERYL_TRIBENZOATE | 0.1789 | 0.1804 | 0.1419 | 0.1419 |
| P-AMINOBENZALDEYDE_c0 | 0.1644 | 0.1503 | 0.1423 | 0.1423 |
| Capsaicin | 0.1793 | 0.1455 | 0.1762 | 0.1455 |
| L-THREONINE | 0.1674 | 0.1523 | 0.1458 | 0.1458 |
| TAUROCHOLIC_ACID | 0.1803 | 0.1476 | 0.1737 | 0.1476 |
| GLYCINE | 0.1803 | 0.1700 | 0.1494 | 0.1494 |
| PHENETHYL_PHENYLACETATE | 0.1857 | 0.1842 | 0.1528 | 0.1528 |
| Xylitol | 0.1782 | 0.1604 | 0.1559 | 0.1559 |
| L-RHAMNOSE | 0.1811 | 0.1587 | 0.1631 | 0.1587 |
| LAURIC_ACID | 0.1804 | 0.1667 | 0.1607 | 0.1607 |
| 2-HYDROXYPIPERITONE | 0.1835 | 0.1681 | 0.1608 | 0.1608 |
| GUAIACYL_PHENYLACETATE | 0.2041 | 0.2097 | 0.1615 | 0.1615 |
| 2-METHYL-4-PHENYL-2-BUTANOL | 0.1857 | 0.1682 | 0.1624 | 0.1624 |
| CINNAMYL_CINNAMATE | 0.2024 | 0.2009 | 0.1663 | 0.1663 |
| L-MENTHYL_LACTATE | 0.2115 | 0.1705 | 0.2080 | 0.1705 |
| Paradol | 0.2105 | 0.1707 | 0.2069 | 0.1707 |

| | | | | |
|---|---|---|---|---|
| P-TOLYL_PHENYLACETATE | 0.2167 | 0.2206 | 0.1749 | 0.1749 |
| 6-ACETOXYDIHYDROTHEASPIRANE | 0.2105 | 0.1756 | 0.2044 | 0.1756 |
| PHENETHYL_ANTHRANILATE | 0.2123 | 0.2076 | 0.1763 | 0.1763 |
| PHENETHYL_CINNAMATE | 0.2152 | 0.2115 | 0.1779 | 0.1779 |
| 1-4-DITHIANE_c0 | 0.2436 | 0.2711 | 0.1811 | 0.1811 |
| P-ISOPROPYLBENZYL_ALCOHOL | 0.2118 | 0.1933 | 0.1839 | 0.1839 |
| UREA_c0 | 0.2443 | 0.1903 | 0.2273 | 0.1903 |
| Sulfacetamide | 0.2281 | 0.1984 | 0.2082 | 0.1984 |
| L-GLUTAMIC_ACID | 0.2465 | 0.1985 | 0.2502 | 0.1985 |
| PHENYL_SALICYLATE | 0.2517 | 0.2583 | 0.1997 | 0.1997 |
| L-GLUTAMINE | 0.2286 | 0.2019 | 0.2020 | 0.2019 |
| D-SORBITOL | 0.2502 | 0.2110 | 0.2336 | 0.2110 |
| 2-MERCAPTOANISOLE_c0 | 0.2819 | 0.3089 | 0.2126 | 0.2126 |
| INOSITOL | 0.2585 | 0.2191 | 0.2355 | 0.2191 |
| BENZOYL_PEROXIDE | 0.2793 | 0.2876 | 0.2207 | 0.2207 |
| EUGENOL_BENZOATE_c0 | 0.2688 | 0.2634 | 0.2230 | 0.2230 |
| MALTOSE | 0.2807 | 0.2267 | 0.2720 | 0.2267 |
| L-SERINE | 0.2639 | 0.2410 | 0.2286 | 0.2286 |
| MYRISTIC_ACID | 0.2638 | 0.2300 | 0.2479 | 0.2300 |
| EUGENYL_ISOVALERATE_c0 | 0.2746 | 0.2628 | 0.2345 | 0.2345 |
| BETA-NAPHTHYL_METHYL_ETHER_c0 | 0.3039 | 0.3212 | 0.2355 | 0.2355 |
| ISOEUGENYL_BENZYL_ETHER | 0.2823 | 0.2706 | 0.2389 | 0.2389 |
| MANNITOL | 0.2941 | 0.2501 | 0.2727 | 0.2501 |
| LACTOSE | 0.3189 | 0.2527 | 0.3206 | 0.2527 |
| TRANS-ANETHOLE_c0 | 0.3286 | 0.3416 | 0.2587 | 0.2587 |
| 4-THUJANOL | 0.2976 | 0.2641 | 0.2646 | 0.2641 |
| PHENETHYL_SALICYLATE | 0.3273 | 0.3244 | 0.2690 | 0.2690 |
| PALMITIC_ACID | 0.3234 | 0.2716 | 0.3158 | 0.2716 |
| SUCROSE | 0.3422 | 0.2730 | 0.3409 | 0.2730 |
| GLYCERIN | 0.3271 | 0.3067 | 0.2775 | 0.2775 |
| 2-THIENYL_DISULFIDE | 0.3703 | 0.3917 | 0.2872 | 0.2872 |
| BETA-NAPHTHYL_ETHYL_ETHER | 0.3704 | 0.3816 | 0.2940 | 0.2940 |
| PHENETHYL_OCTANOATE | 0.3296 | 0.2944 | 0.3011 | 0.2944 |
| L-ARABINOSE | 0.3439 | 0.3125 | 0.2978 | 0.2978 |
| DIPHENYL_ETHER_c0 | 0.3823 | 0.4010 | 0.2986 | 0.2986 |
| ALPHA-TERPINEOL | 0.3518 | 0.3196 | 0.3073 | 0.3073 |
| CHOLIC_ACID | 0.3748 | 0.3082 | 0.3623 | 0.3082 |
| ISOBUTYL_N-METHYLANTHRANILATE | 0.3619 | 0.3435 | 0.3089 | 0.3089 |
| Biphenyl | 0.3993 | 0.4225 | 0.3099 | 0.3099 |
| STEARIC_ACID | 0.3796 | 0.3106 | 0.3805 | 0.3106 |
| AlPHA-D-GLUCOPYRANOSE | 0.3612 | 0.3208 | 0.3165 | 0.3165 |
| 4-HYDROXYMETHYL-2-6-DI-TERTBUTYLPHENOL_c0 | 0.3654 | 0.3177 | 0.3333 | 0.3177 |
| VITAMIN_A_ACETATE | 0.3668 | 0.3198 | 0.3443 | 0.3198 |

| | | | | |
|---|---|---|---|---|
| L-ASPARAGINE | 0.3646 | 0.3224 | 0.3252 | 0.3224 |
| VITAMIN_A | 0.4016 | 0.3351 | 0.3831 | 0.3351 |
| GLYCOCHOLIC_ACID | 0.4316 | 0.3430 | 0.4352 | 0.3430 |
| 4-METHYLBIPHENYL | 0.4625 | 0.4786 | 0.3658 | 0.3658 |
| TRITHIOACETONE | 0.4671 | 0.4718 | 0.3779 | 0.3779 |
| Citronellol | 0.4257 | 0.3805 | 0.3779 | 0.3779 |
| BENZYL_DISULFIDE | 0.4759 | 0.4851 | 0.3818 | 0.3818 |
| FENCHYL_ALCOHOL_c0 | 0.4453 | 0.4121 | 0.3827 | 0.3827 |
| BORNEOL | 0.4547 | 0.4223 | 0.3895 | 0.3895 |
| ISOBORNEOL | 0.4574 | 0.4250 | 0.3917 | 0.3917 |
| BETA-NAPHTHYL_ISOBUTYL_ETHER | 0.5210 | 0.5181 | 0.4276 | 0.4276 |
| MENTHOL | 0.4978 | 0.4533 | 0.4346 | 0.4346 |
| TAURINE_c0 | 0.5504 | 0.5338 | 0.4613 | 0.4613 |
| AZODICARBONAMIDE | 0.5500 | 0.4758 | 0.5096 | 0.4758 |
| OCIMENE | 0.5989 | 0.6018 | 0.4870 | 0.4870 |
| ETHYL_PALMITATE | 0.5940 | 0.4937 | 0.5812 | 0.4937 |
| Vitamin_D | 0.6931 | 0.5628 | 0.6842 | 0.5628 |
| ETHYL_OCTADECANOATE_c0 | 0.6842 | 0.5665 | 0.6733 | 0.5665 |
| CAMPHENE_c0 | 0.7094 | 0.7115 | 0.5767 | 0.5767 |
| LAURYL_ALCOHOL | 0.6755 | 0.5857 | 0.6195 | 0.5857 |
| MYRISTYL_ALCOHOL | 0.7550 | 0.6431 | 0.7060 | 0.6431 |
| 2-DECYLFURAN | 0.8346 | 0.7888 | 0.7198 | 0.7198 |
| STEARYL_ALCOHOL | 0.8716 | 0.7215 | 0.8422 | 0.7215 |

## 6.2 PXRD plots from ornidazole co-crystal screen analysis

PXRD patterns comparing the pure parent components: ornidazole (blue patterns) and co-formers (green patterns), with the product of the co-crystal screen for those two components (red patterns). The figures are labelled by co-former.

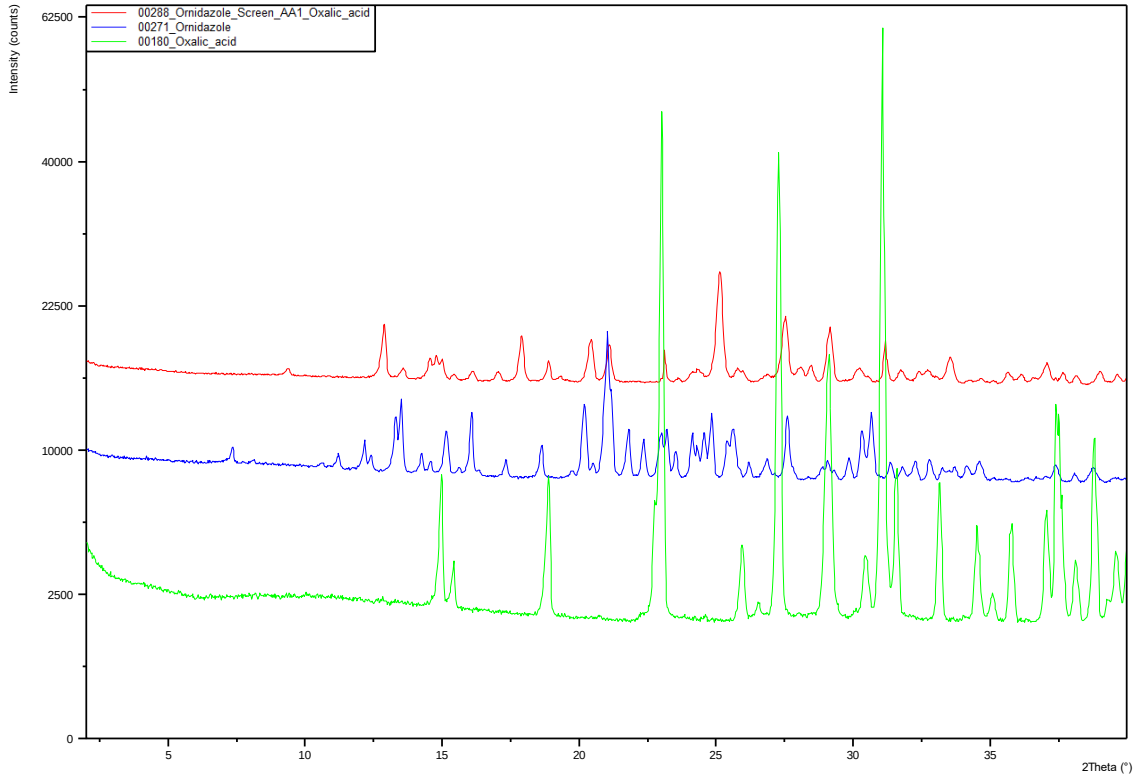


*Figure 1. Oxalic acid.*

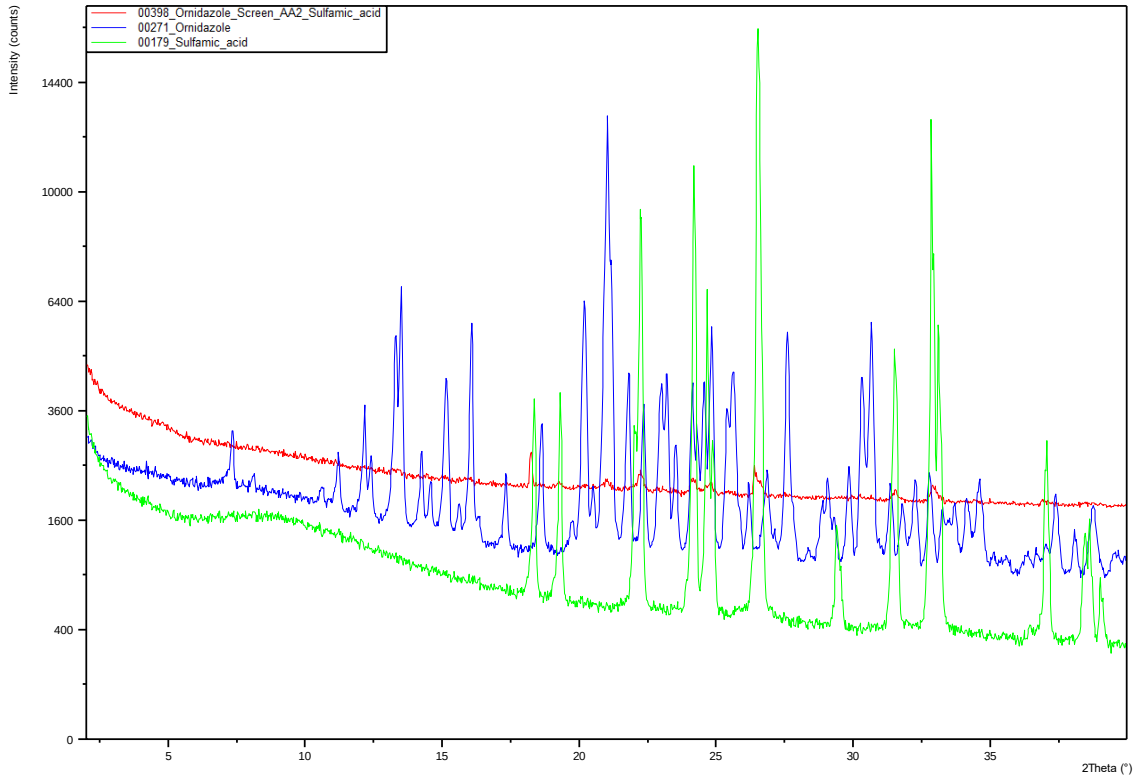


*Figure 2. Sulfamic acid.*

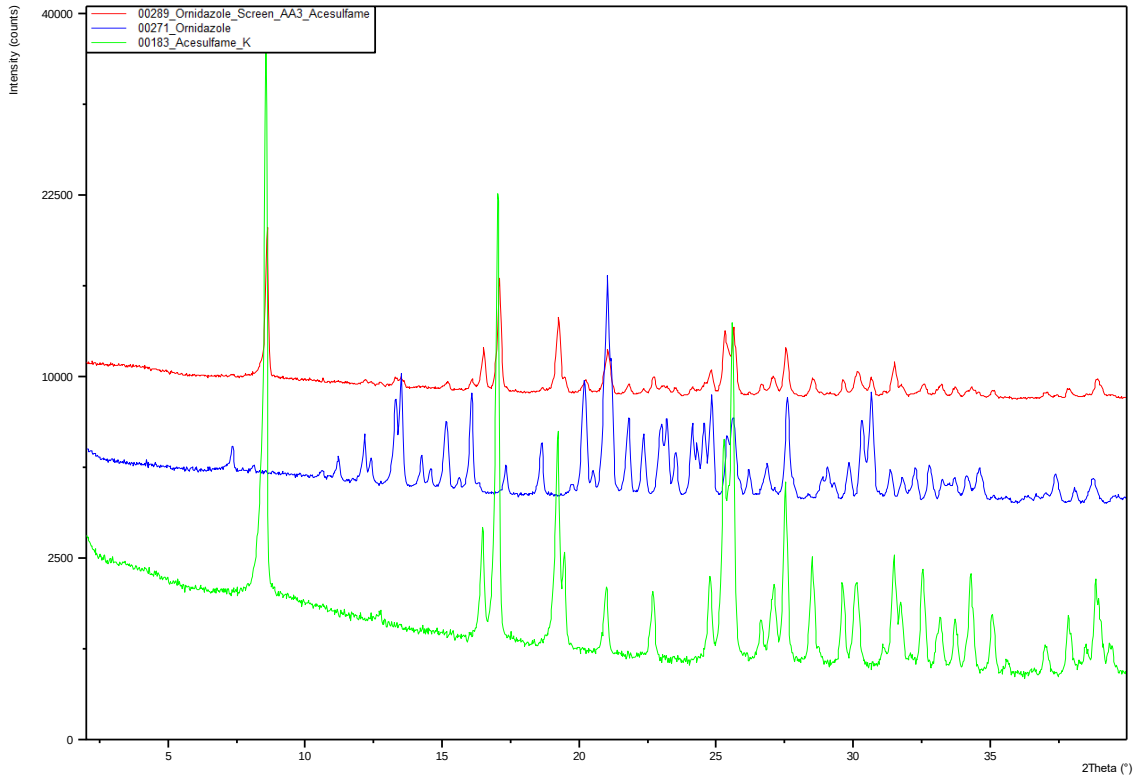


*Figure 3. Acesulfame potassium.*

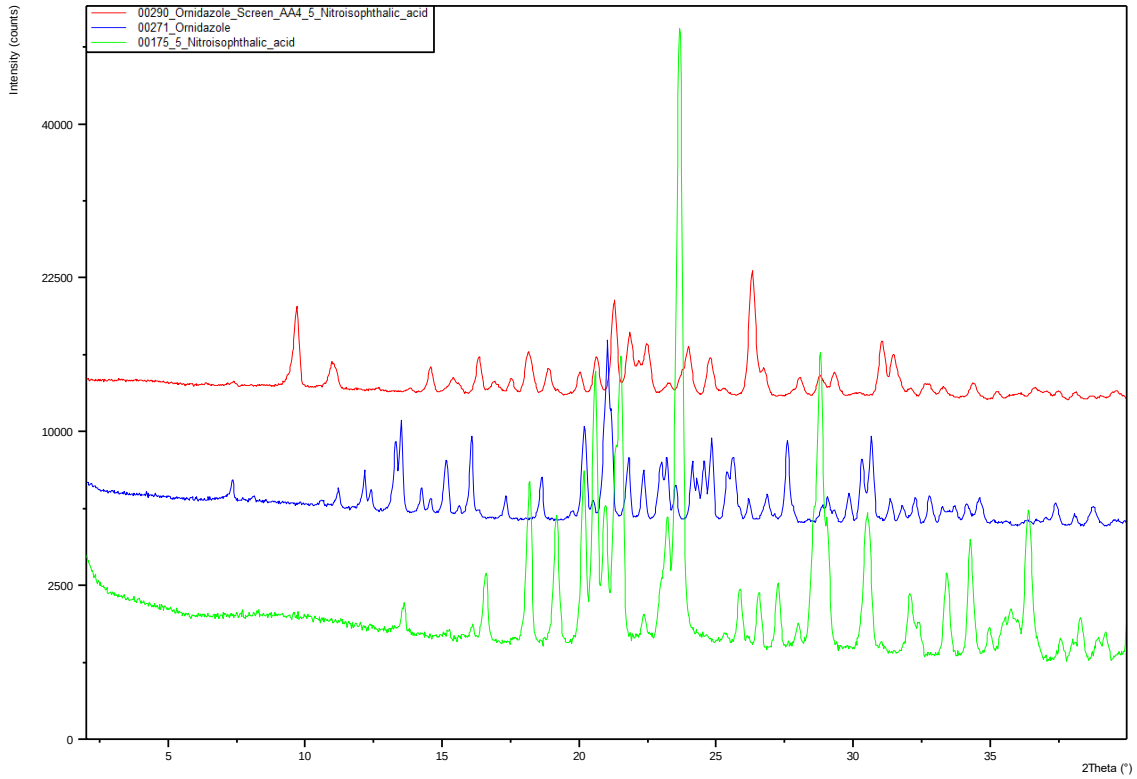


*Figure 4. 5-Nitroisophthalic acid.*

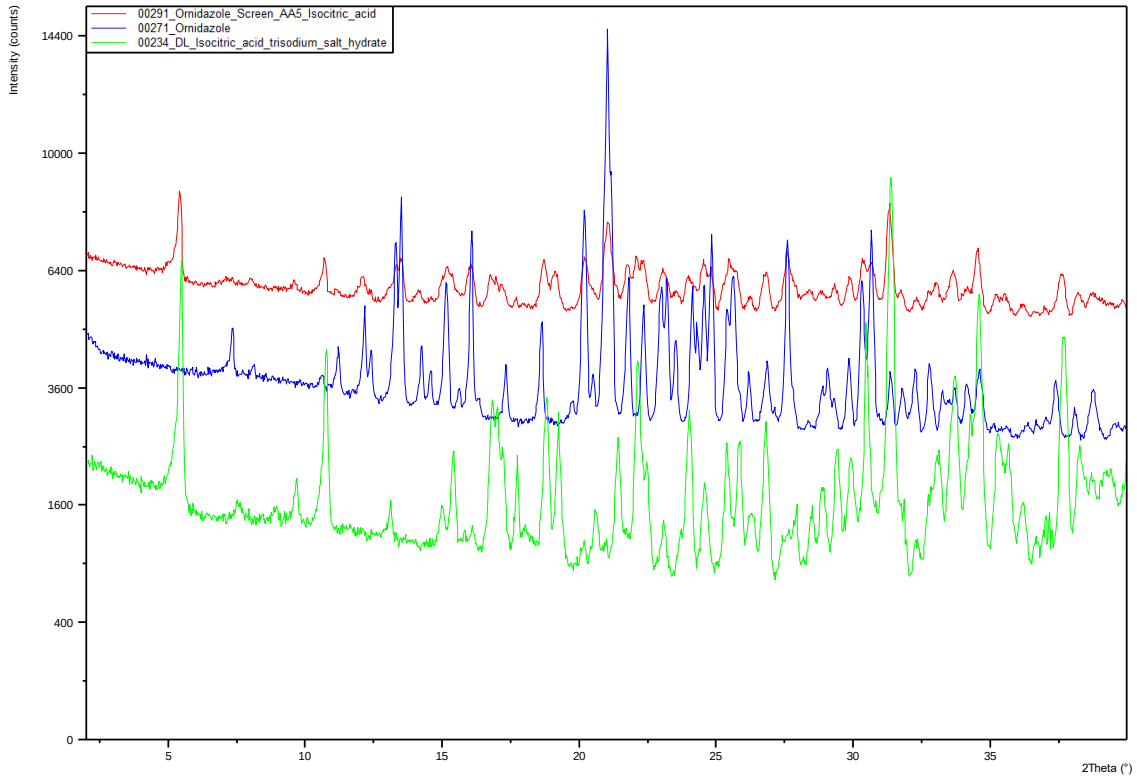


*Figure 5. Isocitric acid trisodium salt hydrate.*

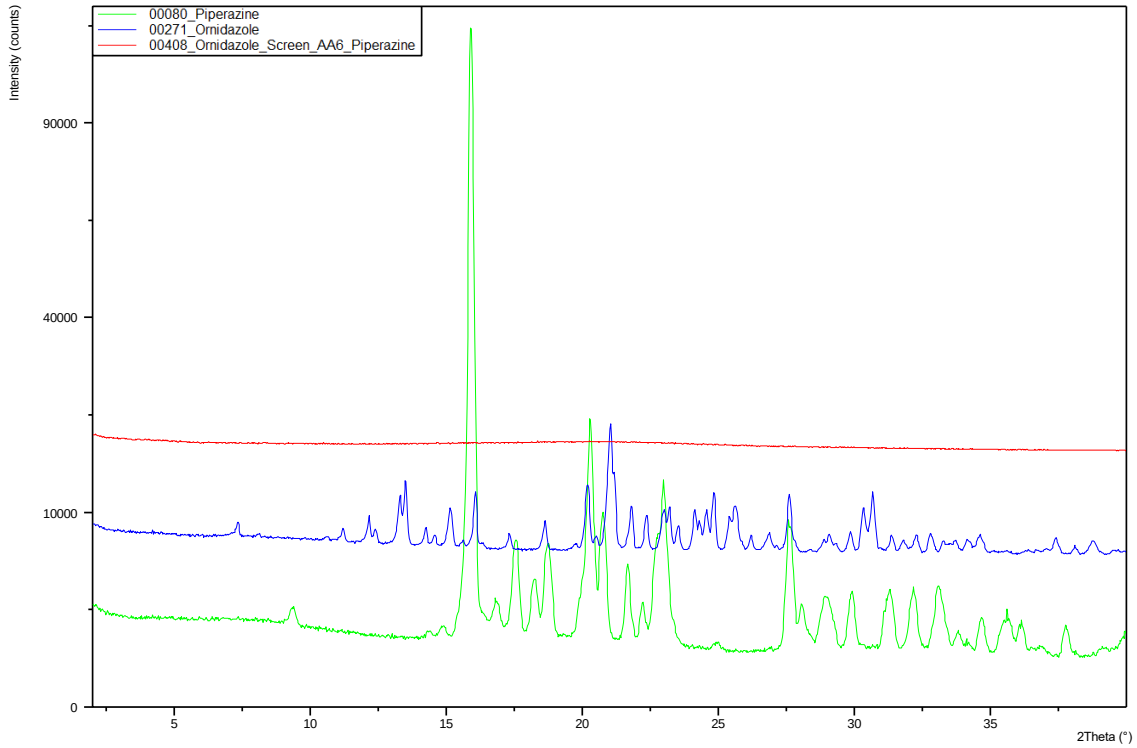


*Figure 6. Piperazine.*

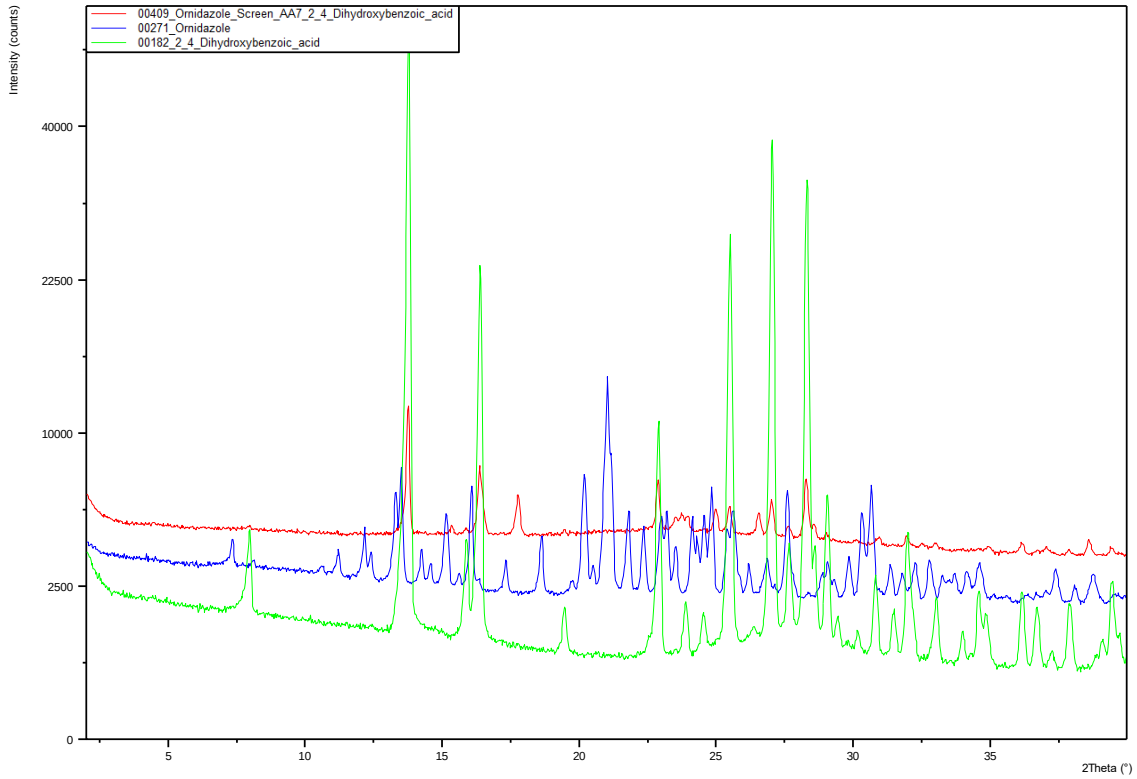


*Figure 7. 2,4-Dihydroxybenzoic acid.*

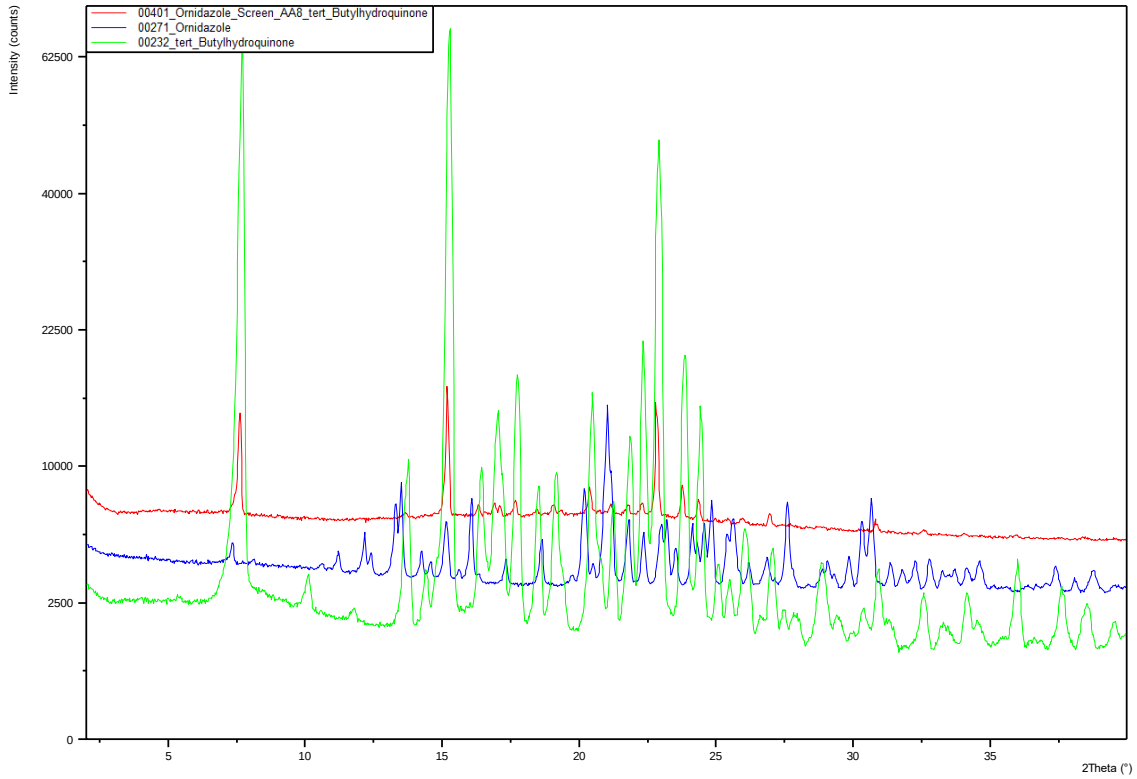


*Figure 8. tert-Butylhydroquinone.*

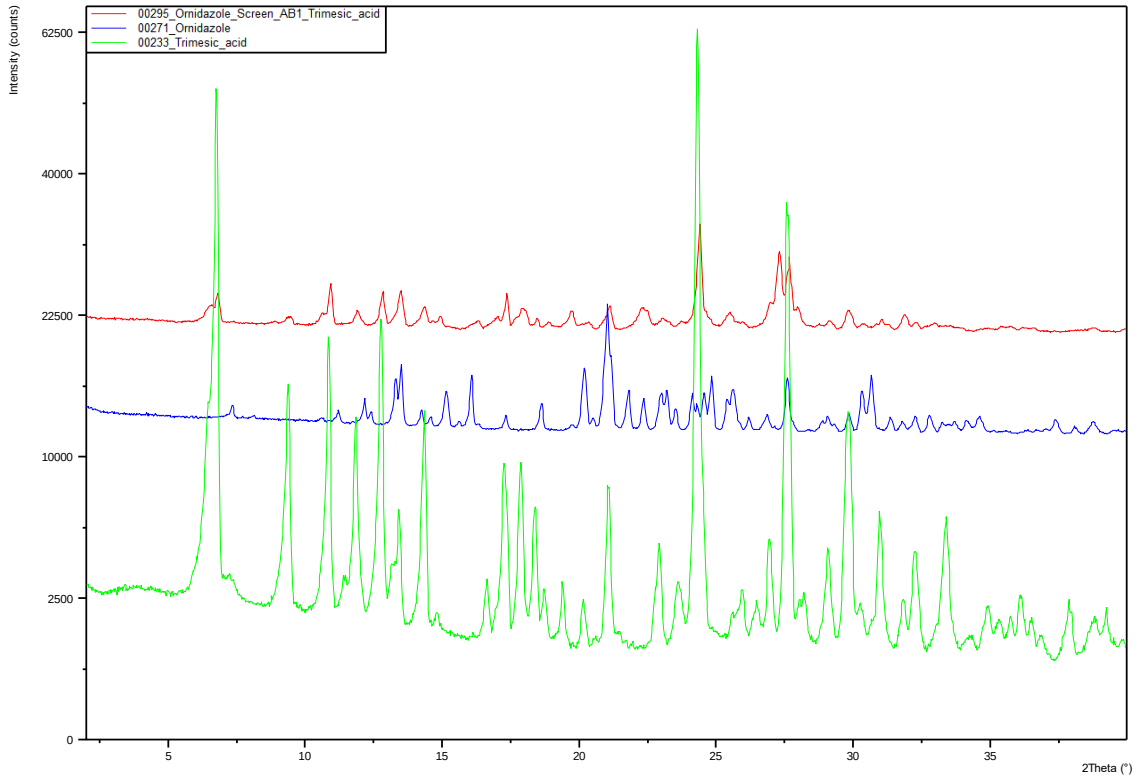


*Figure 9. Trimesic acid.*

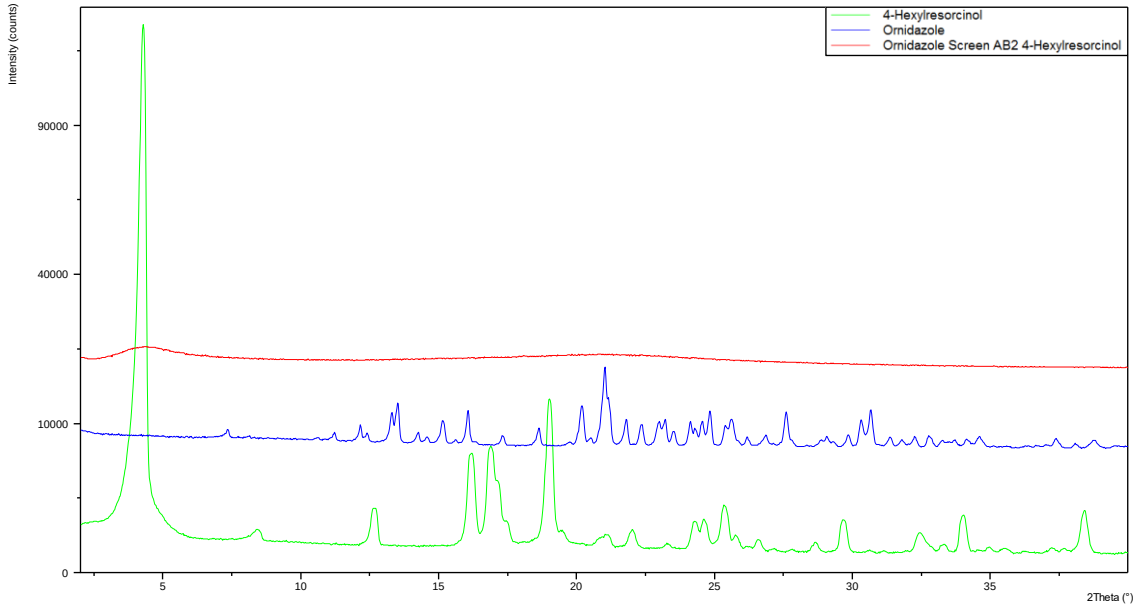


*Figure 10. 4-Hydroxyresorcinol.*

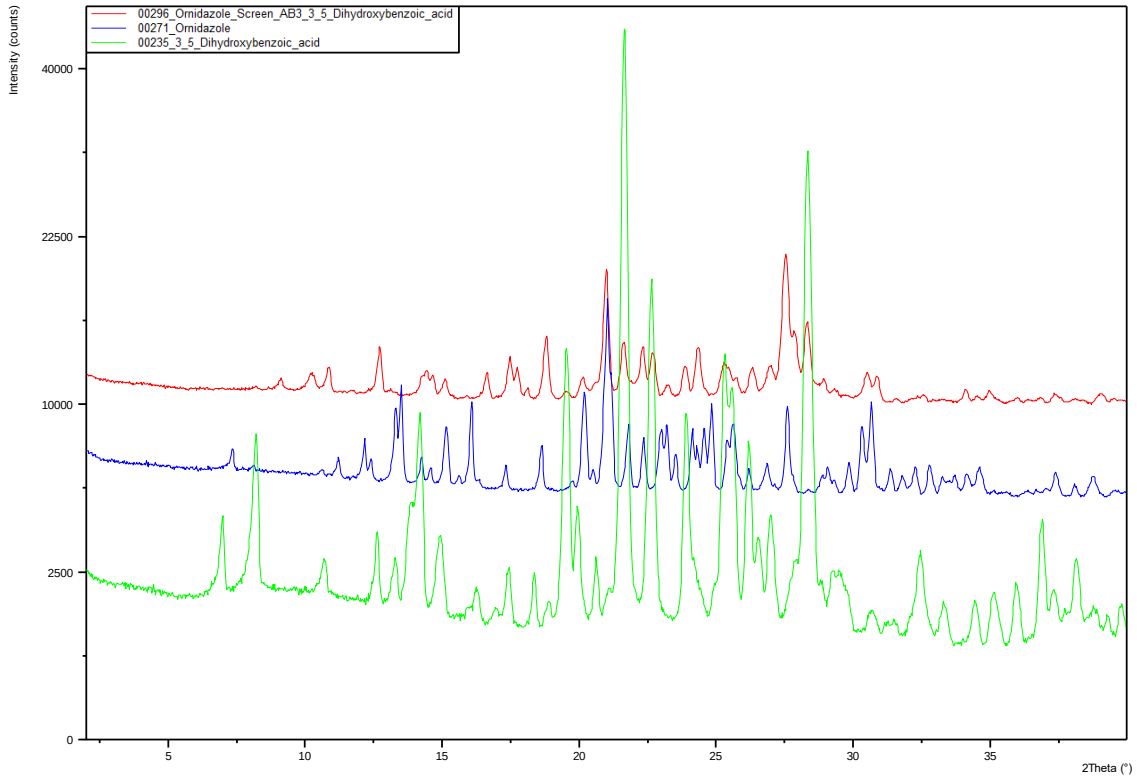


*Figure 11. 3,5-Dihydroxybenzoic acid.*

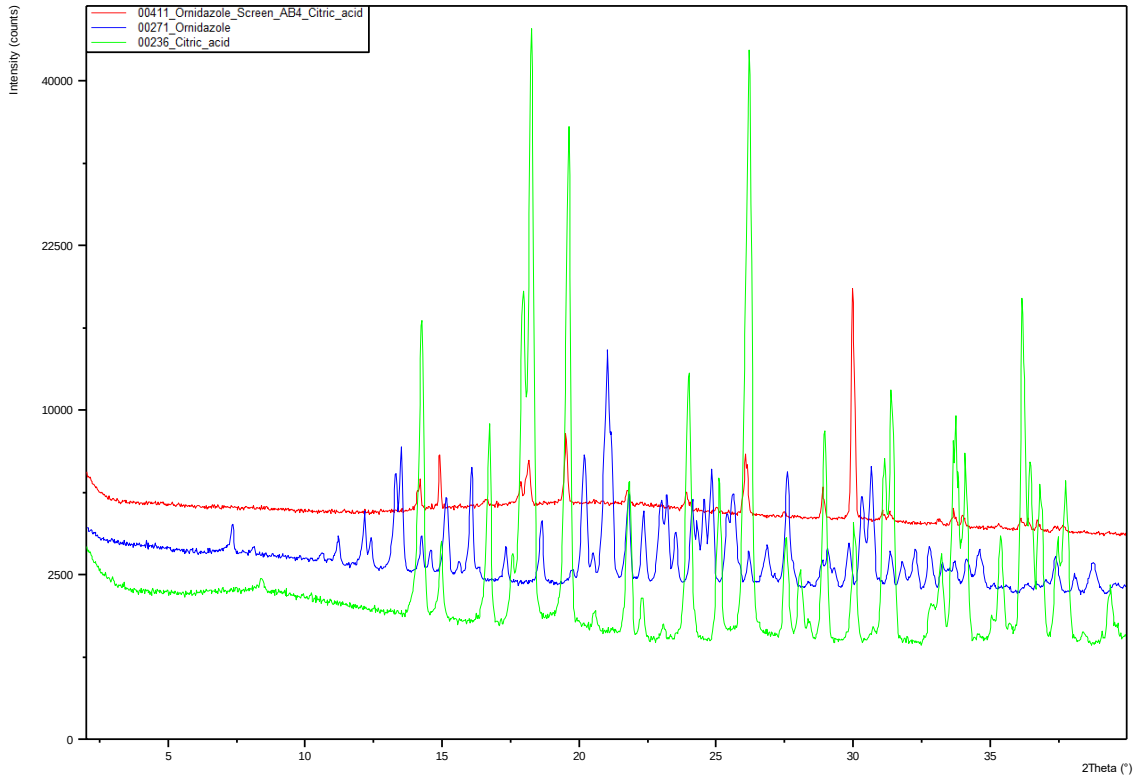


*Figure 12. Citric acid.*

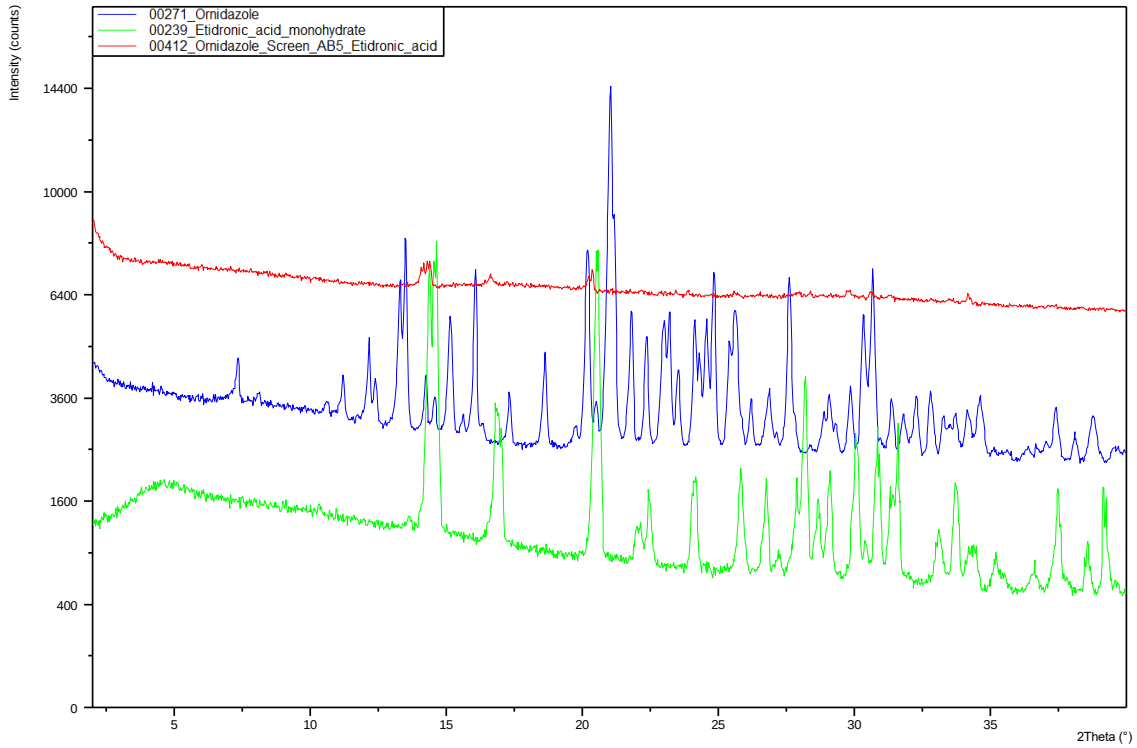


*Figure 13. Etidronic acid monohydrate.*

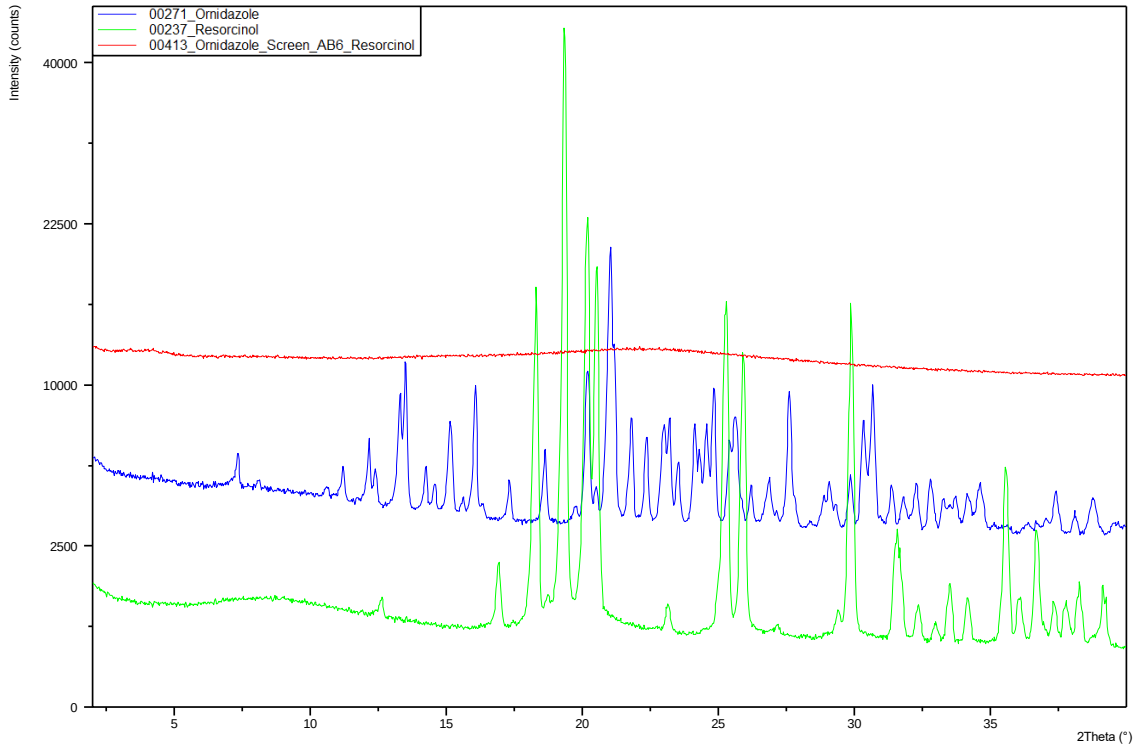


*Figure 14. Resorcinol.*

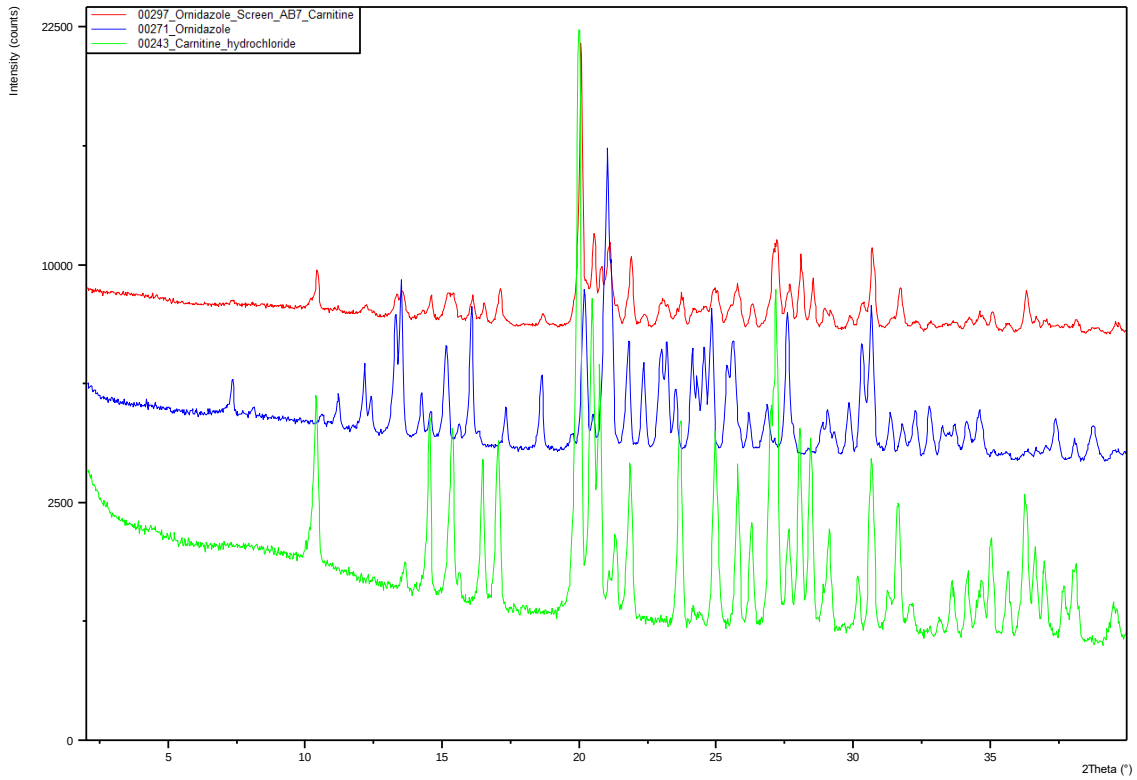


*Figure 15. Carnitine hydrochloride.*

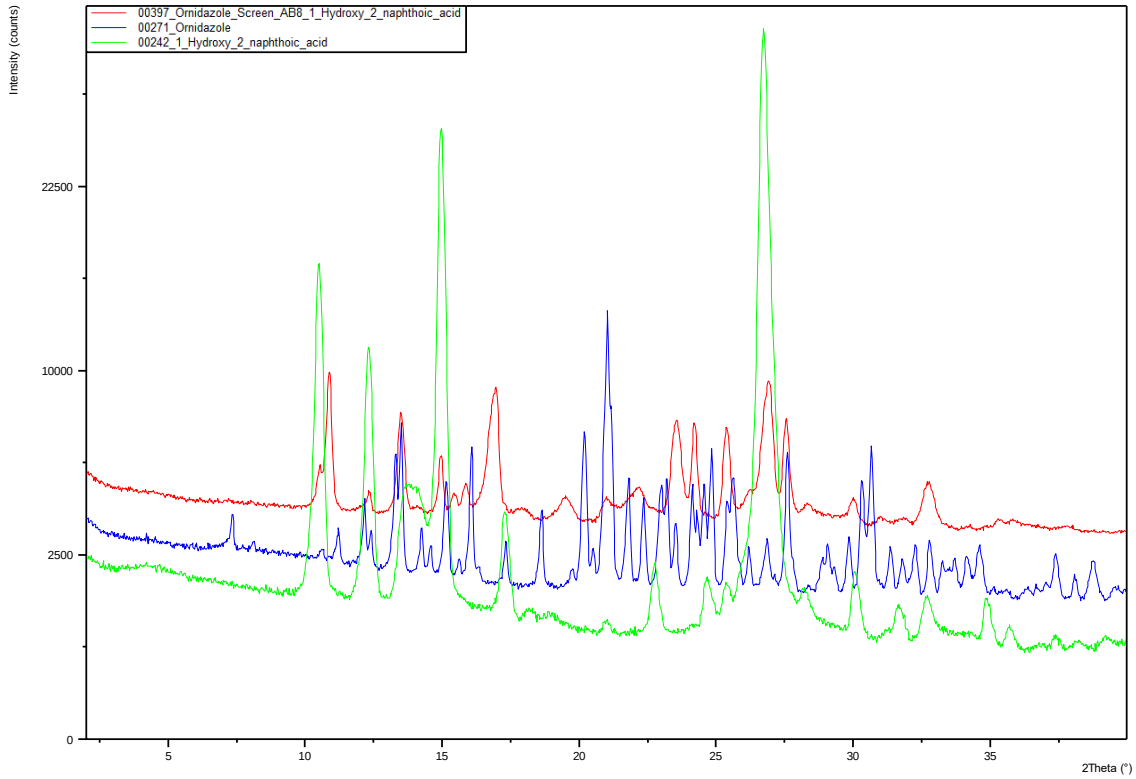


*Figure 16. 1-Hydroxy-2-naphthoic acid.*

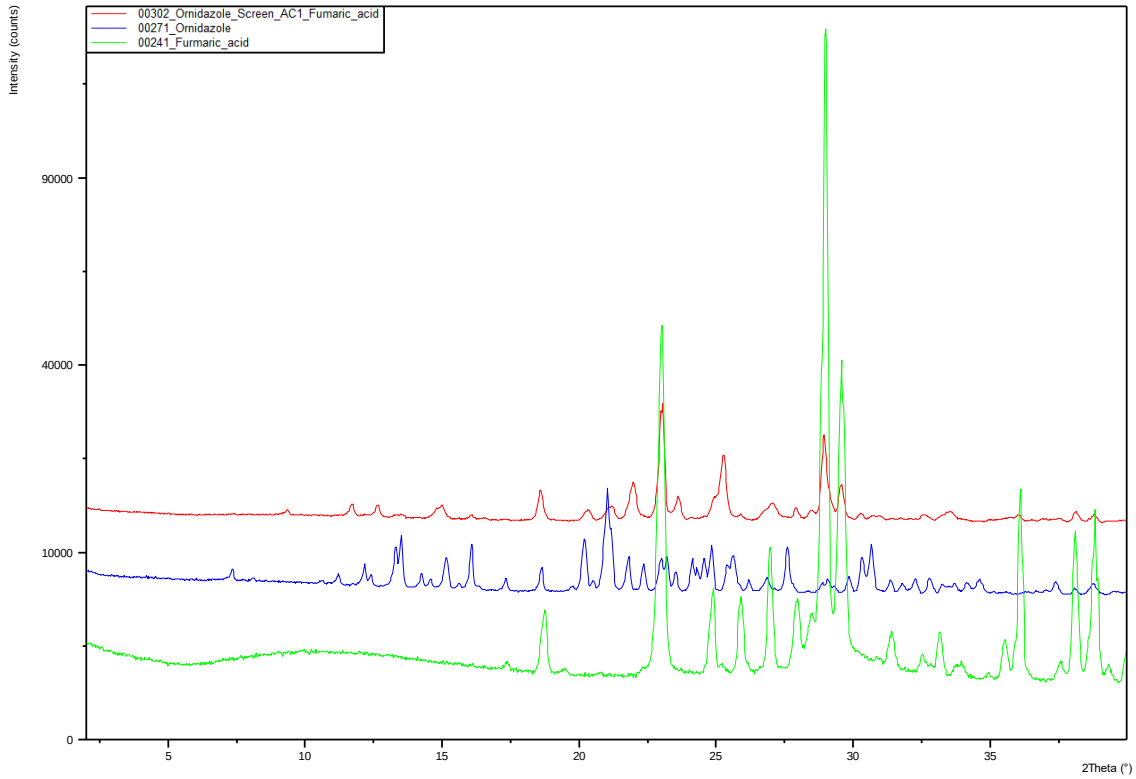


*Figure 17. Fumaric acid.*

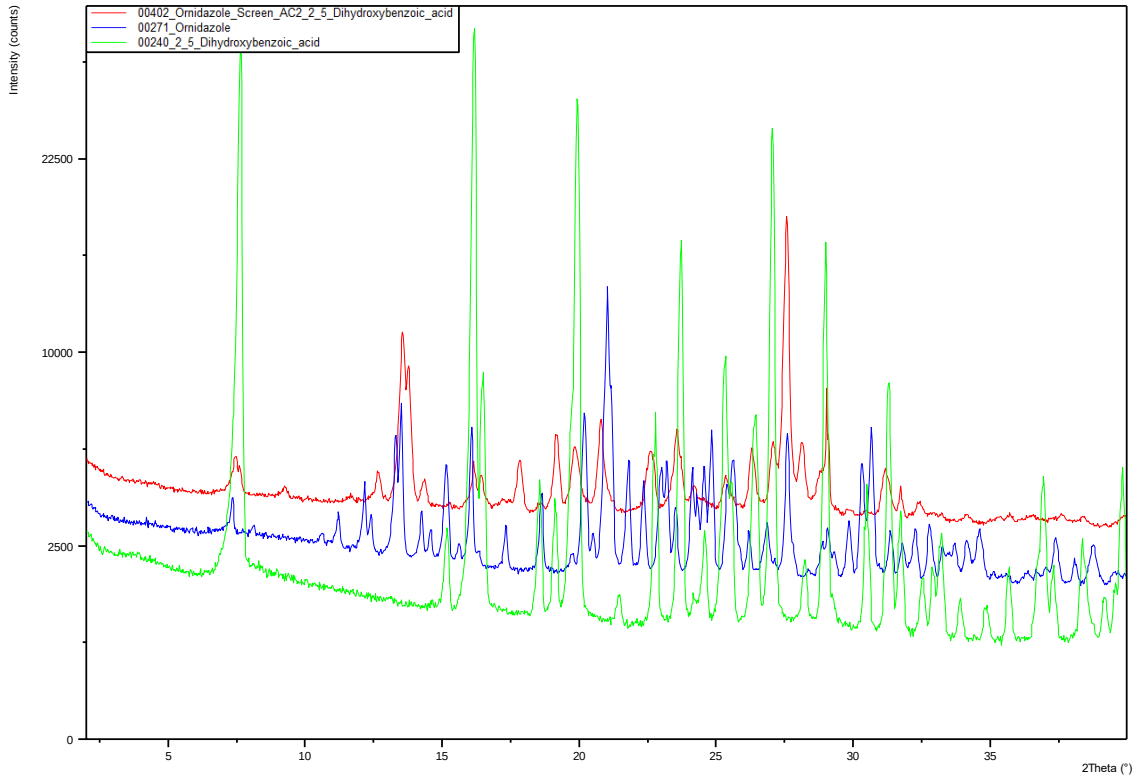


*Figure 18. 2,5-Dihydroxybenzoic acid.*

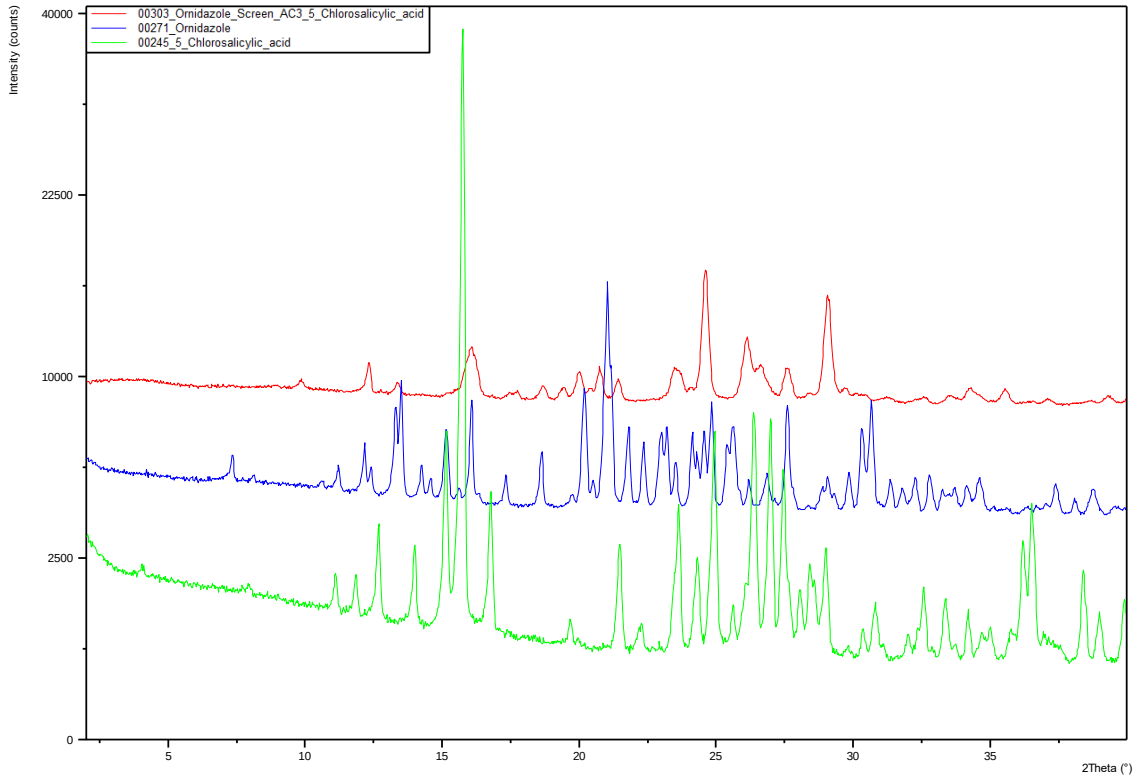


*Figure 19. 5-Chlorosalicylic acid.*

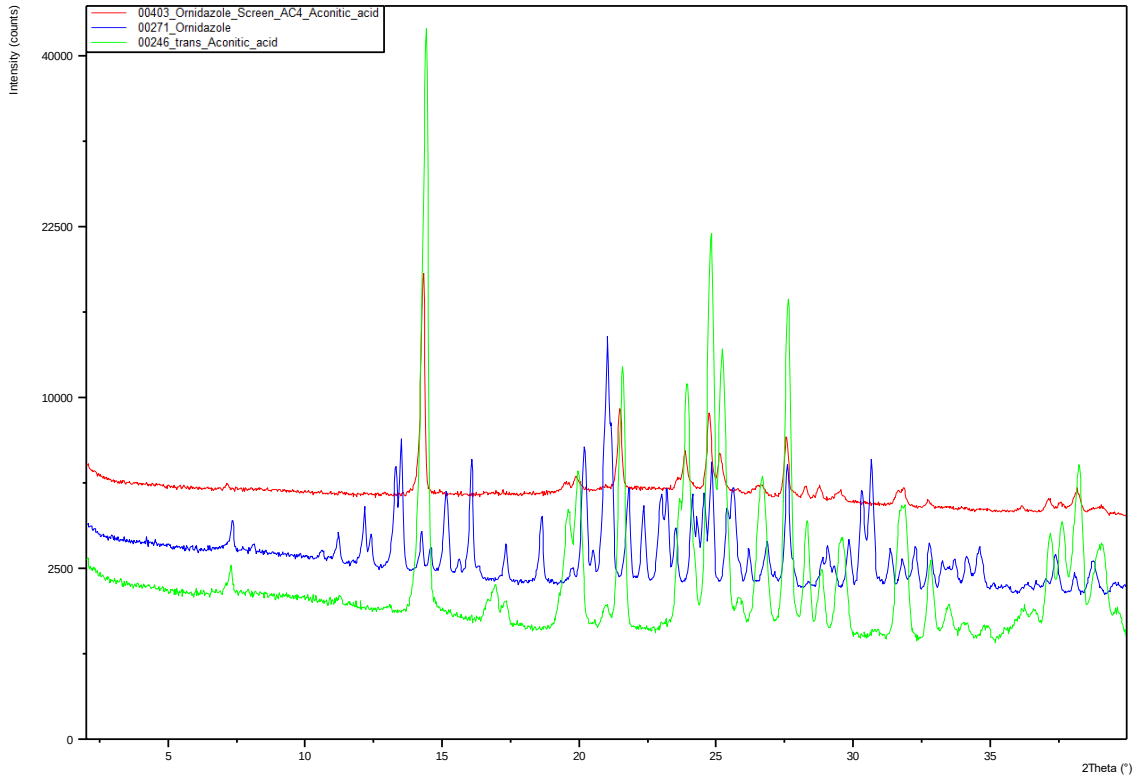


*Figure 20. Aconitic acid.*

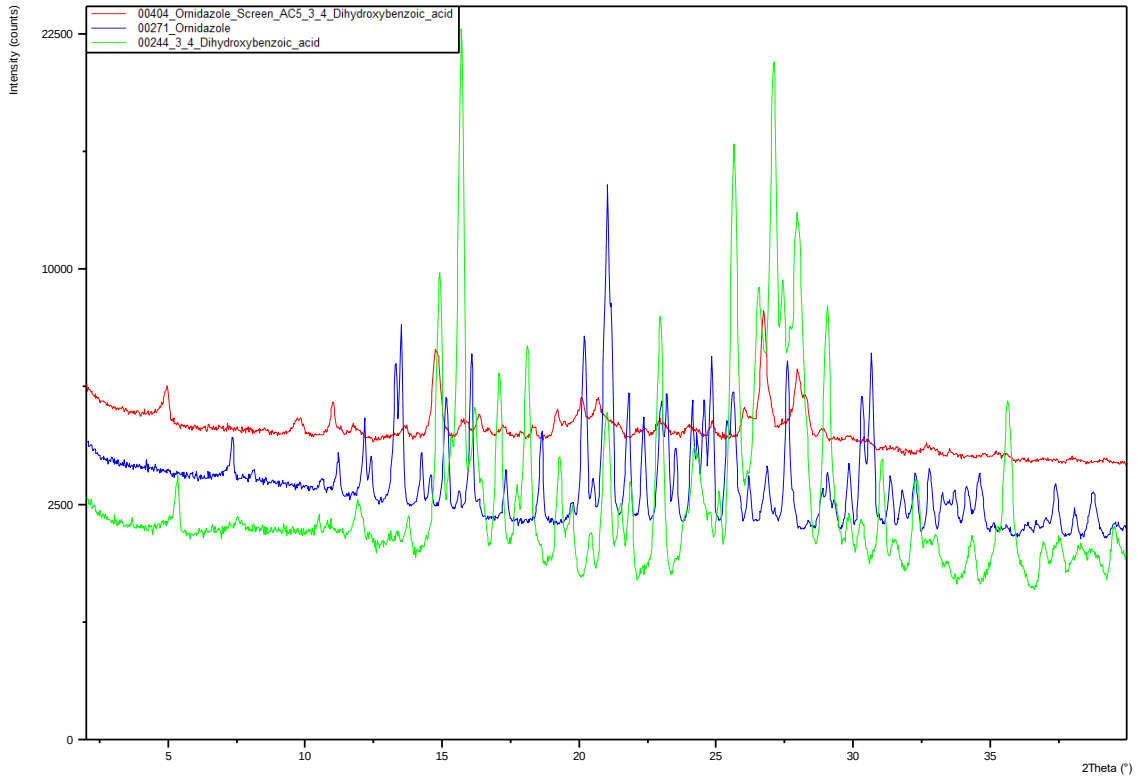


*Figure 21. 3,4-Dihydroxybenzoic acid.*

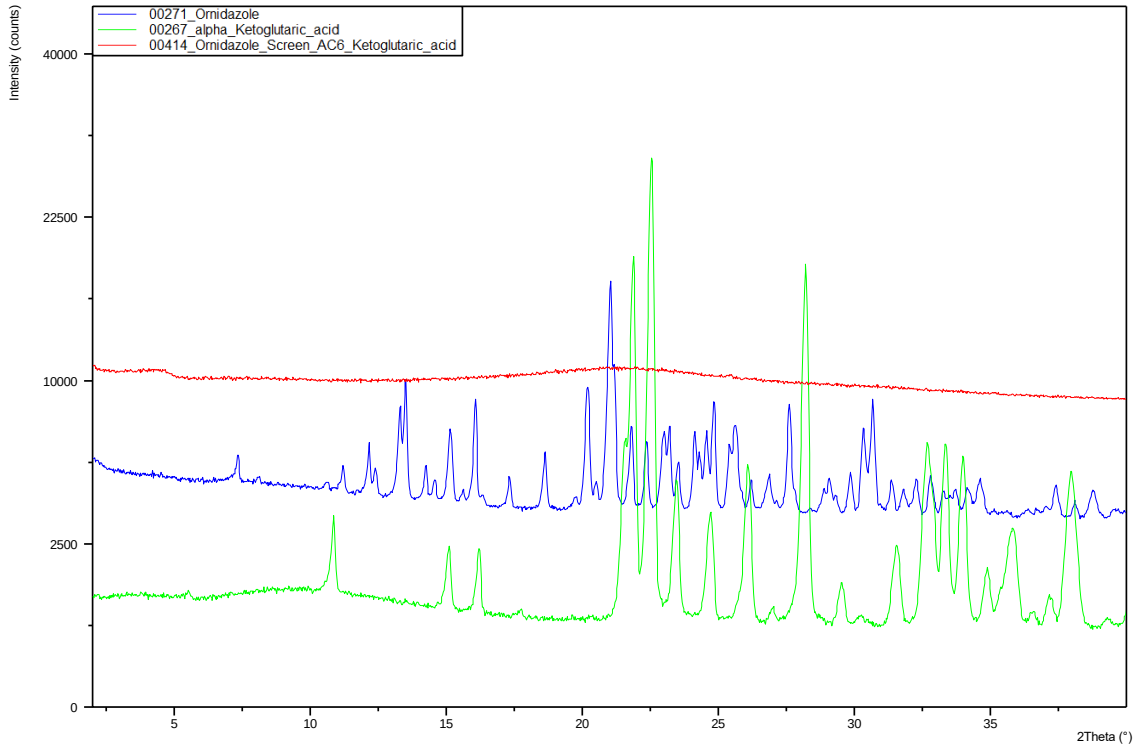


*Figure 22. alpha-Ketoglutaric acid.*

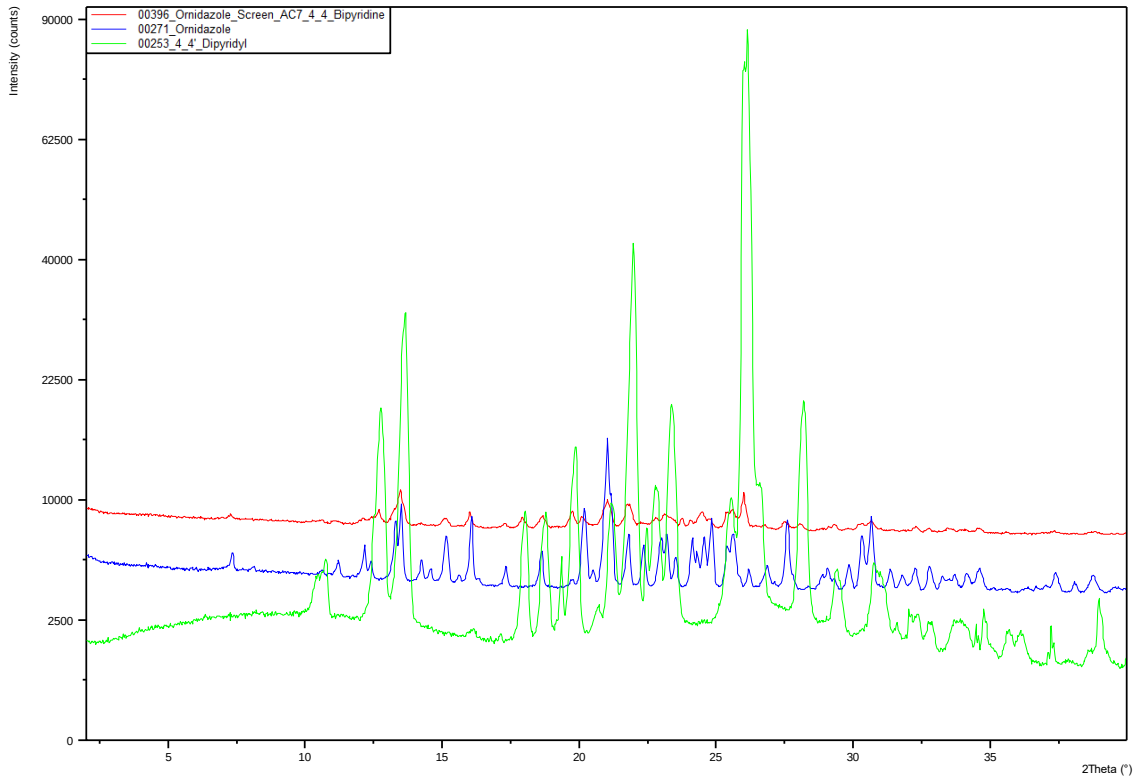


*Figure 23. 4,4-Bipyridine.*

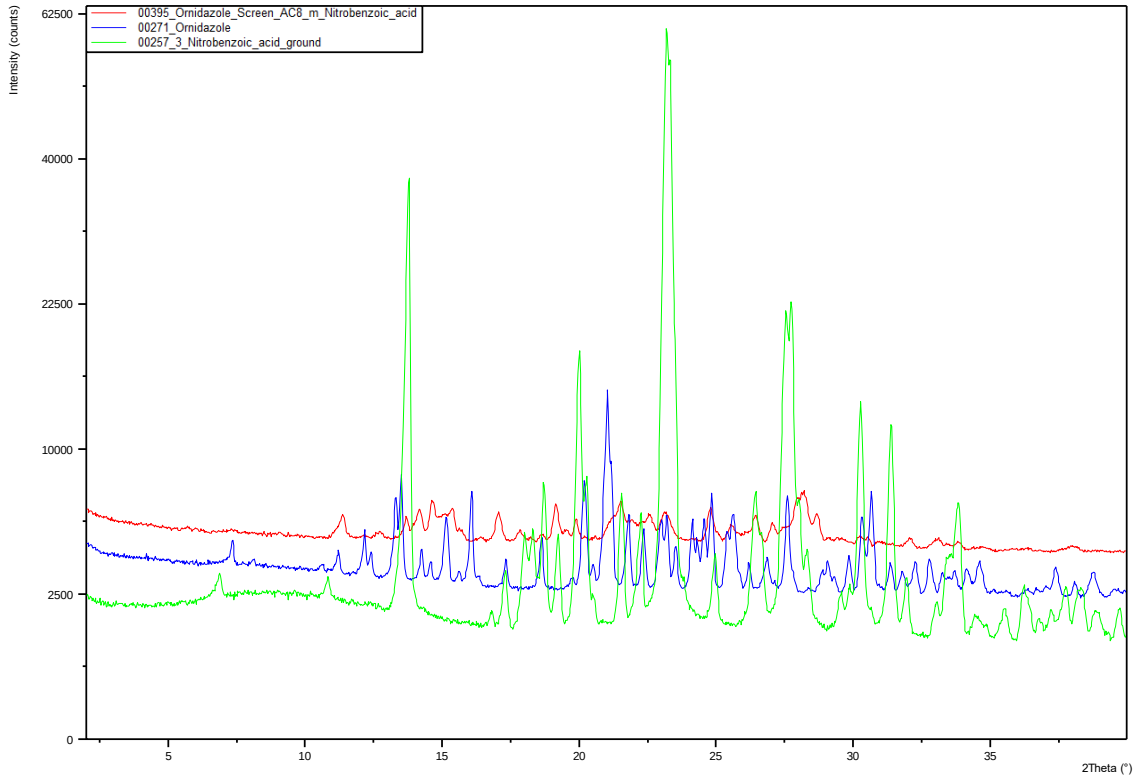


*Figure 24. m-Nitrobenzoic acid.*

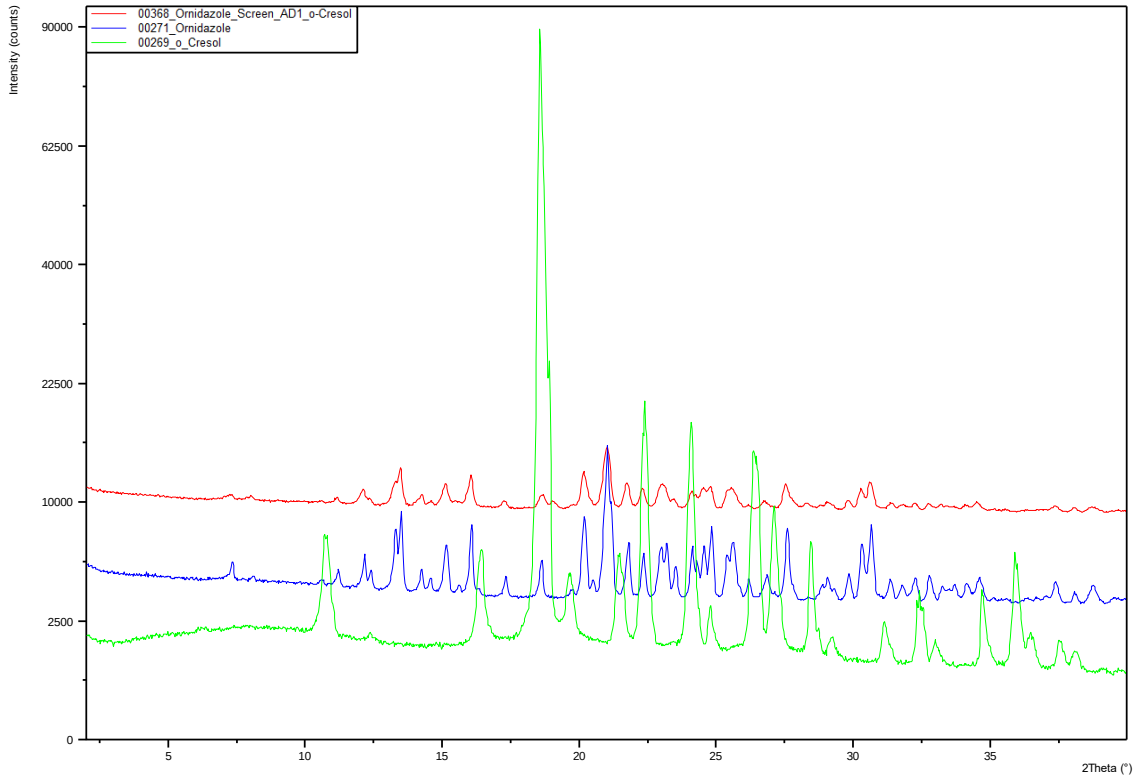


*Figure 25. o-Cresol.*

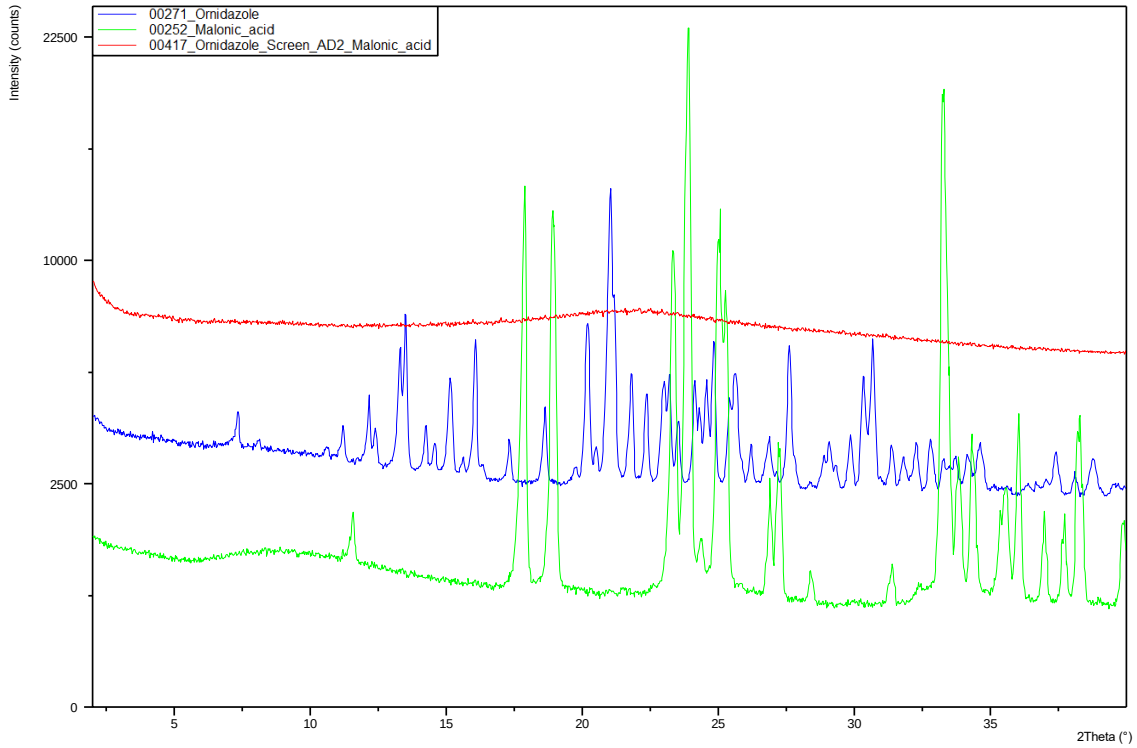


*Figure 26. Malonic acid.*

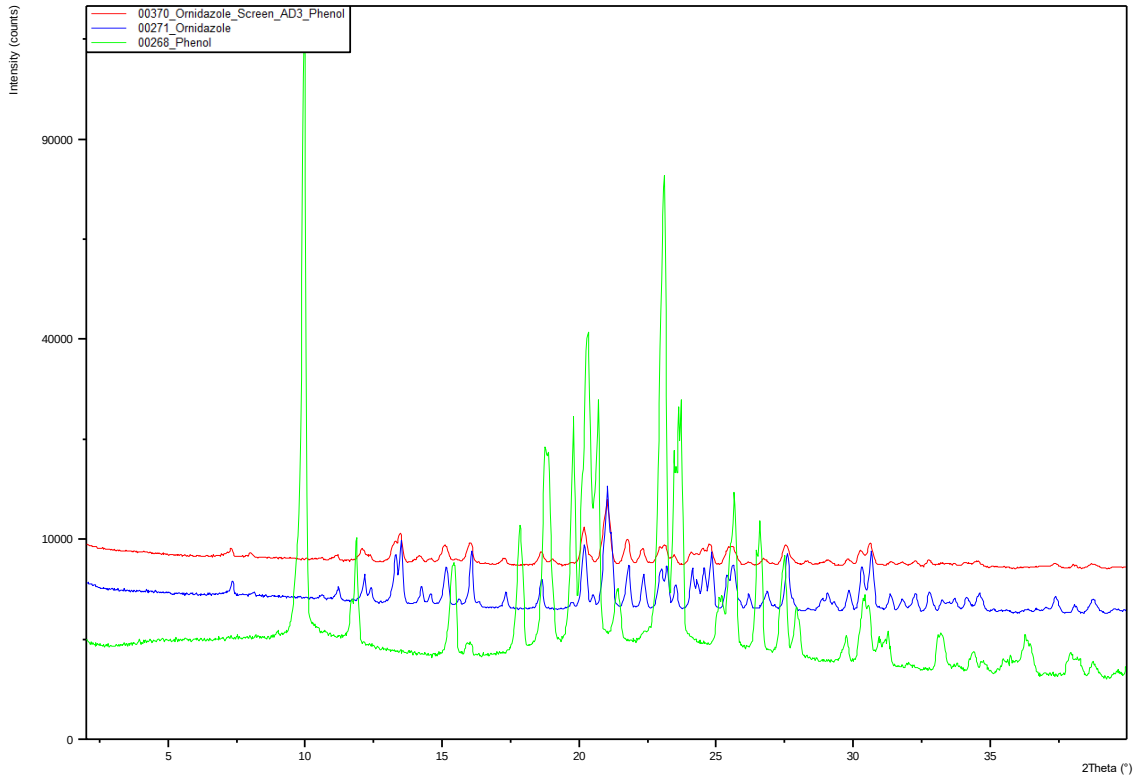


*Figure 27. Phenol.*

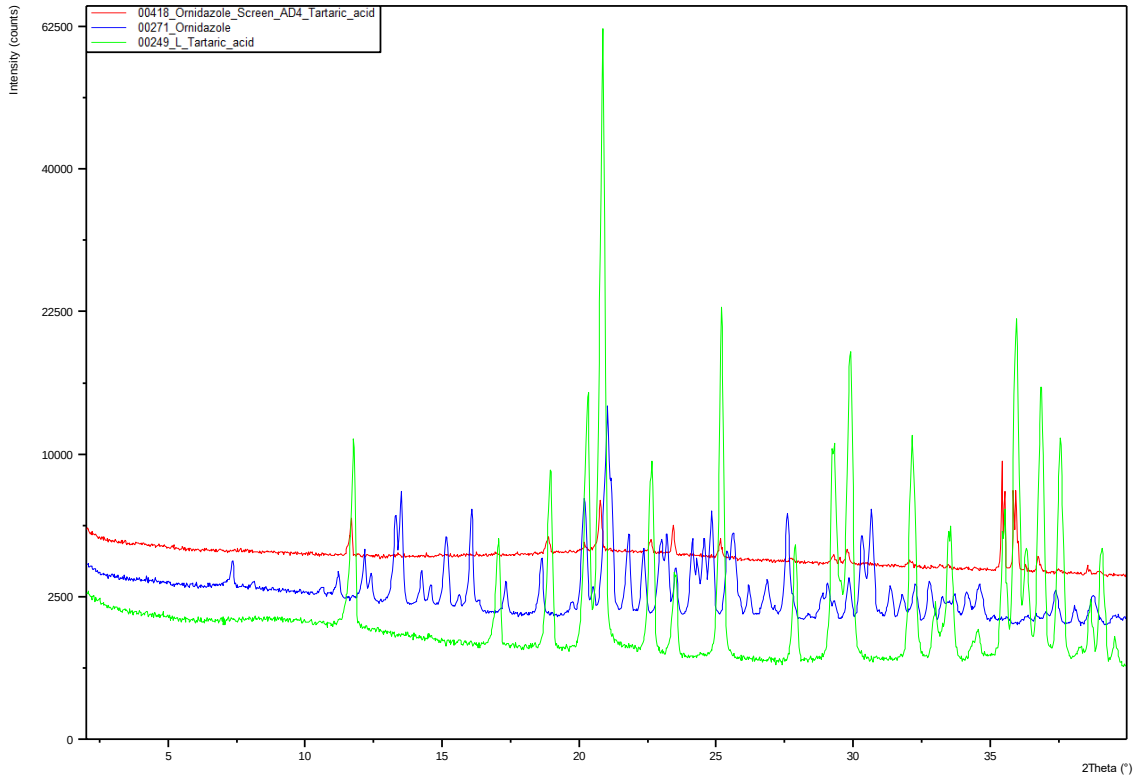


*Figure 28. L-Tartaric acid.*

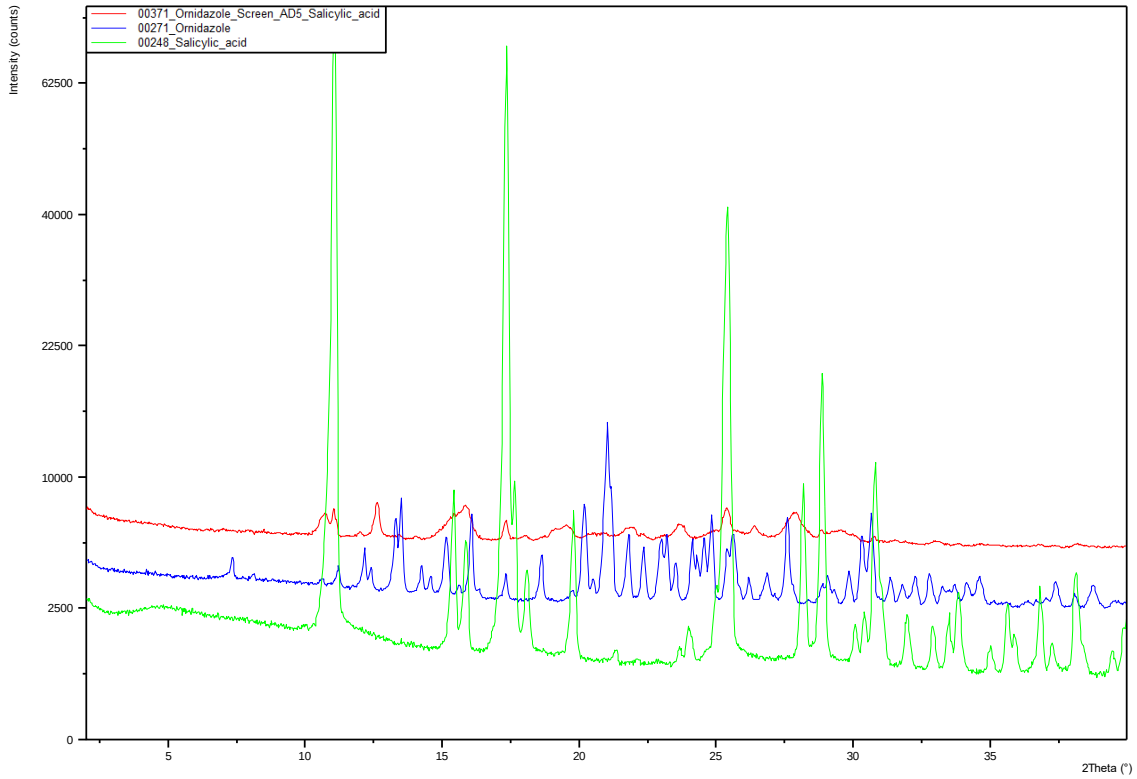


*Figure 29. Salicylic acid.*

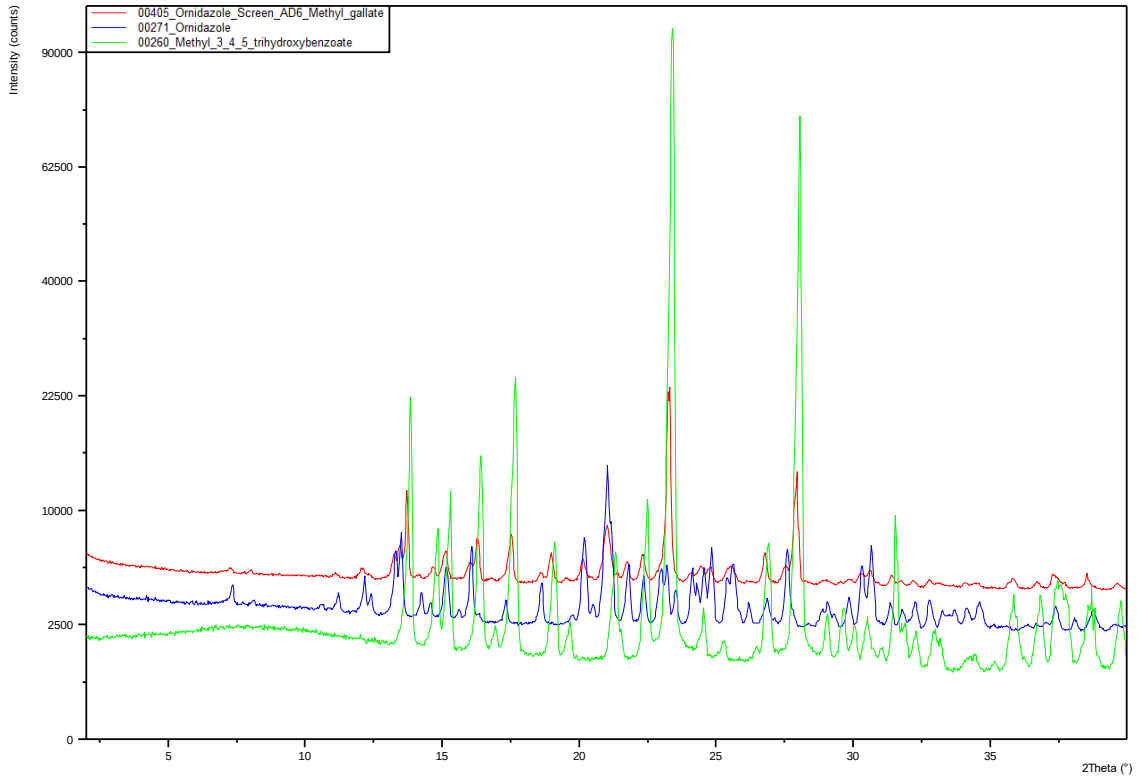


*Figure 30. Methyl gallate.*

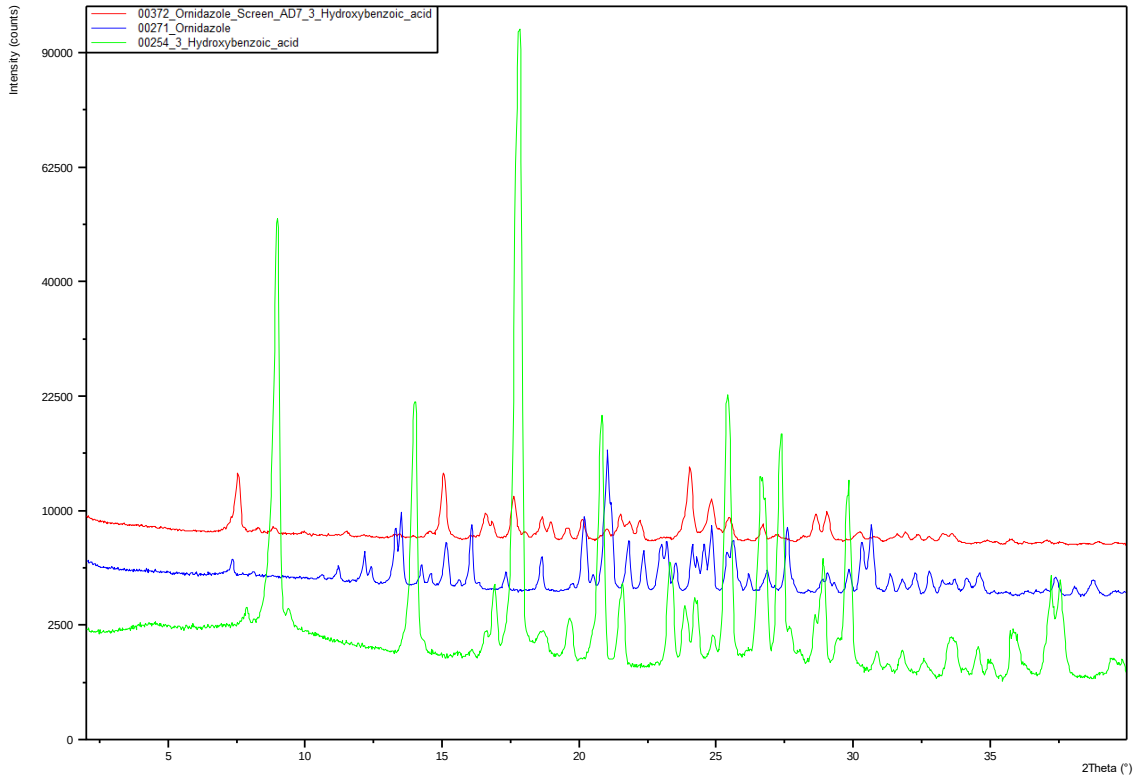


*Figure 31. 3-Hydroxybenzoic acid.*

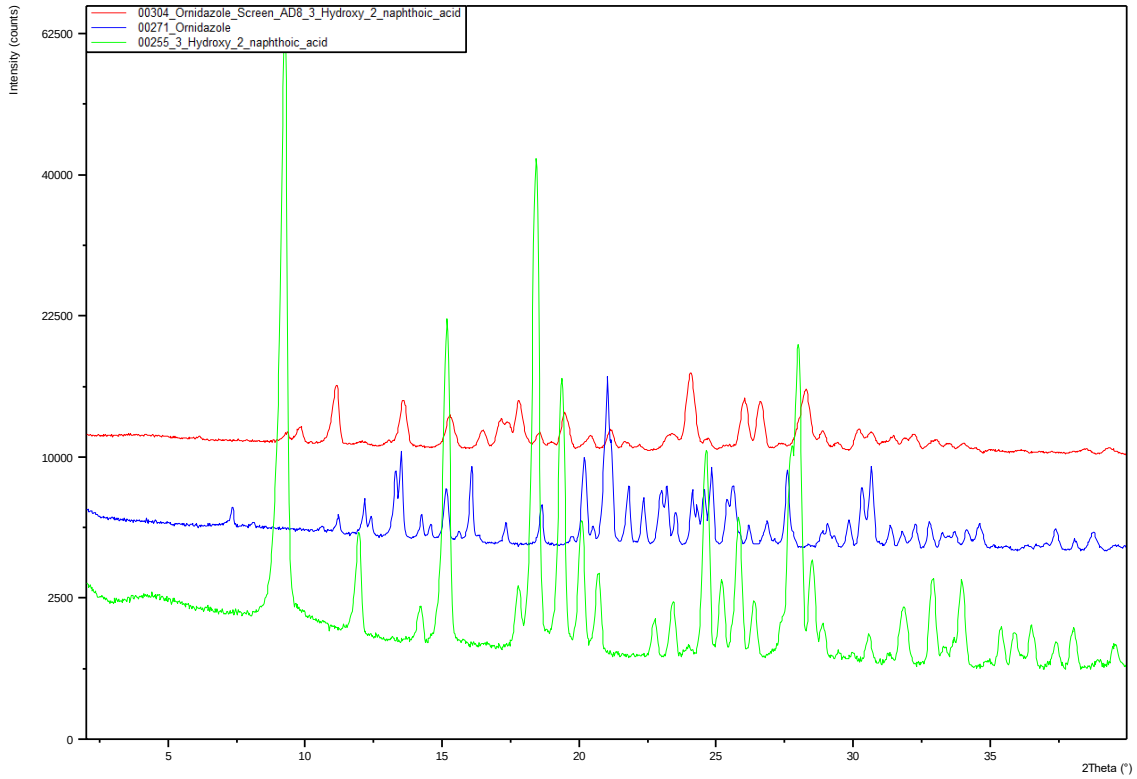


*Figure 32. 3-Hydroxy-2-naphthoic acid.*

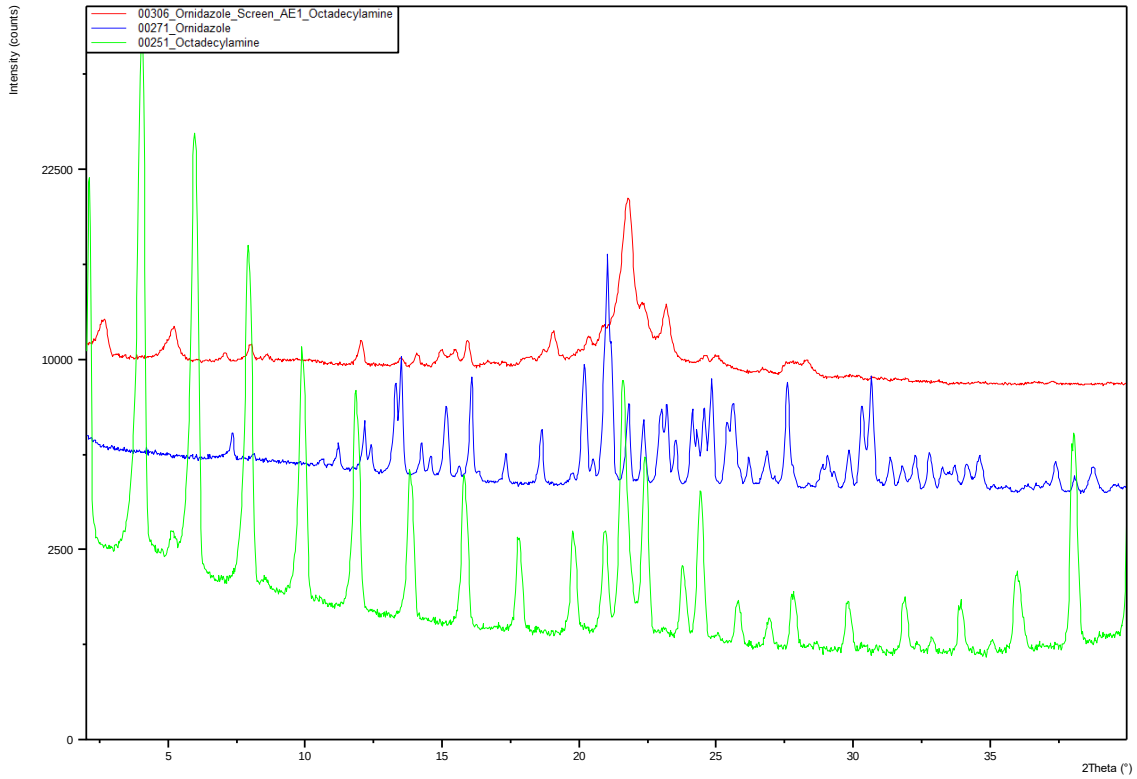


*Figure 33. Octadecylamine.*

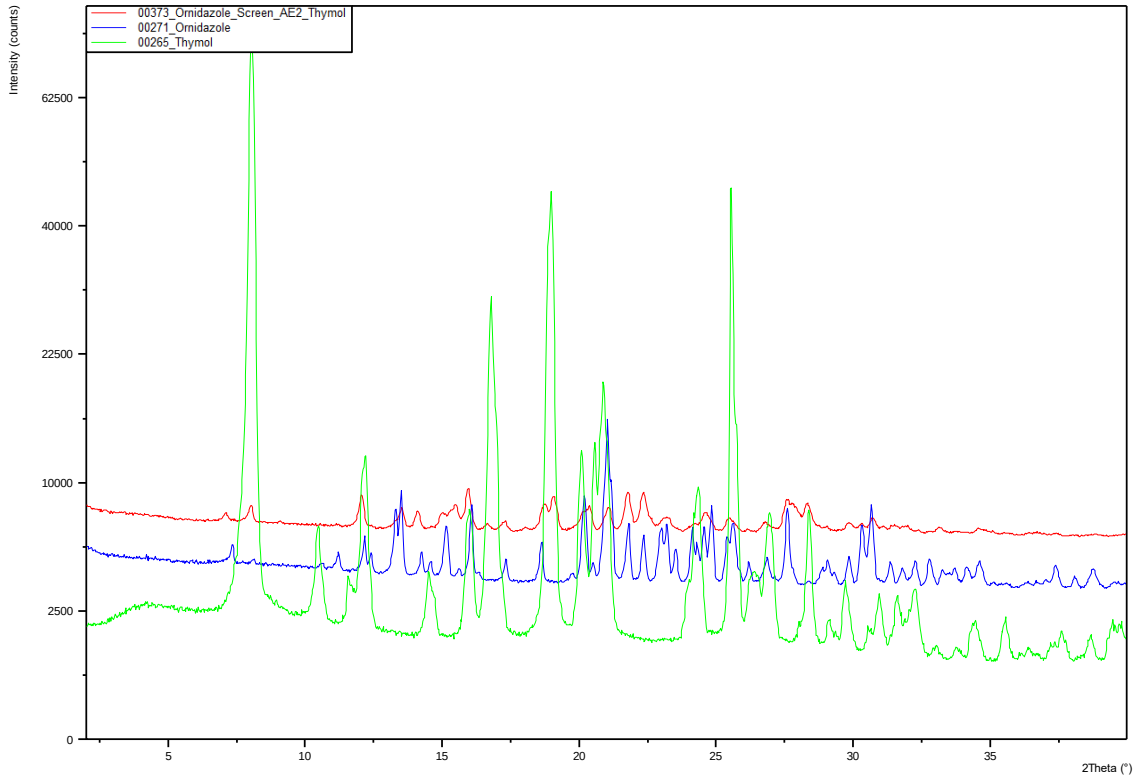


*Figure 34. Thymol.*

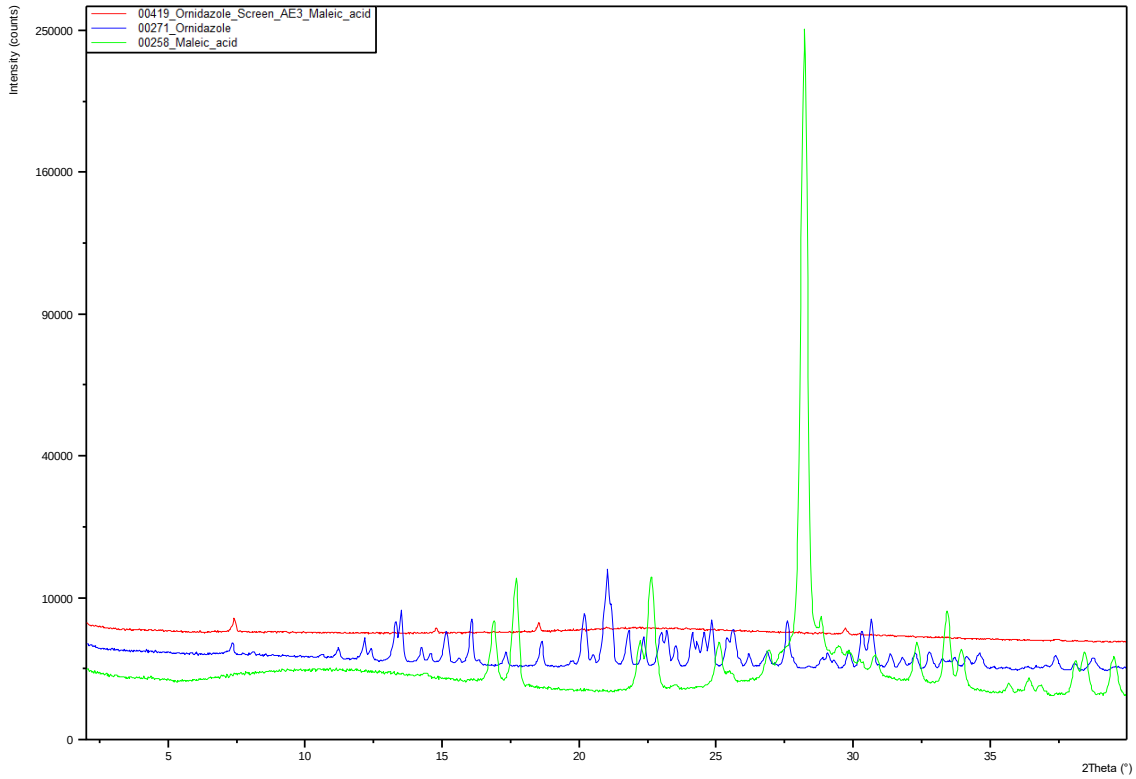


*Figure 35. Maleic acid.*

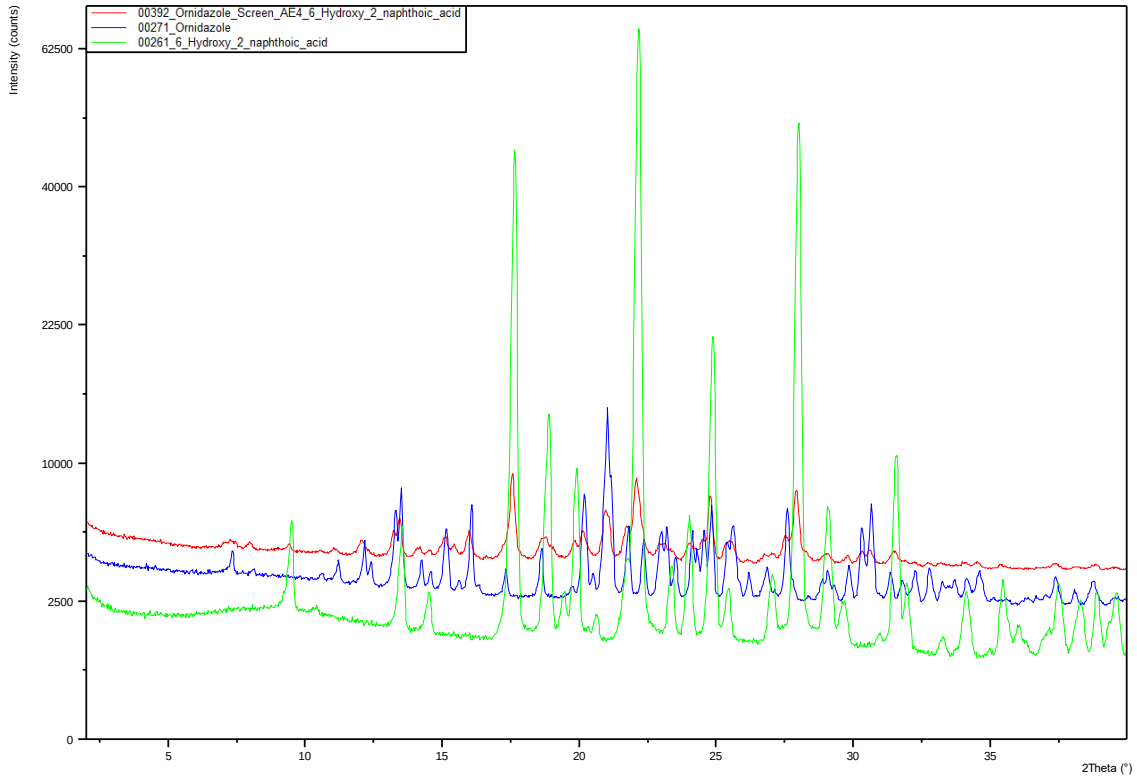


*Figure 36. 6-Hydroxy-2-naphthoic acid.*

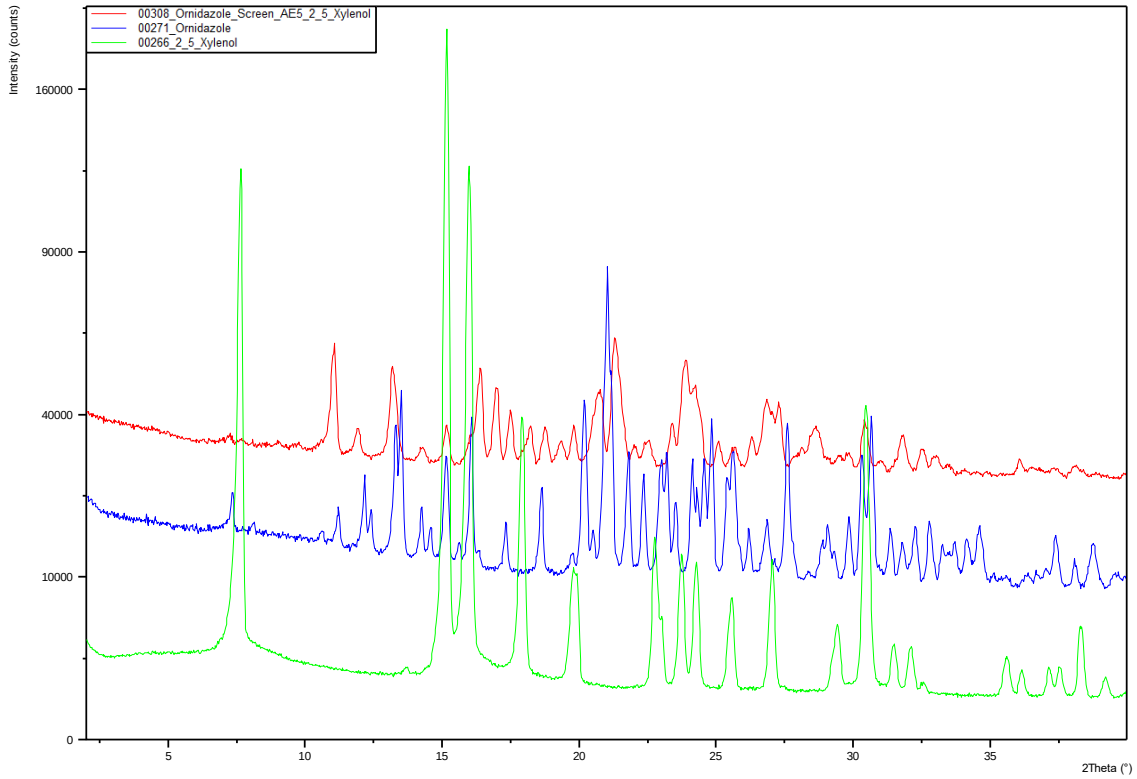


*Figure 37. 2,5-Xylenol.*

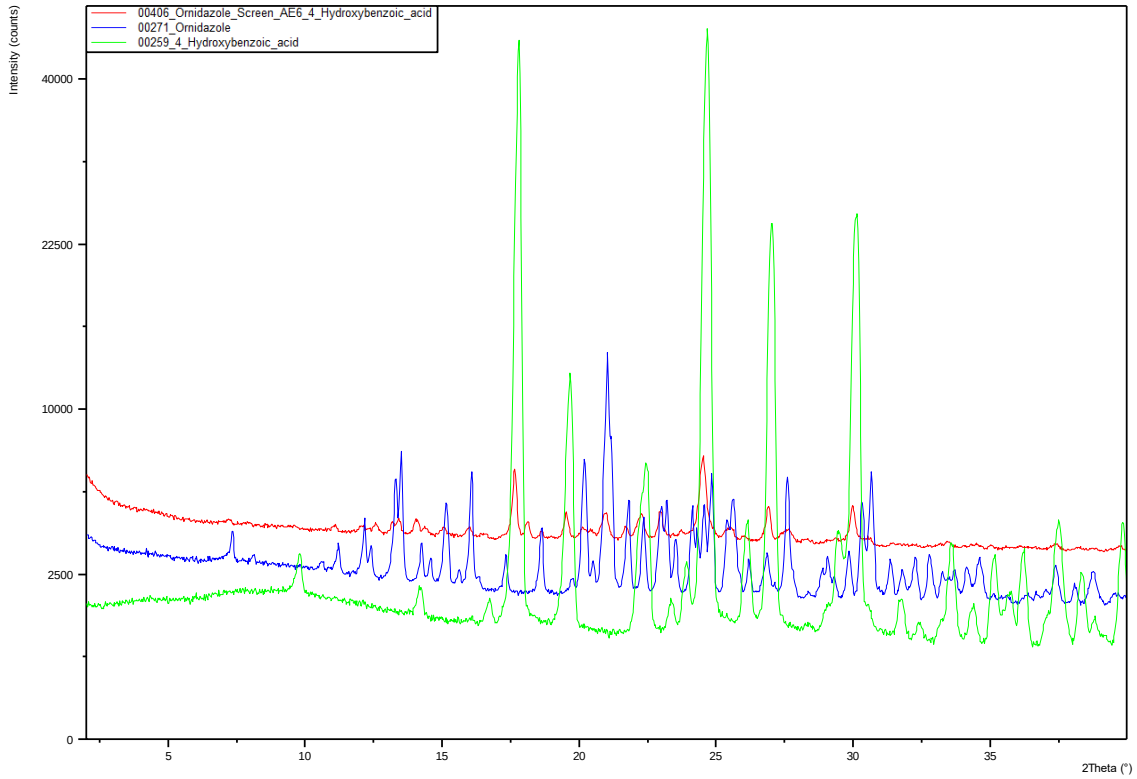


*Figure 38. 4-Hydroxybenzoic acid.*

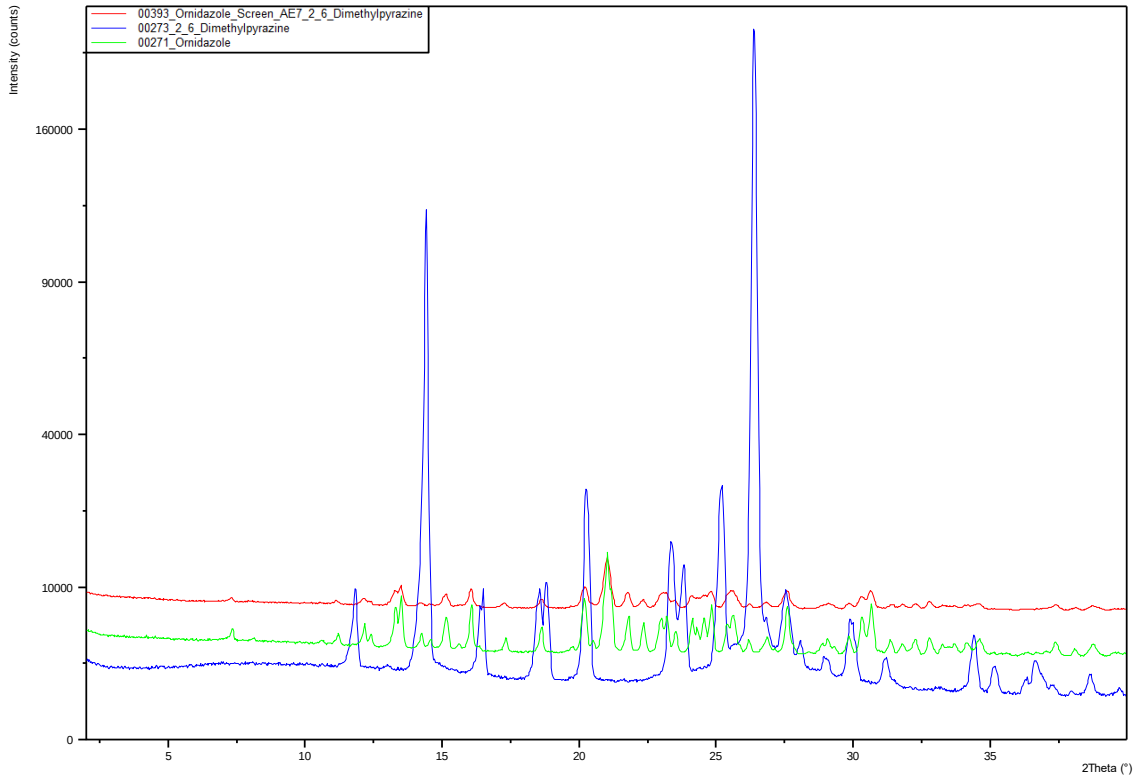


*Figure 39. 2,6-Dimethylpyrazine.*

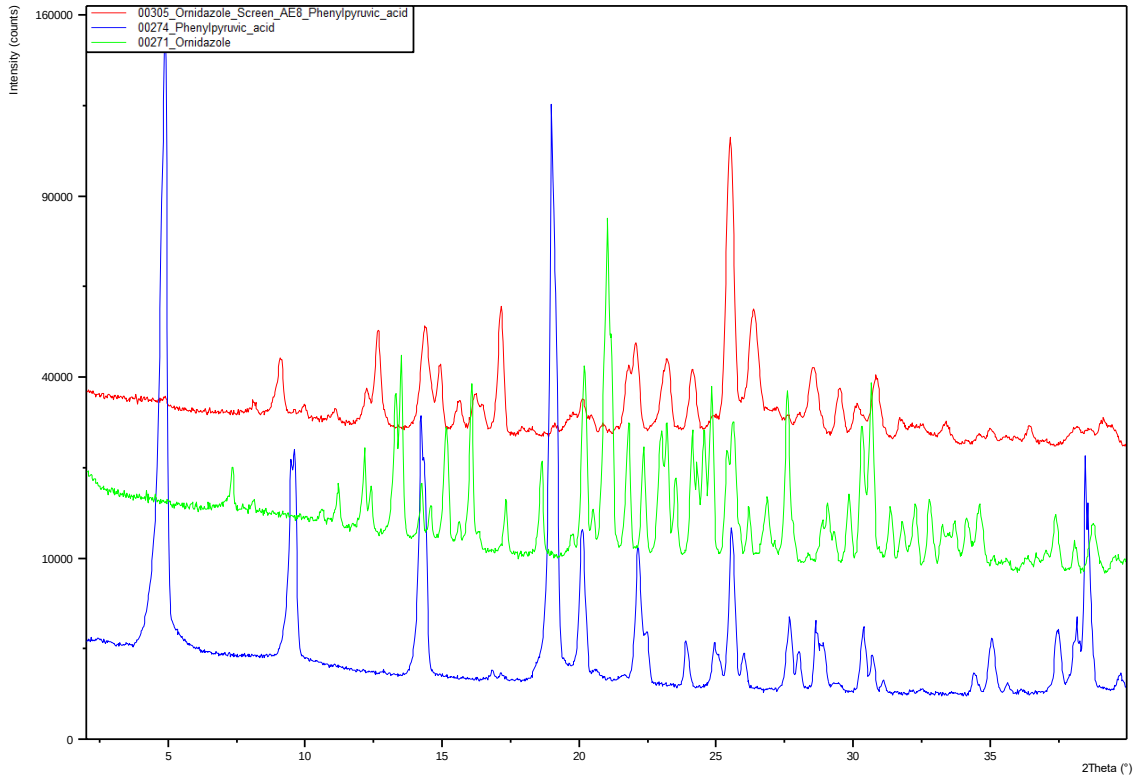


*Figure 40. Phenylpyruvic acid.*

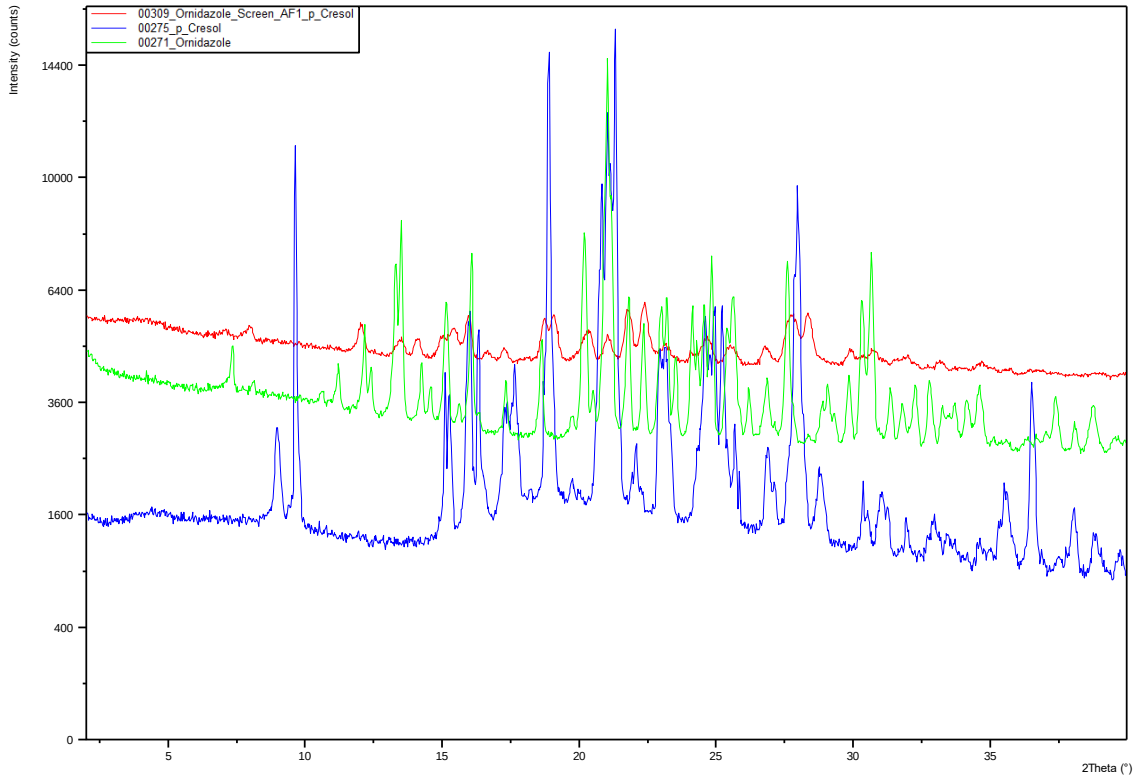


*Figure 41. p-Cresol.*

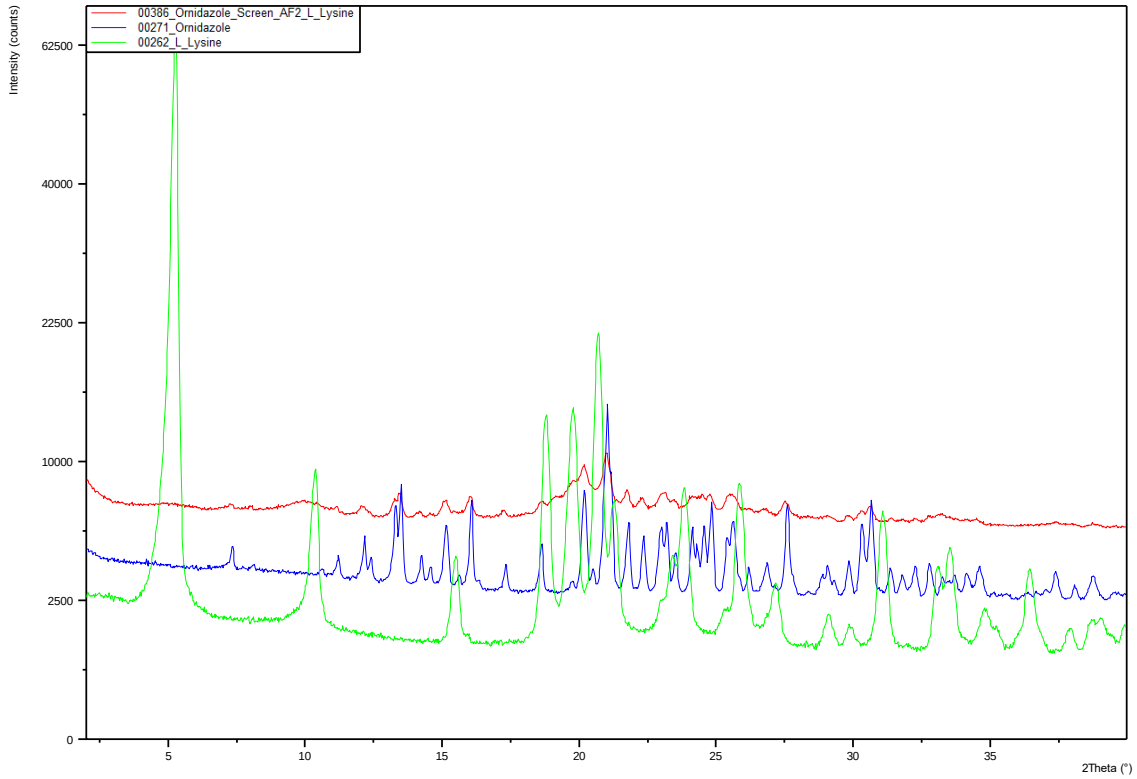


*Figure 42. L-Lysine.*

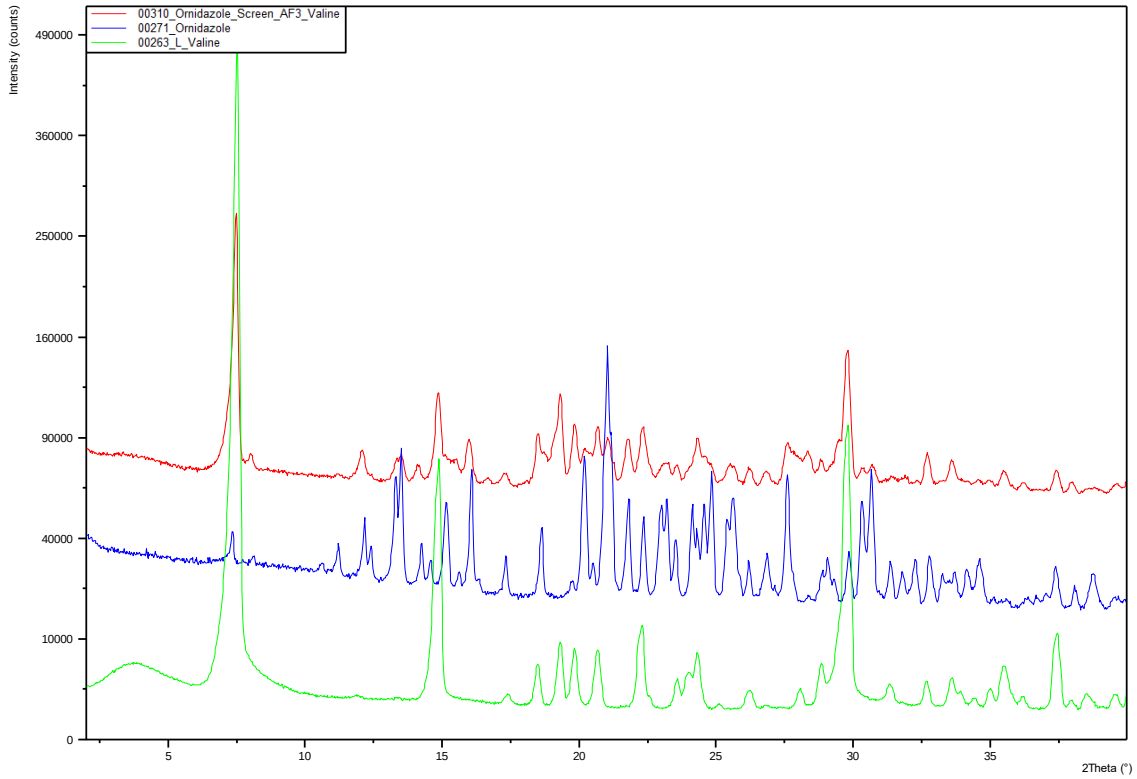


*Figure 43. L-Valine.*

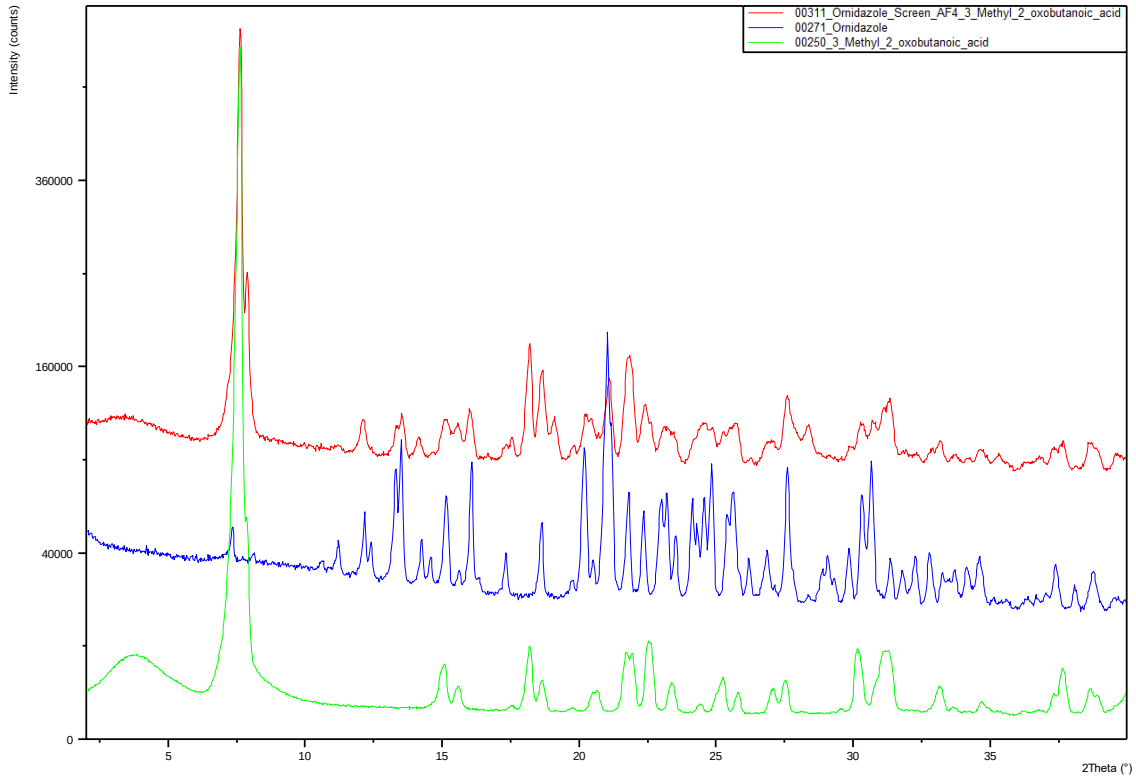


*Figure 44. 3-Methyl-2-oxobutanoic acid.*

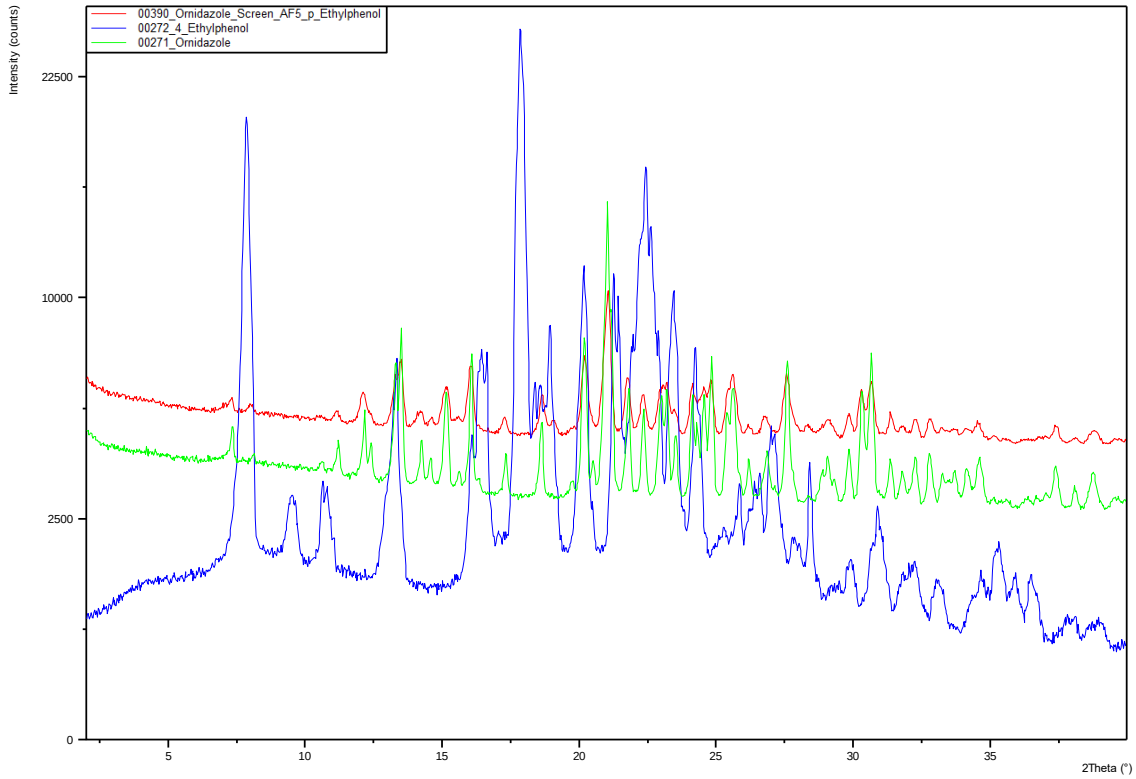


*Figure 45. p-Ethylphenol.*

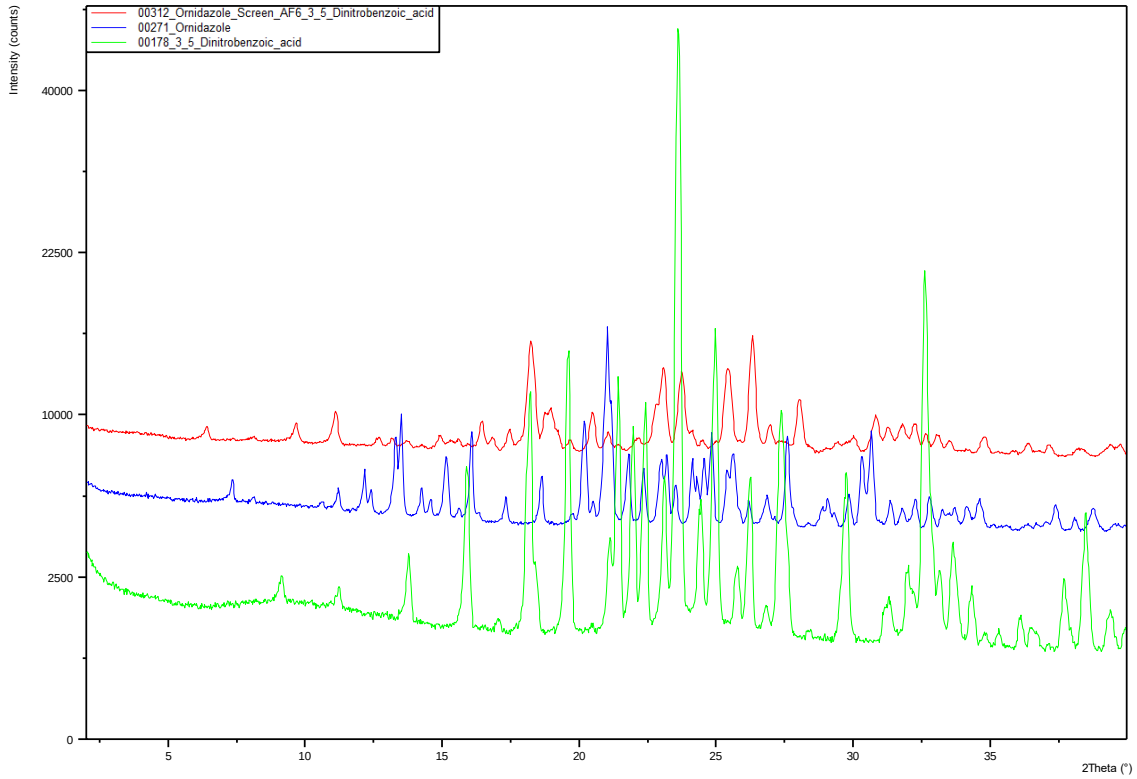


*Figure 46. 3,5-Dinitrobenzoic acid.*

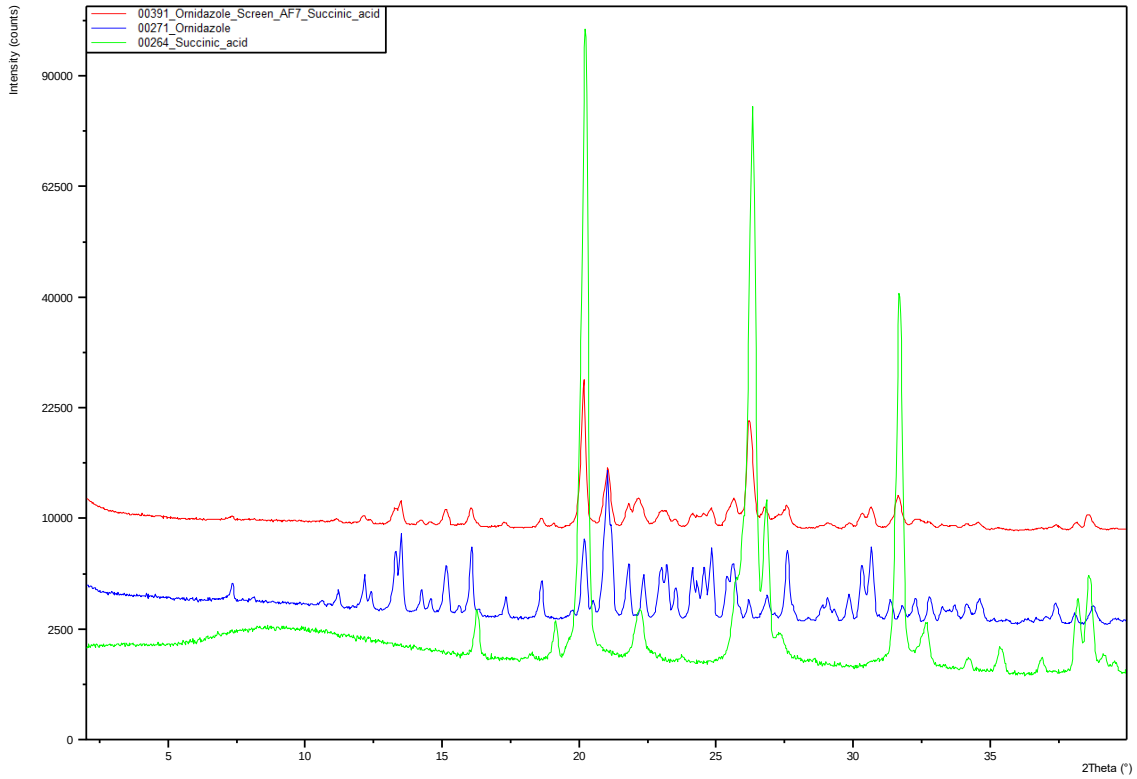


*Figure 47. Succinic acid.*

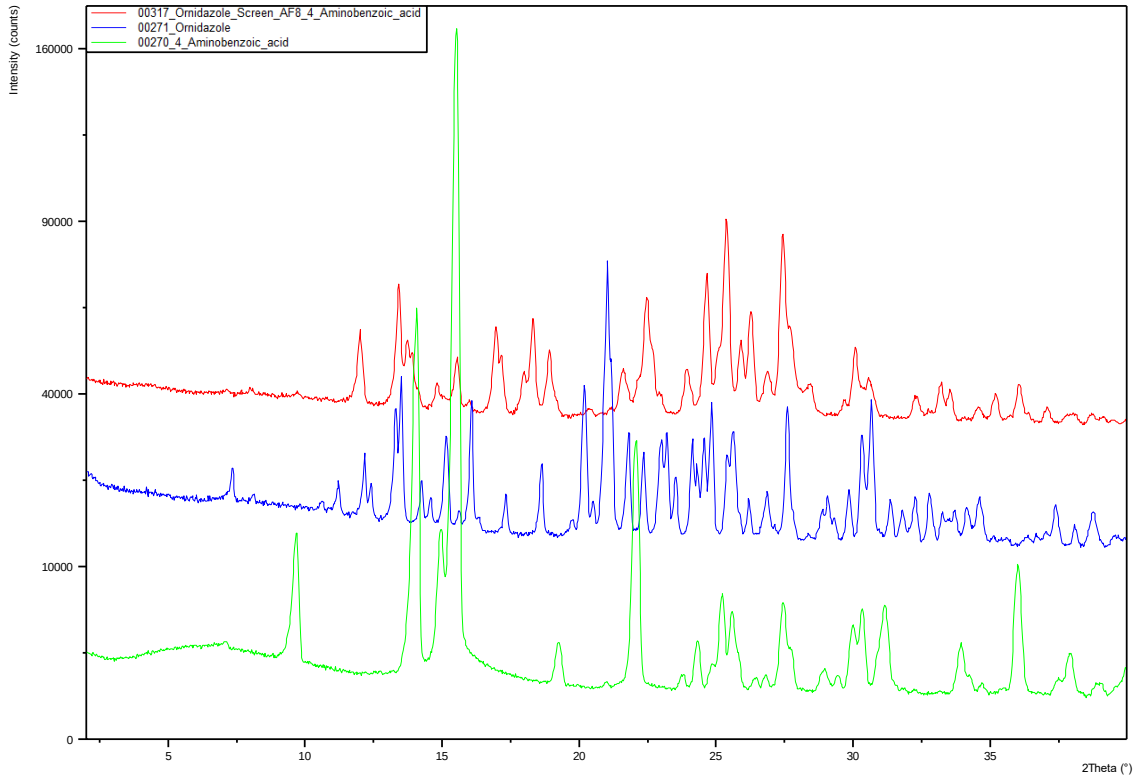


*Figure 48. 4-Aminobenzoic acid.*

## 6.3 DSC and TGA overlay plots from analysis of further investigations into hits

Plots showing an overlay of the DSC and TGA traces for the product of ornidazole and each of the co-formers from the co-crystal screen which resulted in a 'hit' are presented here. Although values for endothermic peaks and mass losses are not displayed, it is still clear to see from the plots whether a single or multiple melting points are present (DSC) and whether desolvation occurs (TGA). Plots are labelled by co-former.

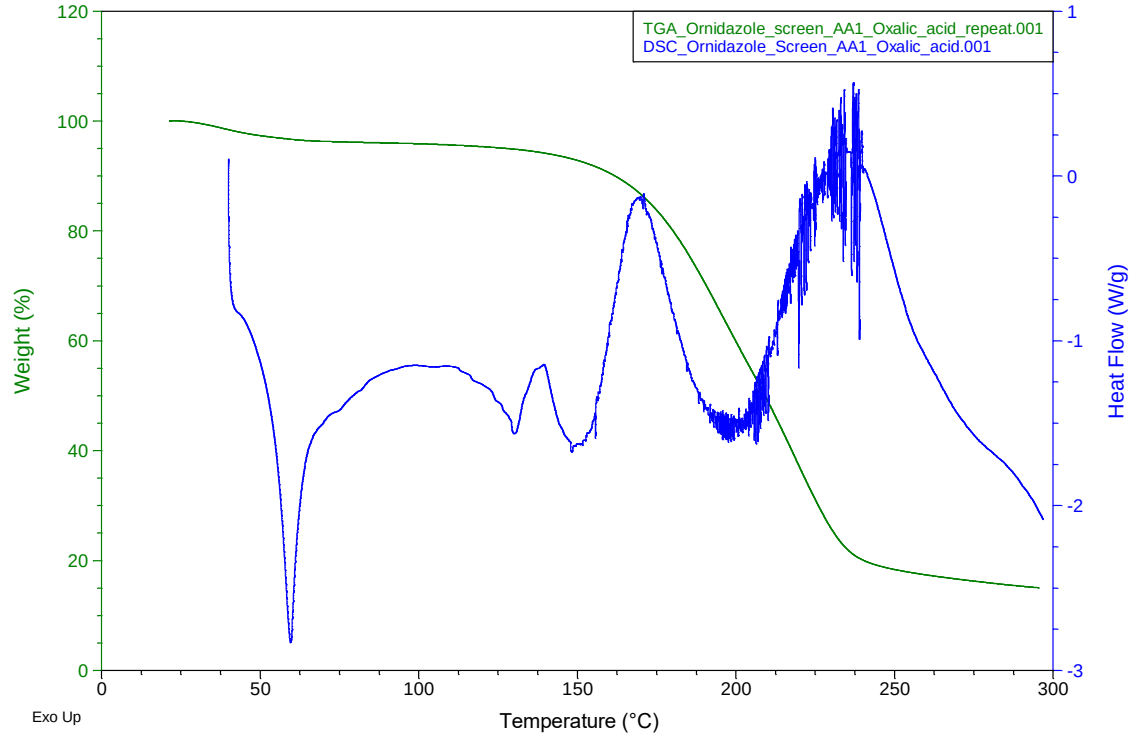


*Figure 49. Oxalic acid.*

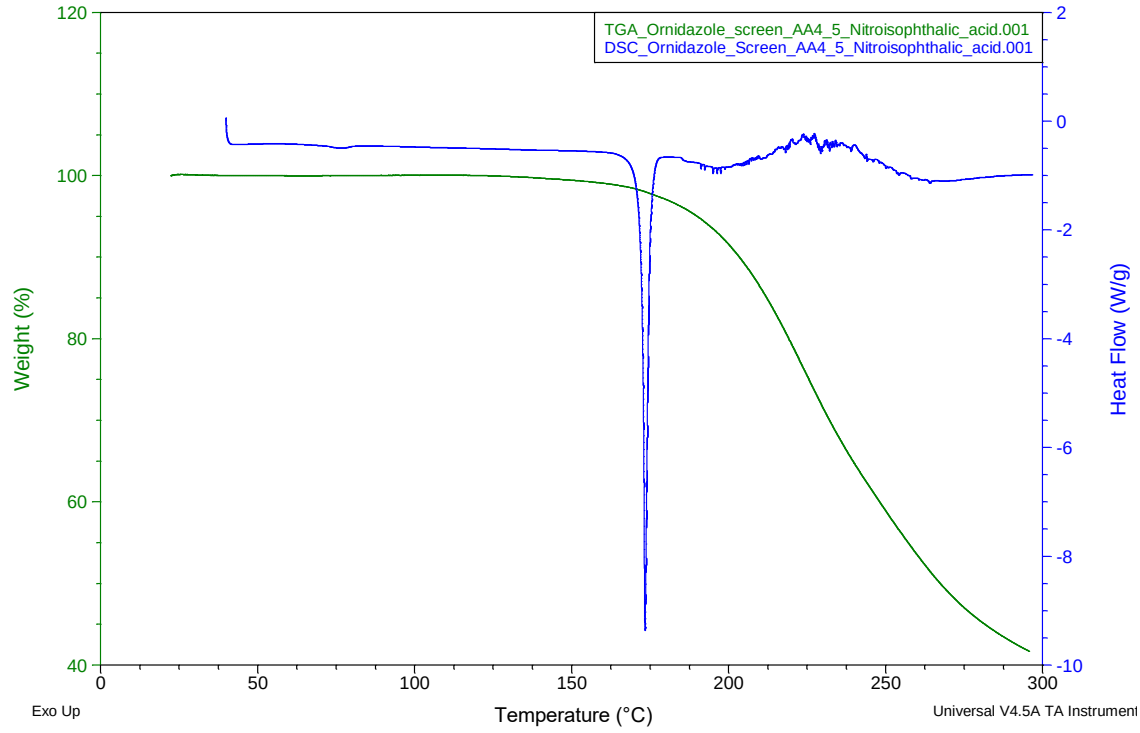


*Figure 50. 5-Nitroisophthalic acid.*

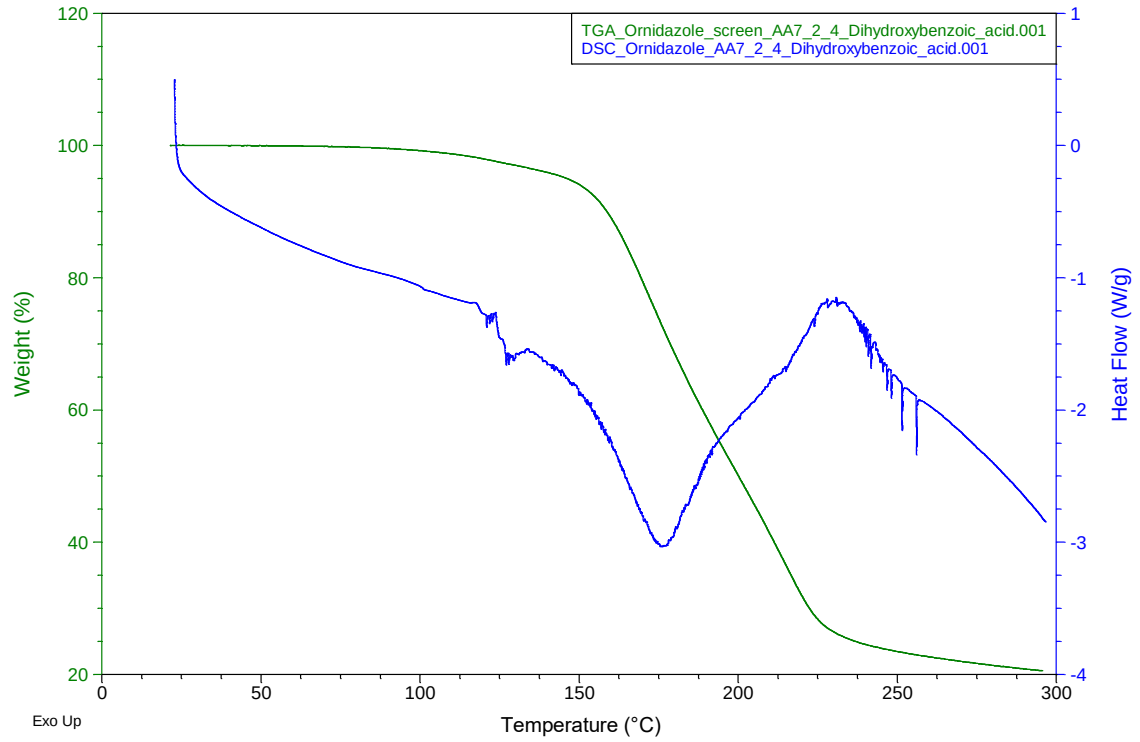


*Figure 51. 2,4-Dihydroxybenzoic acid.*

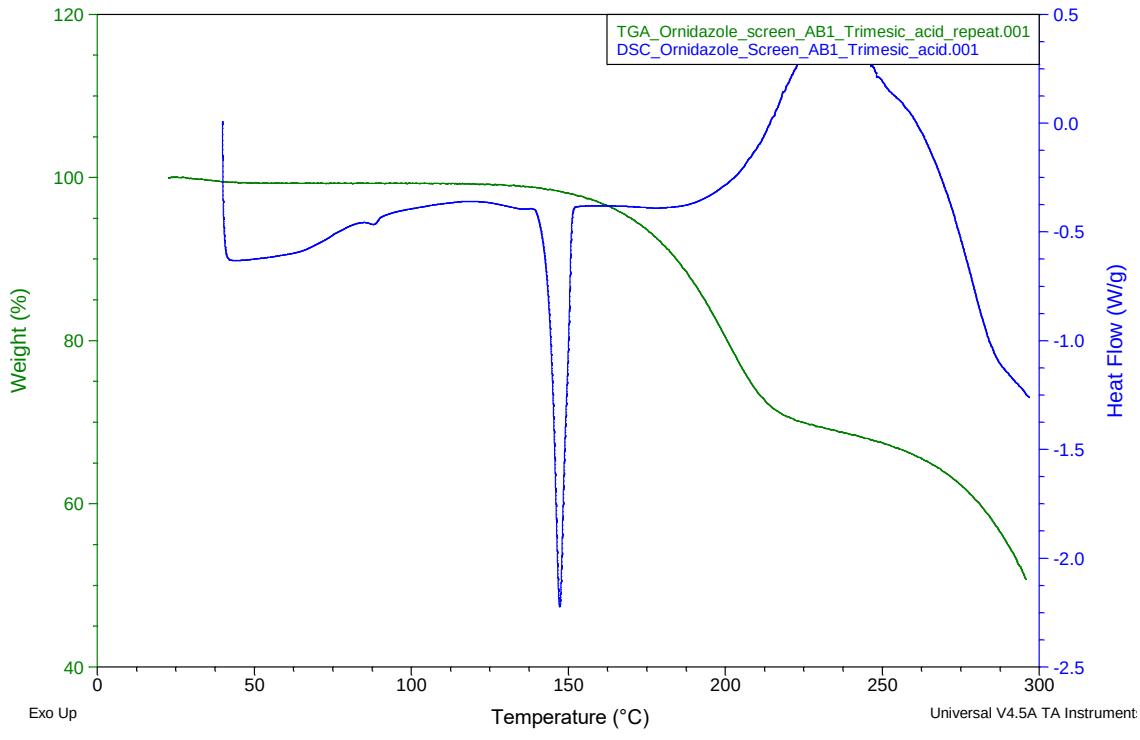


*Figure 52. Trimesic acid.*

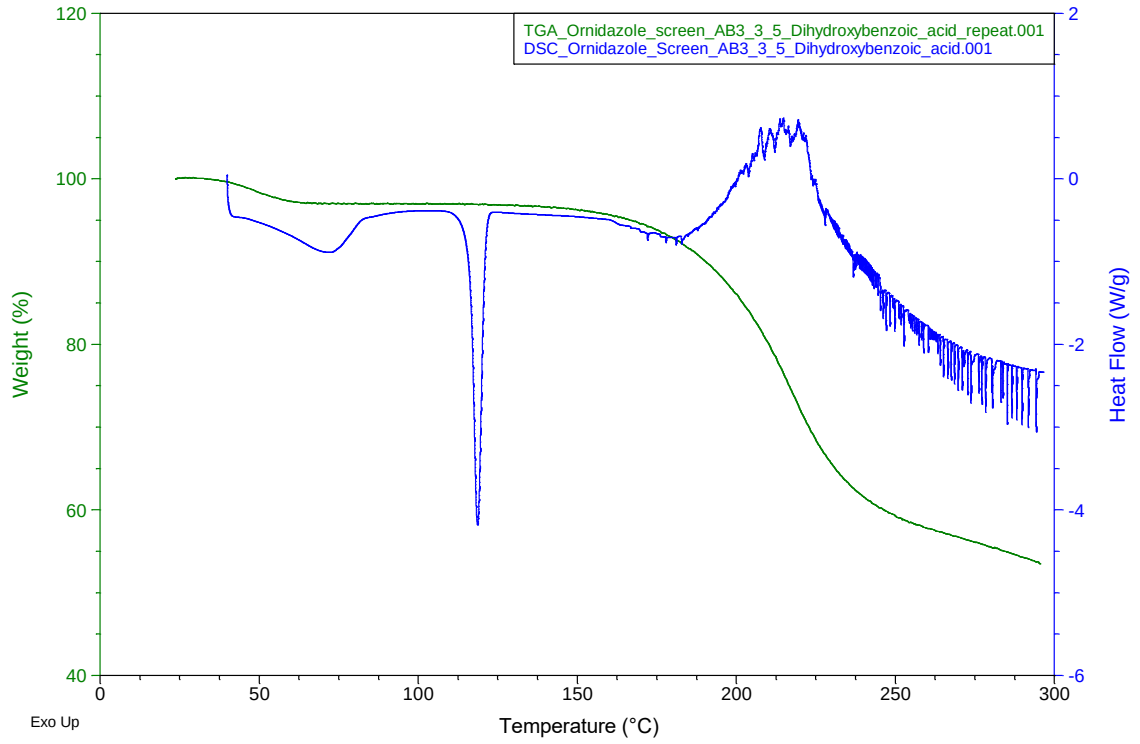


*Figure 53. 3,5-Dihydroxybenzoic acid.*

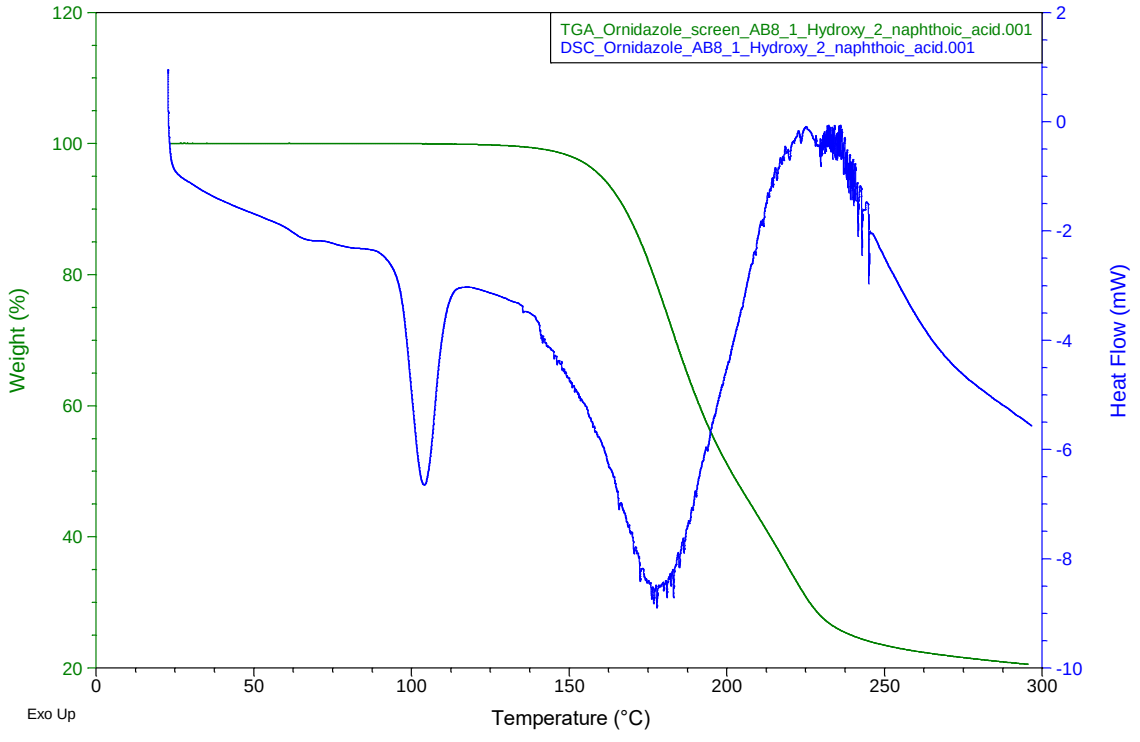


*Figure 54. 1-Hydroxy-2-naphthoic acid.*

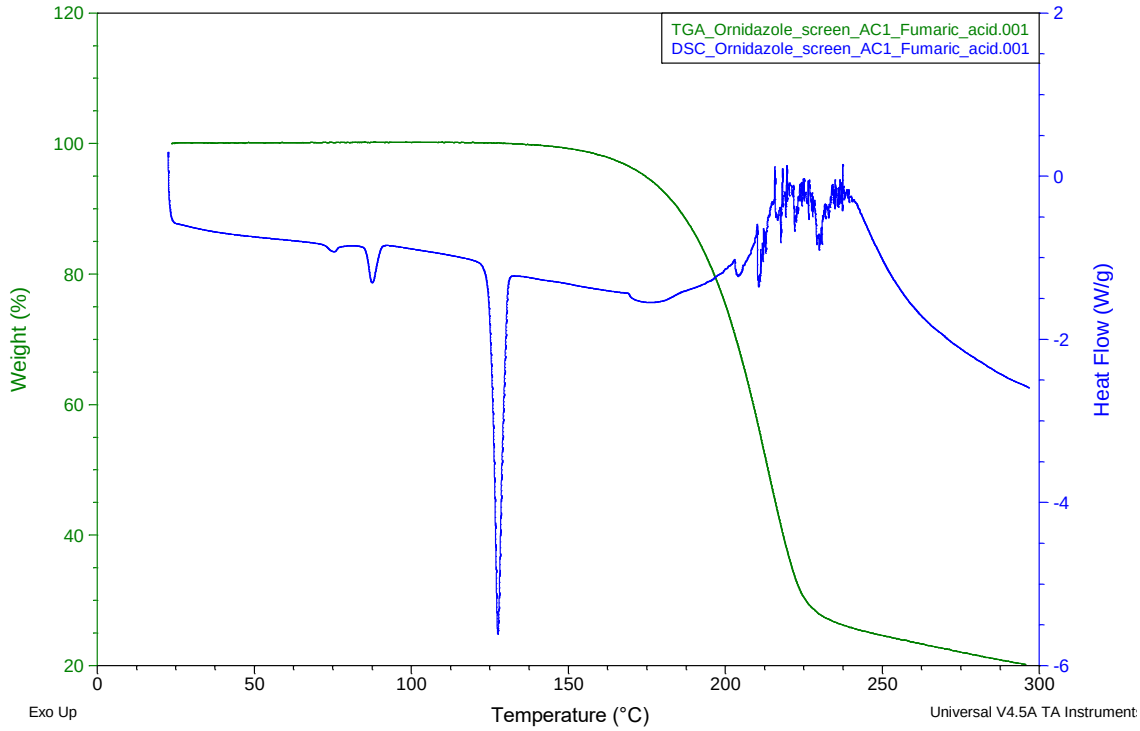


*Figure 55. Fumaric acid.*

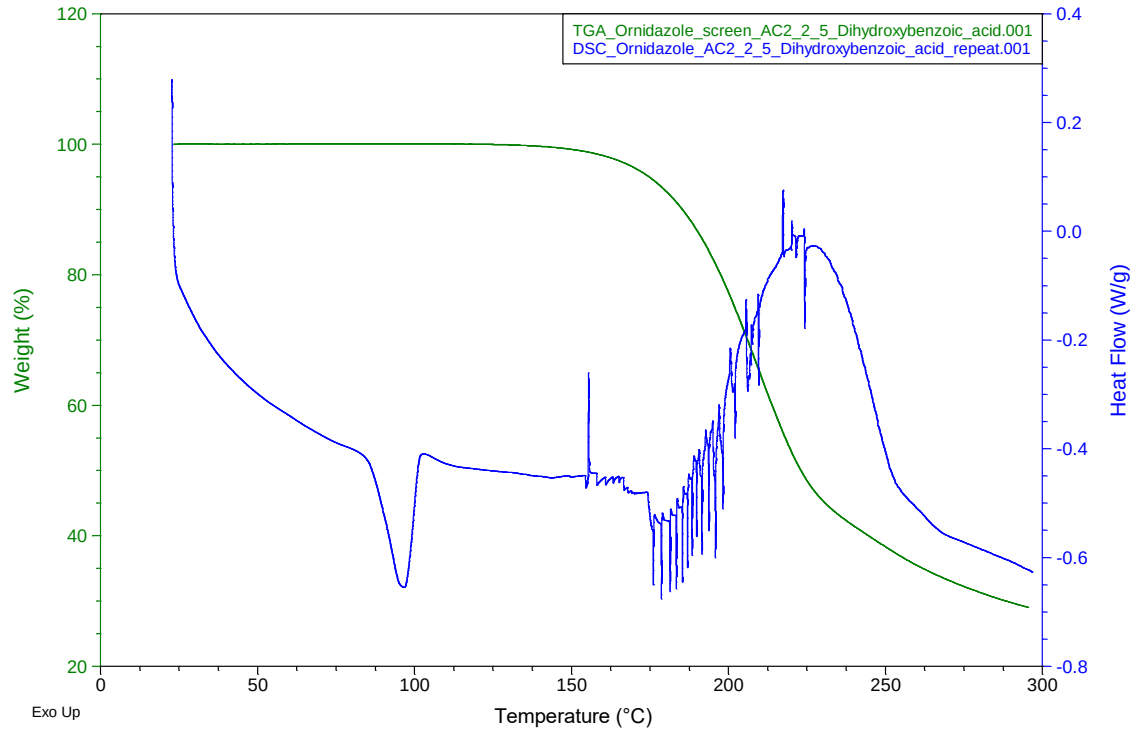


*Figure 56. 2,5-Dihydroxybenzoic acid.*

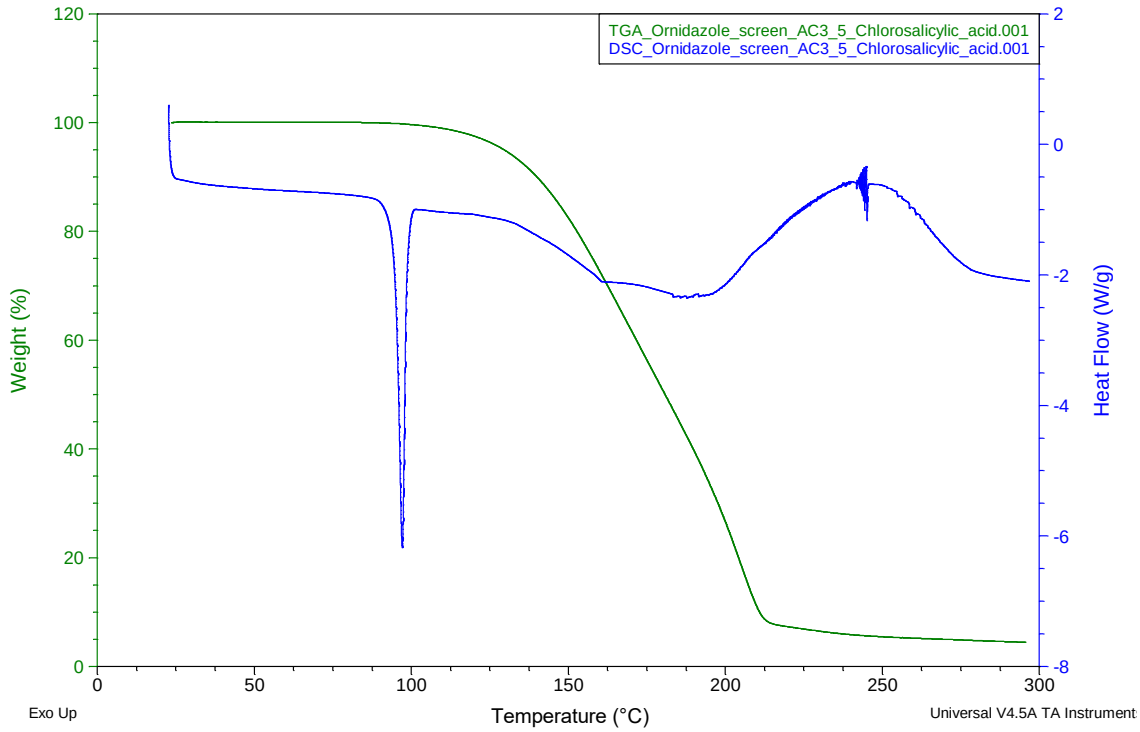


*Figure 57. 5-Chlorosalicylic acid.*

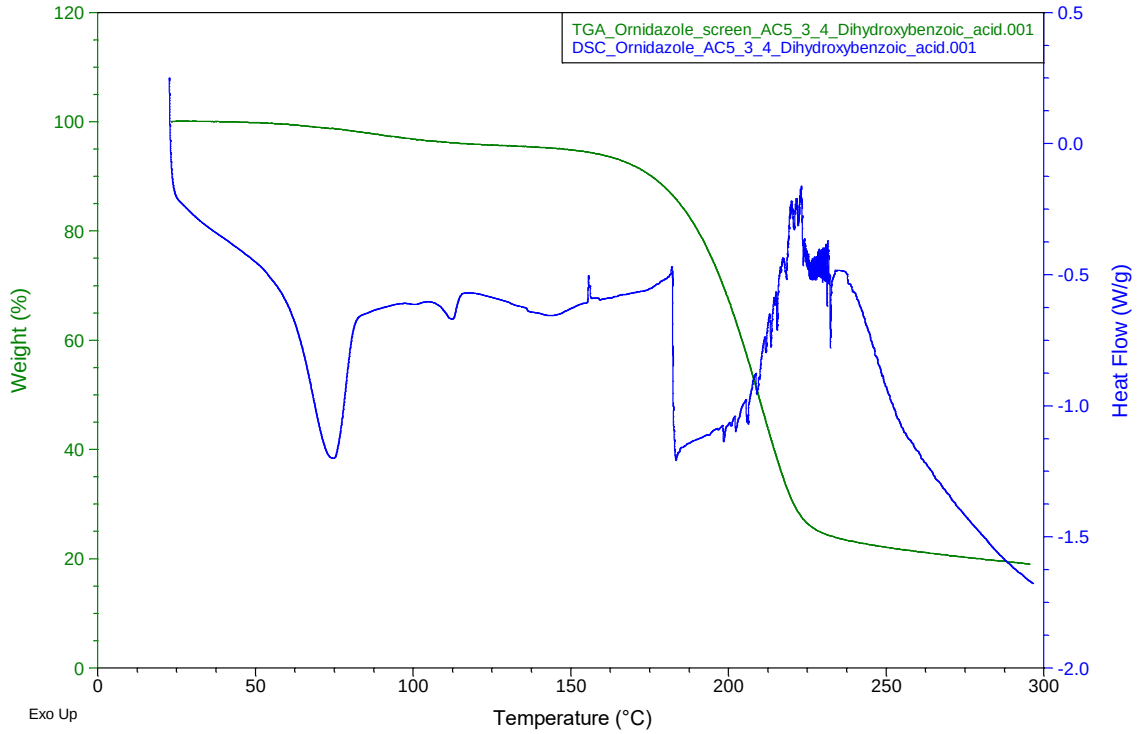


*Figure 58. 3,4-Dihydroxybenzoic acid.*

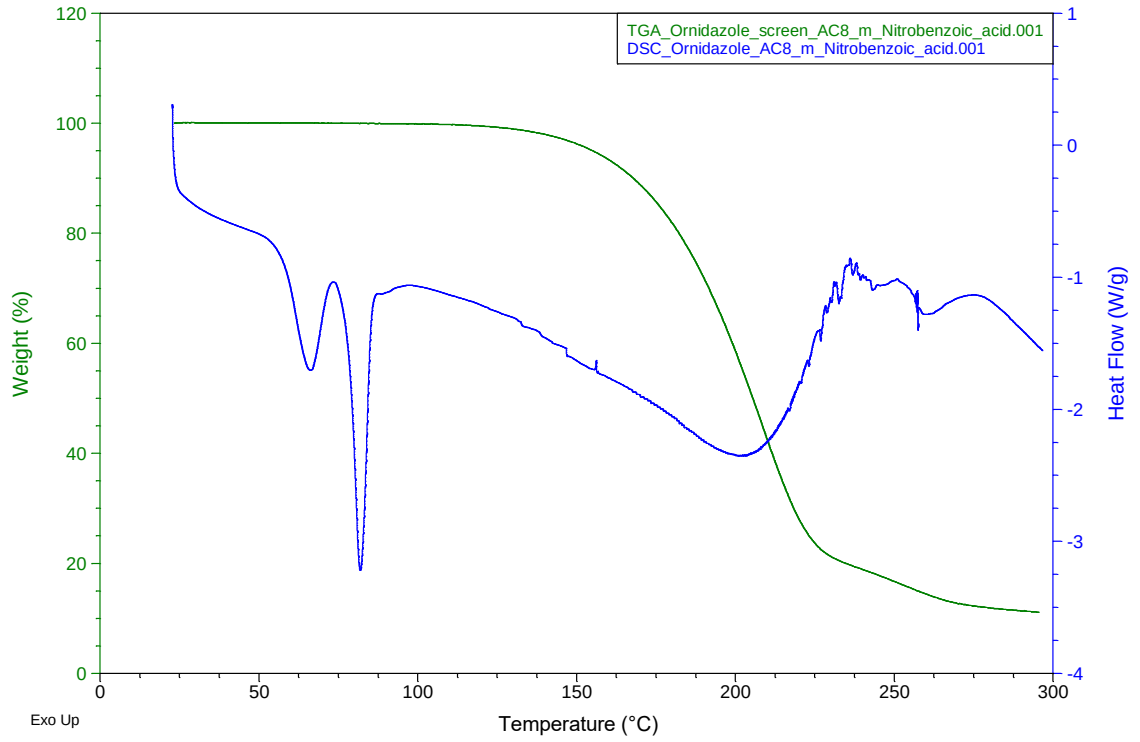


*Figure 59. m-Nitrobenzoic acid.*

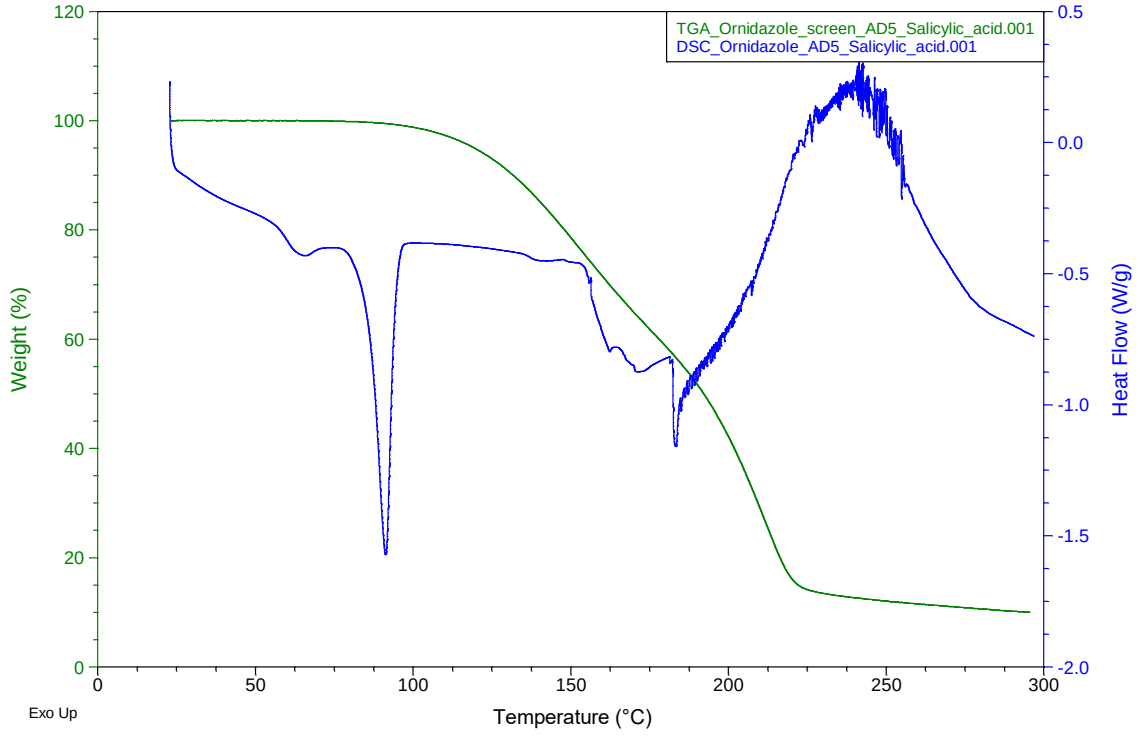


*Figure 60. Salicylic acid.*

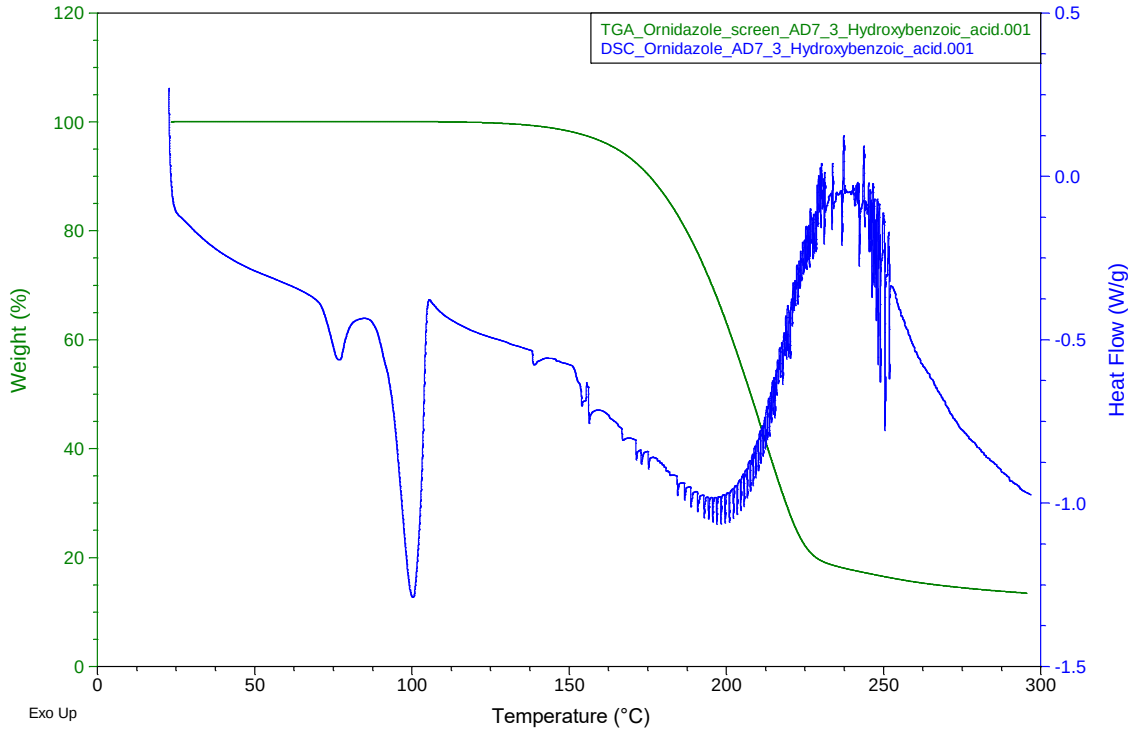


*Figure 61. 3-Hydroxybenzoic acid.*

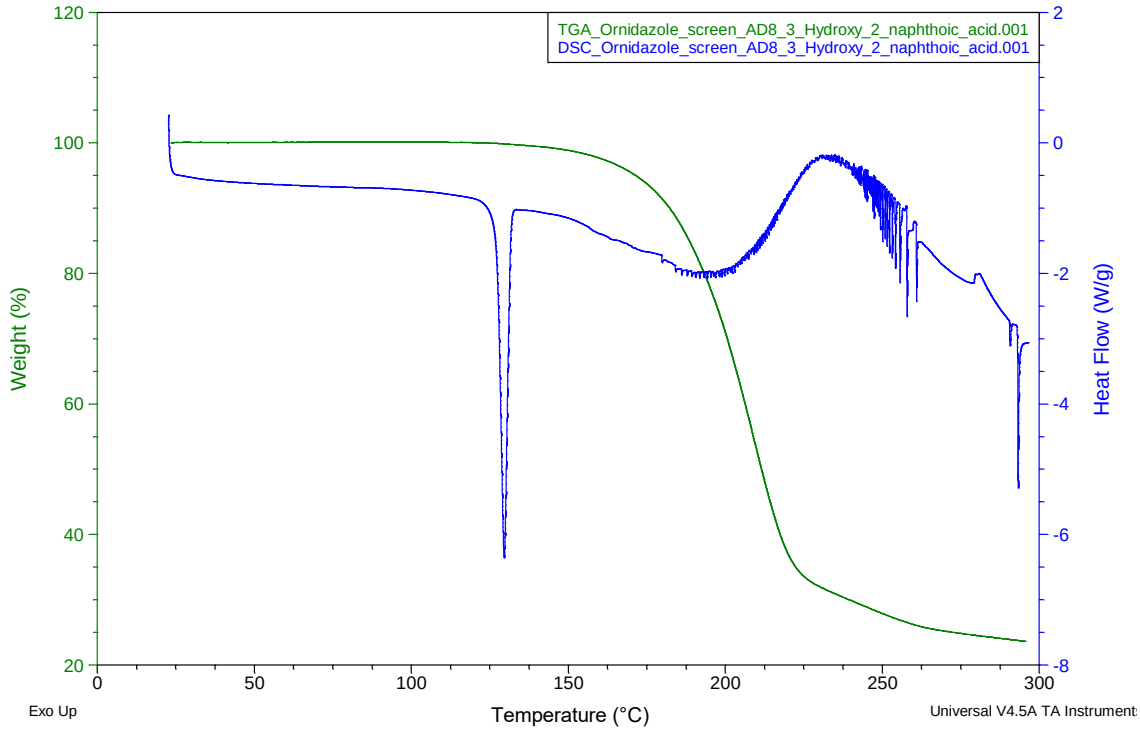


*Figure 62. 3-Hydroxy-2-naphthoic acid.*

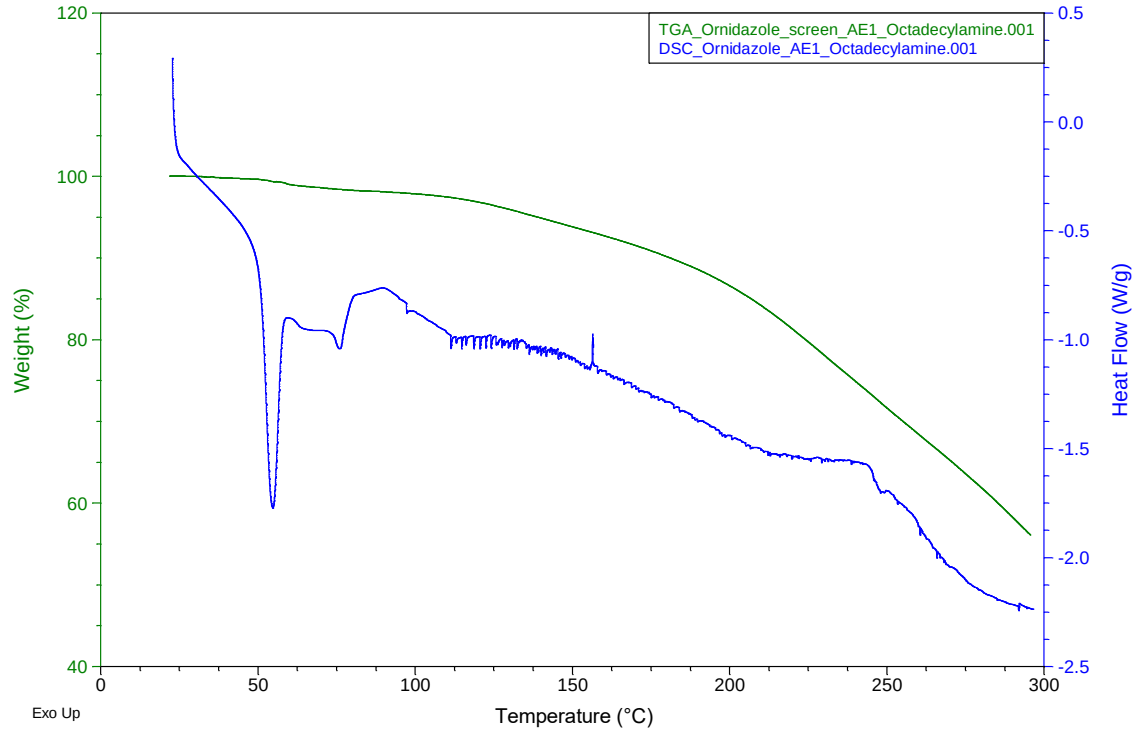


*Figure 63. Octadecylamine.*

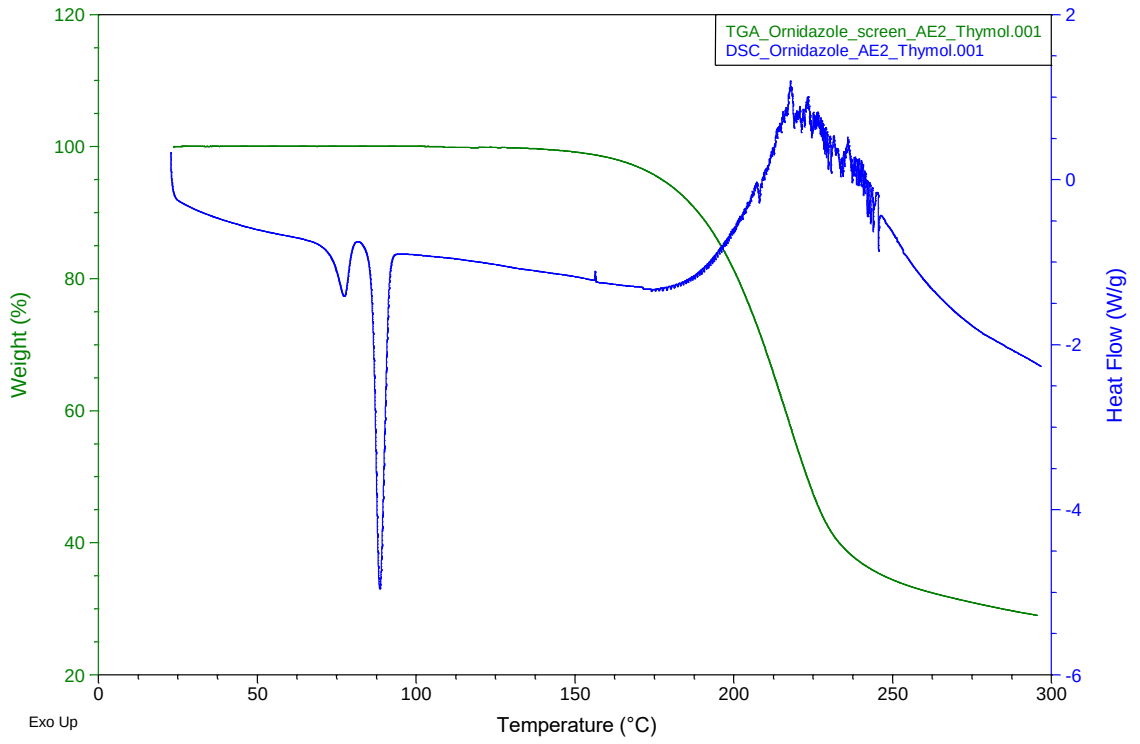


*Figure 64. Thymol.*

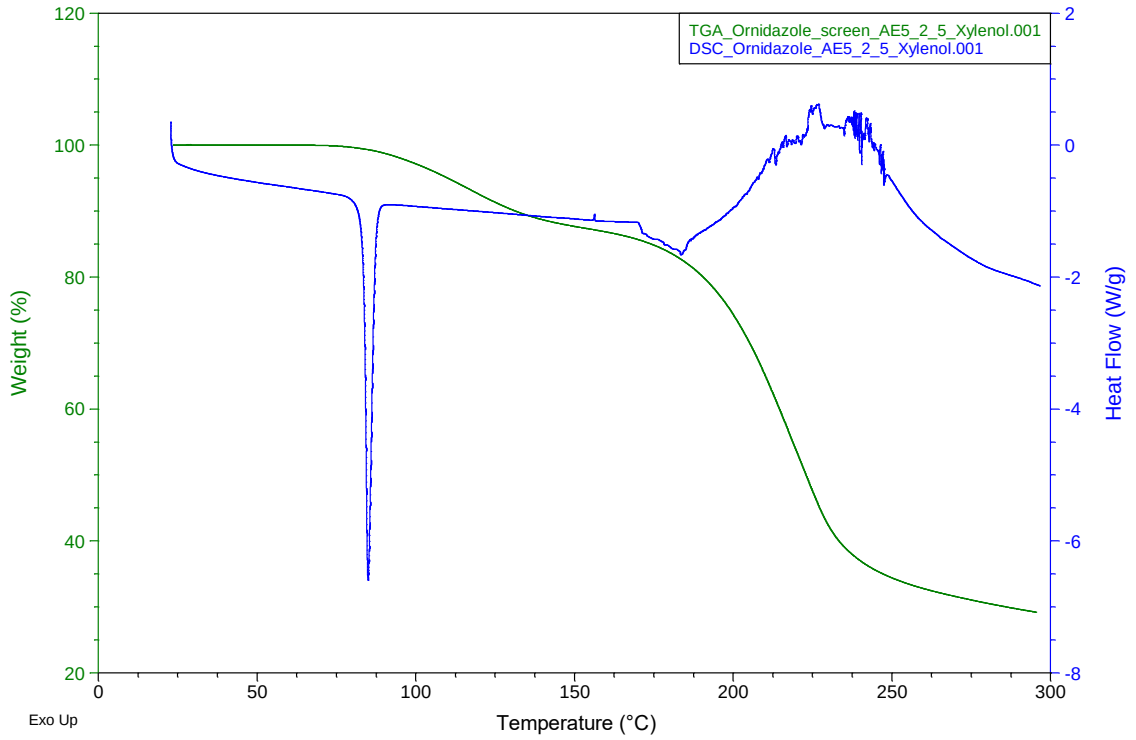


*Figure 65. 2,5-Xylenol.*

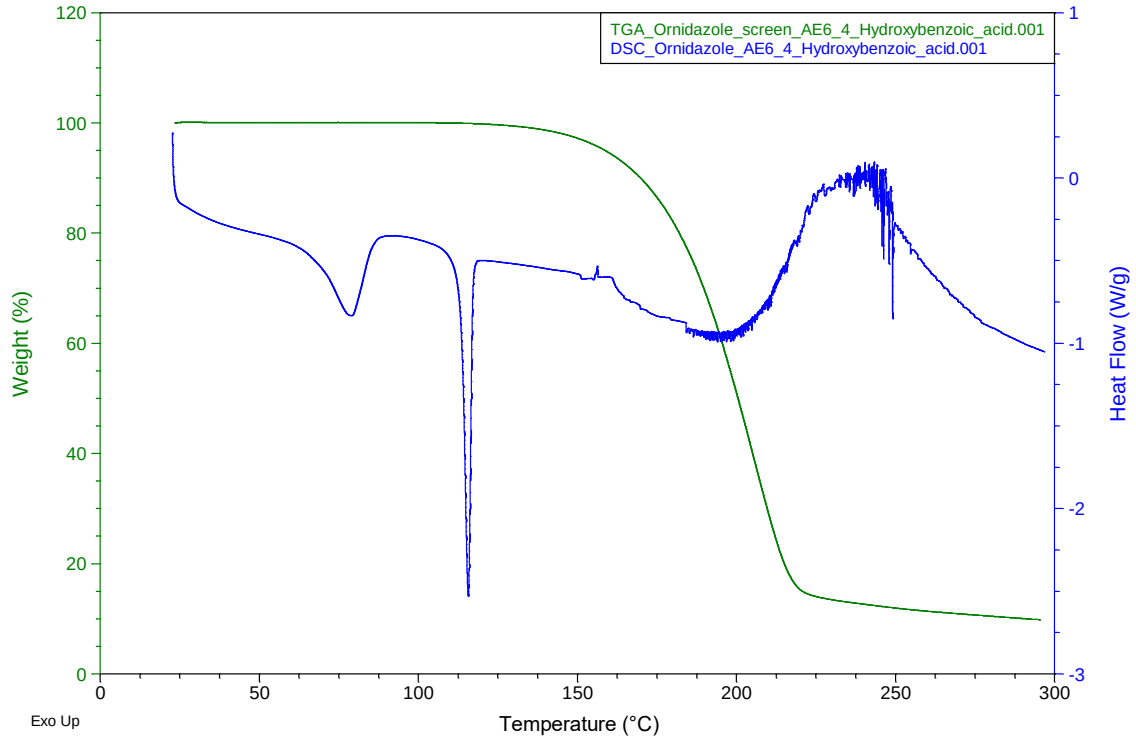


*Figure 66. 4-Hydroxybenzoic acid.*

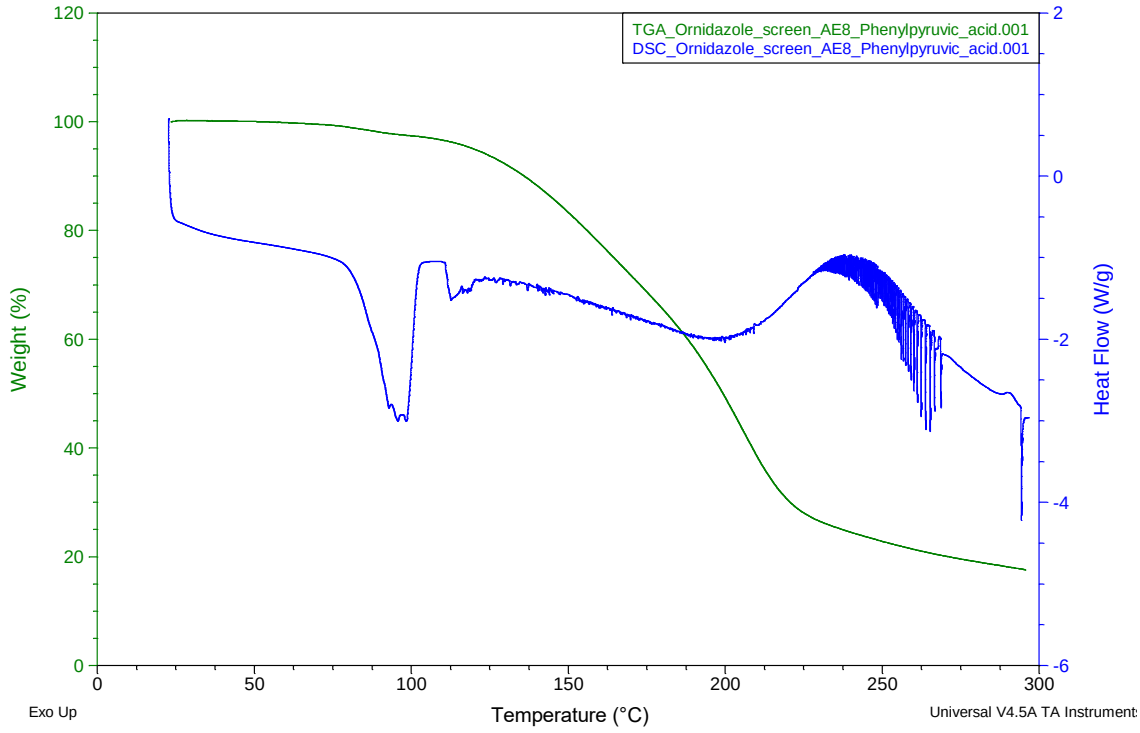


*Figure 67. Phenylpyruvic acid.*

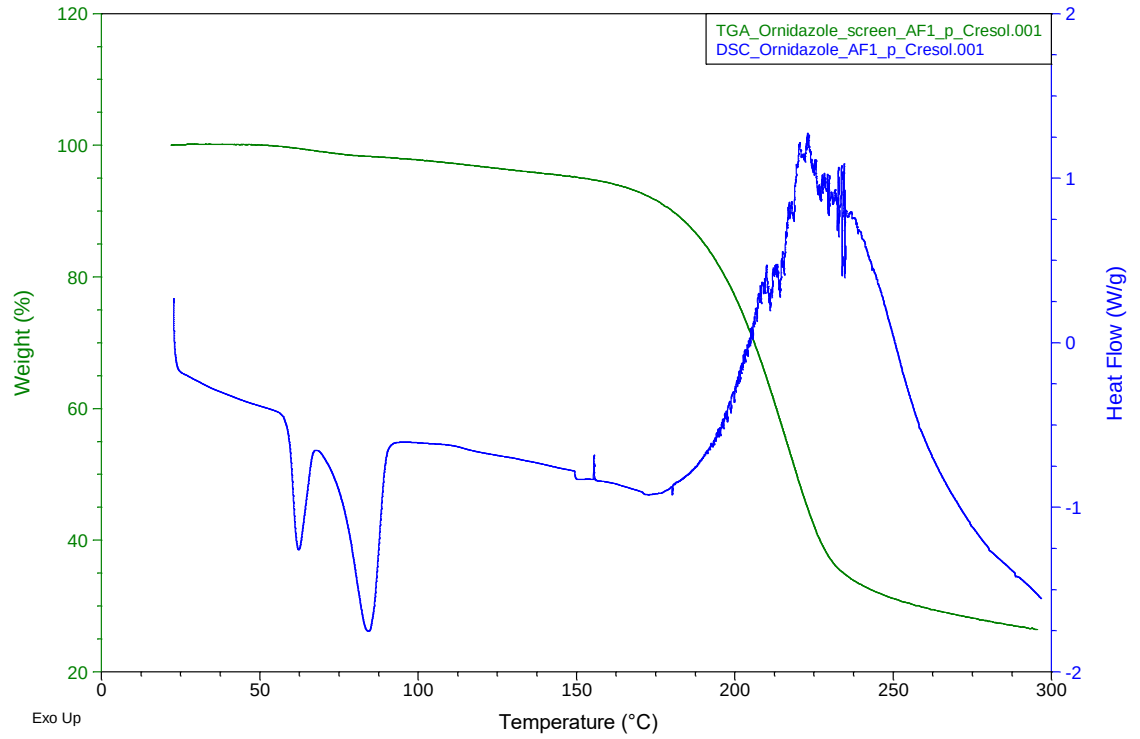


*Figure 68. p-Cresol.*

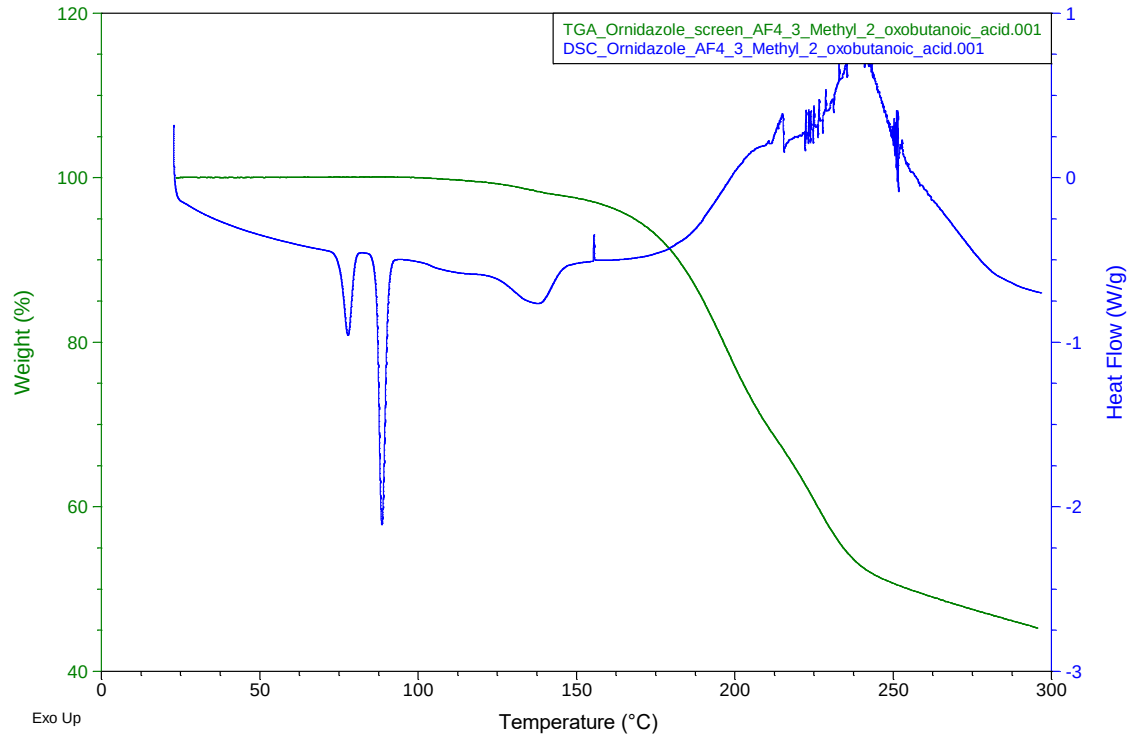


*Figure 69. 3-Methyl-2-oxobutanoic acid.*

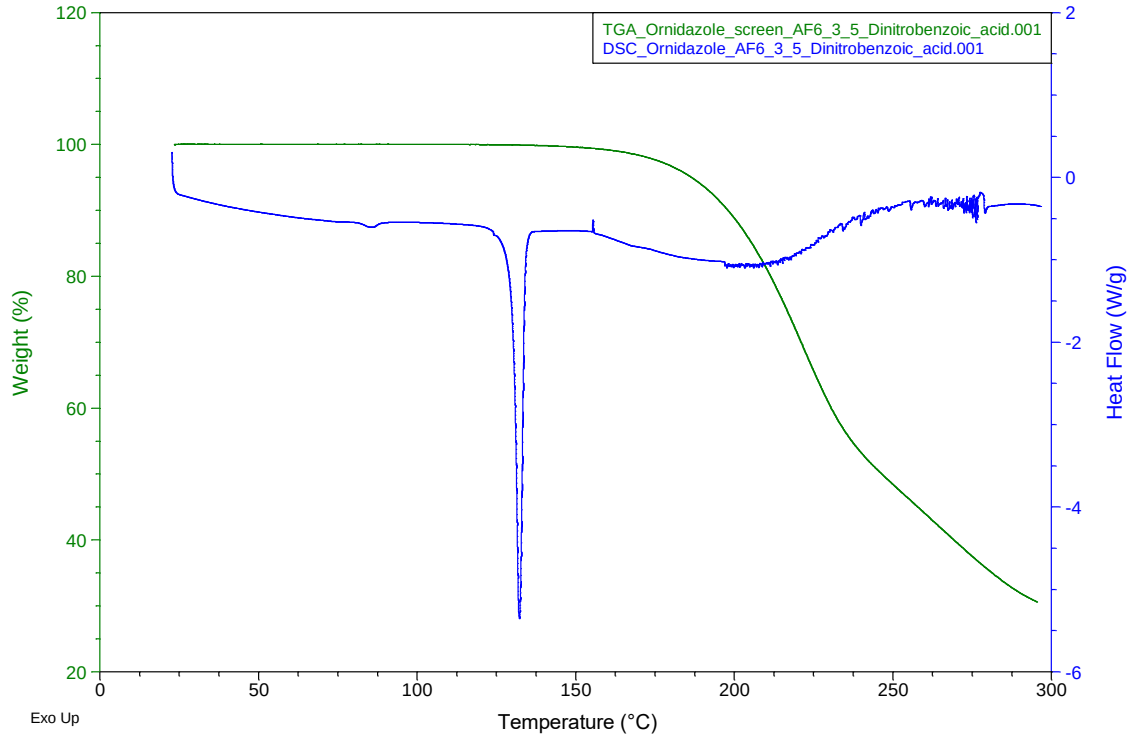


*Figure 70. 3,5-Dinitrobenzoic acid.*

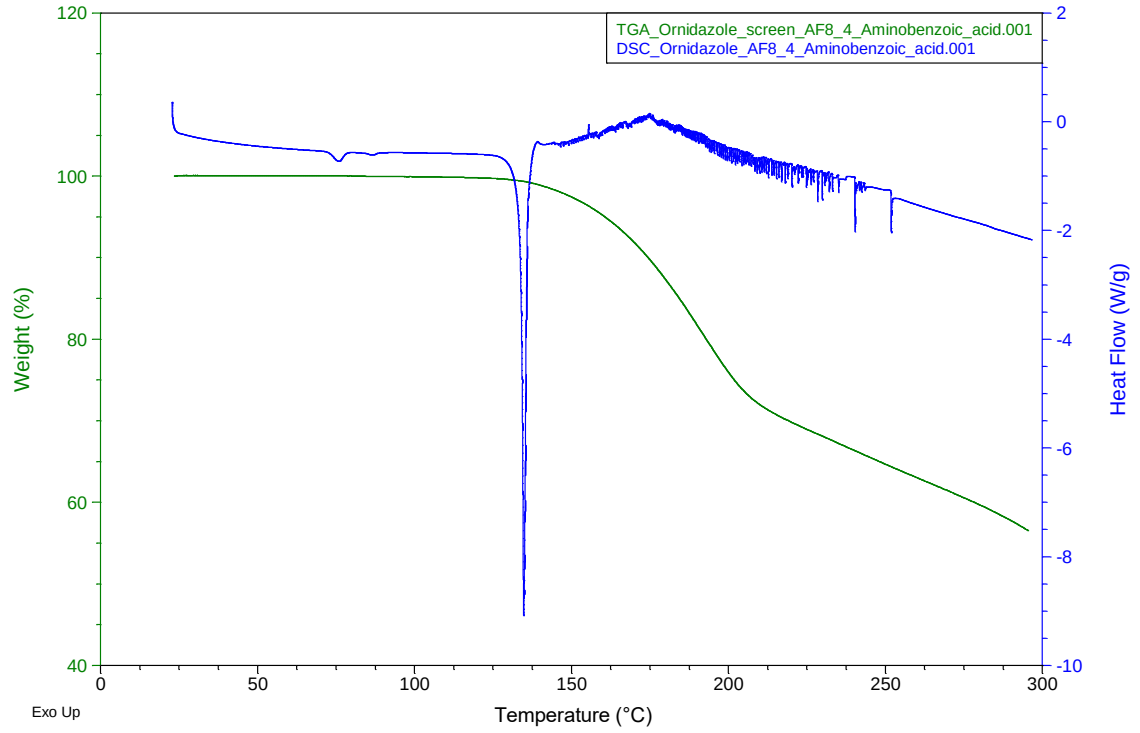


*Figure 71. 4-Aminobenzoic acid.*

## 6.4 PXRD plots from analysis of evaporative crystallisation from DCM solution

PXRD patterns comparing the pure parent components: ornidazole (blue patterns) and co-formers (green patterns), with the product of evaporation of a 1:1 molar solution of the two compounds from DCM (pink patterns) and the product of the co-crystal screen for those two components (red patterns). The figures are labelled by co-former.

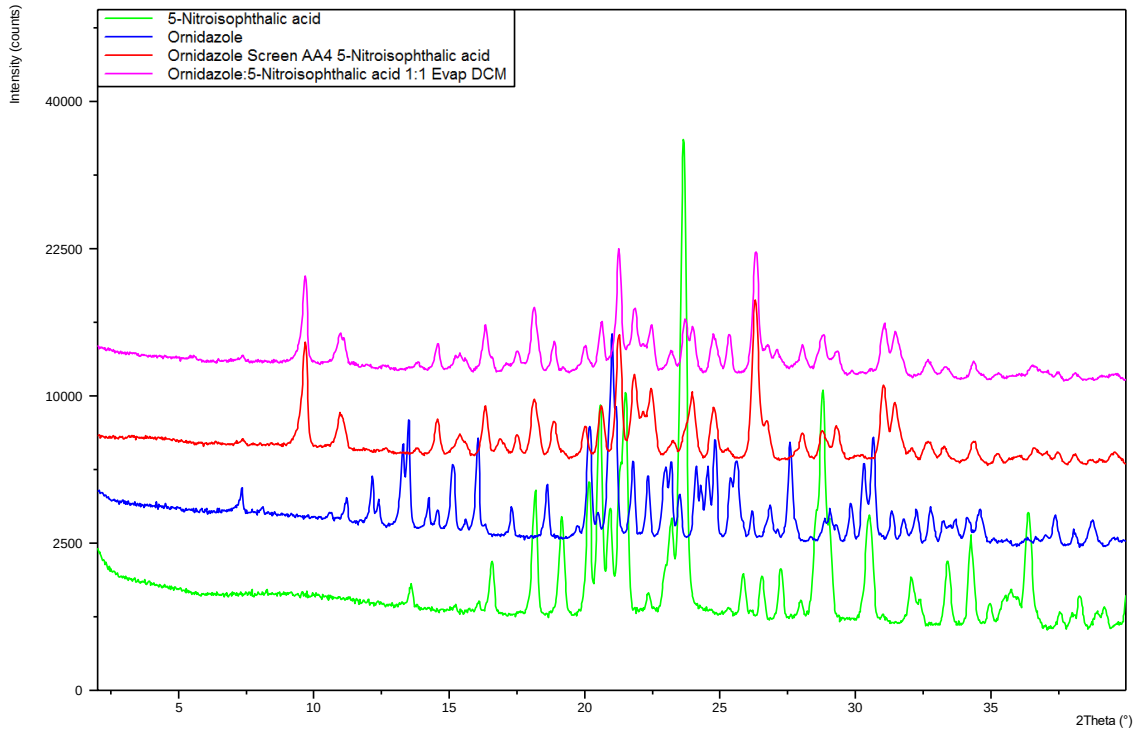


*Figure 72. 5-Nitroisophthalic acid.*

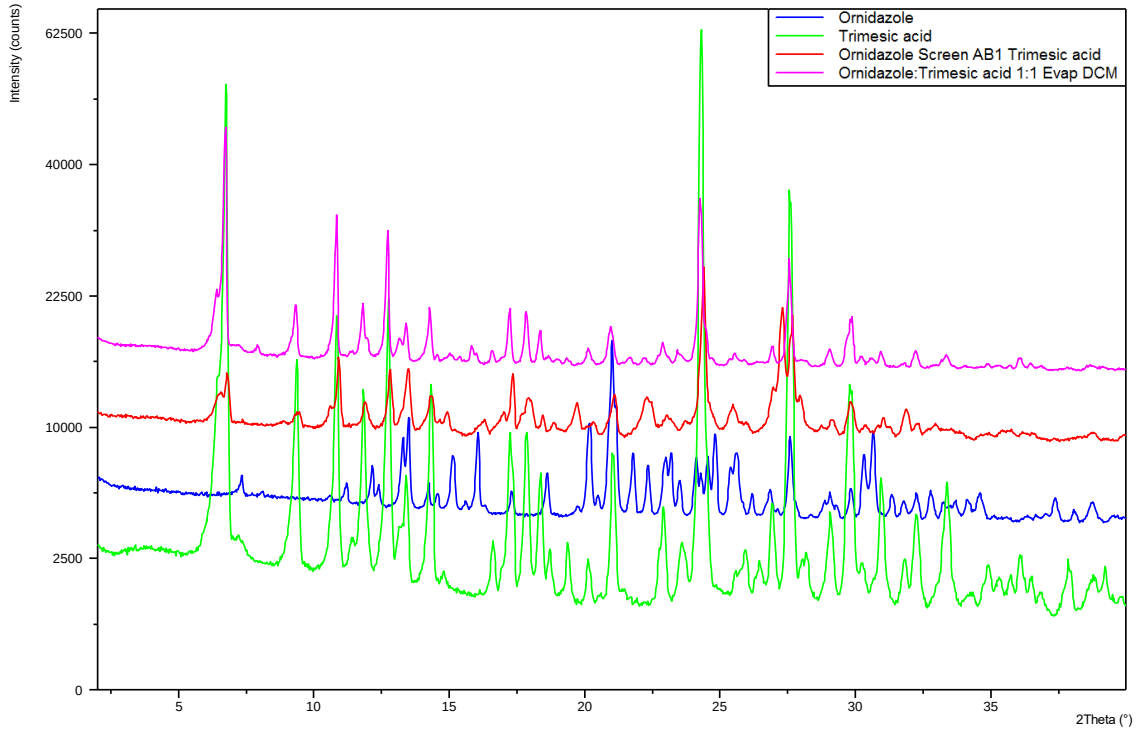


*Figure 73. Trimesic acid.*

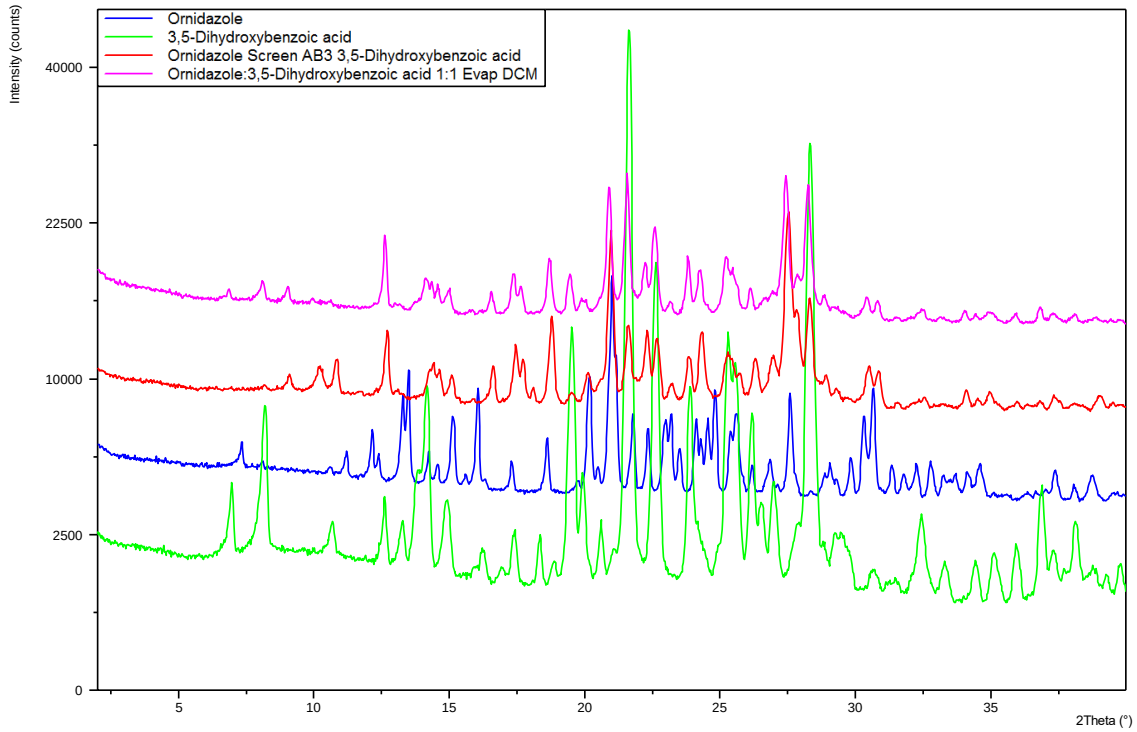


*Figure 74. 3,5-Dihydroxybenzoic acid.*

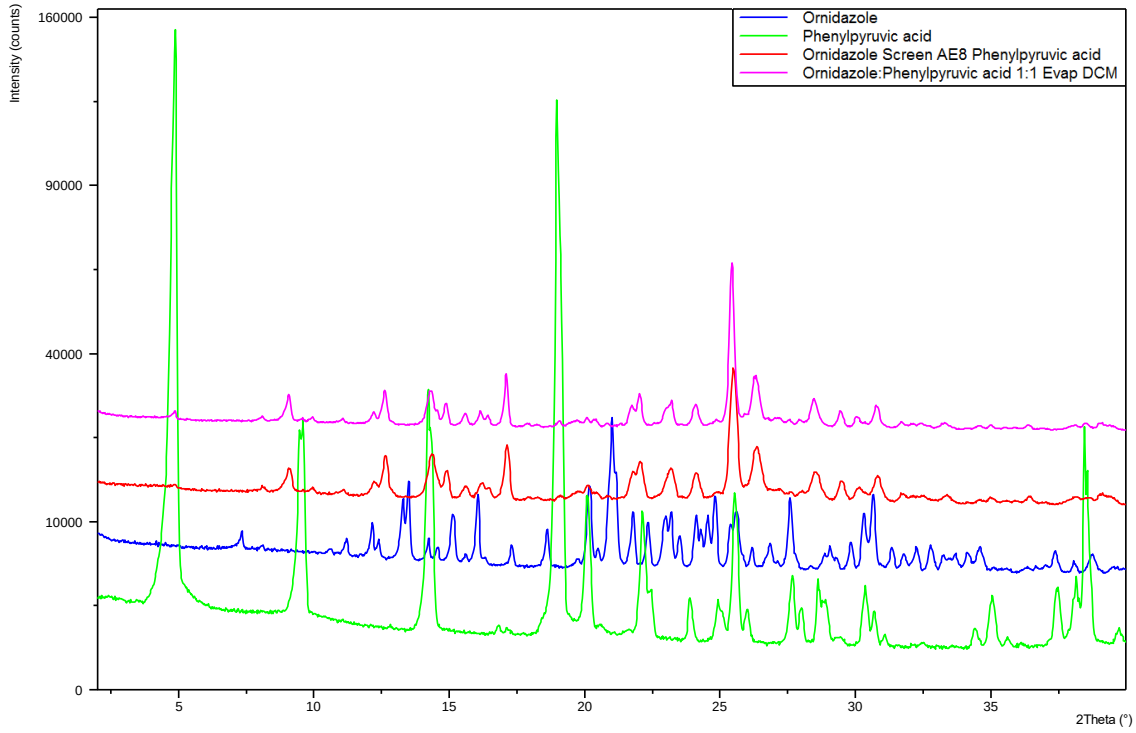


*Figure 75. Phenylpyruvic acid.*

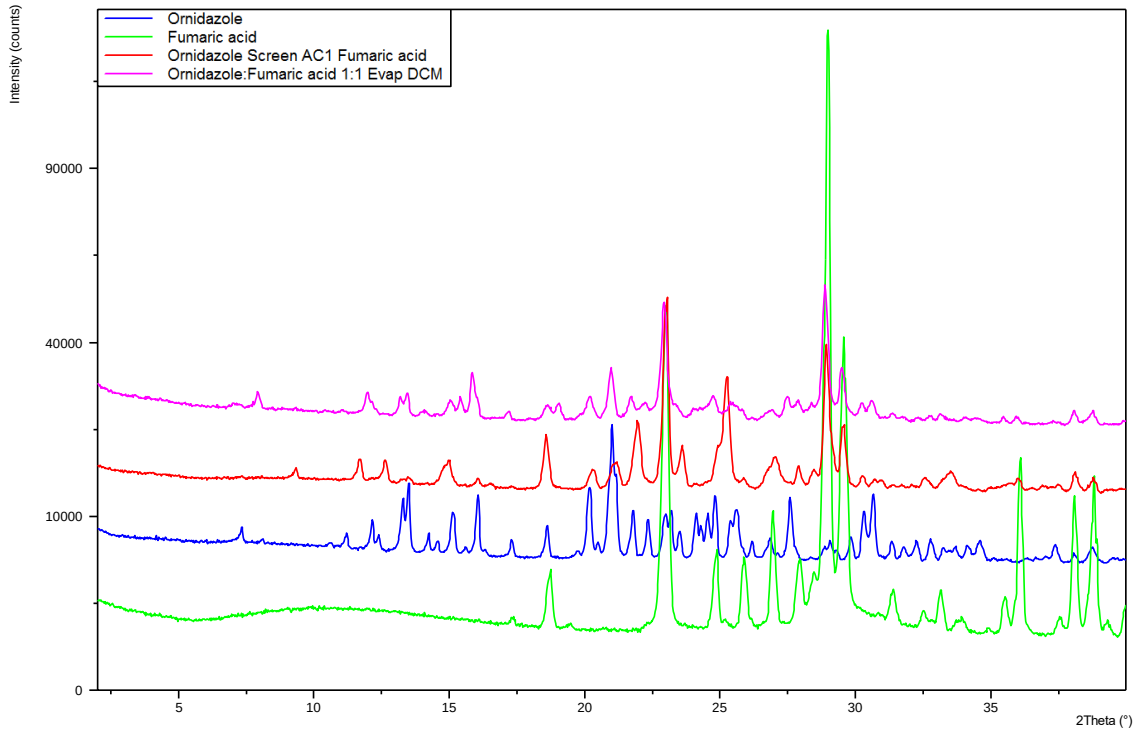


*Figure 76. Fumaric acid.*

## 6.5 Full Intrinsic Dissolution Test Results

*Table 2. Full IDT results for ornidazole.*

| Segment Index | End Time (seconds) | Flow Rate (mL/min) | Surface Conc. (mg/mL) | Intrinsic Dissolution Rate (µg/min/cm²) | Standard Deviation | Sample Mass Released (mg) | Sample Mass % of 7.40mg |
|---|---|---|---|---|---|---|---|
| 1 | 60 | 0.2 | 225.5786 | 125.2183 | 42.9135 | 0.0039 | 0.05 |
| 2 | 120 | 0.2 | 225.4976 | 191.4404 | 5.2656 | 0.0099 | 0.13 |
| 3 | 180 | 0.2 | 224.5979 | 199.6776 | 3.1584 | 0.0162 | 0.22 |
| 4 | 240 | 0.2 | 222.0206 | 191.2116 | 1.7229 | 0.0222 | 0.3 |
| 5 | 300 | 0.2 | 220.9665 | 189.9449 | 2.9125 | 0.0282 | 0.38 |
| 6 | 360 | 0.2 | 222.6274 | 190.1822 | 4.8005 | 0.0342 | 0.46 |
| 7 | 420 | 0.2 | 222.1879 | 189.6431 | 2.0433 | 0.0401 | 0.54 |
| 8 | 480 | 0.2 | 233.7058 | 205.0606 | 5.2824 | 0.0466 | 0.63 |
| 9 | 540 | 0.2 | 231.004 | 206.1359 | 5.916 | 0.053 | 0.72 |
| 10 | 600 | 0.2 | 234.0041 | 209.7367 | 1.8926 | 0.0596 | 0.81 |
| 11 | 660 | 0.8 | 186.0086 | 478.3918 | 155.6717 | 0.0747 | 1.01 |
| 12 | 720 | 0.8 | 172.0074 | 285.3286 | 10.6294 | 0.0836 | 1.13 |
| 13 | 780 | 0.8 | 170.4847 | 279.4885 | 4.5671 | 0.0924 | 1.25 |
| 14 | 840 | 0.8 | 165.3619 | 274.5224 | 3.6465 | 0.101 | 1.37 |
| 15 | 900 | 0.8 | 162.9261 | 274.0695 | 4.8602 | 0.1096 | 1.48 |
| 16 | 960 | 0.8 | 162.1826 | 275.4703 | 8.1595 | 0.1183 | 1.6 |
| 17 | 1020 | 0.8 | 163.5007 | 274.9784 | 4.103 | 0.1269 | 1.72 |
| 18 | 1080 | 0.8 | 162.0631 | 268.2534 | 8.0213 | 0.1354 | 1.83 |
| 19 | 1140 | 0.8 | 163.1435 | 264.9276 | 7.5862 | 0.1437 | 1.94 |
| 20 | 1200 | 0.8 | 167.8849 | 276.6576 | 5.5243 | 0.1524 | 2.06 |

*Table 3. Full IDT results for 5-nitroisophthalic acid.*

| Segment Index | End Time (seconds) | Flow Rate (mL/min) | Surface Conc. (mg/mL) | Intrinsic Dissolution Rate (µg/min/cm²) | Standard Deviation | Sample Mass Released (mg) | Sample Mass % of 7.68mg |
|---|---|---|---|---|---|---|---|
| 1 | 60 | 0.2 | 190.9367 | 85.6288 | 38.6518 | 0.0027 | 0.04 |
| 2 | 120 | 0.2 | 218.214 | 169.2779 | 16.8344 | 0.008 | 0.1 |
| 3 | 180 | 0.2 | 215.666 | 213.7102 | 8.6692 | 0.0147 | 0.19 |
| 4 | 240 | 0.2 | 205.0801 | 241.4155 | 8.9947 | 0.0223 | 0.29 |
| 5 | 300 | 0.2 | 197.543 | 274.3597 | 10.6067 | 0.0309 | 0.4 |
| 6 | 360 | 0.2 | 195.2916 | 322.3068 | 17.372 | 0.0411 | 0.53 |
| 7 | 420 | 0.2 | 193.8619 | 333.2427 | 15.0946 | 0.0515 | 0.67 |
| 8 | 480 | 0.2 | 192.5753 | 263.8173 | 22.9992 | 0.0598 | 0.78 |
| 9 | 540 | 0.2 | 192.0376 | 206.0547 | 9.6573 | 0.0663 | 0.86 |
| 10 | 600 | 0.2 | 192.1486 | 178.4634 | 8.5123 | 0.0719 | 0.94 |
| 11 | 660 | 0.8 | 180.899 | 417.638 | 94.1552 | 0.085 | 1.11 |
| 12 | 720 | 0.8 | 179.244 | 308.8658 | 6.655 | 0.0947 | 1.23 |
| 13 | 780 | 0.8 | 163.1604 | 309.3789 | 27.9119 | 0.1044 | 1.36 |
| 14 | 840 | 0.8 | 161.1805 | 273.2671 | 3.9043 | 0.113 | 1.47 |
| 15 | 900 | 0.8 | 161.2518 | 266.1076 | 3.2178 | 0.1214 | 1.58 |
| 16 | 960 | 0.8 | 161.5072 | 269.4507 | 3.6373 | 0.1298 | 1.69 |
| 17 | 1020 | 0.8 | 161.5256 | 269.8275 | 3.0725 | 0.1383 | 1.8 |
| 18 | 1080 | 0.8 | 162.4197 | 269.0384 | 2.3373 | 0.1468 | 1.91 |
| 19 | 1140 | 0.8 | 162.6555 | 266.7259 | 2.5925 | 0.1551 | 2.02 |
| 20 | 1200 | 0.8 | 162.6295 | 262.7568 | 2.933 | 0.1634 | 2.13 |

*Table 4. Full IDT results for ornidazole:5-nitroisophthalic acid.*

| Segment Index | End Time (seconds) | Flow Rate (mL/min) | Surface Conc. (mg/mL) | Intrinsic Dissolution Rate (μg/min/cm²) | Standard Deviation | Sample Mass Released (mg) | Sample Mass % of 5.58mg |
|---|---|---|---|---|---|---|---|
| 1 | 60 | 0.2 | 93.3978 | 28.4115 | 14.9526 | 0.0009 | 0.02 |
| 2 | 120 | 0.2 | 101.0084 | 73.6409 | 9.4622 | 0.0032 | 0.06 |
| 3 | 180 | 0.2 | 109.0524 | 65.5784 | 7.6925 | 0.0053 | 0.09 |
| 4 | 240 | 0.2 | 105.4413 | 56.5881 | 0.8129 | 0.007 | 0.13 |
| 5 | 300 | 0.2 | 111.3491 | 59.3317 | 1.5037 | 0.0089 | 0.16 |
| 6 | 360 | 0.2 | 102.0853 | 59.1742 | 1.1266 | 0.0108 | 0.19 |
| 7 | 420 | 0.2 | 108.4724 | 62.0071 | 1.0147 | 0.0127 | 0.23 |
| 8 | 480 | 0.2 | 99.4316 | 60.669 | 0.9159 | 0.0146 | 0.26 |
| 9 | 540 | 0.2 | 103.2655 | 62.0892 | 1.4813 | 0.0166 | 0.3 |
| 10 | 600 | 0.2 | 102.3913 | 59.4011 | 1.0227 | 0.0184 | 0.33 |
| 11 | 660 | 0.8 | 16.4747 | 97.7319 | 59.0962 | 0.0215 | 0.39 |
| 12 | 720 | 0.8 | 4.0097 | 40.898 | 1.263 | 0.0228 | 0.41 |
| 13 | 780 | 0.8 | 3.0513 | 40.9952 | 2.8987 | 0.0241 | 0.43 |
| 14 | 840 | 0.8 | 2.3886 | 40.4625 | 1.5066 | 0.0254 | 0.45 |
| 15 | 900 | 0.8 | 3.7503 | 40.5445 | 1.0618 | 0.0266 | 0.48 |
| 16 | 960 | 0.8 | 6.7978 | 41.4478 | 0.8596 | 0.0279 | 0.5 |
| 17 | 1020 | 0.8 | 10.2023 | 40.5244 | 1.4364 | 0.0292 | 0.52 |
| 18 | 1080 | 0.8 | 11.5785 | 40.6874 | 1.6732 | 0.0305 | 0.55 |
| 19 | 1140 | 0.8 | 16.7941 | 42.1832 | 1.554 | 0.0318 | 0.57 |
| 20 | 1200 | 0.8 | 21.9102 | 42.9036 | 0.7518 | 0.0332 | 0.59 |

# Appendix 7

## 7.1 Original zafirlukast co-crystal production methods

**Piperazine cocrystal (2:1) Form A.** It was obtained by slow crystallization from a solution of zafirlukast:piperazine (1:1) in ethanol. Zafirlukast (20mg) and piperazine (3mg), molar ratio 1:1, were dissolved in ethanol (0.3mL) at 60°C. The solution was cooled down at room temperature in 30 minutes and crystals appeared after 4 days, (m.p. 218°C).

**Piperazine cocrystal (1:1) Form D.** It was obtained by slurry in methanol, IPA, acetonitrile, acetone, methyl isobutyl ketone (MiBK) or ethyl acetate (AcOEt) at room temperature. For instance, zafirlukast (50mg) and piperazine (11mg), molar ratio 1:1.5, were slurred in acetonitrile (preferred solvent) (1.0 mL) at room temperature during 24 hours. The solid was filtered and dried under vacuum 48 hours, (m.p. 181°C).

**Piperazine cocrystal (1:1) toluene solvate Form E.** It was obtained by slurry in toluene at room temperature. Zafirlukast (50mg) and piperazine (11mg), molar ratio 1:1.5, were slurred in toluene (1.0mL) at room temperature during 24 hours. The solid was filtered and dried under vacuum 48 hours, (m.p. 106°C).

## 7.2 DSC and TGA overlay plots from analysis of received and produced co-crystals

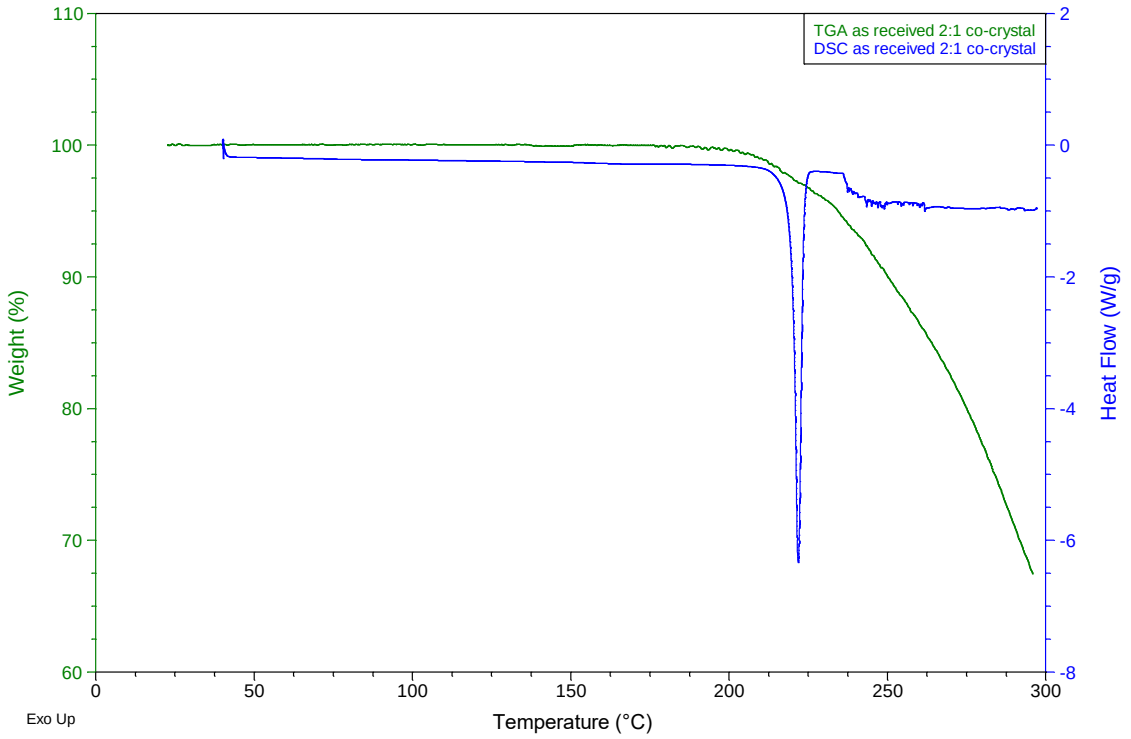


*Figure 1. DSC and TGA overlay plot for the received zafirlukast:piperazine 2:1 co-crystal.*

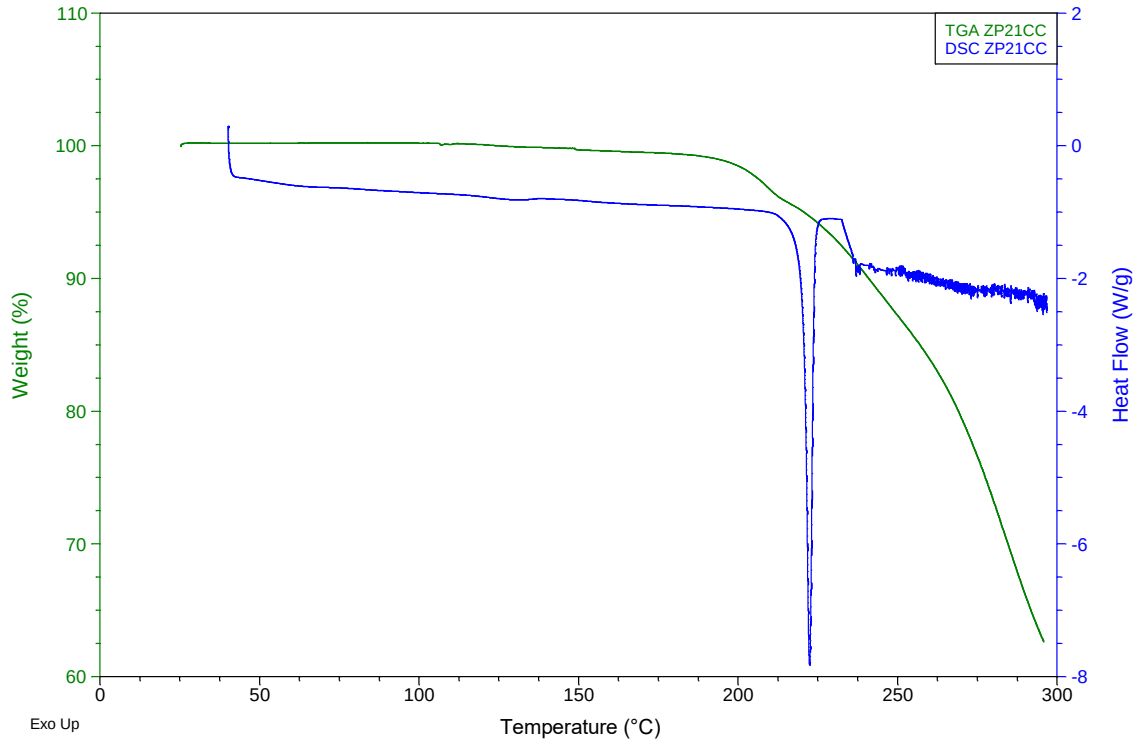


*Figure 2. DSC and TGA overlay plot for the produced zafirlukast:piperazine 2:1 co-crystal (ZP21CC).*

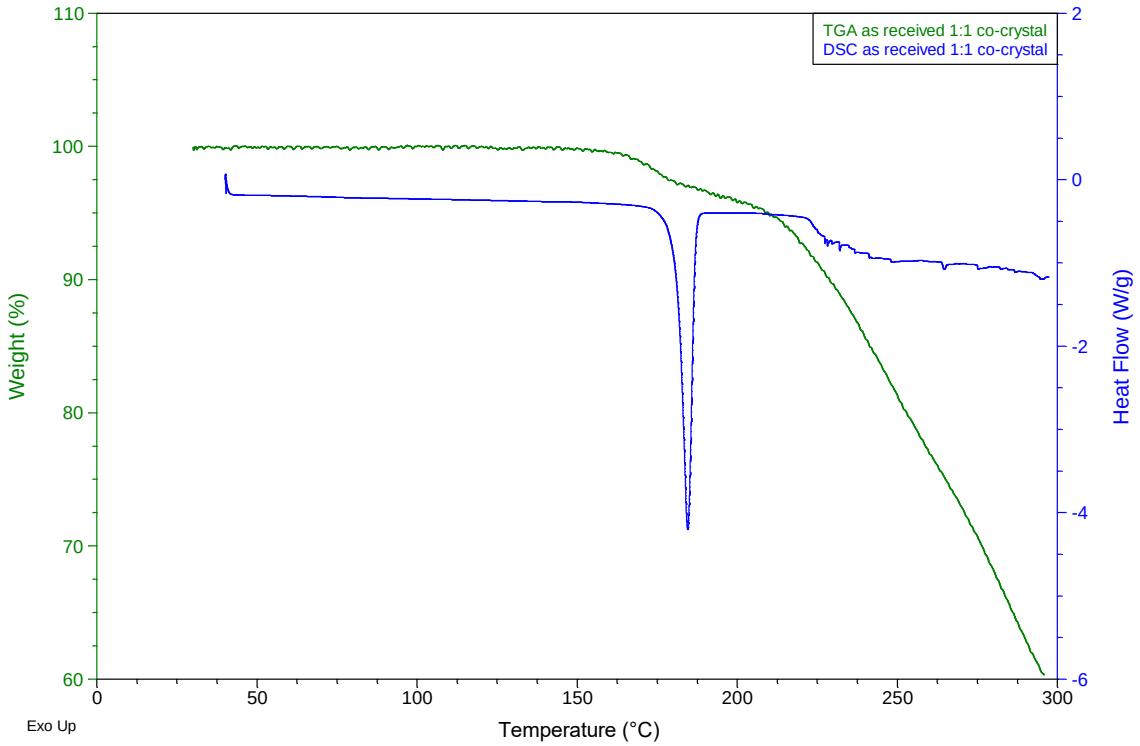


*Figure 3. DSC and TGA overlay plot for the received zafirlukast:piperazine 1:1 co-crystal.*

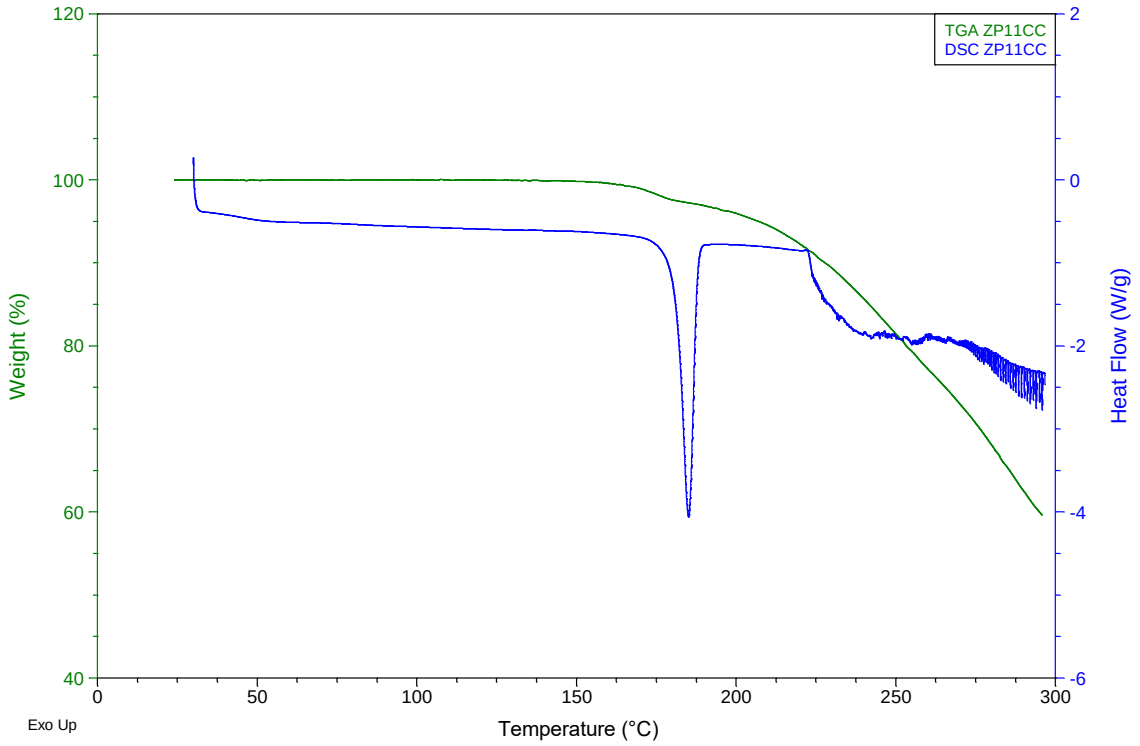


*Figure 4. DSC and TGA overlay plot for the produced zafirlukast:piperazine 1:1 co-crystal (ZP11CC).*

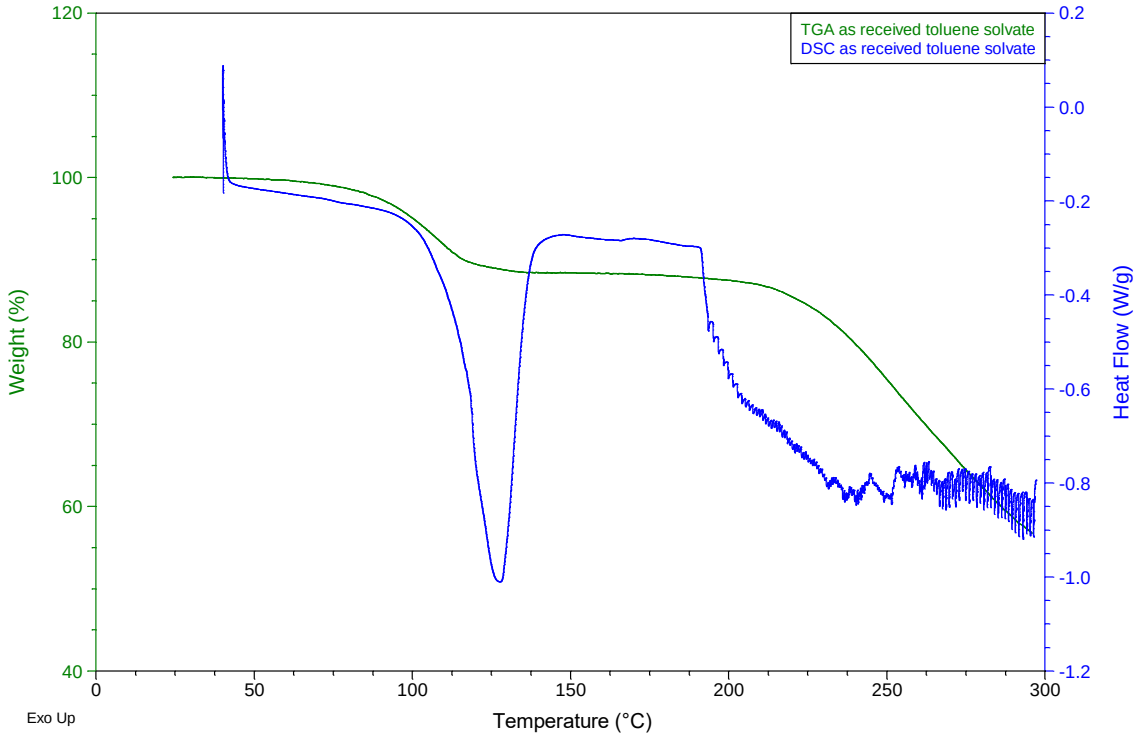


*Figure 5. DSC and TGA overlay plot for the received zafirlukast:piperazine 1:1 co-crystal toluene solvate.*

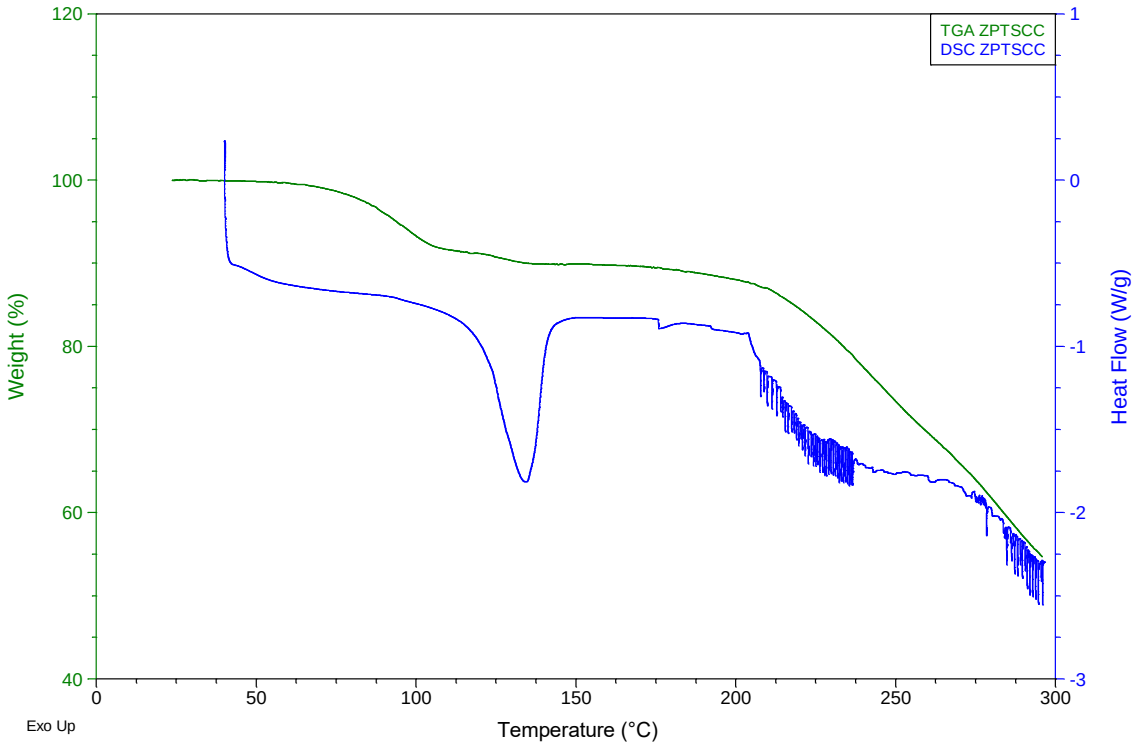


*Figure 6. DSC and TGA overlay plot for the produced zafirlukast:piperazine 1:1 co-crystal toluene solvate (ZPTSCC).*

## 7.3 Calibration curve for HPLC analysis

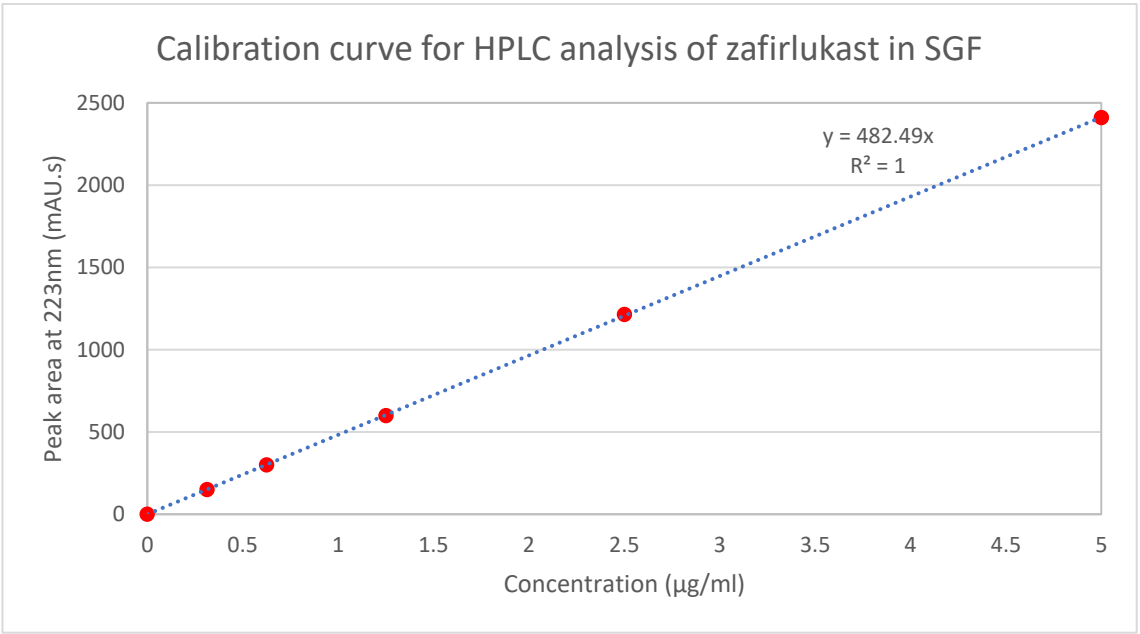


*Figure 7. Calibration curve for the HPLC analysis of zafirlukast in SGF at 223nm.*

7.4 Calibration curves for intrinsic dissolution testing

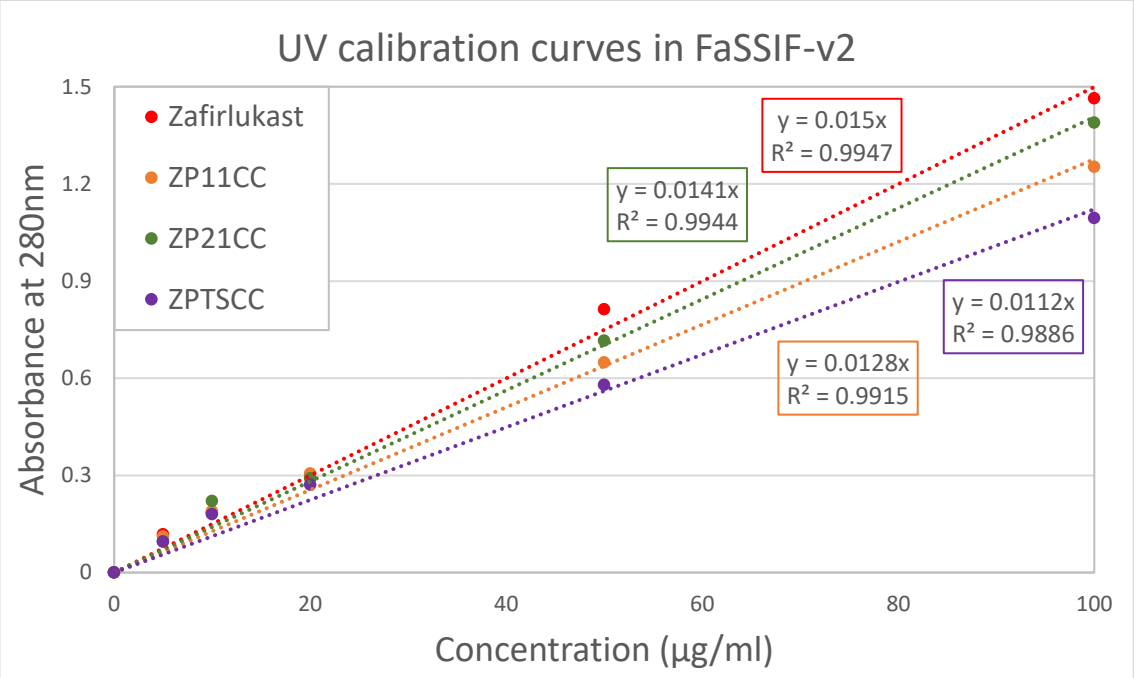


*Figure 8. Calibration curves for the intrinsic dissolution testing of zafirlukast and the three zafirlukast:piperazine co-crystals in FaSSIF-v2 at 280nm*

*Table 1. Molar extinction coefficients determined from UV calibration curves.*

| Material | Molar extinction coefficient ($M^{-1}cm^{-1}$) |
|---|---|
| Zafirlukast | 8630.2 |
| ZP11CC | 8446.3 |
| ZP21CC | 8702.2 |
| ZPTSCC | 8111.9 |

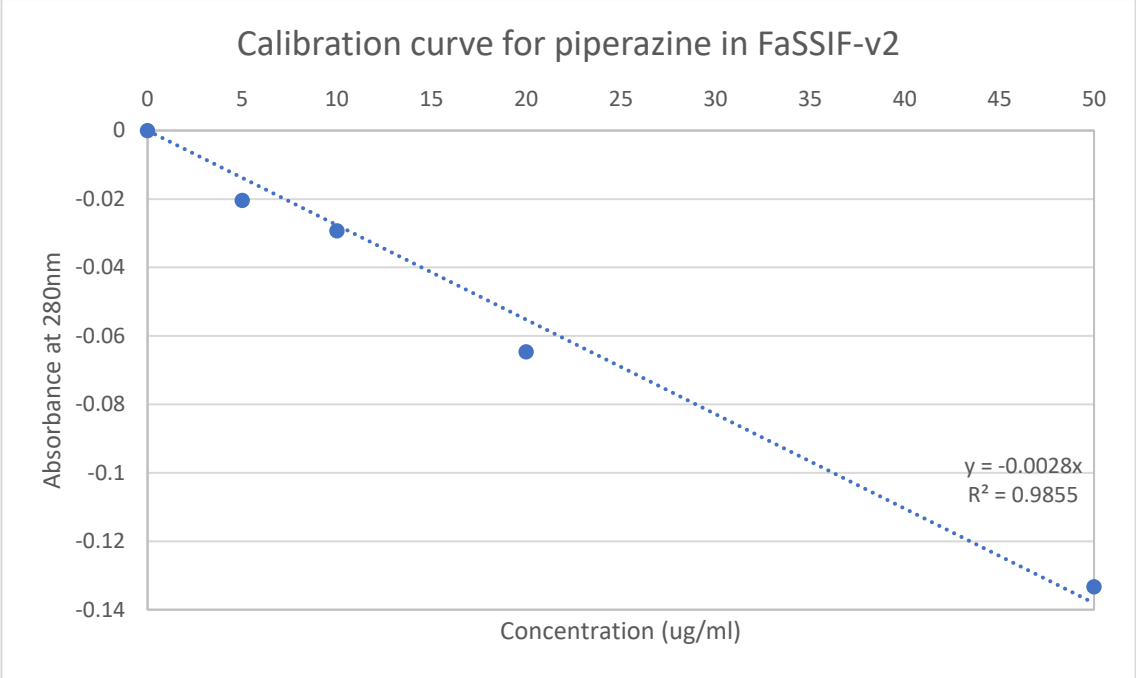


*Figure 9. Calibration curve for piperazine in FaSSIF-v2 at 280nm.*

7.5 Method details for *in* vivo study

The pharmacokinetic parameters of zafirlukast cocrystals (ZP11CC, ZP21CC and ZPTSCC) were compared to those of pure Zafirlukast following oral administration with capsule and intravenously to male Wistar Han Rats (7-9 weeks, approx. 200-300 g). Pure zafirlukast and the cocrystals were encapsulated and orally administered at 5 mg/Kg (with equivalent amounts of pure zafirlukast corrected for each cocrystal stoichiometry). The final number of moles of 1 was 2.171 µmoles in all capsules. The Zaf:Pip:Tol cocrystal dose was calculated based on a 3:3.2 stoichiometry, as suggested by NMR and solid characterisation. Each form was first mixed in a 1:9 ratio with lactose to decrease the error by weight (Granulac 70 for zafirlukast, ZP11CC and ZP21CC and Sorbolac 400 for ZPTSCC). Zafirlukast, ZP11CC and ZP21CC were milled and sieved to achieve same PSD. It was observed that ZPTSCC changed form after the milling, so a different procedure was used; as described in the section on capsule production. The final doses were all within 1.3% of the aimed dose.

IV formulation of zafirlukast: Appropriate weight of zafirlukast was weighed and dissolved into the required volume of vehicle with vortex and sonication applied to reach the target concentration. The vehicle was composed of 5% DMSO, 95% SBE-B-CD (30% w/v in water). This solution was pH adjusted with 1M HCl and 1M NaOH, to the final pH of 7.5. This IV bolus was filtered before administration with formulations stirred at room temperature for at least 2 minutes before dosing. The final measured dose was 1.08 and 1.15 mg/Kg respectively for the two animals. Animals were administered the IV bolus via tail vein. Blood samples (0.2 mL) were collected from the jugular vein at the following intervals: Pre-dose, 2, 5, 10, 30 min, 1, 2, 4, 8, 24 hours post dose.

PO formulations (zafirlukast, ZP11CC, ZP21CC and ZPTSCC): Animals were administered a capsule orally via a dosing needle (Torpac, capsule size 9). Blood samples (0.2 mL) were collected from Jugular vein at the following time intervals: Pre-dose, 15, 30 min, 1, 1.5, 2, 3, 4, 8, 24 hours after oral dosing. Each sample was transferred into plastic micro centrifuge tubes containing K2-EDTA and placed on wet ice prior to centrifugation for plasma. Blood samples were centrifuged at 10000 rpm for 2 min. at 4ºC to obtain plasma. Samples were stored in a freezer at -75±15 ºC prior to analysis. Plasma samples were analysed by an LC-MS/MS method. Pharmacokinetic calculations were performed using WinNonlin (PhoenixTM, version 6.1)

7.6 Plasma concentration plots from the *in vivo* study data

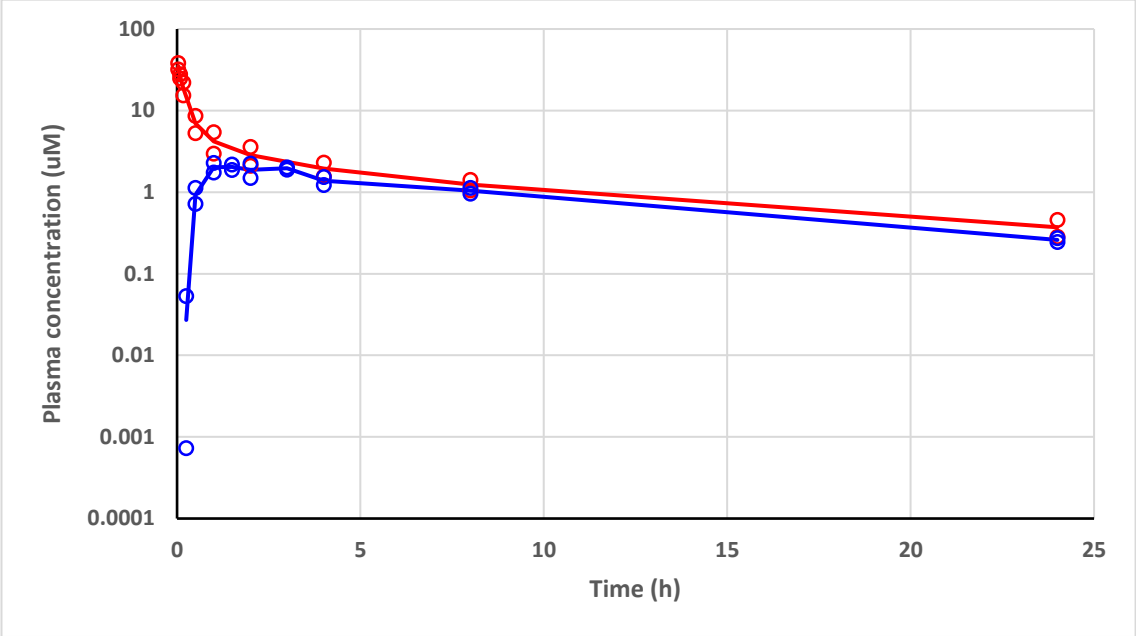


*Figure 10. Plasma concentration of zafirlukast over time plot for orally dosed pure zafirlukast (5mg/Kg, blue) vs IV zafirlukast (1mg/Kg, red) in male Wistar Han rats.*

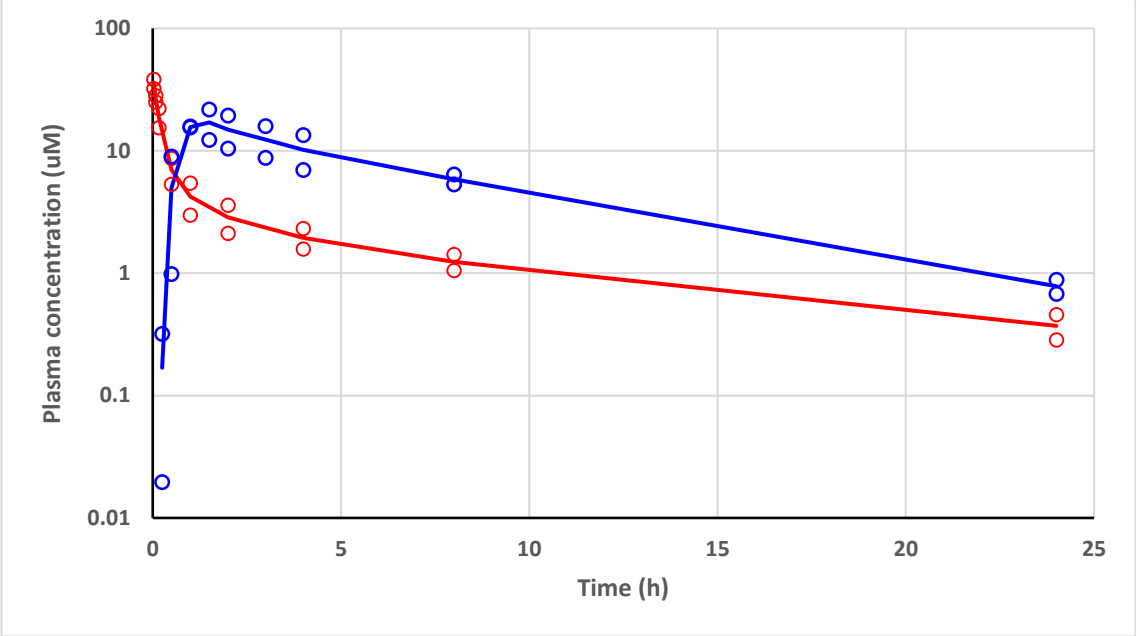


*Figure 11. Plasma concentration of zafirlukast over time plot for orally dosed zafirlukast:piperazine 1:1 co-crystal (5mg/Kg, blue) vs IV zafirlukast (1mg/Kg, red) in male Wistar Han rats.*

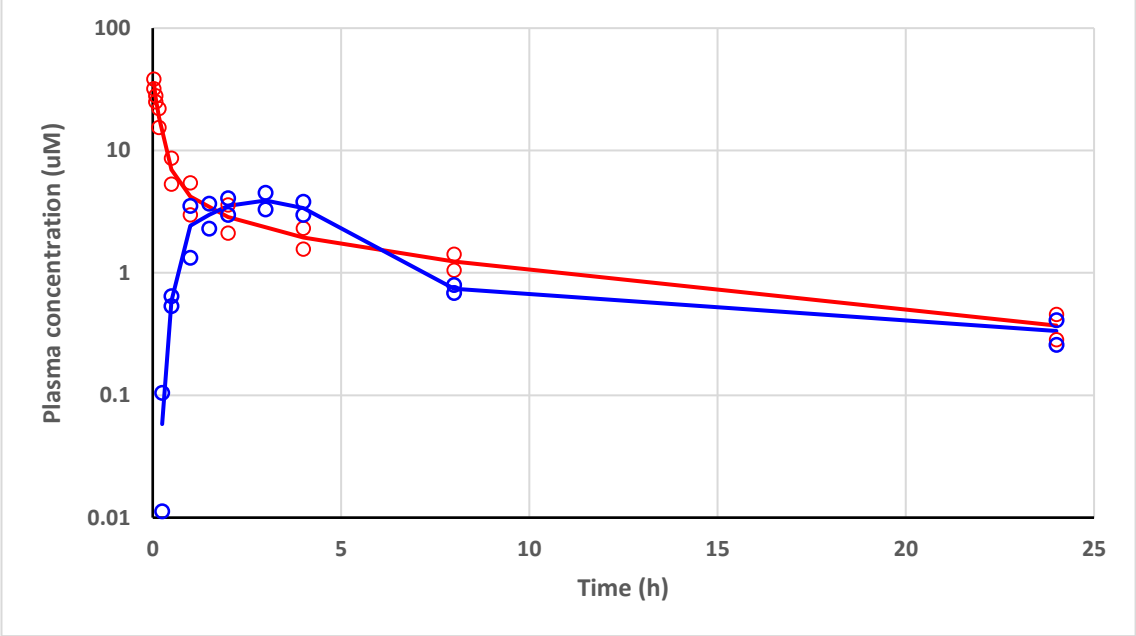


*Figure 12. Plasma concentration of zafirlukast over time plot for orally dosed zafirlukast:piperazine 2:1 co-crystal (5mg/Kg, blue) vs IV zafirlukast (1mg/Kg, red) in male Wistar Han rats.*

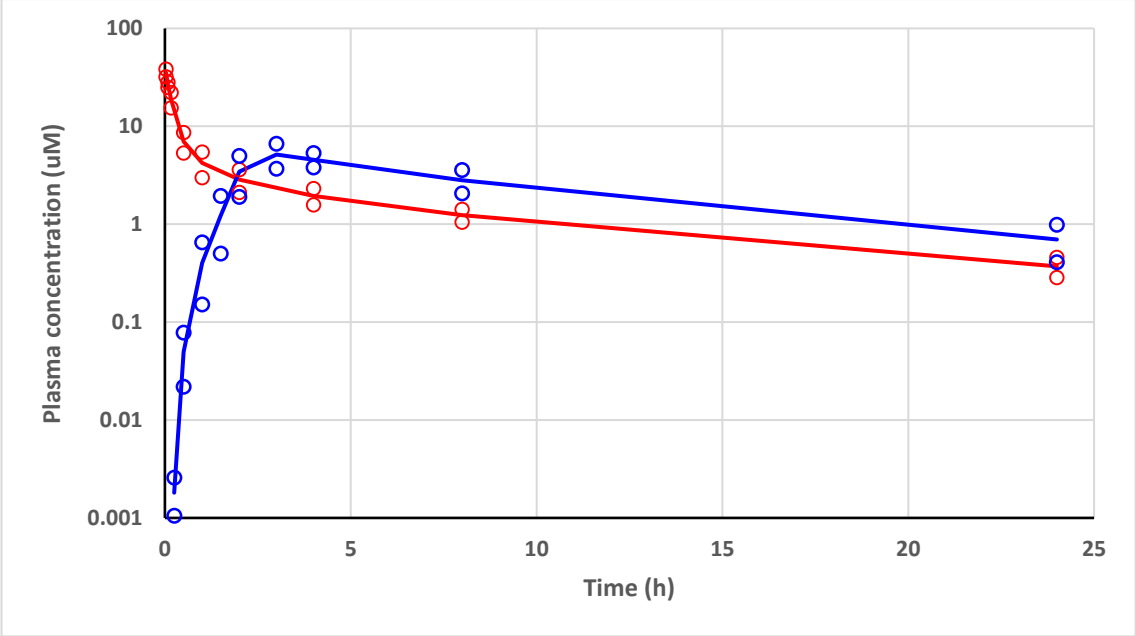


*Figure 13. Plasma concentration of zafirlukast over time plot for orally dosed zafirlukast:piperazine co-crystal toluene solvate (3:3:2) (5mg/Kg, blue) vs IV zafirlukast (1mg/Kg, red) in male Wistar Han rats.*